Investigations of Topological Materials and Thermoelectric Properties of Heavy Metal Chalcogenides

A Thesis

Submitted for the Degree of

Doctor of Philosophy

by

Subhajit Roychowdhury

New Chemistry Unit
Jawaharlal Nehru Centre for Advanced Scientific Research
(A Deemed University)
Bangalore – 560 064, India

May 2019

Dedicated to my parents

DECLARATION

I hereby declare that this thesis entitled "**Investigations of Topological Materials and Thermoelectric Properties of Heavy Metal Chalcogenides**" is a result of studies carried out by me at the New Chemistry Unit, Jawaharlal Nehru Centre for Advanced Scientific Research, Bangalore, India, under the supervision of Prof. Kanishka Biswas. This work has not been submitted elsewhere for the award of any degree or diploma.

In keeping with the general practices of reporting scientific observations, due acknowledgements have been made wherever the work described is based on the findings of other investigators in a collaborative pursuit. Any omission which might have occurred by oversight or error in judgment is regretted.

Bangalore, India

Subhajit Roychowdhury

CERTIFICATE

I hereby certify that the work described in this thesis titled "**Investigations of Topological Materials and Thermoelectric Properties of Heavy Metal Chalcogenides**" has been carried out by Mr. Subhajit Roychowdhury at New Chemistry Unit, Jawaharlal Nehru Centre for Advanced Scientific Research, Bangalore, India under my supervision and that it has not been submitted elsewhere for the award of any degree or diploma.

Bangalore, India

Prof. Kanishka Biswas
(Research Supervisor)

ACKNOWLEDGEMENTS

Completion of my Ph.D. thesis necessitated a lot of guidance and supports from many people. I take this opportunity to mention a few of them. However, my sincere thanks extend to everyone who has played a role in making this dream a reality.

Firstly, I would like to thank my research supervisor, Prof. Kanishka Biswas for suggesting me research problems and guiding me throughout. His valuable instructions and comments in scientific communications have helped me immensely. I express my hearty gratitude to him for giving me an opportunity to work under his guidance.

I would like to thank Bharat Ratna Prof. C. N. R. Rao, FRS, the chairman of New Chemistry Unit (NCU) for his generous support and encouragement throughout my stay in JNCASR. His presence has given me immense inspiration to indulge in active research. I also thank him for providing the infrastructure and facilities to carry out my research work.

I would like to thank Prof. Umesh V. Waghmare, Prof. Swapan K. Pati, Prof. Ranjan Datta, Prof. A. Sundaresan, Prof. A. K. Sood, Prof. Goutam Sheet, Prof. Chandrabhas Narayana, Prof. Dirtha Sanyal, Dr. Sandhya, Raagya, Dr. Jaysree, Rajaji, Dr. Devendra, Dr. Somnath, and Raju for the fruitful scientific collaborations and all the insightful discussions. I have learnt a lot whenever we had meeting or discussion with them.

I am thankful to all my course instructors: Prof. Kanishka Biswas, Prof. A. Sundaresan, Prof. Ranjani Viswanatha, Prof. T. Govindraju, Prof. Sebastian C. Peter, Prof. Subi J. George, Prof. Tapas K. Maji, and Prof. Chandrabhas Narayana, whose courses have been extremely helpful.

I thank all my beloved labmates: Dr. Guin, Dr. Chatterjee, Dr. Jana, Dr. Ghosh, Dr. Shidaling, Dr. P. Chithaiah, Dr. Pal, Dr. Perumal, Dr. Kundu, Dr. Banik, Manisha, Ekashmi, Moinak, Arka, Sujoy, Sushmita, Paribesh, Krishnendu, Debattam, Riddhimoy and Shubhajit for their cheerful company and help in various occasions.

I thank Dr. Somnath Ghara and Mr. Premakumar for their help during Hall measurement, low temperature heat capacity and resistivity measurements and Dr. Rajasekhar (IISc.) for various fruitful discussions. I thank Usha for her help during TEM sample preparation.

I would like to thank all the funding agencies like *CSIR*, *JNCASR*, *DST* and *Synchrotron facilities at DESY-Germany and PF-KEK, Japan*. Without their support, it would have never been possible to conduct research.

Constant assistance and a friendly nature of the technical staff helped me doing my experiments smoothly. Here, I would like to acknowledge Mrs. Usha, Mr. Vasu, Mr.

Anil, Ms. Selvi, Dr. Jay Ghatak, Mr. Mahesh, Mr. Shiva, Mr. Kanan, Mr. N. Kishore, Mr. M. Gowda, Mr. Dileep, Mr. Peer, Mr. Srinivas and others. I am thankful to all the academic, administrative, technical, security, complab and health center staffs for making our campus life smooth and easy.

I express my deep gratitude to all my high school and undergraduate teachers for training me to be disciplined, the basics of science and for growing my interest in research field.

I thank all of my colleagues, juniors and friends in JNCASR.

I have been benefited a lot from my JNC friends. Their help and advice made my academic and non-academic life a memorable and comfortable one here at JNC. I am thankful to all of them. A special thanks to *Rashmi, Manoj, Sudip, Anaranya, Raktim, Arindom, Malabika, Anindita, Ria, Badri, Swastika and Rana* for all the moments I spent with them and also for supporting me any time I required.

Lastly, I would like to acknowledge the most important people of my life, my parents and family. Without their unconditional love and support all my efforts would have gone to vain. I am grateful to you all for whatever you gave me and I dedicate my thesis to you.

PREFACE

Metal chalcogenides constitute one of the most important classes of materials with a rich structural diversity on par with oxides and a plethora of significant properties and applications. This Ph. D. thesis presents the topological materials and thermoelectric properties of heavy metal chalcogenides. I have divided my thesis into five parts.

Part 1 provides a brief introduction to the chemistry of metal chalcogenides covering brief summary of topological materials, thermoelectrics, synthesis, detailed characterizations and measurement techniques.

Part 2 is divided in four chapters. **Chapter 1 and Chapter 2** demonstrate chemical doping (p-type and n-type) in topological crystalline insulator, $Pb_{0.60}Sn_{0.40}Te$ that locally breaks the crystal symmetry and opens up a bulk electronic band gap, which is useful for thermoelectrics. **Chapter 3** reports the large positive non-saturating linear magnetoresistance in topological crystalline insulator, $Pb_{0.60}Sn_{0.40}Te$, at different temperatures between 3 K and 300 K in magnetic field up to 9 T. Magnetoresistance value as high as ~ 200 % was achieved at 3 K at magnetic field of 9 T. In **chapter 4**, I have investigated the intrinsic origin of observed ultralow lattice thermal conductivity (ca. 0.8 W/m.K at 300 K) of *n*-type topological insulator, $TlBiSe_2$ with the help of synchrotron X-ray pair distribution function (PDF) analysis and low-temperature specific heat capacity.

Part 3 is divided in two chapters. In **chapter 1**, I have discussed about the effect of aliovalent cation (Sb and Bi) doping in GeTe which decreases the carrier concentration and enhances the valence band degeneracy by increasing the cubic nature of the sample, which collectively boost Seebeck coefficient of GeTe. Significant thermal conductivity reduction was also achieved due to collective phonon scattering from various meso-structured domain variants, twin and inversion boundaries, nano-structured defect layers, and solid solution point defects. As a result, we have achieved a maximum figure of merit, zT, of ~ 1.85 for $Ge_{0.90}Sb_{0.10}Te$ at 725 K.

Thermoelectric device or module demands both p- and n-type materials. Though there are significant advances of thermoelectric performance of p-type Ge-based chalcogenides, hardly any n-type Ge-based chalcogenide is known hitherto. In **chapter 2**, we have stabilized high temperature and high-pressure rocksalt phase of GeSe at

ambient conditions by alloying with $AgBiSe_2$. Importantly, we also found that cubic $(GeSe)_{1-x}(AgBiSe_2)_x$ exhibits n-type conduction in the measured temperature range, which is rare in Ge-chalcogenide based thermoelectrics.

Part 4 is divided in two chapters. **Chapter 1** presents the high thermoelectric performance in SnTe achieved through two-step design, (a) reduction in lattice thermal conductivity via solid solution alloying and (b) enhancement of Seebeck coefficient (*S*) via modification of electronic structure through co-doping. First, we have demonstrated that introduction of Pb in position of Sn in SnTe decreases the excess p-type carrier concentration in SnTe. $Sn_{0.70}Pb_{0.30}Te$ sample exhibits a κ_{latt} value of ~ 0.67 W/mK at 300 K, which is close to the theoretical minimum limit of the κ_{latt} in SnTe. Secondly, we have achieved S of 121 μV/K at 300 K, which increases to ~ 241 μV/K at 710 K for In and Mg co-doped $Sn_{0.70}Pb_{0.30}Te$ where indium and magnesium act as a resonant dopant and valence band convergent, respectively. **Chapter 2** reports amorphous limit in thermal conductivity (κ_{min} ~ 0.5 W/mK) and high thermoelectric performance (zT_{max} ~1.3 at 854 K) in Ag and In codoped $(SnTe)_{1-2x}(SnSe)_x(SnS)_x$ system *via* three-step approach. Se and S substitution in SnTe increases the configurational entropy of the pseudo-ternary system, $(SnTe)_{1-2x}(SnSe)_x(SnS)_x$. S atoms are off-centered in $(SnTe)_{1-2x}(SnSe)_x(SnS)_x$ lattice which is further confirmed by synchrotron X-ray pair distribution function (PDF) analysis, resulting low energy localized optical phonon modes which strongly couples with heat carrying acoustic phonon modes.

Part 5 is divided in two chapters. In **chapter 1**, I have demonstrated an ultralow κ_{latt} of 0.35 W/mK in AgCuTe, which exhibits a remarkable TE figure-of-merit, zT of 1.6 at 670 K when alloyed with 10 mol% Se. I have investigated the intrinsic origin of observed ultralow lattice thermal conductivity (ca. 0.35 W/m.K at 300 K) in AgCuTe by probing the underlying correlation among structure, chemical bonding, and lattice dynamics. The soft phonon modes, dominated by Ag vibrations, soften further with temperature giving a dynamic cation disorder and plausibly driving the superionic transition. **Chapter 2 and 3** report thermoelectric properties of $AgSbTe_2$. $AgSbTe_2$ is considered as promising thermoelectric material for power generation application in the temperature range of 400 – 700 K due to its glass-like anomalously low thermal conductivity (0.6 - 0.7 $Wm^{-1}K^{-1}$). In **chapter 2**, I have shown that the optimum concentration Zn doping act as an effective p-type dopant and substantially increase the electrical conductivity, which resulted in a

large increase in the power factor in $AgSbTe_2$. With superior electronic transport and ultra-low thermal conductivity, high zT value of ~ 1.9 at 585 K was achieved in $AgSb_{0.96}Zn_{0.04}Te_2$. **Chapter 3** reports ultrahigh thermoelectric figure of merit of 2.6 at 573 K in p-type $AgSb_{1-x}M_xTe_2$ *via* simultaneous carrier engineering and reduction of lattice thermal conductivity. Importantly, $AgSb_{1-x}M_xTe_2$ possesses a device thermoelectric figure of merit, ZT_{dev}, value of ~ 2 in the 300 - 600 K range, which is highest value so far for state-of-the-art thermoelectric materials.

TABLE OF CONTENTS

DECLARATION ..... **III**

CERTIFICATE ..... **V**

ACKNOWLEDGEMENTS ..... **VII**

PREFACE ..... **IX**

PART 1: A Brief Introduction to Topological Materials and Thermoelectric Energy Conversion based on Heavy Metal Chalcogenides **1**

Summary... 3

1.1 Introduction to metal chalcogenides 5

1.2 Chalcogenides of p-block heavy elements 8

1.3 Superionic noble metal chalcogenides 11

1.4 Novel properties of heavy metal based chalcogenides 12

1.4.1 Topological Materials 12

1.4.1.1 Topological insulators 15

1.4.1.2 Topological crystalline insulators 18

1.4.2 Thermoelectrics 22

1.4.3 Correlation between topological materials and thermoelectrics 27

1.5 Synthesis and characterizations 28

1.5.1 Synthesis 28

1.5.2 Characterizations 30

1.5.2.1 Powder X-ray diffraction (PXRD) 30

1.5.2.2 X-ray pair distribution function 31

1.5.2.3 Transmission electron microscope (TEM) 33

1.5.2.4 Field emission scanning electron microscope (FESEM) 33

1.5.2.5 Energy dispersive X-ray analysis (EDAX) 34

1.5.2.6 Positron annihilation spectroscopy (PAS) 34

1.5.2.7 Optical band gap 36

1.5.2.8 Differential scanning calorimetry (DSC) 36

1.5.2.9 Hall effect 37

1.6 Thermoelectric measurements 38

1.6.1 Electronic transport 38

1.6.2 Thermal conductivity 40

1.7 Scope of the thesis 42

1.8 References 45

PART 2: Transport Properties of Topological Materials **49**

Chapter 1: Tailoring of Electronic Structure and Thermoelectric Properties of Topological Crystalline Insulator by Chemical Doping **51**

Summary 53
1.1 Introduction 55
1.2 Methods 56
1.3 Results & Discussion 58
1.4 Conclusions 77
1.5 References 78

Chapter 2: Enhanced Thermoelectric Performance in *n*-type $Pb_{0.60}Sn_{0.40}Te$ by Simultaneous Tuning of the Band Gap and Chemical Potential 81
Summary 83
2.1 Introduction 85
2.2 Methods 86
2.3 Results & Discussion 88
2.4 Conclusions 97
2.5 References 98

Chapter 3: Large Linear Magnetoresistance in Topological Crystalline Insulator, $Pb_{0.60}Sn_{0.40}Te$ 99
Summary 101
3.1 Introduction 103
3.2 Methods 105
3.3 Results & Discussion 106
3.4 Conclusions 114
3.5 References 115

Chapter 4: Dual $6s^2$ Lone Pairs Induced Cation Off-centering Leads to Intrinsically Low Thermal Conductivity in *n*-type Topological Insulator, $TlBiSe_2$ 119
Summary 121
4.1 Introduction 123
4.2 Methods 124
4.3 Results & Discussion 126
4.4 Conclusions 135
4.5 References 136

PART 3: Thermoelectric Properties of Germanium Chalcogenides 139

Chapter 1: High Thermoelectric Performance and Enhanced Mechanical Stability of *p*-type Cation Doped GeTe 141
Summary 143
1.1 Introduction 145
1.2 Methods 147
1.3 Results & Discussion 149
1.4 Conclusions 168
1.5 References 170

Chapter 2: Stabilizing *n*-type Cubic GeSe by Entropy-Driven Alloying of $AgBiSe_2$: Ultralow Thermal Conductivity and Promising Thermoelectric Performance 173
Summary 175
2.1 Introduction 177

2.2 Methods 179
2.3 Results & Discussion 182
2.4 Conclusions 197
2.5 References 198

PART 4: Thermoelectric Properties of Tin Chalcogenides 199

Chapter 1: An Enhanced Seebeck Coefficient and High Thermoelectric Performance in *p*-type In and Mg Co-doped $Sn_{1-x}Pb_xTe$ *via* the Co-adjuvant Effect of Resonance Level and Heavy Hole Valence Band 201

Summary 203
1.1 Introduction 205
1.2 Methods 207
1.3 Results & Discussion 209
1.4 Conclusions 224
1.5 References 225

Chapter 2: Entropy Driven Point Defects and S Atoms Off-centering Instability Lead to Ultralow Thermal Conductivity and Enhanced Thermoelectric Performance in $(SnTe)_{1-2x}(SnSe)_x(SnS)_x$ 229

Summary 231
2.1 Introduction 233
2.2 Methods 235
2.3 Results & Discussion 239
2.4 Conclusions 263
2.5 References 264

PART 5: Thermoelectric Properties of Silver Chalcogenides 267

Chapter 1: Soft Phonon Modes Leading to Ultralow Thermal Conductivity and High Thermoelectric Performance in AgCuTe 269

Summary 271
1.1 Introduction 273
1.2 Methods 274
1.3 Results & Discussion 277
1.4 Conclusions 294
1.5 References 295

Chapter 2: High Thermoelectric Figure of Merit and Enhanced Mechanical Stability of *p*-type $AgSb_{1-x}Zn_xTe_2$ 297

Summary 299
2.1 Introduction 301
2.2 Methods 303
2.3 Results & Discussion 305
2.4 Conclusions 314
2.5 References 315

Chapter 3: Ultrahigh Thermoelectric Figure of Merit, zT> 2.5 in Heavily Doped $AgSbTe_2$ 317
Summary... 319
3.1 Introduction..... 321
3.2 Methods 323
3.3 Results & Discussion..... 325
3.4 Conclusions..... 336
3.5 References..... 337

List of Publications 339
Biography..... 341

PART 1

A Brief Introduction to Topological Materials and Thermoelectric Energy Conversion based on Heavy Metal Chalcogenides

Chapter 1

A Brief Introduction to Topological Materials and Thermoelectric Energy Conversion Based on Heavy Metal Chalcogenides[†]

Summary

Thermoelectric materials can convert waste heat into useful electricity, and constitute a viable means of efficient energy management. The discovery of topological insulators with unique metallic surface states has added a new dimension in the field of electronics and spintronics. Following the initial breakthrough, the topologically non-trivial materials have been extended to various categories namely weak topological insulator, topological crystalline insulator, Dirac semimetal and Weyl semimetal. Interestingly, most of the topological materials are also good candidates for thermoelectric energy conversion because both demand similar material features such as heavy constituent elements, narrow band gap, and high spin-orbit coupling. Heavy metal chalcogenides satisfy these criteria and present a nice platform for exploring both thermoelectrics and topological insulation. This chapter highlights a brief introduction to heavy metal chalcogenides followed by the key issues that make heavy metal chalcogenide as a potential candidates in the field of both thermoelectrics and topological materials. Last part of this chapter is focused on a general discussion of metal chalcogenide synthesis, characterizations and thermoelectric measurements.

[†]*A part of this chapter has been published in the form of review article in J. Solid State. Chem.* **2019**, *275, 103.*

1.1 Introduction to metal chalcogenides

Chalcogenides constitute one of the most important classes in the field of chemistry, exhibiting rich compositional and structural diversity on par with oxides and organic compounds. Chalcogenides are compounds that contain at least one chalcogen Q atom (Q = S/ Se/ Te) in a chemically reduced state compared to its elemental form. Chalcogenides bear few chemical resemblances to oxides, but there are also big dissimilarities in chemical character and physical properties among them which are significant enough to warrant a separate treatment of the chalcogenides as a distinct class of materials. These differences must, of course, originate from the differences between the oxygen atom on the one hand and the atoms of S, Se, Te on the other. Some important differences in the atomic properties of oxygen and the chalcogen are:[1]

(a) The chalcogen atoms are larger (and also heavier) than oxygen atoms.
(b) The chalcogens are less electronegative than oxygen.
(c) The chalcogens have d orbitals of accessible energy (3d for S, 4d for Se and 5d for Te), while oxygen has not.

These differences in the atomic properties cause differences in the bonding of metals to S, Se, and Te relative to the metal-to-oxygen bond. Some of these differences are:

(d) The metal-to-chalcogen bonds are more covalent than metal-to-oxygen bonds (consequence of (b)).
(e) The metal-to-chalcogen bonds often involve the d orbitals of the chalcogen, while this is not possible for the bonding to oxygen (consequence of (c)).
(f) The chalcogenides are more polarizable than oxide ions (consequence of (a) and (c)).

One of the most striking differences between oxides and chalcogenides is the facile ability of the chalcogen to form stable Q−Q bonds: catenation. For instance, there are many allotropes of sulfur, owing to the ability of sulfur to form chains of singly-bonded atoms. This catenation is also observed in metal chalcogenides, for example, in pyrite where S-S (S_2^{2-}) units are found. Similarly, selenides and tellurides also exhibit Q-Q bonding as in Se_2^{2-} and Te_2^{2-} units of pyrite-type structures but in contrast with sulfides, they can form solid-state structures that contain Q_n rings or chains with n>2 as

exemplified by Se_5 moiety in Nb_2Se_9[2] and Te_6 group in $Re_6Te_{16}Cl_6$[3]. In general, as we move from sulfides to selenides to tellurides, the degree of covalent bonding, delocalization of electrons and metallic behaviour increase, and the importance of long range Q-Q interactions (*i.e.*, less than single bond) increases.[4] Te-Te single bonds are ca. 275 pm in length, but in a large number of telluride compounds, Te-Te bonds with distances intermediate between single bonds and van der Waals interactions (ca. 420 pm) exist. These bonds are energetically weak but are structurally important; they also manifest as Te…Te interlayer interactions that essentially stabilize the structures of layered tellurides such as $TaIrTe_4$ and $NbIrTe_4$.[5]

Besides, catenation can produce stable complex polychalcogenide anions (Q_x^{2-}, where x is up to 7 or 8). These anions serve as reactive building blocks for molecules and solid-state materials. Chalcogenides are similar to oxides in that there are as many chalcoanions, particularly with the main-group and early-transition metal atoms (e.g. $[PS_4]^{3-}$, $[P_2S_7]^{4-}$, $[SiS_4]^{4-}$, $[GeS_4]^{4-}$, $[MoS_4]^{2-}$, $[VS_4]^{3-}$ etc.), as there are oxyanions (e.g. $[PO_4]^{3-}$, $[P_2O_7]^{4-}$, $[SiO_4]^{4-}$, $[Si_2O_7]^{6-}$, $[MoO_4]^{2-}$, $[VO_4]^{3-}$ etc.). In fact, chalcogens can form many other chalcoanions which do not have analogous oxyanions, few examples being $[P_2Se_6]^{4-}$, $[P_3Se_7]^{3-}$, $[P_2Se_8]^{2-}$, $[P_8Se_{18}]^{6-}$, $[GeS_4]^{4-}$, $[GeSe_5]^{4-}$, $[Ge_2Se_6]^{6-}$ etc.[6-8]

Metal oxides are usually ionic in character, and they resemble fluorides more than they do chalcogenides. For instance, dioxides such as VO_2, CrO_2, and MnO_2 crystallize in a rutile-type (TiO_2) structure similar to the corresponding fluorides *viz.* VF_2, CrF_2 and MnF_2. On the other hand, while VS_2 and CrS_2 are not known, MnS_2 has a pyrite-type structure characterized by S_2^{2-} units, which is rarely found in oxides. Similarly, $MnSe_2$ and $MnTe_2$ also crystallize in pyrite-type structures. It is noteworthy that although Mn metal atoms have octahedral coordination in both MnO_2 and MnQ_2, the overall structures are significantly different. Besides, layered structures are very common among metal dichalcogenides but seldom found among oxides. The structures of most oxides are well represented by models that treat atoms as hard, charged spheres with ionic radii specific to a given element. The constant-radius approximation is, however, not accurate for metal chalcogenides because of their more covalent character.[4] Some of the important distinctions between metal oxides and metal chalcogenides are summarized in table 1.1

Table 1.1: Some important distinctions between metal oxides and metal chalcogenides.

Feature	Oxides	Chalcogenides
Close packing	Usually	Sometimes
Octahedral/tetrahedral metal-coordination	Yes	Usually
Trigonal prismatic metal-coordination	Very rarely	Groups 5 and 6
Layered structures	Rarely	Usually
Q-Q bonds	Peroxides	Common
Bonding	Ionic	Covalent

Metal chalcogenides are central to many important technologies. They exhibit a broad range of chemical and physical properties associated with diverse scientific phenomena and enable a plethora of applications.[9-16] For example, CdTe and $CuInSe_2$ are high-performing materials for thin-film solar photovoltaics; PbTe, GeTe and $Bi_2Te_{3-x}Se_x$ are the champion thermoelectric materials; Co(Ni)/Mo/S composites are the best available catalysts for hydro-desulphurization of crude oil; $Ge_2Sb_2Te_5$ is a high density memory material; CdHgTe is the key infrared detector material in night-vision cameras etc.

Metal chalcogenides are at the cutting edge of many research areas. Some examples include nonlinear optics,[17] optical information storage,[18] photovoltaic energy conversion,[19] thermoelectric energy conversion,[14,20,21] radiation detectors,[22] thin-film electronics,[23] spintronics,[24] fast-ion conductivity,[25] rechargeable batteries,[26] catalysis,[27] novel magnetism,[28] unconventional superconductivity[29] and science in two dimensions.[15,30] In the recent times, the scientific community has witnessed sensational discoveries pertinent to metal chalcogenides such as quantum spin Hall Effect,[31] topological insulators,[32-35] topological crystalline insulators,[36-37] non-saturating magnetoresistance[38] and many others which will have huge implications, especially in the fields of spintronics and (Opto) electronics. We are currently in the midst of an impressive expansion in solid-state chalcogenide chemistry with emphasis on the synthesis of materials with new compositions and structures on the one hand, and exploration of their novel properties on the other. Most of the aforementioned

applications and phenomena are associated with chalcogenides of transition metals and main group p-block metals. The following sections will brief structural aspects and novel properties pertinent to these metal chalcogenides along with some relevant basics at the end to provide a background to my thesis work.

1.2 Chalcogenides of p-block heavy elements

The p-block metal chalcogenides exhibit rich structural diversity. Wurtzite and zinc blende structures are prevalent in quasi-binary III_2-VI_3 metal chalcogenides. Anisotropic layered structures are also found in III-VI compounds with covalently bonded layers stacked via weak van der Waals interactions. For instance, GaQ (Q = S, Se, Te) and InSe are all found in layered structures stabilized by cation-cation bonds. InTe, TlS and TlSe crystallize in a tetragonal TlSe-type structure [i.e., $Tl^{1+}Tl^{3+}(Se^{2-})_2$] with monovalent and trivalent cations, characterized by anionic and cationic substructures similar to Zintl compounds.

Among IV-VI metal chalcogenides, GeQ and SnQ (Q = S, Se) exhibit orthorhombic puckered layered structure similar to black phosphorous, which can be derived from three-dimensional distortion of the rock salt (NaCl) structures. GeTe and SnTe have rocksalt (NaCl) structures with slight deformations due to phase transitions. The high-temperature phase shows the perfect NaCl-structure, stable above 670 K and 100 K for GeTe and SnTe, respectively. SnQ_2 (Q = S and Se) crystallizes in layered CdI_2-type structure. PbQ (Q = S, Se, Te) crystallizes in cubic rock-salt structure.

Among group V-VI chalcogenides, Sb_2S_3, Sb_2Se_3 and Bi_2S_3 have orthorhombic Sb_2S_3-type stibnite structure with one-dimensional connectivity. Sb_2Te_3, Bi_2Se_3 and Bi_2Te_3 are found in rhombohedral layered structures comprised of covalently bonded Q-M-Q-M-Q (M = Sb/Bi; Q = Se/Te) quintuple layers stacked via weak van der Waals interactions along the c-axis.

It is interesting to note the effect of cation lone pair on the structural stability of group 13-15 metal chalcogenides. The valence ns^2 lone pairs on the cations in these compounds play a key role in their structural, chemical and electronic properties.

For example, as the metal becomes heavier on going down the group 13, the lone pair becomes increasingly stable in the order: $Ga^{+} < In^{+} < Tl^{+}$ and the same applies to groups 14 and 15 where the Pb^{2+} and Bi^{3+} cations possess stable lone pairs. The large stability of ns^2 lone pairs in the heavier elements of the main group is ascribed to relativistic effects that contract the s-orbital and bring it closer to the nucleus thereby lowering its energy level.

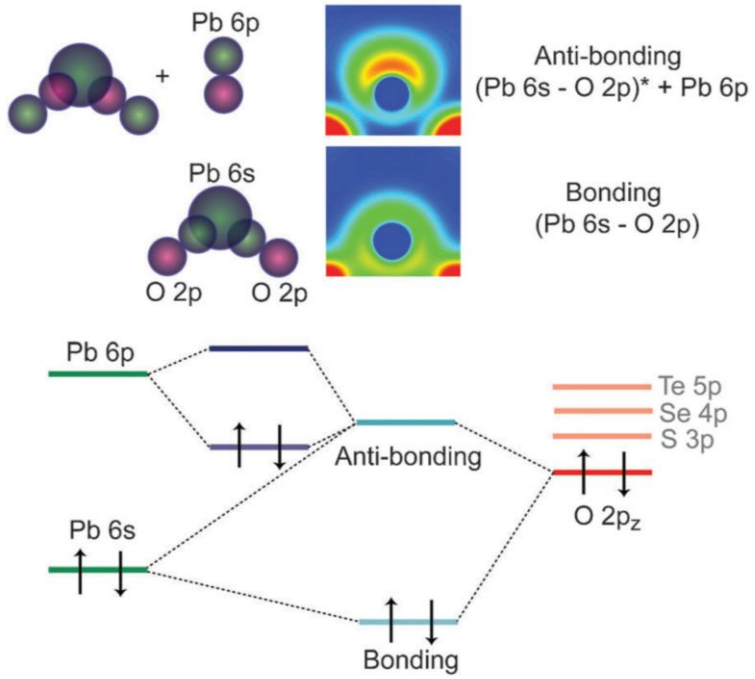

Figure 1.1 *Illustration of orbital interactions leading to stereochemical active lone pair in PbO (upper panel) and the corresponding energy level diagram (lower panel). The cation s and anion p orbital-interaction leads to formation of bonding and antibonding states which appear at the bottom and top of the upper valence band, respectively. The empty cation p states then interact with the filled antibonding state, resulting in stabilization of the cation ns^2 electrons. This interaction becomes symmetry-allowed by lattice distortion accompanied by an asymmetric electron density that is projected into the structural void. Reproduced with permission from ref. 40 © 2011 RSC.*

The cation ns^2 lone pair behaves in different ways depending on the local coordination environment as well as the metal and chalcogen atoms involved.[39,40] It can either express stereochemically by occupying a distinct space around the metal atom or effectively remain 'quenched'. When expressed stereochemically, the ns^2 lone pair can

cause lattice distortion accompanied by lowering of ns^2 energy level. The formation of a stereochemically active lone pair (distortion) depends on the strength of interaction between cation s-states and the anion p-states; the stronger the interaction, the more contribution of cation s-states to the upper valence band (Figure 1.1). Down the group 16, the p-orbital energies increase on going from O to Te. As mentioned above, cation ns^2 energy decreases down the groups 13-15. Therefore, PbO exhibits low symmetry litharge structure (distorted rocksalt structure) with stereochemically active ns^2 lone pairs whereas PbQ (Q = S, Se, Te) occurs in the symmetric rocksalt structure. Similar arguments hold true for orthorhombic Sb_2S_3, Sb_2Se_3 and Bi_2S_3 versus rhombohedral Bi_2Se_3 and Bi_2Te_3, orthorhombic SnSe versus cubic SnTe, and rhombohedral GeTe versus cubic SnTe and PbTe. As the stereochemical expression stabilizes the ns^2 pair which lies above or near the highest occupied state, the energy band gaps are usually higher in the low-symmetry structures relative to symmetric structures.[41] In the latter, the 'quenched' cationic lone pair may experience repulsion from the surrounding anions unlike the former where the structural distortion relieves this repulsion. The structural strain associated with the lone pair repulsion can result in highly anharmonic phonons as in the case of PbTe, Bi_2Se_3 causing low lattice thermal conductivity.[39] It is also worth noting that in PbTe, the stereochemical expression of ns^2 lone pair increases with temperature, a phenomenon dubbed 'emphanisis'.[42] As a consequence, off-centering of Pb atoms occurs from their ideal octahedral sites at high temperatures.

I-V-VI_2 (where I = Cu, Ag, Au or alkali metal; V = As, Sb, Bi; and VI = S, Se, Te) type of compounds are a special class of semiconductors which are renowned for their intrinsically low thermal conductivity due to the strong anharmonicity of their bonding arrangements.[39,43] Some of the members of this class crystallize in cation disordered high symmetry cubic rock salt structure at room temperature (eg. $AgSbSe_2$, $AgSbTe_2$, $NaBiTe_2$, $NaBiSe_2$, $NaSbSe_2$, $NaSbTe_2$ etc).[39,44] However, few of the members show structural phase transitions as a function of temperature ($AgBiS_2$, $AgBiSe_2$, $AgBiTe_2$, etc) and finally transform to cation disordered rock salt cubic structure at high temperatures.[44] Presence of stereochemically active ns^2 lone pair on group V (Sb/Bi) element and disorder cation sublattice results strong anharmonicity in bonding arrangements which gives rise to low thermal

conductivity. I have studied the thermoelectric properties of $AgSbTe_2$ in **chapter 2 and 3 (part 5)** due to their favourable electronic structure and glass like thermal conductivity.

The structural and electronic links to the observed low thermal conductivity and high thermoelectric performance in Ge based and Sn based chalcogenides are investigated in **part 3** and **part 4**, respectively in my thesis.

1.3 Superionic noble metal chalcogenides

Superionic conductors are exciting materials that show unique solid liquid hybrid behaviour. They allow the macroscopic movement of ions through their structure, leading to exceptionally high values (liquid-like) of ionic conductivity in the solid state.[45] The superionic transition normally happens above a critical temperature (mostly at elevated temperature). These materials are generally made of weakly coupled cationic and anionic substructure in which one type constituent species form rigid framework, whereas another type constituent species occupies interstices.[46] At elevated temperature *i.e* above superinoic transition temperature, the rigid framework expands and frequently acquires a new symmetry, and allows the rapid diffusion of a significant fraction of the other constituent species within the rigid framework.[45] Superionic materials has been classified in three different types depending on how the superionicity arises: (a) Type I: superionicity arises due to a first-order structural phase transition (b) Type II: High ionic conductivity arises due to a gradual and continuous disordering process within the same phase (c) Type III: superionicity arises not due to clear phase transition, but via increased mobility of a number of thermally activated defects.[47]

Superionic materials are those that conduct metal ions with an ionic conductivity between 0.1 and 1 S cm^{-1} above a material-dependent transition temperature. Some examples are Ag_4RbI_5, AgI, and $Cu_4RbCl_3I_2$.[48] The superionic noble metal chalcogenides are materials that conduct noble metals (Ag^+, Cu^+) in a fixed lattice of chalcogen atoms (S, Se, or Te), as shown in Figure 1.2. These materials have high enough charge carrier mobility to be considered for use as thermoelectrics, unlike the superionic conductors listed above. Superionic noble metal chalcogenides ensure a low lattice thermal

conductivity; the research on them in this thesis focuses on understanding and optimizing their electronic transport properties. These materials are always present with an excess or a deficiency of metal ions.

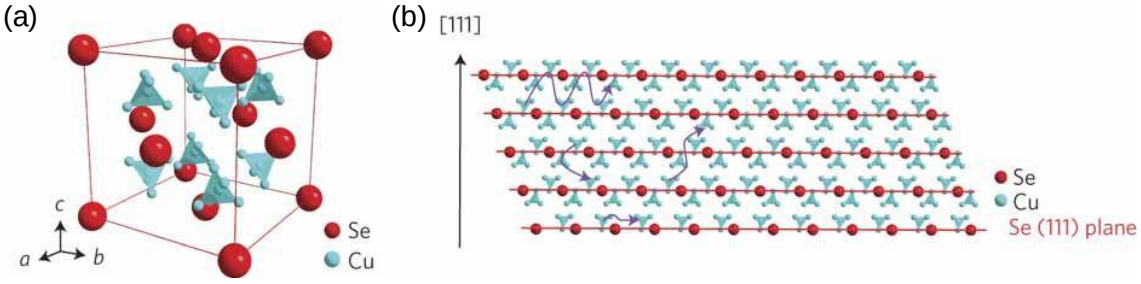

Figure 1.2 *(a) Crystal structure of cubic Cu_2Se where where only the 8c and 32f interstitial positions are shown with Cu atoms. (b) Projected plane representation of the crystal structure along the cubic [1$\bar{1}$0] direction. The arrows indicate that the Cu ions can freely travel among the interstitial sites. There are two Cu layers between the neighbouring Se (111) planes. The structure changes to a monoclinic α-phase by stacking the ordered Cu ions along the cubic [111] direction when cooled to room temperature. Reproduced with permission from ref. 51 © 2012, Springer Nature.*

Some examples of superionic thermoelectrics are $AgCrSe_2$, reported to reach a zT of 1 at 773 K,[49] Ag_2Se, reported to reach a zT of 1 at 300 K,[50] Cu_2Se, reported to reach a zT of 1.5 at 1000 K,[51] and Cu-vacancy doped $Cu_{2-x}S$ ($0 \leq x \leq 0.03$), reported to reach a zT of 1.7 at 1000 K[52] and AgCuSe, reported to reach a zT of ~ 0.7 at 450 K[53]. The structural and electronic links to the observed low thermal conductivity and high thermoelectric performance in AgCuTe is investigated in **chapter 1, part 5** of my thesis.

1.4 Novel properties of heavy metal based chalcogenides

1.4.1 Topological Materials

The past decades have witnessed the rapid growth of topological material research. The discovery of topological insulators with unique metallic surface states has added a new dimension in the field of electronics and spintronics. Following the initial breakthrough, the topologically non-trivial materials have been extended to various categories namely

weak topological insulator, topological crystalline insulator, Dirac semimetal and Weyl semimetal. Prior to the discussion on the details of topological materials (TM), the discovery of topological insulator has conversed in order to elaborate on the evolution of this field. The major breakthrough in the field of topological materials came in 1980 when Klitzing *et al.* discovered the quantum Hall state (QH).[54] The QH states are distinct from previously known states of matter in the context of topological order, where confined electrons in two dimensions exhibit dissipationless transport along the edge of the sample (Figure 1.3).[55] However, the main disadvantage of QH state for device fabrication is the requirement of the high magnetic field to quantize the electrons to get desired properties. In the following years, similar kind of topological order was observed in a new class of topological states known as quantum spin Hall (QSH) state and the materials having QSH are classified as topological insulators (TI).[32-35]

It is very important to understand the origin of band structure for TMs from a solid-state chemistry point of view in order to predict TIs from the library of compounds. The required materials traits for the realization of topologically nontrivial states can be easily understood from a perspective of solid state chemistry. First, the strong interaction between spin and orbital motion of the electron is required which is generally more pronounced in compounds with heavy constituent elements. In the case of ordinary semiconductors, top of the valence band is made up of the orbitals of more electronegative elements whereas the orbital of less electronegative elements form the bottom of the conduction band. Strong SOC splits the energies of the band and inverts the normal ordering of valence and conduction band commonly known as band inversion. In 2006, Bernevig, Hughes, and Zhang have used the concept of band inversion to comprehend topologically active edge states in HgTe thin films.[56] The energy of 6s orbital of Hg is lower compared to a 5p orbital of Te in HgTe because of lanthanide contraction and inert pair effect of Hg, resulting in band inversion at the Γ point. Ahandful number of materials with strong SOC have been proven to be topological insulators. Thus, SOC is one of the required criteria but not the sole criteria for the comprehension of TM.

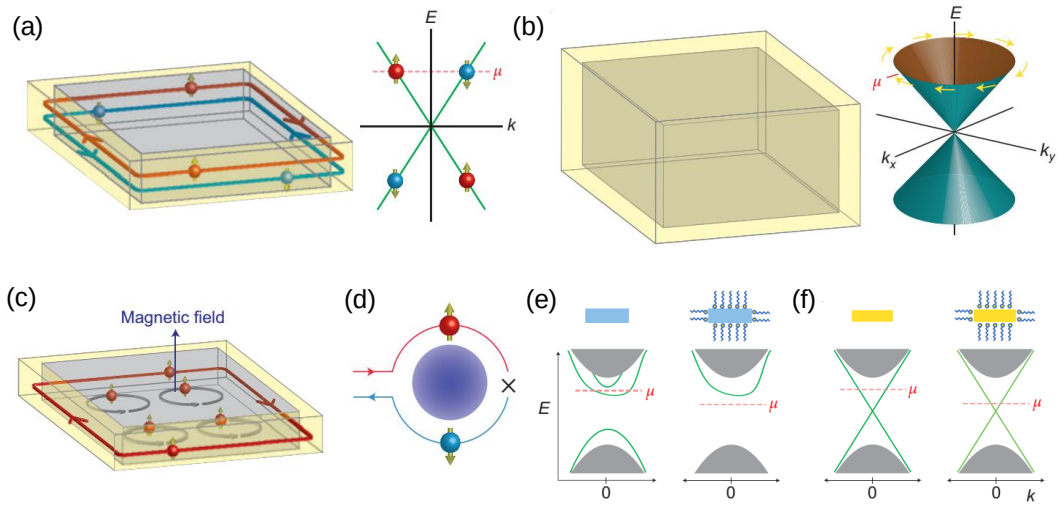

Figure 1.3 *(a) The metallic edge (shown in yellow) of a 2D topological insulator, in which spin-up and spin-down electrons counter-propagate (left), and the corresponding idealized spin-resolved band structure of the edge states (right). The pink line is the chemical potential μ. (b) The metallic surface of 3D topological insulators (left), and the corresponding idealized spin-resolved band structure of the surface states (right) revealing how the electron spin rotates as its momentum moves on the Fermi surface. (c) The quantum Hall effect in a 2D electron system, with a dissipationless metallic edge. (d) Any potential backscattering process on a topological insulator surface with a nonmagnetic impurity (purple circle) is prohibited, owing to the conservation of spin angular momentum. (e) On the left, an ordinary semiconductor and corresponding band diagram with coexisting surface (green lines) and bulk states (grey area). After surface modification, both surface and bulk electronic properties are modified (right). In this particular case, surface states no longer contribute to the transport process (no states available at μ). (f) A topological insulator and the corresponding band structure (left). After surface functionalization, the surface states remain intact, whereas μ shifts (right).* **Reproduced with permission from ref. 33 © 2011, Springer Nature.**

As an example of this illustration, cubic SnTe is a topologically active material (TCI) whereas GeTe and PbTe are trivial semiconductors from the IV-VI family. Coupling between s orbital of cation and p orbital of anion is very strong which leads to band inversion at the L point in case of SnTe whereas this s-p coupling is not strong enough for GeTe and PbTe because of the lower 4s orbital energy of Ge and relativistic effects of Pb, respectively, resulting their normal semiconductor nature.[57] In addition to the spin-orbital coupling, strain and interface dipole fields, the inter-orbital coupling can

also be employed to alter the band structure of a material. In a nutshell, band inversions can be thought of a general guideline for predicting new topological materials.

Interestingly, many topologically nontrivial materials such as Bi_2Te_3 (TI),[58] Bi_2Se_3 (TI),[59] SnTe (TCI)[60] are known for their high thermoelectric performance because both TM and thermoelectricity demand similar material features such as the presence of heavy constituent elements, narrow band gap and high spin-orbit coupling. The robust surface states with linearly dispersed Dirac cones lead to high mobility across the surface of topological materials (Figure 1.3b). Fascinating electronic transport properties of TM originates from the presence of metallic surface states, which offers high carrier mobility and makes them potential candidates for thermoelectric applications also. Moreover, materials with heavy constituent elements have soft vibrational (phonon) modes and consequently have low lattice thermal conductivity which is one of the key requirement to achieve high thermoelectric performance. At the same time, the presence of heavy constituent elements facilitate strong spin-orbit coupling which is one of the essential criteria for band inversion and the realization of topologically nontrivial surface electronic states. However, the optimization of the properties for TM and TE require a different range of carrier concentrations. Targeted bulk carrier concentration range is $<10^{16}$ cm^{-3} for topological materials (TM) in order to avoid the interference coming from the bulk, while the same is in the range 10^{19}-10^{20} cm^{-3} for TE materials.[61]

1.4.1.1 Topological Insulators

Topological insulators (TIs) behave as the normal insulator/semiconductor in bulk with time-reversal symmetry (TRS) protected non-trivial metallic surface states.[62] A TI can be viewed as the counterpart of QH state without applied magnetic field. Here, spin-orbit coupling (SOC) plays a role similar to the magnetic field in QH state, which has potential applications in different fields including spintronics and thermoelectrics. The simplest way to portray a topological insulator is as a non-trivial insulator with metallic boundary when placed next to an ‘ordinary’ insulator (vacuum). These metallic boundaries arise from topological invariants. The exotic metallic surface of TI is known as helical metal, where the electron spin is perpendicularly coupled with its orbital angular momentum

(Figure 1.3b).[63] Interestingly, crystal defects present in the surface of a topological insulator are not able to change the direction of moving electron (forward/backward) because of the 'locked' nature of spin and momentum in helical metal. Hence, the presence of defects at the surface will flip the electron spin due to the changes in momentum sign. To obey the law of conservation of angular momentum, 'U-turn' is prohibited for the surface electron, resulting in dissipationless charge transport along the material's surface (Figure 1.3d). However, it is experimentally observed that mobility of the surface electrons is finite. The spin-momentum locking forbids only recoil (180 degrees) scattering whereas small-angle scattering in a plane is perfectly allowed and known to limit the mobility of topological surface states.[64]

We can distinguish topological insulator from a trivial insulator by introducing novel Z_2 topological index which is classified as Hamiltonian for time-reversal invariant (*T*).[65] The value of topological invariant, ν equals to zero (0) and one (1) for existing even and an odd number of Dirac cones in the BZ, respectively for both 2D and 3D topological insulators.

In case of a 2D-topological insulator, topological edge states were first obtained in quantum wells of mercury telluride (HgTe) with a critical thickness (d_c ~6.5 nm) which is sandwiched between two cadmium telluride (CdTe) layers.[56] HgTe crystallizes in zincblende structure with a space group of *F-43m* (lattice parameter, a = 6.460 Å), similar to group IV (Si & Ge), III-V (GaAs &InP) and II-VI (CdSe) semiconductors. The energy gap between the valence band (p orbitals of anion) and conduction band (s orbital of cation) is 1.5 eV for CdTe, a trivial semiconducting material. The band gap is large for CdTe because of favourable bonding interaction between *s* and *p* bands. On the other hand, in HgTe (Hg and Te occupy the Wyckoff sites 4a and 4c, respectively), the presence of heavy elements such as Hg and Te induces significant SOC that splits the *p* bands into two components ($p_{1/2}$ and $p_{3/2}$) and drive the *p*-orbitals above the *s*-orbitals i.e. the bands are inverted compared to lighter CdTe.[34] Quantum well of HgTe can be established by burying HgTe (strong SOC) between two CdTe (weak SOC) layers with a similar lattice constant. Therefore, it is very important to recognize the critical thickness of HgTe layer to realize the optimum strength of SOC for the whole quantum well which

finally leads to the band inversion and the realization of topological surface states along the edge of the quantum well.[56]

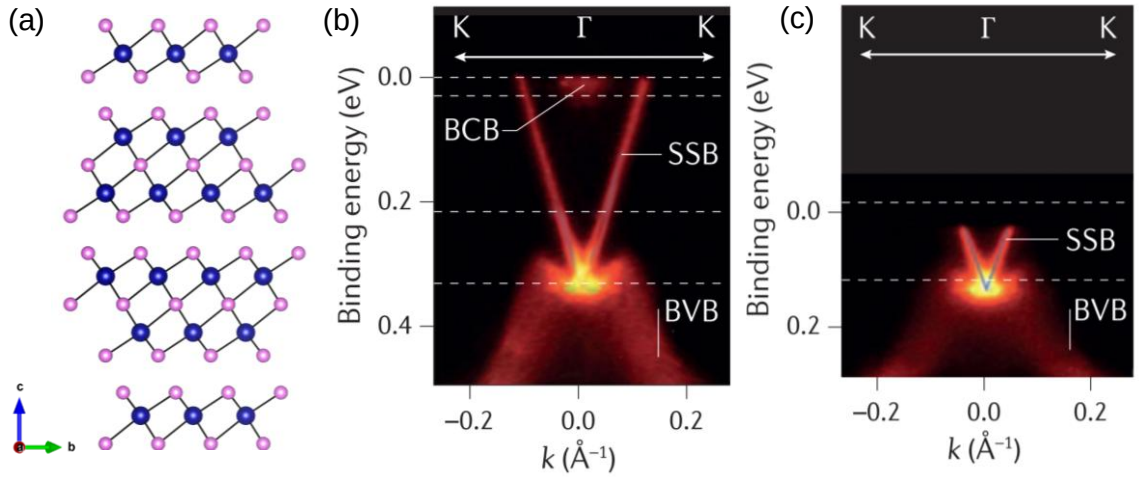

Figure 1.4 *(a) Crystal structure of M_2X_3 (M = Sb/Bi; X = Te/Se), Blue and magenta atom represent M and X, respectively, Energy dispersion for (b) n-type Bi_2Te_3 and (c) p-type Bi_2Te_3 via ARPES study. (b) and (c) Reproduced with the permission from ref 58. © 2009, American Association for the Advancement of Science.*

The next imperative advancement is the recognition of 3D topological insulator. Three dimension topological insulators can be classified into strong and weak topological insulators depending on the nature of the surface states. The 3D weak topological insulator can be created by stacking 2D TI which is identical to the layered Quantum Hall States. Weak topological insulator (WTI) and strong topological insulator (STI) both are characterized by four Z_2 indexes (ν_0, ν_1,ν_2, ν_3). STI has a nontrivial ν_0 which implies the presence of an odd number of Dirac cones in the surface states. For WTI, ν_0 is 0 and ν_1,ν_2,$\nu_3 \neq 0$ and thus it possesses an even number of Dirac cones in the surface states.[66] First 3D strong TI was predicted in $Bi_{1-x}Sb_x$ in 2007 by Fu and Kane[67] which was later experimentally confirmed through angle-resolved photoemission spectroscopy (ARPES) in 2008 by Hsieh *et al*.[68] The surface electronic structure of this alloy is quite complicated which motivates researcher to search for other 3D TI materials with much simpler surface band structure. Layered binary chalcogenides (tetradymite compounds) such as Bi_2Se_3, Bi_2Te_3 and Sb_2Te_3 (Figure 1.4a) are the widely studied compounds as 3D strong TIs (Figure 1.4b-c) because of several enviable properties.[61] Strong SOC alters the order of two p_z orbitals (Bi and X, X = Se/Te) responsible for the formation of the valence band

and conduction band, respectively, thereby band inversion occurs at the Γ point. At room temperature, tetradymite crystallizes in the rhombohedral phase (space group, *R-3m*) (Figure 1.4a). These 3D TIs have typically a bulk band gap of 0.2 - 0.3 eV. Further, the presence of the anti-site defects makes them conducting in nature. Importantly, exotic surface properties of tetradymite compounds can be accessible even at room temperature because of the large band gap. However, it is very challenging to distinguish between the bulk and surface conductivity because of the residual conductivity of bulk states coming from the intrinsic doping and anti-site defects.[61]

$TlBiSe_2$ and $TlBiTe_2$ also display topological surface states which are confirmed experimentally *via* ARPES. Recently, $SnBi_2Te_4$, $GeBi_2Te_4$, $Pb_2Bi_2Se_5$ and $PbBi_4Te_7$ have been also confirmed as topological insulators which have a structural correlation with Bi_2Te_3/Bi_2Se_3. In **chapter 4 (part 2)**, I have discussed the thermoelectric properties of 3D topological insulator, $TlBiSe_2$.

1.4.1.2 Topological Crystalline Insulators (TCI)

Generally, metallic surface states in TI are protected by time-reversal symmetry while the bulk remains insulating. In 3D TI, Dirac point is generally located at the Γ point of the BZ. Motivated by the exciting research on TI, researchers have explored new topologically nontrivial surface states, protected by other symmetries (invariant). Thus, the knowledge of crystal structure and symmetry is essential to understand the electronic properties of materials. In 2011, L. Fu has theoretically predicted a new kind of topological material named as a topological crystalline insulator (TCI).[36] Topological surface states of TCI are protected by crystal symmetries such as rotation, reflection etc. which eventually replace the responsibility of time-reversal symmetry in well studied Z_2 TI. Exploration of new TCI phases both theoretical and experimental investigations are still in their infancy because of the complexity of crystal structure. Unlike Z_2 index for TI, mirror Chern number, N_M helps one to identify the TCI from the library of compounds. Mirror Chern number can be defined as[69]

$$N_M \equiv (N_{+i} - N_{-i})/2 \quad (1.1)$$

Where two integers, N_{+i} and N_{-i} are topological invariants which are the Bloch Eigen states corresponding to Chern numbers. Mirror Chern number must be a non-zero integer for TCI, even if total Chern number is zero, which actually defines mirror symmetry protected TCI phases. In 2012 Hsieh *et al.* have theoretically predicted the TCI phase in SnTe (Figure 1.5a). Till now, the TCI phase is experimentally realized in SnTe, $Pb_{1-x}Sn_xTe$ and $Pb_{1-x}Sn_xSe$ all of which crystallize in rocksalt structure (space group *Fm-3m*).[37,70,71]

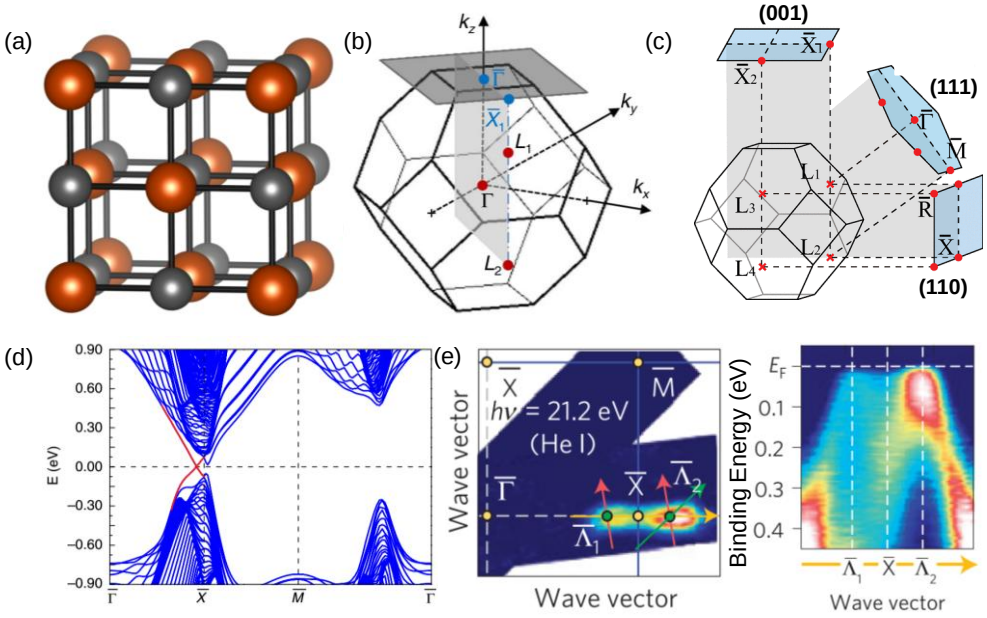

Figure 1.5 *(a) Crystal structure of SnTe (orange and grey atom represent Sn and Te, respectively), (b) the bulk and corresponding surface (001) Brillouin zone of SnTe, (c) Dirac cones in three different surfaces of Brillouin zones, (d) band dispersion of SnTe (e) mapping of the ARPES intensity at the Fermi level, E_F. (b) - (d) Reproduced with the permission from ref 37. © 2012, Springer Nature, (e) Reproduced with the permission from ref 60. © 2012, Springer Nature.*

In SnTe, the existence of non-zero mirror Chern number confirms the presence of topologically protected surface states on the crystal faces which are symmetric with (110) mirror planes (Figure 1.5b-c). Hsieh *et al.* have observed that three surface terminations fulfilling this condition such as (001), (110) and (111) surface (Figure 1.5b).[37] Moreover, surface orientation generates two different types of surface states in TCI like SnTe. One type of surface states exist on the (001) and (110) surface. For the (001) surface, four L

(1, 2 & 3, 4) points of the bulk BZ project onto X (1 and 2) point in the surface BZ (Figure 1.5c). The calculated mirror Chern number, $N_M = 2$ confirms the presence of two pairs of spin-polarized surface states with opposite Eigen values which confirms the existence of four Dirac points in the surface states. Another type of surface state exists on the (111) surface in TCI where three L points of bulk BZ project onto $\bar{M}$ point in the surface BZ and another one L point of bulk BZ projects onto $\bar{\Gamma}$ point in the surface BZ (Figure 1.5c). Interestingly, both types of surface states of SnTe possess even number of Dirac points which make them distinguishable from Z_2 TI with an odd number of Dirac points in the BZ.

After the theoretical prediction of topological surface states in SnTe (Figure 1.5d), Tanaka *et al.* have experimentally confirmed the presence of four Dirac cones in the surface states of SnTe by using ARPES experiment (Figure 1.5e).[60] Experimentally the double Dirac cone structure is observed at $\bar{X}$ point of the surface BZ for the (001) surface of SnTe. Interestingly, none of the Dirac points of (001) surface are located at time reversal invariant momentas of the surface BZ, whereas for (111) surface, four Dirac points are located at time reversal invariant momentas ($1\,\bar{\Gamma} + 3\,\bar{M}$).

PbTe, a champion thermoelectric material from IV-VI chalcogenide family, has the same rocksalt crystal structure like SnTe. However, PbTe is proven to be topologically trivial, unlike SnTe. SnTe and PbTe have small band gaps located at four L points. Low energy theory of band structure indicates the topological distinction between PbTe and SnTe with respect to Dirac mass. Furthermore, ab-initio calculation confirms the electronic structure of PbTe and SnTe. In PbTe, orbitals of Pb contribute in the conduction band and Te orbitals contribute in the valence band. Interestingly, a reverse trend in the electronic structure is observed for SnTe. Mention must be made that the bulk band gap of $Pb_{1-x}Sn_xTe$ alloys initially decreases with increasing the Sn concentration and closes at Sn composition of ~ 0.4; then again reopens.[70] According to the low energy theory, this band inversion leads to a change of sign of the Dirac mass that predicts the presence of TCI phase in SnTe and $Pb_{1-x}Sn_xTe$. By considering all the above facts (low energy theory, ab-initio calculation,and band theory), Hsieh *et al* envisaged that SnTe is a topological crystalline insulator and PbTe is non-topological material.[68]

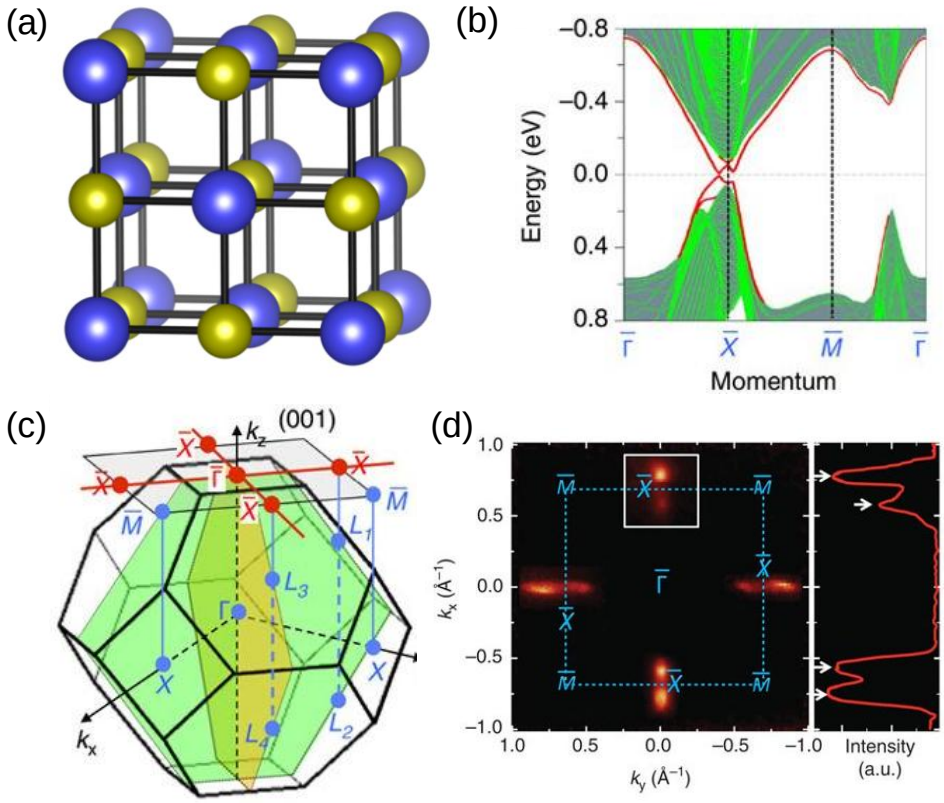

Figure 1.6 *(a) Crystal structure of $Pb_{1-x}Sn_xTe$ (Blue and yellow atom represent Pb/Sn and Te, respectively). (b) Band dispersion of $Pb_{1-x}Sn_xTe$. The bulk and surface states are represented by the red lines and green shaded area, respectively. (c) The face-centered-cubic Brillouin Zone of $Pb_{1-x}Sn_xTe$ showing the mirror planes. (d) Iso-energetic contour mapping of $Pb_{0.6}Sn_{0.4}Te$ (Left panel). ARPES spectral intensity (Right panel). Reproduced with the permission from ref. 70.* © *2012, Springer Nature*

However, the presence of local rhombohedral distortion in SnTe however breaks the mirror symmetry in the crystal structure. Moreover, SnTe is a heavily doped *p*-type degenerate semiconductor because of the intrinsic Sn vacancy which causes a shift of the Fermi level inside the bulk valence band whereas, Pb-rich $Pb_{0.60}Sn_{0.40}Te$ possesses four band inversion at the L point of the BZ similar to its end member, SnTe (Figure 1.6a & b).[70] The detailed theoretical calculation has shown that it is possible to realize mirror symmetry protected topological phase in $Pb_{1-x}Sn_xTe$ due to the presence of momentum space mirror plane along L-Γ-L in BZ of $Pb_{1-x}Sn_xTe$ (Figure 1.6 b & c). $Pb_{0.60}Sn_{0.40}Te$ sample has rock salt structure (Figure 1.6a) without the presence of rhombohedral distortion which preserves the crystal symmetry and it is possible to keep the Fermi level

above the bulk valence band to get information from the surface states *via* photoemission experiments. ARPES experiments have confirmed the presence of four surface states corresponding to the four band inversion in the BZ of $Pb_{0.60}Sn_{0.40}Te$. Spin-resolved ARPES study has revealed the presence of nonzero mirror Chern number (N_M = - 2) for $Pb_{0.60}Sn_{0.40}Te$ which confirms the presence of mirror symmetry protected topological surface states (Figure 1.6d)).[70] In **chapter 1 and 2 (part 2)**, I have discussed the thermoelectric properties of topological crystalline insulator, $Pb_{0.60}Sn_{0.40}Te$. In p**art 4**, I have discussed the thermoelectric properties of topological crystalline insulator, SnTe.

1.4.2 Thermoelectrics

Thermoelectric (TE) materials, by virtue of a unique combination of electrical and thermal properties, are capable of converting thermal gradients into electrical energy or vice versa, and are posited to play a significant role in the energy management.[14,20,21,72] Given the current global energy crisis and the dwindling non-renewable resources, capturing and converting the otherwise wasted heat back into useful electrical power will have a huge impact. When a temperature gradient (ΔT) is applied to a TE couple consisting of n-type and p-type elements, the mobile charge carriers (electrons in n-type and holes in p-type) at the hot end diffuseto the cold end, producing a potential difference (ΔV). This effect known as Seebeck effect, where S= ΔV/ΔT is defined as the Seebeck coefficient, forms the basis of TE power generation. (Figure 1.7a). Conversely, when a potential difference is applied to a TE couple, carriers bring heat from one side to the other so that one side gets cooler while the other gets hotter, an effect known as the Peltier effect (Figure 1.7a) which forms the basis of TE refrigeration.[73]

The thermoelectric conversion efficiency for a material requires both high *zT* values and a large temperature difference across the thermoelectric materials, as given by the following relation:

$$\eta_{TE} = \eta_c \frac{\left(\sqrt{1+zT}-1\right)}{\left(\sqrt{1+zT}+\frac{T_C}{T_H}\right)} \qquad (1.2)$$

where η_c, T_H and T_C are Carnot Efficiency, the temperatures of the hot and cold ends and zT, the dimensionless figure of merit is expressed as

$$zT = \frac{\sigma S^2}{\kappa_{ele} + \kappa_{lat}} T \tag{1.3}$$

Where σ, S, κ_{ele}, κ_{lat} and T are the electrical conductivity, Seebeck coefficient, electrical thermal conductivity, lattice thermal conductivity and absolute temperature, respectively.

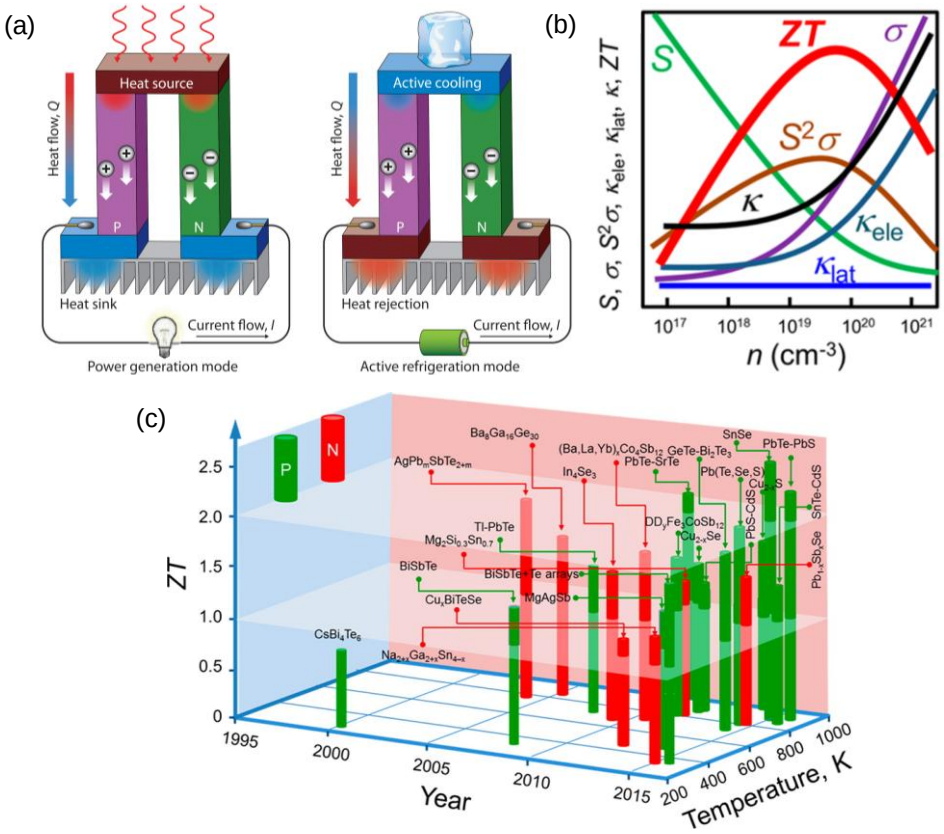

Figure 1.7 *(a) Schematic illustrations of a thermoelectric (TE) module for active refrigeration-Peltier effect (left) and power generation-Seebeck effect (right). (b) Schematic diagram showing the variation of zT and related TE parameters (electrical conductivity (σ), Seebeck coefficient (S), power factor ($S^2\sigma$), electronic thermal conductivity (κ_{ele}), lattice thermal conductivity (κ_{lat}), and total thermal conductivity (κ), as a function of carrier concentration (n). The TE parameters are highly correlatedthereby limiting the maximum zT (~ ZT). (c) TE figure-of-merit (zT) as a function of temperature and year illustrating important milestones. (a) reproduced with permission from ref. 73© 2010 Nature Publishing Group. (b) and (c) are reproduced with permission from ref. 20 © 2016 American Chemical Society.*

An ideal thermoelectric material should have high electrical conductivity similar to metals, large Seebeck coefficient as in semiconductors and ultra-low thermal conductivity like glasses. It is always challenging for the chemists to design a single TE material that meets all the above criteria; moreover, the high interdependence of all the above properties poses an inherent limit to the maximum zT that can be attained in a given material (Figure 1.7b). Figure 1.7c shows the evolution of zT over the past two decades and it clearly shows that the state-of-art TE materials are found among heavy metal chalcogenides, especially those based on Bi and Pb such as Bi_2Te_3, PbTe, and PbSe.[20]

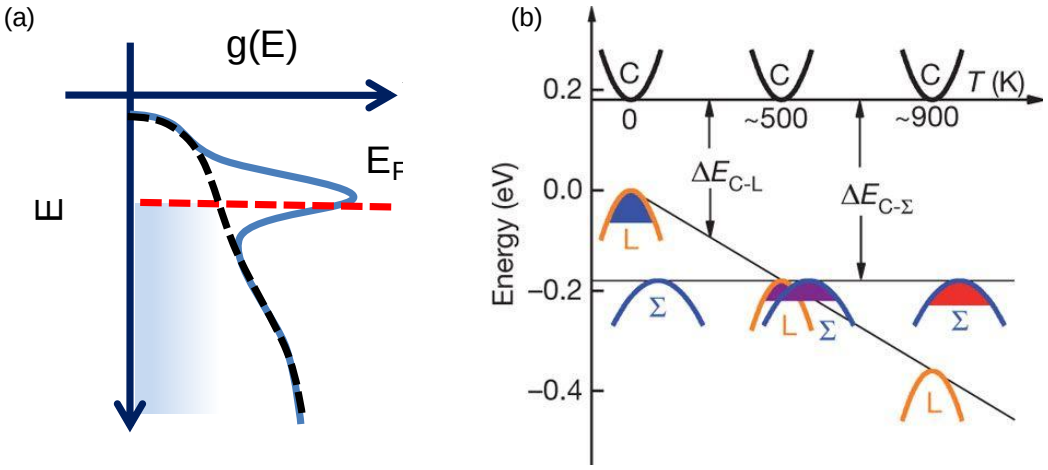

Figure 1.8 *(a) Schematic diagram of resonance level in the valence band. Schematic diagram of density of state (DOS) of the valence band of pristine sample (dotted black line). Tl-doped PbTe shows asymmetric distortion of DOS (blue line) near Fermi level. (b) Relative energy of the valence bands in* $PbTe_{0.85}Se_{0.15}$*. At, 500 K the two valence bands converge, resulting in contributions from both the L and Σ bands in the transport properties. (b) is reproduced with permission from ref. 75 © 2011 Nature Publishing Group.*

Two approaches are employed to boost zT *viz.* enhancement of power factor (σS^2) and reduction of thermal conductivity. Some strategies to enhance power factor include: a) engineering of carrier-concentration through chemical doping, b) enhancement of effective carrier mass (m*) and hence, the Seebeck coefficient either *via* distortion of density of states near Fermi level by resonant impurity levels[74] (Figure 1.8a) or, convergence of multiple valence/conduction band extrema[75] (Figure 1.8b) and c) enhancement of carrier mobility by modulation-doping.[20] On the other hand thermal

conductivity is supressed traditionally through a) point defects, b) endotaxial nanoscale precipitates in the host matrix and c) mesoscale grain boundaries. Sometimes all the above three are incorporated in what are referred to as hierarchical architectures where the atomic scale, nanoscale and mesoscale defects would scatter phonons with a broad range of wavelengths (Figure 1.9).[20,72] The All-scale hierarchical architecting has been shown to be promising especially for the lead chalcogenides. However, in addition to scattering of phonons, an undesirable scattering of carriers can occur limiting the overall zT in most other TE materials. In this respect, materials with intrinsically low thermal conductivity are, therefore, practically more attractive being robust to impurities, doping, grain sizes etc.

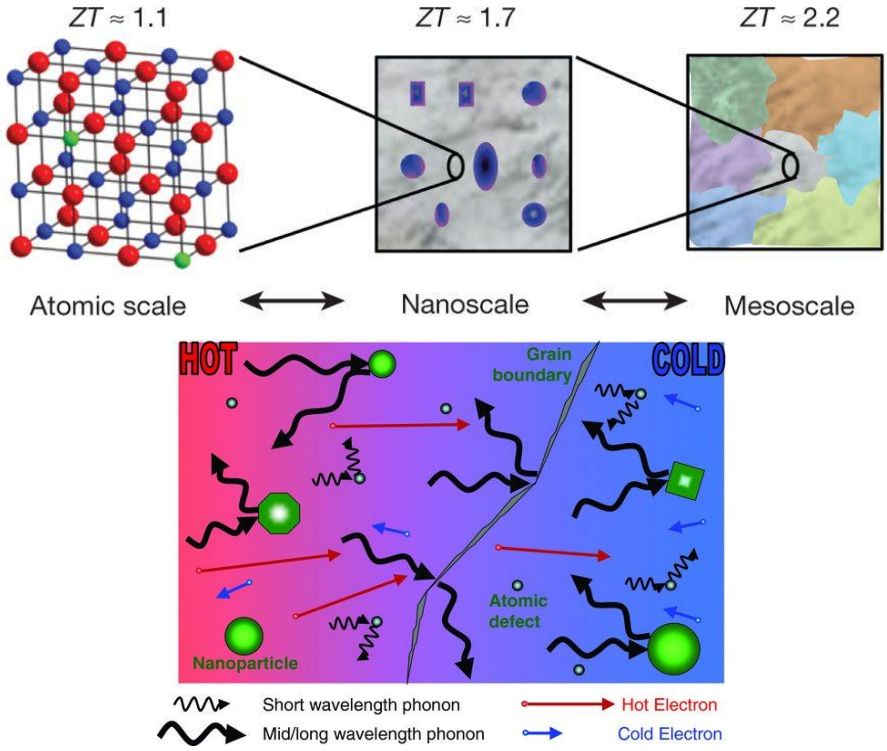

Figure 1.9 *Illustration of atomic scale point defects, endotaxial nanostructures and mesoscale grain boundaries in hierarchical architectures based on PbTe that lead to an all-scale phonon scattering (upper panel). Point defects scatter short-wavelength phonons. Nanoparticles are effective at scattering mid-long wavelength phonons while grain boundaries predominantly scatter the long wavelength phonons. Schematic illustration of phonon-scattering by atomic defects, nanoparticles and grain boundaries in a solid (lower panel). The upper panel is adapted from ref. 72 © 2012 Nature publishing group and the lower panel is reproduced with permission from ref. 21 © 2010 Wiley.*

Slack had originally proposed 'phonon-glass electron-crystal' (PGEC) where the electron and phonon transport channels are decoupled, thus facilitating an independent control of electronic and thermal properties. As the name suggests, a PGEC crystal should possess glass-like low thermal conductivity coexistent with crystal-like high electrical conductivity. PGEC concept has inspired several investigations and led to significant increase in zT in several classes of compounds such as skutterudites,[76] clathrates[77] etc. The latter can be doped with guest-fillers that preferably occupy the intrinsic over-sized structural voids. These guest atoms, not being bonded to the host matrix, randomly rattle within the voids producing localized low-frequency optical vibrations. The latter can couple with the heat-carrying acoustic phonons of the host and lead to ineffective thermal transport via 'phonon resonant scattering'[78] or lowering of acoustic phonon group velocities. Other intrinsic factors leading to low thermal conductivity include large unit cells,[79] complex crystal structures,[80] cation-disorder,[43] liquid-like atomic motion,[51] and weak multicentre bonds.[81]

The high zT of a material demands low lattice thermal conductivity, κ_{lat}. Introduction of micro- and nanostructures in the matrix is the well-known approach to control the phonon propagation and hence thermal conductivity. However, it is essential to understand the influence of chemical bonds on the phonon transport. Room temperature κ_{lat} for GeTe ans SnTe are ~ 2.7 and ~ 2.9 W m^{-1} K^{-1}, respectively whereas for InSb is 16 W m^{-1} K^{-1}.[82] Although the structure of GeTe, SnTe and InSb are different, according to simple mass disorder rule, they should follow the reverse trend as discussed previously by Lee *et al*.[82] Here, chemical bonding plays an important role. Softer chemical bonding in GeTe (SnTe) compared to InSb leads to decrease in the speed of sound and the lattice thermal conductivity (Equation 1.4):

$$\kappa_{lat} = \frac{1}{3} C_V \nu_a l \qquad (1.4)$$

Where, C_v, ν_a and l are heat capacity at constant volume, sound velocity and mean free path respectively. Octahedral coordination in GeTe and SnTe results in softer bonding compared to that of InSb (tetrahedral bonding) which leads to the decrease in the average sound velocity in GeTe (1900 m/s)[83], SnTe (1800 m/s)[83] compared to InSb (2300 m/s),[84] thereby lower lattice thermal conductivity in GeTe and SnTe. Moreover, the presence of soft ferroelectric transverse optical mode in GeTe and SnTe results in reduced

phonon mean free path (~1-100 nm for SnTe and GeTe, ~10-1000 nm for InSb) which further favours in achieving lower lattice thermal conductivity in GeTe and SnTe compared to that of InSb.[82]

1.4.3 Correlation between Topological Materials and Thermoelectrics

Interestingly, many topologically nontrivial materials such as Bi_2Te_3 (TI), Bi_2Se_3 (TI), SnTe (TCI) are known for their high thermoelectric performance because both TM and thermoelectricity demand similar material features such as the presence of heavy constituent elements, narrow band gap and high spin-orbit coupling. The robust surface states with linearly dispersed Dirac cones lead to high mobility across the surface of topological materials. Fascinating electronic transport properties of TM originates from the presence of metallic surface states, which offers high carrier mobility and makes them potential candidates for thermoelectric applications also. Further, we believe that the TE performance of TMs can be improved by using its unique electronic structure (band inversion). Interestingly, band inversion generates many local extrema in the valence or conduction bands during the electronic topological transition, resulting in large DOS and asymmetry near the Fermi level which additionally helps to improve electrical conductivity and Seebeck coefficient. Moreover, materials with heavy constituent elements have soft vibrational (phonon) modes and consequently have low lattice thermal conductivity which is one of the key requirements to achieve high thermoelectric performance. At the same time, the presence of heavy constituent elements facilitate strong spin-orbit coupling which is one of the essential criteria for band inversion and the realization of topologically nontrivial surface electronic states. However, the optimization of the properties for TM and TE require a different range of carrier concentrations. Targeted bulk carrier concentration range is $<10^{16}$ cm^{-3} for topological materials (TM) in order to avoid the interference coming from the bulk, while the same is in the range 10^{19}-10^{20} cm^{-3} for TE. Thus, the intersection of these two ongoing research fields may reveal several new and exciting phenomena and new prospects which are not available in conventional materials. Further, topologically nontrivial boundary states also help to improve the thermoelectric performance of a material compared to the trivial phase

because boundary states act as conducting channels for carriers with minimal backscattering effect. My thesis is centered around the relationship of thermoelectric and topological materials based on heavy metal chalcogenides.

1.5 Synthesis and characterizations

1.5.1 Synthesis

The successful utilization of TE devices depends critically on the synthesis techniques. A great majority of chalcogenides known to date have been synthesized by sealed-tube reactions in vacuum (10^{-3} - 10^{-5} Torr) either by employing high-temperature melt cooling or alkali metal polychalcogenide fluxes A_2Q_n (Q = S/Se/Te) at low temperatures. In high temperature vacuum sealed tube melting reaction, appropriate quantities of starting materials (mostly in their elemental form) are heated above the melting point of the desired product in absence of air, followed by cooling of the subsequent reaction mixture at a specific cooling speed depending upon material's nature (congruent/incongruent). Products of the reactions are generally thermodynamically stable polycrystalline or single-crystalline ingots.

The Spark plasma sintering (SPS) is newly developed technique for the syntheses and processing of thermoelectric materials employing ON-OFF pulse DC voltage / current (Figure 1.10).[85-87] This is considered as an energy-saving sintering technology due to its short processing time and a small number of processing steps. The SPS process is based on the electrical spark discharge phenomenon. Application of a high energy, low voltage spark pulse (spark discharge) momentarily produces a local high temperature state (several to ten thousand degree) in the gap between the particles of a material *via* joule heating (Figure 1.10c, 1.10d and 1.10e). This results in vaporization and melting of the powder particles' surfaces and formation of constricted shapes or "necks" around the contact area between the particles. These constricted shapes gradually develop and plastic transformation progresses during sintering, resulting in a sintered material with density of ≥ 99%. By application of voltage and current repeatedly with this ON-OFF, the discharge

point and the Joule heating point (locally high-temperature generation field) move throughout the sample, resulting in less power consumption and efficient sintering. Since only the surface temperature of the particles rises rapidly by self-heating, particle growth of the starting powder materials is controlled. Therefore, a precision sintered compact is manufactured in a shorter time. At the same time, bulk fabrication of particles with an amorphous structure and crystalline nanostructure formation are now possible without changing their characteristics. Vaporization, melting and sintering are completed in short periods of approximately 5-20 minutes, including temperature rise and holding times. SPS sintering temperatures range from low to over 2000 ℃ which are 200-500 ℃ lower than with conventional sintering.

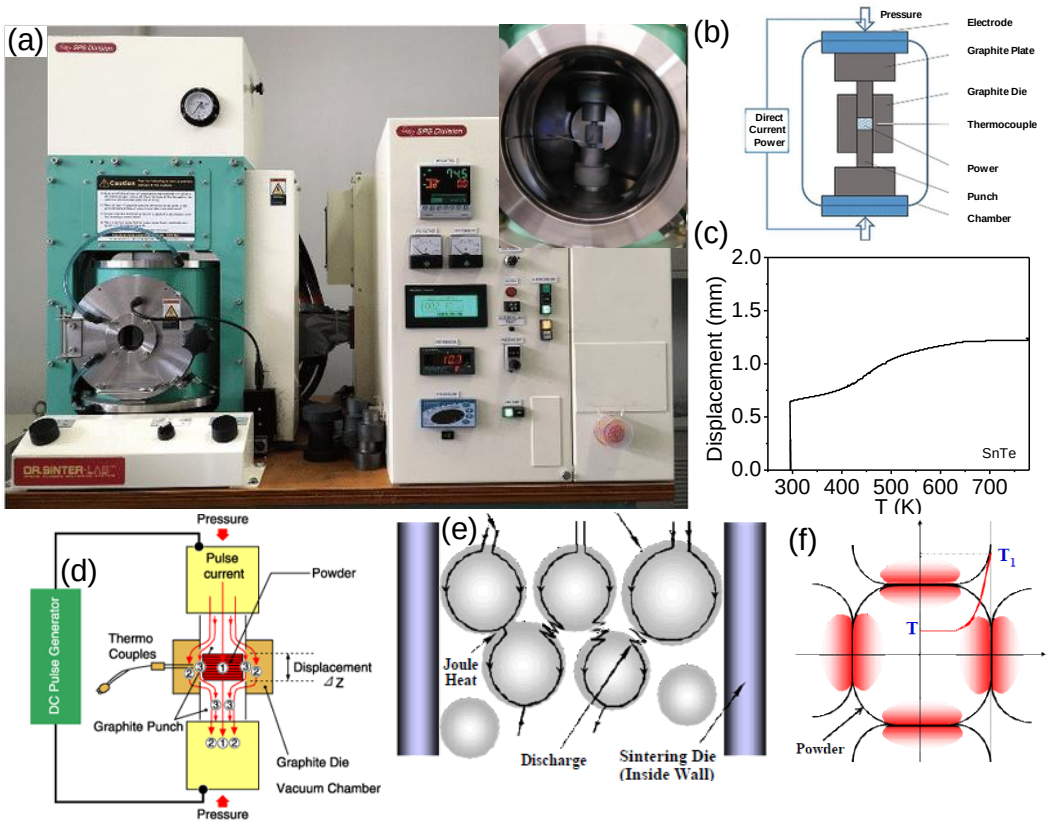

Figure 1.10 *(a) Photograph of SPS-211Lx instrument. The inset image shows sitering chamber. (b) Schematic illustration of a spark plasma sintering equipment. (c) Typical graphite punch displacement rate versus temperature plot for SnTe during SPS processing. (d) Schematic of ON-OFF pulsed current path. (e) Possible electric current path through powder particles inside the die. (f) The temperature image on powder particles surface. Contact surface temperature (T_1) differs significantly from average temperature (T).*[86,87]

In order to prepare high performance thermoelectric materials, we have done spark plasma sintering (SPS) of the melt grown ingots in SPS-211Lx, Fuji Electronic Industrial Co., Ltd. The SPS process and geometrical configuration of the punches, mould and powder are illustrated in figure 1.10. Powders to be consolidated, are placed in a die and heated by applying the electric current. The melt grown ingots were first ground into fine powders using a mortar and pestle to reduce the grains size in an inert glove box. This powder was then pressed into cylindrical shape by SPS method (SPS-211Lx, Fuji Electronic Industrial Co., Ltd.) at specific temperature and pressure under vacuum (Figure 1.10). Highly dense (~ ≥ 98% of theoretical density) disk-shaped pellets with ~ 10 mm diameter and ~ 10 mm thickness were obtained.

1.5.2 Characterizations

I have used the following characterization techniques for my thesis works.

1.5.2.1 Powder X-ray diffraction (PXRD)

Powder X-ray diffraction is the most commonly used technique in solid state inorganic chemistry and has many uses from analysis and assessing phase purity to determining the structure. In this thesis, both lab source X- ray and synchrotron X-ray have been used for structural characterization. In the laboratory, X-rays are generated in a cathode tube. In this technique, a tungsten filament was heated to produce electrons and electron beam was then accelerated towards an anode by applying a voltage (~ 30 - 40 kV). When electrons have sufficient energy to dislodge inner shell electrons of the target material, characteristic X-ray spectra are produced. These spectra consist of several components, the most common being Kα and Kβ. Kα consists, in part, of Kα_1 and Kα_2. Kα_1 has a slightly shorter wavelength and twice intensity than Kα_2. The specific wavelengths are characteristic of the target material (Cu, Fe, Mo, Cr). Cu is the most common target material use for laboratory X-ray. To produce monochromatic X-rays, it is required filtering out Kβ radiation by foils or crystal monochromators. For Cu radiation, a sheet of Ni foil is a very effective filter, but it is difficult to remove Kα_2 from Kα_1 because of close wavelength. The filtering process in laboratory X-ray leads to a reduction in

intensity and hence it is difficult to detect low-intensity peaks in laboratory X-ray diffraction. In addition, it is difficult to distinguish peak splitting when peaks appear closely. These limitations can be ruled out in synchrotron X- ray. Synchrotron radiation is emitted when charged particles such as electrons, traveling at relativistic speeds, are forced to change direction on passing through a magnetic field. To generate synchrotron radiation, electrons or positrons are accelerated to speeds close to that of light and circulate in ultra-high vacuum tubes or storage rings, guided by arrays of magnets.

X-ray diffraction obeys Bragg's law, which states that constructive interference would occur if the path difference between the X-rays scattered from parallel planes were an integer number of the wavelength of radiation. If the planes of atoms, separated by a distance d, make an angle θ with the incident beam, then the path difference would be $2d\sin\theta$. So, for constructive interference, the Braggs law must be satisfied

i.e. $n\lambda = 2d\sin\theta$, $n = 1, 2, 3, \ldots\ldots$ (1.5)

λ= wavelength of the X-ray radiation

In this thesis, room-temperature and high-temperature powder X-ray diffraction experiments on the samples are carried out using Bruker D8 Advance diffractometer using Cu-Kα radiation having wavelength 1.5406 Å. Powder or precipitates of the sample were placed on a glass plate sample holder during measurement. To understand the structural evolution we have also used temperature dependent synchrotron X-ray diffraction measurements under N_2 atm at BL-18B (Indian beamline), Photon Factory, KEK, Tsukuba, Japan. The wavelength of X-ray and temperature ranges for the measurement have been given in the experimental part of the respective chapters. The energy of the beam was set by Si(111) double crystal monochromator, which was cross-checked with Si (640b NIST) standard. All the measurements were carried out in Bragg-Brentano geometry with a divergence slit (300 μm), an anti-scattering slit (350 μm), and a receiving slit (300 μm). High-temperature measurements were carried out with Anton Paar DHS1100 heat cell.

1.5.2.2 X-ray Pair Distribution Function

Pair distribution function (PDF) analysis is a powerful technique for probing atomic-scale disorder that cannot be detected using traditional diffraction methods. Unlike other

crystallographic methods, PDF analysis is a total scattering technique, which means that both Bragg and diffuse scattering are included. The PDF reveals both the long-range periodic structure (Bragg reflections) and the local structure imperfections (diffuse component of the diffraction pattern).

Temperature dependent X-ray PDF data was collected using finely ground powder in beamline P02.1, PETRA III, DESY, Hamburg. Synchrotron beam of fixed energy 59.83 keV and spot size 0.5 X 0.5 mm^2 was used to collect data. From the coherent part $I^{coh}(Q)$ of the measured total diffracted intensity of the material, the total scattering structure function, S(Q), is obtained as

$$S(Q) = \frac{I^{coh}(Q) - \sum C_i |f_i(Q)|^2}{|\sum c_i f_i(Q)|^2} + 1 \quad (1.6)$$

where the coherent intensity is corrected for background and other experimental effects and normalized by theflux and number of atoms in the sample. Here c_i and f_i are the atomic concentration and X-ray atomic form factor, respectively, for the atomic species of type i. The momentum transfer, Q, is given by

$$Q = 4\pi \sin\theta/\lambda \quad (1.7)$$

By Fourier-transforming the expression Q[S(Q)−1], we obtain,

$$G(r) = \left(\frac{2}{\pi}\right) \int_0^{Q_{max}} Q[S(Q) - 1] \sin(Qr)\, dQ \quad (1.8)$$

Where G(r) is the atomic pair distribution function, which is also defined as

$$G(r) = 4\pi r[\rho(r) - \rho_0]$$

Where ρ_0 is the average atomic number density, ρ(r) is the atomic pair density, and r is a radial distance. The function G(r) gives information about the number of atoms in a spherical shell of unit thickness at a distance r from a reference atom. Finally, the experimental G(r) can be compared and refined against the theoretical G(r) from a structural model, given by

$$G(r) + 4\pi r\rho_0 = \frac{1}{r} \sum_v \sum_\mu \frac{f(0)_v f(0)_\mu}{\langle f(0)\rangle^2} \delta(r - r_{v\mu}) \quad (1.9)$$

2D image plate data was collected using a Perkin-Elmer detector which was processed using Fit2D[88] software to obtain the scattering intensities *S*(Q) in the Q-space. The pair distribution *G*(r) was then obtained by Fourier transformation of the scattering structure function *F*(Q) = Q[*S*(Q) - 1] using PDFgetX2[89] software. Finally, the modeling and refinement of *G*(r) was done using the software PDFgui.[90]

1.5.2.3 Transmission electron microscope (TEM)

TEM is one of the important tools in material science for characterization of the microscopic structure of materials. A TEM image represents a two-dimensional projection of a three-dimensional object. TEM operates on the same basic principles as the light microscope, however, uses electrons as "light source" that makes it possible to get a resolution of about thousand times better than a visible light microscope. Instead of glass lenses focusing the light in the light microscope, the TEM uses electromagnetic lenses to focus the electrons into a very thin beam. The electron beam then travels through the specimen you want to study. When the electron beam passes through an ultra thin specimen, it gets absorbed or diffracted through the specimen. Some of the electrons are scattered and disappear from the beam depending on the density of the material present on the focused region. A "shadow image" is formed by the interaction of the electrons transmitted through the specimen focused onto a fluorescent screen or a photographic film or by a sensor such as a charge-coupled device (CCD). TEM study allows to focus electron beam to any part of specimen and electron diffraction data from a different area of the specimen can give us more details about the accurate local structure of the sample.

TEM samples for the solid state materials were prepared by conventional mechanical and tripod polishing. Large electron transparent area was obtained by subsequent Ar ion milling in the precision ion polishing system (PIPS) with the ion energy of 4.5 eV and beam angle of 7 deg. The thickness was restricted to 40-50 μm. Bright field imaging, Diffraction pattern, HRTEM imaging is carried out in aberration corrected FEI TITAN3™ 80–300kV transmission electron microscope.

1.5.2.4 Field emission scanning electron microscope (FESEM)

A FESEM is used to visualize topographic details of the sample surface. Similar to TEM, FESEM microscope also uses electrons as a light source. Electrons are ejected from a field emission source and accelerated in a high electrical field gradient. These electrons (termed as primary electrons) produce a narrow scan beam within the high vacuum column, which bombards the sample material. The incident electrons cause emission of electrons from the sample due to elastic and inelastic scattering. The angle and velocity of

these secondary electrons produced by inelastic collision of accelerated electrons with sample atoms relate to the surface structure of the object. High-energy electrons those are produced by an elastic collision of a primary electrons with atom's nucleus of the sample are termed as backscattered electrons (BSE). Larger atoms (with a high atomic number, *Z*) have a higher chances of producing elastic collisions because of their greater cross-sectional area. Thus, a "brighter" BSE intensity correlates with higher average *Z* in the sample, and "dark" areas have lower average *Z*. BSE images are very helpful for obtaining high-resolution compositional maps of a sample.

In my Ph.D work, I have performed both normal and BSE mode FESEM experiments using NOVA NANO SEM 600 (FEI, Germany) operated at 15 kV to study surface morphology and phase homogeneity. For BSE imaging, I have used a finely polished sample in the back-scattering mode to produce a BSE image of the surface.

1.5.2.5 Energy dispersive X-ray analysis (EDAX)

EDAX is an analytical technique used for elemental composition analysis of the sample. EDAX makes use of the X-ray spectrum emitted by a solid sample bombarded with a focused beam of electrons. For EDAX analysis, an X-ray detector is generally integrated with FESEM instrument. Its characterization capabilities are due in large part to the fundamental principle that each element has a unique atomic structure allowing a unique set of peaks on its electromagnetic emission spectrum. I have performed EDAX using EDAX Genesis instrument attached to FESEM column.

1.5.2.6 Positron annihilation spectroscopy (PAS)

PAS is a nondestructive nuclear solid state technique commonly used for defects and voids study in materials. It is a powerful technique to study open volume defects like dislocation, agglomerates, and vacancies at ppm concentration. Positrons (e^+) is an antiparticle of the electron (e^-) having exactly equal rest-mass of the electron (511 keV) but with apositive charge. One can obtain positrons from the β^+ decay of radioactive isotopes such as ^{22}Na, ^{64}Cu, and ^{58}Co. In the present experiments,^{22}NaCl has been used as positron source. Positrons injected from a radioactive source get thermalized within 1-10 ps and annihilate with a nearby electron inside the material, normally (379 out of 380 cases) emitting two exactly opposite 511 keV gamma rays, in the center of mass frame.

The positron lifetime is inversely proportional to the electron density at the annihilation site. Hence by measuring the positron lifetime (sub nano-second) one can study the electron density distribution in the studied material. Naturally, the lifetime of positrons annihilated at defects is larger compared to the annihilation of positron in the bulk of the material, since theelectron density is lower at such defects and positrons survive relatively longer time before annihilation. Therefore, the measured positron lifetime at defects indicates the nature and type of the open volume and the corresponding intensity (weight of that particular lifetime in the overall spectrum) represents the relative abundance of such defect sites in the studied material.

The other PAS technique is to measure the Doppler broadening of the electron-positron annihilated γ-ray (511 keV) line shape (DBEPARL) with a high purity germanium (HPGe) detectors. The basic concept is that although before annihilation positrons are thermalized but the electron has some energy and the corresponding momentum is p_{el}. Thus the electron-positron pair has some momentum which is translated as a Doppler shift to the 511 keV γ-rays by an amount ($\pm \Delta E = p_L c/2$) in the laboratory frame; where p_L is the component of p_{el} along the direction of measurement. Contributions from all possible p_{el}s are convoluted in the DBEPARL spectrum which looks like an inverted parabola with the centroid at 511 keV ($p_{el} = 0$). The region close to the centroid is formed due to positron annihilation with very low momentum electrons. In the open volume defects, it is more probable for a positron to find a nearly free electron ($p_{el} \sim 0$), the wave function of which are spatially extended. The core electron wave functions are localized and do not span inside the open volumes. Therefore, a more sharpened DBEPARL spectrum represents sample with high concentration of open volume defects. The wing region of DBEPARL spectrum (away from centroid with ahigher value of p_L) carries the information about the annihilation of positrons with the core electrons (which are element specific). De-convolution of DBEPARL spectrum is not straightforward thus ambiguous and in general, a simple methodology is adopted to understand the element specific changes in the wing region of the spectrum. Area-normalized DBEPARL spectrum of a high purity material, either Al, Si single crystal or a single crystal of the respective material is recorded in the same detector assembly. The ratio of counts at each energy is taken and the so-called “ratio curve” is formed. The peak

and dip positions in this ratio curve represent more or less annihilation (respectively) with the electrons of nearby momentum region. The Compton continuum of 1276 keV gamma ray, simultaneously emitted with a positron from the ^{22}Na radioactive source, enhances the background counts in the wing region of the spectrum and thereby blurred the peak or dip shapes as well as positions. Two HPGe detector in coincidence successfully suppresses this Compton continuum and the chemical sensitivity of ratio curves with high precision can be achieved. In general, defects modify thelocal electronic configuration and hence, an intimate relationship is found between PAS parameters (PAL and DBEPARL) and electronic properties of a material.[91,92]

The experimental details about the positron annihilation spectroscopy have been given in the relevant chapter.

1.5.2.7 Optical band gap

In my thesis work, the diffuse reflectance method has been used for the determination of band gap of the solid powdered materials. Diffuse reflectance is an excellent sampling tool for powdered crystalline materials. When light shines onto a powder sample, two types of reflections can occur. Some of the light undergoes specular reflection at the powder surface. Diffuse reflection happens when radiation penetrates into the sample and then emerges at all the angles after suffering multiple reflections and refractions by sample particles. A diffuse reflection accessory is designed to minimize the specular component. To estimate optical energy difference between the valence band and conduction band, optical diffuse reflectance measurements have been done with finely ground powder at room temperature using FT-IR Bruker IFS 66V/S spectrometer and Perkin-Elmer Lambda 900, UV/Vis/NIR spectrometer. Absorption (α/Λ) data were estimated from reflectance data using Kubelka−Munk equation:

$$\alpha/\Lambda=(1-R)^2/(2R) \qquad (1.10)$$

where R is the reflectance, α and Λ are the absorption and scattering coefficients, respectively. The energy band gaps were derived from α/Λ vs E (eV) plots.

1.5.2.8 Differential scanning caloremetry (DSC)

DSC is a thermoanalytical technique in which the difference in the amount of heat required to increase the temperature of a sample and reference is measured as a function

of temperature. Both the sample and reference are maintained at nearly the same temperature throughout the experiment. The basic principle underlying this technique is that when the sample undergoes any physical transformation such as phase transition, melting etc, amount of heat flow required to maintain both of them at the same temperature will be different. When the amount of heat required for the sample is lesser than the reference, the process is termed as exothermic. Endothermic process requires a higher amount of heat flow to maintain the temperature. By observing the difference in heat flow between the sample and reference, differential scanning calorimeters are able to measure the amount of heat absorbed or released during such transitions.

DSC data were collected using TA INSTRUMENT Differential Scanning Calorimeter (DSC Q2000) in N_2 atmosphere. The temperature range has been given in the relevant chapter.

1.5.2.9 Hall effect

The Hall effect describes the behavior of the free carriers in a semiconductor when applying an electric as well as a magnetic field along the perpendicular direction. Thus, measurement of the Hall voltage is used to determine the type of charge carrier present in the system, the free carrier density and the carrier mobility. When a current-carrying semiconductor is kept in a magnetic field, the charge carriers of the semiconductor experience a force in a direction perpendicular to both the magnetic field and the current. At equilibrium, a voltage appears at the semiconductor edges. The ratio of the induced voltage to the product of the current density (I/t, where I is applied current and t is sample thickness) and the applied magnetic field (B) is defined as Hall coefficient (R_H) (Equation 1.11 and 1.12).

$$\boldsymbol{R_H = \frac{Vt}{IB}} \tag{1.11}$$

$$\boldsymbol{n_H = \frac{1}{R_H e}} \tag{1.12}$$

where, e is the charge of an electron (1.602×10^{-19} C).

In this thesis Hall measurement has been done in using an ECOPIA HMS 3000 system, PPMS (Physical Property Measurement System, Quantum Design, USA) system

and in a Hall equipment developed by Excel instrument. We have used a four-contact Hall-bar geometry and a varying magnetic field up for the measurements.

1.6 Thermoelectric measurements

1.6.1 Electronic Transport

The power factor of the *zT* expression depends on the product of the Seebeck coefficient and the electrical conductivity. The Seebeck coefficient is the ratio of a resulting electric field gradient to an applied temperature gradient. In a typical measurement, the temperature is varied around a constant average temperature and the slope of the voltage (V) *vs.* temperature difference (ΔT) curve gives the Seebeck coefficient (the slope method) or just $V/\Delta T$ is measured (single point measurement). Either a specific temperature difference is stabilized before each measurement (steady-state), which takes longer, or measurements are conducted continuously while the temperature difference is varied slowly (quasi- steady-state). Little difference was found between steady-state and quasi-steady-state measurements when good thermal and electrical contact is ensured. The employed temperature difference should be kept small, but too small will lead to decreased accuracy. Usually, 4 - 20 K (or 2 - 10 K) is appropriate for the full temperature span.[93]

In the present thesis, temperature dependent Seebeck coefficient measurement has been done using the most popular commercial instruments ULVAC ZEM 3 RIKO using off-axis 4-point geometry under low-pressure helium (He) atmosphere (Figure 1.11a). In the off-axis, 4-point geometry, the thermocouples, and voltage leads are pressed against the sides of the sample (Figure 1.11b). The instrument uses slope method to extract the Seebeck coefficient from steady-state measurements. In the slope method, the measured raw data is corrected for constant offset voltages by using the slope of several (ΔT, V) points for extracting the Seebeck coefficient. The typical sample for measurement has a rectangular shape with the dimensions of ~ 2 mm × 2 mm × 8 mm and ΔT values 5, 10, 15 K have been used in the measurement. The error in the measurement is ~ 5%. In a

typical measurement, the sample is set in a vertical position between the upper and lower electrode blocks in the heating furnace. For temperature dependent measurement, the sample was first heated to a specified temperature using an infrared (IR) furnace. Thereafter a temperature gradient across the sample was created by heating the lower part of it by a heater. Seebeck coefficient is measured by measuring the upper and lower temperatures T_1 and T_2 with the thermocouples pressed against the side of the sample, followed by measurement of voltage (ΔV) between the same wires on one side of the thermocouple.[94]

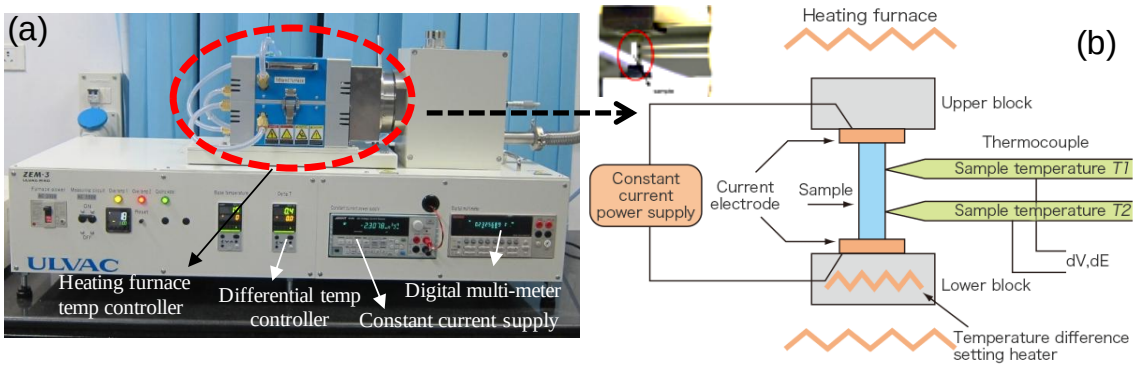

Figure 1.11 *(a) Photograph of sample-chamber in ULVAC-ZEM3 apparatus. (b) Schematic of UlVAC-ZEM 3 four-probe measurement system.*

The electrical conductivity, σ is measured using the four-probe method. Temperature dependent σ has been measured concurrently during Seebeck measurement in ULVAC ZEM 3 RIKO. For the measurement, a constant current I is applied to both ends of the sample to measure the voltage V between the thermocouple. By knowing resistance of sample, R ($R = V/I$), we can calculate σ from resistivity (ρ) of the sample using following equations:

$$\rho = R \times \frac{A}{l} \tag{1.13}$$

$$\sigma = \frac{1}{\rho} \tag{1.14}$$

where A is sample cross section and l is the distance between probes.

1.6.2 Thermal conductivity

The flash diffusivity method most frequently is used for the determination of thermal conductivity (κ_{total}) of material. Non-contact, non-destructive, easy sample preparation, applicability for a wide range of diffusivity values with excellent accuracy and reproducibility makes this method more advantageous than direct method. In the flash diffusivity method, the thermal conductivity is calculated as $\kappa_{total} = DC_p\rho$, where D is thermal diffusivity, ρ is density, and C_p is the constant pressure heat capacity. In this method, the sample is mounted on a carrier system, which is located in a furnace. After the sample reaches a predetermined temperature, a short heat pulse from a pulsed laser is applied to one side of a thin sample, resulting in homogeneous heating. The relative temperature increase on the rear face of the sample is then measured as a function of time by an IR detector. The temperature will rise to a maximum, after which it will decay. The time for the temperature to increase to half-maximum, $t_{1/2}$, is used to calculated the thermal diffusivity using equation 1.15

$$D = 0.1388 \times \frac{l^2}{t_{1/2}} \tag{1.15}$$

where D is thermal diffusivity in cm^2/sec, l is the thickness.[95]

In this thesis, temperature dependent thermal transport measurement has been done using the most popular NETZSCH LFA-457 instrument in N_2 atmosphere (Figure 1.12). Coins with ~ 8 mm diameter and ~ 2 mm thickness were used for all the measurements. The samples were coated with a thin layer of graphite (~ 5 μm) in order to enhance the absorption of laser energy and emission of IR radiation to the detector. It also increases the signal to noise ratio. The error for the κ_{total} measurement is ~ 5%. The samples were placed inside SiC sample holder to mount on carrier system (Figure 1.12c). A Nd-Glass pulsed laser source of wavelength 1054 nm has been used for all the measurement. To measure the increased temperature on the rear face of the sample a liquid N_2 cooled InSb IR detector has been used. The density (ρ) was determined using the dimensions and mass of the sample and C_p, was derived indirectly using a standard sample (pyroceram). The thermal diffusivity data were analyzed using a Cowan model with pulse correction to account for heat losses on the sample faces.

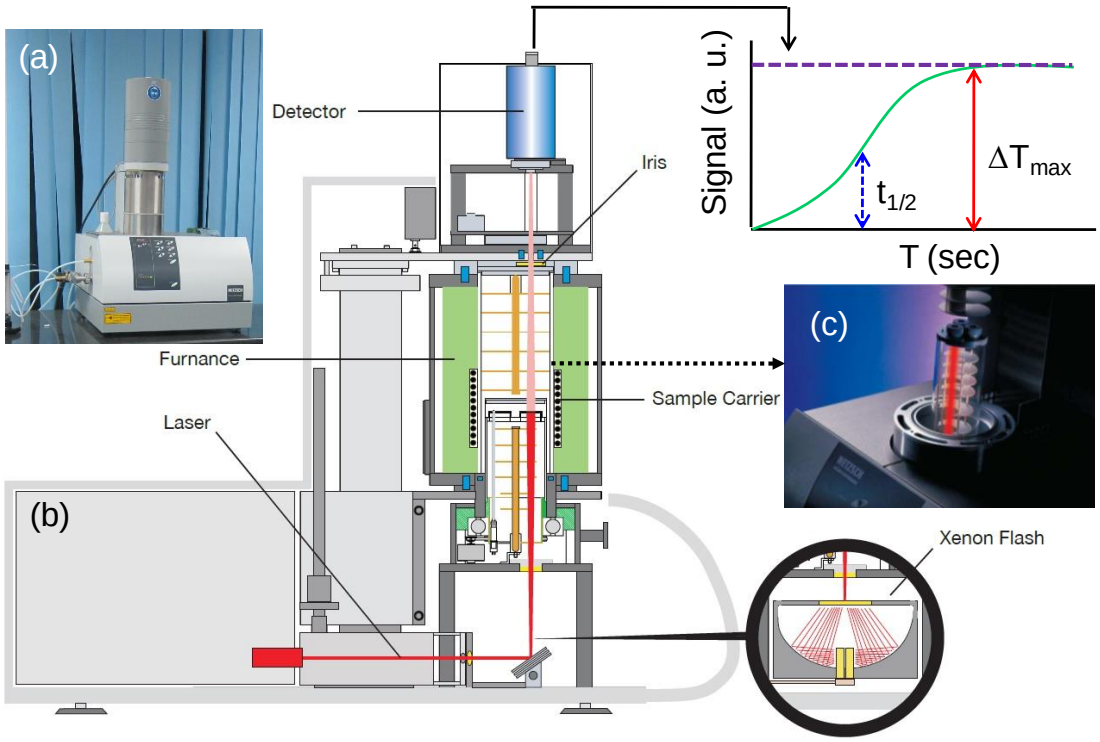

Figure 1.12 *(a) Photograph of NETZSCH LFA-457 instrument. (b) and (c) Schematic of LFA- 457 diffusivity measurement apparatus.*

Lattice thermal conductivity (κ_{lat}) is extracted by subtracting the electronic thermal conductivity (κ_{el}) from total thermal conductivity. κ_{el} is estimated using the Wiedemann Franz law (Equation 1.16).

$$\kappa_{el} = L\sigma T = Lne\mu T \tag{1.16}$$

where, n and μ are carrier concentration and mobility of carrier. Lorenz number, *L* is estimated from the reduced chemical potential and temperature dependent Seebeck coefficient assuming single parabolic band conduction and dominant acoustic phonon scattering of carriers using the following expressions.[96]

$$S = \pm\frac{k_B}{e}\left(\frac{2F_1(\eta)}{F_0(\eta)} - \eta\right) \tag{1.17}$$

$$F_n(\eta) = \int_0^\infty \frac{x^n}{1 + e^{x-\eta}}dx \tag{1.18}$$

$$L = \left(\frac{k_B}{e}\right)^2 \frac{3F_0(\eta)F_2(\eta) - 4F_1(\eta)^2}{F_0(\eta)^2} \quad (1.19)$$

where η is the reduced Fermi energy ($\frac{E_F}{k_B T}$); $F_n(\eta)$ is the nth order Fermi integral $F_n(\eta)$; κ_B, the Boltzmann constant; *e*, the absolute electron charge; *h*, the Planck constant and *x*, the reduced carrier energy. Experimental *S* vs. *T* data is fitted with equation 1.17 to obtain η. *L* is estimated as a function of temperature using the calculated values of $F_n(\eta)$ (Equations 1.18 and 1.19).

1.7 Scope of the thesis

Here, I have synthesized and studied various heavy metal based chalcogenides of varied structures and dimensionality. Apart from the present introductory part, my thesis work is divided into four parts (**2-5**).

In **part 2**, I have discussed the transport properties of main group metal chalcogenides *viz.* $Pb_{0.60}Sn_{0.40}Te$, $TlBiSe_2$. $Pb_{0.60}Sn_{0.40}Te$ and $TlBiSe_2$ are known to be a topological crystalline insulator (TCI) and topological insulator (TI), respectively with insulating bulk and metallic surface states. The fact that these metallic surface states are robust to surface modification or disorder is practically expedient for electronic applications. Due to the vanishingly small bulk band gap, $Pb_{0.60}Sn_{0.40}Te$ has poor thermoelectric properties. Breaking of crystal symmetry can widen the band gap of TCI. While breaking of mirror symmetry in a TCI has been mostly explored by various physical perturbation techniques. In **chapter 1 and 2**, I have tailored the electronic structure and thermoelectric properties of $Pb_{0.60}Sn_{0.40}Te$ by chemical doping. In **chapter 1 and 2**, I have used cation and anion dopant, respectively to break the crystal symmetry locally and open up a bulk electronic band gap in TCI which further improve the thermoelectric performance of $Pb_{0.60}Sn_{0.40}Te$. In **chapter 3**, I have studied the origin of large and linear magnetoresisitance in $Pb_{0.60}Sn_{0.40}Te$. In **chapter 4**, I have investigated the transport properties of *n*-type topological insulator, $TlBiSe_2$. I have found that it

exhibit ultralow lattice thermal conductivity near room temperature that decays close to the theoretical amorphous-limit at elevated temperatures. I have investigated the causes underpinning such intrinsically low lattice thermal conductivity in this compound by probing into the underlying correlation among structure, chemical bonding, and lattice dynamics with the help of synchrotron X-ray pair distribution function (PDF) analysis and low-temperature specific heat capacity.

Part 3 presents the thermoelectric properties of germanium chalcogenides based materials. Germanium chalcogenides have attracted significant attention from the material facet to the device stage owing to their superior thermal and mechanical stability. In **chapter 1**, I have discussed about the effect of aliovalent cation (Sb and Bi) doping in GeTe which decreases the carrier concentration and enhances the valence band degeneracy by increasing the cubic nature of the sample, which collectively boost Seebeck coefficient of GeTe. Significant thermal conductivity reduction was also achieved due to collective phonon scattering from various meso-structured domain variants, twin and inversion boundaries, nano-structured defect layers, and solid solution point defects. Compatibility is another issue for fabrication of any thermoelectric module or device. Better compatibility of any thermoelectric device or module demands both *p*- and *n*-type leg made of same materials. Though there are significant advances of thermoelectric performance of *p*-type Ge-based chalcogenides, hardly any *n*-type Ge-based chalcogenide is known hitherto. High hole carrier concentration in GeTe makes it difficult to change the carrier type from *p*-type to *n*-type. So, new methods/ strategies are required to be developed high-performance *n*-type GeTe based materials. In **chapter 2**, I have stabilized high temperature and high-pressure rocksalt phase of GeSe at ambient conditions by alloying with $AgBiSe_2$. Importantly, we also found that cubic $(GeSe)_{1-x}(AgBiSe_2)_x$ exhibits *n*-type conduction in the measured temperature range, which is extremely rare in Ge-chalcogenide based thermoelectrics.

Part 4 of my thesis is focused on the optimization of the thermoelectric performance of SnTe. SnTe, an environment friendly alternative to lead chalcogenide will have potential impact in thermoelectrics. The major drawbacks of SnTe was its low Seebeck coefficient and high lattice thermal conductivity. I have strived to achieve

minimum κ_{lat} from SnTe. **Chapter 1 and 2** report the reduction of lattice thermal conductivity near to the theoretical minimum limit, κ_{min}, in SnTe. Then, I have tried to improve Seebeck coefficient and power factor *via* carrier concentration optimization and modulation of electronic structure to enhance the thermoelectric performance of SnTe.

Understanding of intrinsic mechanism(s) affecting the phonon transport is not only of fundamental interest but also indispensable to explore and design new materials with ultralow thermal conductivity central to various applications including thermoelectrics. In **part 5**, I have studied thermoelectric properties of two silver chalcogenide based materials *viz.* AgCuTe (**chapter 1**) and $AgSbTe_2$ (**chapter 2 and 3**). $AgSbTe_2$ is considered as promising thermoelectric material for power generation application in the temperature range of 400 – 700 K due to its glass-like anomalously low thermal conductivity (0.6 - 0.7 $Wm^{-1}K^{-1}$). I have found AgCuTe exhibit ultralow lattice thermal conductivity (0.35 $Wm^{-1}K^{-1}$) and a remarkable zT of 1.6 at 670 K. I have investigated the causes underpinning such intrinsically low lattice thermal conductivity in AgCuTe by probing into the underlying correlation among structure, chemical bonding, and lattice dynamics. First-principles DFT calculation reveals the presence of several soft phonon modes in its room-temperature hexagonal phase, which are also evident from low-temperature heat capacity measurement. These phonon modes, dominated by Ag vibrations, soften further with temperature giving a dynamic cation disorder and plausibly driving the superionic transition. **Chapter 2 and 3** report ultrahigh thermoelectric figure of merit of 1.9 and 2.6 at 585 K in *p*-type $AgSb_{1-x}Zn_xTe_2$ and $AgSb_{1-z}M_zTe_2$, respectively *via* simultaneous carrier engineering and reduction of lattice thermal conductivity.

To summarize, in the early work of my thesis (**Part 2**), I have examined the transport properties of topological materials based on heavy metal chalcogenides. Heavy metal chalcogenides present a nice platform for exploring both thermoelectrics and topological insulation. In the rest of my thesis (**Part 3 - 5**), I have strived to understand the correlation between crystal structure, bonding, electronic structure, phonon dispersion and thermoelectric properties of selected heavy metal chalcogenides for future development of thermoelectric modules.

1.8 References

[1] F. Jellinek, *Reactivity of Solids* **1988**, *5*, 323.
[2] A. Meerschaut, L. Guémas, R. Berger, J. Rouxel, *Acta Cryst.* **1979**, *B35*, 1747.
[3] Y. V. Mironov, M. A. Pell, J. A. Ibers, *Angew. Chem. Int. Ed. Engl.* **1996**, *35*, 2854.
[4] in *Transition Metal Sulfides: Chemistry and Catalysis*, eds. T. Weber, R. Prins and R. A. v. Santen, Kluwer Academic Publishers, **1998**.
[5] A. Mar, S. Jobic, J. A. Ibers, *J. Am. Chem. Soc.* **1992**, *114*, 8963.
[6] S. Dehnen, M. Melullis, *Coord. Chem. Rev.* **2007**, *251*, 1259.
[7] M. G. Kanatzidis, *Curr. Opin. Solid State Mater. Sci.* **1997**, *2*, 139.
[8] M. G. Kanatzidis, *Inorg. Chem.* **2017**, *56*, 3158.
[9] M. K. Jana, C. N. R. Rao, *Phil. Trans. R. Soc. A* **2016**, *374*, 20150318.
[10] M. Chhowalla, H. S. Shin, G. Eda, L.-J. Li, K. P. Loh, H. Zhang, *Nat. Chem.* **2013**, *5*, 263.
[11] C. N. R. Rao, U. Maitra, U. V. Waghmare, *Chem. Phys. Lett.* **2014**, *609*, 172.
[12] C. N. R. Rao, H. S. S. Ramakrishna Matte, U. Maitra, *Angew. Chem. Int. Ed.* **2013**, *52*, 13162.
[13] Q. Si, R. Yu, E. Abrahams, *Nat. Rev. Mater*. **2016**, *1*, 16017.
[14] J. R. Sootsman, D. Y. Chung, M. G. Kanatzidis, *Angew. Chem. Int. Ed.* **2009**, *48*, 8616.
[15] Q. H. Wang, K. Kalantar-Zadeh, A. Kis, J. N. Coleman, M. S. Strano, *Nat Nanotechnol.* **2012**, *7*, 699.
[16] G. Eda, T. Fujita, H. Yamaguchi, D. Voiry, M. Chen, M. Chhowalla, *ACS Nano* **2012**, *6*, 7311.
[17] H. Lin, L. Chen, L.-J. Zhou, L.-M. Wu, *J. Am. Chem. Soc*. **2013**, *135*, 12914.
[18] S. Hudgens, B. Johnson, *MRS Bulletin* **2004**, *29*, 829.
[19] S. C. Riha, B. A. Parkinson, A. L. Prieto, *J. Am. Chem. Soc.* **2009**, *131*, 12054.
[20] G. Tan, L. -D. Zhao, M. G. Kanatzidis, *Chem. Rev.* **2016**, *116*, 12123.
[21] C. J. Vineis, A. Shakouri, A. Majumdar, M. G. Kanatzidis, *Adv. Mater.* **2010**, *22*, 3970.
[22] A. Rogalski, *Rep. Prog. Phys.* **2005**, *68*, 2267.
[23] B. Radisavljevic, A. Radenovic, J. Brivio, V. Giacometti, A. Kis, *Nat. Nanotechnol.* **2011**, *6*, 147.
[24] J. J. Cha, J. R. Williams, D. Kong, S. Meister, H. Peng, A. J. Bestwick, P. Gallagher, D. Goldhaber-Gordon, Y. Cui, *Nano Lett.* **2010**, *10*, 1076.
[25] N. Kamaya, K. Homma, Y. Yamakawa, M. Hirayama, R. Kanno, M. Yonemura, T. Kamiyama, Y. Kato, S. Hama, K. Kawamoto, A. Mitsui, *Nat. Mater.* **2011**, *10*, 682.
[26] F. Cheng, J. Liang, Z. Tao, J. Chen, *Adv. Mater*. **2011**, *23*, 1695.
[27] D. Merki, X. Hu, *Energy Environ. Sci.* **2011**, *4*, 3878.
[28] J. M. Caron, J. R. Neilson, D. C. Miller, K. Arpino, A. Llobet, T. M. McQueen, *Phys. Rev. B* **2012**, *85*, 180405.
[29] S. Medvedev, T. M. McQueen, I. A. Troyan, T. Palasyuk, M. I. Eremets, R. J. Cava, S. Naghavi, F. Casper, V. Ksenofontov, G. Wortmann, C. Felser, *Nat. Mater.* **2009**, *8*, 630.

[30] H. S. S. R. Matte, A. Gomathi, A. K. Manna, D. J. Late, R. Datta, S. K. Pati, C. N. R. Rao, *Angew. Chem. Int. Ed.* **2010**, *49*, 4059.
[31] M. König, S. Wiedmann, C. Brüne, A. Roth, H. Buhmann, L. W. Molenkamp, X.-L. Qi, S.-C. Zhang, *Science* **2007**, *318*, 766.
[32] D. Hsieh, Y. Xia, D. Qian, L. Wray, J. H. Dil, F. Meier, J. Osterwalder, L. Patthey, J. G. Checkelsky, N. P. Ong, A. V. Fedorov, H. Lin, A. Bansil, D. Grauer, Y. S. Hor, R. J. Cava, M. Z. Hasan, *Nature* **2009**, *460*, 1101.
[33] D. Kong, Y. Cui, *Nat. Chem.* **2011**, *3*, 845.
[34] L. Müchler, F. Casper, B. Yan, S. Chadov, C. Felser, *Phys. Status Solidi RRL* **2013**, *7*, 91.
[35] Y. Xia, D. Qian, D. Hsieh, L. Wray, A. Pal, H. Lin, A. Bansil, D. Grauer, Y. S. Hor, R. J. Cava, M. Z. Hasan, *Nat. Phys.* **2009**, *5*, 398.
[36] L. Fu, *Phys. Rev. Lett.* **2011**, *106*, 106802.
[37] T. H. Hsieh, H. Lin, J. Liu, W. Duan, A. Bansil, L. Fu, *Nat. Commun.* **2012**, *3*, 982.
[38] M. N. Ali, J. Xiong, S. Flynn, J. Tao, Q. D. Gibson, L. M. Schoop, T. Liang, N. Haldolaarachchige, M. Hirschberger, N. P. Ong, R. J. Cava, *Nature* **2014**, *514*, 205.
[39] M. D. Nielsen, V. Ozolins, J. P. Heremans, *Energy Environ. Sci.* **2013**, *6*, 570.
[40] A. Walsh, D. J. Payne, R. G. Egdell, G. W. Watson, *Chem. Soc. Rev.* **2011**, *40*, 4455.
[41] W. G. Zeier, A. Zevalkink, Z. M. Gibbs, G. Hautier, M. G. Kanatzidis, G. J. Snyder, *Angew. Chem. Int. Ed.* **2016**, *55*, 6826.
[42] E. S. Božin, C. D. Malliakas, P. Souvatzis, T. Proffen, N. A. Spaldin, M. G. Kanatzidis, S. J. L. Billinge, *Science* **2010**, *330*, 1660.
[43] S. N. Guin, A. Chatterjee, D. S. Negi, R. Datta, K. Biswas, *Energy Environ. Sci.* **2013**, *6***,** 2603.
[44] S. Geller, J. H. Wernick, *Acta Crystallogr.* **1959**, *12***,** 46.
[45] T. A. Miller, J. S. Wittenberg, H. Wen, S. Connor, Y. Cui, A. M. Lindenberg, *Nat. Commun.* **2013**, *4***,** 1369.
[46] S. N. Guin, J. Pan, A. Bhowmik, D. Sanyal, U. V. Waghmare, K. Biswas, *J. Am. Chem. Soc.* **2014**, *136***,** 12712.
[47] D. A. Keen, *J. Phys. Condens. Matter*. **2002**, *14***,** R819.
[48] Y. Y. Gurevich and A. K. Ivanov-Shits, Semiconductors and Semimetals, volume *26*, chapter Semiconductor Properties of Superionic Materials. Academic Press, **1988**.
[49] F. Gascoin, A. Maignan, *Chem. Mater*. **2011**, *23*, 2510.
[50] M. Ferhat, J. Nagao, *J. Appl. Phys*. **2000**, *88*, 813.
[51] H. Liu, X. Shi, F. Xu, L. Zhang, W. Zhang, L. Chen, Q. Li, C. Uher, T. Day, G. J. Snyder, *Nat. Mater*. **2012**, *11*, 422.
[52] Y. He, T. Day, T. S. Zhang, H. L. Liu, X. Shi, L. D. Chen, G. J. Snyder, Adv. Mater. **2014**, *26*, 3974.
[53] P. F. Qiu, X. B. Wang, T. S. Zhang, X. Shi, L. D. Chen, *J. Mater. Chem. A* **2015**, *3*, 22454.
[54] K.V. Klitzing, G. Dorda, M. Pepper, *Phys. Rev. Lett.* **1980**, *45*, 494.
[55] S. C. Zhang, X. L. Qi, *Phys. Today* **2010**, *63*, 33.

[56] B. A. Bernevig, T. L. Hughes, S.-C. Zhang, *Science* **2006**, *314*, 1757.
[57] Z. -Y. Ye, H. -X. Deng, H. -Z. Wu, S. -S. Li, S. -H. Wei, J. -W. Luo, *Npj Computat. Mater.* **2015**, *1*, 15001.
[58] Y. L. Chen, J. G. Analytis, J. H. Chu, Z. K. Liu, S. K. Mo, X. L. Qi, H. J. Zhang, D. H. Lu, X. Dai, Z. Fang, S. C. Zhang, I. R. Fisher, Z. Hussain, Z. X. Shen, *Science* **2009**, *325*, 178.
[59] D. Kim, S. Cho, N. P. Butch, P. Syers, K. Kirshenbaum, S. Adam, J. Paglione, M.S. Fuhrer, *Nat. Phys.* **2012**, *8*, 459.
[60] Y. Tanaka, Z. Ren, T. Sato, K. Nakayama, S. Souma, T. Takahashi, K. Segawa, Y. Ando, *Nat. Phys.* **2012**, *8*, 800.
[61] J.P. Heremans, R.J. Cava, N. Samarth, *Nat. Rev. Mater.* **2017**, *2*, 17049.
[62] J.E. Moore, *Nature* **2010**, *464*, 194.
[63] D. Kong, Y. Cui, *Nat. Chem.* **2011**, *3*, 845.
[64] J. Seo, P. Roushan, H. Beidenkopf, Y.S. Hor, R.J. Cava, A. Yazdani, *Nature* **2010**, *466*, 343.
[65] M.Z. Hasan, C.L. Kane, *Rev. Mod. Phys.* **2010**, *82*, 3045
[66] Z. Ringel, Y.E. Kraus, A. Stern, *Phys. Rev. B* **2012**, *86*, 045102.
[67] L. Fu, C.L. Kane, *Phys. Rev. B* **2007**, *76*, 045302.
[68] D. Hsieh, D. Qian, L. Wray, Y. Xia, Y.S. Hor, R.J. Cava, M.Z. Hasan, *Nature* **2008**, *452*, 970.
[69] J. C. Y. Teo, L. Fu, C. L. Kane, *Phys. Rev. B* **2008**, *78*, 045426.
[70] S. -Y. Xu, C. Liu, N. Alidoust, M. Neupane, D. Qian, I. Belopolski, J. D. Denlinger, Y. J. Wang, H. Lin, L. A. Wray, G. Landolt, B. Slomski, J. H. Dil, A. Marcinkova, E. Morosan, Q. Gibson, R. Sankar, F. C. Chou, R. J. Cava, A. Bansil, M. Z. Hasan, *Nat. Commun.* **2012**, *3*, 1192.
[71] P. Dziawa, B.J. Kowalski, K. Dybko, R. Buczko, A. Szczerbakow, M. Szot, E. Lusakowska, T. Balasubramanian, B.M. Wojek, M.H. Berntsen, O. Tjernberg, T. Story, *Nat. Mater.* **2012**, *11*, 1023.
[72] K. Biswas, J. He, I. D. Blum, C.-I. Wu, T. P. Hogan, D. N. Seidman, V. P. Dravid, M. G. Kanatzidis, *Nature*, **2012**, *489*, 414.
[73] J. -F. Li, W. S. Liu, L. -D. Zhao, M. Zhou, *NPG Asia Mater.* **2010**, *2*, 152.
[74] J. P. Heremans, V. Jovovic, E. S. Toberer, A. Saramat, K. Kurosaki, A. Charoenphakdee, S. Yamanaka, G. J. Snyder, *Science* **2008**, *321*, 554.
[75] Y. Pei, X. Shi, A. LaLonde, H. Wang, L. Chen, G. J. Snyder, *Nature* **2011**, *473*, 66.
[76] X. Shi, J. Yang, J. R. Salvador, M. Chi, J. Y. Cho, H. Wang, S. Bai, J. Yang, W. Zhang, L. Chen, *J. Am. Chem. Soc.* **2011**, *133*, 7837.
[77] T. Takabatake, K. Suekuni, T. Nakayama, E. Kaneshita, *Rev. Mod. Phys.* **2014**, *86*, 669.
[78] H. Euchner, S. S. Pailhès, L. T. K. Nguyen, W. Assmus, F. Ritter, A. Haghighirad, Y. Grin, S. Paschen, M. de Boissieu, *Phys. Rev. B* **2012**, *86*, 224303.
[79] S. R. Brown, S. M. Kauzlarich, F. Gascoin, G. J. Snyder, *Chem. Mater.* **2006**, *18*, 1873.
[80] G. J. Snyder, E. S. Toberer, *Nat. Mater.* **2008**, *7*, 105.
[81] S. Wang, J. Yang, L. Wu, P. Wei, J. Yang, W. Zhang, Y. Grin, *Chem. Mater.* **2015**, *27*, 1071.

[82] S. Lee, K. Esfarjani, T. Luo, J. Zhou, Z. Tian, G. Chen, *Nat. Commun.* **2014,** *5*, 3525.
[83] P. Bauer Pereira, I. Sergueev, S. Gorsse, J. Dadda, E. Muller, P. Hermann Raphael, *Phys. Status Solidi (B)* **2013,** *250*, 1300.
[84] X. Cai, J. Wei, *J. Appl. Phys.* **2013,** *114*, 083507.
[85] Z. A. Munir, U. Anselmi-Tamburini, M. Ohyanagi, *J. Mater. Sci.* **2006**, *41*, 763.
[86] http://fuji-sps.sakura.ne.jp/principles/principles.html.
[87] G. Xie, *J. Powder. Metall. Min.* **2013**, *2*, e109.
[88] A. P. Hammersley, S. O. Svensson, M. Hanfland, A. N. Fitch, D. Hausermann, *High Pressure Res.* **1996**, *14*, 235.
[89] X. Qiu, J. W. Thompson, S. J. L. Billinge, *J. Appl. Crystallogr.* **2004,** *37*, 678.
[90] C. L. Farrow, P. Juhas, J. W. Liu, D. Bryndin, E. S. Božin, J. Bloch, P. Th, S. J. L. Billinge, *J. Phys.: Condens. Matter.* **2007**, *19*, 335219.
[91] A. N. Singh, *Appl. Spectrosc. Rev.* **2016**, *51*, 359.
[92] C. Hautojarvi, P. Corbel, *Positron Spectroscopy of Solids,* IOS Press: Amsterdam, The Netherlands, **1995**.
[93] K. A. Borup, J. de Boor, H. Wang, F. Drymiotis, F. Gascoin, X. Shi, L. Chen, M. I. Fedorov, E. Müller, B. B. Iversen, et al., *Energy Environ. Sci.* **2015**, *8*, 423.
[94] ULVAC ZEM3 RIKO, *Seebeck-Coefficient and Eleectric-Resistance-Measuring-System Manual*, **2012**.
[95] NETZSCH, *Operating Instructions LFA 457 Microflash*, **2012**.
[96] K. Biswas, J. He, G. Wang, S. -H. Lo, C. Uher, V. P. Dravid, M. G. Kanatzidis, *Energy Environ. Sci.* **2011**, *4*, 4675.

PART 2

Transport Properties of Topological Materials

Chapter 1

Tailoring of Electronic Structure and Thermoelectric Properties of Topological Crystalline Insulator by Chemical Doping

Chapter 1

Tailoring of Electronic Structure and Thermoelectric Properties of Topological Crystalline Insulator by Chemical Doping†

Summary

Topological crystalline insulators (TCIs) are a new quantum state of matter in which linearly dispersed metallic surface states are protected by crystal mirror symmetry. Due to its vanishingly small bulk band gap, a TCI like $Pb_{0.60}Sn_{0.40}Te$ has poor thermoelectric properties. Breaking of crystal symmetry can widen the band gap of TCI. While breaking of mirror symmetry in a TCI has been mostly explored by various physical perturbation techniques; chemical doping, which may also alter the electronic structure of TCI by perturbing the local mirror symmetry, has not been explored. In the present chapter, we demonstrate that chemical doping (Na and K) in $Pb_{0.60}Sn_{0.40}Te$ locally breaks the crystal symmetry and opens up a bulk electronic band gap, which is confirmed by direct electronic absorption spectroscopy and electronic structure calculations. Cation doping in $Pb_{0.60}Sn_{0.40}Te$ increases p-type carrier concentration and suppresses the bipolar conduction (by widening the band gap), which collectively gives rise to promising zT of ~ 1 at 856 K for $Pb_{0.58}Na_{0.02}Sn_{0.40}Te$ and ~ 1 at 708 K for $Pb_{0.56}K_{0.04}Sn_{0.40}Te$. *Breaking of crystal symmetry by chemical doping widens the bulk band gap in TCI, which uncovers a route to improve TCI for thermoelectric applications.*

†*Papers based on this study have been published in (1) Angew. Chem. Int. Ed., **2015**, 54, 15241; (2) Appl. Phys. Lett., **2016**, 108, 193901*

1.1 Introduction

Topological Crystalline insulators (TCIs) are a new class of topological materials[1-10] which are fundamentally different from conventional topological insulators (TIs)[11-15] in terms of their surface state protection mechanism. TI surface states are protected by time reversal symmetry, while TCI surface states are protected by crystal mirror symmetry.[1-10] Thus, breaking of crystal symmetry can alter the electronic structure of TCI. Recently, crystal symmetry in TCI was broken by various external physical perturbations such as by applying electric field, ferroelectric structural distortion, mechanical strain and thickness engineering.[4-6, 8, 9]

Recently, solid solution composition, $Pb_{0.60}Sn_{0.40}Te$,[16] derived from well known thermoelectric materials, PbTe (E_g ~ 0.29 eV)[17] and SnTe (E_g ~ 0.18 eV, inverted gap),[18] has been discovered to be a TCI by angle-resolved photoemission spectroscopy (ARPES).[16] High-resolution scanning tunnelling microscopy/spectroscopy measurement revealed the crystal symmetry breaking and distortion of the surface of TCI, which resulted in opening of band gap and massive Dirac fermions formation.[5, 9] Furthermore, applying an electric field perpendicular to the thin films of SnTe and $Pb_{1-x}Sn_xSe(Te)$ grown along (001) direction, breaks the mirror symmetry, resulting in opening of a band gap from the edge states.[4] Although chemical doping should alter the electronic structure of TCI by perturbing the local mirror symmetry in the crystal structure, breaking of mirror symmetry in TCI has been mostly explored by physical perturbation techniques so far. Effort to make chemical modification of a TCI has not been reported in literature.

In this chapter, we present the effect of chemical doping (Na and K) on the electronic structure and thermoelectric properties of crystalline ingot of TCI, $Pb_{0.60}Sn_{0.40}Te$. Chemical doping in $Pb_{0.60}Sn_{0.40}Te$ breaks the mirror symmetry locally, resulting in opening of a band gap, which is observed by both direct band gap measurement through electronic absorption spectroscopy and first-principles density functional electronic structure calculations. Na (K) doping increases the *p*-type carrier concentration in $Pb_{0.60}Sn_{0.40}Te$, which pushes the Fermi level deeper into the valence band. Increase in the band gap after chemical doping suppresses the bipolar conduction in $Pb_{0.60}Sn_{0.40}Te$. This pushes the temperature dependent Seebeck maximum to higher temperature and decreases the thermal conductivity further at higher temperature. We

have achieved a maximum thermoelectric figure of merit (zT) of ~ 1 at 856 K for $Pb_{0.58}Sn_{0.40}Na_{0.02}Te$ and ~ 1 at 708 K for $Pb_{0.56}K_{0.04}Sn_{0.40}Te$ sample which is significantly higher compared to undoped TCI, $Pb_{0.60}Sn_{0.40}Te$ (zT ~ 0.38 at 475 K).

1.2. Methods

1.2.1 Reagents

Tin (Sn, Alfa Aesar 99.99+ %), tellurium (Te, Alfa Aesar 99.999+ %), lead (Pb, Alfa Aesar 99.99+ %), sodium (Na, Alfa Aesar 99.95 %) and potassium (K, Sigma Aldrich 99.5 %) were used for synthesis without further purification.

1.2.2 Synthesis

Ingots (~ 10 g) of $Pb_{0.60-x}Na_xSn_{0.40}Te$ (x = 0.0, 0.01, 0.02, 0.03, 0.04) and $Pb_{0.60-x}K_xSn_{0.40}Te$ (x = 0.01, 0.02, 0.03, 0.04) were synthesized by mixing appropriate ratios of high-purity elemental Sn, Pb, Na, K and Te in carbon coated quartz tubes. The tubes were sealed under vacuum (10^{-5} Torr) and slowly heated to 723 K over 12 hrs, then heated up to 1323 K in 5 hrs, soaked for 5 hrs, and cooled down to 1023 K over 2 hrs and soaked for 4 hrs, then slowly cool down to room temperature over a period of 18 hrs.

1.2.3 Powder X-ray diffraction

Powder X-ray diffraction for finely grounded samples were recorded using a Cu K_α (λ = 1.5406 Å) radiation on a Bruker D8 diffractometer.

1.2.4 Band gap measurement

To estimate optical band gap of the as synthesized samples diffuse measurement has been done with finely grounded powder at room temperature using FT-IR Bruker IFS 66V/S spectrometer in a wave-number range 4000-400 cm^{-1} with 2 cm^{-1} resolution and 50 scans. Absorption (α/S) data were calculated from reflectance data using Kubelka-Munk equation: $\alpha/S = (1-R)^2/(2R)$, where R is the reflectance, α and S are the absorption and scattering coefficient, respectively. The energy band gaps were derived from α/S vs E (eV) plot.

1.2.5 Electrical Transport

Electrical conductivity and Seebeck coefficients were measured simultaneously under He atmosphere on a ULVAC-RIKO ZEM-3 instrument system. The typical sample for measurement had a parallelepiped shape with the dimensions of ~ 2×2×8 mm^3. The longer direction coincides with the direction in which the thermal conductivity was measured.

1.2.6 Hall Measurement

To determine carrier concentration, Hall measurements have been carried out using Van der-Pauw method, in a magnetic field of 0.58 T at room temperature (RT) in ECOPIA Hall effect measurement system (HMS 3000).

1.2.7 Thermal transport

Thermal diffusivity, D, was directly measured by using a laser flash diffusivity method in a Netzsch LFA-457. Coins with ~ 8 mm diameter and ~ 2 mm thickness were used in all of the measurements. The temperature dependent heat capacity, C_p, was derived using a standard sample (pyroceram) in LFA-457. The total thermal conductivity, κ_{total}, was calculated using the formula, $\kappa_{total} = DC_p\rho$, where ρ is the density of the sample, measured using the sample dimension and mass. The density of the pellets obtained was in the range ~ 97% of the theoretical density.

1.2.8 Computational details

This part has been done in collaboration with Prof. Umesh V. Waghmare's group in JNCASR. Density Functional Theoretical (DFT) calculations were performed to determine the electronic structure of Na and K substituted $Pb_{10}Sn_6Te_{16}$ using Quantum Espresso package.[19] Effect of the spin-orbit coupling was included in determination of realistic electronic structure since Pb, Sn and Te have high atomic numbers and atomic masses, and the associated relativistic effects cannot be neglected. For this purpose, valence and semicore electronic states of Pb, Sn, Te, Na and K ($5d^{10}\ 6s^2\ 6p^2$, $4d^{10}\ 5s^2\ 5p^2$, $4d^{10}\ 5s^2\ 5p^4$, $3s^1$ and $4s^1$ respectively) were treated with fully relativistic ultra-soft pseudopotentials. The exchange-correlation energy functional was approximated within a Generalized Gradient Approximation (GGA) with parametrized form of Perdew, Burke,

and Erzenhoff (PBE).[20] PbTe and SnTe are known to crystallize in the rocksalt structure with two atoms per unit cell with symmetry given by *Fm3m* space group. To simulate substitutional doping a ($\sqrt{2}$ x $\sqrt{2}$ x 2)a_o supercell of Na (K) doped $Pb_{1-x}Sn_xTe$ containing 32 atoms was used. A 7X7X5 uniform grid of k-points was used in sampling integrations over the Brillouin-zone of the supercell. Energy cutoffs of 40 Ry and 320 Ry were used in truncation of the plane wave basis used for representing wavefunctions and charge density, respectively. Gaussian smearing with a width of 0.003 eV was used to smear the Fermi surface discontinuity in occupation numbers of electronic states. Electronic structure of $Pb_{10}Sn_6Te_{16}$, $Pb_9Sn_6NaTe_{16}$ and $Pb_9Sn_6KTe_{16}$ were determined along high symmetry lines (Γ - X - M - Γ - Z - R - A - Z) in the Brillouin zone, at the experimental lattice constant of 6.388 Å, 6.3745 Å and 6.3953 Å for the pristine $Pb_{10}Sn_6Te_{16}$, ~ 6 % Na and ~ 6 % K doped system, respectively.

1.3. Results & Discussion

Effect of Na doping in $Pb_{0.60}Sn_{0.40}Te$:

Powder X-ray diffraction (PXRD) pattern of $Pb_{0.60-x}Sn_{0.40}Na_xTe$ (x = 0 - 0.04) could be indexed based on the cubic PbTe structure (space group, *Fm-3m*) (see Figure 1.1). No other peak has been observed within the detection limit of the PXRD data, which establishes the formation of single phase materials.

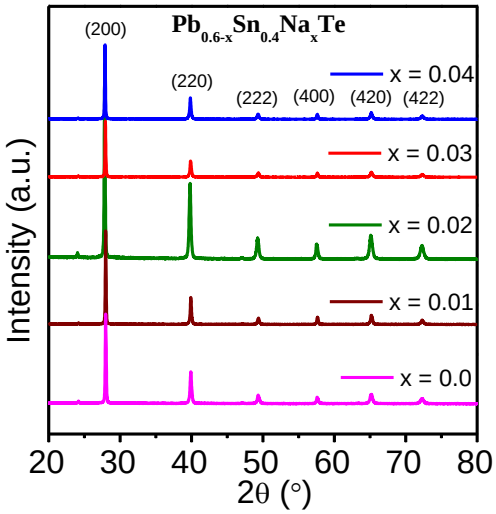

Figure 1.1 *Powder X-ray diffraction pattern for $Pb_{0.60-x}Sn_{0.40}Na_xTe$ (x = 0 - 0.04) samples.*

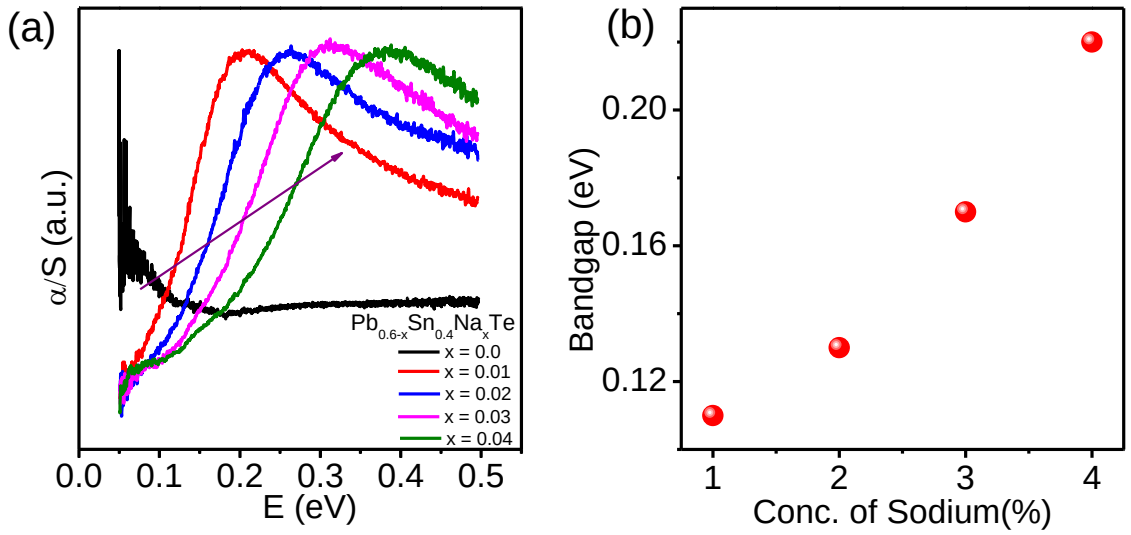

Figure 1.2 *(a) Electronic absorption spectra for $Pb_{0.60-x}Sn_{0.40}Na_xTe$ (x = 0 - 0.04) samples. (b) The variation of band gap with the concentration of Na (x) in $Pb_{0.60-x}Na_xSn_{0.40}Te$ at 300 K.*

Recently, ARPES measurement has confirmed the topological crystalline insulator phase in $Pb_{0.60}Sn_{0.40}Te$ with nearly zero electronic band gap.[16] Previous band inversion model has also predicted zero band gaps in $Pb_{0.60}Sn_{0.40}Te$.[21,22] We have measured the band gap of several samples in the $Pb_{0.60-x}Sn_{0.40}Na_xTe$ (x = 0 - 0.04) composition by infrared (IR) diffuse reflectance spectroscopy. We were not able to resolve the band gap of $Pb_{0.60}Sn_{0.40}Te$ by IR diffuse reflectance spectroscopy as the band gap energy is nearly 0 eV (Figure 1.2a). Interestingly, with increasing sodium doping concentration from 1 to 4 mol% band gap systematically increases from ~ 0.10 eV to ~ 0.22 eV, respectively (see Figure 1.2b). Substitution of Na in place of Pb in $Pb_{0.60}Sn_{0.40}Te$ breaks the crystal mirror symmetry locally, which lifts the protection to the metallic surface states, opening up the band gap.

To understand the effects of Na doping on electronic structure of $Pb_{0.60}Sn_{0.40}Te$ in detail, we determine and compare electronic structure of $Pb_{0.60}Sn_{0.40}Te$ and Na doped (6 mol %) $Pb_{0.60}Sn_{0.40}Te$ (Figure 1.3). We consider two symmetry inequivalent structures of $Pb_9Sn_6NaTe_{16}$, by choosing two inequivalent sets of sites for substitution of Na (Figure 1.3c and e). In the first one (I), the inversion symmetry is retained (1.3c), while the inversion symmetry is broken in the second configuration (II) (1.3e).

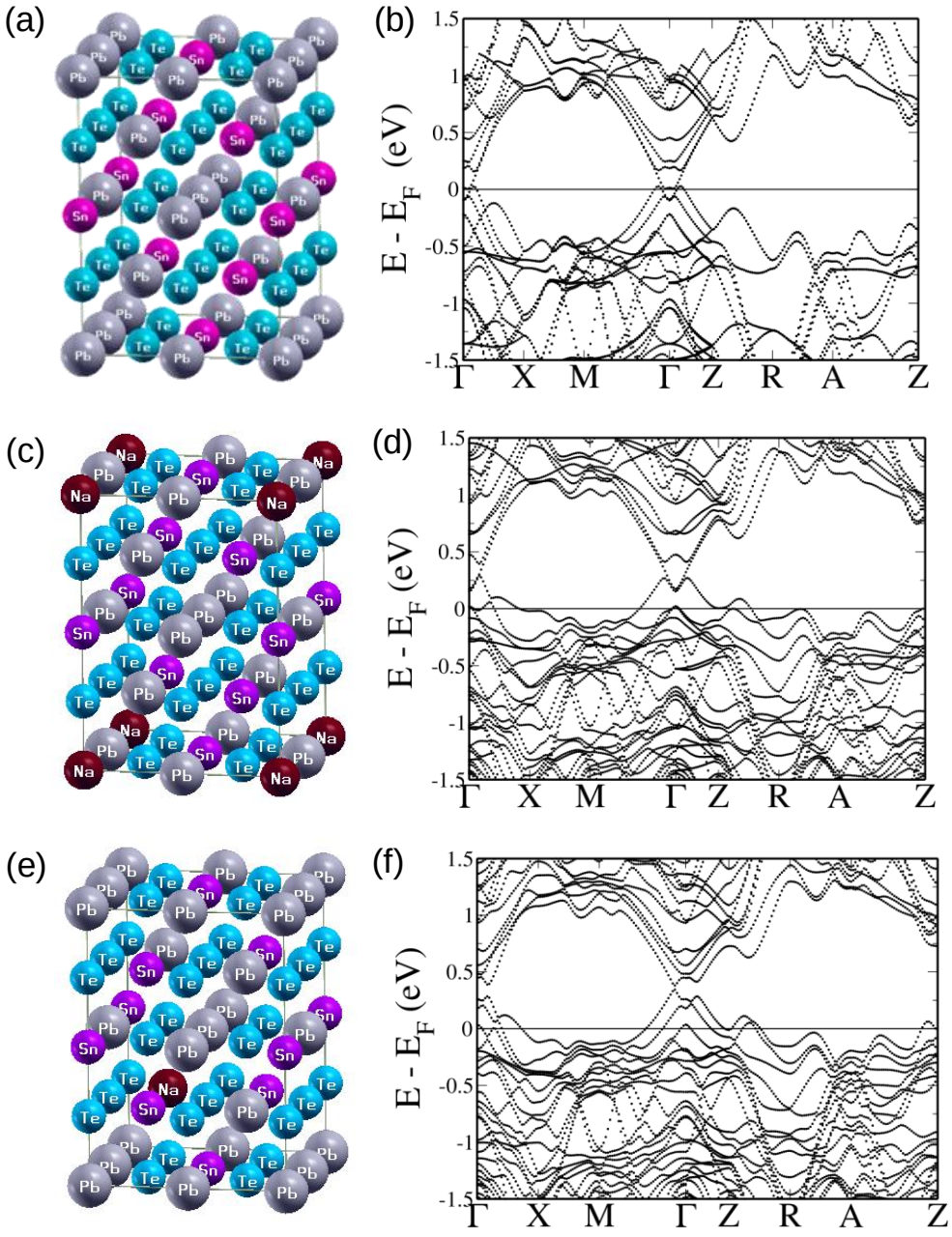

Figure 1.3 *Crystal structure of (a) undoped $Pb_{10}Sn_6Te_{16}$. Crystal structure of $Pb_9Sn_6NaTe_{16}$ (c) with and (e) without retaining mirror symmetry. (b) electronic structure of undoped $Pb_{10}Sn_6Te_{16}$, (d) electronic structure of $Pb_9Sn_6NaTe_{16}$ with retaining mirror symmetry and (e) electronic structure of $Pb_9Sn_6NaTe_{16}$ without retaining mirror symmetry showing opening up of the band gap. All the energies are shifted with respect to the Fermi energy which is equated to zero. The VBM and CBM occurring at L point in the rocksalt cell fold on to the Γ point and the heavy hole valence band appearing along Σ folds on to Z+δ in the case of present 32 atom ($\sqrt{2}$ x $\sqrt{2}$ x 2) tetragonal supercell.*

From the electronic structure of $Pb_{10}Sn_6Te_{16}$, it is clear that the band gap is nearly zero (Figure 1.3b), in agreement with the results of band gap measurements using diffuse reflectance IR spectroscopy. It is also evident that the valence band peaks slightly away from Γ point, giving it a hole-like character, and the conduction band is almost flat barely touching the Fermi level giving it an electron-like character, with high density of states. Upon substitution of Na, the Fermi level shifts to a lower energy such that hole like orbits centred at many low symmetry k points emerge. The contribution of Na atomic orbitals is seen in the higher energy conduction bands (2 eV above the Fermi level). In the centrosymmetric configuration of Na substitution, we see that the electronic structure near Fermi level is symmetric on the two sides of Γ point (M-Γ and Γ -Z) (Figure 1.3d) and the system is almost metallic. In contrast, when Na substitution lowers the structural symmetry a band gap opens up (0.037 eV) (Figure 1.3f), which indeed supports the experimental band gap results. The degeneracy of bands above Fermi level is lifted around Γ point. Visualization of wave functions of states at Γ point and slightly above the Fermi level, reveals primary contribution from *p* orbitals of Pb. We find that the lower symmetry of the configuration (II) results in mixing and reshuffling of bands that open up the gap.

Positive sign of the Hall coefficient suggests *p*-type conduction in $Pb_{0.60-x}Sn_{0.40}Na_xTe$ (x = 0 - 0.04) sample. With increasing of Na doping concentration from 0 to 4 mol%, *p*-type carrier concentration increases from ~ 9.44×10^{18} cm^{-3} to 5.69×10^{19} cm^{-3} (Table 1.1). Each Na^+ substitutes for Pb^{2+}, and from simple valence counting, contributes one extra *p*-type carrier, pushing the Fermi level further inside the valence band of $Pb_{0.60}Sn_{0.40}Te$, which is consistent with the theoretical calculation results.

Opening of electronic band gap and increase in *p*-type carrier concentration by Na doping in $Pb_{0.60}Sn_{0.40}Te$, motivated us to measure the thermoelectric properties in 300-873 K range. Previously, promising thermoelectric properties were evidenced in Na doped PbTe due to the contribution of heavy hole valence band of PbTe in thermoelectric transport at higher temperature. [23,24] Electrical conductivity (σ) of $Pb_{0.60-x}Sn_{0.40}Na_xTe$ (x = 0 - 0.04) samples as a function of temperature is shown in Figure 1.4a. σ for all samples decreases with increasing temperature which is persistent with the behaviour of a degenerate semiconductor. Room temperature σ increases significantly from ~ 1725 S/cm

in $Pb_{0.60}Sn_{0.40}Te$ to ~ 2941 S/cm for 4 mol% Na-doped $Pb_{0.60}Sn_{0.40}Te$ sample, which is mainly attributed to the increase in carrier concentration due to Na doping (Table 1.1).

Table 1.1: Carrier concentration (*p*), carrier mobility (*μ*), electrical conductivity (*σ*), Seebeck coefficient (*S*) and effective mass (*m**) of $Pb_{0.60-x}Sn_{0.40}Na_xTe$ (x = 0 - 0.04) samples at room temperature.

Sample	p (cm^{-3})	μ ($cm^2V^{-1}s^{-1}$)	σ (S/cm)	S (μV/K)	m^*/m_0
$Pb_{0.60}Sn_{0.40}Te$	9.44 x 10^{18}	1148.64	1737.08	61.453	0.13
$Pb_{0.58}Na_{0.02}Sn_{0.40}Te$	1.86 x 10^{19}	812.29	2420.40	39.96	0.14
$Pb_{0.56}Na_{0.04}Sn_{0.40}Te$	5.69 x 10^{19}	320.61	2922.46	45.63	0.36

Temperature dependent σ can be fitted to the equation $\sigma \sim T^{-\delta}$ in order to extract the scattering mechanism, which was earlier employed in Na doped PbTe.[24] Two different values of scattering factor (δ) (δ_1 in low temperature region and δ_2 in the high temperature region) were extracted from ln σ - ln T plot for Na-doped $Pb_{0.60}Sn_{0.40}Te$ samples (Figure 1.4b), which decrease with increasing Na concentration (inset in Figure 1.4b). Two scattering factors denote the contribution from both light hole (L point) and heavy hole (Σ point) valence bands to the temperature dependent electronic transport.[25-27] The smaller δ values in Na doped samples implies a much weaker temperature dependence of hole scattering at higher temperature. The Seebeck coefficient of $Pb_{0.60-x}Sn_{0.40}Na_xTe$ (x = 0 - 0.04) samples as a function of temperature is shown in Figure 1.4c. With increasing temperature, Seebeck coefficient of undoped $Pb_{0.60}Sn_{0.40}Te$ initially increases and reaches a maximum at ~ 550 K, then decreases with further increase in the temperature up to 700 K, which is typical of bipolar conduction in a narrow band gap semiconductor. Na doping in $Pb_{0.60}Sn_{0.40}Te$ opens up a band gap and increases the *p*-type carrier concentration, which suppresses the bipolar conduction and pushes the Seebeck maximum to much higher temperature. All the Na doped samples exhibit lower Seebeck coefficient than the undoped $Pb_{0.60}Sn_{0.40}Te$, which is due to increase in *p*-type carrier concentration at 300 K.

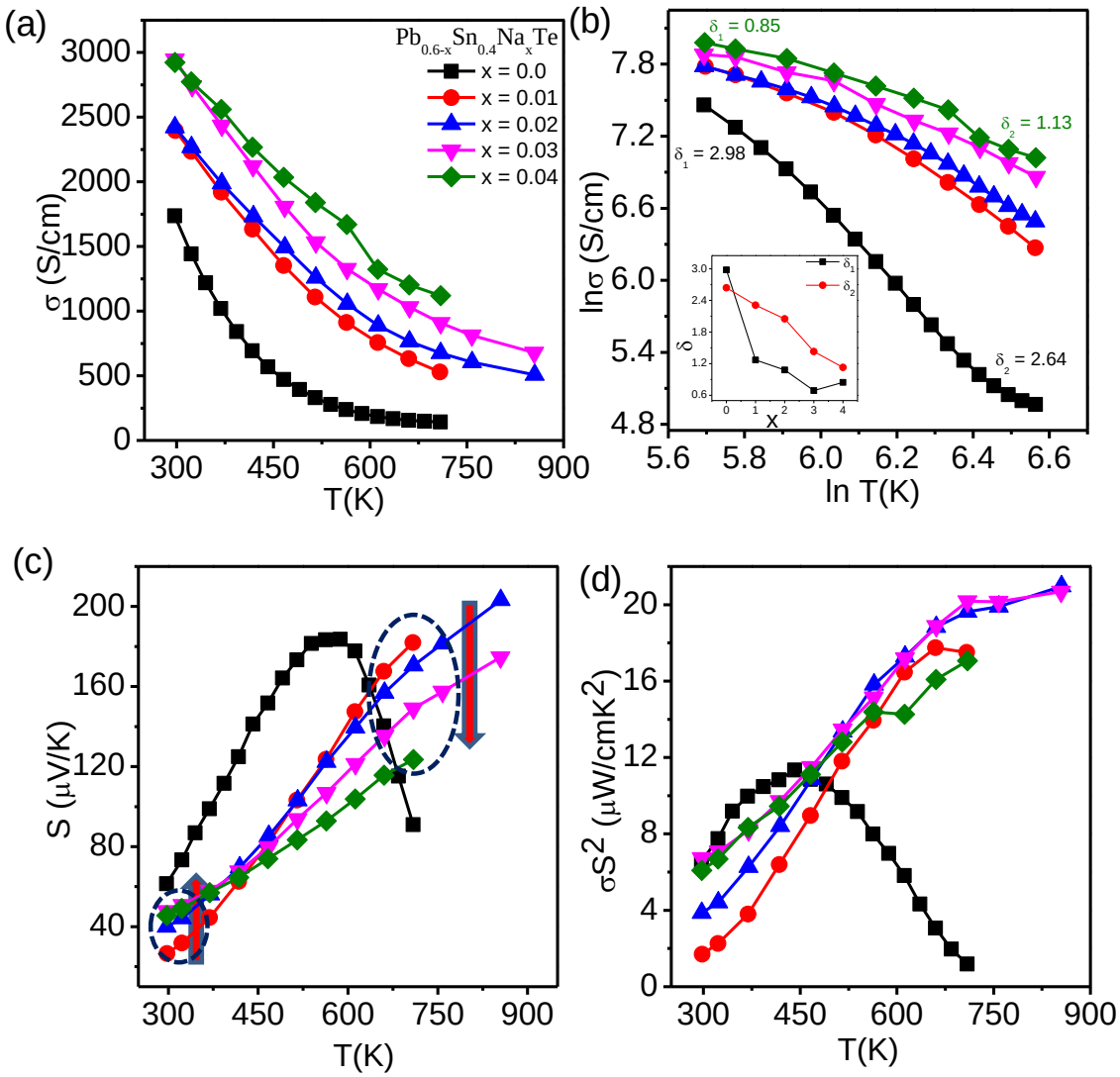

Figure 1.4 *(a) Temperature variations of electrical conductivity (σ) of* $Pb_{0.60-x}Sn_{0.40}Na_xTe$ *(x = 0 - 0.04) samples. (b) lnσ as a function of lnT; inset of (b) shows the Na concentration dependent δ values. Temperature variations of (c) Seebeck coefficient (S) and (d) power factor (σS²) of* $Pb_{0.60-x}Sn_{0.40}Na_xTe$ *(x = 0 - 0.04) samples.*

At 300 K, Seebeck value increases from ~ 27.6 μV/K to ~ 48.5 μV/K with increasing concentration of Na from 1 mol% to 4 mol%, respectively (Figure 1.4c). Interestingly, this trend is reversed at high temperatures. At high temperatures, Seebeck value decreases with increasing Na concentration from 1 mol% to 4 mol% and it passes through a crossover point at ~ 430 K (Figure 1.4c). This can be explained by the two valence band model (light-hole and heavy-hole valence band) of $Pb_{0.60}Sn_{0.40}Te$ (Figure 1.5).[25-28]

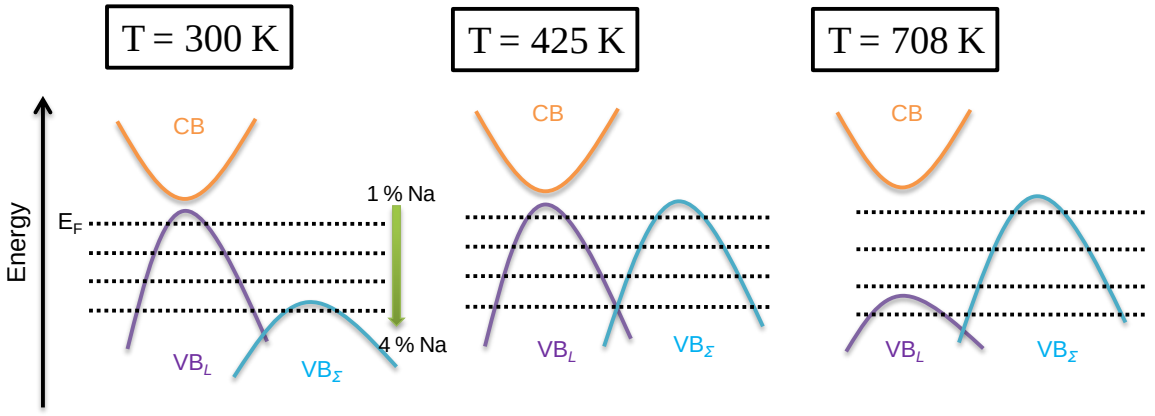

Figure 1.5 *Schematic energy diagram of* $Pb_{0.60-x}Sn_{0.40}Na_xTe$ *with temperature. The relative position of the conduction band (CB), light hole valence band* (VB_L)*, heavy hole valence band* (VB_Σ)*, Fermi level* (E_F) *with addition of sodium with increasing of temperature.*

The energy difference between these two valence band maxima changes with increasing temperature. At about 450 K, the edges of the two valence bands are at approximately the same energy level and above 450 K the main contribution to the transport comes from the heavy-hole valence band.[25-27] At 300 K, increase in Na doping pushes the Fermi level further down into light hole valence band and accesses the heavy hole valence band at high concentration of Na (Figure 1.5), which gives rise to high Seebeck value for 4 mol% Na doped sample compared to 1 mol% Na doped sample. Seebeck coefficient is directly proportional to density of states effective mass (m*).[23,24] In PbTe, heavy hole valence band exhibits higher m* (1.2 - $2m_o$) compared to the light hole valence band ($0.2m_o$).[24] Crossover point at ~ 430 K in *S* vs. *T* data denotes the crossover of light to heavy hole valence band and above 430 K electrical transport in Na-doped $Pb_{0.60}Sn_{0.40}Te$ is mainly contributed by heavy hole valence band (Figure 1.5). At high temperature above 430 K, only heavy hole band contributes to the electronic transport for 1 mol% Na doped sample, whereas both light and heavy hole bands contribute in 4 mol% Na doped sample due lowering of Fermi energy (Figure 1.5). Thus, Seebeck coefficient of 4 mol% Na doped sample is lower compared to 1 mol% Na doped $Pb_{0.60}Sn_{0.40}Te$ at high temperature.

Figure 1.4d presents the power factor (σS^2) of $Pb_{0.60-x}Sn_{0.40}Na_xTe$ (x = 0 - 0.04) samples as a function of temperature. We obtained highest power factor of ~ 21 $\mu Wcm^{-1}K^{-2}$ for 2 mol% Na doped $Pb_{0.60}Sn_{0.40}Te$ sample at ~ 856 K, which is significantly higher compared to that of undoped $Pb_{0.60}Sn_{0.40}Te$ due to increase in both Seebeck coefficient (suppression of bipolar conduction) and electrical conductivity at higher temperatures.

Figure 1.6c represents the temperature dependent total thermal conductivity (κ_{total}) of $Pb_{0.60-x}Sn_{0.40}Na_xTe$ (x = 0 - 0.04) samples. κ_{total} of undoped $Pb_{0.60}Sn_{0.40}Te$ shows significant contribution from bipolar thermal conductivity (κ_{bi}) above 450 K, which is suppressed by Na doping due increase in band gap and carrier concentration (Figure 1.6c). The room temperature κ_{total} value measured for $Pb_{0.58}Sn_{0.40}Na_{0.02}Te$ is ~ 3.10 $Wm^{-1}K^{-1}$ which decreases to ~ 1.83 $Wm^{-1}K^{-1}$ at ~ 873 K. Temperature dependent lattice thermal conductivity, κ_{latt}, values were obtained by subtracting the electronic thermal conductivity, κ_{el}, from the κ_{total}. The κ_{el} were estimated using Wiedemann-Franz law, $\kappa_{el} = L \cdot \sigma \cdot T$; where, L is Lorenz number, σ is electrical conductivity and T is temperature. Temperature dependent L values were extracted based on the fitting of the respective temperature dependent S values (Figure 1.6d) that estimate the reduced chemical potential. The κ_{el} of all the samples are presented in Figure 1.6e. With increasing the Na concentration from 2 to 4 mol%, κ_{latt} value decreases from ~ 1.5 $Wm^{-1}K^{-1}$ to ~ 0.9 $Wm^{-1}K^{-1}$ at 300 K (Figure 1.6f). It was shown earlier in Na doped PbTe that Na doping introduces point defects and nanoscale precipitates, which collectively reduce the κ_{latt}.[24]

We have quantified contribution of κ_{bi} at higher temperature. At high temperature the minority carriers generated in intrinsic excitations not only decrease the Seebeck coefficient, but also increase the thermal conductivity due to the bipolar diffusion. If the bipolar diffusion takes place in semiconductor, generally the lattice thermal conductivity (κ_{latt}) can be overestimated since an extra term (bipolar thermal conductivity, κ_{bi}) contributes to the total thermal conductivity. Therefore, the total thermal conductivity κ_{total} is given by:

$$\kappa_{total} = \kappa_{latt} + \kappa_{el} + \kappa_{bi}$$

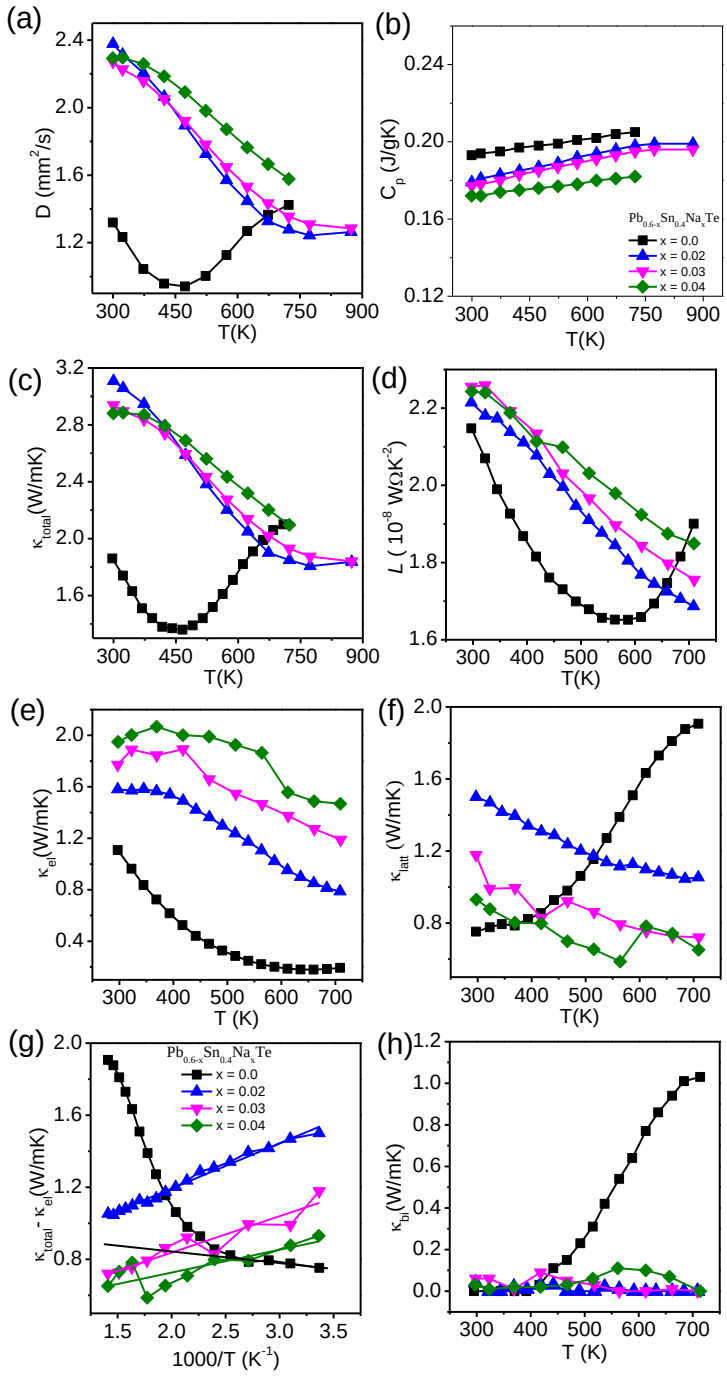

Figure 1.6 *Temperature variations of (a) diffusivity (D), (b) heat capacity (C_p), (c) total thermal conductivity (κ_{total}), (d)Lorenz number (L), (e) electrical thermal conductivity (κ_{el}) and (f) lattice thermal conductivity (κ_{latt}) of $Pb_{0.60-x}Sn_{0.40}Na_xTe$ (x = 0 - 0.04) samples. (g) The difference of total and electronic thermal conductivity (κ_{total} - κ_{el}) as a function of temperature. (h) Bipolar thermal conductivity as a function of temperature for $Pb_{0.60-x}Sn_{0.40}Na_x$ Te (x = 0 - 0.04) samples.*

In order to quantify the contribution of bipolar thermal conductivity (κ_{bi}) at high temperature, the κ_{bi} is separated from the κ_{total} according to the previously reported method.[29] The difference, κ_{total} - κ_{el}, as a function of T^{-1} is shown in Figure 1.6g. Since the acoustic phonon scattering is predominant at low temperatures before bipolar diffusion is significant, κ_{total} - κ_{el} equals to κ_{lat}, which is proportional to T^{-1}. As the temperature is increased to ~ 425 K, the $\kappa_{total} - \kappa_{el}$ starts to gradually deviate from a linear relationship between κ_{lat} and T^{-1} because the bipolar diffusion starts to contribute to the thermal conductivity. Figure 1.6h presents temperature dependent κ_{bi} for $Pb_{0.60-x}Sn_{0.40}Na_xTe$ (x = 0 - 0.04) samples, which indeed indicates that the κ_{bi} significantly decreases with sodium doping.

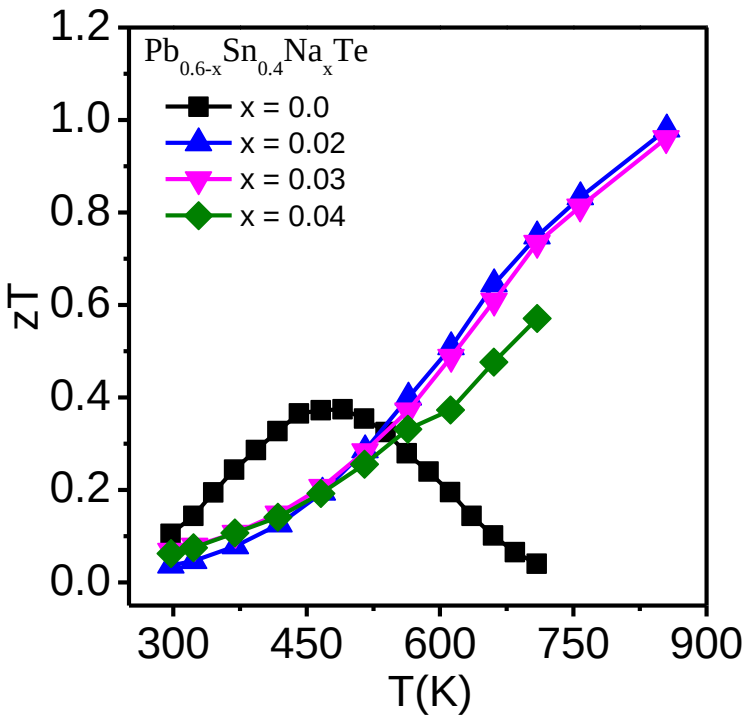

Figure 1.7 *Temperature dependent zT of $Pb_{0.60-x}Sn_{0.40}Na_xTe$ (x = 0 - 0.04) samples.*

Temperature dependence of *zT* of $Pb_{0.60-x}Sn_{0.40}Na_xTe$ (x = 0 - 0.04) samples is shown in Figure 1.7. The highest *zT* value of ~ 1 at 856 K was achieved for $Pb_{0.58}Sn_{0.40}Na_{0.02}Te$ sample which is significantly higher compared to undoped $Pb_{0.60}Sn_{0.40}Te$ sample.

Effect of K doping in $Pb_{0.60}Sn_{0.40}Te$:

To generalize and validate our concept of chemical doping on topological crystalline insulator (TCI), we have further studied the effect of K^+ doping on Pb^{2+} site of $Pb_{0.60}Sn_{0.40}Te$. Potassium (K) is more electro positive than Na, thus K doping in $Pb_{0.6}Sn_{0.4}Te$ expected to further push the Fermi level down in to the heavy hole valence band and modify its electronic structure. Additionally, K doping in PbTe is known to show high thermoelectric performance. We found a significant improvement in the electronic transport in $Pb_{0.60-x}Sn_{0.40}K_xTe$ (x = 0 - 0.04) compared to that of pristine $Pb_{0.60}Sn_{0.40}Te$, resulting in high thermoelectric performance.

$Pb_{0.60-x}K_xSn_{0.40}Te$ (x = 0.0, 0.01, 0.02, 0.03, 0.04) samples were characterized by powder XRD. The PXRD patterns could be indexed on cubic PbTe structure (space group: *Fm-3m*). Figure 1.8a indicates the absence of any other impurity peaks within the detection limit of PXRD.

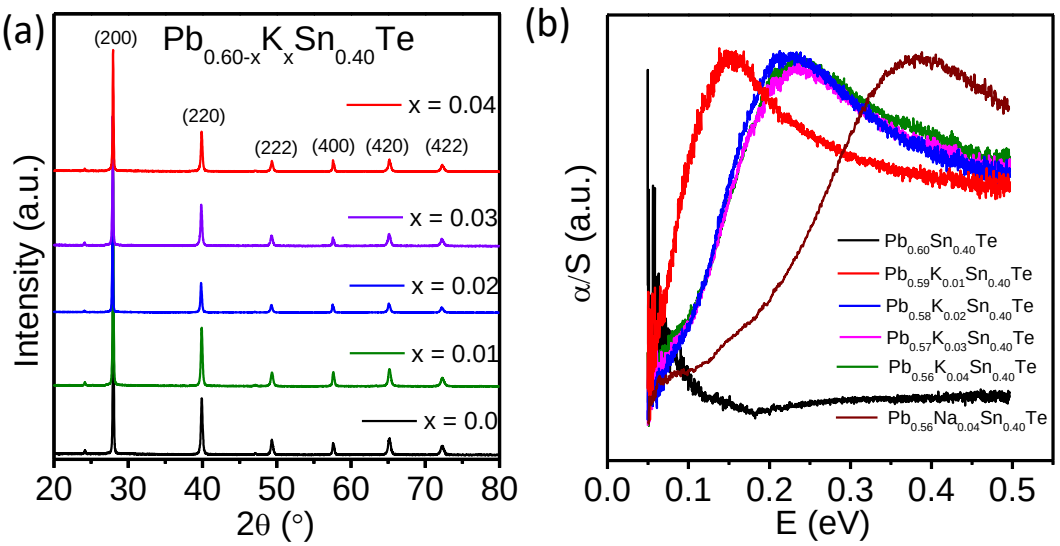

Figure 1.8 *(a) Powder X-ray diffraction pattern and (b) electronic absorption spectra for $Pb_{0.60-x}Sn_{0.40}Na_xTe$ (x = 0-0.04) samples.*

We have measured the optical band gap for $Pb_{0.60-x}K_xSn_{0.40}Te$ (x = 0.0, 0.01, 0.02, 0.03, 0.04) samples by using infrared (IR) diffuse reflectance spectroscopy (Figure 1.8b). Bulk band gap of $Pb_{0.60}Sn_{0.40}Te$ is nearly zero which was confirmed by ARPES measurement previously,[16] thus we were not able to resolve it by diffuse reflectance IR spectroscopy. With increasing potassium doping concentration up to 2 mol% band gap systematically increases to ~ 0.12 eV (Figure 1.8b), which is similar to that of 2 mol% Na

doped $Pb_{0.60}Sn_{0.40}Te$ sample (Figure 1.2a). Substitution of K in place of Pb in $Pb_{0.60}Sn_{0.40}Te$ breaks the crystal mirror symmetry locally, which lifts the protection to the metallic surface states and widens up the band gap. Interestingly, with further addition of K above 2 mol%, there is no change in band gap. 4 mol% K doped sample $Pb_{0.60}Sn_{0.40}Te$ show lower band gap (~ 0.12 eV) compared to that of 4 mol% Na doped sample (~ 0.22 eV) (Figure 2.1.2a).

In order to understand the effects of K doping in electronic structure of TCI, we determine the electronic structure of K doped (6 mol%) $Pb_{0.60}Sn_{0.40}Te$ (Figure 1.9) and compare it with the electronic structure of pristine $Pb_{0.60}Sn_{0.40}Te$ (Figure 1.3b). Density Functional Theoretical (DFT) based calculations were performed to determine the electronic structure using Quantum Espresso package. Two configurations of $Pb_9Sn_6KTe_{16}$ were constructed in which two symmetry in-equivalent sites for substitution of K were chosen as shown in Figure 1.9a (where inversion symmetry is retained) and Figure 1.9c (where the inversion symmetry is broken).

Un-doped $Pb_{10}Sn_6Te_{16}$ has a nearly zero band gap with a valence band having hole-like states, as it peaks slightly away from Γ point, and a conduction band having electron-like states, which is almost flat and barely touches the Fermi level (Figure 1.3b). Upon substitution of K, the Fermi level lowers in energy such that hole-like orbits centred at many low symmetry points emerge, similar to those in the case of Na doping. In the centrosymmetric configuration of K substitution, the electronic structure is symmetric with respect to Γ point on either side (M-Γ and Γ -Z) near Fermi level (Figure 1.9b) and the system is nearly metallic. In contrast, when K doping lowers the structural symmetry, a band gap opens up (0.034 eV, Figure 1.9d), which indeed supports the experimental band gap results. The degeneracy of states around Γ point with energies above Fermi level is also lifted as the symmetry of the system is lowered. *p* orbitals of Pb contribute primarily to the states slightly above the Fermi level at Γ point, as revealed in the isosurfaces of wave functions of these states. The contribution of K atomic orbitals is seen in higher energy conduction bands (2 eV above the Fermi level). Lower symmetry structure (shown in Figure 1.9c) exhibits electronic structure that involves in mixing and reshuffling of bands while opening up the gap.

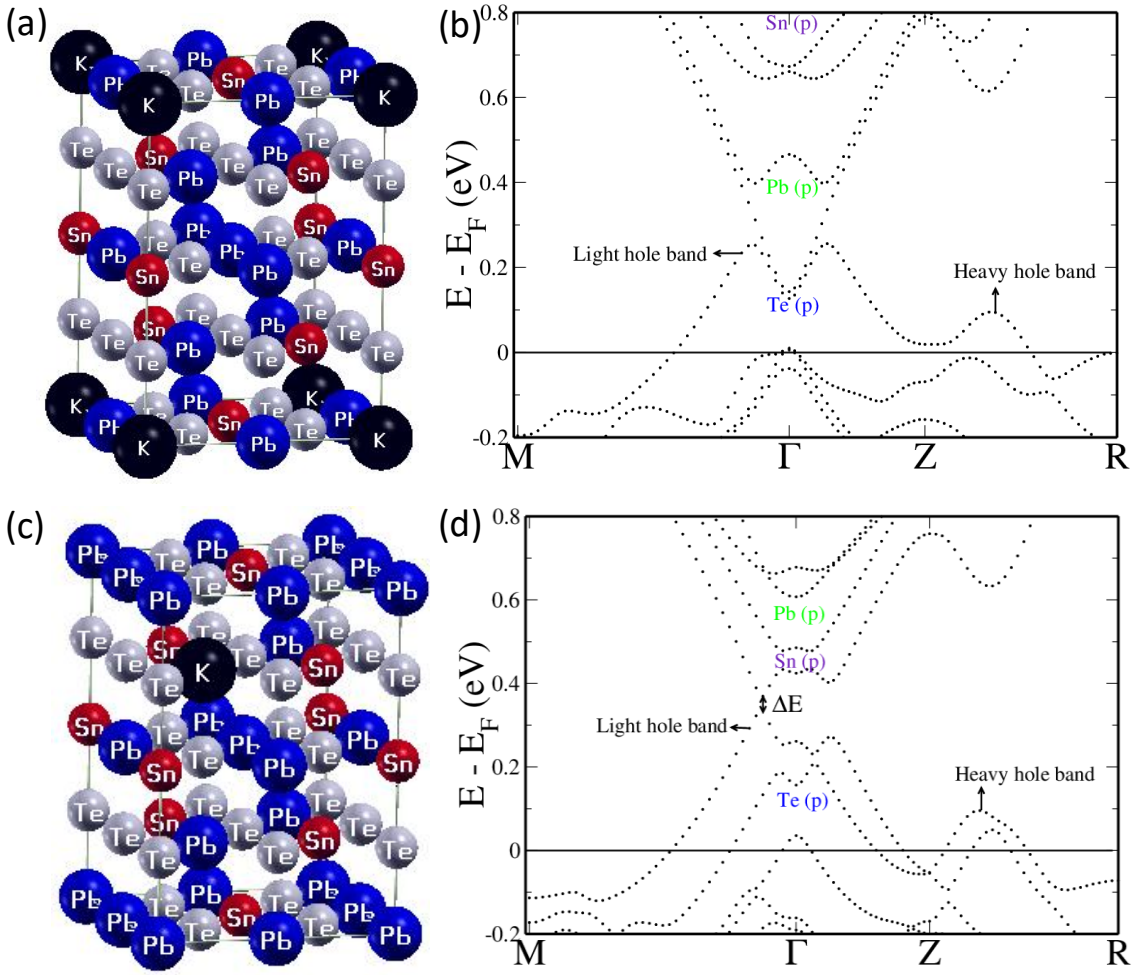

Figure 1.9 *(a) configuration of $Pb_9Sn_6KTe_{16}$ with mirror symmetry and its corresponding electronic structure (b). (c) Configuration of $Pb_9Sn_6KTe_{16}$ without mirror symmetry and its corresponding electronic structure (d) showing opening up of the band gap. All the energies are relative to the Fermi energy, (which is set to zero). The VBM and CBM occurring at L point in the primitive cell of rocksalt structure fold on to the Γ point, and the heavy hole valence band appearing along Σ fold onto Z + δ in the case of the present 32 atom ($\sqrt{2}$ x $\sqrt{2}$ x 2) tetragonal supercell shown in (a) and (c).*

The positive sign of the Hall coefficient suggests *p*-type carriers in $Pb_{0.60-x}K_xSn_{0.40}Te$ (x = 0 – 0.04) samples. K doping increases the carrier concentration from 9.44 x 10^{18} cm^{-3} to 1.87 x 10^{20} cm^{-3} for 0 to 4 mol% substitution of K, respectively (Table 1.2) which is higher than that of 4 mol% Na doped sample (Table 1.1). K doping pushes

the Fermi level further down in energy of the valence band of $Pb_{0.60}Sn_{0.40}Te$, consistent with the results of theoretical calculation.

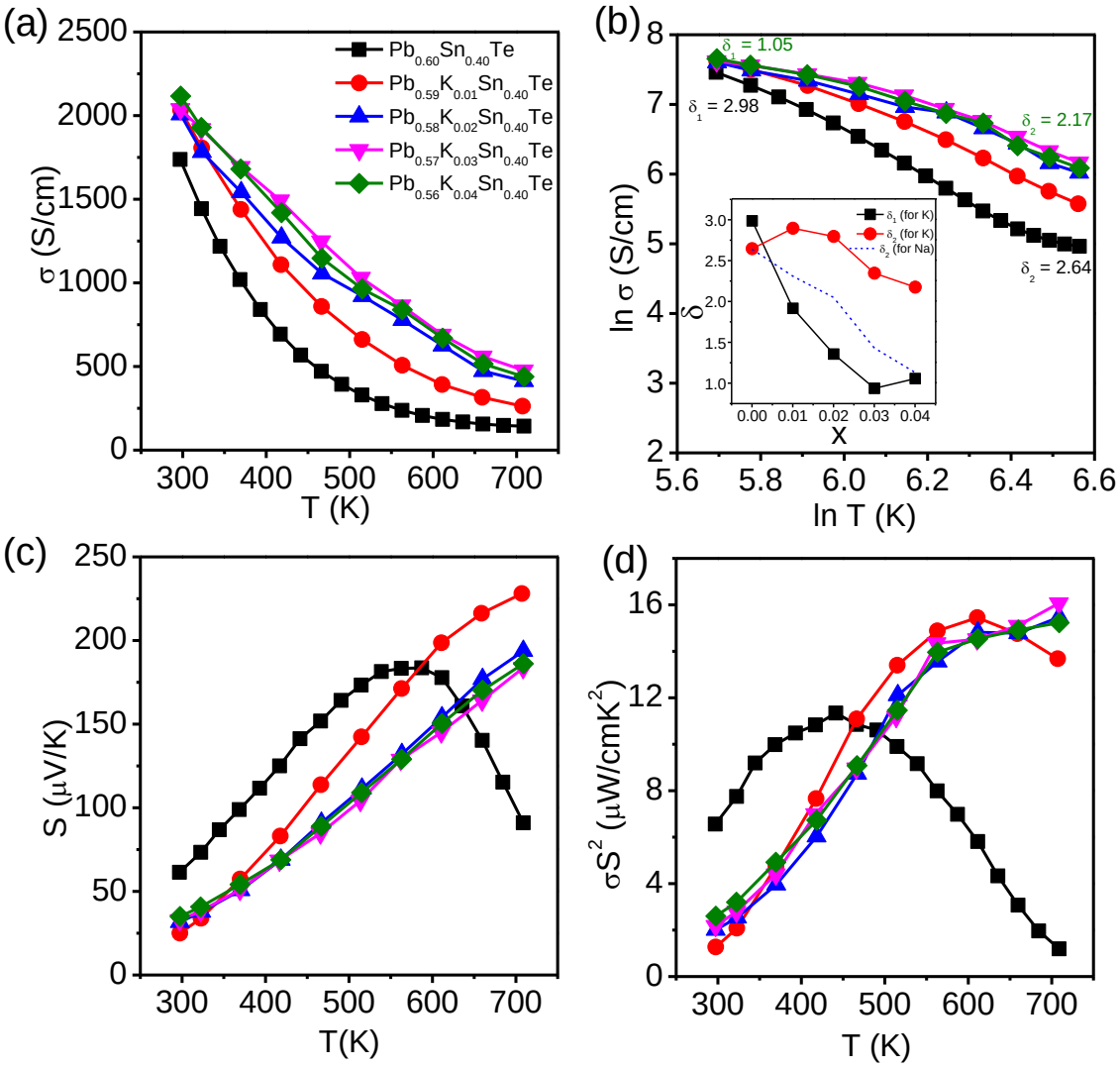

Figure 1.10 *(a) Temperature variations of electrical conductivity (σ) of* $Pb_{0.60-x}Sn_{0.40}K_xTe$ *(x = 0 - 0.04) samples. (b) lnσ as a function of lnT; inset of (b) shows the Na concentration dependent δ values. Temperature variations of (c) Seebeck coefficient (S) and (d) power factor (*σS^2*) of* $Pb_{0.60-x}Sn_{0.40}K_xTe$ *(x = 0 - 0.04) samples.*

Increase in *p*-type carrier concentration and widening of band gap with K doping in $Pb_{0.60}Sn_{0.40}Te$ influenced us to measure its thermoelectric properties in 300 - 725 K range. Figure 1.10a represents temperature dependent electrical conductivity (σ) of $Pb_{0.60-x}K_xSn_{0.40}Te$ (x = 0.0, 0.01, 0.02, 0.03, 0.04) samples. The σ values decrease with increasing temperature for all samples due to their degenerate semiconductor behaviour.

At room temperature, σ value of undoped $Pb_{0.60}Sn_{0.40}Te$ is to be ~ 1725 S/cm, which increases to ~ 2130 S/cm for 4 mol% K doped sample, due to significant increase in the *p*-type carrier concentration. To understand the mechanism of carrier scattering process, temperature dependent σ was fitted to the equation $\sigma \sim T^{-\delta}$, which was earlier employed in Na doped PbTe[24] and $Pb_{0.60}Sn_{0.40}Te$ samples. From ln σ vs. ln T plot of K doped $Pb_{0.60}Sn_{0.40}Te$ (Figure 1.10b), we have extracted two different type of scattering factors (δ) (δ_1 in low temperature region and δ_2 in high temperature region), which decrease with increasing K concentration . Two scattering factors denote the contributions from the both light (L) and heavy hole (Σ) valence bands to the temperature dependent electronic transport. The exponent δ_2 (at high T) is higher for K doped sample compared to Na doped one at higher doping concentration, which indicates that the carrier-carrier scattering is higher in the case of K doped sample than in the Na doped sample. Although K doped samples exhibit higher carrier concentration compared to Na doped sample, K doped samples show lower σ value compared to Na doped samples due to enhanced carrier-carrier scattering which predominantely affects the carrier mobility (Table 1.2).

Table 1.2: Carrier concentration (*p*), electrical conductivity (*σ*) and carrier mobility (*μ*), of $Pb_{0.60-x}Sn_{0.40}K_xTe$ (x = 0.02 and 0.04) samples at room temperature.

Sample	p (cm^{-3})	σ (S/cm)	μ ($cm^2V^{-1}s^{-1}$)
$Pb_{0.58}K_{0.02}Sn_{0.40}Te$	2.99×10^{19}	2006	418
$Pb_{0.56}K_{0.04}Sn_{0.40}Te$	1.87×10^{20}	2166	70

Temperature dependent Seebeck coefficient of $Pb_{0.60-x}K_xSn_{0.40}Te$ (x = 0.0, 0.01, 0.02, 0.03, 0.04) samples is presented in Figure 1.10c. Positive sign of the *S* for all samples indicate *p*-type conduction, which also supports the Hall coefficient data. Undoped $Pb_{0.60}Sn_{0.40}Te$ exhibits bipolar conduction at ~ 550 K, which is evident in the temperature dependent Seebeck measurement. As the temperature increases, bipolar effects degrade Seebeck coefficients, because minority carriers, thermally excited across the band gap, have Seebeck coefficients with the opposite sign, and will offset that of the

majority ones for narrow-band-gap semiconductors. K doping in $Pb_{0.60}Sn_{0.40}Te$ enhances the *p*-type carrier concentration and widens the band gap, which suppresses the bipolar conduction and shifts the Seebeck maximum to a higher temperature. At 300 K, Seebeck coefficients for all the K doped samples are lower than the undoped $Pb_{0.60}Sn_{0.40}Te$ due to enhancement in *p*-type carrier concentration.

At 300 K the Seebeck value of 1 mol% K doped $Pb_{0.6}Sn_{0.4}Te$ is ~ 25 μV/K, which increase with increasing concentration of K (4 mol%) to ~ 35 μV/K. This trend is reversed at high temperatures. At high temperatures, Seebeck coefficient decreases with increasing K concentration from 1 mol% to 4 mol% and it passes through a crossover point at ~ 375 K (Figure 1.10c). This behaviour is similar to Na doped $Pb_{0.60}Sn_{0.40}Te$, but the crossover point there was measured at ~ 430 K (Figure 1.4c). This can be explained by the two valence band model (light-hole and heavy-hole valence band) of $Pb_{0.60}Sn_{0.40}Te$ (Figure 1.11).[24-28] The energy difference between these two valence band maxima changes with increasing temperature. Recently, A. Glatz *et al.* have shown that large Seebeck coefficient can be achieved by tuning chemical potential of the system or due to asymmetry of the density of states (DOS).[30,31] At room temperature, increase in the K doping pushes the Fermi level (chemical potential) further down into light hole valence band and accesses the heavy hole valence band at high concentration of K, which results in higher Seebeck value for 4 mol% K doped sample compared to 1 mol% K doped sample.

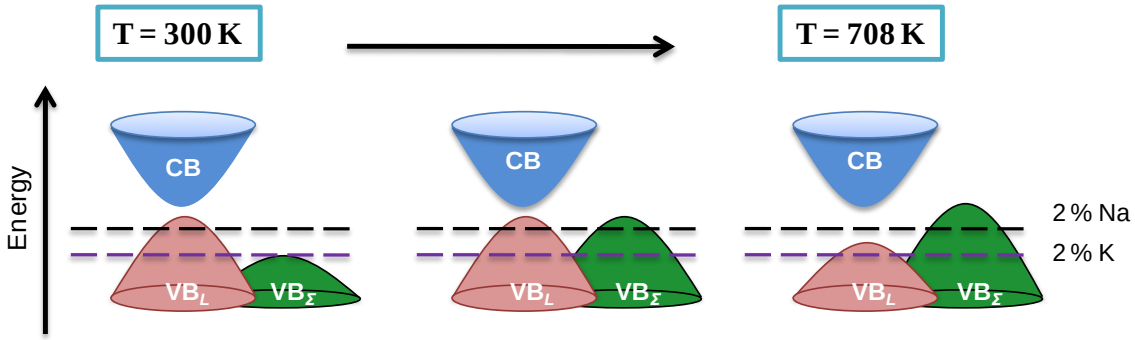

Figure 1.11 *Schematic of the electronic structure of $Pb_{0.6-x}M_{0.02}Sn_{0.4}Te$ (M = Na, K) at different temperatures.*

Crossover point at ~ 375 K in *S* vs. *T* data denotes the crossover of light to heavy hole valence band, and above 375 K electrical transport in K-doped $Pb_{0.60}Sn_{0.40}Te$ is mainly contributed by heavy hole valence band. K doped $Pb_{0.60}Sn_{0.40}Te$ exhibits higher *p*-type carrier concentration (2.99 X 10^{19} cm^{-3}, 2 mol% K) compared to Na doped sample (1.86 X 10^{19} cm^{-3}, 2 mol% Na), thus K doping pushes the Fermi level deeper into the valence band. Thus, access to the heavy hole valence band is faster compared to Na doped sample at high T (Figure 1.11). Thus, the crossover point occurs at lower temperature (~ 375 K) for K doped $Pb_{0.60}Sn_{0.40}Te$ compared to Na doped sample (~ 430 K). At high temperature above 375 K, only heavy hole band contributes to the electronic transport for 1 mol% K doped sample, whereas both light and heavy hole bands contribute in 4 mol% K doped sample due lowering of Fermi energy. Thus, Seebeck coefficient of 4 mol% K doped sample is lower compared to 1 mol% K doped $Pb_{0.6}Sn_{0.4}Te$ at high temperature.

Significant enhancement in the Seebeck coefficient (suppression of bipolar conduction) and electrical conductivity of K doped $Pb_{0.60}Sn_{0.40}Te$ provide high power factor (σS^2) at higher temperatures compared to that of undoped $Pb_{0.60}Sn_{0.40}Te$. We obtained highest power factor of ~ 16.2 $\mu W\ cm^{-1}\ K^{-2}$ for 3 mol% K doped $Pb_{0.60}Sn_{0.40}Te$ sample at ~ 708 K (Figure 1.10d).

Figure 1.12b displays the total thermal conductivity (κ_{total}) of $Pb_{0.60-x}K_xSn_{0.40}Te$ (x = 0 - 0.04) samples. Undoped $Pb_{0.60}Sn_{0.40}Te$ exhibits significant contribution of bipolar thermal conductivity (κ_{bi}) starting at 450 K, which is suppressed by K doping due to widening of band gap and increase in carrier concentration. Typically, κ_{total} measured for $Pb_{0.56}Sn_{0.40}K_{0.04}Te$ is ~ 2.2 $Wm^{-1}K^{-1}$ at 300 K, which decreases to ~1.17 $Wm^{-1}K^{-1}$ at ~ 725 K. Temperature dependent lattice thermal conductivity, (κ_{latt}) values were obtained by subtracting the electronic thermal conductivity, κ_{el}, from the κ_{total} for higher concentration of K (2 - 4 mol%) doped $Pb_{0.60}Sn_{0.40}Te$ which do not show bipolar thermal conduction. The κ_{el} was estimated using Wiedemann-Franz law, $\kappa_{el} = L \cdot \sigma \cdot T$; where, *L* is Lorenz number, σ is electrical conductivity and T is temperature.

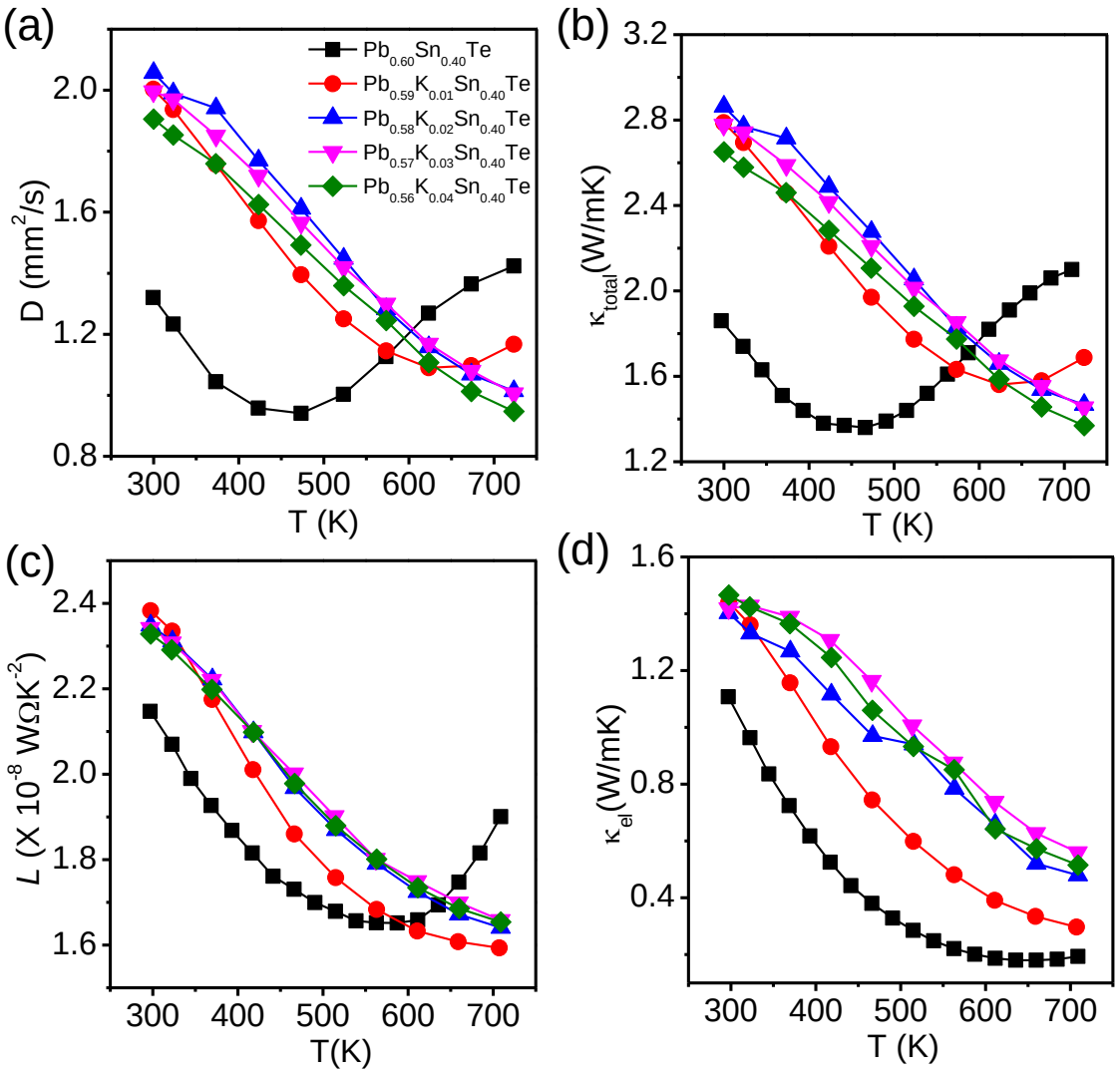

Figure 1.12 *Temperature variations of (a) diffusivity (D), (b) total thermal conductivity (κ_{total}), (c) Lorenz number (L) and (d) electrical thermal conductivity (κ_{el}) of $Pb_{0.60-x}Sn_{0.40}K_xTe$ (x = 0 - 0.04) samples.*

Temperature dependent *L* values were extracted based on the fitting of the respective temperature dependent *S* values (Figure 1.12c) that estimate the reduced chemical potential, which was elaborated elsewhere.[21] The κ_{el} of all the samples are given in Figure 1.12d. K doping affects the phonon transport in $Pb_{0.60}Sn_{0.40}Te$ which is clearly observed from κ_{lat} values which decreases with increasing K concentration (Figure 1.13a). At room temperature, κ_{latt} decreases from 1.10 $Wm^{-1}K^{-1}$ to 0.7 $Wm^{-1}K^{-1}$ with increasing concentrations of K from 1 mol % to 4 mol %, respectively (Figure 1.13a).

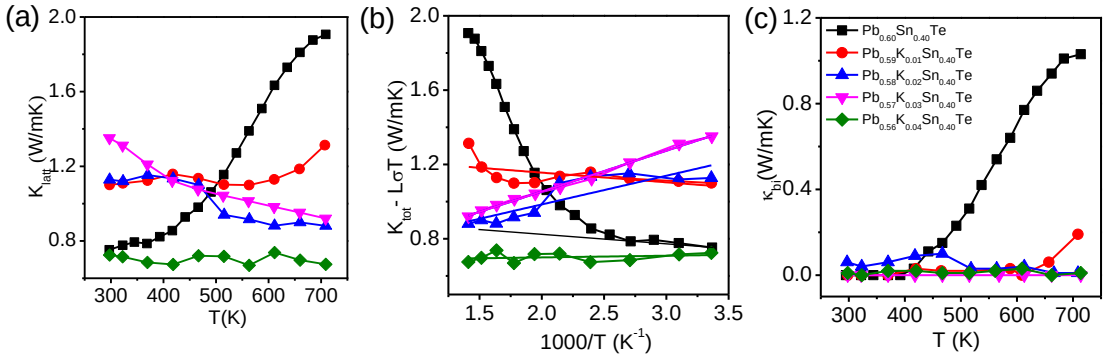

Figure 1.13 *(a) Temperature variations of lattice thermal conductivity (κ_{latt}) of $Pb_{0.60-x}Sn_{0.40}K_xTe$ (x = 0 - 0.04) samples. (b) The difference of total and electronic thermal conductivity (κ_{total} - LσT) and (c) bipolar thermal conductivity as a function of temperature for $Pb_{0.60-x}Sn_{0.40}K_xTe$ (x = 0 - 0.04) samples.*

Previous reports on K or Na doping in PbTe show existence of point defects and nanoscale precipitates, which collectively scatter the phonon and reduces the κ_{latt}.[24] We have observed that phonon thermal conductivity is being almost temperature independent for x = 0.04 in $Pb_{0.60-x}Sn_{0.40}K_xTe$ sample which is similar to the previously reported 2.5% K-doped $PbTe_{0.70}S_{0.30}$ sample.[32] Phonon mean free path of heat carrier depends on both impurity scattering and U scattering. As the temperature increases, the effect of Umklapp (U) scattering increases which reduces lattice thermal conductivity but effect of impurity scattering decreases due to the average thermal speed of heat carrier phonon increases. Thus carrier spends less time near an ionized impurity as they pass. This two scattering factors compensate each other for $Pb_{0.60-x}Sn_{0.40}K_xTe$ (x = 0.04) sample with increasing temperature and we get almost temperature independent behavior of phonon thermal conductivity for the same sample. We have estimated the contribution of κ_{bi} for $Pb_{0.60-x}Sn_{0.40}K_xTe$ (x = 0 - 0.04) samples at higher temperatures in figure 1.13c.

We have estimated the zT of $Pb_{0.60-x}K_xSn_{0.40}Te$ (x = 0 - 0.04) samples by using measured value of σ, S and κ in 300 - 725 K range (Figure 1.14), and find the highest zT ~ 1 for $Pb_{0.56}K_{0.04}Sn_{0.40}Te$ at ~ 708 K which is considerably higher than that of the undoped $Pb_{0.60}Sn_{0.40}Te$ sample. The zT of K doped $Pb_{0.60}Sn_{0.40}Te$ is comparable to the Na doped $Pb_{0.60}Sn_{0.40}Te$ (Figure 1.7).

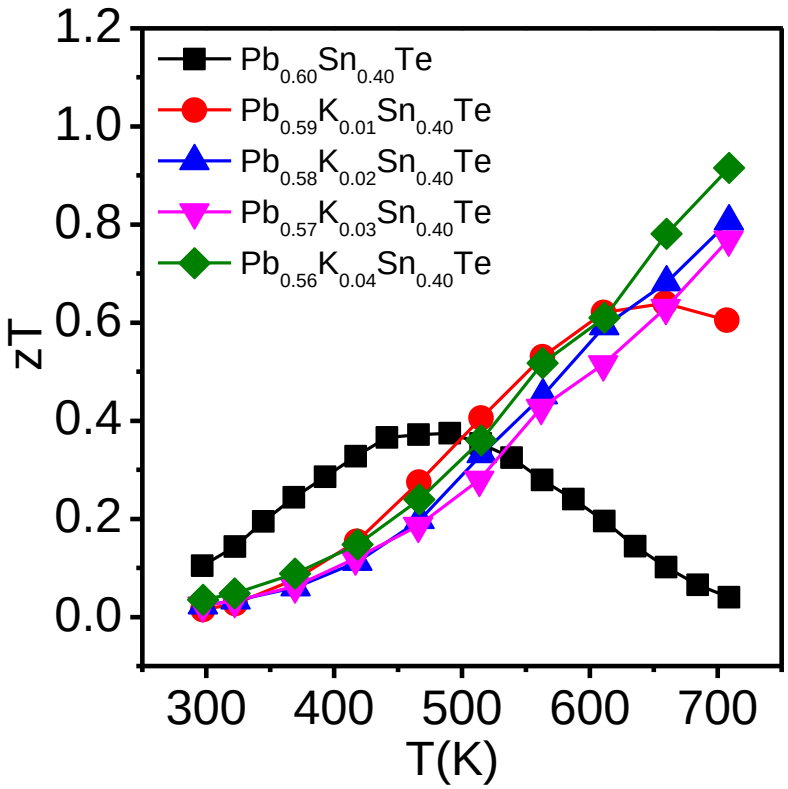

Figure 1.14 *Temperature variations of zT of* $Pb_{0.60-x}Sn_{0.40}K_xTe$ *(x = 0 - 0.04) samples.*

1.4 Conclusions

In conclusion, chemical doping (Na and K) in TCI, $Pb_{0.60}Sn_{0.40}Te$, breaks the crystal mirror symmetry locally, which results in modification of electronic structure and opening of an electronic band gap. Although previous attempts to break the mirror symmetry of TCIs are reported mainly by physical perturbation techniques, present work demonstrates that chemistry has a major role in order to tune the electronic structure and thermoelectric properties of TCIs. Na (K) doping pushes the Fermi level deeper inside the valence band, which accesses the heavy hole valence band, resulting in improvement in Seebeck coefficient. Na (K) doping in $Pb_{0.60}Sn_{0.40}Te$ increases *p*-type carrier concentration and suppresses the bipolar conduction (by opening up a band gap), which collectively improve thermoelectric properties. Our study should motivate chemists to explore various doping strategies, which may modify/tune electronic structure and properties of TCIs.

1.5 References

[1] T. Sato, Y. Tanaka, K. Nakayama, S. Souma, T. Takahashi, S. Sasaki, Z. Ren, A. A. Taskin, K. Segawa, Y. Ando, *Phys. Rev. Lett*. **2013**, *110*, 206804.

[2] Y. Ando, L. Fu, *Ann. Rev. Cond. Mat. Phys.* **2015**, *6*, 361.

[3] L. Fu, *Phys. Rev. Lett*. **2011**, *106*, 106802.

[4] J. Liu, T. H. Hsieh, P. Wei, W. Duan, J. Moodera, L. Fu, *Nat. Mater*. **2014**, *13*, 178.

[5] I. Zeljkovic, Y. Okada, M. Serbyn, R. Sankar, D. Walkup, W. Zhou, J. Liu, G. Chang, Y. J. Wang, M. Z. Hasan, F. Chou, H. Lin, A. Bansil, L. Fu ,V. Madhavan, *Nat. Mater*. **2015**, *14*, 318.

[6] T. Liang, Q. Gibson, J. Xiong, M. Hirchberger, S. P. Koduvayur, R. J. Cava, N. P. Ong, *Nat. Commun.* **2013**, *4*, 2696.

[7] K. V. Mitrofanov, A. V. Kolobov, P. Fons, M. Krbal, J. Tominaga, T. Uruga, *J. Phys.: Condens. Matter.* **2014**, *26*, 475502.

[8] I. Zeljkovic, Y. Okada, C.-Y. Huang, R. Sankar, D.Walkup, W.Zhou, M. Serbyn, F. Chou, W.-F. Tsai, H. Lin, A. Bansil, L. Fu, M. Z. Hasan, V. Madhavan, *Nat. Phys.* **2014**, *10*, 572.

[9] Y. Okada, M. Serbyn, H. Lin, D. Walkup, W. Zhou, C. Dhital, M. Neupane, S. Xu, Y. Jui Wang, R. Sankar, F. Chou, A. Bansil, M. Z. Hasan, S. D. Wilson, L. Fu, V. Madhavan, *Science* **2013**, *341*, 1496.

[10] A. S. Erickson, J. -H. Chu, M. F. Toney, T. H. Geballe, I. R. Fisher, *Phys. Rev. B* **2009**, *79*, 024520.

[11] L. Müchler, H. Zhang, S. Chadov, B. Yan, F. Casper, J. Kübler, S. C. Zhang, C. Felser, *Angew. Chem. Int. Ed.* **2012**, *51*, 7221.

[12] D. Hsieh, D. Qian, L. Wray, Y. Xia, Y. S. Hor, R. J. Cava, M. Z. Hasan, *Nature* **2008**, *452*, 970.

[13] X. L. Qi, S. C. Zhang, *Phys. Today* **2010**, *63*, 33.

[14] M. Z. Hasan, C. L. Kane, *Rev. Mod. Phys.* **2010**, *82*, 3045.

[15] J. Moore, *Nature* **2010**, *464*, 194.

[16] S. Y. Xu, C. Liu, N. Alidoust, M. Neupane, D. Qian, I. Belopolski, J. D. Denlinger, Y. J. Wang, H. Lin, L. A. Wray, G. Landolt, B. Slomski, J. H. Dil, A. Marcinkova, E. Morosan, Q. Gibson, R. Sankar, F. C. Chou, R. J. Cava, A. Bansil, M. Z. Hasan, *Nat. Commun.* **2012**, *3*, 1192.

[17] K. Biswas, J. He, I. D. Blum, C. I. Wu, T. P. Hogan, D. N. Seidman, V. P. Dravid, M. G. Kanatzidis, *Nature* **2012**, *489*, 414.

[18] Q. Zhang, B. Liao, Y. Lan, K. Lukas, W. Liu, K. Esfarjani, C. Opeil, D. Broido, G. Chen, Z. Ren, *Proc. Natl. Acad. Sci. USA* **2013**, *110*, 13261.

[19] P. Giannozzi, S. Baroni, N. Bonini, M. Calandra, R. Car, C. Cavazzoni, D. Ceresoli, G. L. Chiarotti, M. Cococcioni, I. Dabo, A. L. Corso, S. de. Gironkoli, S. Fabris, G. Fratesi, R. Gebauer, U. Gerstmann, C. Gougoussis, A. Kokalj, M. Lazzeri, L. Martin-Samos, N. Marzari, F. Mauri, R. Mazzarello, S. Paolini, A.

Pasquarello, L. Paulatto, C. Sbraccia, S. Scandolo, G. Sclauzero, A. P. Seitsonen, A. Smogunov, P. Umari, R. M. Wentzcovitch, *J. Phys. Condens. Matter*. **2009**, *21*, 395502.

[20] J. P. Perdew, K. Burke, M. Ernzerhof *Phys. Rev. Lett*. **1996**, *77*, 3865.

[21] J. O. Dimmock, I. Melngailis, A. J. Strauss, *Phy. Rev. Lett.* **1966**, *16*, 1193.

[22] X. Gao, M. S. Daw, *Phys. Rev. B* **2008**, *77*, 033103.

[23] Y. Pei, A. LaLonde, S. Iwanaga, G. J. Snyder, *Energy Environ. Sci*. **2011**, *4*, 2085.

[24] J. Androulakis, I. Todorov, D.-Y. Chung, S. Ballikaya, G. Wang, C. Uher, M. Kanatzidis, *Phys. Rev. B* **2010**, *82*, 115209.

[25] R. S. Allgaier, *J. Appl. Phys.* **1961**, *32*, 2185.

[26] R. S. Allgaier, B. B. Houston, *J. Appl. Phys.* **1966**, *37*, 302.

[27] S. V. Airapetyants, M. N. Vinogradova, I. N. Dubrovskaya, N. V. Kolomoets, I. M. Rudnik, *Sov. Phys. Solid State* **1966**, *8*, 1069.

[28] Y. Pei, X. Shi, A. LaLonde, H. Wang, L. Chen, G. J. Snyder, *Nature* **2011**, *473*, 66.

[29] L. D. Zhao, H. J. Wu, S. Q. Hao, C. I. Wu, X. Y. Zhou, K. Biswas, J. Q. He, T. P. Hogan, C. Uher, C. Wolverton, V. P. Dravid and M. G. Kanatzidis, *Energy Environ. Sci.* **2013**, *6*, 3346.

[30] A. Glatz, I. S. Beloborodov, *Europhys. Lett.* **2009**, *87*, 57009.

[31] A. Glatz, I. S. Beloborodov, *Phys. Rev. B* **2009**, *80*, 245440.

[32] H. J. Wu, L. –D. Zhao, F. S. Zheng, D. Wu, Y. L. Pei, X. Tong, M. G. Kanatzidis, J. Q. He, *Nat. Commun*. **2014**, *5*, 4515.

Chapter 2

Enhanced Thermoelectric Performance in *n*-type $Pb_{0.60}Sn_{0.40}Te$ by Simultaneous Tuning of the Band Gap and Chemical Potential

Chapter 2

Enhanced Thermoelectric Performance in *n*-type $Pb_{0.60}Sn_{0.40}Te$ by Simultaneous Tuning of the Band Gap and Chemical Potential[†]

Summary

Tailoring of the electronic structure of the topological crystalline insulators (TCIs) is necessary to enhance its thermoelectric (TE) performance. p-type chemical doping in TCI like $Pb_{0.60}Sn_{0.40}Te$ exhibited significantly high TE figure of merit (zT), but n-type $Pb_{0.60}Sn_{0.40}Te$ is still elusive, which is urgently needed for the thermoelectric application. In this chapter, we present enhanced thermoelectric performance in n-type iodine (I) doped $Pb_{0.60}Sn_{0.40}Te$. Aliovalent I^- doping in Te^{2-} sublattice of $Pb_{0.60}Sn_{0.40}Te$ widens the band gap via breaking of local crystal mirror symmetry, which decreases the bipolar conduction and pushes the Seebeck maxima towards high temperatures. Iodine doping in $Pb_{0.60}Sn_{0.40}Te$ significantly increases the n-type carrier concentration and move the chemical potential (Fermi level) inside the conduction band of $Pb_{0.60}Sn_{0.40}Te$, which improve the electrical transport properties. We report a maximum zT of 1.05 in the n-type $Pb_{0.60}Sn_{0.40}Te_{0.995}I_{0.005}$ sample at 620 K which is 483 % higher than pristine $Pb_{0.60}Sn_{0.40}Te$.

[†]*Paper based on this study has been published in J. Mater. Chem. A* ***2018****, 6, 24216.*

2.1 Introduction

Pristine $Pb_{0.60}Sn_{0.40}Te$ is not a good thermoelectric materials because of its vanishingly small energy gap between valence and conduction band. An energy gap can be opened at Dirac point in TCI by breaking of the crystal mirror symmetry as discussed in chapter 2.1.

Importantly, the thermoelectric device demands both *p*-type and *n*-type semiconductor.[1] Although *p*-type TCI (like $Pb_{0.60}Sn_{0.40}Te$) shows significantly high thermoelectric performance,[2-5] the search for effective *n*-type $Pb_{0.60}Sn_{0.40}Te$ is still elusive. Unearthing of such a material having characteristic compatibility and performance like its *p*-type counterpart would be a key for the practical applications.

This chapter demonstrate the significantly enhanced thermoelectric properties of a series of 0.5-3 mol% iodine (I)-doped $Pb_{0.60}Sn_{0.40}Te$ in the 300-723 K range. Iodine acts as a donor dopant in $Pb_{0.60}Sn_{0.40}Te$ and alters its carrier type from *p* to *n*, thereby enhances thermoelectric performance. I^- chemically dope in the Te^{2-} sublattice and break the mirror symmetry locally in the crystal structure, resulting in widening the band gap which is confirmed *via* experimental band gap measurement by diffuse reflectance spectroscopy. Iodine doping increases the carrier concentration from 9.44×10^{18} cm^{-3} for $Pb_{0.60}Sn_{0.40}Te$ to 4.9×10^{19} cm^{-3} for $Pb_{0.60}Sn_{0.40}Te_{0.97}I_{0.03}$ sample which shifts the Fermi level into the conduction band. The widening in band gap alongwith high *n*-type carrier concentration in I-doped $Pb_{0.60}Sn_{0.40}Te$ suppresses the bipolar conduction which (a) shifts Seebeck maxima at a higher temperature and (b) decreases the thermal conductivity. We present a notable enhanced thermoelectric figure of merit, zT of 1.05 for *n*-type $Pb_{0.60}Sn_{0.40}Te_{0.995}I_{0.005}$ sample which is significantly higher (483 %) compared with that of the undoped $Pb_{0.60}Sn_{0.40}Te$ sample at 620 K.

2.2 Methods

2.2.1 Reagents

Tin (Sn, Alfa Aesar 99.99+ %), tellurium (Te, Alfa Aesar 99.999+ %), lead (Pb, Alfa Aesar 99.99+ %) and tellurium iodide (TeI_4, Alfa Aesar 99%) were used for synthesis without further purification.

2.2.2 Synthesis

Ingots (~ 10 g) of $Pb_{0.60}Sn_{0.40}Te_{1-x}I_x$ (x = 0.0, 0.005, 0.01, 0.02, 0.03) were synthesized by mixing stoichiometric ratios of high-purity elemental Sn, Pb, Te and TeI_4 in quartz tubes. The tubes were sealed under vacuum (10^{-5} Torr) and slowly heated to 723 K over 12 h (58 K/hr), then heated up to 1323 K in 5 h (120 K/hr), annealed for 5 h (0 K/hr), and cooled down to 1023 K over 2 h (150 K/hr) and annealed for 4 h (0 K/hr), then slowly cool down to room temperature over a period of 18 h (55 K/hr).

In order to achieve homogeneity in the samples without any surface crack or defects, we have taken two step annealing strategies. First, we have given 5 hrs annealing time at 1323 K during synthesis and shaken the tubes several times and secondly, we have given 4 hrs annealing time at 1023 K to get good quality (high density, ~ 97 %) ingot samples. We have executed thermoelectric measurements for all samples as synthesized ingot from melt.

2.2.3 Powder X-ray diffraction

Powder X-ray diffraction for finely ground samples were recorded using a Cu K_α (λ = 1.5406 Å) radiation on a Bruker D8 diffractometer.

2.2.4 Band gap measurement

To estimate optical band gap of the as synthesized samples, diffuse reflectance measurement has been done with finely ground powder at room temperature using FT-IR Bruker IFS 66V/S spectrometer in wave number range 4000-400 cm^{-1} with 2 cm^{-1} resolution and 50 scans. Absorption (α/ S) data were calculated from reflectance data using Kubelka-Munk equation: $\alpha/S= (1-R)^2/(2R)$, where R is the reflectance, α and S are the absorption and scattering coefficient, respectively. The energy band gaps were derived from α/S vs E_g (eV) plot.

2.2.5 Electrical transport

Electrical conductivity and Seebeck coefficients were measured simultaneously in He atmosphere from room temperature to 723 K using a ULVAC-RIKO ZEM-3 instrument system. The specimens used for this have typical parallelepiped shape with dimensions of ~ 2×2×8 mm^3. The longer direction coincides with the direction in which the thermal conductivity was measured.

2.2.6 Hall measurement

For determining the carrier concentrations, Hall measurements were carried out on the same rectangular specimens used for electrical transport measurement in four-contact geometry up to a magnetic field of 0.57 T at room-temperature using custom-built equipment developed by Excel Instruments.

2.2.7 Thermal transport

Thermal diffusivity, D, was directly measured in the range 300–723 K by laser flash diffusivity method using a Netzsch LFA-457 instrument. Coins with ~ 8 mm diameter and ~ 2 mm thickness were used for these thermal diffusivity measurements. The temperature dependent heat capacity, C_p, was derived using a standard sample (pyroceram) in LFA-457. Then, the total thermal conductivity, κ_{total}, was calculated using the formula, $\kappa_{total} = DC_p\rho$, where ρ is the density of the sample. C_p of pristine $Pb_{0.60}Sn_{0.40}Te$ was used for iodine doped $Pb_{0.60}Sn_{0.40}Te$ samples also. The measured density of the samples was found to be in the range of ~ 97% of the theoretically expected density.

2.2.8 Kelvin probe force microscopy

To investigate the relative position of the Fermi level, Kelvin probe force microscopy has been done with coins (~ 8 mm diameter and ~ 1 mm thickness) at room temperature using Bruker's dimension icon atomic force microscopy (AFM) system. A Pt-Ir coated Si cantilever (SCM-PIT-V2 from Bruker) with 25 nm radius was used for KPFM measurement.

2.3 Results & Discussion

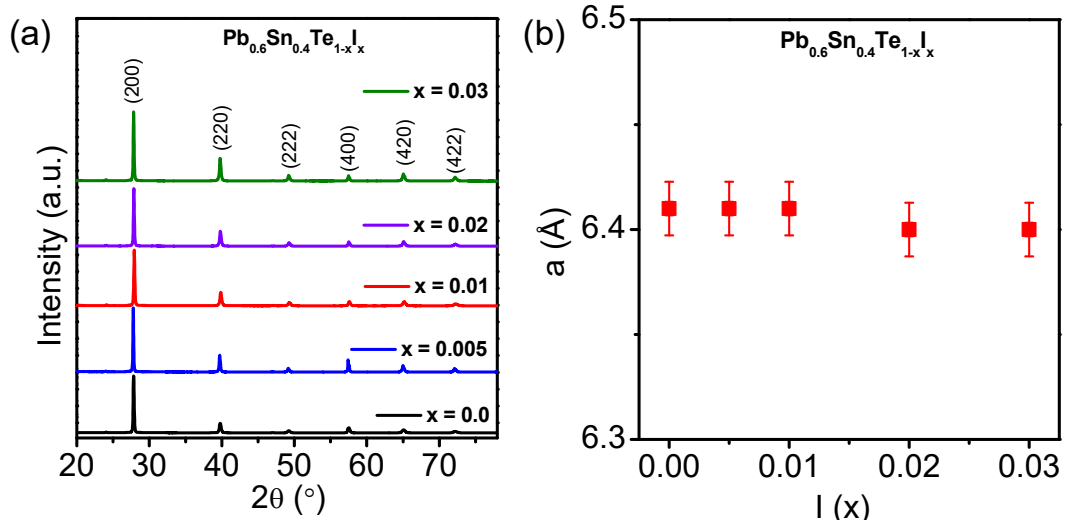

Figure 2.1 *(a) Powder X-ray diffraction (PXRD) and (b) variation of lattice parameter of* $Pb_{0.60}Sn_{0.40}Te_{1-x}I_x$ *(x = 0, 0.005, 0.01, 0.02 and 0.03) samples.*

Figure 2.1a affirms the formation of single phase materials within the detection limit of PXRD and measured PXRD patterns could be indexed based on the cubic PbTe structure (space group, *Fm-3m*). It is worth noting that lattice parameter almost remains unchanged after iodine substitution in $Pb_{0.60}Sn_{0.40}Te$ owing to the similar ionic radii of I^- (206 pm) and Te^{2-} (207 pm) and form a complete solid solution with the $Pb_{0.60}Sn_{0.40}Te$ system (Figure 2.1b).

Figure 2.2a represents optical absorption spectra of $Pb_{0.60}Sn_{0.40}Te_{1-x}I_x$ (x = 0.0, 0.005, 0.01 0.02 and 0.03) samples. We were not able to resolve the bulk band gap of $Pb_{0.60}Sn_{0.40}Te$ by diffuse reflectance spectroscopy due to its nearly zero band gap.[2] The systematic increase in band gap is observed for iodine doped $Pb_{0.60}Sn_{0.40}Te$ samples (Figure 2.2a) which is consistent with that of previously reported Na/K/Se doped $Pb_{0.60}Sn_{0.40}Te$ sample.[2,3,6] Topological crystalline insulator, $Pb_{0.60}Sn_{0.40}Te$ possesses inversion symmetry (mirror symmetry) in its crystal structure. In chapter 1, we have shown that addition of *p*-type dopant (chemically) in the topological crystalline insulator, $Pb_{0.60}Sn_{0.40}Te$ lowers the structural symmetry and lifts the degeneracy of electronic states around Γ point, resulting in the widening of the band gap.[2,3] Substitution of iodine in place of Te in $Pb_{0.60}Sn_{0.40}Te$ breaks the crystal mirror symmetry locally, which lifts the protection from the metallic surface states thereby widening the band gap. Apart from

this, iodine perturbs the chemical potential of $Pb_{0.60}Sn_{0.40}Te$ and shifts the Fermi level into the conduction band (Figure 2.2b).

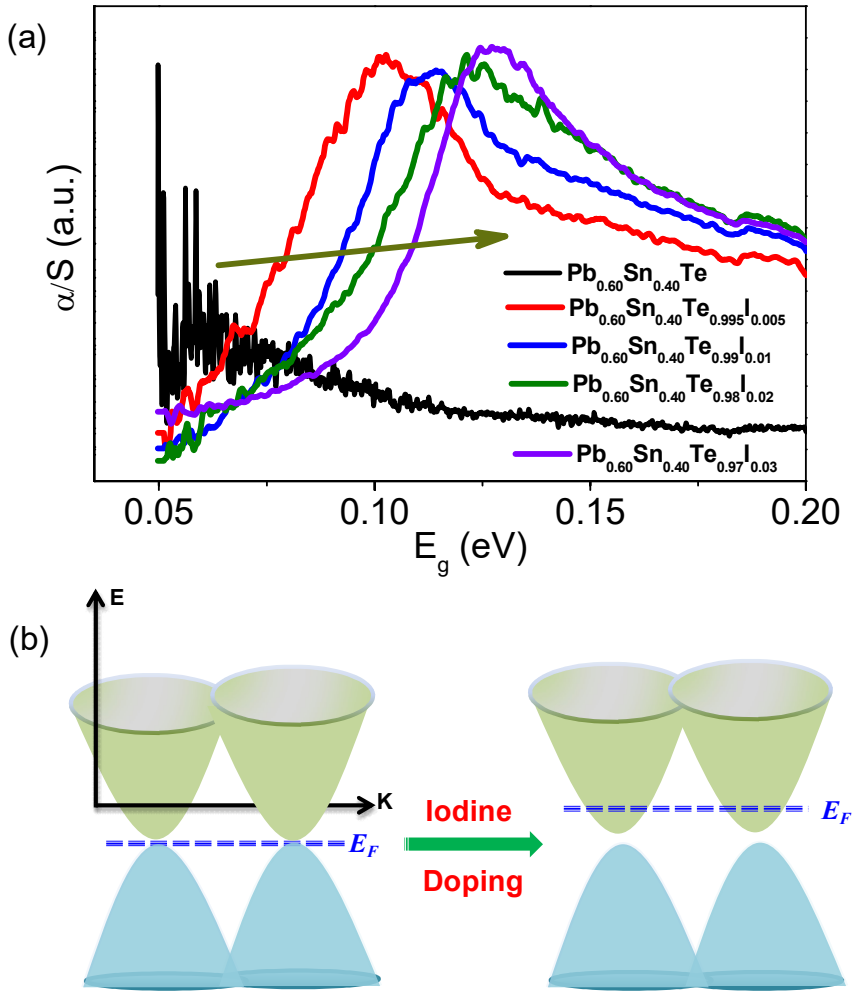

Figure 2.2 *(a) Optical absorption spectra of $Pb_{0.60}Sn_{0.40}Te_{1-x}I_x$ (x = 0, 0.005, 0.01, 0.02 and 0.03) samples. (b) Schematic representation of effect of iodine doping on the electronic structure of topological crystalline insulator, $Pb_{0.60}Sn_{0.40}Te$.*

The negative sign of the measured Hall coefficients confirms *n*-type conduction for $Pb_{0.60}Sn_{0.40}Te_{1-x}I_x$ (x = 0.005, 0.01, 0.02, 0.03) samples which is actually in contrast to *p*-type conduction observed for undoped $Pb_{0.60}Sn_{0.40}Te$. Substitution of I^- in Te^{2-} sublattice in $Pb_{0.60}Sn_{0.40}Te$ releases one extra electron into the conduction band which can be understood using simple valence counting. Iodine doping increases the carrier

concentration from 9.44 x 10^{18} cm^{-3} for $Pb_{0.6}Sn_{0.4}Te$ to 4.9 x 10^{19} cm^{-3} for $Pb_{0.60}Sn_{0.40}Te_{0.97}I_{0.03}$ sample (Table 2.1).

Table 2.1: Carrier concentration (*n*), carrier mobility (μ), effective mass (m^*) and band gap (E_g) of $Pb_{0.60}Sn_{0.40}Te_{1-x}I_x$ (x = 0, 0.005, 0.01, 0.02 and 0.03) samples at room temperature.

Sample	*n* (cm^{-3})	μ ($cm^2V^{-1}S^{-1}$)	m^*
$Pb_{0.60}Sn_{0.40}Te$	9.44 x 10^{18} *p-type*	1148	0.14 m_0
$Pb_{0.60}Sn_{0.40}Te_{0.995}I_{0.005}$	1.03 x 10^{19} *n-type*	788	0.18 m_0
$Pb_{0.60}Sn_{0.40}Te_{0.99}I_{0.01}$	2.4 x 10^{19} *n-type*	704	0.18 m_0
$Pb_{0.60}Sn_{0.40}Te_{0.98}I_{0.02}$	4.2 x 10^{19} *n-type*	400	0.22 m_0
$Pb_{0.60}Sn_{0.40}Te_{0.97}I_{0.03}$	4.9 x 10^{19} *n-type*	292	0.24 m_0

Increase in *n*-type carrier concentration and widening of electronic bandgap with I doping in $Pb_{0.60}Sn_{0.40}Te$ inspired us to measure its thermoelectric transport properties in 300-725 K range. The temperature dependences of the electrical conductivity (σ) and the Seebeck coefficient (*S*) for $Pb_{0.60}Sn_{0.40}Te_{1-x}I_x$ (x = 0.0, 0.005, 0.01, 0.02 and 0.03) samples are shown in Figure 2.3. With increasing temperature, the linearly increasing absolute Seebeck coefficient and the monotonically decreasing electrical conductivity indicate degenerate semiconducting behavior for all samples. At room temperature, σ value for undoped $Pb_{0.60}Sn_{0.40}Te$ is to be ~ 1725 S/cm which increases to ~ 2691 S/cm for 2 mol% I doped sample, due to a significant increase in the *n*-type carrier concentration. Electrical conductivity decreases with further increasing iodine concentration due to the enhanced carrier-carrier and point defect scattering in $Pb_{0.60}Sn_{0.40}Te_{0.97}I_{0.03}$ sample, which decreases the carrier mobility (Table 2.1). To estimate the scattering rate, temperature dependent σ was fitted to the equation $\sigma \sim 1/T^{\delta}$, δ is the scattering factor. Interestingly, two distinct δ (δ_1 in the low-temperature regime and δ_2 in the high-temperature regime) values can be extricated from the ln σ – ln T plot, Figure 2.3b. The inset of Figure 2.3b exhibits the plot δ as a function of iodine concentration, which decreases with doping concentration. δ_1 (δ_2) decrease from 2.98 (2.64) for $Pb_{0.60}Sn_{0.40}Te$ to 1.30 (1.63) for 3 mol

% I doped $Pb_{0.60}Sn_{0.40}Te$ sample. The smaller δ values in iodine-doped samples involve a much weaker temperature-dependence of carrier scattering, which maintained high electrical conductivity at a higher temperature. Two scattering factors probably represent the contributions from the two conduction bands of $Pb_{0.60}Sn_{0.40}Te$ to the electronic transport.[2,3] Previous electronic structure calculation of $Pb_{0.60}Sn_{0.40}Te$ showed signature of two conduction bands at Γ and Z+ δ point of Brillouin zone (32 atoms, √2 x √2 x 2 tetragonal supercell).[2,3]

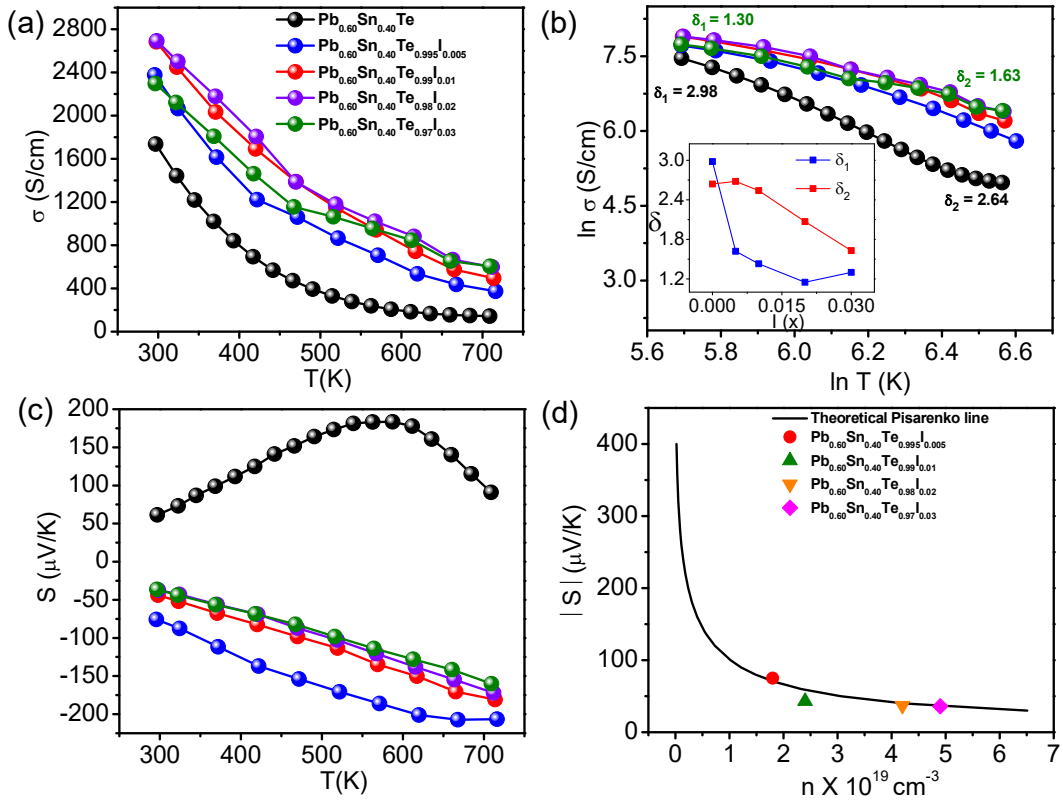

Figure 2.3 *Temperature dependent (a) electrical conductivity (σ), (b) ln σ vs. ln T plot to extract the scattering factor, δ (inset: Iodine concentration dependent δ values) and (c) Seebeck coefficient (S) of $Pb_{0.60}Sn_{0.40}Te_{1-x}I_x$ (x = 0, 0.005, 0.01, 0.02 and 0.03) samples. (d) Seebeck coefficient (S) as a function of carrier concentration (n) (Pisarenko plot) at T = 300 K for $Pb_{0.60}Sn_{0.40}Te_{1-x}I_x$ (x = 0.005, 0.01, 0.02 and 0.03) samples.*

Pristine TCI, $Pb_{0.60}Sn_{0.40}Te$, exhibits bipolar conduction at ~ 550 K, which is confirmed from temperature dependent Seebeck coefficient data (Figure 2.3c). It is interesting to note that pristine $Pb_{0.60}Sn_{0.40}Te$ sample exhibits positive *S* value over the

300-725 K range. The negative sign of *S* for $Pb_{0.60}Sn_{0.40}Te_{1-x}I_x$ (x = 0.005, 0.01, 0.02, 0.03) samples means that electrons are the major carriers which are also consistent with our Hall coefficient data. The sign of *S* changes from positive (+ 50 μV/K) to negative (-70 μV/K) at room temperature with increasing x from 0 to 0.005 in $Pb_{0.60}Sn_{0.40}Te_{1-x}I_x$ sample. Previously, substitution of Na or K in cation sublattice of $Pb_{0.6}Sn_{0.4}Te$ provides holes in the valence band and makes it *p*-type.[2,3] Whereas, in this study we use iodine as a dopant in Te sublattice which provides one extra electron per iodine doping in the conduction band of $Pb_{0.6}Sn_{0.4}Te$. We have been able to synthesize both *p*-type and *n*-type from the same material ($Pb_{0.6}Sn_{0.4}Te$) which is intriguing. This result has significant importance in making a thermoelectric device for practical application because of favorable compatibility between both *p*- and *n*-type materials. Due to the enhancement of carrier concentration (*n*-type) and widening of band gap after iodine substitution, it suppresses the bipolar conduction in $Pb_{0.60}Sn_{0.40}Te_{1-x}I_x$, resulting in the shifting of Seebeck maximum to higher temperatures (Figure 2.3c). Typically, $Pb_{0.60}Sn_{0.40}Te_{0.995}I_{0.005}$ sample shows room temperature Seebeck value of ~ -75 μV/K which further increases to ~ -208 μV/K at 710 K (Figure 2.3c). We have plotted experimental *S* vs. *n* data with the calculated Pisarenko line (Figure 2.3d). The effective mass, *m** used to plot the Pisarenko line is 0.18 m_0 which is corresponding to single conduction band transport. Evidently, at room temperature, there is no augmentation in *S* for iodine doped samples (Figure 2.3d). Electronic structure of $Pb_{0.60}Sn_{0.40}Te$ exhibits two conduction bands, one at Γ (light electron conduction band, 0.18 m_0) and second one at Z+ δ (comparatively heavy electron conduction band, 0.27 m_0) point in the Brillouin zone (32 atoms, √2 x √2 x 2 tetragonal supercell).[2] With increase in the iodine concentration, carrier concentration increases and it shifts the Fermi level deeper into the conduction band and essentially touches the second heavy conduction band. As a result, we observe increase in effective mass with iodine content in $Pb_{0.60}Sn_{0.40}Te$ sample (Table-2.1).

Figure 2.4 illustrates the power factor, $S^2\sigma$, of the $Pb_{0.60}Sn_{0.40}Te_{1-x}I_x$ (x = 0, 0.005, 0.01, 0.02 and 0.03) samples as a function of temperature. Typically, $Pb_{0.60}Sn_{0.40}Te_{0.995}I_{0.005}$ sample shows an $S^2\sigma$ value of ~13.6 μWcm^{-1} K^{-2} at 300 K, which reaches a maximum of ~25 μWcm^{-1} K^{-2} at 570 K. Enhancement in power factor for $Pb_{0.60}Sn_{0.40}Te_{1-x}I_x$ samples compared to that of pristine $Pb_{0.6}Sn_{0.4}Te$ is due to the

suppression of bipolar effect in Seebeck coefficient and increase in electrical conductivity.

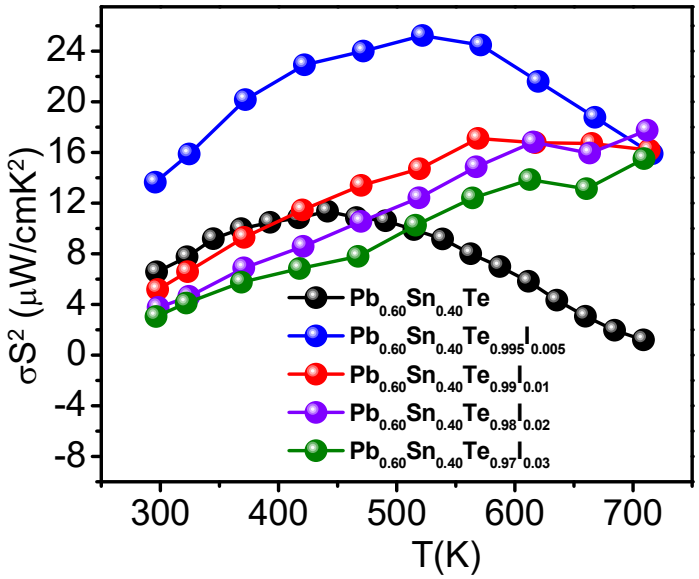

Figure 2.4 *Temperature dependent power factor (σS^2) of $Pb_{0.60}Sn_{0.40}Te_{1-x}I_x$ (x = 0, 0.005, 0.01, 0.02 and 0.03) samples.*

Kelvin probe force microscopy (KPFM) is an important tool to understand the relative position of Fermi level in solids.[7] The work function in $Pb_{0.60}Sn_{0.40}Te_{1-x}I_x$ (x = 0.0, 0.005 and 0.02) samples were measured by using KPFM. KPFM quantifies the local contact potential difference (CPD) between the tip and sample. The CPD is described as,[7]

$$CPD = \varphi_{tip} - \varphi_{sample}$$

where, φ_{tip} and φ_{sample} represent the work function of the metallic tip and sample surface, respectively. The work function of Pt-Ir coated tip (SCM-PIT-V2 from Bruker) is first calibrated with highly ordered pyrolytic graphite (HOPG) (φ_{HOPG}= 4.68 eV). The work function of the sample can be estimated as follows[7]

$$\varphi_{sample} = 4.68\ eV + CPD_{HOPG} - CPD_{sample}$$

A scan of larger than 2 μm^2 is performed on both the sample and HOPG to determine CPD_{sample} and CPD_{HOPG} respectively. KPFM based measurements confirm that the surface work functions of iodine doped $Pb_{0.60}Sn_{0.40}Te$ samples are lower compared to that of the pristine $Pb_{0.60}Sn_{0.40}Te$ sample, representing the accumulation of electron on the surface.

Table 2.2: Contact potential difference (CPD) of highly ordered pyrolytic graphite (HOPG) and $Pb_{0.60}Sn_{0.40}Te_{1-x}I_x$ (x = 0, 0.005 and 0.02) samples at room temperature.

Sample	CPD_{HOPG} (eV)	CPD_{Sample} (eV)
$\mathbf{Pb_{0.60}Sn_{0.40}Te}$	0.23	0.463
$\mathbf{Pb_{0.60}Sn_{0.40}Te_{0.995}I_{0.005}}$	0.23	0.496
$\mathbf{Pb_{0.60}Sn_{0.40}Te_{0.98}I_{0.02}}$	0.23	0.514

The calculated surface work functions of pristine $Pb_{0.60}Sn_{0.40}Te$ (*p*-type), $Pb_{0.60}Sn_{0.40}Te_{0.995}I_{0.005}$ (*n*-type) and $Pb_{0.60}Sn_{0.40}Te_{0.98}I_{0.02}$ (*n*-type) are 4.45 eV, 4.41 eV and 4.39 eV, respectively (Table 2.2). The lower work function of iodine doped $Pb_{0.60}Sn_{0.40}Te$ can be attributed to the excess available of electron in the Fermi level because the work function represents the energy required to remove an electron from the Fermi level to the vacuum. Thus, substitution of iodine at the position of Te in $Pb_{0.60}Sn_{0.40}Te$ provides one extra electron and shifts the Fermi level to the conduction band which is consistent with our Hall coefficient and Seebeck coefficient measurements.

Figure 2.5b presents the total thermal conductivity, κ_{total}, of the $Pb_{0.60}Sn_{0.40}Te_{1-x}I_x$ (x = 0, 0.005, 0.01, 0.02 and 0.03) samples as a function of temperature. Pristine $Pb_{0.6}Sn_{0.4}Te$ sample shows significant contribution of bipolar thermal conductivity (κ_{bi}) above 450 K. Substitution of iodine suppresses bipolar thermal conductivity significantly due to the increase in carrier concentration and widening of the band gap. At 300 K, $Pb_{0.60}Sn_{0.40}Te_{0.995}I_{0.005}$ sample shows the κ_{total} value of ~ 2.35 $Wm^{-1}K^{-1}$ which decreases to ~ 1.30 $Wm^{-1}K^{-1}$ at ~723K. Temperature dependent lattice thermal conductivity, κ_{latt}, values were estimated by subtracting the electronic thermal conductivity, κ_{el}, from the κ_{total} (Figure 2.6a). The κ_{el} were estimated using Wiedemann-Franz law, $\kappa_{el} = L \cdot \sigma \cdot T$; (Figure 2.5d) where, L is Lorenz number, σ is electrical conductivity and T is temperature.

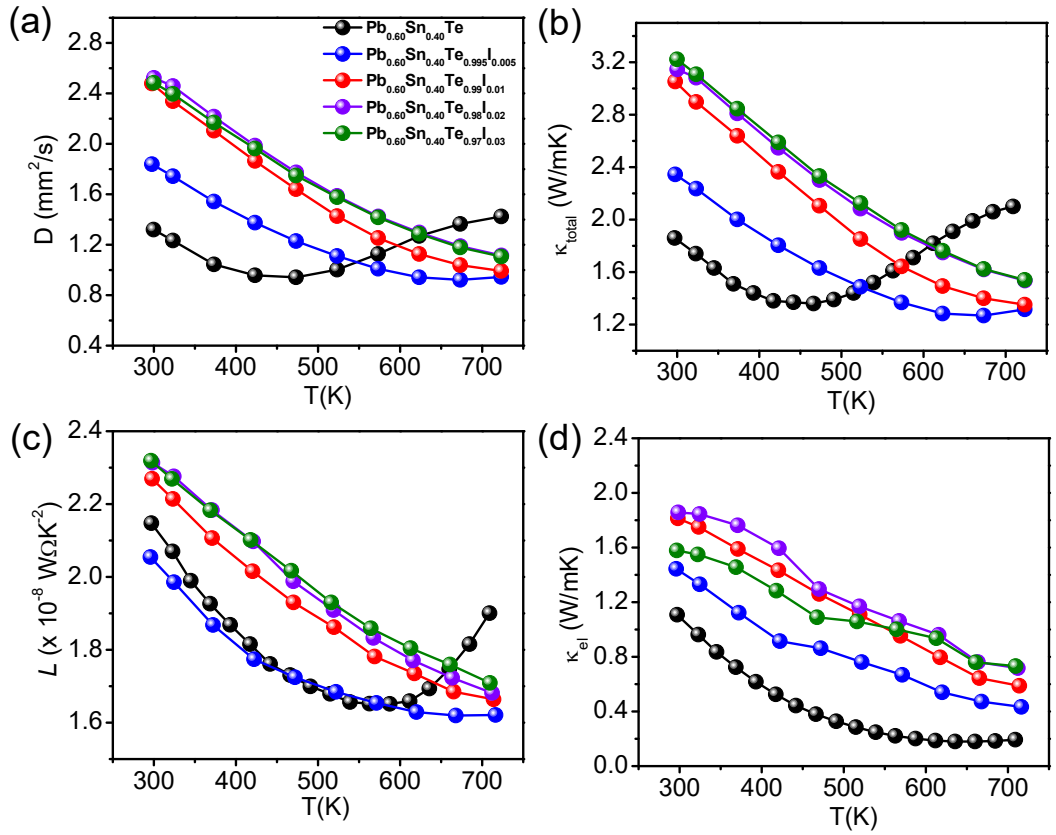

Figure 2.5 *Temperature variations of (a) diffusivity (D), (b) total thermal conductivity (κ_{total}), (c) Lorenz number (L) and (d) electrical thermal conductivity (κ_{el}) of $Pb_{0.60}Sn_{0.40}Te_{1-x}I_x$ (x = 0, 0.005, 0.01, 0.02 and 0.03) samples.*

In principle, lattice thermal conductivity should decrease with iodine concentration owing to point defect phonon scattering. However the reverse trend is observed for $Pb_{0.60}Sn_{0.40}Te_{1-x}I_x$ (x = 0.005, 0.01, 0.02 and 0.03) samples. This can be attributed to interband charge transfer which is common for a degenerate semiconductor with multiple valleys near Fermi level.[8,9] Thus, Lorenz number used for the calculation of κ_{el} is not so accurate, leading to an underestimation of κ_{el}. The higher Lorenz number compared to that of degenerate semiconductor (L_0) indicates the transfer of large amount of heat by carrier than what is anticipated by L_0 when they (carriers) travel from one band to the other.Thus, an increase in κ_{latt} with iodine concentration is observed for $Pb_{0.60}Sn_{0.40}Te$ samples because of interband carrier transport. Typically, the room temperature κ_{latt} value measured for $Pb_{0.60}Sn_{0.40}Te_{0.995}I_{0.005}$ is ~ 0.9 $Wm^{-1}K^{-1}$ which decreases to ~ 0.86 $Wm^{-1}K^{-1}$ at 715 K (Figure 2.6a).

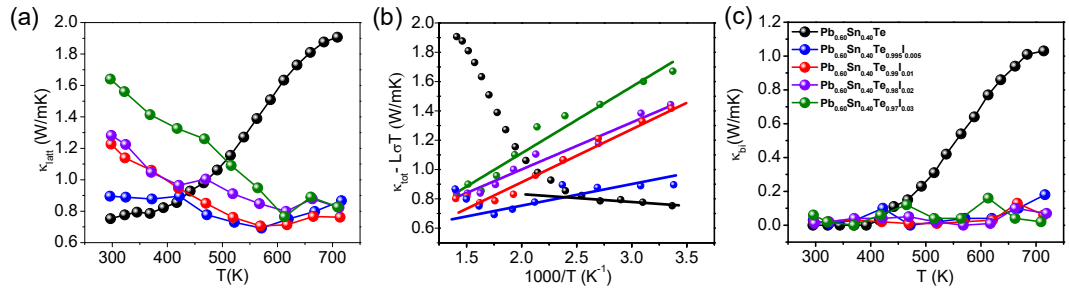

Figure 2.6 *(a) Temperature variations of lattice thermal conductivity (κ_{latt}) of $Pb_{0.60}Sn_{0.40}Te_{1-x}I_x$ (x = 0, 0.005, 0.01, 0.02 and 0.03) samples. (b) The difference of total and electronic thermal conductivity (κ_{total} - $L\sigma T$) as a function of temperature. Deviation from linear region indicates a significant contribution bipolar thermal conductivity (κ_{bi}). (c) Temperature dependent bipolar thermal conductivity (κ_{bi}) of $Pb_{0.60}Sn_{0.40}Te_{1-x}I_x$ (x = 0, 0.005, 0.01, 0.02 and 0.03) samples.*

We have estimated the contribution of bipolar thermal conductivity (κ_{bi}) to the κ_{total} at higher temperatures for all samples by using a previously reported method.[2] At lower temperatures, (κ_{total} - κ_{el}) equals to κ_{lat} which is inversely proportional to T as the contribution of κ_{bi} to κ_{total} is insignificant. Whereas, with rising temperature to ~ 425 K for pristine $Pb_{0.60}Sn_{0.40}Te$ sample, κ_{total} - κ_{el} values does not follow the linear relationship between κ_{lat} and T^{-1} because of the significant contribution of κ_{bi}. We plotted the subtracted value of total thermal conductivity and electrical thermal conductivity i.e. κ_{total} - $L \cdot \sigma \cdot T$ as a function of inversion of temperature (figure 2.6b). The solid lines in figure 2.6b represent linear fit to the experimental data, in which divergence from the linear fit indicates the contribution of κ_{bi}. Figure 2.6c presents temperature dependent κ_{bi} for $Pb_{0.60}Sn_{0.40}Te_{1-x}I_x$ (x = 0, 0.005, 0.01, 0.02 and 0.03) samples, which indeed indicates that the κ_{bi} significantly decreases with iodine doping.

Figure 2.7 illustrates the thermoelectric figure of merit, zT, of the $Pb_{0.60}Sn_{0.40}Te_{1-x}I_x$ (x = 0.005-0.03) samples as a function of temperature. A maximum zT of ~ 1.05 is achieved for the *n*-type $Pb_{0.60}Sn_{0.40}Te_{0.995}I_{0.005}$ at 620 K which significantly higher (483 %) than that of the undoped $Pb_{0.60}Sn_{0.40}Te$ sample. The observed zT for *n*-type iodine doped sample is comparable to that of previously reported *p*-type Na/K doped $Pb_{0.60}Sn_{0.40}Te$ samples.[2,3] Moreover, zT of the present $Pb_{0.60}Sn_{0.40}Te_{1-x}I_x$ is comparable to that of iodine doped PbTe but the TCI samples are consist of lesser content of lead.[10]

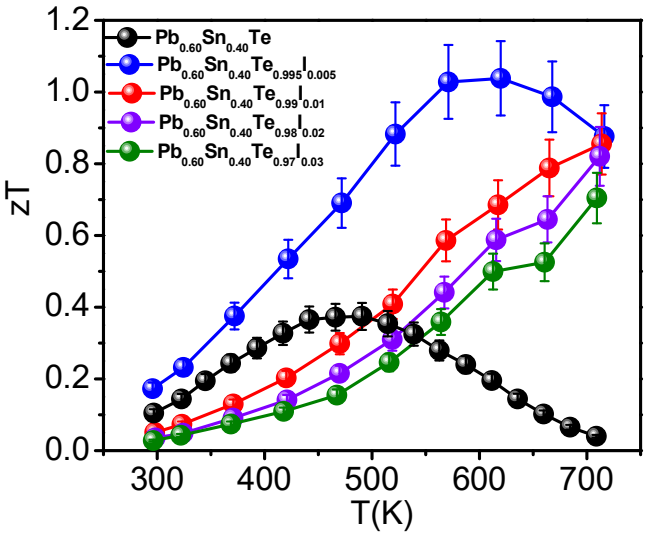

Figure 2.7 *Temperature dependent zT of* $Pb_{0.60}Sn_{0.40}Te_{1-x}I_x$ *(x = 0, 0.005, 0.01, 0.02 and 0.03) samples.*

2.4 Conclusions

In conclusion, iodine doping perturbs the local mirror symmetry and widens the band gap in TCI, $Pb_{0.60}Sn_{0.40}Te$, which makes it a promising *n*-type thermoelectric material. Iodine acts as a donor dopant in $Pb_{0.60}Sn_{0.40}Te$, thereby increases the *n*-type carrier concentration. Increase in the *n*-type carrier concentration and enlarging of the band gap in $Pb_{0.60}Sn_{0.40}Te_{1-x}I_x$, suppress the bipolar conduction, which shifts the Seebeck maxima to high temperatures and decreases the total thermal conductivity above 550 K. A maximum zT of ~ 1.05 is achieved for the composition of $Pb_{0.60}Sn_{0.40}Te_{0.995}I_{0.005}$ at 620 K which is notably higher compared to that of pristine $Pb_{0.60}Sn_{0.40}Te$. The improvement of zT is mainly due to the combined effect of improvement of power factor and reduction of total thermal conductivity at 620 K. The measured zT for iodine doped *n*-type sample is comparable to that of previously reported *p*-type Na/K doped $Pb_{0.60}Sn_{0.40}Te$ samples.[2,3] Thermoelectric performance of *n*-type $Pb_{0.60}Sn_{0.40}Te$ system can be further enhanced by increasing phonon scattering *via* all-scale hierarchical architectures.

2.5 References

[1] Y. Xiao, H. Wu, J. Cui, D. Wang, L. Fu, Y. Zhang, Y. Chen, J. He, S. J. Pennycook, L. -D. Zhao, *Energy Environ. Sci.* **2018**, *11*, 2486.

[2] S. Roychowdhury, U. S. Shenoy, U. V. Waghmare, K. Biswas, *Angew. Chem. Int. Ed.* **2015**, *54*, 15241.

[3] S. Roychowdhury, U. S. Shenoy, U. V. Waghmare, K. Biswas, *Appl. Phys. Lett.* **2016**, *108*, 193901.

[4] S. Shenoy, D. K. Bhat, *J. Phys. Chem. C* **2017**, *121*, 20696.

[5] D. Ginting, C. -C. Lin, G. Kim, J. H. Yun, B. -K. Yu, S. -J. Kim, K. Ahn, J.-S. Rhyee, *J. Mater. Chem. A* **2018**, *6*, 5870.

[6] D. Ginting, C.-C. Lin, L. Rathnam, G. Kim, J. H. Yun, H. S. So, H. Lee, B. -K. Yu, S.-J. Kim, K. Ahn, J. -S. Rhyee, *ACS Appl. Mater. Interface*, **2018**, *10*, 11613.

[7] W. Melitz, J. Shen, S. Lee, J. S. Lee, A. C. Kummel, R. Droopad, E. T. Yu, *J. Appl. Phys.* **2010**, *108*, 023711.

[8] J. Androulakis, I. Todorov, D. –Y. Chung, S. Ballikaya, G. Wang, C. Uher, M. Kanatzidis, *Phys. Rev. B* **2010**, *82*, 115209.

[9] M. K. Jana K. Pal, U. V. Waghmare, K. Biswas, *Angew. Chem. Int. Ed.* **2016**, *55*, 7592.

[10] A. D. LaLonde, Y. Pei, G. J. Snyder, *Energy Environ. Sci*. **2011**, *4*, 2090.

Chapter 3

Large Linear Magnetoresistance in Topological Crystalline Insulator, $Pb_{0.60}Sn_{0.40}Te$

Chapter 3

Large Linear Magnetoresistance in Topological Crystalline Insulator, $Pb_{0.60}Sn_{0.40}Te$[†]

Summary

Classical magnetoresistance generally follows the quadratic dependence of the magnetic field at lower field and finally saturates when field is larger. In this chapter, we present the large positive non-saturating linear magnetoresistance in topological crystalline insulator, $Pb_{0.60}Sn_{0.40}Te$, at different temperatures between 3 K and 300 K in magnetic field up to 9 T. Magnetoresistance value as high as ~ 200 % was achieved at 3 K at magnetic field of 9 T. Linear magnetoresistance observed in $Pb_{0.60}Sn_{0.40}Te$ is mainly governed by the spatial fluctuation carrier mobility due to distortions in the current paths in inhomogeneous conductor.

[†]*Paper based on this study has been published in J. Solid State Chem.* ***2016****, 233, 199.*

3.1 Introduction

The Magnetoresistance (MR) of a material describes the changes of the electrical resistance with an external magnetic field.[1,2] Materials exhibiting large MR have attracted enormous attention due to their potential application in magnetic sensors,[1] magnetic memories,[2] and in hard drives.[3] Due to immense technological importance of MR, scientific community has been taken a great interest to search for new materials which show large MR.[4] It has been well established that classical MR in most metals follows the quadratic dependence of the magnetic field at lower field because of vector nature of the magnetic field and finally saturates when field is larger.[5,6] Giant magnetoresistance (GMR), which is a quantum mechanical phenomenon,[7] was first observed in multilayered thin-film of a pair of ferromagnetic Fe layers separated by a non-magnetic Cr layer.[6] Colossal magnetoresistance (CMR) was observed in manganite perovskite oxides and Zintl phases during the transition from high temperature paramagnetic insulator to low temperature ferromagnetic metal.[8-11]

The MR of nonmagnetic metals with open Fermi surfaces can be linear and non-saturating at high magnetic fields.[12] Recently, materials exhibiting large linear magnetoresistance (LMR) have attracted intense research interest due to the fundamental science of bi-stability and nonlinearity, as well as of its technological importance.[13,14] Large LMR effect has been observed in narrow band gap metal chalcogenide semiconductors, such as doped polycrystalline silver chalcogenides,[13] topological insulators,[15,16] 3D Dirac semimetal[17,18] and multilayer graphene.[19,20] Mention must be made that mechanism of positive large LMR is not fully understood till date. Among the theoretical models, Abrikosov proposed that the quantum LMR is observed in material with gapless linearly dispersed energy levels, in which all carriers lie in the lowest Landau level, i.e. the extreme quantum limit.[21, 22] Classically, Parish and Littlewood have proposed that LMR can originate in an inhomogeneous conductor from distortions in the current paths induced by macroscopic spatial fluctuations in the carrier mobility;[23] this type of non-saturating LMR has been observed in narrow-gap self-doped $Ag_{2+\delta}Te$ and $Ag_{2+\delta}Se$ chalcogenides semiconductors.[13,14] Recent discovery of large LMR in topological insulators, Bi_2Te_3,[15,16] Bi_2Se_3,[24] $Hg_{1-x}Cd_xTe$,[25] and YPdBi,[26] has again stimulated intensive research interest in LMR, because of nontrivial zero-gap Dirac-like

surface states in topological insulators. Zero band gap InSb also shows large LMR due to contribution from both classical and quantum MR.[27] Positive GMR has been observed in β-$Cu_{1-x}Ni_xAgSe$ due to its very high carrier mobility.[28] Recently, Heusler topological insulators[29] and WTe_2[30] also showed large non saturating MR.

Rock salt type IV-VI narrow band gap (E_g) chalcogenides, PbTe (E_g ~ 0.29 eV) and SnTe (E_g ~ 0.18 eV, inverted gap), are known for their excellent thermoelectric properties.[31-37] PbTe and SnTe form the complete solid solution in the range $Pb_{1-x}Sn_xTe$ ($0 \leq x \leq 1$) as indicated by phase diagram in Figure 3.1a.[38] Recently, solid solution composition $Pb_{0.60}Sn_{0.40}Te$ has been created sensation, when it has been identified as topological crystalline insulator by angle-resolved photoemission spectroscopy (ARPES).[39] Topological crystalline insulator is different from topological insulator (e.g. Bi_2Te_3, Bi_2Se_3) with respect to their surface state protection. In topological insulator surface states are protected by time reversal symmetry, while in topological crystalline insulator surface states are protected by crystal symmetry.[39-41] Topological crystalline insulators have an even number of surface states with distinct band structures depending on crystal surfaces, while topological insulators have an odd number of surface states.[39-41] Till now, research on the topological insulator has been mainly focused on the prediction of new topological insulator and the determination of topological surface states by using ARPES.[42-44] However, transport property investigations that can realize the practical application of topological insulators are essential.

This chapter demonstrate the observation of the large positive non-saturating linear magnetoresistance (LMR) in the topological crystalline insulator, $Pb_{0.60}Sn_{0.40}Te$, at different temperatures between 3 K and 300 K in magnetic field up to 9 T. Highest magnetoresistance value as high as ~200 % was achieved at 3 K at magnetic field of 9 T. LMR in $Pb_{0.60}Sn_{0.40}Te$ is mainly governed by the spatial fluctuation of the carrier mobility, thus the fundamental understanding has been developed based on classical Parish and Littlewood model.[23]

3.2 Methods

3.2.1 Reagents

Tin (Sn, Alfa Aesar 99.99+ %), tellurium (Te, Alfa Aesar 99.999+ %) and lead (Pb, Alfa Aesar 99.99+ %) were used for synthesis without further purification.

3.2.2 Synthesis

Ingots (~ 10 g) of $Pb_{1-x}Sn_xTe$ (x = 0.1 - 0.85) were synthesized by mixing appropriate ratios of high-purity elemental Sn, Pb and Te in quartz tube. The tubes were sealed under vacuum (10^{-5} torr) and slowly heated to 723 K over 12 hrs, then heated up to 1323 K in 5 hrs, annealed for 5 hrs, and cooled down to 1023 K over 2 hrs and annealed for 4 hrs, then slowly cool down to room temperature over a period of 18 hrs.

3.2.3 Powder X-ray diffraction

Powder X-ray diffraction for finely ground samples were recorded using a Cu K_α (λ = 1.5406 Å) radiation on a Bruker D8 diffractometer.

3.2.4 Band gap measurement

To estimate optical band gap of the as synthesized samples, diffuse reflectance measurement has been done with finely ground powder at room temperature using FT-IR Bruker IFS 66V/S spectrometer in wave number range 4000-400 cm^{-1} with 2 cm^{-1} resolution and 50 scans. Absorption (α/ S) data were calculated from reflectance data using Kubelka-Munk equation: $\alpha/S= (1-R)^2/(2R)$, where R is the reflectance, α and S are the absorption and scattering coefficient, respectively. The energy band gaps were derived from α/S vs E (eV) plot.

3.2.5 Field dependence magnetic measurement

Temperature and magnetic field dependent resistivity was measured with the physical property measurement system (PPMS, Quantum Design) using conventional four probe method with current of 5000 µA between 3 K and 300 K. Hall measurements were performed with the using conventional five probe method with the AC transport option in PPMS (Quantum Design) in a magnetic field of 9 T. The longitudinal magnetoresistance was measured with the magnetic field perpendicular to the current direction.

3.3 Results & Discussion

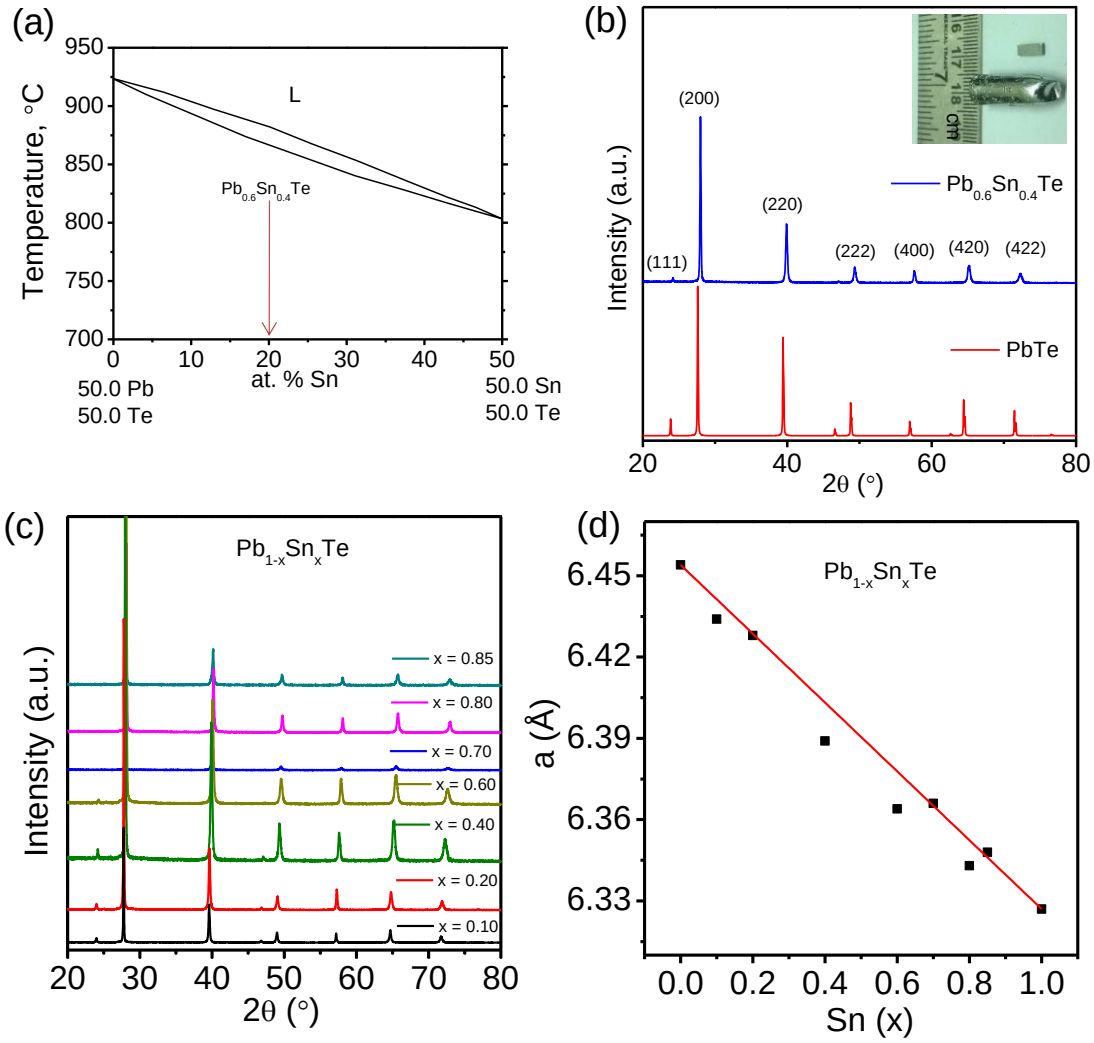

Figure 3.1 *(a) Schematic of the phase diagram of PbTe-SnTe system.[38] Labeled arrow shows the composition of $Pb_{0.6}Sn_{0.4}Te$. (b) Powder X-ray diffraction pattern of $Pb_{0.60}Sn_{0.40}Te$. Inset in (b) shows the photograph of high quality ingot of $Pb_{0.60}Sn_{0.40}Te$ synthesized by melting reaction. (c) Powder X-ray diffraction patterns of $Pb_{1-x}Sn_xTe$ ($0.10 \leq x \leq 0.85$) and (d) Variation of the lattice parameter as a function of Sn concentration (x) in $Pb_{1-x}Sn_xTe$ ($0.10 \leq \times \leq 0.85$).*

Powder X-ray diffraction (PXRD) pattern of $Pb_{0.60}Sn_{0.40}Te$ could be index based on cubic PbTe structure (space group, *Fm-3m*) (see Figure 3.1b). No other impurity peak has been observed within the detection limit of the PXRD data. PXRD patterns of other $Pb_{1-x}Sn_xTe$ (x = 0.1 - 0.85) compositions can also be indexed in PbTe structure (space group, *Fm-3m*) (see Figure 3.1c). Incorporation of smaller Sn atom (~ 141 pm) in the Pb (~ 147

pm) position results linear decrease in the lattice parameter, follow solid solution Vegard's law (Figure 3.1d). This result confirms solid solution nature of $Pb_{1-x}Sn_xTe$ (x = 0.1 - 0.85), which was as indicated earlier in the PbTe-SnTe phase diagram (Figure 3.1a).[38] In the inset of Figure 3.1b, we show a typical photograph of the "as-synthesized" $Pb_{0.6}Sn_{0.4}Te$ ingot. Bar shaped sample (Figure 3.1b) obtained after cutting and polishing such ingot, was used for MR measurement.

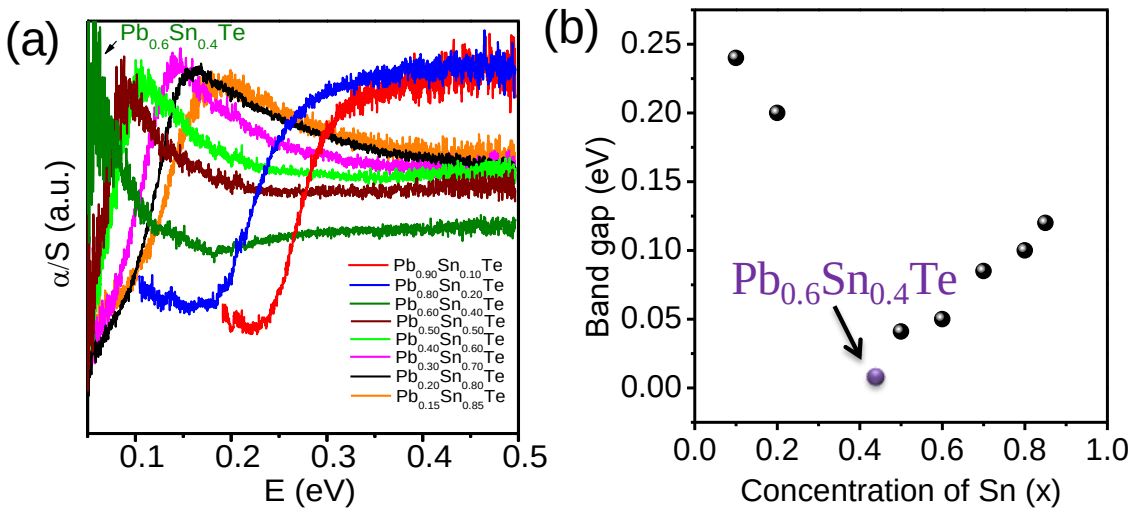

Figure 3.2 *(a) Absorption spectra of the several compositions in $Pb_{1-x}Sn_xTe$ ($0.10 \leq x \leq 0.85$). (b) The variation of band energies with the concentration of Sn (x) in $Pb_{1-x}Sn_xTe$ solid solution at room temperature.*

We have measured the band gap of several samples in the $Pb_{1-x}Sn_xTe$ (x = 0.10 - 0.85) composition by infrared (IR) diffuse reflectance spectroscopy. Spectroscopically measured optical band gap of $Pb_{1-x}Sn_xTe$ (x = 0.10 - 0.85) has been presented in Figure 3.2a. Band gap energy strongly depends on Sn concentration in $Pb_{1-x}Sn_xTe$. With increasing Sn concentration band gap decreases from ~ 0.24 eV to nearly 0 eV (Figure 3.2b), when the composition was reached to $Pb_{0.6}Sn_{0.4}Te$, *i.e.*, topological crystalline insulator phase. We could not able to resolve the actual band gap of $Pb_{0.6}Sn_{0.4}Te$ by IR diffuse reflectance spectroscopy (Figure 3.2a), as the band gap energy is very near to 0 eV.[39] Further increasing the Sn concentration in $Pb_{1-x}Sn_xTe$, band gap increases from ~ 0.04 eV to ~ 0.15 eV, when the composition reached close to pure SnTe (Figure 3.2b). Sn concentration dependent anomalous band gap evolution in $Pb_{1-x}Sn_xTe$ supports existence

of topological crystalline insulator phase near $Pb_{0.60}Sn_{0.40}Te$ composition, which was earlier confirmed by ARPES study[39] and *ab initio* electronic structure calculations.[45]

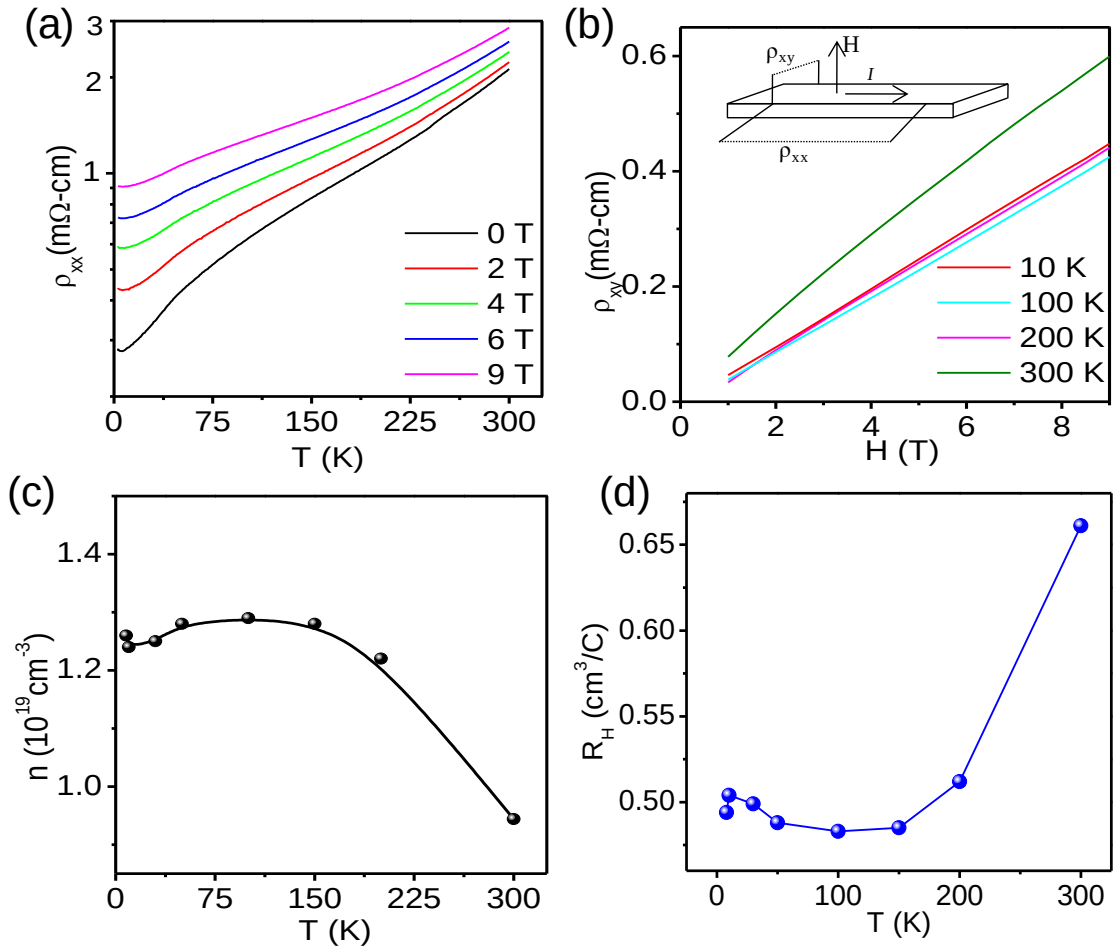

Figure 3.3 *(a) Temperature-dependent resistivity (ρ_{xx}) of $Pb_{0.60}Sn_{0.40}Te$ under various magnetic fields, H = 0, 2, 4, 6 and 9 T. (b) Hall resistivity (ρ_{xy}) of $Pb_{0.60}Sn_{0.40}Te$ as a function of magnetic field. Inset of (b) represents measurement configuration. (c) Temperature dependent carrier concentration (n) and (d) Hall coefficient (R_H) for $Pb_{0.60}Sn_{0.40}Te$ sample.*

In this chapter, we have selected the topological crystalline insulator phase, $Pb_{0.60}Sn_{0.40}Te$, from several $Pb_{1-x}Sn_xTe$ (x = 0.10 - 0.85) compositions, for further MR measurement. We have measured MR using a Physical Properties Measurement System (PPMS) from Quantum Design up to a 9 T magnetic field, in which magnetic field is perpendicular to the direction of current (inset in Figure 3.3b). The temperature dependent resistivity (ρ_{xx}) of $Pb_{0.60}Sn_{0.40}Te$ under various applied magnetic field is shown in Figure 3.3a. The zero field ρ_{xx} increases with increasing temperature, indicating metallic

behaviour of the sample. The ρ_{xx} in presence of magnetic field follows similar trend compared of that of zero field curve, thus the metallic behaviour of the sample retained after application of magnetic field. The room temperature zero field ρ_{xx} value of ~ 2.11 mΩ-cm decreases to 0.28 mΩ-cm at 3 K, yielding residual resistivity ratio, [ρ(300K)/ρ(3K)] of 7.54. In presence of 9 T magnetic fields, room temperature ρ_{xx} decreases from ~ 2.86 mΩ-cm to 0.91 mΩ-cm at 3 K, yielding residual resistivity ratio of 3.14.

In Figure 3.3b, we present hall resistivity (ρ_{xy}) as a function of magnetic field, H, at different temperatures. The positive slope of ρ_{xy} confirms the *p*-type nature of $Pb_{0.60}Sn_{0.40}Te$. We have estimated the temperature dependent carrier density, n (Figure 3.3c), from the formula: $n = 1/eR_H$, where e is the electronic charge and R_H is Hall coefficient (Figure 3.3d). The room temperature carrier density for $Pb_{0.60}Sn_{0.40}Te$ is 9.4×10^{18} cm^{-3}. The carrier density in $Pb_{0.60}Sn_{0.40}Te$ increases with decreasing temperature up to ~ 150 K, then remain almost same below 150 K.

Figure 3.4a shows the variation of resistivity (ρ_{xx}) with magnetic field (H) of $Pb_{0.60}Sn_{0.40}Te$ at different temperature (3 K to 300 K). Linear magnetic field dependence of ρ_{xx} was observed up to 100 K. Non-linearity in the ρ_{xx} *vs*. H curve was evidenced in the lower field region (below ~ 3.85 T) for 200 K and 300 K measurements. Interestingly, in the higher field (3.85 - 9 T) region, ρ_{xx} became linear during high temperature (200 K and 300 K) measurements.

In Figure 3.4b, we present longitudinal MR of $Pb_{0.60}Sn_{0.40}Te$ with field (0 - 9 T) at different temperature ranging from 3 K to 300 K. The MR is defined as, $MR = [\{\rho_{xx}(H) - \rho_{xx}(0)\}/ \rho_{xx}(0)] \times 100\%$, where $\rho_{xx}(H)$ and $\rho_{xx}(0)$ are the resistivity with and without the magnetic field H. Typically, linear magnetoresistance (LMR) behaviour was observed at 3 K in magnetic field range of 1.8 - 9 T, while the magnetic field below ~ 1.8 T, MR follows the quadratic law dependence (Figure 3.4c). A large MR, as large as ~ 200 %, was observed under a 9 T magnetic field at 3 K.

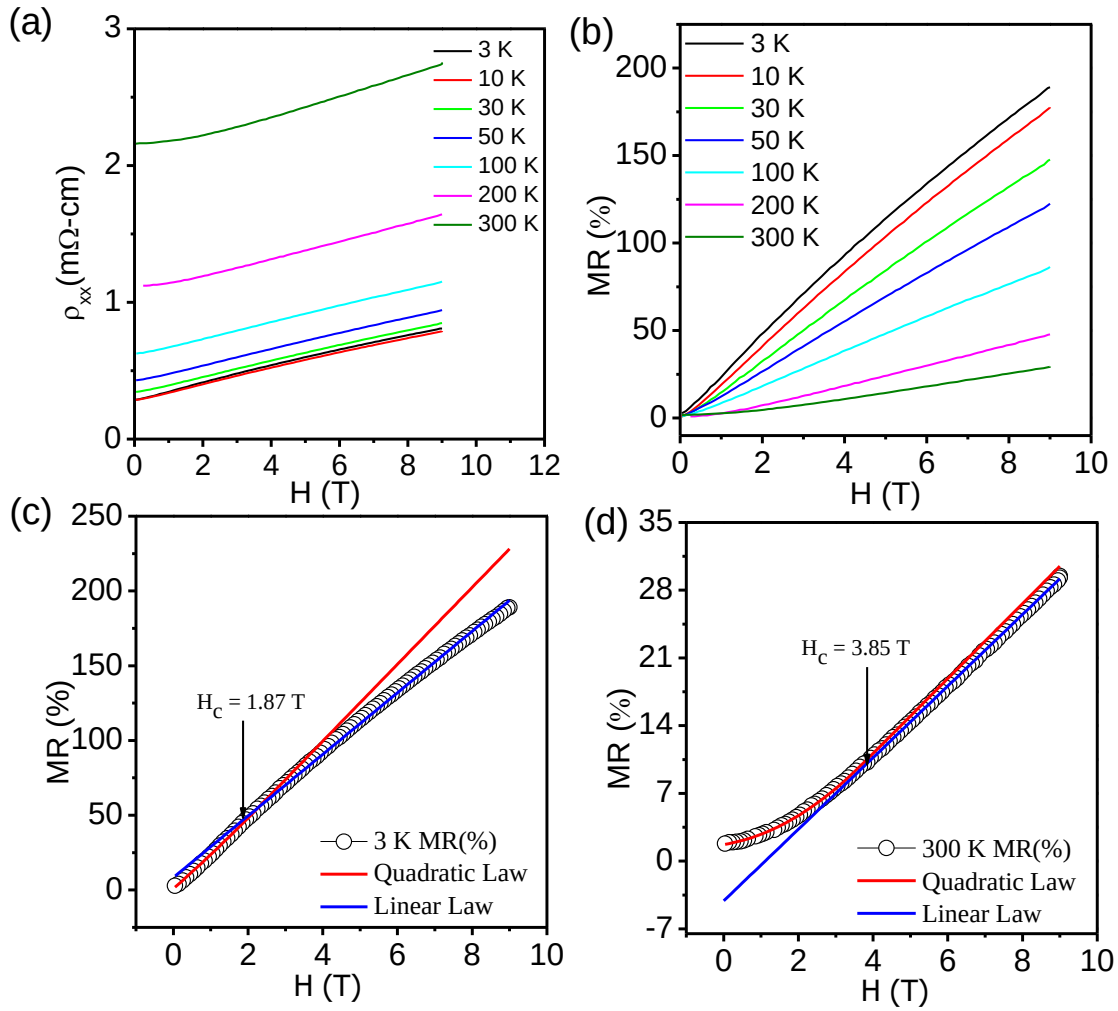

Figure 3.4 *(a) The magnetic field (H) dependence of ρ_{xx} measured at different temperatures. (b) Magnetoresitance (MR) of $Pb_{0.60}Sn_{0.40}Te$ as a function of magnetic field (H) at a series of temperatures T = 3, 10, 30, 50, 100, 200 and 300 K. Here, MR = [ρ(H) – ρ(0)/ ρ(0)] × 100%, where ρ(H) and ρ(0) are the resistivity with and without the magnetic field H, respectively. Magnetic field dependent magnetoresistance of $Pb_{0.60}Sn_{0.40}Te$ at (c) 3 K and (d) 300 K with quadratic and linear fitting. H_c is the crossover field (i.e. the field at which the MR curve becomes linear).*

Fitting formula: For linear fitting, MR (%) = a + b*H

For quadratic fitting, MR (%) = $a + b_1*H + b_2*H^2$

Fitting parameters: At 3 K: For linear fitting, a = 8.368; b = 20.593

For quadratic fitting, a = 0.877; b_1 = 21.985; b_2 = 0.832

At 300 K: For linear fitting, a = -3.992; b = 3.685

For quadratic fitting, a = 1.691; b_1 = 0.676; b_2 = 0.418

At high temperatures (e.g. 300 K), magnetic field dependent MR follows a quadratic law dependence below ~ 3.85 T, while above 3.85 T, MR follows linear magnetic field dependence (Figure 3.4d). Crossover field, H_c, the field at which the MR curve becomes linear, decreases markedly from ~ 3.85 T to 1.8 T with decreasing the measurement temperature from 300 K to 3 K. Thus, MR of $Pb_{0.6}Sn_{0.4}Te$ becomes more linear with decreasing the temperature up to 3 K.

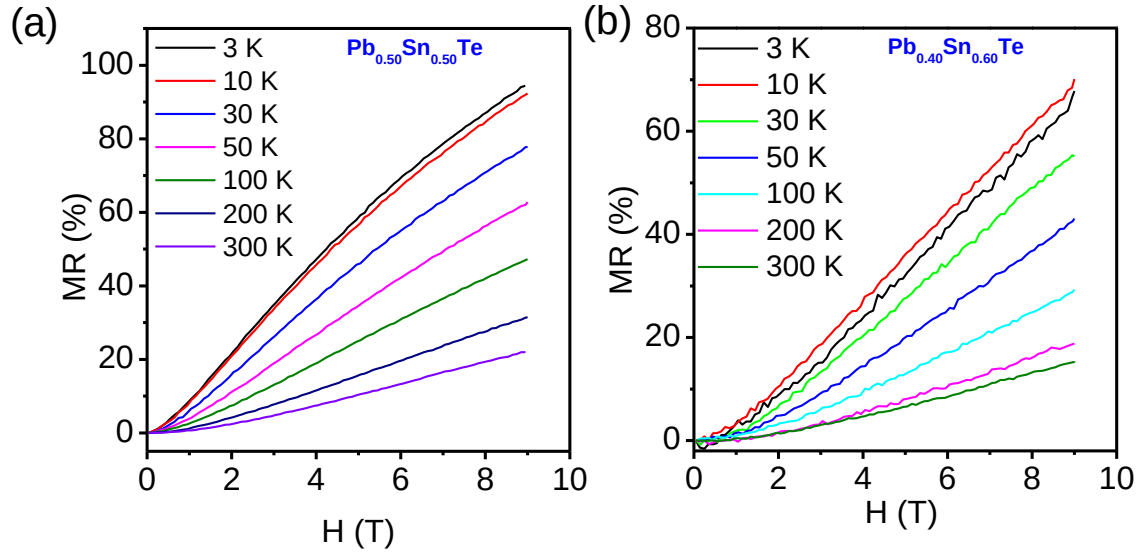

Figure 3.5 *Magnetoresitance (MR) as a function of magnetic field (H) at a series of temperatures T = 3, 10, 30, 50, 100, 200 and 300 K for (a) $Pb_{0.50}Sn_{0.50}Te$ and (b) $Pb_{0.40}Sn_{0.60}Te$.*

We have also measured the field dependent MR of $Pb_{0.50}Sn_{0.50}Te$ and $Pb_{0.40}Sn_{0.60}Te$, which show LMR behaviour with highest MR of ~ 95% and ~ 70 %, respectively, at 3 K under 9 T magnetic fields (Figure 3.5 (a and b)). We observe the systematic decrease of MR from ~ 200% to 70% with increasing Sn concentration in $Pb_{1-x}Sn_xTe$ at 3 K under 9 T magnetic field (Figure 3.6a). According to Parish and Littlewood model[23] the slope of the linear part of MR, *i.e.* $\Delta R/\Delta H$, should be proportional to the carrier mobility. Figure 3.6b represents the slopes of LMR for $Pb_{0.60}Sn_{0.40}Te$, $Pb_{0.50}Sn_{0.50}Te$ and $Pb_{0.40}Sn_{0.60}Te$ as a function of temperature. Slopes of LMR, $\Delta R/\Delta H$, which is proportional to carrier mobility, is lower for $Pb_{0.40}Sn_{0.60}Te$ compared that of $Pb_{0.60}Sn_{0.40}Te$. Thus, we believe that carrier mobility of $Pb_{0.40}Sn_{0.60}Te$ sample is lower

than that in $Pb_{0.60}Sn_{0.40}Te$, which results in lower MR (~ 70 %) in $Pb_{0.40}Sn_{0.60}Te$ compared to $Pb_{0.60}Sn_{0.40}Te$ (~ 200 %).

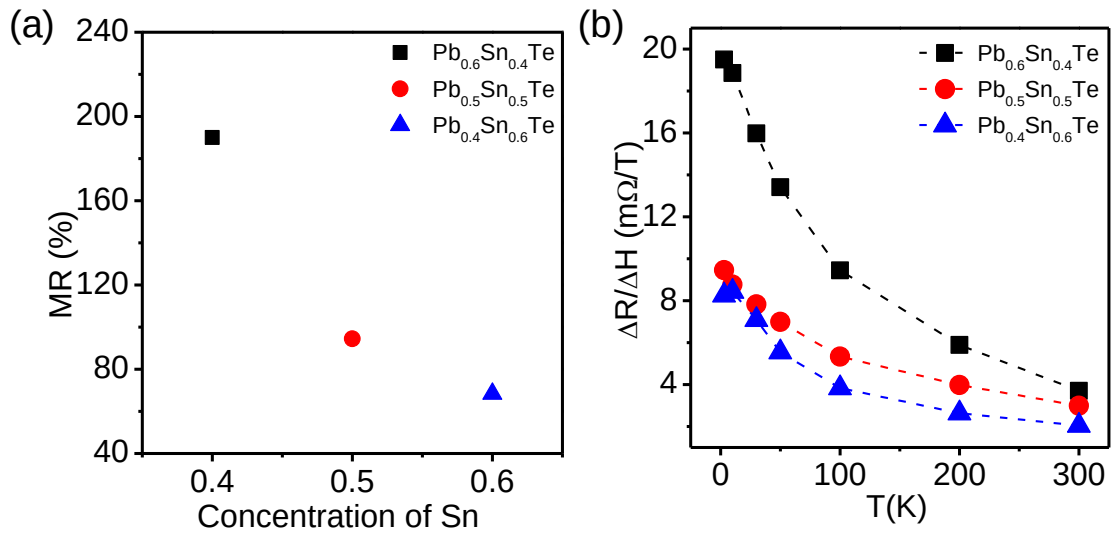

Figure 3.6 *(a) Progression of MR behavior as a function of Sn concentration in* $Pb_{1-x}Sn_xTe$ *and (b) Slopes of LMR, ΔR/ΔH, as a function of temperature for* $Pb_{0.60}Sn_{0.40}Te$, $Pb_{0.50}Sn_{0.50}Te$ *and* $Pb_{0.40}Sn_{0.60}Te$.

In order to explain the LMR behaviour, several mechanisms mainly in the two classes have been proposed. In the Abrikosov model, quantum LMR arises from the linear energy dispersion of the topological metallic surface states, which can persist both low and high temperatures.[21, 22] The LMR in epitaxial graphene[19] and topological insulator Bi_2Te_3 nanosheets[15] were found to increase with increasing temperature and were therefore interpreted as due to Abrikosov's linear quantum magnetoresistance. However, $Pb_{0.60}Sn_{0.40}Te$ exhibited a MR value of 200 % at 3 K, while with increasing temperature to 300 K, MR decrease to 40 % at 300 K. In previous report on magnetoresistance of single crystal of *p*-type PbTe, Schneider *et. al.* observed sublinear magnetoresistance for undoped *p*-type PbTe and nonsaturating LMR for BaF_2 doped PbTe sample.[47] The slopes LMR, $\Delta R/\Delta H$, for PbTe and BaF_2 doped PbTe are independent with temperature which is consistent with the theory of quantum linear magnetoresistance.[47] In the case of polycrystalline $Pb_{0.60}Sn_{0.40}Te$, slopes LMR, $\Delta R/\Delta H$, decreases with increasing the temperature (Figure 3.6b), which strongly supports the Parish and Littlewood model. Thus, LMR effect in $Pb_{0.6}Sn_{0.4}Te$ is not due to quantum LMR as proposed by Abrikosov.

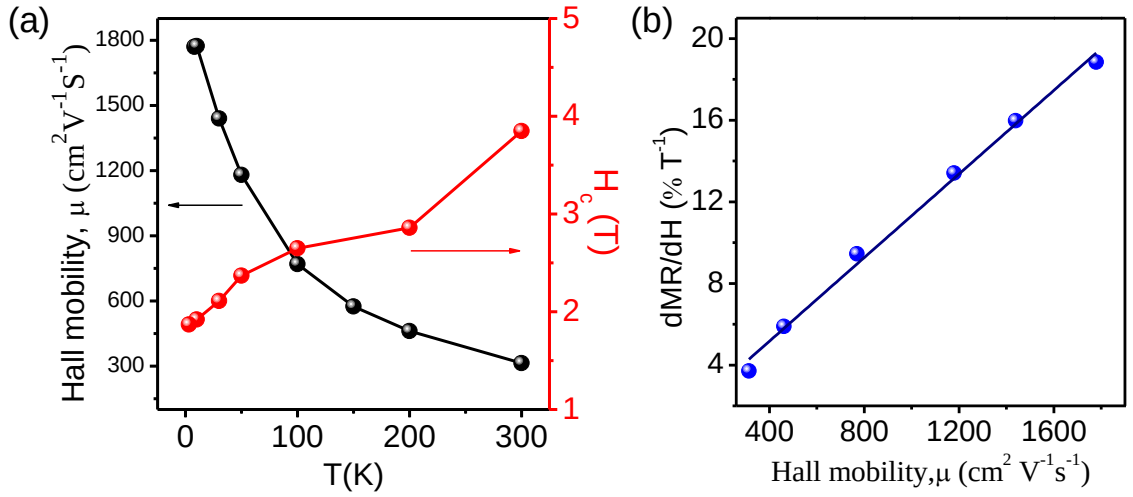

Figure 3.7 *(a) The cross over field H_C on right y-axis and Hall mobility (μ) on left y-axis as a function of temperature (T). (b) Slope of the Linear part of MR, i.e., dMR(T)/dH as a function of carrier mobility (μ) for $Pb_{0.60}Sn_{0.40}Te$.*

To gain deeper understanding of the observed LMR in $Pb_{0.60}Sn_{0.40}Te$ sample, we recalled the classical Parish and Littlewood model,[23] in which the LMR is expected to be governed by the carrier mobility. Classically, Parish and Littlewood have proposed that LMR can originate in an inhomogeneous conductor from distortions in the current paths induced by macroscopic spatial fluctuations in the carrier mobility.[23] This model predicts that the crossover field, H_c, the field at which the MR curve becomes linear, should be inversely proportion to carrier mobility, and H_c should continually increase with increasing temperature due to decreasing mobility.[26, 46] In Figure 3.7a, we present the H_c and carrier mobility as a function of temperature. The carrier mobility, $\mu = R_H/\rho$, was extracted from the measured Hall coefficient, R_H. We have estimated H_c from the first-order derivative of the MR curve with respect to the magnetic field. Here, we observe that μ and H_c follow the inverse relationship as stated by Parish and Littlewood model. Parish and Littlewood model also predicts that the slope of the linear part of MR, i.e. dMR (T)/dH, should be proportional to the μ. Figure 3.7b shows the plot of dMR(T)/dH versus μ. Interestingly, we found that dMR(T)/dH depends linearly on the μ for $Pb_{0.60}Sn_{0.40}Te$. Thus, MR and μ simply follow the relation MR(T) = μ(T)H, which has been evidenced earlier in polycrystalline Heusler topological insulators.[26,29] Hence, the LMR observed in

$Pb_{0.60}Sn_{0.40}Te$ is mainly governed by its carrier mobility, thus LMR effect can be explain based on classical Parish and Littlewood model.

3.4 Conclusions

In conclusion, we have synthesized samples of several compositions in PbTe-SnTe phase diagram and measured the band gaps in order identify the unusual band inversion. Infrared diffuse reflectance spectroscopy probes the initiation of band inversion in $Pb_{0.60}Sn_{0.40}Te$ among the various $Pb_{1-x}Sn_xTe$ (x = 0.10 - 0.85) compositions. Topological crystalline insulator composition, $Pb_{0.60}Sn_{0.40}Te$, was identified by combined solid state inorganic synthesis and band gap measurement. We have demonstrated large non-saturating LMR in $Pb_{0.60}Sn_{0.40}Te$ at different temperatures between 3 K and 300 K in magnetic field up to 9 T. Highest MR value of ~ 200 % was achieved at 3 K, which decreases to ~ 30 % at 300 K at measured field of 9 T. Magnitude of MR increases significantly with increasing carrier mobility as the temperature decreases. The proportional relation between carrier mobility and LMR shows a clear evidence of the phenomenological model of Parish and Littlewood, which attributes the spatial fluctuation of the conductivity in the material. This result demonstrates the first observation of large non-saturating LMR in $Pb_{0.60}Sn_{0.40}Te$ and sheds light on the fundamental mechanism of MR in narrow band gap chalcogenides material. It will be worth searching for large LMR effect in other narrow band gap chalcogenides.

3.5 References

[1] J. E. Lenz, *Proc. IEEE* **1990**, *78*, 973.

[2] Y. Moritomo, A.Asamitsu, H.Kuwahara, Y.Tokura, *Nature* **1996**, *380*, 141.

[3] J. Daughton, *J. Magn. Magn. Mater.* **1999**, *192*, 334.

[4] A. Urushibara, Y. Moritomo, T. Arima, A. Asamitsu, G. Kido, Y. Tokura, *Phys. Rev. B* **1995**, *51*, 14103.

[5] J. R. Ziman, Principles of the Theory of Solids Cambridge University Press, Cambridge, **1972**, 250.

[6] H. Gu, X. Zhang, H. Wei, Y.Huang, S. Wei, Z. Guo, *Chem. Soc. Rev.* **2013**, *42*, 5907.

[7] M. N. Baibich, J. M. Broto, A. Fert, F. Nguyen Van Dau, F. Petroff, P. Etienne, G. Creuzet, A. Friederich, J. Chazelas, *Phys. Rev. Lett.* **1988**, *61*, 2472.

[8] C. N. R. Rao, A. K. Cheetam, R. Mahesh, *Chem. Mater.* **1996**, *8*, 2421.

[9] A. P. Ramirez, *J. Phys.: Cond. Matter.* **1997**, *9*, 8171 and the references therein.

[10] E. J. Wildman, J. M. S. Skakle, N.Emery, A. C.Mclaughlin, *J. Am. Chem. Soc.* **2012**, *134*, 8766.

[11] J. Jiang, S. M. Kauzlarich, *Chem. Mater.* **2006**, *18*, 435.

[12] J. L. Olsen, Electron Transport in Metals (Interscience, New York, **1962**).

[13] R. Xu, A. Husmann, T. F. Rosenbaum, M. -L. Saboungi, J. E. Enderby, P. B. Littlewood, *Nature* **1997**, *390*, 57.

[14] A. Husmann, J. B. Betts, G. S. Boebinger, A. Migliori, T. F. Rosenbaum, M. -L. Saboungi, *Nature* **2002**, *417*, 421.

[15] X.Wang, Y. Du, S. Dou, C. Zhang, *Phys. Rev. Lett.* **2012**, *108*, 266806.

[16] D. X. Qu, Y. S. Hor, J. Xiong, R. J. Cava, N. P. Ong, *Science* **2010**, *329*, 821.

[17] J. Feng, Y. Pang, D.Wu, Z. Wang, H. Weng, J. Li, X. Dai, Z. Fang, Y. Shi, L. Lu, *Phys. Rev. B* **2014**, *92*, 081306.

[18] L. P. He, X. C. Hong, J. K. Dong, J. Pan, Z. Zhang, J. Zhang, S. Y. Li, *Phys. Rev. Lett.* **2014**, *113*, 246402.

[19] A. L.Friedman, J. L. Tedesco, P. M.Campbell, J. C. Culbertson, E. Aifer, F. K. Perkins, R. L. Myers-Ward, J. K. Hite, C. R. Eddy, Jr., G. G. Jernigan, D. K. Gaskill, *Nano Lett.* **2010**, *10*, 3962.

[20] Z. -M. Liao, H. -C. Wu, S. Kumar, G. S. Duesberg, Y. –B. Zhou, G. L. W. Cross, I. V. Shvets, D. -P. Yu, *Adv. Mater.* **2012**, *24*, 1862.

[21] A. A.Abrikosov, *Phys. Rev. B* **1998**, *58*, 2788.

[22] A. A.Abrikosov, *Phys. Rev. B* **2000**, *61*, 7770.

[23] M. M.Parish, P. B.Littlewood, *Nature* **2003**, *426*, 162.

[24] H.Tang, D.Liang, R. L. J.Qiu, X. P. A.Gao, *ACS Nano* **2011**, *5*, 7510.

[25] T. Thio, S. A. Solin, J. W. Bennett, D. R. Hines, M.Kawano, N. Oda, M.Sano, *Phys. Rev. B* **1998**, *57*, 12239.

[26] W. Wang, Y. Du, G. Xu, X. Zhang, E. Liu, Z. Liu, Y. Shi, J. Chen, G. Wu, X. -X.Zhang, *Sci. Rep.* **2013,** *3*, 2181.

[27] J. Hu, T. F. Rosenbaum, *Nat. Mater.* **2008**, *7*, 697.

[28] S. Ishiwata, Y.Shiomi, J. S.Lee, M. S. Bahramy, T. Suzuki, M. Uchida, R. Arita, Y. Taguchi, Y. Tokura, *Nat. Mater.* **2013**, *12*, 512.

[29] C. Shekhar, S. Ouardi, A. K. Nayak, G. H. Fecher, W. Schnelle, C. Felser, *Phys. Rev. B* **2012**, *86*, 155314.

[30] M. N. Ali, J. Xiong, S. Flynn, J. Tao, Q. D. Gibson, L. M. Schoop, T. Liang, N. Haldolaarachchige, M. Hirschberger, N. P. Ong, R. J. Cava, *Nature* **2014**, *514*, 205.

[31] K. Biswas, J. He, I. D. Blum, C. Wu, T. P. Hogan, D. N. Seidman, V. P. Dravid, M. G. Kanatzidis, *Nature* **2012**, *489*, 414.

[32] K. Biswas, J. He, Q. Zhang, G. Wang, C. Uher, V. P. Dravid, M. G. Kanatzidis, *Nat. Chem.* **2011**, *3*, 160.

[33] Y. Pei, X. Shi, A. LaLonde, H. Wang, L. Chen, G. J. Snyder, *Nature* **2011**, *473*, 66.

[34] Q. Zhang, B. Liao, Y. Lan, K. Lukas, W. Liu, K. Esfarjani, C. Opeil, D. Broido, G. Chen, Z. Ren, *Proc. Natl. Acad. Sci. USA* **2013**, *110*, 13261.

[35] G. Tan, F. Shi, J. W. Doak, H. Sun, L. D. Zhao, P. Wang, C. Uher, C. Wolverton, V. P. Dravid, M. G. Kanatzidis, *Energy Environ. Sci.* **2015**, *8*, 267.

[36] A. Banik, U. S. Shenoy, S. Anand, U. V. Waghmare, K. Biswas, *Chem. Mater.* **2015**, *27*, 581.

[37] A. Banik, K. Biswas, *J. Mater. Chem. A* **2014,** 2, 9620.

[38] U. Kattner, H. L. Lukas, G. Petzow, B. Gather, E. Irle, R. Blachnik, *Z. Metallkd.* **1988**, *79*, 32.

[39] S. Y. Xu, C. Liu, N. Alidoust, M. Neupane, D. Qian, I. Belopolski, J. D. Denlinger, Y. J. Wang, H. Lin, L. A. Wray, G. Landolt, B. Slomski, J. H. Dil, A. Marcinkova, E. Morosan, Q. Gibson, R. Sankar, F. C. Chou, R. J. Cava, A. Bansil, M. Z. Hasan, *Nat. Commun.* **2012**, *3*, 1192.

[40] Y. Okada, M. Serbyn, H. Lin, D. Walkup,W. Zhou,C. Dhital, M. Neupane, S. Xu, Y. J. Wang, R. Sankar, F. Chou, A. Bansil, M. Z. Hasan, S. D. Wilson, L. Fu, V. Madhavan, *Science* **2013**, *341*, 1496.

[41] T. H. Hsieh, H. Lin, J. Liu, W. Duan, A. Bansil, L. Fu, *Nat. Commun.* **2012**, *3*, 982.

[42] D. Hsieh, D. Qian, L.Wray, Y. Xia, Y. S. Hor, R. J. Cava, M. Z. Hasan, *Nature* **2008**, *452*, 970.

[43] Y. Xia, D. Qian, D. Hsieh, L.Wray, A. Pal, H. Lin, A. Bansil, D. Grauer, Y. S. Hor, R. J. Cava, M. Z. Hasan, *Nat. Phys.* **2009**, *5*, 398.

[44] Y. L.Chen, J. G. Analytis, J. –H. Chu, Z. K. Liu, S. K. Mo, X. L. Qi, H. J. Zhang, D. H. Lu, X. Dai, Z. Fang, S. C. Zhang, I. R. Fisher, Z. Hussain, Z. -H. Shen, *Science* **2009**, *325*, 178.

[45] X. Gao, M. S. Daw, *Phys. Rev. B* **2008**, *77*, 033103.

[46] Z. H.Wang, L.Yang, X. J.Li, X. T.Zhao, H. L.Wang, Z. D.Zhang, X. P. A.Gao, *Nano Lett.* **2014**, *14*, 6510.

[47] J. M. Schneider, M. L. Peres, S. Wiedmann, U. Zeitler, V. A. Chitta, E. Abramof, P. H. O. Rappl, S. de Castro, D. A. W. Soares, U. A. Mengui, N. F. Oliveira, Jr., *Appl. Phys. Lett.* **2014**, *105*, 162108.

Chapter 4

Dual $6s^2$ Lone Pairs Induced Cation Off-centering Leads to Intrinsically Low Thermal Conductivity in *n*-type Topological Insulator, $TlBiSe_2$

Chapter 4

Dual $6s^2$ Lone Pairs Induced Cation Off-centering Leads to Intrinsically Low Thermal Conductivity in *n*-type Topological Insulator, $TlBiSe_2$[†]

Summary

Topological insulators (TI) being a new quantum material have drawn enormous interest in solid-state chemistry and material science because of their distinctive surface properties. TIs have been considered as promising candidate for thermoelectric applications because both demand similar characteristic features in electronic structure. However, understanding of thermal transport of topological insulators is imperative to enhance thermoelectric efficiency for waste heat recovery. Herein, we report ultralow lattice thermal conductivity, κ_{latt} (1.1-0.48 W/mK) in n-type $TlBiSe_2$ in the temperature range of 300-715 K. This low κ_{latt} is ascribed to the large anharmonicity in the lattice, resulting from significant structural distortion locally while keeping the global structure rhombohedral, owing to the presence of stereochemically active $6s^2$ lone pair of Tl and Bi which is further confirmed by synchrotron X-ray pair distribution function analysis. Moreover, low temperature heat capacity measurement confirms the presence of low energy optical phonon modes which scatter heat carrying acoustic phonon modes significantly and suppressed the κ_{latt}. The κ_{latt} further decreases to 0.33 W/mK at 723 K for TlBiSeS due to the point defect scattering. We report a maximum thermoelectric figure of merit (zT) of 0.8 in n-type TlBiSeS at 715 K.

[†]*Manuscript under preparation*

4.1 Introduction

Thermoelectric innovation has increased enormous consideration from researchers in light of their potential applications in the field of waste-heat recovery, energy harvesting and solid-state energy conversion.The recent breakthrough of topological insulators (TIs) reveals new insight into this pursuit.[1-4] TIs are insulating/semiconducting materials with time-inversion symmetry protected surface states which make them different from conventional insulator and metal.[1] Topological insulators (TI) are getting to be a standout amongst the most examined classes of novel materials because of their extraordinary potential for applications extending from spintronics to waste-heat recovery.[3,4] Numerous TIs (Bi_2Te_3, Sb_2Te_3) are known to be superior thermoelectric materials due to the prerequisite of comparable highlights in the materials properties and electronic band structure.[4,5] The performance of a thermoelectric material is governed by dimensionless figure of merit, $zT = \sigma S^2T/(\kappa_{el} + \kappa_{latt})$, where, σ, S, κ_{el} and κ_{latt}, and T are electrical conductivity, Seebeck coefficient, electrical thermal conductivity and lattice thermal conductivity and absolute temperature, respectively.[6-8] Importantly, κ_{latt} is the only parameter which can tailor independently to improve the zT. Extrinsic approaches such as all-scale hierarchical architecting and endotaxial nanostructuring etc.have been employed to reduce κ_{latt} of inorganic solids.[5,9-11] On the other hand, recent studies reveal that solids with complex crystal structures,[12] soft phonon modes,[13] anharmonic ratting modes,[14] liquid-like cation disordering in superionic substructures[15] and layered structures[16] exhibit strong phonon resistance intrinsically and suppressed the thermal conductivity without affecting electrical transport.

Materials with intrinsically strong lattice anharmonicity in the crystal open up opportunities to decouple phonon and electron transport, alleviating concerns of device cost and longevity.[17] Notably, I-V-VI_2 chalcogenides exhibit ultralow thermal conductivity, originating from stereochemically active ns^2 lone pair of Group V cations.[18,19] Intrinsically low κ_{latt} has also been observed in layered SnSe due to anharmonic and strong anisotropic bonding.[16] The bond anharmonicity in SnSe can be attributed to local off-centering of Sn, resulting from active $5s^2$ lone pair.[20] Therefore, materials with characteristically low thermal conductivity are exceedingly attractive in the look for high TE performance.

In this chapter, we report an ultralow lattice thermal conductivity, κ_{latt} ~ 1.1 - 0.48 W/mK in 3D topological insulator, *n*-type $TlBiSe_2$ in a temperature range of 300–723 K. Low temperature heat capacity measurement confirms the presence of low energy optical phonon modes (Einstein modes) which scatter heat carrying acoustic phonon modes significantly. We have investigated the structural aspect of $TlBiSe_2$ and compared to well-known layered 3D topological insulator, Bi_2Te_3. The low lattice thermal conductivity is recognized to the strong anharmonicity in the lattice owing to the presence of $6s^2$ lone pair on both Tl^+ and Bi^{3+}. These stereochemically active dual lone pairs distorted the structure locally while keeping the global structure rhombohedral which is confirmed from the X-ray pair distribution function analysis. We have observed a further decrease in the κ_{latt} to 0.33 W/mK at 715 K for TlBiSeS, which is attributed to solid solution point defect scattering. As a result, a maximum zT of ~ 0.8 is achieved in *n*-type TlBiSeS at 715 K.

4.2 Methods

4.2.1 Reagents

Thallium (Tl, Aldrich 99.99 %), bismuth (Bi, Aldrich 99.999 %), selenium (Se, Alfa Aesar 99.9999%) and sulfur (S, Alfa Aesar 99.999%) were used for synthesis without further purification.

4.2.2 Synthesis

Ingots (~ 10 g) of $TlBiSe_{2-x}S_x$ (x = 0 and 1) were synthesized by mixing appropriate ratios of high-purity elemental Tl, Bi, Se and S in quartz tubes. The tubes were sealed under vacuum (10^{-6} Torr) and slowly heated to 723 K over 12 hrs, then heated up to 1173 K in 4 hrs, annealed for 10 hrs and then slowly cool down to room temperature over a period of 15 hrs.

The as-synthesized ingots were crushed and ground to fine powders using a mortar and pestle. The powders were pressed into cylindrical-shaped pellets (10 mm diameter) using spark plasma sintering system (SPS211-LX, Dr. Sinter Lab) where 40 MPa of axial pressure was applied for 5 min at 450 °C in vacuum. The SPS-processed

cylindrical-shaped sample was further cut and polished for electrical and thermal transport measurement.

4.2.3 Powder X-ray diffraction

Powder X-ray diffraction for finely ground samples were recorded using a Cu K_α (λ = 1.5406 Å) radiation on a Bruker D8 diffractometer.

4.2.4 X-ray Pair Distribution Function

Room temperature X-ray PDF data was collected using finely ground powder in beamline P02.1, PETRA III, DESY, Hamburg. Synchrotron beam of fixed energy 59.83 keV and spot size 0.5 X 0.5 mm^2 was used to collect data. 2D image plate data was collected using a Perkin-Elmer detector which was processed using Fit2D[21] software to obtain the scattering intensities S(Q) in the Q-space. The pair distribution G(r) was then obtained by Fourier transformation of the scattering structure function F(Q) = Q[S(Q) - 1] using PDFgetX2[22] software. Finally, the modeling and refinement of G(r) was done using the software PDFgui.[23]

4.2.5 Electrical transport

Electrical conductivity and Seebeck coefficients were measured simultaneously under He atmosphere from room temperature to 723 K on a ULVAC-RIKO ZEM-3 instrument system. The typical sample for measurement had a parallelepiped shape with the dimensions of ~ 2×2×8 mm^3. The longer direction coincides with the direction in which the thermal conductivity was measured.

4.2.6 Hall measurement

To determine carrier concentration, Hall measurements have been carried out using four-contact Hall-bar geometry, in a magnetic field of 0.57 T at room temperature in equipment developed by Excel Instruments.

4.2.7 Thermal transport

Thermal diffusivity, D, was directly measured in the range 300 – 723 K by using a laser flash diffusivity method in a Netzsch LFA-457 instrument. Coins with ~ 8 mm diameter and ~ 2 mm thickness were used in all of the measurements. The total thermal

conductivity, κ_{total}, was calculated using the formula, $\kappa_{total} = DC_p\rho$, where ρ is the density of the sample and C_p is the heat capacity using the Dulong–Petit limit. The density of the pellets obtained was in the range ~95 % of the theoretical density.

4.3 Results & Discussion

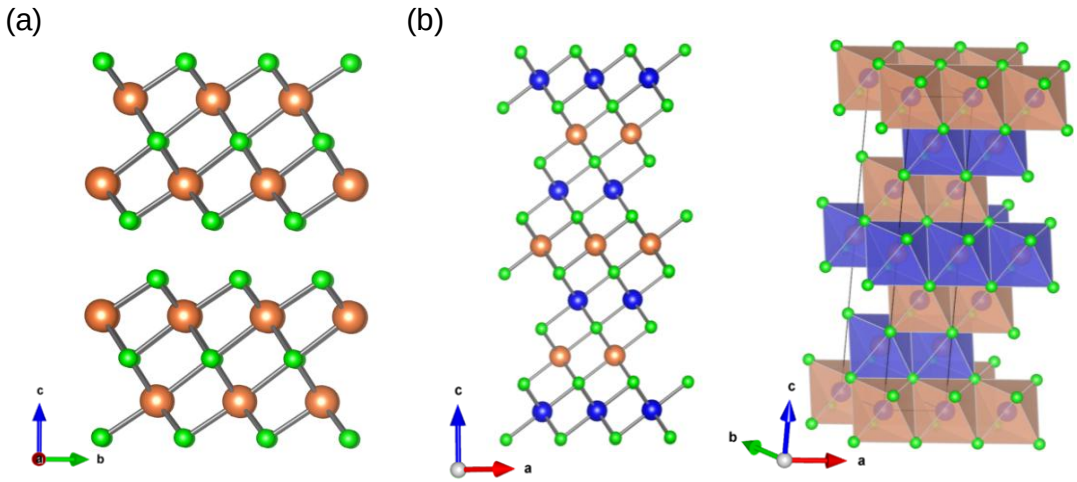

Figure 4.1 *(a) Crystal structure of tetradymites, M_2X_3 (M = Sb/Bi; X = Se/Te). (b) Left panel: Crystal structure of $TlBiSe_2$ (Green, Blue and Orange atoms represent Se, Tl and Bi, respectively); Right panel represent a 3D edge sharing octahedral network of Tl/ Bi atom which is coordinated by six Se atoms.*

Till now, tetradymites such as Bi_2Se_3 and Bi_2Te_3 are considered as archetypical topological insulators.[4] Tetradymites crystallize in rhombohedral structure (space group *R-3m*) in which quintuple layers (X1–M–X2–M–X1; M= Bi/Sb, X=Se/Te) stacked (along c axis) *via* weak van der Waals forces in the crystallographic unit cell (Figure 4.1a).[4] Recently, a single Dirac cone in the surface Brillouin Zone has been experimentally confirmed for Tl-based III-V-VI_2 ternary chalcogenides such as $TlBiSe_2$, $TlBiTe_2$ etc. which also adopt a rhombohedral structure with space group *R-3m*.[24-27] Interestingly, unlike tetradymites, $TlBiSe_2$ forms a three-dimensional crystal structure by stacking [-Tl-Se-Bi-Se-]$_n$ layers along the c axis of its unit cell without van-der-Waals gap (Figure 4.1b). In the unit cell Tl, Bi and Se occupy 3a, 3b and 4c Wyckoff sites respectively. Both

Tl and Bi atoms are coordinated with six Se atoms and a three-dimensional edge sharing octahedral arrangement is established (Figure 4.1b).

Another uniqueness of this Tl-based III-V-VI_2 ternary chalcogenide family is the existence of a topologically trivial compound such as $TlBiS_2$ whose crystal structure is indistinguishable and persistently associated with nontrivial compound, $TlBiSe_2$.[26] Thus, a phase transition (topological) from trivial to nontrivial phase is recognized in this family which is extremely unique in 3D topological insulator systems. Previous angle resolved photoemission spectroscopy (ARPES) confirmed this quantum phase transition in the solid solution $TlBi(Se_{1-x}S_x)_2$ system.[26] Importantly, topological transition happen particularly at x = 0.50 associated with a band inversion which is mainly responsible for the transition from trivial to nontrivial phase. Later, Singh *et al.* predicted that a Weyl semimetal phase can be obtained for TlBiSeS.[28] In this work we try to understand the thermal transport properties of topologically non-trivial $TlBiSe_2$ and TlBiSeS system.

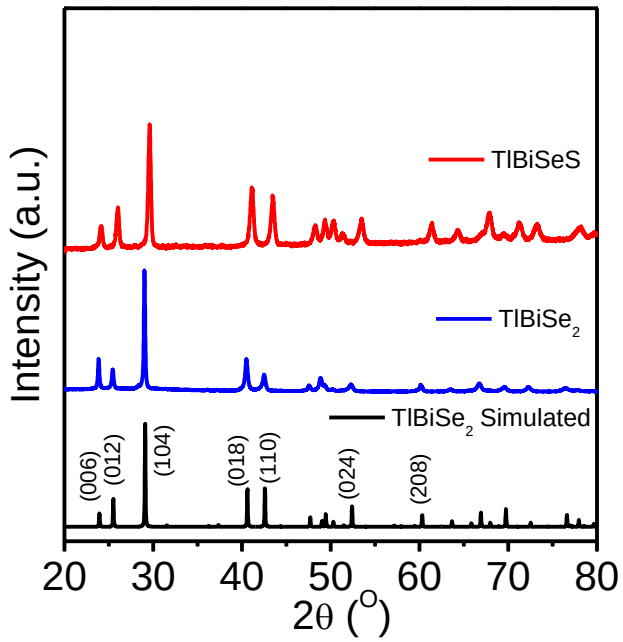

Figure 4.2 *Powder X-ray diffraction pattern for $TlBiSe_{2-x}S_x$ (x = 0, 1) samples.*

The diffraction pattern of the samples show the retention of the rhombohedral structure of $TlBiSe_2$. Substitution of S in$TlBiSe_2$ shifts the Bragg peaks towards higher

angle (2θ) because of the decrease in the lattice parameter because of the inclusion of smaller size of S (1.00 Å) in the position of Se (1.20 Å) in the $TlBiSe_2$ lattice (Figure 4.2).

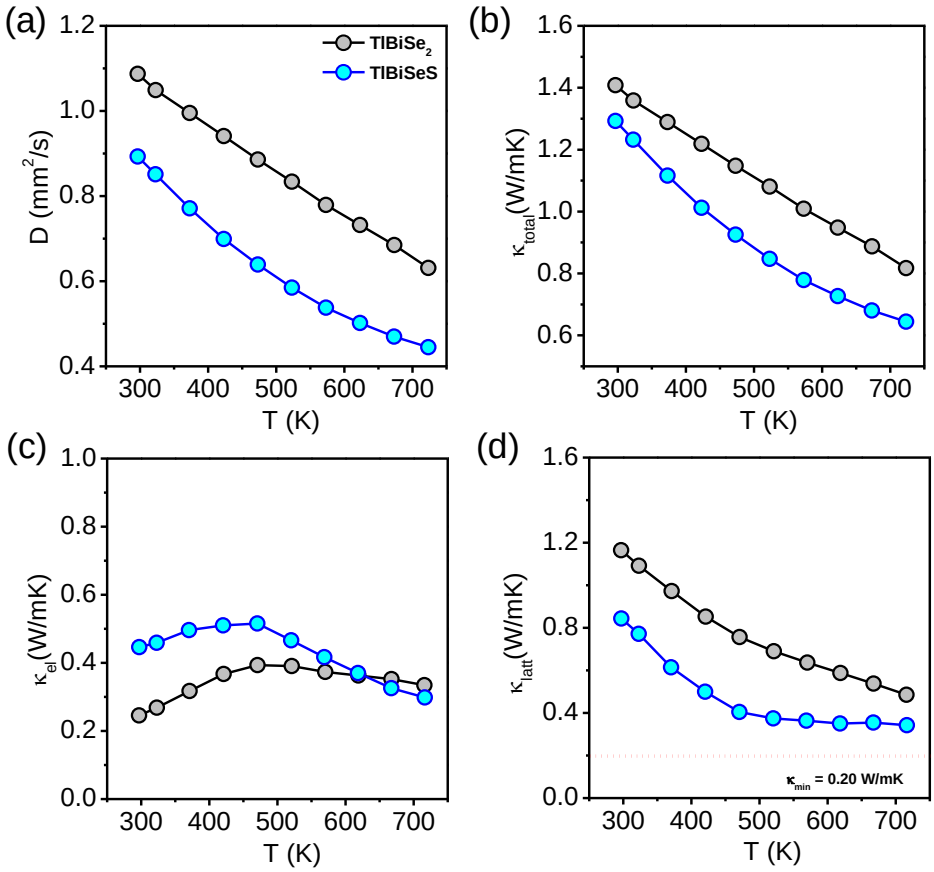

Figure 4.3 *Temperature dependent (a) thermal diffusivity (D), (b) total thermal conductivity (κ_{total}), (c) electrical thermal conductivity (κ_{el}) and (d) lattice thermal conductivity (κ_{latt}) of $TlBiSe_{2-x}S_x$ (x = 0, 1) samples.*

Figure 4.3b represents the total thermal conductivity of $TlBiSe_{2-x}S_x$ (x = 0, 1) samples as a function of temperature. At 300 K, $TlBiSe_2$ has the κ_{total} value of ~ 1.40 W/mK which decreases to ~ 1.29 W/mK for TlBiSeS sample. The lattice thermal conductivity (κ_{latt}) was obtained after subtracting the electronic contribution (κ_{el}) from κ_{total}. The κ_{el} (Figure 4.3c) were calculated by using Wiedemann-Franz relation, $\kappa_{el} = L\sigma T$, where σ is measured electrical conductivity and L is the Lorenz number calculated from reduced Fermi energy, which is acquired from the fitting of the temperature dependent Seebeck coefficient. Pristine $TlBiSe_2$ exhibits κ_{latt} of 1.16 W/mK at 300 K which further decreases to 0.49 W/mK at 715 K (Figure 4.3d). For TlBiSeS, κ_{latt} reduces to ~ 0.84 W/mK at 300 K which further deceases to ~ 0.33 W/mK at 715 K (Figure 4.3d).

Unexpectedly, Bi_2Se_3 with layered structure shows high lattice thermal conductivity, κ_{latt} of 1.82 W/mK at 300 K and further reduces to 1.2 W/mK at 715 K which is considerably higher compared to the non-layered $TlBiSe_2$ compound. Previous ab-initio calculations reveal the existence of lower transverse/longitudinal acoustic phonon velocity compared to Bi_2Se_3.[29] The calculated in-plane longitudinal and transverse sound velocities for $TlBiSe_2$ are 1650 m/s and 976 m/s respectively.[29] Thus, one possible reason for this low thermal conductivity is the presence of the low frequencies (< 50 cm^{-1}) and low group velocities induced by the heavy constituents like Tl and Bi of this compound.[29] These give hints about the presence of soft bonding interaction in the crystal which affects phonon-phonon interaction and their propagation throughout the crystals. The calculated Grüneisen parameter (γ), for $TlBiSe_2$ is 2.8 which is larger than that of Bi_2Se_3 (1.49) and Bi_2Te_3 (1.40).[29] The high γ specifies the presence of strong lattice anharmonicity in $TlBiSe_2$ compared to the layered tetradymites. The origin of this high γ will be discussed in later in details. Sulphur substitutions in $TlBiSe_2$ increases solid solution point defect scattering and decreases the lattice thermal conductivity further.

To understand the underlying mechanism for low lattice thermal conductivity, κ_{latt}, we have measured the specific heat capacity C_p of $TlBiSe_2$ in the temperature range of 2 -30 K and fitted the C_p/T *vs.* T^2 plot by using combined Debye-Einstein model (Equation 4.1 and Figure 4.4):[13,14]

$$\frac{C_p}{T} = \gamma + \beta T^2 + \sum_n \left(A_n(\theta_{E_n})^2 .\ (T^2)^{-3/2} .\ \frac{e^{\theta_{E_n}/T}}{\left(e^{\theta_{E_n}/T}-1\right)^2} \right) \qquad (4.1)$$

Where, γ and βT^2 represent electronic contribution and Debye mode contribution, respectively. β is given as $\beta = C\left(\frac{12\pi^4 N_A k_B}{5}\right).(\theta_D^{-3})$ (where, N_A, κ_B and θ_D are the Avogadro number, Boltzmann constant and Debye temperature, respectively). Here, C is presented as $C = 1 - \sum_n A_n/(3NR)$, where N and R are the number of atoms per formula unit and the gas constant, respectively.

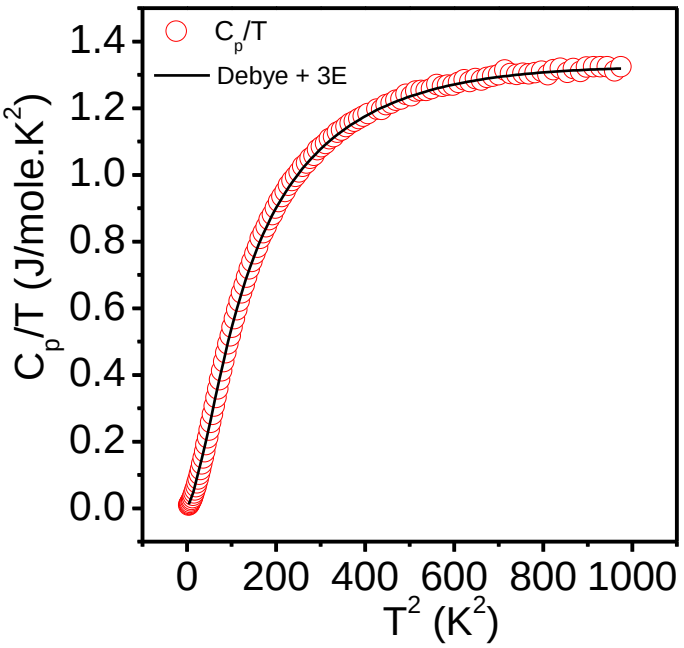

Figure 4.4 *C_p/T versus T^2 plot for $TlBiSe_2$. The solid line is calculated using the combined Debye-Einstein model.*

The last term in the above equation offers the contribution of Einstein modes and A_n is the pre-factor of the n^{th} mode. The calculated Debye temperature (θ_D) from the β value is 195 K for $TlBiSe_2$. The low temperature specific heat capacity, C_p of $TlBiSe_2$ cannot be fitted with the Debye model only and requires at least three Einstein modes whose typical temperatures are obtained from the fits are 25 K (θ_{E1} ~ 17.40 cm^{-1}), 55 K (θ_{E2} ~ 38.20 cm^{-1}) and 115 K (θ_{E3}~ 79.93 cm^{-1}) (Table 4.1).

Table 4.1: Derived parameters obtained by modeling low temperature C_p/T vs T^2 data of $TlBiSe_2$ by using combined Debye-Einstein modes.

Parameters	Debye-Einstein Model
γ /10^{-3} J mol^{-1} K^{-2}	9.99
β /10^{-4} J mol^{-1} K^{-2}	2.32
Θ_{E1} (K)	25
Θ_{E2} (K)	55
Θ_{E3} (K)	115
Debye temperature, Θ_D (K)	195
R^2	0.9997

These low-frequency Einstein modes arise because of the soft vibrations of Tl and/or Bi cations in $TlBiSe_2$ which is consistent with previous ab-initio molecular dynamics (MD) calculation.[29] These low-frequency optical phonons couple with the heat-carrying acoustic phonons effectively and play a pivotal role to suppress the lattice thermal conductivity of $TlBiSe_2$.

In tin chalcogenides (SnTe, SnSe) and lead chalcogenides (PbTe, PbSe and PbS), cations are off centered from its crystallographic position, resulting local structural distortion and strong anharmonicity in the system. ns^2 lone pair of Sn^{2+} and Pb^{2+} is mainly responsible for this local structural distortion in the globally high symmetry structure. Herein, we anticipated strong local distortion in rhombohedral $TlBiSe_2$ because both Tl^+ and Bi^{3+} possess $6s^2$ lone pair which makes this system unique compared to other system where only one atom contains active ns^2 lone pair. Interplay of dual $6s^2$ lone pair expected to create strong local anharmonicity in the system which may help to reduce κ_{latt} of $TlBiSe_2$.

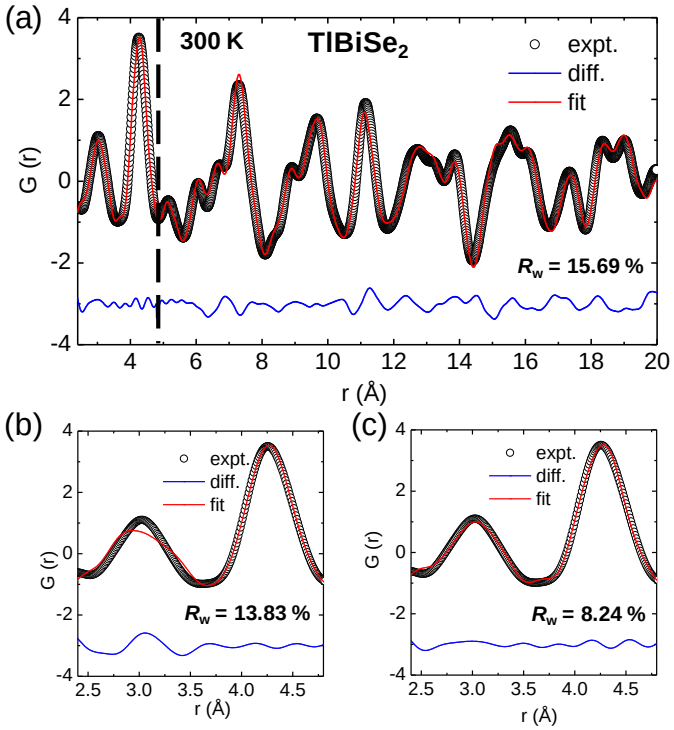

Figure 4.5 *(a) Global fit of x-ray PDF with rhombohedral structure in $TlBiSe_2$ at 300 K. Fit of x-ray PDF for the nearest neighbor atomic correlation with the consideration of (b) rhombohedral structure and (c) cation (Tl and Bi) off-centering at 300 K in $TlBiSe_2$. Although, the global structure is well fitted with rhombohedral phase, the local structure fits better with cation off-centering.*

To investigate the local structure of $TlBiSe_2$, we have performed the atomic pair distribution function (PDF) analysis which provide information about both long periodic global (Bragg scattering) along with imperfection in the local structure (diffuse scattering). The experimental X-ray PDF for $TlBiSe_2$ is shown in figure 4.5a. The long-range ordering from 4.8 – 20 Å is in good agreement with the average rhombohedral structure (*R-3m*) of $TlBiSe_2$ and yields a rational goodness of fit (R_w) of around 15.69 %.

However, in the low r region (2.4 - 4.8 Å), we observed irregularities which cannot be explained by average structure model. The experimentally obtained first peak which corresponds to the nearest atom-atom distance (*i.e.*, Tl/Bi – Se distance) do not match with the modelled rhombohedral fitting (Figure 4.5b). It can be clearly seen that the modelled peak tails of early as compared to the experimental data. Such abnormalities clearly indicate a local structural distortion under a global rhombohedral arrangement of atoms. To understand the nature of the structural distortion, we have allowed the cations (*i.e.*, Tl^+ and Bi^{3+}) to distort slightly from their parent position. We have noticed that the distortion of the cations is equal in x- and y-axis, whereas the distortion is higher in the z direction (Figure 4.5c). We have noticed both the cations to have identical distortion when we tried to refine their positions individually, making it difficult to apprehend which cation has a larger influence. We noticed that the distortion along x- and y-direction is ~ 0.163 Å whereas in the z-direction it is ~ 0.279 Å. This unique distortion in them could result from the presence of $6s^2$ lone pairs around both cations and makes $TlBiSe_2$ unique compared to the conventional I-V-VI_2 compounds.[19]

Figure 4.6a and 4.6b represent the temperature-dependent electrical conductivity (σ) and Seebeck coefficient (S) of $TlBiSe_2$ and TlBiSeS, respectively. With increasing temperature, electrical conductivity (σ) decreases and Seebeck coefficient (absolute value) increases for both the samples which represents the degenerate semiconducting transport. The σ of pristine $TlBiSe_2$ is 400 S/cm at 300 K, which decreases to ~ 275 S/cm at 715 K. Solid solution of $TlBiSe_2$ with sulfur increases the σ notably due to the enhancement in the carrier concentration from 1.76X 10^{19} cm^{-3} for pristine $TlBiSe_2$ to 2.44 X 10^{19} cm^{-3} for TlBiSeS.

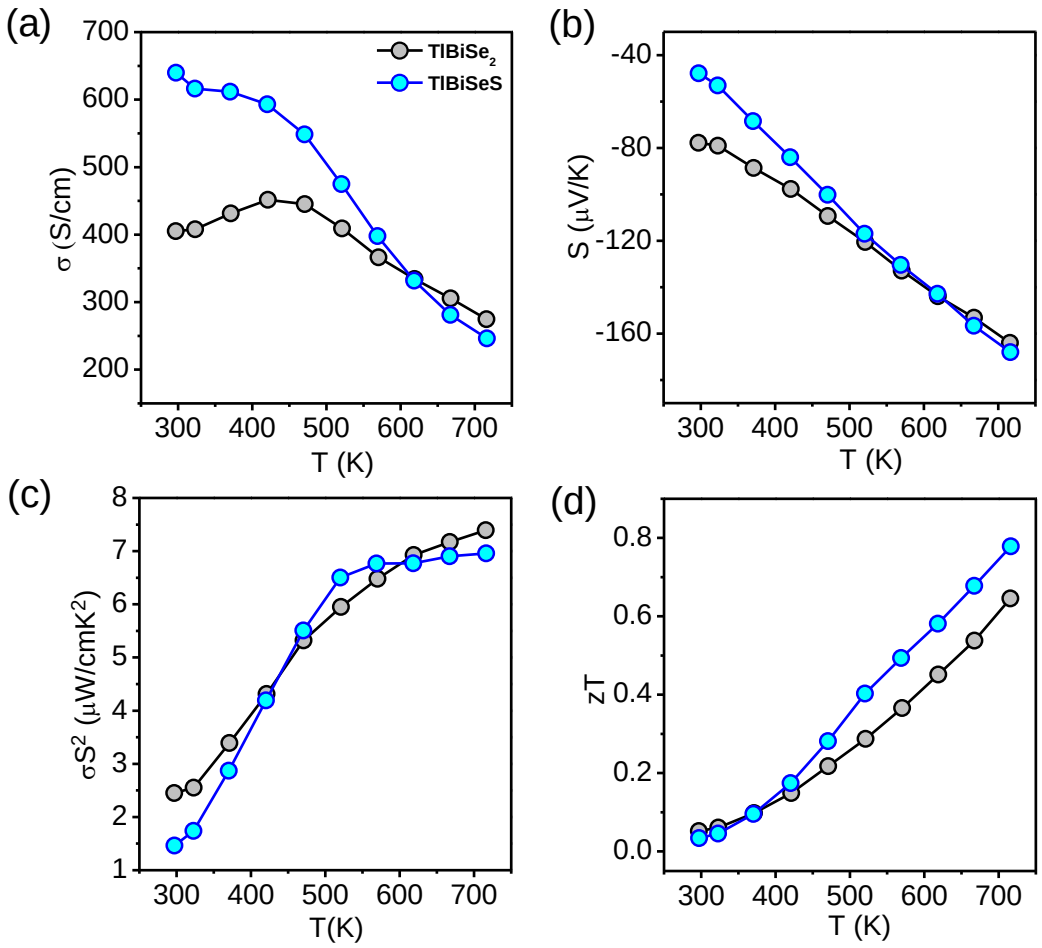

Figure 4.6 *Temperature dependent (a) electrical conductivity (σ), (b) Seebeck coefficient (S), (c) power factor (σS^2) and (d) thermoelectric figure of merit (zT) of* $TlBiSe_{2-x}S_x$ *(x = 0, 1) samples.*

S substitutions in $TlBiSe_2$ creates defects at Se site and enhances the carrier concentration of the system as each Se vacancy provides two intrinsic electrons in the crystal ($Se_{Se} \rightarrow V_{Se}^{\bullet\bullet} + Se + 2e$). Typically, the room temperature σ of TlBiSeS is found to be ~650 S/cm,which decreases to ~245 S/cm at 715 K.

Pristine $TlBiSe_2$ shows a room temperature Seebeck coefficient value of -80 μV/K which further increases to -164 μV/K at 715 K. Therefore, electrons are the majority carriers in $TlBiSe_2$, which is consistent with our Hall coefficient data (negative sign). Till now, Tl-chalcogenides based thermoelectric materials exhibit *p*-type conducting behavior whereas both *p* and *n*-type semiconductor of same material is required for thermoelectric

device fabrication due to the compatibility issue.[30-33] Thus *n*-type $TlBiSe_2$ is indeed a new addition in the family of Tl-chalcogenides for practical applications.

Figure 4.6c represents temperature-dependent power factor of all the samples. Typically, a maximum power factor of ~ 7.5 $\mu W/cm.K^2$ is achieved for $TlBiSe_2$ at 715 K. Sulfur substitutions in $TlBiSe_2$ decreases thermal conductivity further due to the enhanced solid solution point defect scattering and exhibits a maximum zT of ~ 0.8 at 715 K (Figure 4.6d) in *n*-type TlBiSeS which is higher compared to pristine *n*-type $TlBiSe_2$ (~ 0.6 at 715 K) and comparable with state-of-the-art *p*-type Tl-chalcogenides based thermoelectrics.[30-33]

4.4 Conclusions

In conclusion, topological insulator, $TlBiSe_2$ exhibits ultralow lattice thermal conductivity (1.1-0.48 W/mK) in the measured temperature range (300-715 K). This low lattice thermal conductivity is recognized to the strong anharmonicity in the lattice owing to $6s^2$ lone pair of both Tl^+ and Bi^{3+}. These stereochemically active dual lone pairs distorted the structure locally while keeping the global structure rhombohedral which is confirmed from the X-ray pair distribution function analysis also. Moreover, low temperature heat capacity experiment on $TlBiSe_2$ confirms the presence of low-energy optical phonon modes which effectively scatter heat carrying acoustic phonon and decreases the lattice thermal conductivity. The κ_{latt} further decreases 0.33 W/mK at 723 K for TlBiSeS due to the point defect scattering. Interestingly, both $TlBiSe_2$ and TlBiSeS have *n*-type conduction which is exceptionally rare in the Tl-chalcogenide thermoelectrics. We achieve a zT of ~ 0.7 and ~ 0.8 at 715 K for $TlBiSe_2$ and TlBiSeS, respectively. The thermoelectric performance of $TlBiSe_2$ can be further enhanced *via* halide doping. These results provide the fundamental understanding of thermal transport properties of topological insulators and will help further to design new topological material with intrinsically low thermal conduction.

4.5 References

[1] L. Müchler, H. Zhang, S. Chadov, B. Yan, F. Casper, J. Kübler, S. C. Zhang, C. Felser, *Angew. Chem. Int. Ed.* **2012**, *51*, 7221.

[2] L. Muchler, F. Casper, B. Yan, S. Chadov, C. Felser, *Phys. Status Solidi RRL* **2012**, *7*, 913.

[3] R. J. Cava, H. Ji, M. K. Fuccillo, Q. D. Gibson, Y. S. Hor, *J. Mater. Chem. C* **2013**, *1*, 3176.

[4] J. P. Heremans, R. J. Cava, N. Samarth, *Nat. Rev. Mater*. **2017**, *2*, 17049.

[5] B. Poudel, Q. Hao, Y. Ma, Y. Lan, A. Minnich, B. Yu, X. Yan, D. Wang, A. Muto, D. Vashaee, X. Chen, J. Liu, M. S. Dresselhaus, G. Chen, Z. Ren, *Science* **2008**, *320*, 634.

[6] J. Sootsman, D. Y. Chung, M. G. Kanatzidis, *Angew. Chem. Int. Ed*. **2009**, *48*, 8616.

[7] G. Tan, L. D. Zhao, M. G. Kanatzidis, *Chem. Rev*. **2016**, *116*, 12123.

[8] A. Banik, S. Roychowdhury, K. Biswas, *Chem. Comm*. **2018**, *54*, 6573.

[9] K. Biswas, J. He, I. D. Blum, C. I. Wu, T. P. Hogan, D. N. Seidman, V. P. Dravid, M. G. Kanatzidis, *Nature* **2012**, *489*, 414.

[10] L. D. Zhao, S. Hao, S. H. Lo, C. I. Wu, X. Zhou, Y. Lee, H. Li, K. Biswas, T. P. Hogan, C. Uher, C. Wolverton, V. P. Dravid, M. G. Kanatzidis, *J. Am. Chem. Soc.* **2013**, *135*, 7364.

[11] A. Banik, B. Vishal, S. Perumal, R. Datta, K. Biswas, *Energy Environ. Sci.* **2016**, *9*, 2011.

[12] Y. Pei, X. Shi, A. La Londe, H. Wang, L. Chen, G. J. Snyder, *Nature* **2011**, *473*, 66.

[13] M. Samanta, K. Pal, P. Pal, U. V. Waghmare, K. Biswas, *J. Am. Chem. Soc.* **2018**, *140*, 5866.

[14] M. K. Jana, K. Pal, A. Warankar, P. Mandal, U. V. Waghmare, K. Biswas, *J.Am. Chem. Soc*. **2017**, *139*, 4350.

[15] S. Roychowdhury, M. K. Jana, J. Pan, S. N. Guin, D. Sanyal, U. V. Waghmare, K. Biswas, *Angew. Chem., Int. Ed*. **2018**, *57*, 4043.

[16] L.-D. Zhao, S.-H. Lo, Y. Zhang, H. Sun, G. Tan, C. Uher, C. Wolverton, V. P. Dravid, M. G. Kanatzidis, *Nature* **2014**, *508*, 373.

[17] M. K. Jana, K. Biswas, *ACS Energy Lett.* **2018**, *3*, 1315.

[18] D. T. Morelli, V. Jovovic, J. P. Heremans, *Phys. Rev. Lett*. **2008**, *101*, 035901

[19] M. D. Nielsen, V. Ozolins, J. -P. Heremans, *Energy Environ. Sci.* **2013**, *6*, 570.

[20] C. W. Li, J. Hong, A. F. May, D. Bansal, S. Chi, T. Hong, G. Ehlers, O. Delaire, *Nat. Phys*. **2015**, *11*, 1063.

[21] A. P. Hammersley, S. O. Svensson, M. Hanfland, A. N. Fitch, D. Hausermann, *High Pressure Res.* **1996**, *14*, 235.

[22] X.Qiu, J. W Thompson,. S. J. L. Billinge, *J. Appl. Crystallogr.* **2004,** *37*, 678.

[23] C. L. Farrow, P. Juhas, J. W. Liu, D. Bryndin, E. S. Božin, J. Bloch, P. Th, S. J. L. Billinge, *J. Phys.: Condens. Matter*. **2007**, *19*, 335219.

[24] K. Kuroda, M. Ye, A. Kimura, S. V. Eremeev, E. E. Krasovskii, E. V.Chulkov, Y. Ueda, K. Miyamoto, T. Okuda, K. Shimada, H. Namatame, M. Taniguchi, *Phys. Rev. Lett.* **2010**, *105*, 146801.

[25] T. Sato, K. Segawa, H. Guo, K. Sugawara, S. Souma, T. Takahashi, Y.Ando, *Phys. Rev. Lett*. **2010**, *105*, 136802.

[26] T. Sato, K. Segawa, K. Kosaka, S. Souma, K. Nakayama, K. Eto, T. Minami, Y. Ando, T. Takahashi, *Nat. Phys*. **2011**, *7*, 840.

[27] C. Niu, Y. Dai, L. Yu, M. Guo, Y. Ma, B. Huang, *Appl. Phys. Lett*. **2011**, *99*, 142502.

[28] B. Singh, A. Sharma, H. Lin, M. Z. Hasan, R. Prasad, A. Bansil, *Phys. Rev. B* **2012**, *86*, 115208.

[29] G. Ding, J. Carrete, W. Li, G. Y. Gao, K. Yao, *Appl. Phys. Lett*. **2016**, *108*, 233902.

[30] Q. Guo, M. Chan, B. A. Kuropatwa, H. Kleinke, *Chem. Mater.* **2013**, *25*, 4097.

[31] V. S. Aswathy, C. R. Sankar, M. R. Varma, A. Assoud, M. Bieringer, H. Kleinke, *Dalton Trans*. **2017**, *46*, 17053.

[32] Y. Shi, A. Assoud, S. Ponou, S. Lidin, H. Kleinke, *J. Am. Chem. Soc*. **2018**, *140*, 8578.

[33] Q. Guo, M. Chan, B. A. Kuropatwa, H. Kleinke, *J. Appl. Phys.* 2014, 116, 183702.

PART 3

Thermoelectric Properties of Germanium Chalcogenides

Chapter 1

High Thermoelectric Performance and Enhanced Mechanical Stability of *p*-type Cation Doped GeTe

Chapter 1

High Thermoelectric Performance and Enhanced Mechanical Stability of *p*-type Cation Doped GeTe[†]

Summary

Thermoelectric materials can convert untapped heat to electricity and are expected to have an important role in future energy utilization. IV−VI metal chalcogenides are the most promising candidates for mid-temperature thermoelectric power generation. Among them, PbTe and their alloys have been proven to be the superior thermoelectric materials. Unfortunately, the toxicity of lead (Pb) prevents the application of lead chalcogenides and demands the search for lead-free high-performance solids. As an alternative, GeTe-rich alloys such as TAGS ($GeTe–AgSbTe_2$) have been largely investigated since the 1960s. In the present chapter, we show that aliovalent cation (Sb and Bi) doping act as effective donor dopants and decreases the carrier concentration of GeTe. Sb and Bi doping in GeTe enhances the valence band degeneracy by increasing the cubic nature of the sample, which collectively boost Seebeck coefficient in the 300 - 773 K temperature range. Significant thermal conductivity reduction was achieved due to collective phonon scattering from various meso-structured domain variants, twin and inversion boundaries, nano-structured defect layers, and solid solution point defects. High thermoelectric figure of merit, zT, of ~ 1.85 at 725 K along with significant cyclable temperature stability was achieved in Pb-free p-type $Ge_{1-x}Sb_xTe$ samples through simultaneous enhancement in Seebeck coefficient and reduction of thermal conductivity. A maximum zT of ~ 1.3 at 725 K was obtained for $Ge_{0.94}Bi_{0.06}Te$ sample. The high performance $Ge_{0.90}Sb_{0.10}Te$ and $Ge_{0.94}Bi_{0.06}Te$ samples show mechanical stability (Vickers microhardness) of ~ 206 H_v and ~ 165 H_v which is significantly higher compared to other popular thermoelectric materials such as Bi_2Te_3, PbTe, PbSe, Cu_2Se and TAGS.

[†]*Papers based on this study have been published in (1) Chem. Mater.* ***2015****, 27, 7171; (2) Inorg. Chem. Front.* ***2016****, 3, 125.*

1.1 Introduction

Lead telluride (PbTe) based materials are so far considered to be leading thermoelectric materials for intermediate 600-900 K temperature range power generation.[1,2] However, environmental concern about Pb limits its usage in the large scale thermoelectric applications. Although GeTe based alloys known for their promising thermoelectric properties since 1960s,[3,4] GeTe has not attracted as much attention as others in the IV-VI semiconductor family. Pristine GeTe is a *p*-type degenerate semiconductor with large carrier density (~ 10^{21} cm^{-3}) due to its intrinsic Ge-vacancy,[5-7] which is resulting high electrical conductivity of 8500 S/cm, low Seebeck coefficient value of ~ 34 μV/K, and perversely high total thermal conductivity of ~ 8 W/mK at room temperature, thus leading to a maximum *zT* value of 0.8 at 720 K.[8] GeTe undergoes the ferroelectric structural phase transition from high temperature cubic (*β*-phase) to low temperature rhombohedral (*α*- phase) at ~ 700 K due to the thermal strain induced shift in Ge atoms (Figure 1.1), which thrusts the distortion in the unit cell along [111] direction with an angular distortion of α = 1.65°.[9-11]

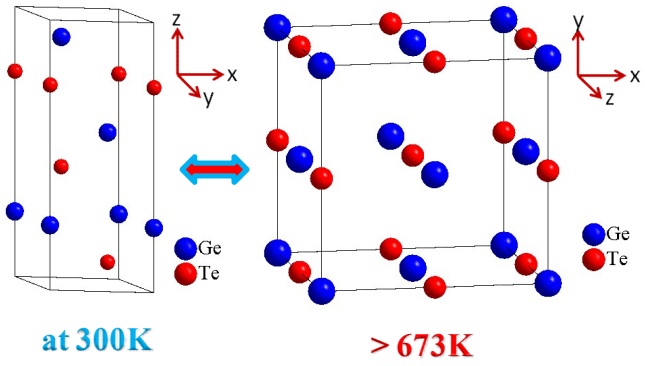

Figure 1.1 *Rhombohedral to cubic structural phase transition in GeTe.*

Pseudo-binary solid solution of GeTe-$AgSbTe_2$, generally known as TAGS-80 & TAGS-85 depending on composition, illustrated the promising thermoelectric performance.[12-16] Recently, $Ge_xPb_{1-x}Te$ is considered to be high performance thermoelectric materials due to the donor dopant nature of Pb which increases Seebeck coefficient drastically by reducing carrier density and the presence of low thermal conductivity generated from the thermodynamically driven various nanoscale

modulations.[17-20] Recently, *zT* of ~ 1.9 at 773 K was obtained in 3 mol % Bi_2Te_3 doped $Ge_{0.87}Pb_{0.13}Te$ samples due to the thermal conductivity reduction from point defect scattering of phonons and enhancement of power factor through valence band convergence.[21] Although Pb-free thermoelectric is desirable for mass-market applications, high performance $Ge_xPb_{1-x}Te$ composition contains 13 mol % of Pb.

In this chapter, we present an extraordinary thermoelectric performance and high mechanical stability in Pb-free *p*-type $Ge_{1-x}M_xTe$ (M = Sb and Bi). The maximum figure of merit, *z*T, of ~ 1.85 and ~ 1.30 were achieved for the composition of $Ge_{0.90}Sb_{0.10}Te$ and $Ge_{0.94}Bi_{0.06}Te$, respectively at 725 K. We achieve significant enhancement in *zT* due to the following collective reasons: (i) aliovalent substitution of Sb^{3+} / Bi^{3+} at Ge^{2+} site in GeTe decreases the *p*-type carrier concentration due to donor dopant nature of Sb^{3+}/ Bi^{3+}, which resulted in enhanced Seebeck coefficient; (ii) Sb (Bi) doping in GeTe significantly increases the cubic nature at room temperature and decreases the rhombohedral to cubic phase transition temperature, thus enhance the valence band degeneracy, which in turn increases Seebeck coefficient, and (iii) significant reduction in the lattice thermal conductivity was obtained due to phonon scattering of various nano/meso-scale structures such as domain variants, twin and inversion boundaries, defect layers, nanoprecipitates and solid solution point defects. A maximum thermoelectric conversion efficiency (η_{max}) of ~ 12% was calculated by considering virtual thermoelectric module consisting of present *p*-type $Ge_{0.90}Sb_{0.10}Te$ and previously reported *n*-type 8% of Sn doped PbTe-PbS,[22] by maintaining the temperature difference of ΔT = 400 K. Mechanical stability is also an important issue for thermoelectric material when it used in devices for power generation. We have measured Vickers micro-hardness (H_v) of 206 and 165 for the present *p*-type $Ge_{0.90}Sb_{0.10}Te$ and $Ge_{0.94}Bi_{0.06}Te$, respectively which is significantly higher than pristine GeTe (~ 145 H_V) and other state-of-art thermoelectric materials such as Bi_2Te_3, PbTe, PbSe, Cu_2Se and TAGS.[23-30]

1.2 Methods

1.2.1 Reagents

Germanium (Ge, Aldrich 99.999%), antimony (Sb, Alfa Aesar 99.9999%), bismuth (Bi, Alfa Aesar 99.9999%) and tellurium (Te, Alfa Aesar 99.999+ %) were used for synthesis without further purification.

1.2.2 Synthesis

High quality crystalline ingots (~ 10 g) of $Ge_{1-x}Sb_xTe$ (x = 0 − 0.10) and $Ge_{1-x}Bi_xTe$ (x = 0 − 0.10) were synthesized by mixing appropriate ratios of high purity starting materials of Ge, Sb, Bi and Te in a quartz tube. The tube was sealed under vacuum (10^{-6} Torr) and slowly heated to 1223 K over 10 h then annealed for 6 h, and cooled slowly to room temperature over 10 h.

1.2.3 Powder X-ray diffraction

Room-temperature Powder X-ray diffraction for finely grounded samples were recorded using a Cu K_α (λ = 1.5406 Å) radiation on a Bruker D8 diffractometer. Temperature dependent XRD patterns were recorded using the attached high temperature chamber.

1.2.4 Band gap measurement

To estimate optical band gap of the as synthesized samples, diffuse reflectance measurement has been done with finely grounded powder at room temperature using FT-IR Bruker IFS 66V/S spectrometer in the wave number range 4000-400 cm^{-1} with 2 cm^{-1} resolution and 50 scans. Absorption (α/S) data were calculated from reflectance data using Kubelka-Munk equation: $\alpha/S = (1-R)^2/(2R)$, where R is the reflectance, α and S are the absorption and scattering coefficient, respectively. The energy band gaps were derived from α/S vs E_g (eV) plot.

1.2.5 TEM measurements.

TEM imaging was performed using an aberration corrected FEI TITAN cubed 80 – 300 kV transmission electron microscopes, operating at 300 kV.

1.2.6 Electrical transport.

Electrical conductivity and Seebeck coefficients were measured simultaneously under He atmosphere from room temperature to 773 K on a ULVAC-RIKO ZEM-3 instrument system. The typical sample for measurement had a parallelepiped shape with the dimensions of ~ 2×2×8 mm^3. The longer direction coincides with the direction in which the thermal conductivity was measured.

1.2.7 Hall measurement.

Hall measurement was carried out at room temperature in the home made setup, where fixed magnetic field and dc-current were used to be 0.25 T and 5 mA, respectively. The carrier concentration of holes (n) was calculated from the equations of $n = 1/(eR_H)$, where R_H is the Hall coefficient and e is the electron charge.

1.2.8 Thermal transport.

Thermal diffusivity, D, was directly measured in the range 300 − 773 K by using the laser flash diffusivity method in a Netzsch LFA-457. Coins with ~ 8 mm diameter and ~ 2mm thickness were used in all of the measurements. Temperature dependent heat capacity, C_p, was derived using standard sample (pyroceram) in LFA-457, which is in good agreement with Dulong-Petit C_p value. The total thermal conductivity, κ_{total}, was calculated using the formula $\kappa_{total} = DC_p\rho$, where ρ is the density.

1.2.9 Mechanical properties.

Microhardness of all the samples was measured in the home-made microhardness machine using the diamond indenter on the Vickers hardness scale, where the force was used to be 1 N and the indent was kept for 10s. Vickers hardness (kg/mm^2) values were determined by the equation of $H_v = 1.854 \times L/(2d)^2$, where L is the indentation load and 2d is the diagonal length of the indentation. The uncertainity of microhardenss measurement is about 5%.

1.2.10 Methods for calculation of theoretical device figure of merit and thermoelectric efficiency.

(a) Device figure of merit, $(ZT)_m$ for single pair (p and n- type legs).

$(ZT)_m$ value was theoretically calculated from the following equation where previously reported $Pb_{1-x}Sn_xTe$-PbS was used as *n*-type leg[22] and present $Ge_{0.90}Sb_{0.10}Te$ was kept to *p*-type leg, and hot and cold side temperatures are kept to be 700 K and 300 K, respectively.

$$(ZT)m = \int_{T_c}^{T_h} \frac{(S_p - S_n)^2 \,.\, T}{[\sqrt{\rho_p.\kappa_p} + \sqrt{\rho_n.\kappa_n}]^2.\ \Delta T} dT \quad (1.1)$$

Where (S_p and S_n), (ρ_p and ρ_n) and (κ_p and κ_n) represent the Seebeck coefficient, electrical resistivity and total thermal conductivity of *p*-and *n*-type materials, respectively.

(b) Thermoelectric efficiency.

The conversion efficiency of the aforesaid pair of the materials was theoretically calculated from the equation,

$$\eta_{TE} = (\Delta T/T_h)\frac{\left(\sqrt{1+(ZT)_{avg}}-1\right)}{\left(\sqrt{1+(ZT)_{avg}}+\frac{T_c}{T_h}\right)} \quad (1.2)$$

Where $\Delta T/T_h$ refers the Carnot efficiency, T_h and T_c are the hot and cold side temperature and $(ZT)_{avg}$ is an average figure-of-merit of a pair of thermoelectric materials.

1.3 Results & Discussion

Room temperature powder X-ray diffraction (PXRD) patterns of $Ge_{1-x}Sb_xTe$ (x = 0 - 0.10) samples could be indexed based on rhombohedral GeTe structure (space group, *R3m*) with no other impurity phase being observed within the detection limits of PXRD (Figure 1.2a). Additionally, presence of double-peaks [(024) and (220)] in between 2θ = 41 - 45˚ indicates the rhombohedral structure at room temperature, but these two peaks approach closer with the increasing of Sb doping concentration in GeTe (Figure 1.2b), which suggests that cubic nature of $Ge_{1-x}Sb_xTe$ increases with increasing Sb doping concentration. High temperature (323-773K) PXRD patterns of $Ge_{0.90}Sb_{0.10}Te$ indicates the rhombohedral to cubic transition temperature to be ~ 573 K, which is significantly lower than that for pristine GeTe (~723 K) (Figure 1.2c and d). Sb doping in GeTe enhances the cubic nature of the sample, which may have significant impact on the Seebeck coefficient (discussed later).

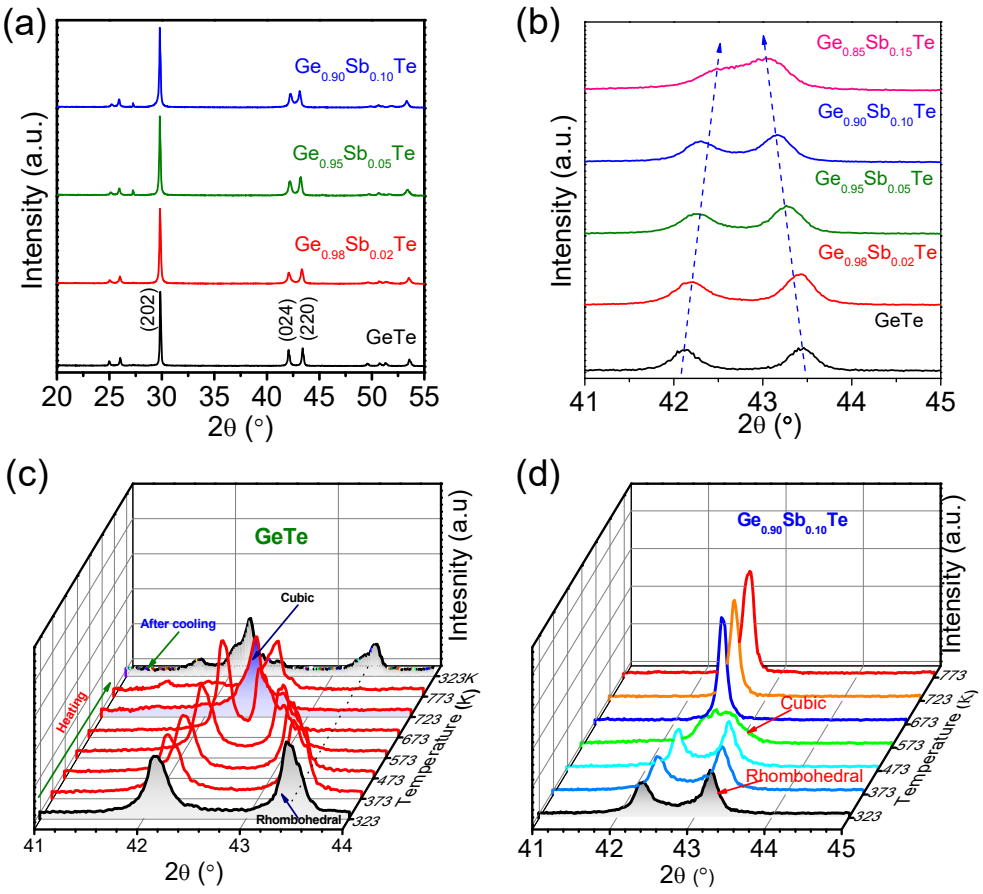

Figure 1.2 *(a) PXRD pattern of $Ge_{1-x}Sb_xTe$ (x = 0 – 0.10) samples at 300 K. (b) Sb doping in GeTe merges the double peaks of (024) and (220), which confirms the increase in cubic nature with the increase in Sb doping in GeTe. High temperature PXRD pattern of (c) GeTe and (d) $Ge_{0.90}Sb_{0.10}Te$ showing structural transition.*

Figure 1.3 represents the optical absorption spectra of $Ge_{1-x}Sb_xTe$ samples. With increasing the concentration of Sb doping from 0 mol% to 10 mol% in GeTe, the band gap decreases from ~ 0.2 eV to ~ 0.08 eV. Electronegitivity of Te (2.10, Pauling electronegative scale) is more than that of Ge (2.01). In GeTe, valence and conduction bands are mostly constituted by Te and Ge orbitals, respectively. Substituting Sb (electronegetivity, 2.05) in place of Ge lowers the conduction band energy, which gives rise to decrease in the band gap of $Ge_{1-x}Sb_xTe$. Previous first principle electronic structure calculations also indicated decreases in the band gap of GeTe after Sb doping due to lowering of conduction band energy.[31]

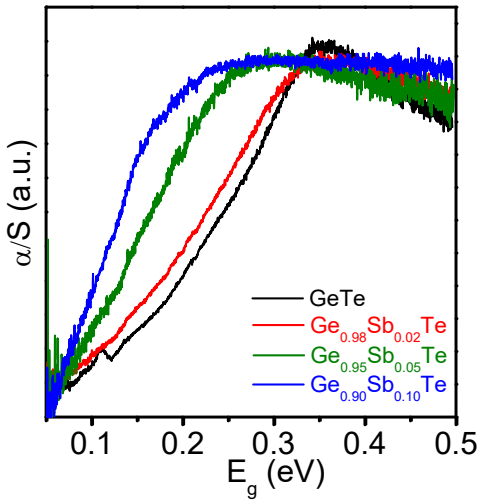

Figure 1.3 *Optical absorption spectra of $Ge_{1-x}Sb_xTe$ (x = 0 – 0.10) samples at 300 K.*

Aberration corrected transmission electron microscope (TEM) was used to examine the nano/meso-scale architectures of $Ge_{0.90}Sb_{0.10}Te$ sample (see Figure 1.4). TEM investigation of $Ge_{0.90}Sb_{0.10}Te$ exemplifies the following features: (i) formation of ordered domain variants, surrounded by (001), (0-10) and (11-1) planes, usually referred as herringbone structures with successive bright and dark contrasts; (ii) inversion boundaries and twin boundaries along <110> direction; (iii) nanoscale ordered layer structures of cation vacancies and (iv) the formation of van der Waals gaps due to relaxation of Te atom in the vicinity of the defect layer, which are observed throughout the sample.[32-36] Figure 1.4a shows bright field TEM image representing the domain variants with bright and dark contrasts in the <110> direction. The sucessive contrast variation occurs due to the breakdown of Friedel symmetry of non-centrosymmetric crystals.[21] Figure 1.4b represents the high resolution TEM (HRTEM) micrograph of the matrix with the measured interplanar distance of d = 0.34 nm which corresponds to (021) planes of GeTe. Fast Fourier transforms (FFTs) and dark field pattern of electron diffraction analysis confirm the rhombohedral structure. Selected area electron diffraction pattern (SAED) along <001> zone axis obtained from same area indicates the single crystalline nature of the material.

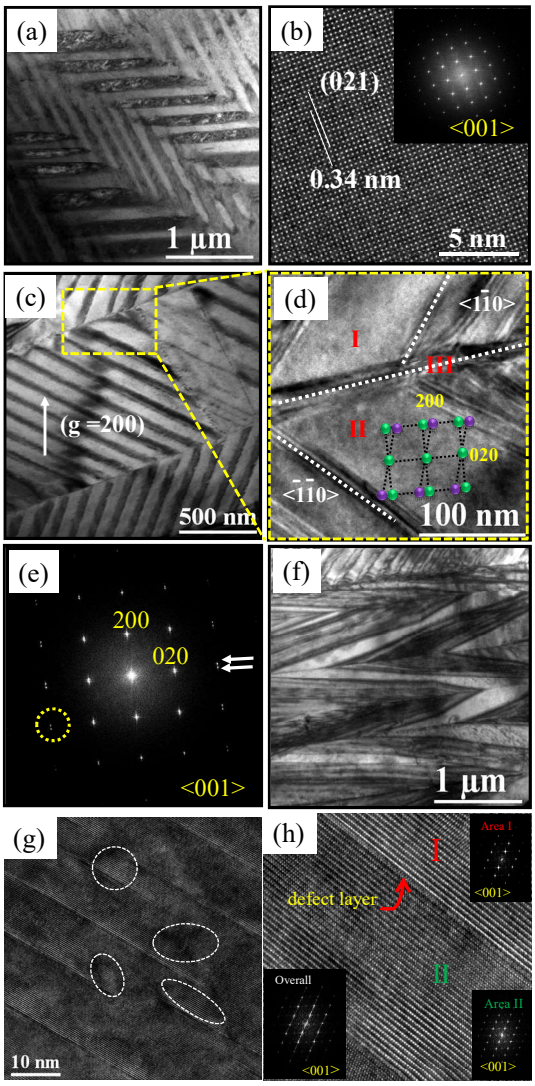

Figure 1.4 *(a) Low magnification TEM micrograph of $Ge_{0.90}Sb_{0.10}Te$ showing domain variants called herringbone structure. (b) HRTEM image of $Ge_{0.90}Sb_{0.10}Te$. SAED pattern along the <001> zone axis as an inset in (b). (c) TEM micrograph shows the twin boundaries along <110> direction. (d) Zoomed version of TEM micrograph in (c) showing the twin boundaries. Inset in (d) shows the schematic twin structure formation. (e) SAED pattern along zone axis of <001> confirms the twin boundaries with clear spots splitting. (f) TEM image shows the presence of inversion boundaries between two domains with different polarity. (g) HRTEM of defect layers. Dotted circle in (g) denotes the nanoprecipitates. (h) Zoomed area of defect layers with SAED pattern in different regions, where defect-free regions (I and II) show clear SAED pattern and overall region shows the diffused SAED pattern.*

Figure 1.4c indicates the formation of "reflection twins" along <110> direction with different domain variants in terms of contrast difference. Figure 1.4d shows the zoomed version of twin boundaries where domains were clearly distinguished. In addition, the corresponding SAED pattern (Figure 1.4e) shows spot splitting, which confirms the twins. Twin free regions (I and II in Figure 1.4d, twin planes along <-1-10> and <1-10>, respectively) showed no spots splitting, whereas overall region (region III) shows clear indication of spot splitting in the electron diffraction patterns, thus confirming the twins. Twins are formed due to the cubic to rhombohedral distortion while cooling from melting.

Additionally, presence of inversion domain boundaries were clearly seen in Figure 1.4f, which is formed because of the existence of two domain region, where trigonal axis are parallel but of opposite polarity.[33] Nanoscale planar defect layers were also observed in $Ge_{0.90}Sb_{0.10}Te$ sample (Figure 1.4g and h), which are formed due to Ge vacancies.[34-36] These defect layer regions show a diffused SAED pattern, whereas defect free regions depict relatively perspicuous SAED pattern (Figure 1.4h). HRTEM imaging shows the presence of strained endotaxial nanoprecipitates in a few regions of the $Ge_{0.90}Sb_{0.10}Te$ sample (Figure 1.4g).

Figure 1.5 represents the thermoelectric properties of $Ge_{1-x}Sb_xTe$ (x = 0- 0.10) samples in the measured 300 - 800 K temperature range. Electrical conductivity (σ) and Seebeck coefficient (S) were measured simultaneously under He atmosphere on a ULVAC-RIKO ZEM3 instrument. σ values of the $Ge_{1-x}Sb_xTe$ samples decrease with increasing the temperature (Figure 1.5a), indicating degenerate semiconductor behavior. Substitution of Sb in GeTe drastically decreases the σ from ~ 8067 S/cm for GeTe to ~ 1529 S/cm for $Ge_{0.90}Sb_{0.10}Te$ at 300 K. This confirms that the Sb alloying indeed suppresses the Ge vacancies and decrease the carrier concentrations. Typically, the room temperature σ of pristine GeTe is to be ~ 8067 S/cm, which decreases to ~ 2152 S/cm at 710 K. $Ge_{0.90}Sb_{0.10}Te$ sample exhibits σ value of ~ 1529 S/cm at room temperature, which decreases to ~ 778 S/cm at 775 K. Temperature dependent σ curves show a signature of structural phase transition in between 570 - 670 K $Ge_{1-x}Sb_xTe$ samples.

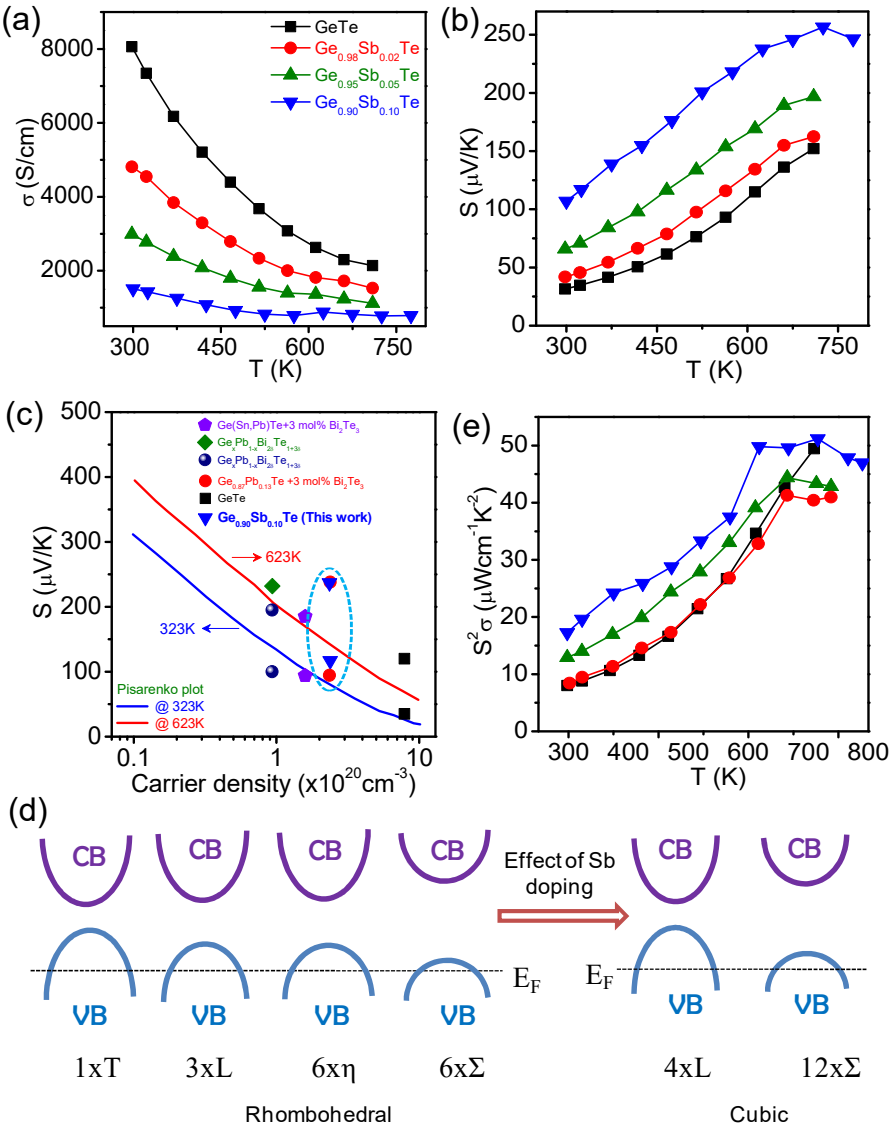

Figure 1.5 *Temperature dependent (a) electrical conductivity (σ) and (b) Seebeck coefficient (S) of $Ge_{1-x}Sb_xTe$ (x = 0 - 0.10) samples. (c) S vs. n data of $Ge_{1-x}Sb_xTe$ compared with Pisarenko plot of GeTe and state of the art GeTe based samples[17,20,21] (d) Schematic shows that the valence band valley degeneracy is more in high symmetry cubic phase (Fm-3m) compared to that of the low symmetry rhombohedral (R3m) phase of GeTe. With Sb-doping in GeTe[37], one T pocket and three L pockets merge to four L pockets; and 6 η pockets and 6 Σ pockets merge into 12 Σ pockets, thus valence band degeneracy increases, which resulted in an enhanced Seebeck coefficient. (e) Temperature dependent power factor ($S^2\sigma$) of $Ge_{1-x}Sb_xTe$ (x = 0 - 0.10) samples.*

The Hall coefficients, R_H, at room temperature for pristine and Sb doped GeTe samples are positive, which indicate *p*-type conduction in this system. Assuming parabolic bands and a single band conduction process at 300 K, we estimated the carrier concentration, n, from the formula: $n = 1/eR_H$, where e is the electronic charge. GeTe, $Ge_{0.98}Sb_{0.02}Te$, $Ge_{0.95}Sb_{0.05}Te$, and $Ge_{0.90}Sb_{0.10}Te$ samples exhibit *n*-values to be ~ 8.72×10^{20} cm^{-3}, ~ 5.8×10^{20} cm^{-3}, ~ 3.68×10^{20} cm^{-3}, and ~ 2.38×10^{20} cm^{-3}, respectively, at room temperature (see Table 1.1). Decrease in the hole concentrations indicates aliovalent donor doping of Sb^{3+} in Ge^{2+} sublattice of GeTe.

Table 1.1: Hall Carrier Concentration of $Ge_{1-x}Sb_xTe$ (x = 0 − 0.10) Samples.

Sample	**Carrrier concentration, n, ($\times10^{20}$ cm^{-3})**
GeTe	8.72
$Ge_{0.98}Sb_{0.02}Te$	5.80
$Ge_{0.95}Sb_{0.05}Te$	3.68
$Ge_{0.90}Sb_{0.10}Te$	2.38

Temperature dependences of Seebeck coefficients (S) of $Ge_{1-x}Sb_xTe$ (x = 0 − 0.10) are presented in Figure 1.5b. Positive sign of the S values indicates *p*-type conduction, which also supports the Hall coefficient data. The S-value of pristine GeTe is ~ 32 μV/K at 300 K, which reaches ~ 150 μV/K at 710 K. The S-value gradually increases with the addition of Sb in GeTe in the 300 − 773 K temperature range (Figure 1.5b). Typically, $Ge_{0.90}Sb_{0.10}Te$ exhibits an S-value of ~ 107 μV/K at 300 K, which reaches a maximum of ~ 256 μV/K at 725 K. We have compared our experimental *S* versus *n* data with the previously reported Pisarenko plots[21] both at 323 and 623 K and also with the S of previously reported 3 mol % Bi_2Te_3 doped $Ge_{0.87}Pb_{0.13}Te$,[21] $Ge_{1-x}Pb_xTe$,[20] and $(GeTe)_{1-x}[(PbTe)(SnTe)\ (Bi_2Te_3)]_x$[17] in Figure 1.5c. At 323 K, the experimental S-value of $Ge_{0.90}Sb_{0.10}Te$ falls slightly above to Pisarenko line; however, at 623 K, experimental S-values lie significantly above the Pisarenko line.

This increase in *S* could be attributed to following collective reasons: (i) reduction of *p*-type carrier concentration due to the donor dopant nature of Sb in GeTe and (ii) Sb substitution in GeTe enhances the cubic nature of the sample (see PXRD section), which resulted in an increase in valence band valley degeneracy. Valence band valley degeneracy is more in high symmetry cubic phase (*Fm-3m*) compared to that of the low symmetry rhombohedral (*R3m*) phase of GeTe (Figure 1.5d). With Sb-doping in GeTe, one T pocket and three L pockets merge to four L pockets; and 6 η pockets and 6 Σ pockets merge into 12 Σ pockets (Figure 1.5d),[34] thus valence band degeneracy increases, which resulted in enhanced Seebeck coefficient. We have estimated effective mass (*m**) of the carriers in $Ge_{1-x}Sb_xTe$ using measured *S* and Hall carrier concentration (*n*) at room temperature following equations 1.3-1.5.[38]

$$m^* = \frac{h^2}{2k_BT}\left[\frac{n}{4\pi F_{1/2}(\eta)}\right]^{2/3} \tag{1.3}$$

$$S = \pm \frac{k_B}{e}\left(\frac{(r+3/2)F_{r+3/2}(\eta)}{(r+3/2)F_{r+1/2}(\eta)} - \eta\right) \tag{1.4}$$

$$F_n(\eta) = \int_0^\infty \frac{x^n}{1+e^{x-\eta}}dx \tag{1.5}$$

Where, η , $F_n(\eta)$, k_B , e , h , and r stand for reduced Fermi energy, n[th] order Fermi integral, the Boltzmann constant, electron charge, Planck constant and scattering factor, respectively. By fitting the respective Seebeck data, the reduced Fermi energy was extracted. Although accurate calculation of *m** require consideration of non-parabolic band and multiple band model, present calculation of *m** considers only single parabolic band with acoustic phonon scattering (r = -1/2) for simplicity.[21] The *m** value of $Ge_{0.90}Sb_{0.10}Te$ is to be $2.07m_0$, which is significantly higher than that of pristine GeTe ($1.43m_0$), which also suggests the effect of valence band degeneracy. Increase in the cubic nature in $Ge_{1-x}Sb_xTe$ increases the possibility of occupancy of the *p*-type carriers to the more numbers of degenerate band valleys, which results in increases in the Seebeck coefficient.

Temperature dependence of power factors of ($S^2\sigma$) $Ge_{1-x}Sb_xTe$ (x = 0 - 0.10) are presented in the Figure 1.5e. Typically, GeTe show the $S^2\sigma$ value of ~ 8 $\mu Wcm^{-1}K^{-2}$ at 300 K, which rises to ~ 49.4 $\mu Wcm^{-1}K^{-2}$ at 710 K, whereas $Ge_{0.90}Sb_{0.10}Te$ sample exhibits the $S^2\sigma$ value of ~ 17.2 $\mu Wcm^{-1}K^{-2}$ at 300 K, then reaches the maximum value of ~ 51.4 $\mu Wcm^{-1}K^{-2}$ at 725 K.

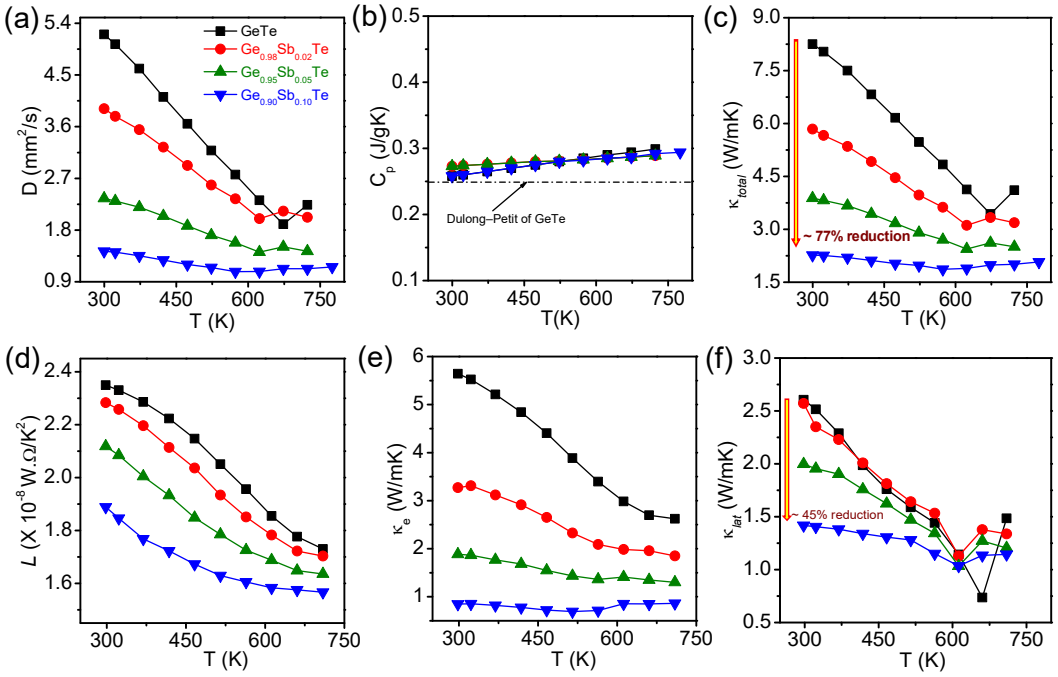

Figure 1.6 *Temperature dependent (a) diffusivity (D), (b) heat capacity (C_p), (c) total thermal conductivity (κ_{total}), (d) Lorenz number (L), (e) electrical thermal conductivity (κ_e) and (f) lattice thermal conductivity (κ_{lat}) of $Ge_{1-x}Sb_xTe$ (x = 0 - 0.10) samples.*

The total thermal conductivities, κ_{total}, of the samples were estimated in the temperature range of 300 - 773 K using the formula, $\kappa_{total} = DC_p\rho$, where, D is the thermal diffusivity (Figure 1.6a), C_p is specific heat (Figure 1.6b) and ρ is density (~ 99 % of the theoretical density) of the sample. D was measured by the laser flash diffusivity technique by using NETZSCH LFA-457 instrument over 300 - 773 K range. Temperature dependent total thermal conductivity (κ_{total}) of $Ge_{1-x}Sb_xTe$ (x = 0 - 0.10) are illustrated in Figure 1.6c. Substitution of Sb in GeTe substantially reduces κ_{total} value. At 300K, GeTe has the κ_{total} value of ~ 8.24 $Wm^{-1}K^{-1}$, whereas $Ge_{0.90}Sb_{0.10}Te$ shows the κ_{total} value of ~ 2.25 $Wm^{-1}K^{-1}$, which is about ~ 77 % reduction with respect to the κ_{total} of pristine

GeTe. Observed significant reduction in κ_{total} can be attributed due to the reduction in both electronic and lattice thermal conductivity. Mention must be made that slight upturn of κ_{total} at ~ 673 K was observed for pristine GeTe, which is attributed to the rhombohedral to cubic structural phase transition. This was earlier observed for other GeTe based materials. [12, 20] Up-turn temperature decreases to lower value from 673 to 573 K with increasing the Sb concentration from 0 to 10 mol % (Figure 1.6c). Sb doping in GeTe decreases the rhombohedral to cubic phase transition temperature, which was confirmed by temperature-dependent PXRD (Figure 1.2d).

The electronic thermal conductivities, $\kappa_e = L \cdot \sigma \cdot T$, were presented in Figure 1.6e. Temperature dependent Lorenz number, L, can be obtained based on the fitting of the respective Seebeck values that estimate the reduced chemical potential (Figure 1.6d). The κ_e value of all the $Ge_{1-x}Sb_xTe$ samples are substantially lower than that of pristine GeTe, which is due to the significantly lower electrical conductivity of Sb doped samples compared to that of GeTe.

The temperature dependent lattice thermal conductivity (κ_{lat}) was estimated by subtracting the κ_e from κ_{total} and plotted in Figure 1.6f. Sb alloying in GeTe significantly reduces κ_{lat} values both at room and high temperatures because of mass-fluctuation phonon scattering where vibrations of atoms with different frequencies damps the phonons transport. In addition, formation of domain structures, twin and inversion boundaries and grain boundaries play a predominant role on reduction in κ_{lat} by scattering mid to long wavelength phonons at room temperature. Typically, $Ge_{0.90}Sb_{0.10}Te$ sample exhibits the κ_{lat} value of ~1.4 $Wm^{-1}K^{-1}$ at room temperature, which decreases to ~1.1 $Wm^{-1}K^{-1}$ at 710 K, which is comparable to that of previously reported 3% Bi_2Te_3 doped $Ge_{0.87}Pb_{0.13}Te$.[21] We have achieved reduction of κ_{lat} of ~ 45 % after Sb (10 mol%) doping in GeTe, which is lower compared to that in reported 3% Bi_2Te_3 doped $Ge_{0.87}Pb_{0.13}Te$ (~ 28 % reduction in κ_{lat})[21] and Ge-rich $Ge_{1-x}Pb_xTe$ (~ 31 % reduction in κ_{lat})[18] at room temperatures.

Temperature dependence of the dimensionless thermoelectric figure of merits, zT, of $Ge_{1-x}Sb_xTe$ (x = 0-0.10) samples is illustrated in Figure 1.7a. The maximum zT achieved is ~ 1.85 at 725 K for $Ge_{0.90}Sb_{0.10}Te$, which is ~ 110 % higher compared to pristine GeTe.

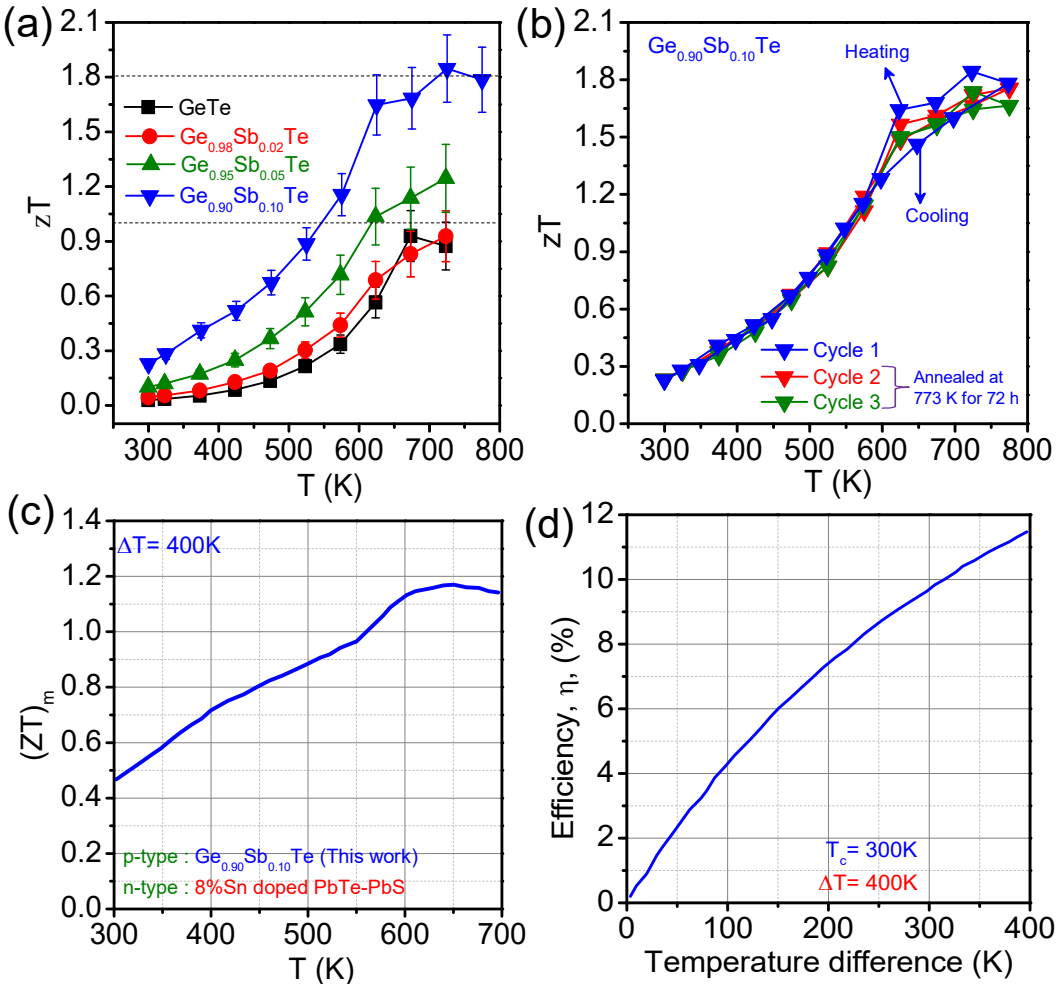

Figure 1.7 *(a) Temperature dependent thermoelectric figure of merit (zT) of* $Ge_{1-x}Sb_xTe$ *(x = 0 - 0.10) samples. (b) Three cycles of heating and cooling temperature dependent zT data of* $Ge_{0.90}Sb_{0.10}Te$*. Cycle 2 (red) and Cycle 3 (green) represent the zT vs. T data of the same* $Ge_{0.9}Sb_{0.1}Te$ *sample which was annealed at 773 K for 72 h. (c) Theoretical device thermoelectric figure of merit* $(ZT)_m$ *for one pair of p-type (present* $Ge_{0.90}Sb_{0.10}Te$*) and n-type (previously reported 8% of Sn doped PbTe-PbS)*[22] *legs as a function of temperature. (d) Calculated thermoelectric efficiency as a function of temperature difference.*

Three cycles of heating-cooling (300 - 773 K) *zT* vs. T data clearly show high temperature stability and reproducibility of the thermoelectric performance of the $Ge_{0.90}Sb_{0.10}Te$ (Figure 1.7b). Additionally, *zT vs.* T of the $Ge_{0.90}Sb_{0.10}Te$ sample which was annealed at 773 K (above phase transition temperature) for 72 h also confirms long

term high temperature stability (Figure 1.7b) $Ge_{0.95}Sb_{0.05}Te$ sample shows the highest zT of ~ 1.25 at 725 K.

Theoretical device thermoelectric figure of merit $(ZT)_m$ for a pair of legs of *p*-type (present $Ge_{0.90}Sb_{0.10}Te$) and *n*-type (previously reported 8% of Sn doped PbTe-PbS)[22] was estimated as a function of temperature (Figure 1.7c, using equation 1.1), in which the temperature difference was maintained to be 400 K throughout the estimated temperature range. Theoretically calculated average devices' thermoelectric figure of merit, $(ZT)_{avg}$, was estimated to be ~ 0.85 considering ΔT = 400 K. The estimated $(ZT)_{avg}$ was used for theoretical calculation of the thermoelectric conversation efficiency (Figure 1.7d) in equation (1.2). A maximum efficiency of ~ 12% was achieved for the temperature difference of 400 K.

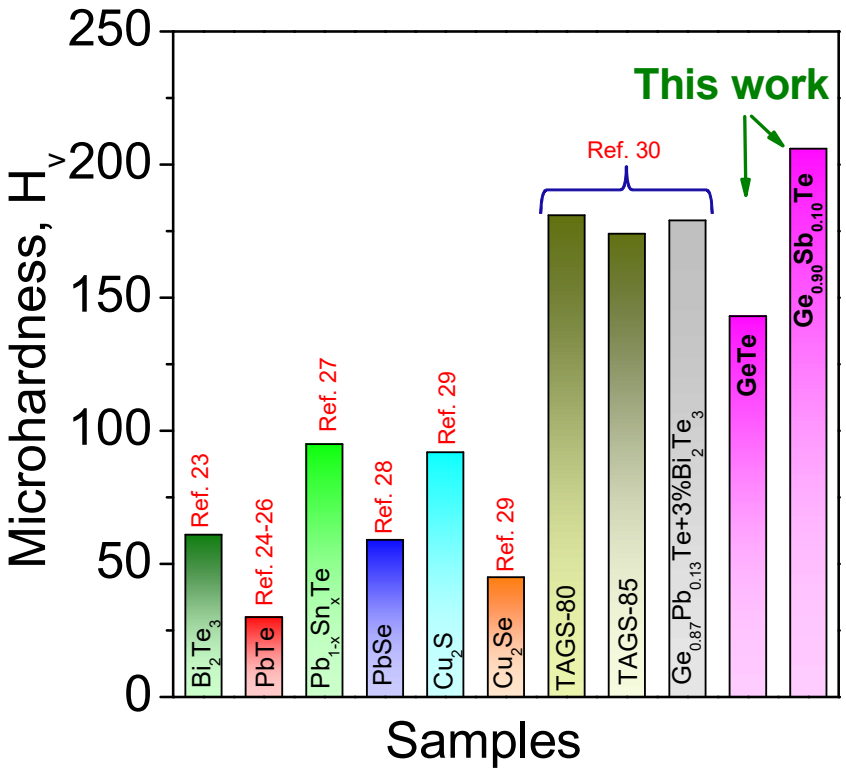

Figure 1.8 *Vickers microhardness value (H_v) of $Ge_{1-x}Sb_xTe$ (x = 0 – 0.10) samples compared with other thermoelectric materials.*

Besides the high *zT* and promising theoretical thermoelectric efficiency, one has to look for the good mechanical properties of thermoelectric materials for mass-market applications. We have measured Vicker's micro-hardness to estimate the mechanical strength and hardness of $Ge_{1-x}Sb_xTe$ (x = 0 - 0.10) samples and experimental values are presented in Figure 1.8. Present micro-hardness (H_v) values were compared with previously reported popular thermoelectric materials, such as Bi_2Te_3,[23] PbTe,[24-26] $Pb_{1-x}Sn_xTe$,[27] PbSe,[28] Cu_2S,[29] Cu_2Se,[29] TAGS-80[30] and TAGS-85.[30] High performance $Ge_{0.90}Sb_{0.10}Te$ exhibits a H_v value of 206 ± 0.5, which is higher compared to that of Bi_2Te_3,[23] PbTe,[24-26] $Pb_{1-x}Sn_xTe$,[27] PbSe,[28] Cu_2S,[29] Cu_2Se,[29] TAGS-80,[30] TAGS-85[30] and pristine GeTe.

To validate our aliovalent cation doping concept on GeTe, we have further studied the effect of Bi doping on Ge site of GeTe. We found a significant reduction in lattice thermal conductivity in $Ge_{1-x}Bi_xTe$ (x = 0.02, 0.06 and 0.10) samples compared to that of pristine GeTe, resulting in high thermoelectriuc performance. We have chosen Bi^{3+} substitution in in a Ge^{2+} sublattice of GeTe due to the aliovalent donor dopant nature of Bi^{3+}. We show that 2 - 10 mol% of Bi acts as an effective donor dopant and reduces the excess hole carrier concentration and subsequently enhances the Seebeck coefficient in GeTe.

Powder X-ray diffraction (XRD) patterns of the $Ge_{1-x}Bi_xTe$ (x = 0 - 0.15) samples are presented in Figure 1.9a. PXRD patterns of $Ge_{1-x}Bi_xTe$ could be indexed based on rhombohedral GeTe (*R*3*m*) structure. Typically, presence of double peaks in the range 2θ = 23˚ to 27˚ and 2θ = 41˚ to 45˚ further confirms the rhombohedral phase. Additionally, substitution of Bi in GeTe tends to merge these double peaks into single peak (Figure 1.9b). Substitution of Bi tries to rearrange the positions of Ge from (½-x ½-x ½-x) to (½ ½ ½), which indicates that the cubic nature of the system increases with Bi doping in GeTe.

Spectroscopically measured band gaps of $Ge_{1-x}Bi_xTe$ samples are shown in Figure 1.9c. Optical band gap of pure GeTe is observed to be ~ 0.21 eV. Substitution of Bi at GeTe substantially reduces the band gap from ~ 0.21 eV to 0.08 eV (Figure 1.9c). In GeTe, Te (electronegativity ~ 2.10 in Pauling scale) forms valence band, whereas Ge (electronegativity ~ 2.01) contributes to the conduction band.

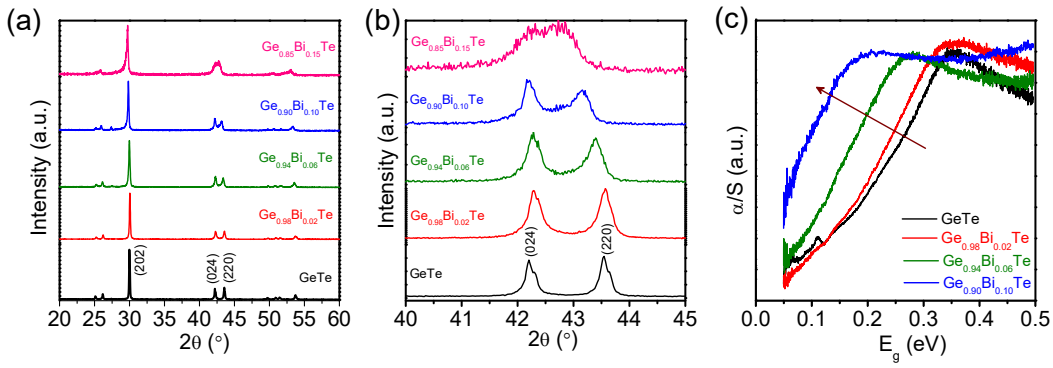

Figure 1.9 *(a) Powder XRD patterns of $Ge_{1-x}Bi_xTe$ (x = 0 - 0.15) samples. (b) Zoomed XRD pattern of Figure 3.1.9a in between the angles (2θ) of 40° to 45°, that shows the merging of (024) and (220) peaks with increasing the Bi doping. (c) Optical absorption spectra of $Ge_{1-x}Bi_xTe$ (x = 0.00, 0.02, 0.06 and 0.10) samples.*

The reduction in band gap is due to the formation of Bi states below the conduction band because of its donor dopant nature and the slightly higher electronegativity of Bi (~ 2.02) compared to Ge. Previously reported first principle electronic structure calculations also indicated the decreases in the band gap of GeTe after Bi doping due to lowering of conduction band energy.[31]

Nano/microstructures of $Ge_{0.90}Bi_{0.10}Te$ are investigated by aberration corrected TEM and are shown in Figure 1.10. Low magnification TEM micrograph of $Ge_{0.90}Bi_{0.10}Te$ is presented in Figure 1.10a, which clearly shows the presence of nanoprecipitates of Bi-rich phase (dark area) in the matrix of GeTe. In Figure 1.10b, high magnification micrograph illustrates ~ 100 - 200 nm sized fine grains of GeTe (marked in yellow dotted circle). Nanoprecipitates with size in the range 5 - 20 nm are observed in high resolution TEM micrograph in Figure 1.10c. Presence of the nanoscale parallel cation-position like defect layers in the van der Waals gaps are also clearly seen throughout the samples (Figure 1.10d). These defect layers are formed because of strongly disordered octahedral voids between the successive Te-Te layers. Moreover, inset of Figure 1.10d shows the diffused selected area diffraction pattern (SAED), which is obtained from the defect layers region. Additionally, these defects seemed to be thermodynamically less stable as it disappears upon prolonging exposure of high energy electron beam, even for 1 min exposure.

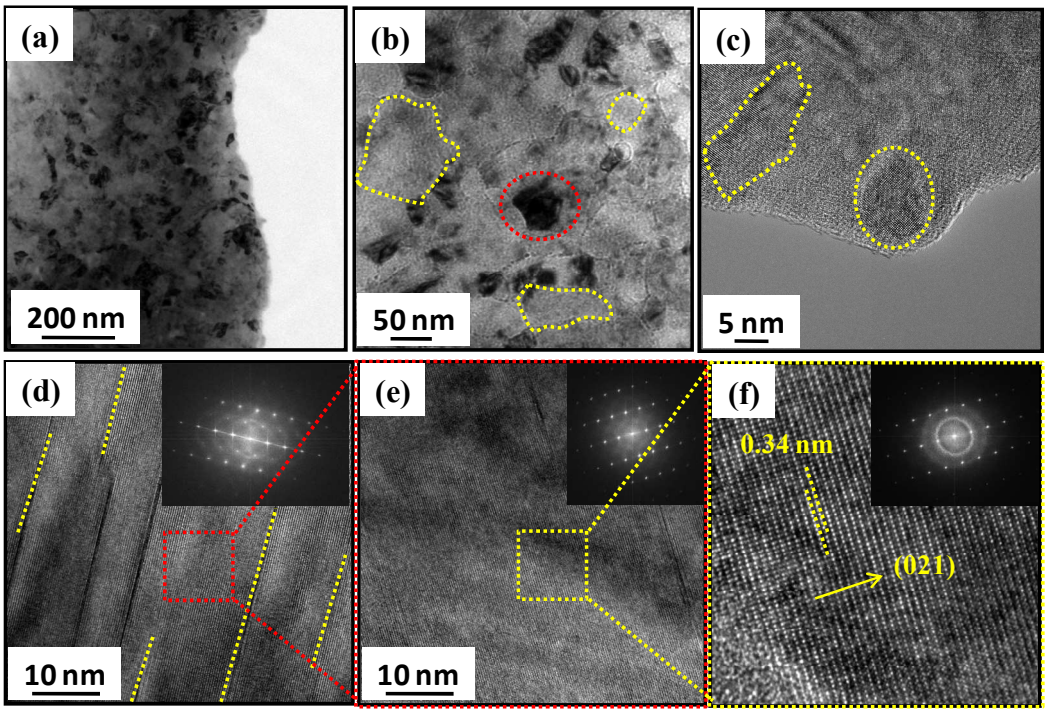

Figure 1.10 *(a) Low magnification TEM micrograph of $Ge_{0.90}Bi_{0.10}Te$ with Bi-rich nano-precipitates, (b) TEM image shows mesoscale grain boundaries (dotted yellow circle), (c) HRTEM images shows nanoprecipitates, (d) Parallel defect layers and their corresponding SAED pattern with diffusive spots, (e) HRTEM micrographs in the defect free region with clear SAED spots, (f) HRTEM micrograph of $Ge_{0.90}Bi_{0.10}Te$ shows a inter planar spacing of 0.34 nm (inset shows the corresponding SAED pattern).*

Figure 1.10e illustrates the HRTEM micrographs of defect-free region, zoomed area from Figure 3.1.10d, with corresponding SAED pattern with clear spots (inset of Figure 1.10e). HRTEM micrograph on defect-free region illustrates the interplanar spacing of ~0.34 nm that corresponds to (021) lattice planes of GeTe, (Figure 1.10f), which further confirms rhombohedra *R3m* phase. Defect-free regions shows the clearly separated diffraction spots (inset Figure 1.10f).

Figure 1.11a presents the electrical conductivity, σ, of $Ge_{1-x}Bi_xTe$ (x = 0 - 0.10) samples as a function of temperature. The σ of all the samples decreases with increasing the temperature, which is typically observed for the degenerate semiconductors. Pristine GeTe exhibits the σ value of ~ 8067 S/cm at 300 K, which decreases to ~ 2158 S/cm at 708 K.

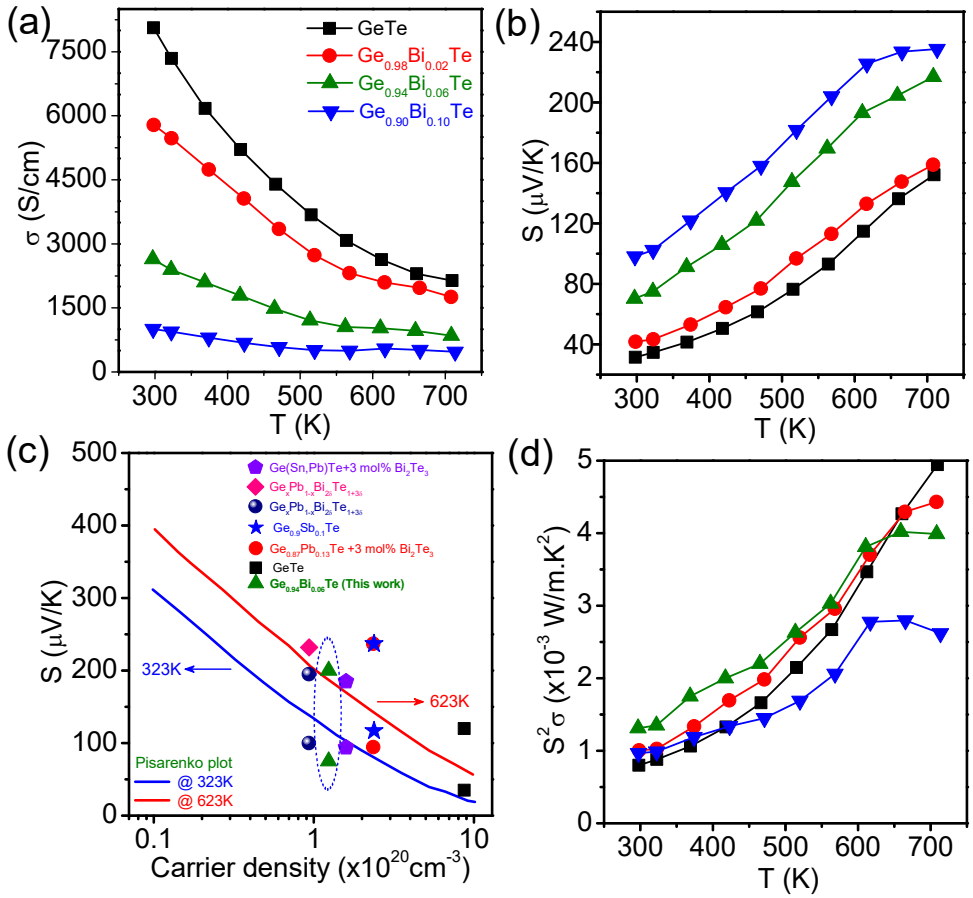

Figure 1.11 *Temperature dependent (a) electrical conductivity (σ) and (b) Seebeck coefficient (S) of $Ge_{1-x}Bi_xTe$ (x = 0.00, 0.02, 0.06 and 0.10) samples. (c) Pisarenko plots (S vs. n data) for $Ge_{1-x}Bi_xTe$ samples which compared with earlier reported data.*[17,20,21] *(d) Temperature dependence power factor ($S^2\sigma$) of $Ge_{1-x}Bi_xTe$ (x = 0.00, 0.02, 0.06 and 0.10) samples.*

Around 673 K, σ *vs.* T data shows an anomaly which is due to structural transition (*R3m* to *Fm-3m*) in GeTe. Furthermore, addition of Bi of 10 mol% in GeTe drastically reduces the σ value from ~ 8067 S/cm to ~ 986 S/cm, due to the reduction in the carrier concentration. Hall measurement was performed to measure the room temperature hole concentration. Typically, the calculated carrier density, *n*, is ~ 8.7 x 10^{20} cm^{-3} GeTe which decreases to ~ 1.24 x10^{20} cm^{-3} for $Ge_{0.94}Bi_{0.06}Te$, respectively. This reduction in *p*-type carrier concentration is attributed to the aliovalent dopant nature of Bi^{3+} at Ge^{2+} site in GeTe which gives rise to the extra electron to the system.

Figure 1.11b presents the Seebeck coefficient value, *S*, of $Ge_{1-x}Bi_xTe$ (x = 0 - 0.10) samples as a function of temperature. For all the samples, positive sign of the *S* indicate that holes are responsible for thermoelectric transport, which supports the Hall coefficient data. At 300 K, GeTe has the *S* value of ~ 34 μV/K which increases with temperature, then reaches to ~ 153 μV/K at 708 K.[8] It is expected that doping of Bi in GeTe would increase the *S* value as it drastically reduces the holes concentration. Typically, 10 mol % of Bi doping in GeTe increases the *S* value to ~ 98 μV/K at 300K, which reaches to maximum value ~ 236 μV/K at 708 K. Increase of Seebeck coefficient by Bi substitution is mainly due to decreases in hole concentration, which will be clear from Pisarenko plot (next section).

Figure 1.11c shows the measured Seebeck values, *S*, as a function of holes density, *n*, for GeTe and $Ge_{0.94}Bi_{0.06}Te$, which are compared with the Pisarenko plot at different temperatures of 323 K and 623 K.[17,20,21] We have also compared the present *S* vs. *n* data with $Ge_{1-x}Sb_xTe$ and previously reported other high performance GeTe based materials such as $(GeTe)_{1-x}[(PbTe)(SnTe)(Bi_2Te_3)]_x$,[17] $Ge_{1-x}Pb_xTe$,[20] and 3 mol% Bi_2Te_3 doped $Ge_{0.87}Pb_{0.13}Te$.[21] *S* vs. *n* data of $Ge_{1-x}Bi_xTe$ follows the Pisarenko relation, which indicates enhancement in Seebeck coefficient upon Bi doping in GeTe is mainly due to decreases in carrier concentration.

Figure 1.11d illustrates the power factor, $S^2\sigma$, of $Ge_{1-x}Bi_xTe$ (x = 0 - 0.10) samples as a function of temperature. Typically, $Ge_{0.94}Bi_{0.06}Te$ samples shows $S^2\sigma$ value of ~ 12 $\mu Wcm^{-1}K^{-2}$ at 300K, which reaches to maximum ~ 40 $\mu Wcm^{-1}K^{-2}$ at 712 K. Though *S* values increases upon Bi doping in GeTe, it does not improve the $S^2\sigma$ values due to large reduction in electrical conductivity.

Figure 1.12b presents the total thermal conductivity, κ_{total}, of $Ge_{1-x}Bi_xTe$ (x = 0 - 0.10) samples as a function of temperature. Typically, pristine GeTe has the κ_{total} value of ~ 8.3 W/mK at 300 K, which decreases to ~ 3.4 W/mK at 673 K. Mention must be made that increase in κ_{total} above 673 K in undoped GeTe is due to the rhombohedral to cubic structural phase transition. This trend was earlier observed for other GeTe based materials. With increasing the Bi concentration, the κ_{total} drastically reduces from ~ 8.3 W/mK for GeTe to ~ 1.6 W/mK for $Ge_{0.90}Bi_{0.10}Te$ at 300 K.

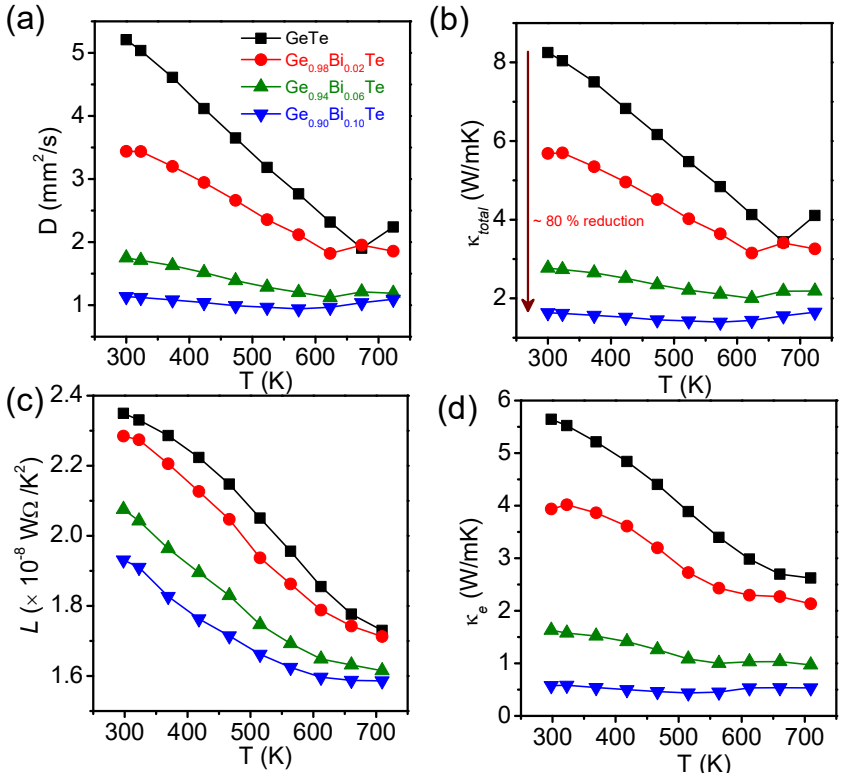

Figure 1.12 *Temperature dependent (a) diffusivity (D), (b) total thermal conductivity (κ_{total}), (c) Lorenz number (L) and (e) electrical thermal conductivity (κ_e) of $Ge_{1-x}Bi_xTe$ (x = 0.00, 0.02, 0.06 and 0.10) samples.*

The electronic thermal conductivity, κ_e was calculated *via* Wiedemann-Franz law, $\kappa_e = \sigma \cdot L \cdot T$, where L is the Lorenz number. *L*, can be obtained based on the fitting of the respective Seebeck values that estimate the reduced chemical potential assuming single parabolic band model (Figure 1.12c). κ_e as a function of temperature for $Ge_{1-x}Bi_xTe$ (x = 0-0.10) were presented in Figure 1.12d.

Pristine GeTe has the κ_e value of ~ 5.6 W/m.K at 300 K, which suggests that carriers are mainly responsible for heat transport in GeTe. Due to the donor dopant nature of Bi in GeTe, it reduces the *p*-type carrier density and significantly decreases the κ_e. Typically, 10 mol % of Bi in GeTe reduces the κ_e value from 5.66 W/mK to 0.58 W/mK, which is about 90% reduction as compared to undoped GeTe.

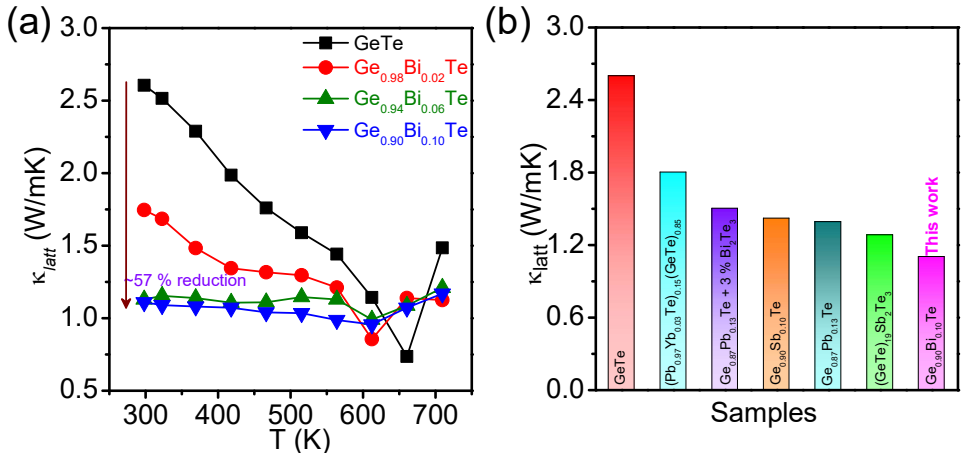

Figure 1.13 *(a) Temperature dependent lattice thermal conductivity, κ_{latt}, of $Ge_{1-x}Bi_xTe$ (x = 0.00, 0.02, 0.06 and 0.10) samples. (b) Comparison of the κ_{latt} of the present $Ge_{0.90}Bi_{0.10}Te$ sample with previously reported high performance GeTe based materials.21,*

The κ_{latt} of all the samples was obtained by subtracting the κ_e from κ_{total} (Figure 1.13a). κ_{latt} value of $Ge_{1-x}Bi_xTe$ decrease with increase the Bi concentration. At 300 K, κ_{lat} of GeTe is ~ 2.6 W/m.K, which is reduced to ~ 1.1 W/m.K for $Ge_{0.90}Bi_{0.10}Te$, which is ~ 57% reduction in κ_{latt}. We have compared the κ_{latt} of present $Ge_{0.90}Bi_{0.10}Te$ sample with previously reported high performance GeTe based materials (Figure 1.13b). $Ge_{0.90}Bi_{0.10}Te$ sample exhibits one of lowest values of κ_{latt} among the reported GeTe based materials. The low κ_{latt} in $Ge_{1-x}Bi_xTe$ is attributed due to the increased phonon scattering of meso-scale grain boundaries, nano-scale Bi rich precipitates, defect layers and atomic-scale point defects due to mass fluctuations.

Figure 1.14a illustrates the thermoelectric figure of merit, zT, of $Ge_{1-x}Bi_xTe$ (x = 0.00, 0.02, 0.06 & 0.10) samples as a function of temperature. Maximum zT of ~ 1.30 is achieved for the composition of $Ge_{0.94}Bi_{0.06}Te$ at 725 K. High zT samples were re-measured and subjected to cyclic measurement (heating and cooling cycle), which shows a good reproducibility, that indicates prepared samples are thermally stable during thermal treatments/cycles (Figure 1.14b).

Besides high zT, materials should be mechanically stable during machining in order to use for large scale device application. We have measured mechanical properties by Vickers microhardness indentation method (Figure 1.14c).

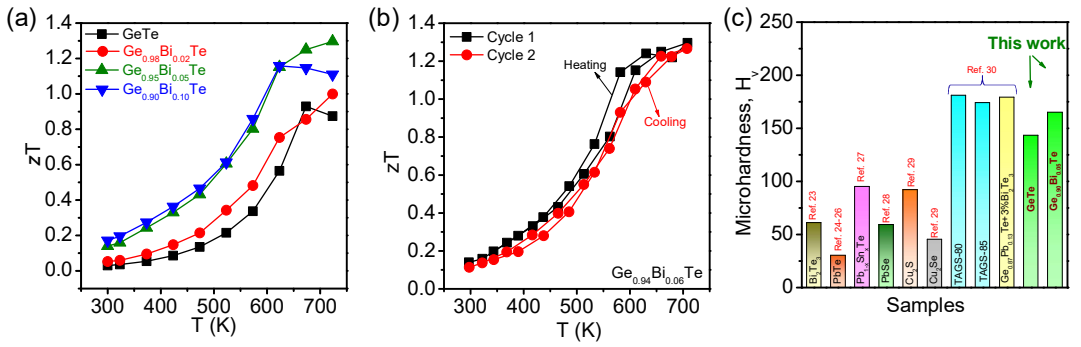

Figure 1.14 *(a) Temperature dependent zT of $Ge_{1-x}Bi_xTe$ (x = 0.00, 0.02, 0.06 and 0.10) samples. (b) Two cycles of heating and cooling zT data of $Ge_{0.94}Bi_{0.06}Te$. (c) Vickers microhardness values, H_V, of $Ge_{0.94}Bi_{0.06}Te$ which is compared with selected popular thermoelectric materials.*

$Ge_{0.94}Bi_{0.06}Te$ sample shows the measured microhardness value of ~ 165 H_V, which is considerably higher than that of the state-of-art thermoelectric materials such as, Bi_2Te_3,[23] PbTe,[24-26] Pb-Sn-Te,[27] PbSe,[28] Cu_2S,[29] Cu_2Se[29] and relatively comparable that of other GeTe based materials.[30]

1.4 Conclusions

In conclusion, we have synthesized high quality samples of $Ge_{1-x}Sb_xTe$ (x = 0 - 0.10) and $Ge_{1-x}Bi_xTe$ (x = 0 - 0.10) by simple melting reactions. Substitution of Sb and Bi in GeTe significantly decreases the *p*-type carrier concentration due to the donor dopant nature of Sb and Bi, which resulted in enhanced Seebeck coefficients. Sb and Bi doping GeTe also increases the cubic nature of the sample and enhances the valence band degeneracy effect, which boosts the Seebeck throughout the measured temperature range. At the same time, significant reduction of thermal conductivity was achieved due to collective phonon scattering of various meso-structured domain variants and twin and inversion boundaries; nano-structured defect layers and precipitates; and solid solution point defects. The highest *zT* value of ~ 1.85 for $Ge_{0.90}Sb_{0.10}Te$ and ~ 1.30 for $Ge_{0.94}Bi_{0.06}Te$ at 725 K were achieved, which is higher compared to that of pristine GeTe.

Additionally, the thermoelectric performance of $Ge_{0.90}Sb_{0.10}Te$ and $Ge_{0.94}Bi_{0.06}Te$ is stable under several heating-cooling cycles. A maximum thermoelectric conversion efficiency (η_{max}) of ~ 12% was estimated by considering virtual thermoelectric module consisting of present *p*-type $Ge_{0.90}Sb_{0.10}Te$ and previously reported *n*-type 8% of Sn doped PbTe-PbS,[22] by maintaining the temperature difference of ΔT = 400 K. We have achieved Vickers micro-hardness of ~ 206 H_v and ~ 165 H_v for high performance $Ge_{0.90}Sb_{0.10}Te$ and $Ge_{0.94}Bi_{0.06}Te$, which are significantly higher compared to other high performance thermoelectric materials such as Bi_2Te_3, PbTe, PbSe, Cu_2Se and TAGS. Present results on synthesis, fundamental understanding of the structure-property relationship, extraordinary performance, significant temperature and mechanical stability of Sb (Bi) doped GeTe reflect the promise to do further research in GeTe based materials and replace PbTe for mass-market application.

1.5 References

[1] G. J. Snyder, E. S. Toberer, *Nat. Mater.* **2008**, *7*, 105.

[2] K. Biswas, J. He, I. D. Blum, C. I. Wu, T. P. Hogan, D. N. Seidman, V. P. Dravid, M. G. Kanatzidis, *Nature* **2012**, *489*, 414.

[3] F. D. Rosi, J. P. Dismukes, E. F. Hockings, *Electr. Eng.* **1960**, *79*, 450.

[4] E. A. Skrabek, D. S. Trimmer, *Thermoelectrics Handbook* ed. D. M. Rowe, (Boca Raton, FL: CRC), chapter 22, **1995**.

[5] T. A. Christakudi, S. K. Plachkova, G. Ch. Christakudis, *Phys. Status Solidi A* **1995**, *147*, 211.

[6] J. E. Lewis, *Phys. Status Solidi A* **1970**, *38*, 131.

[7] D. H. Damon, M. S. Lubell, R. Mazelsky, *J. Phys. Chem. Solids* **1967**, *28*, 520.

[8] E. M. Levin, M. F. Besser, R. Hanus, *J. Appl. Phys*. **2013**, *114*, 083713.

[9] T. Chattopadhyay, J. X. Boucherle, H. G. von Schnering, *J. Phys. C* **1987**, *20*, 143.

[10] M. J. Polking, M. -G. Han, A. Yourdkhani, V. Petkov, C. F. Kisielowski, V. V. Volkov, Y. Zhu, G. Caruntu, A. P. Alivisatos, R. Ramesh, *Nat. Mater.* **2012**, *11*, 700.

[11] P. B. Pereira, I. Sergueev, S. Gorsse, J. Dadda, E. Muller, R. P. Hermann, *Phys. Status Solidi B* **2013**, *250*,1300.

[12] J. K. Lee, M. W. Oh, B. S. Kim, B. K. Min, H. W. Lee, S. D. Park, *Electron. Mater. Lett.* **2014**, *10*, 813.

[13] E. M. Levin, B. A. Cook, J. L. Harringa, S. L. Bud'ko, R. Venkatasubramanian, K. Schmidt-Rohr, *Adv. Funct. Mater.* **2011**, *21*, 441.

[14] S. K. Plachkova, T. I. Georgiev, *J. Phys.: Condens. Matter*. **1993**, *5*, 67.

[15] J. R. Salvador, J. Yang, X. Shi, H. Wang, A. A. Wereszczak, *J. Solid State Chem*. **2009**, *182*, 2088.

[16] L. Zhang, W. Wang, B. Ren, J. Guo, *J. Electron. Mater*. **2013**, *42*, 7.

[17] Y. Gelbstein, O. Ben-Yehuda, E. Pinhas, T. Edrei, Y. Sadia, Z. Dashevsky, M. P. Dariel, *J. Electron. Mater*. **2009**, *38*, 1478.

[18] Y. Gelbstein, B. Dado, O. Ben-Yehuda, Y. Sadia, Z. Dashevsky, M. P. Dariel, *J. Electron. Mater.* **2010**, *39*, 2049.

[19] Y. Gelbstein, J. Davidow, S. N. Girard, D. Y. Chung, M. Kanatzidis, *Adv. Energy Mater.* **2013**, *3*, 815.

[20] Y. Gelbstein, J. Davidow, *Phys. Chem. Chem. Phys.* **2014**, *16*, 20120.

[21] D. Wu, L.-D. Zhao, S. Hao, Q. Jiang, F. Zheng, J. W. Doak, H. Wu, H. Chi, Y. Gelbstein, C. Uher, C. Wolverton, M. G. Kanatzidis, J. He, *J. Am. Chem. Soc*. **2014**, *136*, 11412.

[22] J. Androulakis, C. -H. Lin, H. -J. Kong, C. Uher, C-I. Wu, T. Hogan, B. A. Cook, T. Caillat, K. M. Paraskevopoulos, M. G. Kanatzidis, *J. Am. Chem. Soc.* **2007**, *129*, 9780.

[23] L. -D. Zhao, B. -P. Zhang, J. -F. Li, M. Zhou, W.-S. Liu, J. Liu, *J. Alloys Compd.* **2008**, *455*, 259.

[24] M. S. Ablova, M. N. Vinogradova, M. I. Karklina, *Sov. Phys.–Sol. State*. **1969**, *10*, 1929.
[25] A. J. Crocker, M. Wilson, *J. Mater. Sci*. **1978**, *13*, 833.
[26] Y. Gelbstein, G. Gotesman, Y. Lishzinker, Z. Dashevsky, M. P. Dariel, *Scripta Materialia* **2008**, *58*, 251.
[27] J. L. Cui, X. Qian and X. B. Zhao, *J. Alloy. Compd*. **2003**, *358*, 228.
[28] W. B. W. M. S. Darrow, R. Roy, *J. Mater. Sci.* **1969**, 313.
[29] L. Zhao, X. Wang, F. Y. Fei, J. Wang, Z. Cheng, S. Dou, J. Wanga, G. J. Snyder, *J. Mater. Chem. A* **2015**, *3*, 9432.
[30] J. Davidow, Y. Gelbstein, *J. Eelectron. Mater.* **2013**, *42*, 1542.
[31] K. Hoang, S. D. Mahanti, M. G. Kanatzidis, *Phys. Rev. B* **2010**, *81*, 115106.
[32] T. Rosenthal, M. N. Schneider, C. Stiewe, M. Doblinger, O. Oeckler, *Chem. Mater.* **2011**, *23*, 4349.
[33] H. S. Lee, B-S. Kim, C-W. Cho, M-W. Oh, B-K. Min, S-D, Park, H-W. Lee, *Acta Materialia* **2015**, *91*, 83.
[34] B. A. Cook, M. J. Kramer, X. Wei, J. L. Harringa, E. M. Levin, *J. Appl. Phys.* **2007**, *101*, 053715.
[35] B. A. Cook, X. Z. Wei, J. L. Harringa, M. J. Kramer, *J. Mater. Sci.* **2007**, *42*,7643.
[36] B. J. Kooi, W. M. G. Groot, J. T. M. De Hosson, *J. Appl. Phys*. **2004**, *95*, 924.
[37] Y. Chen, C. M. Jaworski, Y. B. Gao, H. Wang, T. J. Zhu, G. J. Snyder, J. P. Heremans, X. B. Zhao, *New J. Phys.* **2014**, *16*, 013057.
[38] S. N. Guin, A. Chatterjee, D. S. Negi, R. Datta, K. Biswas, *Energy Environ. Sci.* **2013**, *6*, 2603.
[39] F. Fahrnbauer, D. Souchay, G. Wagner, O. Oeckler, *J. Am. Chem. Soc.* **2015**, *137*, 12633.
[40] J. F. Deng, J. Q. Li, R. F. Ye, X. Y. Liu, F. S. Liu, W. Q. Ao, *J. Alloys Compd*. **2014**, *585*, 173.

Chapter 2

Stabilizing *n*-type Cubic GeSe by Entropy-Driven Alloying of $AgBiSe_2$: Ultralow Thermal Conductivity and Promising Thermoelectric Performance

Chapter 2

Stabilizing *n*-type Cubic GeSe by Entropy-Driven Alloying of $AgBiSe_2$: Ultralow Thermal Conductivity and Promising Thermoelectric Performance[†]

Summary

n-type Ge-chalcogenides with promising thermoelectric performance is urgently needed to match their p-type counterparts. However, their realization remains elusive due to intrinsic Ge vacancies which make them p-type semiconductors. GeSe crystallizes into a layered orthorhombic structure similar to the SnSe at ambient conditions. High symmetry cubic phase of GeSe is predicted to be stabilized either by applying external pressure of 7 GPa or by enhancing the entropy via increasing the temperature to 920 K. In this chapter, we present the stabilization of n-type cubic phase of GeSe at ambient conditions by alloying with $AgBiSe_2$ (30 - 50 mol %), which enhances the entropy through solid solution mixing. The interplay of positive and negative chemical pressure anomalously changes the band gap of GeSe with increasing the $AgBiSe_2$ concentration. The band gap of n-type cubic $(GeSe)_{1-x}(AgBiSe_2)_x$ ($0.30 \leq x \leq 0.50$) posses a value in the 0.3 - 0.4 eV range, which is significantly lower than orthorhombic GeSe (1.1 eV). Cubic $(GeSe)_{1-x}(AgBiSe_2)_x$ exhibits an ultralow lattice thermal conductivity ($\kappa_L \sim 0.43\ Wm^{-1}K^{-1}$) in the 300 - 723 K temperature range. The low κ_L is attributed to significant phonon scattering by entropy driven enhanced solid solution point defects.

[†]*Paper based on this study has been published in Angew. Chem. Int. Ed.* ***2018****, 57, 15167.*

2.1 Introduction

Most of the high-performance thermoelectric materials are based on metal tellurides such as Bi_2Te_3, PbTe, SnTe and GeTe.[1,2] However, the abundance of Te is scarce in the Earth crust, which leads to the quest for the design and discovery of new thermoelectric materials comprising earth-abundant elements with less toxicity, like Se. Moreover, both *p*-type and *n*-type materials are required to construct a thermoelectric device, interestingly *n*-type thermoelectric materials with ultralow thermal conductivity are very rare in the literatures.

Ge-chalcogenides (especially GeTe) is one of the most efficient thermoelectric materials in the group IV-VI family (as discuused in chapter 1, part 3) and are being used for power generation in the mid-temperature range (600–800 K) since the 1960s.[3-5] However, these Ge-chalcogenide based thermoelectric materials are all *p*-type, limited by their intrinsic Ge vacancies.[3-5] Thus, a speedy development of promising *n*-type Ge-chalcogenide based thermoelectric materials is a forthwith requirement.

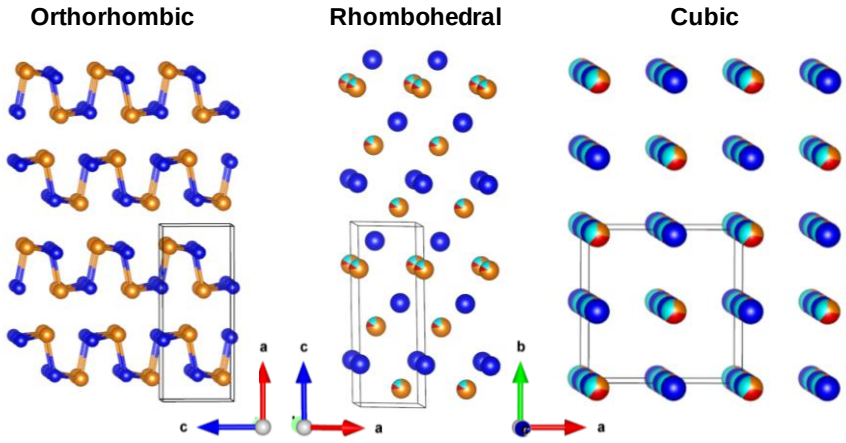

Figure 2.1 *Crystal structure of different phases of GeSe, orthorhombic (O), rhombohedral (R) and cubic (C) (Yellow: Ge; Blue: Se; Red: Ag; Cyan: Bi).*

GeSe crystallizes in three different structures: orthorhombic (*Pnma*), rhombohedral (*R3m*) and cubic phases (*Fm-3m*) (Figure 2.1) depending on the temperature and pressure conditions.[6,7] At ambient conditions, GeSe posses the orthorhombic structure similar to that of SnSe which shows an unprecedented zT in the single crystal form due to ultralow thermal conductivity.[8] Recently, by using first-

principles density functional calculations, Hao *et al.* predicted the high thermoelectric performance in GeSe through carrier engineering.[9] However, the orthorhombic GeSe is experimentally found to be a *p*-type semiconductor with poor thermoelectric performance.[10,11] Recently, Huang *et al.*[6] have been able to stabilize the *p*-type rhombohedral GeSe by alloying it with $AgSbSe_2$, which showed a zT of 0.86 at 710 K in $GeAg_{0.2}Sb_{0.2}Se_{1.4}$. They have achieved a low κ_L of 0.9 $Wm^{-1}K^{-1}$, which is, however, still higher than the theoretical κ_{min} of GeSe (0.4 $Wm^{-1}K^{-1}$).[10] The room temperature orthorhombic GeSe undergoes to a first-order structural transition to a face-centered cubic (FCC) structure at 920 K.[12] This cubic phase of GeSe is unstable at ambient conditions because of the presence of several imaginary vibration modes in its phonon dispersion. Theoretical calculations, however, indicate that the application of external pressure of 7 GPa would lead to the stabilization of the cubic phase.[7] The high symmetric cubic phases are in general much sought-after for high-performance thermoelectrics as they possess degenerate electronic band valleys. Therefore, the stabilization of cubic GeSe is worthwhile for improving its thermoelectric performance.

Here, we demonstrate the experimental realization of high temperature and high-pressure cubic rocksalt phase of GeSe at ambient conditions by alloying with $AgBiSe_2$ ($0.30 \leq x \leq 0.50$). Importantly, we also found that cubic $(GeSe)_{1-x}(AgBiSe_2)_x$ exhibits *n*-type conduction in the 300 - 723 K range, which is extremely rare in Ge-chalcogenide based thermoelectrics. Cubic $(GeSe)_{1-x}(AgBiSe_2)_x$ possesses an ultralow lattice thermal conductivity (κ_L) of 0.43 - 0.70 $Wm^{-1}K^{-1}$ in the 300 - 723 K range. Solid solution mixing of $AgBiSe_2$ with GeSe enhances the entropy and consequently leads to the stabilization of the cubic phase of GeSe at ambient conditions. The band gap of orthorhombic GeSe (1.1 eV) decreases to 0.05 eV with the initial formation of rhombohedral $(GeSe)_{1-x}(AgBiSe_2)_x$ phase ($x = 0.1$), and thereafter slightly increases to a value in the 0.3 - 0.4 eV range in cubic $(GeSe)_{1-x}(AgBiSe_2)_x$ ($0.30 \leq x \leq 0.50$). The combination of this ultralow κ_L, high Seebeck coefficient and narrow band gap generates a promising thermoelectric figure of merit, zT of 0.45 at 677 K in *n*-type $(GeSe)_{0.50}(AgBiSe_2)_{0.50}$.

2.2 Methods

2.2.1 Reagents

Germanium (Ge, Aldrich 99.999%), silver (Ag, Aldrich 99.999%), bismuth (Bi, Alfa Aesar 99.9999%) and selenium (Se, Alfa Aesar 99.9999%) were used for synthesis without further purification.

2.2.2 Synthesis

Ingots (~ 10 g) of $(GeSe)_{1-x}(AgBiSe_2)_x$ (x = 0 – 0.6) were synthesized by mixing stoichiometric ratios of elemental Ge, Ag, Bi and Se in quartz tubes. The tubes were sealed under vacuum (10^{-5} Torr) and slowly heated to 673 K over 12 hrs, soaked for 4 hrs and then heated up to 1223 K in 7 hrs followed by annealing for 10 hrs and then slowly cooled down to room temperature over a period of 18 hrs.

2.2.3 Powder X-ray diffraction

Room-temperature powder X-ray diffraction patterns were recorded using Cu K_α (λ = 1.5406 Å) radiation in a Bruker D8 diffractometer.

Temperature-dependent synchrotron X-ray diffraction measurements (300 - 623 K) under N_2 flow were carried out with synchrotron X-ray beam of λ = 0.7749 Å, at BL-18B (Indian beam line), Photon Factory, KEK, Tsukuba, Japan. The energy of the beam was set by a Si (111) double crystal monochromator, which was cross-checked with Si (640b NIST) standard. All the measurements were carried out in Bragg−Brentano geometry with a divergence slit (300 μm), an anti-scattering slit (350 μm), and a receiving slit (300 μm). High-temperature measurements were carried out with Anton Paar DHS 1100 heating stage.

2.2.4 Band gap measurement

To estimate optical band gap of the as-synthesized specimens of $(GeSe)_{1-x}(AgBiSe_2)_x$ (x = 0, 0.02, 0.04, 0.10, 0.20, 0.30, 0.40, 0.50), diffuse reflectance measurements were carried out with finely grounded powder at room temperature using a Perkin-Elmer Lambda 900 UV/Vis/near-IR spectrometer in reflectance mode (λ = 2500 - 250 nm) and FT-IR Bruker IFS 66V/S spectrometer (λ = 4000 - 400 cm^{-1}), respectively. Absorption (α/S) data were

calculated from the reflectance data using Kubelka-Munk equation: $\alpha/S = (1-R)^2/(2R)$, where R is the reflectance, α and S are respectively the absorption and scattering coefficients. The energy band gaps were then determined from α/S *vs.* E (eV) plot.

2.2.5 Field emission scanning electron microscopy.

FESEM experiments were performed using NOVA NANO SEM 600 (FEI, Germany) operated at 15 KV.

2.2.6 Transmission electron microscopy.

The TEM images of $(GeSe)_{1-x}(AgBiSe_2)_x$ (x = 0 and 0.50) were taken using a JEOL (JEM3010) TEM instrument (300 kV accelerating voltage) fitted with a Gatan CCD camera and also using a FEI TECNAI G2 20 STWIN TEM instrument (operating at 200 kV).

2.2.7 Electrical transport.

Electrical conductivity and Seebeck coefficients were measured simultaneously in He atmosphere from room temperature to 723 K using a ULVAC-RIKO ZEM-3 instrument system. The specimens used for this have typical parallelepiped shape with dimensions of $\sim 2 \times 2 \times 8$ mm^3. The longer direction coincides with the direction in which the thermal conductivity was measured.

2.2.8 Hall measurement.

For determining the carrier concentrations, Hall measurements were carried out on the same rectangular specimens used for electrical transport measurement in four-contact geometry up to a magnetic field of 0.57 T at room-temperature using custom-built equipment developed by Excel Instruments.

2.2.9 Thermal transport.

Thermal diffusivity, D, was directly measured in the range 300 – 723 K by laser flash diffusivity method using a Netzsch LFA-457 instrument. Coins with ~ 8 mm diameter and ~ 2 mm thickness were used for these thermal diffusivity measurements. Then, the total thermal conductivity, κ_{total}, was calculated using the formula, $\kappa_{total} = DC_p\rho$, where ρ

is the density of the sample and C_p is heat capacity. The measured density of the samples was found to be in the range of ~ 97% of the theoretically expected density.

2.2.10 Computational details.

This part has been done in collaboration with Prof. Umesh V. Waghmare's group in JNCASR. We use density functional theoretical (DFT) methods as implemented in QUANTUM ESPRESSO (QE) code.[13] We used a generalized gradient approximation (GGA)[14] to the exchange-correlation energy functional as parameterized by Perdew, Burke, and Ernzerhof (PBE).[15] To describe the interactions between valence electrons and ions we used Projected Augmented–Wave (PAW) potentials. Electronic wave functions and charge density were represented in plane wave basis sets truncated with cut-off energies of 45 Ry and 360 Ry respectively. The discontinuity in occupation numbers of electronic states was smeared using a Fermi-Dirac distribution function with broadening of k_BT = 0.003 Ry. We determined electronic structure of GeSe, $(GeSe)_{0.90}(AgBiSe_2)_{0.10}$ and $(GeSe)_{0.60}(AgBiSe_2)_{0.40}$ using their fully optimized structures. At ambient conditions, GeSe stabilizes in the orthorhombic phase containing eight atoms in the unit cell, and we consider this phase in our theoretical analysis. Integrations over Brillouin Zone (BZ) were sampled on a uniform 8 × 8 × 8 mesh of k-points. Electronic spectrum was determined at Bloch vectors along high symmetry lines (Γ - X - S - Y -Γ - Z - U - R - T - Z - Y - T -U - X - S) in the Brillouin zone. $(GeSe)_{0.90}(AgBiSe_2)_{0.10}$ exists in the rhombohedral phase and to simulate the desired concentration a 2 × 2 × 1 supercell was considered. Electronic spectrum was determined at Bloch vectors along high symmetry lines (Γ - M - K - Γ -A - L - H - A - L - M - K - H) in the Brillouin zone of rhombohedral lattice. With further increase in concentration of $AgBiSe_2$, a rocksalt phase is stabilized. $(GeSe)_{0.60}(AgBiSe_2)_{0.40}$ exists in the cubic structure consisting of 8 atoms in the unit cell. To simulate this composition, a 1 × 1 × 2 supercell was considered, and Brillouin Zone (BZ) integrations were sampled on a uniform 10 × 12 × 12 mesh of k-points. Electronic spectrum was determined at Bloch vectors along high symmetry lines (Γ - X - M - Γ -Z - R - A–Z) in the Brillouin zone of FCC lattice. We compared electronic structures with and without spin-orbit coupling (SOC) using fully relativistic and scalar relativistic potentials respectively. Our optimized lattice parameters for pristine GeSe in the

orthorhombic structure (*Pnma*) are a = 11.10 Å, b = 3.88 Å, c = 4.47 Å, which agree with the typical GGA errors with experimental lattice parameters (a = 10.92 Å, b = 3.87 Å, c = 4.41 Å). The estimated lattice parameters of $(GeSe)_{0.90}(AgBiSe_2)_{0.10}$ in the rhombohedral structure are a = b = 3.92 Å and c = 10.29 Å, which agree well with experimental values of a = b = 3.98 Å and c = 10.17 Å. While the experimental lattice parameters of the cubic $(GeSe)_{1-x}(AgBiSe_2)_x$ at x = 0.4 are a = b = c = 5.76 Å, the theoretical estimates are a = b = 5.77 Å and c = 11.58 Å (for the 1 × 1 × 2 supercell), which was used for understanding the effect of disordering .

2.3 Results & Discussion

The room-temperature powder X-ray diffraction (PXRD) pattern of pristine GeSe obtained using laboratory x-ray source could be indexed based on orthorhombic phase at room temperature (Figure 2.2a). Orthorhombic GeSe, when alloyed with $AgBiSe_2$, gradually transforms to the face-centered cubic structure *via* an intermediate rhombohedral phase (Figure 2.2a) at ambient conditions. With the addition of a small amount of $AgBiSe_2$ ($x \leq 0.04$) in GeSe, the rhombohedral phase starts to appear along with the orthorhombic phase and finally the pure rhombohedral phase stabilizes in the range of x = 0.08 - 0.29 in $(GeSe)_{1-x}(AgBiSe_2)_x$ at ambient conditions. With further increase in the concentration of $AgBiSe_2$, an pure rocksalt phase starts to appear at x = 0.30. The Rietveld refinements of the PXRD patterns of $(GeSe)_{1-x}(AgBiSe_2)_x$ (x = 0, 0.10 and 0.40) (Figure 2.2b-d and Tables 2.1 - 2.3) indicate that when $AgBiSe_2$ is added into the GeSe system, the Ag and Bi atoms preferentially occupies the Ge sites and create substitutional disorder.

In order to understand the microstructure of cubic $(GeSe)_{1-x}(AgBiSe_2)_x$, we have performed back scattered mode field emission scanning electron microscopy (FESEM), EDAX (Figure 2.3) and transmission electron microscopy (TEM) (Figure 2.4) of $(GeSe)_{1-x}(AgBiSe_2)_x$ samples. We did not find any phase separation in microscopy experiments up to x = 0.50 in $(GeSe)_{1-x}(AgBiSe_2)_x$ samples as similar to PXRD experiment.

Pure phase cubic compound is obtained up to x = 0.50 in $(GeSe)_{1-x}(AgBiSe_2)_x$ composition (Figure 2.5a). With further addition of $AgBiSe_2$ (more than x = 0.50), we

observe the presence of minor impurity phases such as BiSe, Ag_2Se and Bi_2Se_3 along with the cubic $(GeSe)_{1-x}(AgBiSe_2)_x$ (Figure 2.5b).

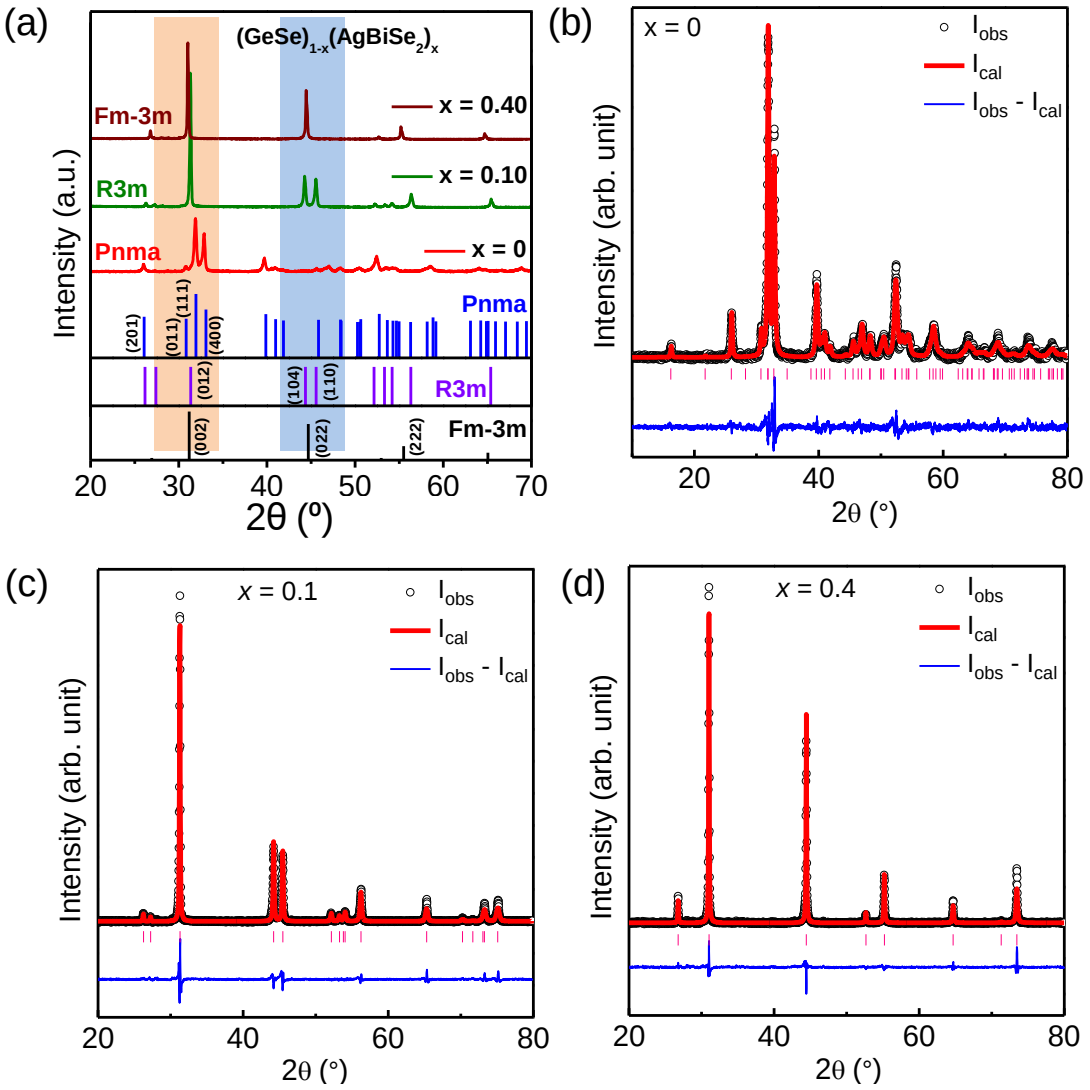

Figure 2.2 *(a) Room temperature PXRD patterns (Laboratory source, Cu K_α; λ = 1.5406 Å) of $(GeSe)_{1-x}(AgBiSe_2)_x$ (x = 0, 0.10, 0.40) manifesting the structural phase evolution from orthorhombic to cubic via an intermediate rhombohedral phase. Rietveld refinement of room-temperature PXRD data of $(GeSe)_{1-x}(AgBiSe_2)_x$ (x = 0, 0.10 and 0.40) samples using GSAS software.[16] (b) x = 0, orthorhombic (Pnma), (c) x = 0.10, rhombohedral (R3m) and (d) x = 0.40, cubic phase (Fm-3m) of GeSe were used for the refinements.*

Table 2.1: Structural parameters of Rietveld refinement for pristine GeSe.

Space group: *Pnma*; a= 10.9208(4) Å, b=3.8708(3) Å, c= 4.4075(4) Å, α = β = γ = 90º

Constituent Element	x/a	y/b	z/c	U_{iso} (Å^2)	Occupancy	GOF
Ge	0.8758(2)	0.25	0.8939(6)	0.096(1)	1	1.53
Se	0.1460(2)	0.25	0.4948(6)	0.0847(9)	1	

R-factors: R_{wp}: 0.0803; R_{exp}: 0.0525.

Table 2.2: Structural parameters of Rietveld refinement for $(GeSe)_{0.90}(AgBiSe_2)_{0.10}$ sample.

Space group: *R3m*; a=b = 3.98656(8) Å, c= 10.1689(3) Å, α = β = 90º, γ = 120º

Constituent Element	x/a	y/b	z/c	U_{iso} (Å^2)	Occupancy	GOF
Ge	0	0	0.7630(4)	0.124(4)	0.74(3)	2.98
Se	0	0	0.2357(5)	0.098(3)	1	
Ag	0	0	0.7630(4)	0.124(4)	0.09(3)	
Bi	0	0	0.7630(4)	0.124(4)	0.17(3)	

R-factors: R_{wp}: 0.1317; R_{exp}: 0.0442.

Table 2.3: Structural parameters of Rietveld refinement for $(GeSe)_{0.60}(AgBiSe_2)_{0.40}$ sample.

Space group: *Fm-3m*; a=b = c = 5.75991(4) Å, α = β = γ = 90º

Constituent Element	x/a	y/b	z/c	U_{iso} (Å^2)	Occupancy	GOF
Ge	0	0	0	0.1361(8)	0.33(2)	2.25
Se	0.5	0.5	0.5	0.1205(9)	1	
Ag	0	0	0	0.1361(8)	0.29(2)	
Bi	0	0	0	0.1361(8)	0.38(2)	

R-factors: R_{wp}: 0.1050; R_{exp}: 0.0467.

The increasing substitutional disorder with the increase of $AgBiSe_2$ concentration in the system leads to the enhancement of configurational entropy and the consequent stabilization of the high symmetry cubic phase at room temperature. This is similar to the phenomenon generally found in high entropy alloys where the addition of extra elements stabilizes high symmetry phases due to the enhancement of entropy of the alloy system.[4,17,18]

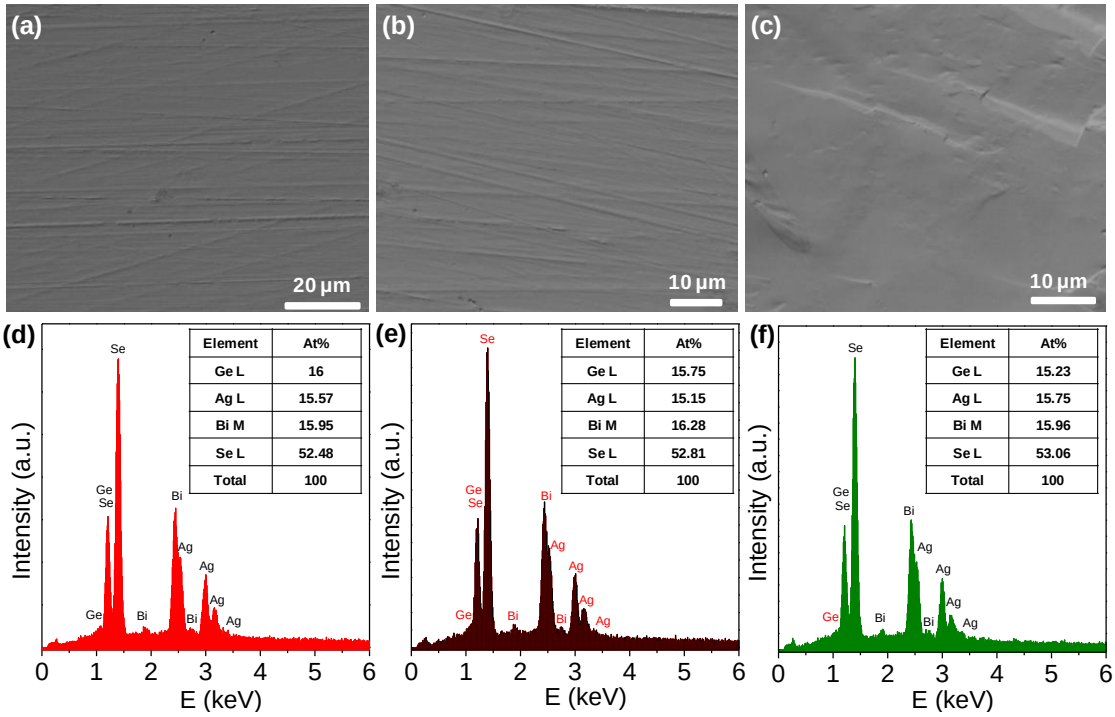

Figure 2.3 *(a)-(c) Backscattered electron images taken during FESEM and (d)-(f) EDAX spectra of (a)-(c) respectively for* $(GeSe)_{0.50}(AgBiSe_2)_{0.50}$ *sample.*

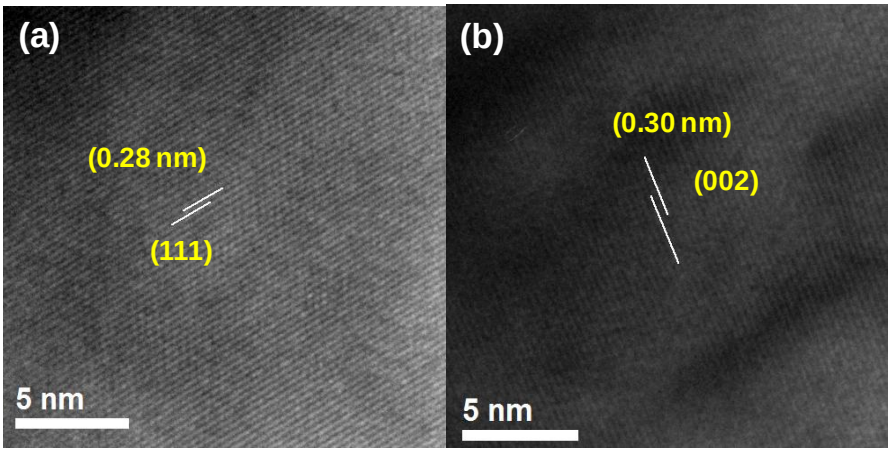

Figure 2.4 *HRTEM of (a) orthorhombic GeSe and (b) cubic* $(GeSe)_{0.50}(AgBiSe_2)_{0.50}$ *samples.*

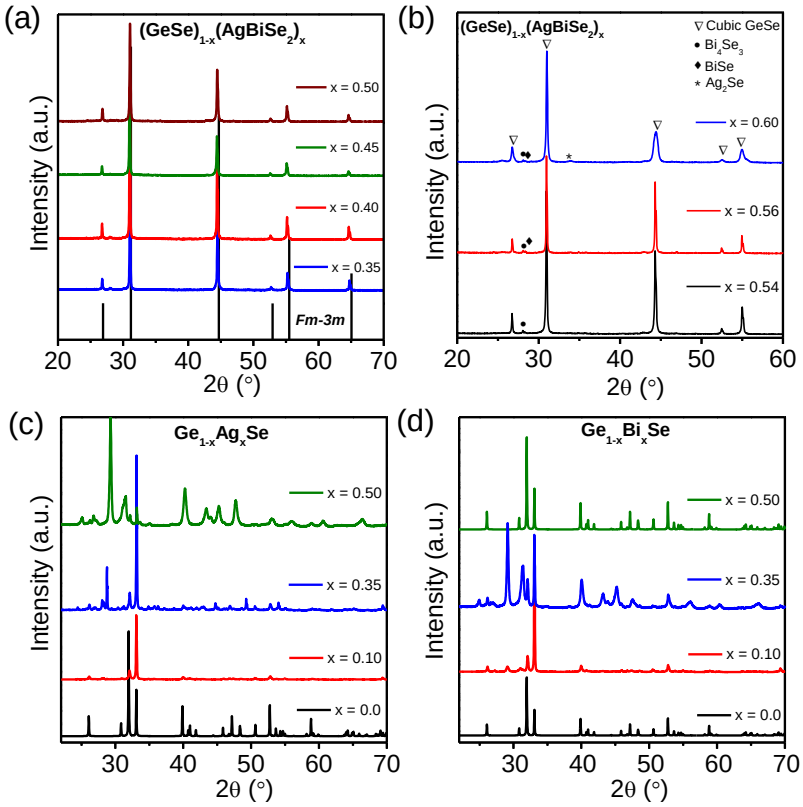

Figure 2.5 *Powder XRD patterns of (a) cubic $(GeSe)_{1-x}(AgBiSe_2)_x$ (x = 0.35, 0.40, 0.45, 0.50), (b) $(GeSe)_{1-x}(AgBiSe_2)_x$ (x = 0.54, 0.56 and 0.60), (c) $Ge_{1-x}Ag_xSe$ (x = 0, 0.10, 0.35, 0.50) and (d) $Ge_{1-x}Bi_xSe$ (x = 0, 0.10, 0.35, 0.50) samples. However, only the single element (Ag or Bi) mixing in GeSe, does not stabilizes the cubic structure.*

The entropy engineering is an effective approach to optimize the thermoelectric performance of a material because it elevates the symmetry of the crystal structure which in turn helps to achieve high Seebeck coefficient and reduces thermal conductivity by increasing the point defect concentrations which can scatter heat carrying phonons effectively.

In this context, mention must be made that only small amount of Ge substitution (~ 9 mol%) in the hexagonal phase of $AgBiSe_2$ does not stabilize high symmetry cubic phase at ambient conditions.[19] $AgBiSe_2$ rich $(AgBiSe_2)_{1-x}(GeSe)_x$ [x = 0 - 0.09], however, undergoes a temperature dependent hexagonal (*P-3m1*; room temperature phase) to cubic (*Fm-3m*) structural phase transition with increasing temperature *via* an intermediate rhombohedral phase (*R-3m*),[19] which is an well known phase transition in pristine $AgBiSe_2$.[20]

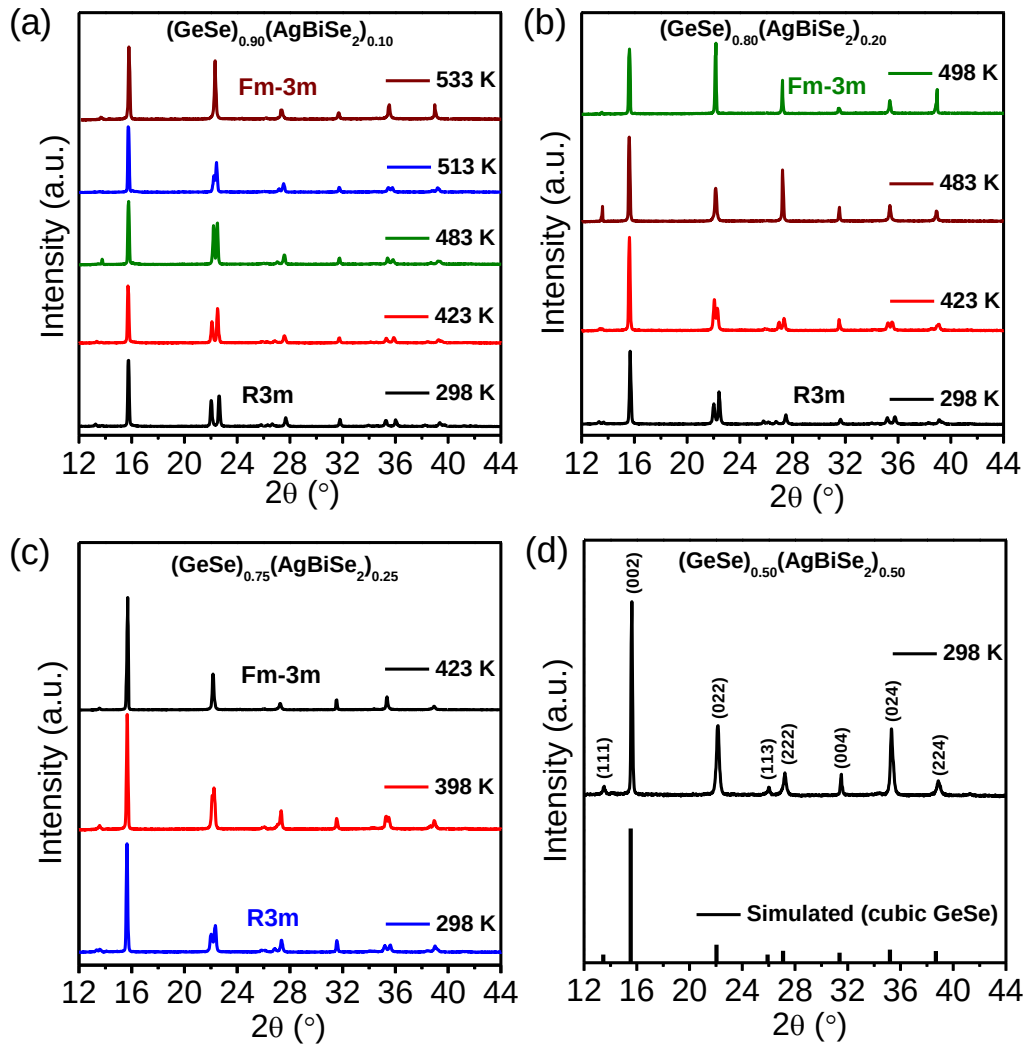

Figure 2.6 *(a)-(c) Temperature-dependent synchrotron (λ = 0.7749 Å) PXRD patterns of* $(GeSe)_{1-x}(AgBiSe_2)_x$ *(x = 0.10, 0.20 and 0.25) showing the decrease of rhombohedral to rocksalt structural transition temperature with increasing* $AgBiSe_2$ *concentration. (d) Synchrotron (λ = 0.7749 Å) powder XRD patterns of* $(GeSe)_{0.50}(AgBiSe_2)_{0.50}$ *(298 K) sample.*

In order to capture the evolution of phase transition temperature with respect to alloying concentration in present GeSe rich $(GeSe)_{1-x}(AgBiSe_2)_x$ (x = 0.1 - 0.25), we have studied temperature dependent synchrotron (λ = 0.7749 Å) PXRD (Figure 2.6a-c) and DSC analysis (Figure 2.7a). The rhombohedral phase of $(GeSe)_{1-x}(AgBiSe_2)_x$ undergoes a structural phase transition into a rocksalt structure at high temperatures. The phase transition (rhombohedral to rocksalt) temperature, however, decreases with increasing $AgBiSe_2$ concentration (e.g., 533 K for x = 0.10, 498 K for x = 0.20 and 423 K for x =

0.25) and finally, the rocksalt phase stabilizes at ambient conditions for x = 0.30 in $(GeSe)_{1-x}(AgBiSe_2)$ (Figure 2.6d).

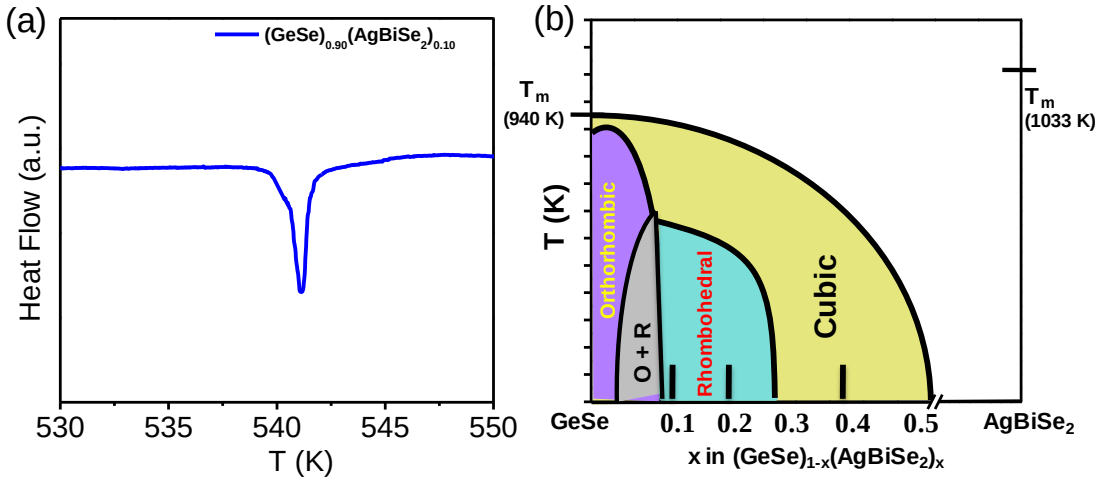

Figure 2.7 *(a) DSC curve for of $(GeSe)_{0.90}(AgBiSe_2)_{0.10}$ sample. (b) The possible schematic phase diagram of the GeSe-$AgBiSe_2$ system based on temperature dependent PXRD and DSC data.*

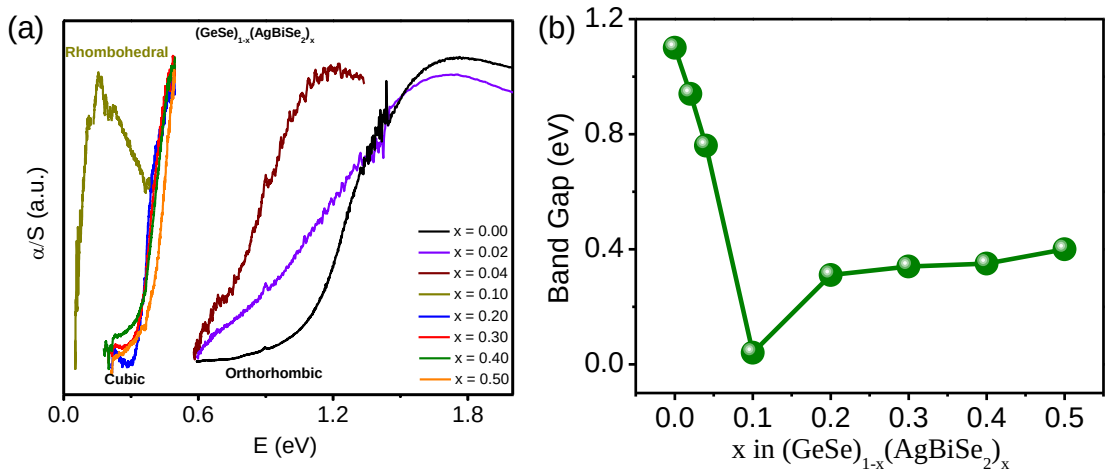

Figure 2.8 *(a) Electronic absorption spectra for $(GeSe)_{1-x}(AgBiSe_2)_x$ (x = 0 - 0.50) samples. (b) The evolution of experimental band gap of GeSe with increasing $AgBiSe_2$ concentration in $(GeSe)_{1-x}(AgBiSe_2)_x$.*

The schematic phase diagram of the GeSe-$AgBiSe_2$ system, as inferred from room and high temperatures PXRD and DSC analysis is shown in Figure 2.7b. The phase boundaries are, however, relative to the position of the orthorhombic, rhombohedral, and cubic phases because of the limited amount of data set studied in this work. However, this phase diagram helps one to identify that the increase of $AgBiSe_2$ concentration in GeSe

causes a structural phase evolution from orthorhombic to rhombohedral phase followed by an rocksalt structure as the $AgBiSe_2$ concentration increases further.

The band gap of pristine orthorhombic GeSe is measured to be ~ 1.1 eV (Figure 2.8a-b), which is much higher than the state of the art thermoelectric materials like Bi_2Te_3 (0.15 eV), PbTe (0.28 eV) and GeTe (0.22 eV). However, when GeSe is alloyed with $AgBiSe_2$, band gap rapidly decreases to ~ 0.05 eV at x ~ 0.10 in the rhombohedral phase (Figure 2.8a-b) due to increase in chemical pressure originating from a sharp decrease in unit cell volume from 186 $Å^3$ (orthorhombic) to 140 $Å^3$ (rhombohedral) (Figure 2.9).

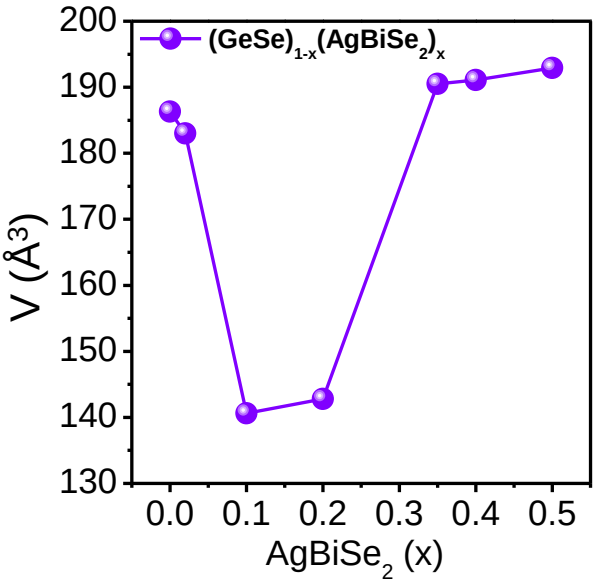

Figure 2.9 *Unit cell volume of* $(GeSe)_{1-x}(AgBiSe_2)_x$ *vs.* $AgBiSe_2$ *concentration.*

When the concentration of $AgBiSe_2$ increases above $x > 0.1$, the band gap slightly increases and stays in 0.3 - 0.4 eV range (2.8a-b) in the cubic phase ($0.30 \leq x \leq 0.50$). The expansion of the unit cell during rhombohedral (140 $Å^3$) to cubic phase (192 $Å^3$) transition releases the chemical pressure, which consequently opens up the band gap slightly.

To study the evolution of band gap with respect to the alloying concentration, we calculated the electronic band structure at three concentrations: pristine GeSe (orthorhombic, Figure 2.10a), $(GeSe)_{0.90}(AgBiSe_2)_{0.10}$ (rhombohedral, Figure 2.10b) and $(GeSe)_{0.60}(AgBiSe_2)_{0.40}$ (rocksalt, Figure 2.10c-d) by density functional theoretical (DFT) calculation with and without spin orbit coupling (SOC). The theoretical band gap of GeSe in the orthorhombic structure is 0.93 eV irrespective of the inclusion of SOC, which is slightly lower than that of the experimental band gap of 1.1 eV (Figure 2.10a), that is common DFT calculation of gaps.

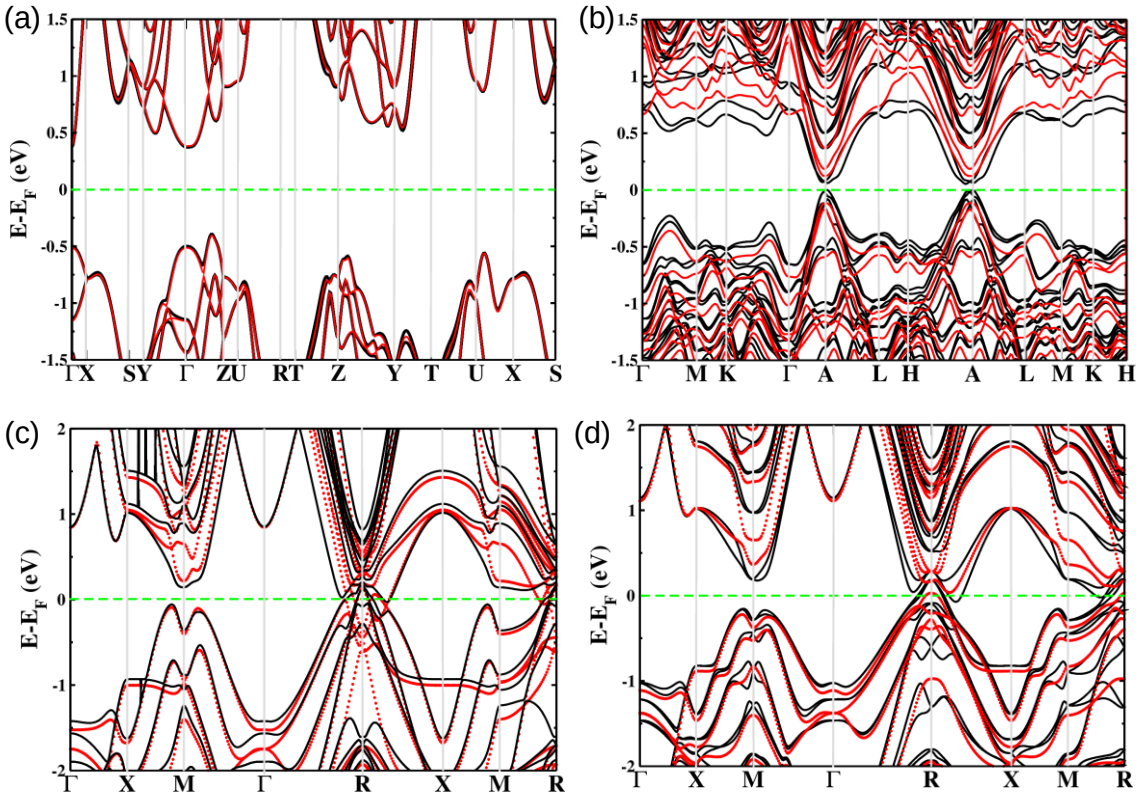

Figure 2.10 *Electronic band structure of (a) orthorhombic GeSe, (c) rhombohedral* $(GeSe)_{0.90}(AgBiSe_2)_{0.10}$. *Electronic structure of eight atoms FCC (1X1X1) (c)* $(GeSe)_{0.60}(AgBiSe_2)_{0.40}$ *and (d) off-centered structure calculated with (black color lines) and without (red color lines) the inclusion of spin-orbit coupling (SOC).*

We find that the band gap of GeSe decreases with $AgBiSe_2$ alloying, consistent with the trend observed in experimental measurements. Our estimates of the band gap of rhombohedral $(GeSe)_{0.90}(AgBiSe_2)_{0.10}$ is ~ 0.05 eV (with SOC) (Figure 2.10b). Electronic structures of the 8 atoms cubic FCC unit cell (1X1X1) of $(GeSe)_{0.60}(AgBiSe_2)_{0.40}$

calculated with and without SOC reveal vanishing band gaps with overlapping bands at the Fermi level (Figure 2.10c). To get a more accurate estimate of band gap theoretically, we investigated the role of local structural distortions in cubic phase (Figure 2.10d). We determined the extent of off-centring by introducing displacements in Bi atom along the <111> direction (Table 2.4).

Table 2.4: Off-centering displacements of atoms in the cubic structure of $(GeSe)_{0.60}(AgBiSe_2)_{0.40}$ obtained after relaxation of the structure.

	Along x direction (Å)	Along y direction (Å)	Along z direction (Å)
Ge	0.17	0.08	0.06
Ag	0.19	0.24	0.19
Bi	0.03	0.02	0.03
Ge	0.06	0.08	0.17
Se	0.01	0.18	0.03
Se	0.14	0.03	0.14
Se	0.03	0.03	0.05
Se	0.11	0.04	0.02

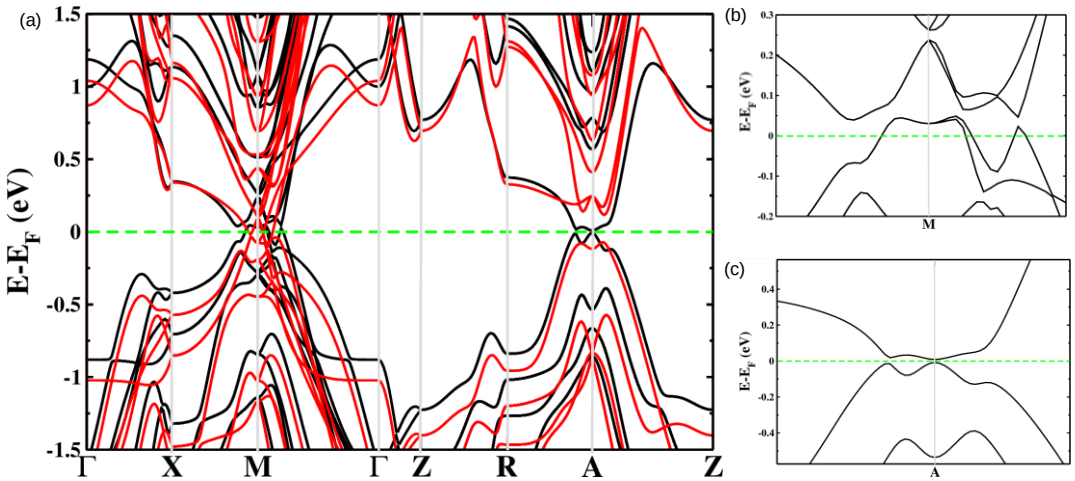

Figure 2.11 *Electronic band structure of (a) cubic $(GeSe)_{0.60}(AgBiSe_2)_{0.40}$ with (black color lines) and without (red color lines) the inclusion of spin-orbit coupling (SOC). Zoomed version at (b) M point and (c) A point which clearly shows conduction band minima and valence band maxima don't cross each other.*

Electronic bands of the relaxed structure calculated without SOC show vanishing gap, whereas, with SOC, we find weakly overlapping bands at R point and the Fermi level (Figure 2.10d). We then simulated chemical disorder in the cubic system with a 1x1x2 supercell. Electronic structure calculated with SOC of this supercell of cubic $(GeSe)_{0.60}(AgBiSe_2)_{0.40}$ reveals no overlap between valence and conduction band (Figure 2.11a-c) emphassing the role of chemical disorder. The band gap in the cubic structure stabilized at higher $AgBiSe_2$ concentration is strongly influenced by the chemical disorder in occupation of Bi, Ag and Ge at the cationic site.

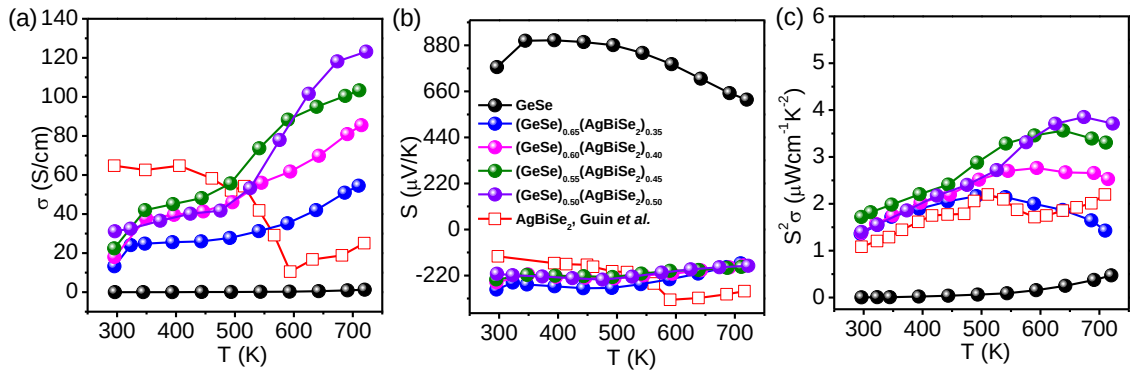

Figure 2.12 *Temperature variations of (a) electrical conductivity (σ), (b) Seebeck coefficient (S) and (c) power factor (σS^2) of $(GeSe)_{1-x}(AgBiSe_2)_x$ (x = 0 - 0.50) and comparison with that of $AgBiSe_2$[20].*

In all the $(GeSe)_{1-x}(AgBiSe_2)_x$ (x = 0 - 0.50) compositions, electrical conductivity (σ) increases with increasing temperature which indicates the semiconducting transport (Figure 2.12a). The σ of pristine orthorhombic GeSe is 0.0046 S/cm at 300 K, which increases to ~ 1.2 S/cm at 723 K. Such a low σ is mainly caused by the low carrier concentration (*p*-type, 1.2 X 10^{17} cm^{-3}) of orthorhombic GeSe and leads to its poor thermoelectric performance. Several attempts have been made in the past to increase the carrier concentration in GeSe using *p*-type dopants such as Ag, Cu, Na or *n*-type dopants like Sb, Bi, La, As, I, however, the carrier concentration remained far away from the theoretical value for promising thermoelectric properties.[10]

Table 2.5: Room temperature electrical conductivity (σ), Seebeck coefficient (S) and carrier concentration (n) of $(GeSe)_{1-x}(AgBiSe_2)_x$ (x = 0, 0.40, 0.45, 0.50) samples.

Sample	σ (S/cm)	S (μV/K)	n (cm^{-3})
GeSe	0.0047	+770	1.20×10^{17}
$\mathbf{(GeSe)_{0.60}(AgBiSe_2)_{0.40}}$	18	-171	2.38×10^{18}
$\mathbf{(GeSe)_{0.55}(AgBiSe_2)_{0.45}}$	23	-179	2.71×10^{18}
$\mathbf{(GeSe)_{0.50}(AgBiSe_2)_{0.50}}$	31	-211	3.29×10^{18}

Solid solution of GeSe with $AgBiSe_2$ increases the σ significantly due to the enhancement in the carrier concentration from 1.2×10^{17} cm^{-3} (p-type) for pristine GeSe to 3.29×10^{18} cm^{-3} (n-type) for $(GeSe)_{0.50}(AgBiSe_2)_{0.50}$ (Table 2.5). Typically, the room temperature σ of $(GeSe)_{0.50}(AgBiSe_2)_{0.50}$ is found to be ~ 32 S/cm, which increases to ~ 124 S/cm at 723 K. We have compared the electrical transport behavior of cubic $(GeSe)_{1-x}(AgBiSe_2)_x$ with pristine $AgBiSe_2$ (Figure 2.12) which distinctly exhibits the differences between these two compounds: while a clear signature of structural phase transition is visible in the temperature dependent electrical transport behavior of pristine $AgBiSe_2$,[20] cubic $(GeSe)_{0.50}(AgBiSe_2)_{0.50}$ exhibits no such signature.

The measured value of the Seebeck coefficient (S) of pristine orthorhombic GeSe is 770 μV/K at 300 K, which decreases to 640 μV/K at 720 K (Figure 2.12b). Holes are the majority carriers in orthorhombic GeSe making it a p-type semiconductor, which is also confirmed by the *positive* value of Hall coefficient. Ge-chalcogenide based thermoelectric materials are generally p-type semiconductors due to intrinsic Ge vacancies, and so far, the pristine orthorhombic GeSe seems to be no exception to this. However, the cubic $(GeSe)_{1-x}(AgBiSe_2)_x$ ($0.35 \leq x \leq 0.50$) show *negative S* values (Figure 2.12b) indicating a n-type conduction. The n-type carrier conduction is also in agreement with the *negative* sign of Hall coefficients. Bi^{3+} substitution in place of Ge^{2+} acts as a donor dopant and increases the n-type carrier concentration which is also evident from the projected density of states (PDOS) analysis (Figure 2.13). While, the contribution of Ge-p orbital is significant in the formation of the conduction band (CB) edge of orthorhombic and

rhombohedral GeSe, the contribution of Bi *p*-orbital considerably increases and Ge-*p* vanishes in the CB edge of cubic phase.

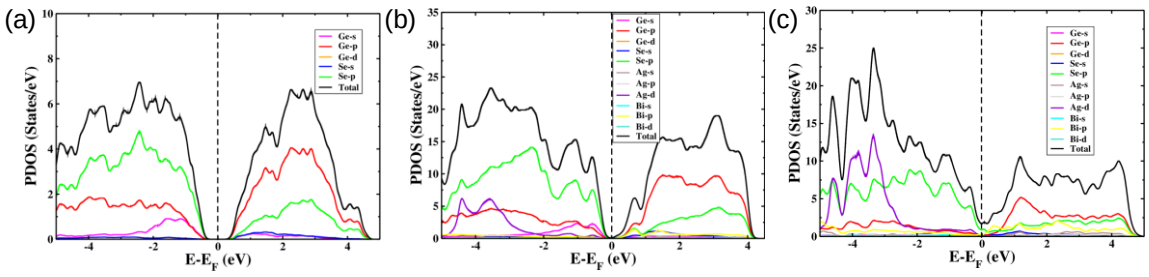

Figure 2.13 *Electronic density of states (DOS) and projected density of states (PDOS) of (a) GeSe (orthorhombic), (b) $(GeSe)_{0.90}(AgBiSe_2)_{0.10}$ (rhombohedral) and (c) $(GeSe)_{0.60}(AgBiSe_2)_{0.40}$ (cubic) calculated with inclusion of the spin-orbit coupling.*

In pure GeSe, we find that valence band (VB) is contributed mostly by Se-p orbitals, and weakly by Ge-s and Ge-p orbitals. Its conduction band (CB) is contributed by Ge-p orbitals. In the rhombohedral phase, contributions to valence band are dominated by Se-p, Ge-s and Ge-p orbitals as was seen in pure GeSe, while the CB is contributed by Ge-p orbitals and weakly by Bi-p and Se-p orbitals. In the cubic phase, contributions of Ge-s and Ge-p orbitals to the VB vanish and Bi-p, Se-p and Ge-p orbitals contribute to the CB.

Typically, $(GeSe)_{0.50}(AgBiSe_2)_{0.50}$ exhibits a *S* value of - 210 μV/K at 300 K, which decreases to -174 μV/K at 724 K. Therefore, our finding of the stabilization of high symmetry cubic phase of $(GeSe)_{1-x}(AgBiSe_2)_x$ ($0.35 \leq x \leq 0.50$) at ambient conditions with dominant *n*-type carrier (>10^{18} carriers/cm^3) and high *S* value is an intriguing new development in the area of Ge-chalcogenide based thermoelectrics.

Cubic $(GeSe)_{1-x}(AgBiSe_2)_x$ ($0.35 \leq x \leq 0.50$) exhibits higher power factor, $S^2\sigma$, compared to that of the orthorhombic GeSe (Figure 2.12c) due to higher electrical conductivity. The measured maximum power factor of $(GeSe)_{0.50}(AgBiSe_2)_{0.50}$ is found to be 3.8 μWcm^{-1}K^{-2} at 677 K.

Orthorhombic pristine GeSe exhibits total thermal conductivity (κ_{total}) of 1.78 Wm^{-1}K^{-1} at 300 K, which decreases to 0.54 Wm^{-1}K^{-1} at 720 K (Figure 2.14c). When GeSe is alloyed with $AgBiSe_2$, κ_{total} in the cubic $(GeSe)_{0.50}(AgBiSe_2)_{0.50}$ significantly decreases to 0.43 Wm^{-1}K^{-1} at 300 K (Figure 2.14c). Electrical thermal conductivities, κ_{el} were

estimated (Figure 2.14e) using Wiedemann-Franz Law, $\kappa_{el} = L\sigma T$, where L is the Lorenz number which is calculated by fitting the reduced chemical potential derived from temperature-dependent Seebeck coefficient considering single parabolic band conduction and dominant acoustic phonon scattering of carriers. Temperature dependent lattice thermal conductivities, κ_L were obtained by subtracting κ_{el} from κ_{total}. κ_L of orthorhombic pristine GeSe decreases with increasing temperature (Figure 2.14f). At 720 K, the value of κ_L of pristine GeSe (κ_{min} of ~ 0.4 $Wm^{-1}K^{-1}$)[10] becomes nearly one-third (0.54 $Wm^{-1}K^{-1}$) of its room temperature value (1.78 $Wm^{-1}K^{-1}$). However, in the cubic $(GeSe)_{1-x}(AgBiSe_2)_x$ ($0.35 \leq x \leq 0.50$), κ_L becomes nearly temperature independent and exhibits ultralow values that ranges between 0.43 - 0.70 $Wm^{-1}K^{-1}$ in the temperature range 300 - 723 K (Figure 2.14f).

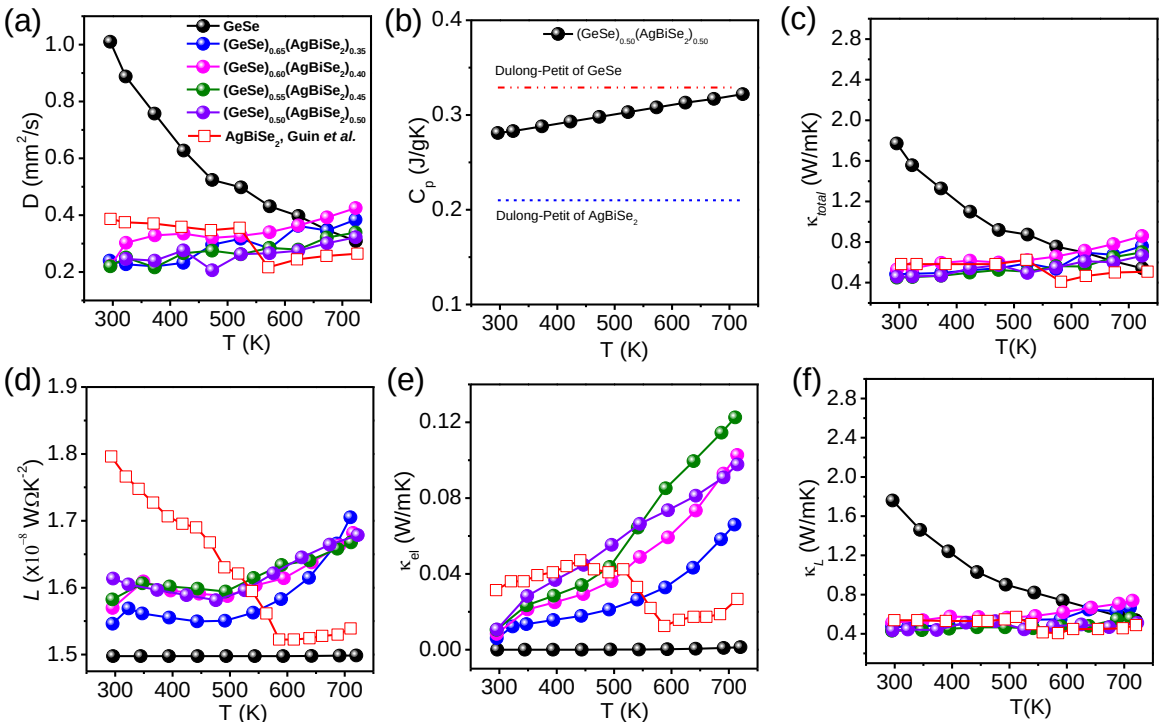

Figure 2.14 *Temperature variations of (a) diffusivity (D), (b) heat capacity (C_p), (c) total thermal conductivity (κ_{total}), (d) Lorenz number (L), (e) electrical thermal conductivity (κ_{el}) and (f) lattice thermal conductivity (κ_L) of $(GeSe)_{1-x}(AgBiSe_2)_x$ (x = 0-0.50) and comparison with that of $AgBiSe_2$[20].*

The value of κ_L in $(GeSe)_{0.50}(AgBiSe_2)_{0.50}$ is 0.43 $Wm^{-1}K^{-1}$ at 300 K. The origin of low κ_L can be attributed to the increased phonon scattering by enhanced point defects due

to entropy driven solid solution in GeSe-$AgBiSe_2$. We have also compared the both κ_{total} and κ_L of cubic $(GeSe)_{1-x}(AgBiSe_2)_x$ ($0.35 \leq x \leq 0.50$) samples with $AgBiSe_2$ in Figure 2.14c and f. Similar to the temperature dependent electrical transport behaviors, a clear signature of structural phase transition is also present in the temperature variation of thermal conductivities of pristine $AgBiSe_2$ which is absent in cubic $(GeSe)_{1-x}(AgBiSe_2)_x$.

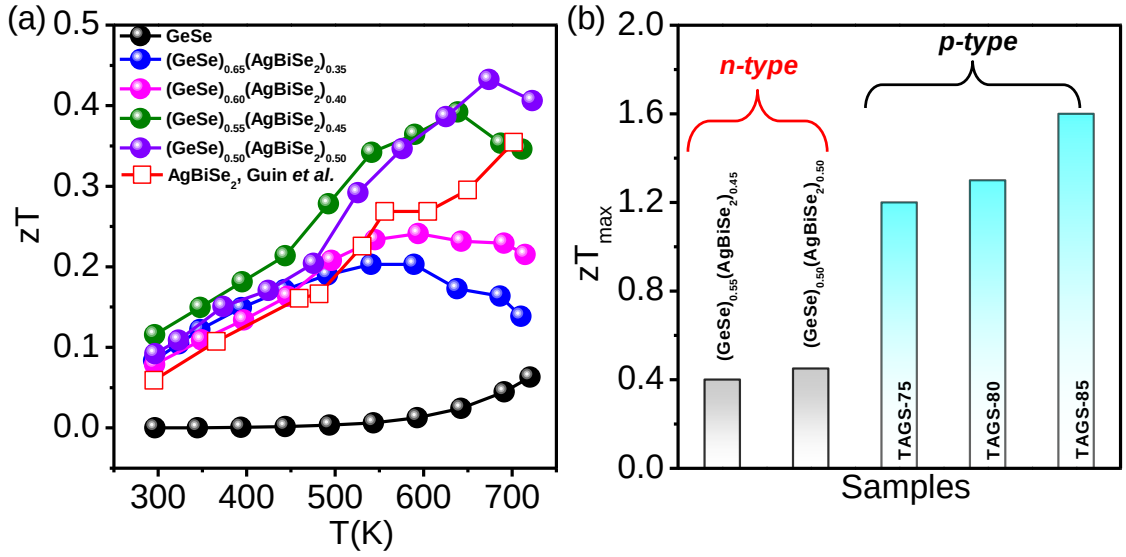

Figure 2.15 *(a) Temperature dependent thermoelectric figure of merit (zT) of* $(GeSe)_{1-x}(AgBiSe_2)_x$ *(x = 0- 0.50) and compared with that of* $AgBiSe_2$[20]*. (b) Comparison of* zT_{max} *of* $(GeSe)_{1-x}(AgBiSe_2)_x$ *(x = 0.45 and 0.50) samples with well known TAGS-x (x = 75, 80 and 85).*[21,22]

Alloying of GeSe with $AgBiSe_2$ increases the electrical conductivity while κ_L approaches ultralow value of ~ 0.43 $Wm^{-1}K^{-1}$. Consequently, *zT* increases to a maximum value of 0.45 at 677 K for *n*-type $(GeSe)_{0.50}(AgBiSe_2)_{0.50}$ (Figure 2.15a) that is promising for Ge-chalcogenide based thermoelectrics considering that they are mostly of *p*-type materials/compositions with high *zT* like well known TAGS-x (x = 75, 80 and 85) (see the comparison Figure 2.15b).[21,22]

2.4 Conclusions

In conclusion, the high temperature and high-pressure cubic rocksalt phase of GeSe has been stabilized at ambient conditions by entropy driven solid solution alloying with $AgBiSe_2$. The anomalous closing and opening of the band gap of GeSe with increasing $AgBiSe_2$ concentration is due to the influence of positive (rhombohedral phase) and negative (cubic phase) chemical pressure. Interestingly, cubic $(GeSe)_{1-x}(AgBiSe_2)_x$ posses *n*-type conduction with reasonable high carrier concentration, which is rare in Ge-chalcogenides based thermoelectrics. This cubic $(GeSe)_{1-x}(AgBiSe_2)_x$ demonstrates an ultralow κ_L of 0.43 $Wm^{-1}K^{-1}$. Ultralow thermal conductivity is attributed to the enhanced point defect phonon scattering due to entropy driven extended solid solutions. This report establishes cubic $(GeSe)_{1-x}(AgBiSe_2)_x$ as a promising *n*-type thermoelectric materials and their performance can be improved further by carrier engineering such as aliovalent halide doping.

2.5 References

[1] G. Tan, L.-D. Zhao, M. G. Kanatzidis, *Chem. Rev.* **2016**, *116*, 12123.

[2] Z. Ge, L. Zhao, D. Wu, X. Liu, B. Zhang, J. Li, J. He, *Mater.Today* **2016**, *19*, 227.

[3] F. D. Rosi, J. P. Dismukes, E. F. Hockings, *Electr. Eng.* **1960**, *79*, 450.

[4] M. Samanta, K. Biswas, *J. Am. Chem. Soc.* **2017**, *139*, 9382.

[5] S. Roychowdhury, M. Samanta, S. Perumal, K. Biswas, *Chem. Mater*. **2018**, *30*, 5799.

[6] Z. Huang, S. A. Miller, B. Ge, M. Yan, S. Anand, T. Wu, P. Nan, Y. Zhu, W. Zhuang, G. J. Snyder, P. Jiang, X. Bao, *Angew. Chem. Int. Ed.* **2017**, *56*, 14113.

[7] V. L. Deringer, R. P. Stoffel, R. Dronskowski, *Phys. Rev*. B **2014**, *89*, 094303.

[8] L.-D. Zhao, S.-H. Lo, Y. Zhang, H. Sun, G. Tan, C. Uher, C. Wolverton,V. P. Dravid, M. G. Kanatzidis, *Nature* **2014**, *508*, 373.

[9] S. Hao, F. Shi, V. P. Dravid, M. G. Kanatzidis, C. Wolverton, *Chem. Mater.* **2016**, *28*, 3218.

[10] X. Zhang, J. Shen, S. Lin, J. Li, Z. Chen, W. Li, Y. Pei, *J. Materiomics*, **2016**, *2*, 331.

[11] M. A. Hughes, Y. Fedorenko, B. Gholipour, J. Yao, T.-H. Lee, R. M. Gwilliam, K. P. Homewood, S. Hinder, D. W. Hewak, S. R. Elliott, R. J. Curry, *Nat. Commun*. **2014**, *5*, 5346.

[12] M. Sist, C. Gatti, P. Nørby, S. Cenedese, H. Kasai, K. Kato, B. B. Iversen, *Chem. Eur. J.* **2017**, *23*, 6888.

[13] P. Giannozzi, S. Baroni, N. Bonini, M. Calandra, R. Car, C. Cavazzoni, D. Ceresoli, G. L. Chiarotti, M. Cococcioni, I. Dabo, A. L. Corso, S. de Gironkoli, S. Fabris, G. Fratesi, R. Gebauer, U. Gerstmann, C. Gougoussis, A. Kokalj, M. Lazzeri, L. Martin-Samos, N. Marzari, F. Mauri, R. Mazzarello, S. Paolini, A. Pasquarello, L. Paulatto, C. Sbraccia, S. Scandolo, G. Sclauzero, A. P. Seitsonen, A. Smogunov, P. Umari, R. M. Wentzcovitch, *J. Phys. Condens. Matter*. **2009**, *21*, 395502.

[14] X. Hua, X. Chen, W. A. Goddard, *Phys. Rev. B* **1997**, *55*, 16103.

[15] J. P. Perdew, K. Burke, M. Ernzerhof, *Phys. Rev. Lett.* **1996**, *77*, 3865.

[16] B. J. Toby, *Appl. Cryst.* **2001**, *34*, 210.

[17] C. M. Rost, E. Sachet, T. Borman, A. Moballegh, E. C. Dickey, D. Hou, J. L. Jones, S. Curtarolo, J.-P. Maria, *Nat. Commun*. **2015**, *6*, 8485.

[18] R. Liu, H. Chen, K. Zhao, Y. Qin, B. Jiang, T. Zhang, G. Sha, X. Shi, C. Uher, W. Zhang, L. Chen, *Adv. Mater*. **2017**, *29*, 1702712.

[19] H.-J. Wu, P.-C. Wei, H.-Y. Cheng, J.-R. Deng, Y.-Y. Chen, *Acta. Mater.* **2017**, *141*, 217.

[20] S. N. Guin, V. Srihari, K. Biswas, *J. Mater. Chem. A* **2015**, *3*, 648.

[21] L. Zhang, W. Wang, B. Ren J. Guo, *J. Electron. Mater.* **2013**, *42*, 1303

[22] J. Davidow, Y. Gelbstein, *J. Electron. Mater.* **2013**, *42*, 1542.

PART 4

Thermoelectric Properties of Tin Chalcogenides

Chapter 1

An Enhanced Seebeck Coefficient and High Thermoelectric Performance in *p*-type In and Mg Co-doped $Sn_{1-x}Pb_xTe$ *via* the Co-adjuvant Effect of Resonance Level and Heavy Hole Valence Band

Chapter 1

An Enhanced Seebeck Coefficient and High Thermoelectric Performance in *p*-Type In and Mg Co-doped $Sn_{1-x}Pb_xTe$ *via* the Co-adjuvant Effect of Resonance Level and Heavy Hole Valence Band[†]

Summary

Recently, tin telluride (SnTe) has drawn much attention as a potential candidate for thermoelectric power generation. In this chapter, we present the high thermoelectric performance in SnTe achieved through two-step design, (a) reduction in lattice thermal conductivity via solid solution alloying and (b) enhancement of Seebeck coefficient (S) via modification of electronic structure through co-doping. First, we demonstrate that introduction of Pb in position of Sn in SnTe decreases the excess p-type carrier concentration in SnTe. Notably, $Sn_{0.70}Pb_{0.30}Te$ sample exhibits a κ_{latt} value of ~ 0.67 W/mK at 300 K, which is close to the theoretical minimum limit of the κ_{latt} in SnTe, which results mainly from scattering of heat carrying phonons by solid solution point defects. Secondly, we achieve S of 121 μV/K at 300 K, which increases to ~ 241 μV/K at 710 K for In and Mg co-doped $Sn_{0.70}Pb_{0.30}Te$, which is the highest Seebeck coefficient among all the state-of-the-art SnTe based materials known so far. Indium acts as a resonant dopant, leading to a remarkable enhancement in Seebeck coefficient mainly near room temperature, whereas Mg doping enables the valence band convergence in $Sn_{0.70}Pb_{0.30}Te$, which is confirmed by density functional theoretical (DFT) calculation of its electronic structure. As a result of co-doping, remarkable enhancement in Seebeck coefficient over a wide range of temperature is achieved due to synergistic effect of resonance level formation and valence band convergence. Hence, we have achieved a maximum zT of 1 at 710 K for In and Mg co-doped $Sn_{0.70}Pb_{0.30}Te$. Notably, average zT (zT_{avg}) of ~ 0.6 is achieved in the temperature range of 300 – 710 K for $Sn_{0.655}Mg_{0.04}In_{0.005}Pb_{0.30}Te$ sample.

[†]*Paper based on this study has been published in J. Mater. Chem. C* ***2017****, 5, 5737.*

1.1 Introduction

Significant enhancement in zT has been achieved through (a) the enhancement of Seebeck coefficient by the manipulation of density of states *via* introduction of resonance states near Fermi level in the electronic structure,[1,2] band convergence[3-7] and carrier engineering;[8] and/or (b) by reducing the lattice thermal conductivity by introducing point defects, second phase nano-precipitates,[9-12] meso-scale grain boundaries[13,14] and bond anharmonicity[15-18] which can effectively scatter heat carrying phonons.

Lead Telluride (PbTe) is an efficient thermoelectric material for power generation application in the temperature range of 600 – 900 K.[9,13] Heremans *et al.* reported that substitution of Tl in PbTe can enhance its Seebeck coefficient due to the formation of resonance levels in the valence band.[1] Furthermore, Mg doping in PbTe widens the principal band gap and reduces the energy between light and heavy hole valence band (*i.e.* valence band convergence), resulting in significant enhancement in Seebeck coefficient.[19] PbTe serves as a classical isostructural model for SnTe, which has a similar electronic structure as PbTe.[2,20,21] However, pristine SnTe is not considered as a promising thermoelectric material because of its high electrical and thermal conductivity and low Seebeck coefficient at room temperature, resulting low zT ~ 0.35 at 900 K.[3,22,23] The reason of this low thermoelectric efficiency is mainly arising from: (a) very high *p*-type carrier concentration caused by intrinsic Sn vacancies[22,23] and (b) a large energy separation between light hole and heavy hole valence band (~ 0.3 - 0.4 eV) compared to that of PbTe (~ 0.18 eV),[20-22] which effectively hinders the heavy hole band contribution to the electronic transport, resulting in low Seebeck coefficient. Recently, thermoelectric performance of SnTe is significantly enhanced by modulation of its electronic structure[2-4,6,7,24-27] and introducing nanostructures in the SnTe matrix.[11,12] For example, Zhang *et al.* demonstrated that addition of indium in SnTe increases the Seebeck coefficient significantly at room temperature due to the formation of resonance level in the valence band.[2] Moreover, Mg doping in SnTe modifies its electronic band structure (*via* valence band convergence), enhancing its Seebeck coefficient.[4]

SnTe and PbTe form solid solution throughout the complete range of compositions ($Sn_{1-x}Pb_xTe$; $0 \leq x \leq 1$) and their physical properties like hole concentration and band gap have been tailored previously by changing the ratio of Sn and Pb.[28-35]

Introduction of Pb in SnTe reduces its lattice thermal conductivity due to scattering of heat carrying phonons by solid solution point defects.[29-34] Previously, Han *et al.* showed that Cd doping in Sn rich $Sn_{1-x}Pb_xTe$ reduced the carrier concentration and the lattice thermal conductivity.[36] A *zT* value of ~ 0.7 at 560 K is reported for $(Sn_{1-x}Pb_x)_{0.97}Cd_{0.03}Te$ (x = 0.36) sample.[36] However, the thermoelectric performance of Sn rich $Sn_{1-x}Pb_xTe$ system is not well studied in the intermediate temperature range (400 - 700 K). Previous studies on SnTe indicate that In and Mg have distinct and complementary roles in the improvement of thermoelectric performance.[2,4] Motivated by these facts, we have studied here the effect of co-doping of In and Mg in Sn rich $Sn_{1-x}Pb_xTe$ system, which may enhance the Seebeck coefficient *via* synergistic effect of resonance level and valence band convergence, thereby improving the zT over a wide temperature range.

In this chapter, we demonstrate high thermoelectric performance in SnTe that is achieved through two-step design, (a) reduction of lattice thermal conductivity *via* solid solution alloying with PbTe, which scatters heat carrying phonons effectively and (b) enhancement of Seebeck coefficient *via* synergistic effect of indium and magnesium co-doping in $Sn_{1-x}Pb_xTe$, where In acts as a resonant dopant and Mg doping enables the valence band convergence. With first-principles density functional (DFT) calculations we determine the electronic structure of In and Mg co-doped $Sn_{1-x}Pb_xTe$, and corroborate the simultaneous introduction of resonance level and valence band convergence. In and Mg co-doped $Sn_{0.70}Pb_{0.30}Te$ samples show significantly high Seebeck coefficient compared to controlled $Sn_{0.70-x}In_xPb_{0.30}Te$ and $Sn_{0.70-y}Mg_yPb_{0.30}Te$ samples. We have achieved *S* value of ~ 121 μV/K at 300 K, which increases to ~ 241 μV/K at 710 K for $Sn_{0.70-x-y}In_xMg_yPb_{0.30}Te$, which is one of the highest Seebeck values measured among all SnTe based materials reported so far.[3,4-7,12] Finally, we have achieved maximum zT ~ 1 at 710 K for In and Mg co-doped sample, which is higher than that of undoped, In doped and Mg doped $Sn_{0.70}Pb_{0.30}Te$ sample. Notably, an average thermoelectric figure of merit (zT_{avg}) of ~ 0.6 was obtained in the temperature range of 300 – 710 K for $Sn_{0.6550}Mg_{0.04}In_{0.0050}Pb_{0.30}Te$ sample, which is comparable to other high performance SnTe - based materials.[2, 4, 6,7, 36, 37]

1.2 Methods

1.2.1 Reagents

Tin (Sn, Alfa Aesar 99.99+ %), tellurium (Te, Alfa Aesar 99.999+ %), lead (Pb, Alfa Aesar 99.99+ %), indium (In, Alfa Aesar 99.99+ %) and magnesium (Mg, Alfa Aesar 99.999+ %) were used for synthesis without further purification.

1.2.2 Synthesis

Ingots (~ 10 g) of $Sn_{1-x}Pb_xTe$ (x = 0, 0.15, 0.20, 0.30), $Sn_{0.70-x}In_xPb_{0.30}Te$ (x = 0.0005, 0.001, 0.0025, 0.005), $Sn_{0.70-y}Mg_yPb_{0.30}Te$ (y = 0.02, 0.04, 0.06) and $Sn_{0.70-x-y}In_xMg_yPb_{0.30}Te$ (y= 0.04; x = 0.0005, 0.0025, 0.0050) were synthesized by mixing appropriate ratios of high-purity elemental Sn, Pb, In, Mg and Te in quartz tubes. The tubes were sealed under vacuum (10^{-5} Torr) and slowly heated to 723 K over 12 hrs, then heated up to 1323 K in 5 hrs, annealed for 5 hrs, and cooled down to 1023 K over 2 hrs and annealed for 4 hrs, then slowly cool down to room temperature over a period of 18 hrs.

1.2.3 Powder X-ray diffraction

Powder X-ray diffraction of samples were recorded using a Cu K_α (λ = 1.5406 Å) radiation on a Bruker D8 diffractometer.

1.2.4 Electrical transport

Electrical conductivity and Seebeck coefficients were measured simultaneously under He atmosphere from room temperature to 723 K on a ULVAC-RIKO ZEM-3 instrument system. The typical sample for measurement had a parallelepiped shape with the dimensions of ~ 2×2×8 mm^3. The longer direction coincides with the direction in which the thermal conductivity was measured.

1.2.5 Hall measurement

To determine carrier concentration, Hall measurements have been carried out using four-contact Hall-bar geometry, in a magnetic field of 0.57 T at room temperature in equipment developed by Excel Instruments.

1.2.6 Thermal transport

Thermal diffusivity, D, was directly measured in the range 300 – 723 K by using a laser flash diffusivity method in a Netzsch LFA-457 instrument. Coins with ~ 8 mm diameter and ~ 2 mm thickness were used in all of the measurements. The temperature dependent heat capacity, C_p, was derived using a standard sample (pyroceram) in LFA-457. The total thermal conductivity, κ_{total}, was calculated using the formula, $\kappa_{total} = DC_p\rho$, where ρ is the density of the sample. The density of the pellets obtained was in the range ~ 97% of the theoretical density.

1.2.7 Computational details

This part has been done in collaboration with Prof. Umesh V. Waghmare's group in JNCASR. We modeled a configuration of solid solution $Sn_{0.7}Pb_{0.3}Te$ with a periodic supercell containing $Sn_{11}Pb_5Te_{16}$. Electronic structure of $Sn_{11-x-y}Pb_5Mg_xIn_yTe_{16}$ was determined within density functional theory (DFT) using Quantum Espresso package.[38] Since most of these atoms have high atomic numbers and masses, we included the effects of spin orbit coupling in determination of realistic electronic structure. A Generalized Gradient Approximation (GGA) to exchange-correlation energy with parametrized functional of Perdew, Burke, and Erzenhoff (PBE) was used.[39] Valence and semicore electronic states of Sn, Pb, Te, Mg and In (in $4d^{10}\ 5s^2\ 5p^2$, $5d^{10}\ 6s^2\ 6p^2$, $4d^{10}\ 5s^2\ 5p^4$, $3s^2$ and $4d^{10}\ 5s^2\ 5p^1$ configurations respectively) were treated with fully relativistic ultra-soft pseudopotentials.[40] Pristine, Mg and In substituted SnTe were simulated with a tetragonal supercell ($\sqrt{2}$ x $\sqrt{2}$ x 2)a_0 containing 32 atoms. Plane wave basis set used in representation of Kohn sham wavefunctions was terminated with kinetic energy cut-off of 50 Ry, and that for charge density at an energy of 400 Ry. A fine and uniform 14X14X10 mesh of k points was used in sampling Brillouin zone integrations. The discontinuity in occupation numbers of electronic states near the gap was smeared using a Gaussian function and a smearing with a width (k_BT) of 0.04 eV. We analyzed electronic structure along high symmetry directions (Γ - X - M - Γ - Z - R - A - Z) in the Brillouin zone.

1.3 Results & Discussion

Optimization of thermoelectric properties of SnTe through Pb alloying.

Powder X-ray diffraction pattern of $Sn_{1-x}Pb_xTe$ (x = 0, 0.15, 0.20, 0.30) samples show no impurity phase within the detection limit of PXRD (Figure 1.1a). Linear increase in lattice parameter of SnTe with the addition of lead follows Vegard's law for solid solution (Figure 1.1b).

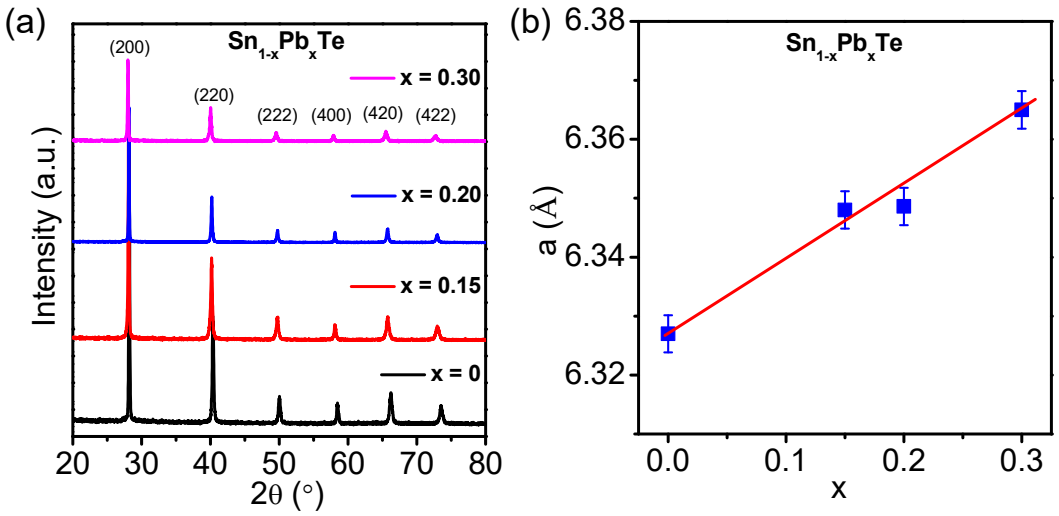

Figure 1.1 *(a) Powder XRD patterns and (b) variation of lattice parameter as a function of Pb concentration of $Sn_{1-x}Pb_xTe$ (x = 0 - 0.30) samples.*

The room temperature electrical conductivity of pristine SnTe are ~ 8320 S/cm due to intrinsic Sn vacancy regardless of growth condition.[3,4] Previously, it was reported that solid solution alloying with Se in SnTe optimizes the lattice thermal conductivity.[41]

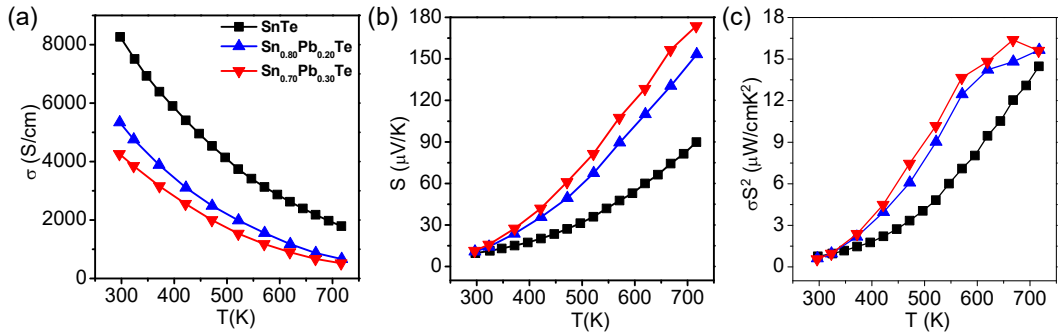

Figure 1.2 *Temperature variations of (a) electrical conductivity (σ), (b) Seebeck coefficient (S) and (c) power factor (σS^2) of $Sn_{1-x}Pb_xTe$ (x = 0 - 0.30) samples.*

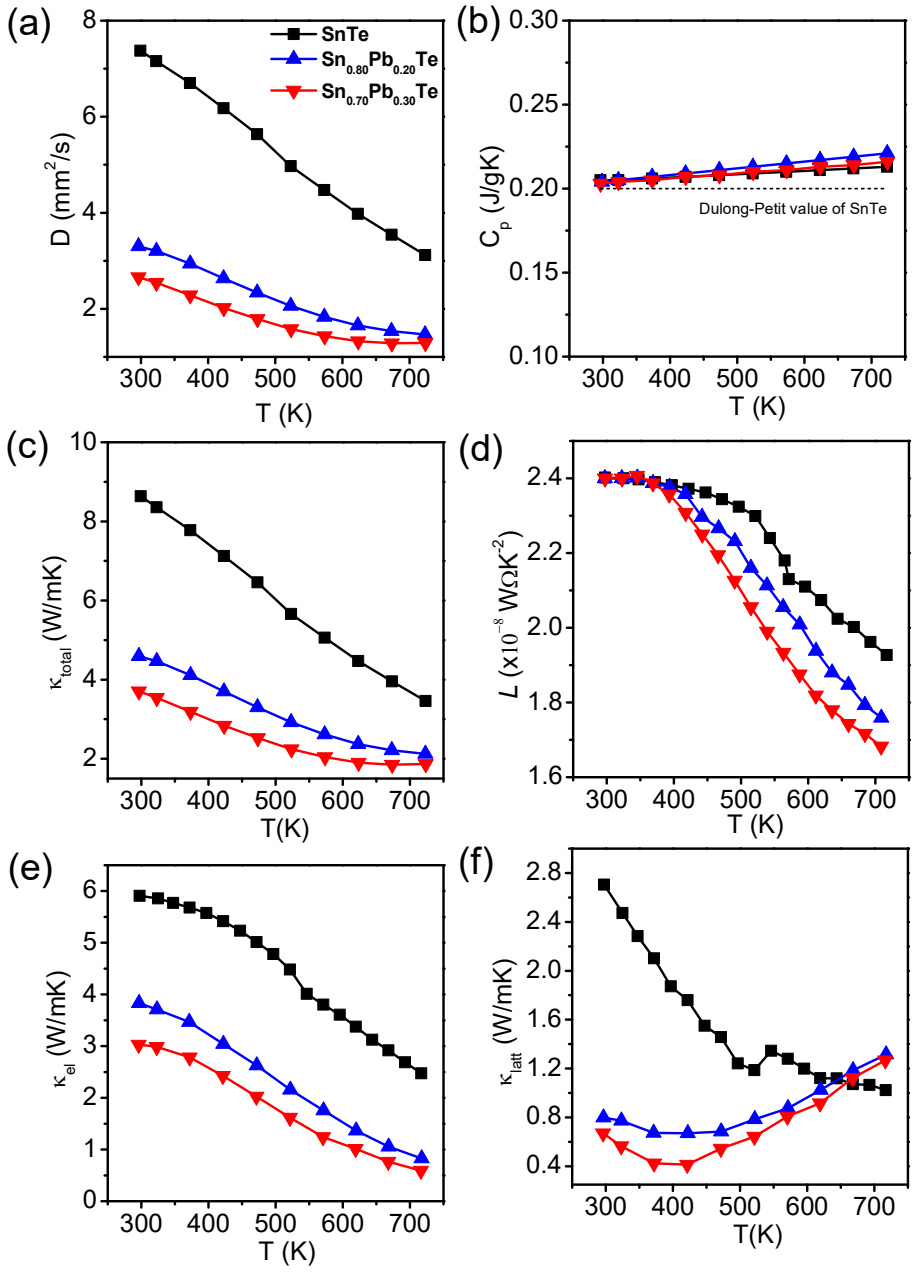

Figure 1.3 *Temperature variations of (a) diffusivity (D), (b) heat capacity (C_p), (c) total thermal conductivity (κ_{total}), (d)Lorenz number (L), (e) electrical thermal conductivity (κ_{el}) and (f) lattice thermal conductivity (κ_{latt}) of $Sn_{1-x}Pb_xTe$ (x = 0 – 0.30) samples.*

Similarly, alloying with Pb can limit the formation of Sn vacancy and control the *p*-type carrier concentration and electrical conductivity of SnTe. Isovalent Pb acts as a

donor dopant in SnTe, which decreases the carrier concentration from 3.2 X 10^{20} cm^{-3} (SnTe) to 8 X 10^{19} cm^{-3} ($Sn_{0.70}Pb_{0.30}Te$) (Table 1.1). Substitution of 30 mol% Pb in SnTe decreases the electrical conductivity from ~ 8320 S/cm to ~ 4280 S/cm at room temperature (Figure 1.2a). The temperature dependence of Seebeck coefficient of $Sn_{1-x}Pb_xTe$ (x = 0, 0.20, 0.30) samples is presented in Figure 1.2b. At room temperature there is no such improvement in *S* value after Pb alloying, but high temperature S significantly increases compared to pristine. The energy gap between light and heavy hole valence band in SnTe (~ 0.38 eV)[3] slightly decreases to 0.3 eV with the substitution of Pb, which is estimated by the DFT electronic structure calculation (discussed later). Thus, higher S value at high temperature for Pb alloyed sample is due to the increasing contribution of heavy hole valence band in the electronic transport.

Table 1.1: Room temperature electrical conductivity (σ), Seebeck coefficient (S), carrier concentration (p) and mobility (μ) of $Sn_{1-x}Pb_xTe$ samples.

Samples	σ (S/cm)	S (μV/K)	p ($10^{20}cm^{-3}$)	μ (cm^2/Vs)
SnTe	8265	9.50	3.20	160
$Sn_{0.80}Pb_{0.20}Te$	5375	10.7	1.05	319
$Sn_{0.70}Pb_{0.30}Te$	4265	11.50	0.80	333

Figure 1.3c and 1.3f show the total and lattice thermal conductivity of $Sn_{1-x}Pb_xTe$ (x = 0, 0.20, 0.30) samples as a function of temperature. Substitution of Pb in SnTe decreases the κ_{total} values significantly. At 300 K, SnTe has the κ_{total} value of ~ 8.64 W/mK which decreases to ~ 3.68 W/mK for $Sn_{0.70}Pb_{0.30}Te$ sample (Figure 1.3c). The lattice thermal conductivity (κ_{latt}) was obtained after subtracting the electronic contribution (κ_{el}) from κ_{total}. The κ_{el} (Figure 1.3e) were calculated by using Wiedemann-Franz relation, $\kappa_{el} = L\sigma T$, where σ is measured electrical conductivity and L is the Lorenz number calculated from reduced Fermi energy, which is acquired from the fitting of the temperature dependent Seebeck coefficient (Figure 1.3d). Typically, $Sn_{0.70}Pb_{0.30}Te$ sample exhibits a κ_{latt} of ~ 0.67 W/mK at 300 K which is significantly lower than that of pristine SnTe (κ_{latt} ~ 2.8 W/mK at 300 K) due to the mass fluctuation and formation of solid solution point defects,

which can effectively scatter phonon (Figure 1.3f). Substitution of 30 mol% Pb gives rise to lowest κ_{latt} in $Sn_{1-x}Pb_xTe$; hence, $Sn_{0.70}Pb_{0.30}Te$ sample has been used for further thermoelectric studies. The zT value for $Sn_{0.70}Pb_{0.30}Te$ sample reaches to ~ 0.6 at ~ 716 K, which is higher than that of the pristine SnTe (Figure 1.4).

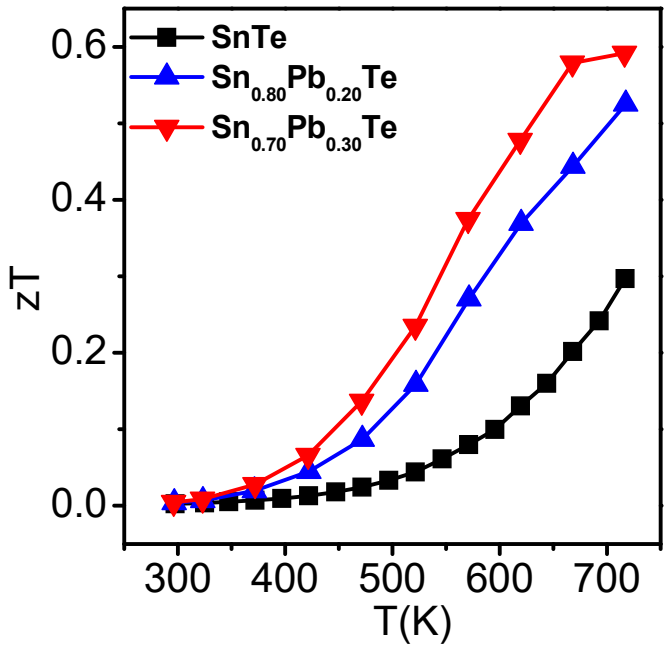

Figure 1.4 *Temperature variations of thermoelectric figure of merit (zT) of $Sn_{1-x}Pb_xTe$ (x = 0 – 0.30) samples.*

Enhancement of thermoelectric performance of $Sn_{0.70}Pb_{0.30}Te$ *via* In and Mg co-doping.

The lattice thermal conductivity, $\kappa_{latt,}$ for $Sn_{0.70}Pb_{0.30}Te$ is ~ 0.67 W/mK at 300 K which is close to theoretical minimum limit (κ_{min}) of 0.5 W/mK in SnTe calculated by Cahil's formalism.[11] Thus, our main concern is to modify the electronic structure to improve the Seebeck coefficient of $Sn_{0.70}Pb_{0.30}Te$. Previously, it was reported that co-doping of In, Cd and In, Ag enhanced the Seebeck coefficient of SnTe through synergistic effect of resonance level formation and valence band convergence.[3,6]

Here, we choose In and Mg as a co-dopant for modification of electronic structure of low thermal conducting $Sn_{0.70}Pb_{0.30}Te$.

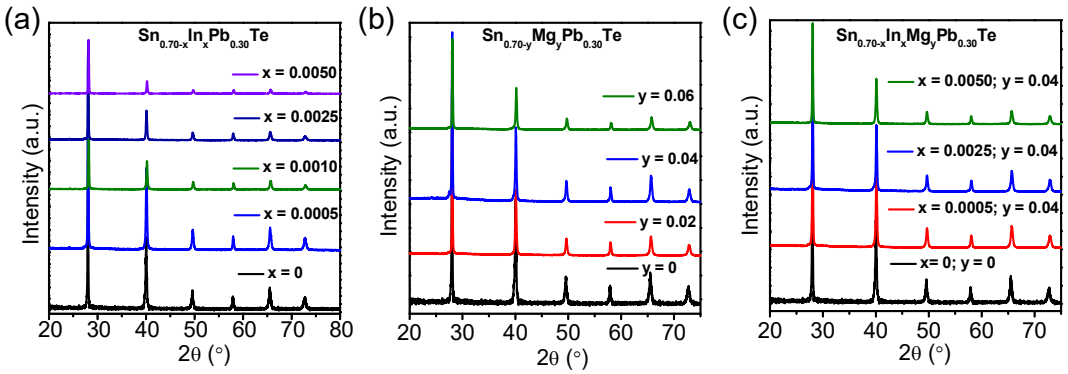

Figure 1.5 *Powder XRD patterns of (a) $Sn_{0.70-x}In_xPb_{0.30}Te$, (b) $Sn_{0.70-y}Mg_yPb_{0.30}Te$ and (c) $Sn_{0.70-x-y}In_xMg_yPb_{0.30}Te$ samples.*

To understand the effect of co-doping of In and Mg on the thermoelectric properties $Sn_{0.70}Pb_{0.30}Te$, we have synthesized $Sn_{0.70-x}In_xPb_{0.30}Te$ and $Sn_{0.70-y}Mg_yPb_{0.30}Te$ for comparison. We have indexed powder X-ray diffraction pattern for all sample on the basis of cubic SnTe pattern (space group *Fm-3m*) without any impurity phase (Figure 1.5).

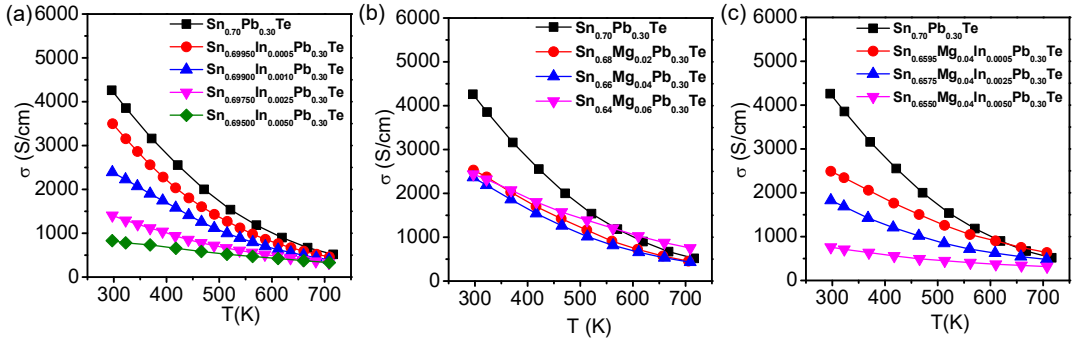

Figure 1.6 *Temperature variations of electrical conductivities (σ) of (a) $Sn_{0.70-x}In_xPb_{0.30}Te$, (b) $Sn_{0.70-y}Mg_yPb_{0.30}Te$ and (c) $Sn_{0.70-x-y}In_xMg_yPb_{0.30}Te$ samples.*

Figure 1.6 represents the temperature dependent electrical conductivities (σ) of $Sn_{0.70-x}In_xPb_{0.30}Te$, $Sn_{0.70-y}Mg_yPb_{0.30}Te$ and co-doped $Sn_{0.70-x-y}In_xMg_yPb_{0.30}Te$ samples. σ decreases with increasing temperature for all samples which is similar to heavily doped degenerate semiconductor. The room temperature electrical conductivity for all sample decreases with increasing In, Mg and co-dopant (In-Mg) concentration due to decrease of

carrier mobility (Table 1.2). Typically, at 300 K σ value for $Sn_{0.695}In_{0.005}Pb_{0.30}Te$, $Sn_{0.66}Mg_{0.04}Pb_{0.30}Te$ and $Sn_{0.655}Mg_{0.04}In_{0.005}Pb_{0.30}Te$ samples are ~ 836 S/cm, ~ 2366 S/cm and ~ 786 S/cm, respectively. Notably, In and Mg co-doped samples has the lower electrical conductivity value than that of the singly In and Mg doped samples.

Table 1.2: Room temperature electrical conductivity (σ), Seebeck coefficient (S), carrier concentration (p) and mobility (μ) of In and/or Mg doped $Sn_{1-x}Pb_xTe$ samples.

Samples	σ (S/cm)	S (μV/K)	p (10^{20}cm^{-3})	μ (cm^2/Vs)
$Sn_{0.699}In_{0.0010}Pb_{0.30}Te$	2388	59	0.698	213
$Sn_{0.695}In_{0.005}Pb_{0.30}Te$	841	96	0.78	67
$Sn_{0.68}Mg_{0.02}Pb_{0.30}Te$	2530	21	0.75	210
$Sn_{0.66}Mg_{0.04}Pb_{0.30}Te$	2364	32	1.22	121
$Sn_{0.64}Mg_{0.06}Pb_{0.30}Te$	2435	47	1.39	109
$Sn_{0.6595}Mg_{0.04}In_{0.0005}Pb_{0.30}Te$	2488	38	1.06	146
$Sn_{0.6575}Mg_{0.04}In_{0.0025}Pb_{0.30}Te$	1827	59	1.02	111
$Sn_{0.6550}Mg_{0.04}In_{0.0050}Pb_{0.30}Te$	760	121	2.07	23

Hall measurements were performed to evaluate the carrier concentration of singly doped samples and In and Mg co-doped $Sn_{0.70}Pb_{0.30}Te$ samples. Hall coefficients are positive for all measured samples indicate hole is major carrier. The resultant carrier concentration (p) and carrier mobility (μ) are summarized in Table 1.2. Undoped SnTe has carrier concentration of ~ 3.2 X 10^{20} cm^{-3} due to presence of intrinsic Sn vacancy, whereas, $Sn_{0.70}Pb_{0.30}Te$ sample has carrier concentration of ~ 8 X 10^{19} cm^{-3}. p-type carrier concentration of $Sn_{0.70}Pb_{0.30}Te$ sample increases with increasing co-dopant (In & Mg) concentration (Table 1.2). This result indicates that In /Mg substitute Sn in SnTe and increases the p-type carrier density. We have also measured carrier concentration of the controlled sample. Initially, with addition of lower concentration of In in $Sn_{0.70}Pb_{0.30}Te$, carrier concentration slightly decreases (Table 1.2). Similar kind of behavior of low concentration In doped SnTe is known in literature.[2,37] Carrier concentration of the Mg

doped $Sn_{0.70}Pb_{0.30}Te$ samples increases with increasing the concentration of Mg (Table 1.2).[4] Thus, we believe the increase in the carrier concentration in the co-doped (In & Mg) $Sn_{0.70}Pb_{0.30}Te$ sample is mainly due to Mg doping.

$Sn_{0.70}Pb_{0.30}Te$ sample exhibit high hole mobility (μ ~ 333 $cm^2V^{-1}S^{-1}$) compared to that of the pristine SnTe (μ ~ 160 $cm^2V^{-1}S^{-1}$). Co-substitution of In and Mg in $Sn_{0.70}Pb_{0.30}Te$ sample decreases the carrier mobility significantly (Table 1.2) due to point defect scattering and possibly impurity scattering originated from In doping.[2] Controlled samples also show the decrease in carrier mobility with increase of doping concentration. Notably, co-doped $Sn_{0.6550}Mg_{0.04}In_{0.0050}Pb_{0.30}Te$ sample has significantly low carrier mobility of ~ 23 $cm^2V^{-1}S^{-1}$ at 300 K. This is possibly due to the rise of heavy hole band energy compared to the light hole valence band due to the synergistic effect of In and Mg co-substitution. We will discuss this result later in more details.

Figure 1.7 represents the temperature dependent Seebeck coefficients of $Sn_{0.70-x}In_xPb_{0.30}Te$, $Sn_{0.70-y}Mg_yPb_{0.30}Te$ and co-doped $Sn_{0.70-x-y}In_xMg_yPb_{0.30}Te$ samples. Seebeck coefficients for all samples show positive value, represents hole is the major carrier which is consistent with Hall coefficient data. Room temperature Seebeck coefficient values significantly enhances from 11 μV/K ($Sn_{0.70}Pb_{0.30}Te$) to 97 μV/K for $Sn_{0.695}In_{0.005}Pb_{0.30}Te$ sample (Figure 1.7a). Substitution of Mg in $Sn_{0.70}Pb_{0.30}Te$ also enhances S value (Figure 1.7b). Typically, *S* value for $Sn_{0.66}Mg_{0.04}Pb_{0.30}Te$ sample at 300 K is ~ 33 μV/K which increase to ~ 202 μV/K at ~ 710 K. Interestingly, for co-doped $Sn_{0.70-x-y}In_xMg_yPb_{0.30}Te$ samples, the S value synergistically increased compared to those of singly doped (In and Mg) sample over the whole temperature range (Figure 1.7c). Typically, for $Sn_{0.6550}Mg_{0.04}In_{0.0050}Pb_{0.30}Te$ sample, *S* value is ~ 121 μV/K at 300 K which increases to ~ 241 μV/K at 710 K. We have obtained significantly higher Seebeck value over whole temperature range for In and Mg co-doped $Sn_{0.70}Pb_{0.30}Te$ sample compared to the previously reported In and Cd co-doped SnTe[6] and In and Ag co-doped SnTe[3]. This clearly indicates that In and Mg co-doped $Sn_{0.70}Pb_{0.30}Te$ sample exhibits synergistic Seebeck enhancement and combine the advantage of In and Mg doping in $Sn_{0.70}Pb_{0.30}Te$.

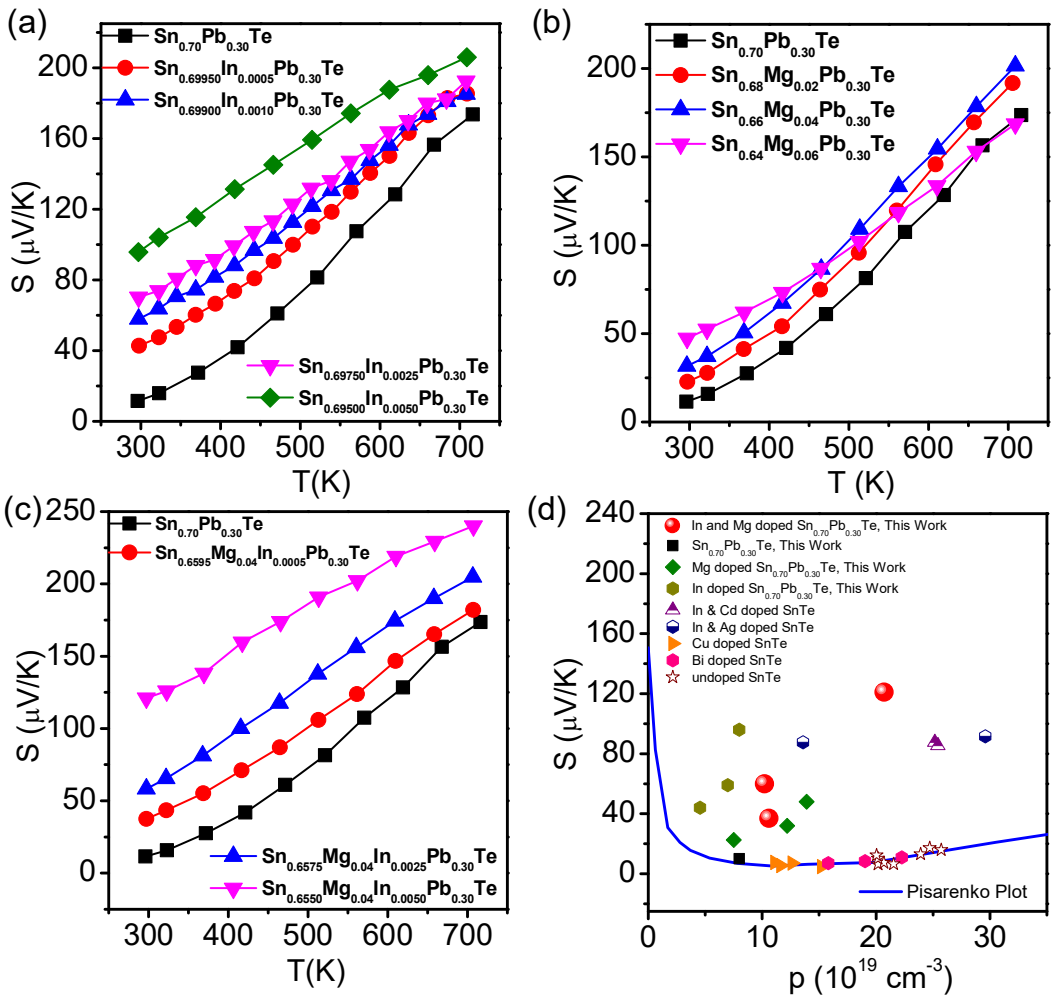

Figure 1.7 *Temperature variations of Seebeck coefficients (S) of (a) $Sn_{0.70-x}In_xPb_{0.30}Te$, (b) $Sn_{0.70-y}Mg_yPb_{0.30}Te$ and (c) $Sn_{0.70-x-y}In_xMg_yPb_{0.30}Te$ samples. (d) Seebeck coefficient of $Sn_{0.70-x-y}In_xMg_yPb_{0.30}Te$ samples as a function of carrier concentration at 300 K. For comparison, Pisarenko curve of SnTe,[2] S vs. p experimental data of un-doped $Sn_{0.70}Pb_{0.30}Te$ (present work), controlled Mg doped SnTe (present work), controlled In doped SnTe (present work) and In & Cd co-doped SnTe,[6] In & Ag co-doped SnTe[3] and undoped, Bi doped and Cu doped SnTe[21] are given in (d).*

We have plotted the room temperature *S* value of $Sn_{0.70-x}In_xPb_{0.30}Te$, $Sn_{0.70-y}Mg_yPb_{0.30}Te$ and co-doped $Sn_{0.70-x-y}In_xMg_yPb_{0.30}Te$ samples with respect to the carrier concentration and compared with the Pisarenko plot of SnTe, which is calculated first by Ren and co-workers by using two-valence band model.[2] We have also compared the room temperature Seebeck coefficient of $Sn_{0.70-x-y}In_xMg_yPb_{0.30}Te$ samples with previously reported In and Cd co-doped SnTe[6] and In and Ag doped SnTe sample[3]. $Sn_{0.70}Pb_{0.30}Te$

sample follows the Pisarenko plot which indicates the efficacy of the adopted physical model. In doped $Sn_{0.70}Pb_{0.30}Te$ samples show comparatively higher Seebeck coefficient than Pisarenko curve due to the formation of resonance level in the valence band of $Sn_{0.70}Pb_{0.30}Te$. In doping decreases the hole carrier mobility significantly (Table 1.2) due to enhancement of effective mass of holes and carrier scattering. The Mg doped $Sn_{0.70}Pb_{0.30}Te$ samples also show higher *S* value than that of predicted by Pisarenko curve. However these values are close to previously reported S value of Mg/Cd doped SnTe, where enhanced Seebeck coefficient values are obtained due to the valence band convergence.[4,5] Interestingly, we have observed that the co-doped samples, especially, $Sn_{0.6550}Mg_{0.04}In_{0.0050}Pb_{0.30}Te$ exhibits significantly higher Seebeck coefficient value as compared to singly In and Mg doped $Sn_{0.70}Pb_{0.30}Te$ sample. This result indicates that resonance level instigated by In and valence band convergence originated from Mg synergistically enhance the Seebeck coefficient in In and Mg co-doped $Sn_{0.70}Pb_{0.30}Te$ sample.

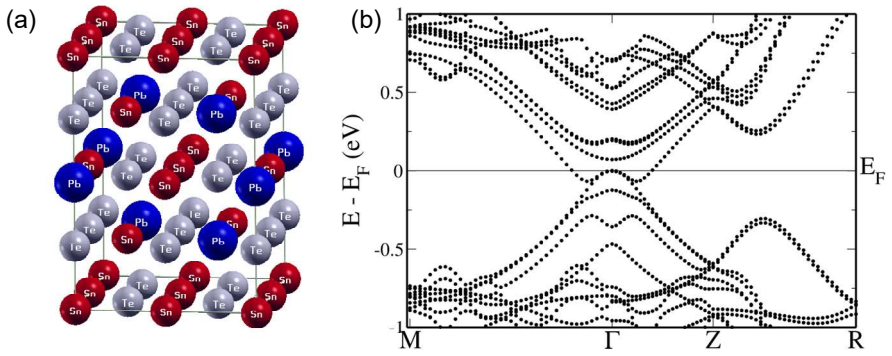

Figure 1.8 *(a) Structure of $Sn_{11}Pb_5Te_{16}$. (b) electronic structure of $Sn_{11}Pb_5Te_{16}$. Energies are shifted so as to maintain the Fermi level at 0.*

To understand the origin of enhanced Seebeck coefficient of co-doped sample, we determined electronic structure of undoped, Mg-doped, In-doped and In & Mg co-doped $Sn_{11}Pb_5Te_{16}$ within DFT. In the Brillouin Zone of the ($\sqrt{2}$ x $\sqrt{2}$ x 2) tetragonal supercell used in our simulations (Figure 1.8a), the principal valence band (light hole) maximum (VBM) and conduction band minimum (CBM) occur at the zone centre Γ point, and a maximum due to heavy hole band occurs at Z + δ along the Z → R direction.

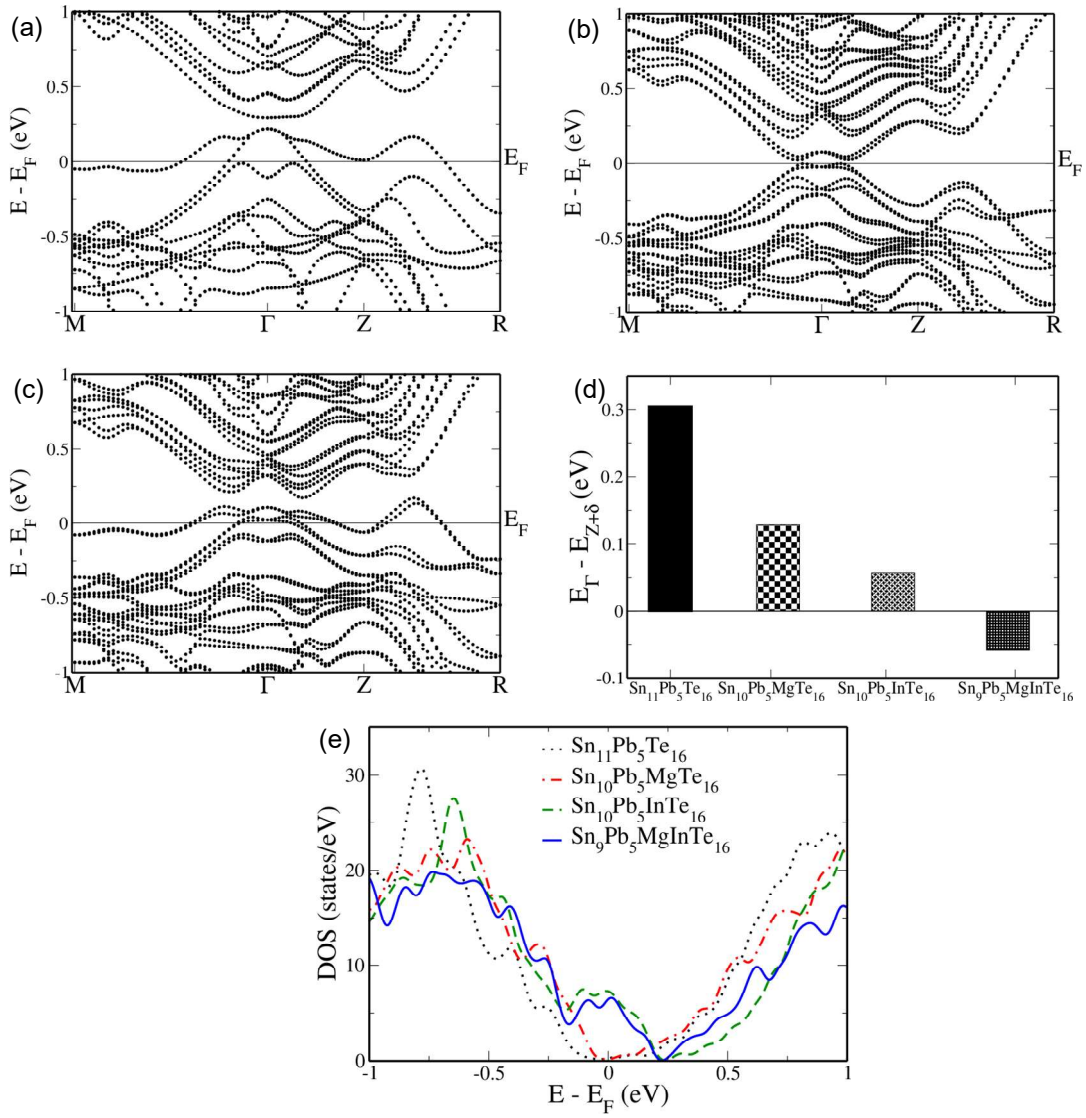

Figure 1.9 *Electronic structures of (a) $Sn_{10}Pb_5InTe_{16}$, b) $Sn_{10}Pb_5MgTe_{16}$ and (c) $Sn_9Pb_5MgInTe_{16}$. (d) Energy separations between the light hole valence band (at Γ point) and heavy hole valence band (at Z + δ point) and e) density of states (DOS) of $Sn_{11}Pb_5Te_{16}$, $Sn_{10}Pb_5InTe_{16}$, $Sn_{10}Pb_5MgTe_{16}$ and $Sn_9Pb_5MgInTe_{16}$.*

We note that the VBM and CBM occurring normally at the L point in the Brillouin zone of the cubic cell of pristine SnTe fold onto the Γ point, while the heavy hole valence band maximum appearing along Σ folds onto Z + δ point in the Brillouin zone of the 32 atoms ($\sqrt{2} \times \sqrt{2} \times 2$) tetragonal supercell of the $Sn_{11}Pb_5Te_{16}$. In the calculated electronic structure of $Sn_{11}Pb_5Te_{16}$ (Figure 1.8b), it is evident that the system is weakly metallic as the DFT is unable to capture the tiny experimental band gap due to

typical underestimation of the gaps by DFT. We find that the band gap of $Sn_{11}Pb_5Te_{16}$ widens with In or Mg substitution at Sn sites (Figure 1.9a-b), and the band gap of $Sn_{11}Pb_5Te_{16}$ opens up to ~ 0.029 eV at Γ- δ' in M→Γ direction with Mg substitution. The separation between energies of light and heavy hole valence bands reduces from ~ 0.305 eV (undoped) to ~ 0.129 eV (Mg doped) (Figure 1.9b and d). In the case of substitution of indium for Sn, we see that the band gap opens up at Γ point to ~ 0.073 eV and the energy separation between the two valence bands decreases significantly from ~ 0.305 eV (undoped) to ~ 0.057 eV (In doped) (Figure 1.9d). Well-defined peaks in the valence bands near the Fermi level (see density of states, Figure 1.9e) confirm the formation of resonance state arising from In doping. Thus, incorporation of In or Mg leads to increase in the valence band degeneracy, and such valence band convergence gives rise to an asymmetric increase in the density of electronic states near the Fermi energy.[4] Similar modifications in the electronic structure have been seen in the electronic structures of Ag-In, Mg, Cd, Cd-In and Bi/Hg doped SnTe. [3, 4-7] Electronic structure of In and Mg co-doped $Sn_{11}Pb_5Te_{16}$ clearly reveals the resonance level appearing as the peaks in the DOS near the Fermi level (see Figure 1.9e). Interestingly, we also see that the heavy hole band rises in energy more than the light hole valence band by about ~ 0.058 eV in In and Mg co-doped $Sn_{11}Pb_5Te_{16}$ (Figure 1.9c). While this kind of behaviour is usually seen at high temperatures, we see it here to be leading to ultra-high Seebeck coefficient observed in co-doped sample at low temperature. Furthermore, co-doped $Sn_{0.655}Mg_{0.04}In_{0.005}Pb_{0.30}Te$ sample has a significantly low carrier mobility of ~ 23 $cm^2V^{-1}S^{-1}$ at 300 K, which is actually due to the sole involvement of heavy hole valence band in the electronic transport of co-doped sample. Therefore, coexisting resonant levels and the cross-over of heavy hole valence band in In and Mg co-doped sample synergistically cause high Seebeck coefficient in 300 - 710 K range.

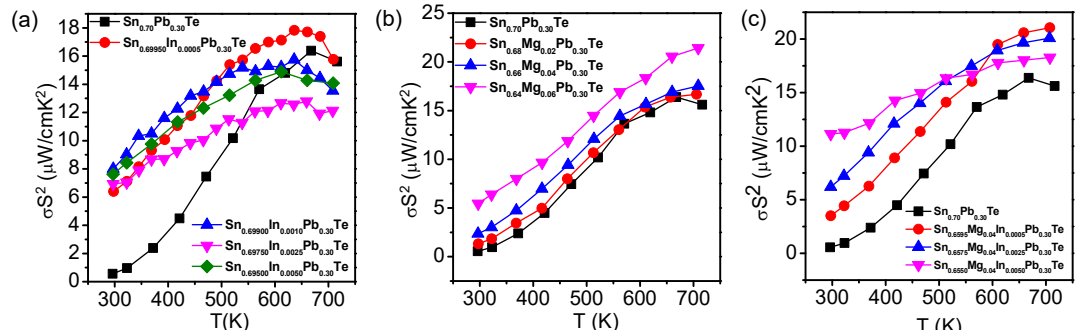

Figure 1.10 *Temperature variations of power factors (σS^2) of (a) $Sn_{0.70-x}In_xPb_{0.30}Te$; (b) $Sn_{0.70-y}Mg_yPb_{0.30}Te$ and (c) $Sn_{0.70-x-y}In_xMg_yPb_{0.30}Te$ samples.*

Figure 1.10 represents the temperature dependent power factors (σS^2) of $Sn_{0.70-x}In_xPb_{0.30}Te$, $Sn_{0.70-y}Mg_yPb_{0.30}Te$ and $Sn_{0.70-x-y}In_xMg_yPb_{0.30}Te$ samples. In and Mg co-doped $Sn_{0.70}Pb_{0.30}Te$ samples show higher σS^2 value over a wide range of temperature due to presence of high Seebeck coefficient and optimal electrical conductivity compared to those of singly doped $Sn_{0.70}Pb_{0.30}Te$ samples. Typically, $Sn_{0.6550}Mg_{0.04}In_{0.0050}Pb_{0.30}Te$ sample exhibits σS^2 value of ~ 11 μW/cmK^2 at 300 K which increases to ~ 18 μW/cmK^2 at 710 K.

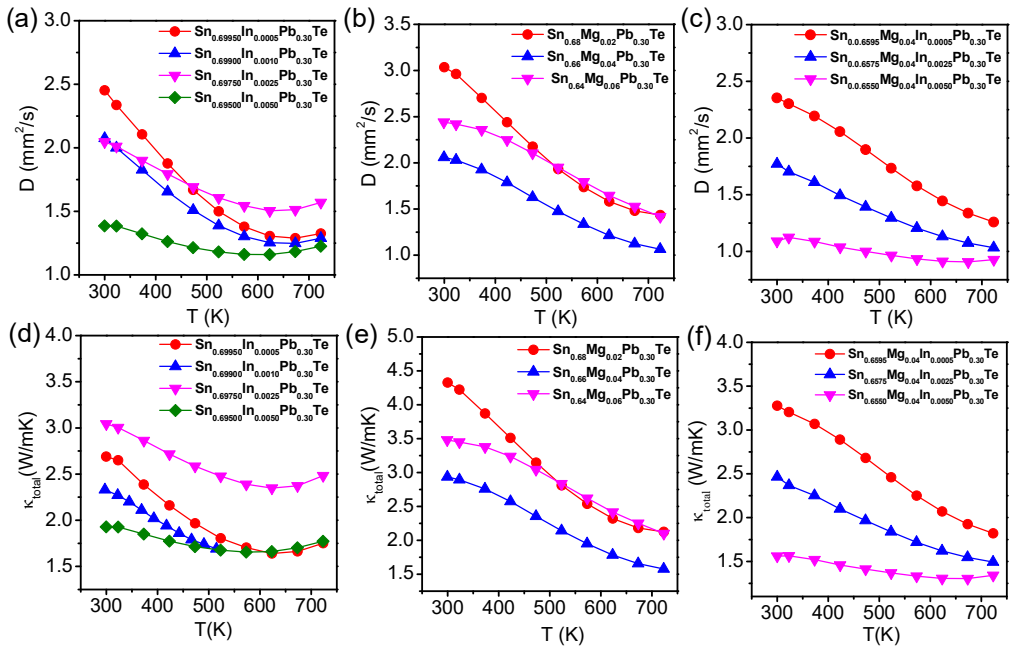

Figure 1.11 *Temperature variations of diffusivity (D) (a)–(c) and total thermal conductivity (κ_{total}) (d-f) of $Sn_{0.70-x}In_xPb_{0.30}Te$, $Sn_{0.70-y}Mg_yPb_{0.30}Te$ and $Sn_{0.70-x-y}In_xMg_yPb_{0.30}Te$ samples.*

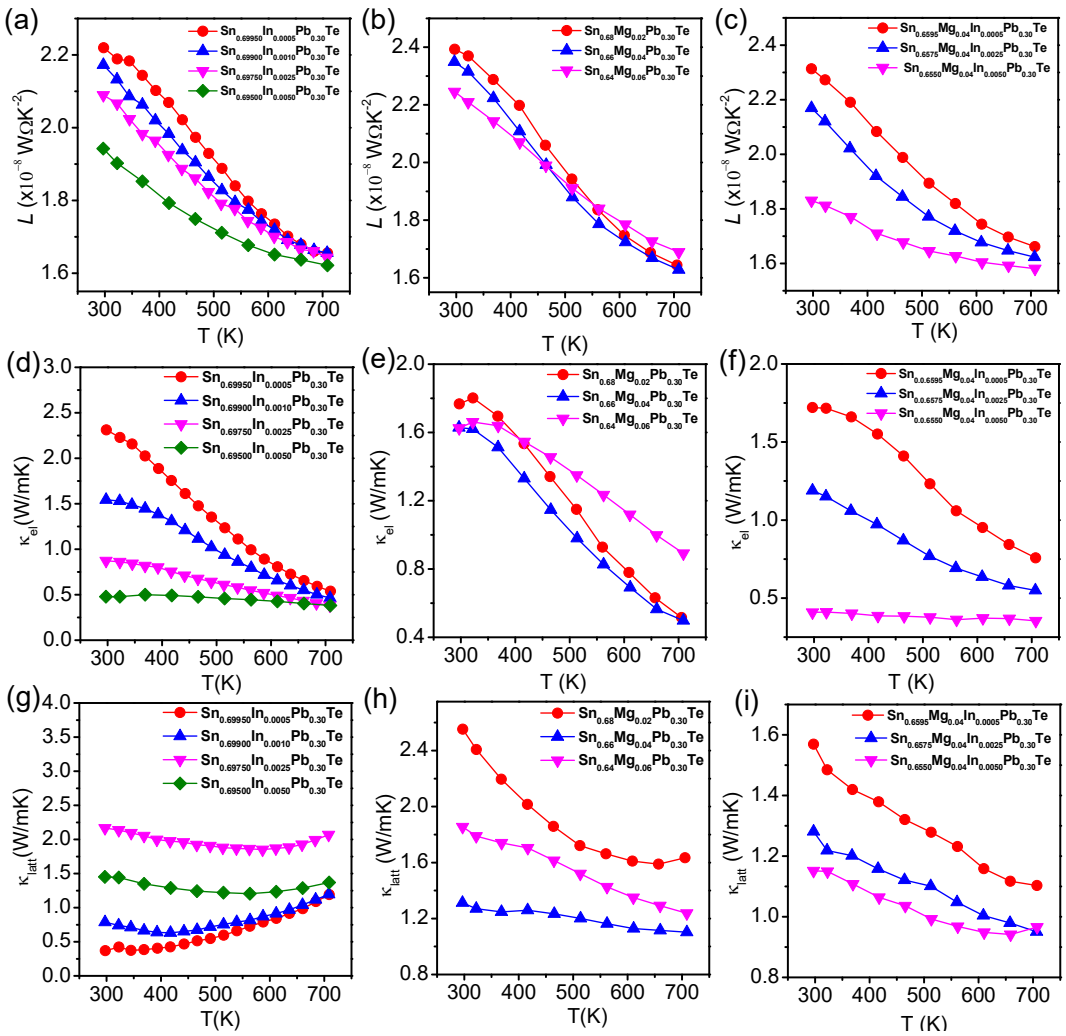

Figure 1.12 *Temperature variations of Lorenz number (L) (a)–(c), electrical thermal conductivity (κ_{el}) (d-f) and lattice thermal conductivity (κ_{latt}) (g-i) of $Sn_{0.70-x}In_xPb_{0.30}Te$, $Sn_{0.70-y}Mg_yPb_{0.30}Te$ and $Sn_{0.70-x-y}In_xMg_yPb_{0.30}Te$ samples.*

Figure 1.11d-f represents the temperature dependent total thermal conductivities (κ_{total}) of $Sn_{0.70-x}In_xPb_{0.30}Te$, $Sn_{0.70-y}Mg_yPb_{0.30}Te$ and $Sn_{0.70-x-y}In_xMg_yPb_{0.30}Te$ samples. It is evident that for all samples κ_{total} decreases with increasing dopant concentration which is mainly governed by the systematic decrease in electrical thermal conductivity (κ_{el}) (Figure 1.12 d-f). The κ_{el} were calculated by using Wiedemann-Franz relation, $\kappa_{el} = L\sigma T$, where σ is measured electrical conductivity and L is calculated Lorenz number from reduced Fermi energy, which is acquired from the fitting of the temperature dependent Seebeck coefficient value.[5] Typically, $Sn_{0.6550}Mg_{0.04}In_{0.0050}Pb_{0.30}Te$ sample has κ_{total} ~

1.56 W/mK at 300 K which decreases to 1.33 W/mK at 723 K. The κ_{latt} values are calculated by subtracting electronic part (κ_{el}) from κ_{total} and plotted in Figure 1.12g-i for all samples. $Sn_{0.6550}Mg_{0.04}In_{0.0050}Pb_{0.30}Te$ sample has κ_{latt} ~ 1.16 W/mK at 300 K which decreases to 0.97 W/mK at 723 K. Moreover, κ_{latt} does not show any systematic trend irrespective of dopant type and/or concentration. It is worth to mention that singly doped (In and Mg) and In and Mg co-doped $Sn_{0.70}Pb_{0.30}Te$ sample show higher κ_{latt} than those of undoped $Sn_{0.70}Pb_{0.30}Te$ sample. In principle, increased point defects in the In/Mg doped $Sn_{0.70}Pb_{0.30}Te$ sample are expected to lower the κ_{lat} value. The above result indicates that the Lorenz number value used cannot properly account for the electronic contribution to the thermal conductivity, which is similar to previously reported Na and K doped PbTe[42] and In-Ag co-doped SnTe[3] samples, where complex inter-valley scattering occur that underestimate κ_{el}.

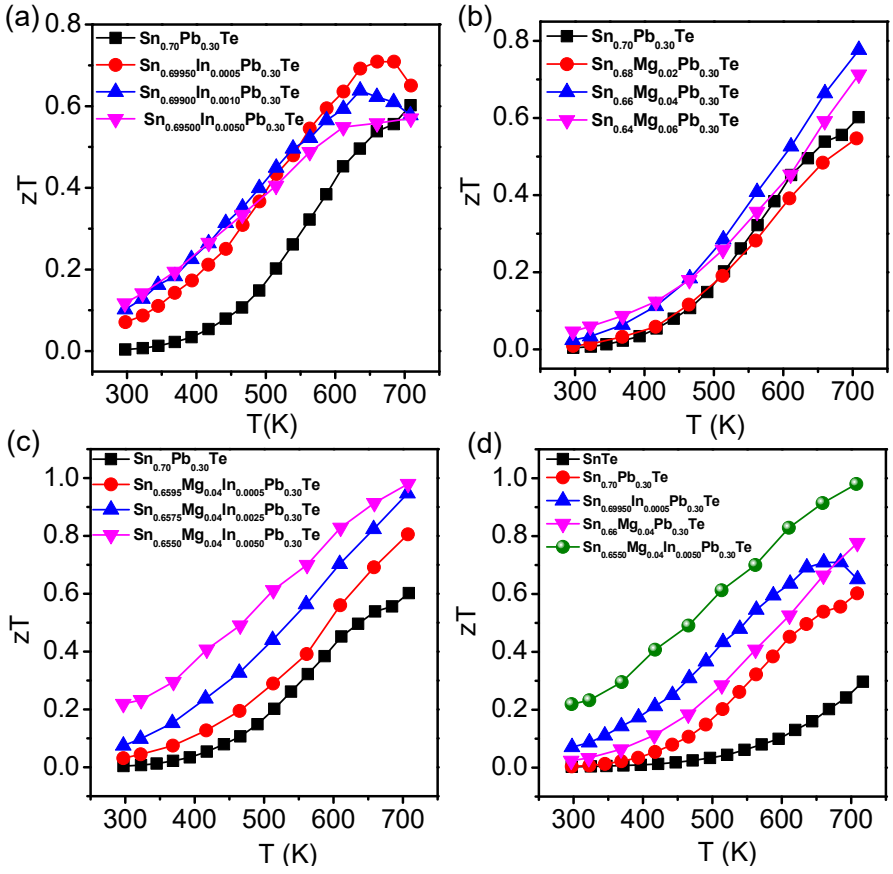

Figure 1.13 *Temperature variations of zT of (a) $Sn_{0.70-x}In_xPb_{0.30}Te$, (b) $Sn_{0.70-y}Mg_yPb_{0.30}Te$ and (c) $Sn_{0.70-x-y}In_xMg_yPb_{0.30}Te$ samples. (d) Comparison of zTs between undoped and single/co-doped samples.*

Figure 1.13 represents the temperature dependent thermoelectric Figure-of-merit (zT) of $Sn_{0.70-x}In_xPb_{0.30}Te$, $Sn_{0.70-y}Mg_yPb_{0.30}Te$ and $Sn_{0.70-x-y}In_xMg_yPb_{0.30}Te$ samples. In doping in $Sn_{0.70}Pb_{0.30}Te$ sample increases the zT in the lower temperature range compared to that of undoped sample but the enhancement is marginal at high temperature (Figure 1.13a). However, Mg doping increases zT of $Sn_{0.70}Pb_{0.30}Te$ sample rapidly at high temperature (Figure 1.13b). Co-doping of In and Mg in $Sn_{0.70}Pb_{0.30}Te$ sample combines the effect of both In and Mg and enhances the zT significantly over whole temperature range (Figure 1.13c). The highest zT values for SnTe, $Sn_{0.70}Pb_{0.30}Te$, $Sn_{0.70-x}In_xPb_{0.30}Te$, $Sn_{0.70-y}Mg_yPb_{0.30}Te$ and co-doped $Sn_{0.70-x-y}In_xMg_yPb_{0.30}Te$ samples are ~ 0.35, ~ 0.6, ~ 0.7, ~ 0.8 and ~ 1 at ~ 710 K, respectively (Figure 1.13d). It is observed that co-doped sample has higher zT over singly doped $Sn_{0.70}Pb_{0.30}Te$ samples, which is due to the enhancement of the significant Seebeck coefficient.

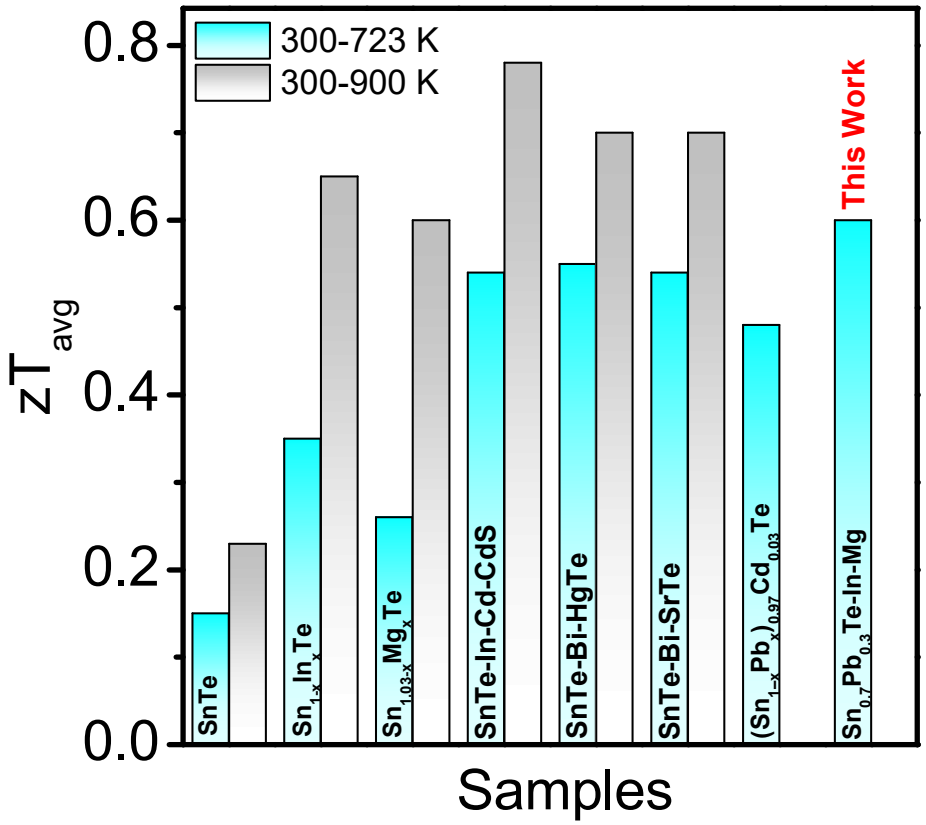

Figure 1.14 *zT_{avg} values for several popular SnTe based thermoelectric materials compared with the present result ($Sn_{0.70-x-y}In_xMg_yPb_{0.30}Te$ sample).*

Figure 1.14 compares the average thermoelectric figure (zT_{avg}) between the present In-Mg co-doped $Sn_{0.70}Pb_{0.30}Te$ and previously reported state-of-art SnTe based system at two different temperature ranges (300 - 723 K and 300 – 900 K). It is worth to mention that zT_{avg} of $Sn_{0.6550}Mg_{0.04}In_{0.0050}Pb_{0.30}Te$ is ~ 0.6 in the temperature range of 300 – 710 K which is comparable value to other high performance SnTe-based materials.

1.4 Conclusions

In conclusion, high quality crystalline ingots of In and Mg co-doped $Sn_{0.70}Pb_{0.30}Te$ samples have been synthesized by vacuum sealed tube melting reaction. Solid solution alloying with PbTe (0 - 30 mol%) decreases carrier concentration and lowers the lattice thermal conductivity of SnTe close to its theoretical minimum. In and Mg co-doped $Sn_{0.70}Pb_{0.30}Te$ samples exhibit synergistically enhanced Seebeck coefficient over a wide range of temperature due to co-adjuvant effect of resonance level formation and significant contribution from heavy hole valence band. In acts as a resonant dopant in $Sn_{0.70}Pb_{0.30}Te$, whereas Mg doping enables the valence band convergence, which have been confirmed with DFT calculation of electronic structure. Remarkably high Seebeck coefficient of ~ 121 μV/K at room temperature has been achieved for $Sn_{0.70-x-y}In_xMg_yPb_{0.30}Te$ sample, which is the highest among all optimized SnTe based materials reported so far. Thus, the highest zT ~ 1 was measured at 710 K for In and Mg co-substituted $Sn_{0.70}Pb_{0.30}Te$ sample. Moreover, zT_{avg} of ~ 0.6 was obtained in the temperature range of 300 – 710 K for $Sn_{0.6550}Mg_{0.04}In_{0.0050}Pb_{0.30}Te$. Present results suggest that $Sn_{1-x}Pb_xTe$ is an important candidate for mid-temperature thermoelectric power generation. Further improvement in the thermoelectric performance of $Sn_{1-x}Pb_xTe$ can be achieved by introducing second phase nanostructuring and/or all-scale hierarchical phonon scattering.

1.5 References

[1] J. P. Heremans, V. Jovovic, E. S. Toberer, A. Saramat, K. Kurosaki, A. Charoenphakdee, S. Yamanaka, G. J. Snyder, *Science* **2008**, *321*, 554.

[2] Q. Zhang, B. Liao, Y. Lan, K. Lukas, W. Liu, K. Esfarjani, C. Opeil, D. Broido, G. Chen, Z. Ren, *Proc. Natl. Acad. Sci. USA* **2013**, *110*, 13261.

[3] A. Banik, U. S. Shenoy, S. Saha, U. V. Waghmare, K. Biswas, *J. Am. Chem. Soc*. **2016**, *138*, 13068.

[4] A. Banik, U. S. Shenoy, S. Anand, U. V. Waghmare, K. Biswas *Chem. Mater*. **2015**, *27*, 581.

[5] G. Tan, L. -D. Zhao, F. Shi, J. W. Doak, S.-H. Lo, H. Sun, C. Wolverton, V. P. Dravid, C. Uher, M. G. Kanatzidis, *J. Am. Chem. Soc*. **2014**, *136*, 7006.

[6] G. Tan, F. Shi, S. Hao, H. Chi, L.-D. Zhao, C. Uher, C. Wolverton, V. P. Dravid, M. G. Kanatzidis, *J. Am. Chem. Soc*. **2015,** *137*, 5100.

[7] G. J. Tan, F. Y. Shi, J. W. Doak, H. Sun, L. D. Zhao, P. L. Wang, C. Uher, C. Wolverton, V. P. Dravid, M. G. Kanatzidis, *Energy Environ. Sci*. **2015**, *8*, 267.

[8] S. N. Guin, A. Chatterjee, D. S. Negi, R. Datta, K. Biswas, *Energy Environ. Sci*. **2013**, *6*, 2603.

[9] K. Biswas, J. He, Q. Zhang, G. Wang, C. Uher, V. P. Dravid, M. G. Kanatzidis, *Nat. Chem*. **2011**, *3*, 160.

[10] L. D. Zhao, S. Hao, S. H. Lo, C. I. Wu, X. Zhou, Y. Lee, H. Li, K. Biswas, T. P. Hogan, C. Uher, C. Wolverton, V. P. Dravid, M. G. Kanatzidis, *J. Am. Chem. Soc.* **2013**, *135*, 7364.

[11] A. Banik, B. Vishal, S. Perumal, R. Datta, K. Biswas, *Energy Environ. Sci*. **2016**, *9*, 2011.

[12] R. A. R. A. Orabi, N. A. Mecholsky, J. Hwang, W. Kim, J.-S.Rhyee, D. Wee, M. Fornari, *Chem. Mater*. **2016**, *28*, 376.

[13] K. Biswas, J. He, I. D. Blum, C.-I. Wu, T. P. Hogan, D. N. Seidman, V. P. Dravid, M. G. Kanatzidis, *Nature* **2012**, *489*, 414.

[14] B. Poudel, Q. Hao, Y. Ma, Y. Lan, A. Minnich, B. Yu, X. Yan, D. Wang, A. Muto, D. Vashaee, X. Chen, J. Liu, M. S. Dresselhaus, G. Chen, Z. Ren, *Science* **2008**, *320*, 634.

[15] L. D. Zhao, S. H. Lo, Y. Zhang, H. Sun, G. Tan, C. Uher, C. Wolverton, V. P. Dravid and M. G. Kanatzidis, *Nature* **2014**, *508*, 373.

[16] D. T. Morelli, V. Jovovic and J. P. Heremans, *Phys. Rev. Lett.* **2008**, *101*, 035901.

[17] S. N. Guin, J. Pan, A. Bhowmik, D. Sanyal, U. V. Waghmare, K.Biswas, *J. Am. Chem. Soc*. **2014**, *136*, 12712.

[18] M. K. Jana, K. Pal, U. V. Waghmare, K. Biswas, *Angew. Chem. Int. Ed*. **2016**, *55*, 7592.

[19] L. D. Zhao, H. J. Wu, S. Q. Hao, C. I. Wu, X. Y. Zhou, K. Biswas, J. Q. He, T. P. Hogan, C. Uher, C. Wolverton, V. P. Dravid, M. G. Kanatzidis, *Energy Environ. Sci*. **2013**, *6*, 3346.

[20] L. M. Rogers, *J. Phys. D: Appl. Phys.* **1968**, *1*, 845.

[21] R. F. Brkbrick, A. J. Strauss, *Phys. Rev*. **1963**, *131*, 104.

[22] R. Brebrick, A. Strauss, *Phys. Rev.* **1963**, *131*, 104.

[23] E. I. Rogacheva, *J. Phys.Chem. Solids* **2008**, *69*, 259.

[24] L. Zhang, J. Wang, Z. Cheng, Q. Sun, Z. Li, S. Dou, *J. Mater. Chem. A* **2016**, *4*, 7936.

[25] M. Zhou, Z. M. Gibbs, H. Wang, Y. Han, C. Xin, L. Li, G. J. Snyder, *Phys. Chem. Chem. Phys*. **2014**, *16*, 20741.

[26] M. H. Lee, D.-G. Byeon, J. -S. Rhyee, B. Ryu, *J. Mater. Chem. A* **2017**, *5*, 2235.

[27] A. Banik and K. Biswas, *J. Solid State Chem*. 2016, **242**, 43.

[28] J. He, J. Xu, G. Liu, X. Tan, H. Shao, Z. Liu, J. Xu, J. Jianga, H. Jianga, *RSC Adv*. **2015**, *5*, 59379.

[29] J. W. Wagner, R. K. Willardson, *Trans. Metall. Soc. AIME* **1968**, *242*, 366.

[30] E. Abramof, S. O. Ferreira, P. H. O. Rappl, H. Closs, I. N. Bandeira, *J. Appl. Phys*. **1997**, *82*, 2405.

[31] V. Jovovic, S. J. Thiagarajan, J. P. Heremans, T. Komissarova, D. Khokhlov, A. Nicorici, *J. Appl. Phys*. **2008**, *103*, 053710.

[32] I. U. Arachchig, M. G. Kanatzidis, *Nano Lett.* **2009**, *9*, 1583.

[33] M. K. Han, J. Androulakis, S. J. Kim, M. G. Kanatzidis, *Adv. Energy Mater.* **2012**, *2*, 157.

[34] M. Orihashi, Y. Noda, L.-D. Chen, T. Goto, T. Hirai, *J. Phys. Chem. Solids* **2000**, *61*, 919.

[35] S. Roychowdhury, S. Ghara, S. N. Guin, A. Sundaresan, K. Biswas, *J. Solid State Chem.* **2016**, *233*, 199.

[36] M. –K. Han, X. Zhou, C. Uher, S.-J. Kim, M. G. Kanatzidis, *Adv. Energy Mater*. **2012**, *2*, 1218.

[37] L.-D. Zhao, X. Zhang, H. Wu, G. Tan, Y. Pei, Y. Xiao, C. Chang, D. Wu, H. Chi, L. Zheng, S. Gong, C. Uher, J. He, M. G. Kanatzidis, *J. Am. Chem. Soc*. **2016**, *138*, 2366.

[38] P. Giannozzi, S. Baroni, N. Bonini, M. Calandra, R. Car, C. Cavazzoni, D. Ceresoli, G. L. Chiarotti, M. Cococcioni, I. Dabo, A. L. Corso, S. de Gironkoli, S. Fabris, G. Fratesi, R. Gebauer, U. Gerstmann, C. Gougoussis, A. Kokalj, M. Lazzeri, L. Martin-Samos, N. Marzari, F. Mauri, R. Mazzarello, S. Paolini, A. Pasquarello, L. Paulatto, C. Sbraccia, S. Scandolo, G. Sclauzero, A. P. Seitsonen, A. Smogunov, P. Umari, R. M. Wentzcovitch, *J. Phys. Condens. Matter.* **2009**, *21*, 395502.

[39] J. P. Perdew, K. Burke, M. Ernzerhof, *Phys. Rev. Lett*. **1996**, *77*, 3865.

[40] D. Vanderbilt, *Phys. Rev. B* **1990**, *41*, 7892(R).

[41] A. Banik, K. Biswas, *J. Mater. Chem. A* **2014**, *2*, 9620.

[42] J. Androulakis, I. Todorov, D.-Y. Chung, S. Ballikaya, G. Wang, C. Uher, M. Kanatzidis, *Phys. Rev. B* **2010**, *82*, 115209.

Chapter 2

Entropy Driven Point Defects and S Atoms Off-centering Instability Lead to Ultralow Thermal Conductivity and Enhanced Thermoelectric Performance in $(SnTe)_{1-2x}(SnSe)_x(SnS)_x$

Chapter 2

Entropy Driven Point Defects and S atoms Off-centering Instability Lead to Ultralow Thermal Conductivity and Enhanced Thermoelectric Performance in $(SnTe)_{1-2x}(SnSe)_x(SnS)_x$[†]

Summary

Understanding of the thermodynamics of phase stability, chemical bonding and phonon transport are essential to realizing ultralow thermal conductivity in crystalline solids to design high-performance thermoelectric materials. Pristine SnTe, an alternative of PbTe from IV-VI family, exhibit poor thermoelectric performance because of high p-type hole concentration (10^{21} cm^{-3}), high lattice thermal conductivity, κ_{lat} (~ 3.1 W/mK) and large energy separation between two valence bands. Herein, we demonstrated a unique strategy to achieve amorphous limit in lattice thermal conductivity (κ_{min} ~ 0.5 W/mK) via engineering of configurational and vibrational entropies and introducing local off-centering instability in pseudo-ternary $(SnTe)_{1-2x}(SnSe)_x(SnS)_x$. Initially, self-compensated $Sn_{1.03}Te$ is synthesized to optimize the excess Sn vacancy and hole carrier concentration. Then, co-substitution of Se and S in the Te lattice in SnTe reduces the κ_{lat} to its theoretical minimum. First-principles density functional theoretical (DFT) calculations reveal that S atoms are locally off-centered in global rock salt structure of SnTe lattice which is further confirmed by synchrotron X-ray pair distribution function (PDF) analysis, resulting low energy localized optical phonon modes which strongly couples with heat carrying acoustic phonon modes. Moreover, Se and S substitution in SnTe increases the configurational entropy and points defects in the pseudo-ternary system, $(SnTe)_{1-2x}(SnSe)_x(SnS)_x$, which decreases the κ_{lat} further. In the final step, improvement of the Seebeck coefficient is achieved via the synergistic effect of indium and silver co-doping in $(SnTe)_{1-2x}(SnSe)_x(SnS)_x$, where In acts as a resonant dopant and Ag serves as valence band convergent, respectively. We achieve a high thermoelectric figure of merit, zT_{max}, of ~1.3 at 854 K in $Sn_{1.03}Te_{0.85}Se_{0.075}S_{0.075}$ - 2 mol% Ag and 2 mol% In sample.

[†]*Manuscript submitted*

2.1 Introduction

Thermodynamics govern the material's capacity to chemical modification, which can dramatically influence the thermoelectric properties of inorganic solids. The entropy is measure of the number of microscopic configuration present in macrostates of a material.[1] Introduction of extensive alloying (site or size disorder)[2-7] increases the configurational entropy of the system and simultaneously decreases the lattice thermal conductivity, providing the opportunity to realize better thermoelectric performance.

Here we present a unique strategy for the reduction of lattice thermal conductivity of a crystalline solid to its amorphous limit by simultaneously engineering vibrational and configurational entropy. Vibrational entropy originates from the vibration of atoms around equilibrium.[1] In alloys, vibrational entropy is used to calculate the solubility of the second phase in the host matrix.[8] The large size mismatch between the constituent atoms may generate locally strained region in the global structure. Recently, effect of large size mismatch between Te and S is observed in PbTe-PbS alloys where S atoms are off-centered from their ideal crystallographic position, resulting local dipole moments and soft phonon modes which scatter heat carrying acoustic phonon effectively.[9] On the other hand, configurational entropy arises due to the occupation of one crystallographic site by multi-elements.[1] Multi-component chalcogenides such as $(PbTe)_{1-2x}(PbSe)_x(PbS)_x$ and $(GeTe)_{1-2x}(GeSe)_x(GeS)_x$ are known to show low thermal conductivity due to increase configurational entropy driven point defect phonon scattering, resulting from strong strain and mass fluctuations between different components.[4,5]

Pristine SnTe exhibits lattice thermal conductivity of ~ 3.1 W/mK which is significantly higher than its theoretical limit of minimum lattice thermal conductivity (κ_{min} ~ 0.5 W/mK) at 300 K.[3e] Thermal conductivity of SnTe has been significantly reduced *via* multi-element alloy scattering (~ 0.8 W/mK at 300K)[8] and introducing matrix encapsulated layered intergrowth compounds of $Sn_mSb_{2n}Te_{3n+m}$ (~ 0.67 W/mK at 300K).[10] The observed κ_{lat} values are still far from the theoretical limit of SnTe. The decrease of the thermal conductivity of a crystalline solid without degrading the carrier mobility has recently been demonstrated in SnTe *via* engineering ferroelectric instability which effectively scatters heat carrying acoustic modes and results in low thermal conductivity (~ 0.67 W/mK at 300 K).[11]

We envisaged that the simultaneous the effects of configurational entropy engineering and the introduction of local instability related to vibrational entropy *via* off-centering of the selective atom would be a promising approach to realize the κ_{min} of SnTe *via* co-alloying it with SnSe and SnS. Pseudo-ternary $(SnTe)_{1-x-y}(SnSe)_x(SnS)_y$ system has several possible compositions, but in the present study we narrowed it down by choosing the equal fraction of SnSe and SnS in SnTe, *i.e.* $(SnTe)_{1-2x}(SnSe)_x(SnS)_x$.

Here, we report ultralow κ_{lat} of ~ 0.52 W/mK in $(SnTe)_{1-2x}(SnSe)_x(SnS)_x$ [x = 0-0.10]. We achieved ultralow thermal conductivity and high thermoelectric performance in SnTe *via* three successive steps. Initially, we used the self-compensation in SnTe *i.e.* $Sn_{1.03}Te$ to optimize the excess hole carrier concentration which arises due to a significant amount of intrinsic Sn vacancies. Subsequently, the reduction of κ_{lat} of $Sn_{1.03}Te$ is achieved *via* co-alloying SnSe and SnS. Configurational entropy for pseudo-ternary $(SnTe)_{1-2x}(SnSe)_x(SnS)_x$ system is significantly higher compared to the conventional binary systems SnTe-SnSe or SnSe-SnS, which enhances the point defect phonon scattering markedly. Using first-principles density functional theoretical (DFT) calculations, we discover that S atoms are off-centered in cubic $(SnTe)_{1-2x}(SnSe)_x(SnS)_x$, resulting in local strain and strong overlap between heat carrying acoustic and low energy optical phonons, which reduces κ_{lat} significantly in $(SnTe)_{1-2x}(SnSe)_x(SnS)_x$. The off-centering behavior of S atoms in the global rock salt lattice of $(SnTe)_{1-2x}(SnSe)_x(SnS)_x$ was further experimentally verified by synchrotron X-ray pair distribution function (PDF) analysis. Finally, improvement of the Seebeck coefficient is achieved *via* the co-doping of indium and silver in $(SnTe)_{1-2x}(SnSe)_x(SnS)_x$, where In and Ag act as a resonant dopant and valence band convergent, respectively, which is confirmed by electronic structure determined using first-principles DFT calculation. Consequently, a peak zT of ~ 1.3 at 854 K is achieved for *p*-type $Sn_{1.03}Te_{0.85}Se_{0.075}S_{0.075}$ - 2 mol% Ag and 2 mol% In sample which is markedly higher compared to that of pristine SnTe.

2.2 Methods

2.2.1 Reagents

Tin (Sn, Alfa Aesar 99.99+ %), tellurium (Te, Alfa Aesar 99.999+ %), selenium (Se, Alfa Aesar 99.9999%), sulfur (S, 99.999%, metal basis, Alfa Aesar), indium (In, Alfa Aesar 99.99+ %) and silver (Ag, Aldrich 99.999%) were used for synthesis without further purification.

2.2.2 Synthesis

IngotsIngots (~ 10 g) of $Sn_{1.03}Te_{1-2x}Se_xS_x$ (x = 0 − 0.10), $Sn_{1.03}Te_{0.85}Se_{0.075}S_{0.075}$ – y% Ag and y % In (y = 1 - 3), $Sn_{1.03}Te_{0.85}Se_{0.075}S_{0.075}$ – 2% Ag and $Sn_{1.03}Te_{0.85}Se_{0.075}S_{0.075}$ –2% In were synthesized by mixing appropriate ratios of high-purity elemental Sn, Se, Te, S, Ag and In in quartz tubes. The tubes were sealed under vacuum (10^{-5} Torr) and slowly heated to 723 K over 12 hrs, then heated up to 1173 K in 5 hrs, annealed for 10 hrs and then slowly cool down to room temperature over a period of 15 hrs.

The as-synthesized ingots were crushed and ground to fine powders using a mortar and pestle. The powders were pressed into cylindrical-shaped pellets (10 mm diameter) using spark plasma sintering system (SPS211-LX, Dr. Sinter Lab) where 40 MPa of axial pressure was applied for 5 min at 500 °C in vacuum. The SPS-processed cylindrical-shaped sample was further cut and polished for electrical and thermal transport measurement.

2.2.3 Powder X-ray diffraction

Powder X-ray diffraction of samples were recorded using a Cu K_α (λ = 1.5406 Å) radiation on a Bruker D8 diffractometer.

2.2.4 X-ray pair distribution function

Powder Temperature dependent X-ray PDF data was collected using finely ground powder in beamline P02.1, PETRA III, DESY, Hamburg. Synchrotron beam of fixed energy 59.83 keV and spot size 0.5 X 0.5 mm^2 was used to collect data. 2D image plate data was collected using a Perkin-Elmer detector which was processed using Fit2D[12] software to obtain the scattering intensities *S*(Q) in the Q-space. The pair distribution *G*(r) was then obtained by Fourier transformation of the scattering structure function *F*(Q) =

Q[*S*(Q) - 1] using PDFgetX2[13] software. Finally, the modeling and refinement of *G*(r) was done using the software PDFgui.[14]

2.2.5 Band gap measurement

To estimate optical band gap of the as synthesized samples diffuse reflectance measurement has been done with finely ground powder at room temperature using FT-IR Bruker IFS 66V/S spectrometer in a wave-number range 4000-400 cm^{-1} with 2 cm^{-1} resolution and 50 scans. Absorption (α/S) data were calculated from reflectance data using Kubelka-Munk equation: $\alpha/S= (1-R)^2/(2R)$, where R is the reflectance, α and S are the absorption and scattering coefficient, respectively. The energy band gaps were derived from α/S *vs* E (eV) plot.

2.2.6 Field emission scanning electron microscopy

FESEM experiments were performed using NOVA NANO SEM 600 (FEI, Germany) operated at 15 KV.

2.2.7 Electrical transport

Electrical conductivity and Seebeck coefficients were measured simultaneously under He atmosphere from room temperature to 860 K on a ULVAC-RIKO ZEM-3 instrument system. The typical sample for measurement had a parallelepiped shape with the dimensions of ~ 2×2×8 mm^3. The longer direction coincides with the direction in which the thermal conductivity was measured.

2.2.8 Hall measurement

To determine carrier concentration, Hall measurements have been carried out using four-contact Hall-bar geometry, in a magnetic field of 0.57 T at room temperature in equipment developed by Excel Instruments.

2.2.9 Thermal transport

Thermal diffusivity, D, was directly measured in the range 300–873 K by using a laser flash diffusivity method in a Netzsch LFA-457. Coins with ~ 8 mm diameter and ~ 2 mm thickness were used in all of the measurements. The temperature dependent heat capacity, C_p, was derived using a standard sample (pyroceram) in LFA-457. The total thermal conductivity, κ_{tot}, was calculated using the formula, $\kappa_{tot} = DC_p\rho$, where ρ is the density of

the sample. The density of the pellets obtained was in the range ~ 97% of the theoretical density. To determine the total thermal conductivity of the other samples, the C_p of SnTe was used.

2.2.10 Estimation of κ_{lat} from Klemens model

According to Klemens theory of disordered alloys,[15] the lattice thermal conductivity of a disordered alloy, κ_{lat}^{d} is determined by:

$$\kappa_{lat}^{d} = \frac{\tan^{-1}(u)}{u}\kappa_{lat}^{p} \quad (2.1)$$

Where κ_{lat}^{p} is the lattice thermal conductivity of a pure alloy and u can be expressed by

$$u^2 = \frac{\pi^2 \Theta_D \Omega}{h\upsilon^2}\kappa_{lat}^{p}\Gamma \quad (2.2)$$

Here u is the disorder scaling parameter, Θ_D is the Debye temperature (Θ_D = 140 K for SnTe[10]), h is the Plank constant, υ is the sound velocity (υ = 1800 m s^{-1}, for SnTe[10]), and Ω is the average volume per atom and Γ is the scattering parameter that combines the influences from mass, bonding force, and strain contrasts, described as

$$\Gamma = c(1-c)\left[\left(\frac{\Delta M}{M}\right)^2 + \varepsilon\left(\frac{\Delta a}{xa}\right)^2\right] \quad (2.3)$$

where c is concentration of dopant, ε is a phenomenological parameter (163) related to the Grüneisen parameter γ ($\sim$ 2.1 for SnTe), M and a are the molar mass and lattice constant of the alloy, ΔM and Δa are the differences in mass and lattice constant between the two constituents.

2.2.11 Computational details

This part has been done in collaboration with Prof. Swapan K. Pati's group in JNCASR. First principle calculation based on Density Functional Theory (DFT) method as implemented in Quantum Espresso package has been used.[16] Ag and In Co-doped SnTeSeS, Ag-doped SnTeSeS, In-doped SnTeSeS has been simulated to perform electronic band structure and density of states (DOS) calculations. Scalar relativistic norm-conserving pseudopotentials and GGA approximated exchange-correlation energy with functional of Perdew, Burke, Erzenhoff (PBE) has been considered because of the presence of heavy elements in the supercell. We also take into consideration the spin-orbit coupling to elucidate electronic structure calculations. The wave function cut-off is considered to be 70 Ry. The Monkhorst-pack grid with 12 x 12 x 10 k-points is used in

sampling Brillouin zone integrations. A tetragonal supercell (√2x√2x2) containing 32 atoms are considered for electronic structure calculation. SnTe forms rocksalt crystal structure with two atoms per unit cell with space group *Fm-3m*. The crystal structures are fully relaxed to minimize the energy until the magnitude of Hellman-Feynman force on each atom is less than 0.025 eV/Å. The Gaussian spreading is considered to be 0.003 Ry. Electronic structures of $Sn_{16}Te_{16}$, $Sn_{16}Te_{14}SeS$, $Sn_{15}AgTe_{14}SeS$, $Sn_{15}InTe_{14}SeS$ and $Sn_{14}AgInTe_{14}SeS$ are determined along high symmetry points (M-Γ-Z-R).

Density functional perturbation theory (DFPT) has been used to calculate phonon dispersion properties of SnTeSeS and pristine SnTe. SnTe unit cell containing 8 atoms is considered for phonon frequency calculation. A uniform grid of 4 x 4 x 4 q-mess is taken into consideration. We compute vibrational entropy using Quasi-Harmonic approximation (QHA) code in quantum espresso package.

Vibrational entropy originates with the vibration of atoms around equilibrium.[1] The key difference between vibrational entropy with configurational entropy is used to calculate the solubilities of dilute solutions. The vibrational entropy has temperature dependence whereas the configurational entropy does not. Vibrational entropy has been calculated with the harmonic expressions for the phonon frequencies using the following equations.

Partition function, $Z = \prod_{k,\nu} \frac{\exp\left(-\frac{\hbar\omega(k,\nu)}{2\kappa_B T}\right)}{1-exp\left(-\frac{\hbar\omega(k,\nu)}{\kappa_B T}\right)}$ (2.4)

Free energy, $F = -k_B T\, lnZ$ (2.5)

Substituting the value of Z, free energy $F = k_B T \sum_{k,\nu} \ln[2 \sinh\left(\frac{\hbar\omega(k,\nu)}{2k_B T}\right)]$ (2.6)

Vibrational entropy expression,

$S = \frac{1}{2T}\sum_{k,\nu} \hbar\omega(k) Coth\left(\frac{\hbar\omega(k,\nu)}{2k_B T}\right) - k_B \sum_{k,\nu} \ln[2 \sinh\left(\frac{\hbar\omega(k,\nu)}{2k_B T}\right)]$ (2.7)

Where T is the temperature, k is phonon momentum vector, ω is phonon frequency, ν is phonon mode, k_B is the Boltzmann constant.

Configurational entropy arises due to the location of the constituent particles. Configuration entropy also characterizes a disorder in the systems. The entropy of mixing or configuration entropy is calculated using the formula,

$\Delta S_{mix} = -nR\,(x_1 lnx_1 + x_2 lnx_2)$ (2.8)

Where, x_1 and x_2 are mole fraction of species 1 and 2 respectively.

The average phonon group velocity is given by ($\nu_g = d\omega/dq$) where ν_g = average acoustics phonon group velocity, ω = phonon frequency and q = wave vector of phonon. The expression, we have used to calculate Debye temperature,

$$\kappa_B \Theta_D = \frac{h\nu_g}{2\pi}(6\pi^2 N/V)^{1/3} \quad (2.9)$$

Where, κ_B = Boltzmann constant, Θ_D = Debye temperature, N/V = carrier concentration per unit volume.

2.3 Results & Discussion

The effectiveness of SnTe as a potential thermoelectric material has limited because of its high *p*-type concentration originating from inherent Sn vacancy in the crystal structure, resulting in high electrical conductivity and electrical thermal conductivity.[17] Addition of donor dopants such as iodine and Sb/Bi in SnTe is an effective approach to enhance thermoelectric performance by decreasing the excess hole carrier concentration.[10,18,19] Recently, G. Tan *et al.* have optimized the Sn vacancy in SnTe by utilizing the self-compensation ($Sn_{1+x}Te$) approach.[20] First, we have synthesized SnTe sample with slight excess Sn, *i.e.* $Sn_{1.03}Te$ which exhibits lower *p*-type carrier concentration (1.08 X 10^{20} cm^{-3}) compared to that of pristine SnTe (4.5 X 10^{20} cm^{-3}). Further, we have taken two-step strategies to optimize the thermoelectric performance of the self-compensated $Sn_{1.03}Te$ sample.

Despite of the fact that the research on thermoelectric properties of pseudo-binary SnTe-SnSe and SnSe-SnS systems has reported,[21-24] so far, there is no report on pseudo-ternary SnTe-SnSe-SnS system for thermoelectrics because of its complex chemistry. A notable miscibility gap is observed between SnTe and SnS due to the significant difference in atomic radii between Te (1.40 Å) and S (1.00 Å) which is investigated by powder X-ray diffraction, backscattering FESEM analysis, and vibrational entropy calculation. Here, we described the structure, thermodynamical aspect and thermoelectric properties of SnTe rich $Sn_{1.03}Te_{1-2x}Se_xS_x$ system in details.

All $Sn_{1.03}Te_{1-2x}Se_xS_x$ (x = 0-0.10) samples are synthesized by vacuum sealed tube melting followed by spark plasma sintering (SPS) (see Method). Room temperature

powder XRD patterns (Figure 2.1a) for $Sn_{1.03}Te_{1-2x}Se_xS_x$ (x = 0-0.10) samples has been indexed based on cubic SnTe (space group *Fm-3m*). Simultaneous substitution of Se and S in SnTe shifts the Bragg peaks towards higher angle (2θ) because of the decrease in the lattice parameter which was further confirmed from the plot of lattice parameter *vs.* substituted Se/S concentration (Figure 2.1b). The decrease in lattice parameter for $Sn_{1.03}Te_{1-2x}Se_xS_x$ samples is due to the incorporation of the smaller size of Se (1.20 Å) and S (1.00 Å) in the position of Te (1.40 Å) in the SnTe lattice. However, PXRD patterns (Figure 2.1a) for higher SnSe/SnS concentration ($x \geq 0.05$) in SnTe show additional weak reflections of SnS, indicating the lower solubility limit of SnS in SnTe matrix compared to that of SnSe which is further studied in detail *via* backscattered FESEM and vibrational entropy calculation. Vibrational entropy plays an important role to understand the phase stability and solubility of the second phase in the host matrix which is discussed later in details.

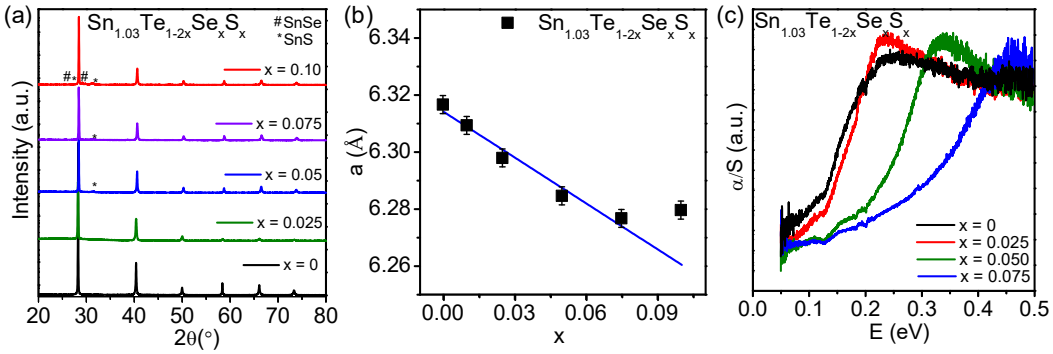

Figure 2.1 *(a) Powder X-ray diffraction pattern of $Sn_{1.03}Te_{1-2x}Se_xS_x$ (x = 0–0.10) samples. (b) Lattice parameter of $Sn_{1.03}Te_{1-2x}Se_xS_x$ as a function of the Se/S concentration, x. (c) Optical absorption spectra of $Sn_{1.03}Te_{1-2x}Se_xS_x$ samples (x = 0–0.10).*

To understand the effect of Se and S substitution into the SnTe, optical absorption spectra of $Sn_{1.03}Te_{1-2x}Se_xS_x$ (x = 0-0.075) samples were measured near room temperature (Figure 2.1c). Redshift in the absorption spectra is observed with increasing SnSe and SnS content. The optical band gap increases from 0.14 eV for $Sn_{1.03}Te$ to 0.27 eV for $Sn_{1.03}Te_{0.85}Se_{0.075}S_{0.075}$ sample.

To realize the surface morphology and microstructure compositions of $Sn_{1.03}Te_{1-2x}Se_xS_x$ sample backscattered electron imaging (BSE) FESEM and EDS are performed. Figure 2.2a and 2.2b represent the BSE-FESEM micrograph of $Sn_{1.03}Te_{0.85}Se_{0.075}S_{0.075}$ sample. We have observed the presence of micrometer size precipitate with dark contrast in the light contrast matrix.

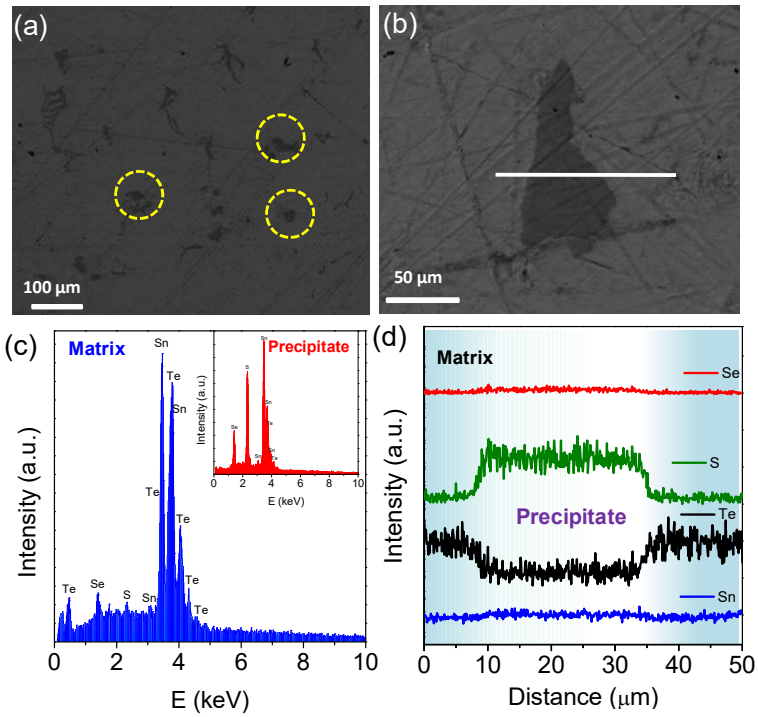

Figure 2.2 *(a)-(b) BSE-FESEM images of $Sn_{1.03}Te_{0.85}Se_{0.075}S_{0.075}$ sample. (c) EDS performed on both matrix and precipitate (inset of figure c). (d) EDS line scans along the precipitate (highlighted in image b).*

EDS analysis reveals the composition of both matrix and precipitate (Figure 2.2c, Table 2.1). The matrix is $SnTe_{1-x}Se_x$ rich whereas the dark contrast precipitate observed in FESEM is $SnS_{1-x}Se_x$ rich. In order to understand the phase composition of both matrix and precipitates simultaneously, EDS line scanning was performed on a precipitate along with the matrix which confirms the presence of $SnS_{1-x}Se_x$ rich precipitate on $SnTe_{1-x}Se_x$ rich matrix (Figure 2.2b and 2.2d). These observations are consistent with the solubility limit of SnSe and SnS in the SnTe matrix owing to the smaller size of S compared to that of Te.

Table 2.1: Elemental identification and quantification by EDS of matrix and precipitate of $Sn_{1.03}Te_{0.85}Se_{0.075}S_{0.075}$ sample.

Matrix			Precipitate		
Element	**Wt %**	**At %**	**Element**	**Wt %**	**At %**
Sn	46.98	46.79	Sn	65.68	45.85
Te	48.56	44.98	Te	8.40	5.60
Se	3.75	5.61	Se	11.91	12.50
S	0.71	2.62	S	14.01	36.19
Total	100	100	Total	100	100

Temperature-dependent total thermal conductivity (κ_{tot}) values for $Sn_{1.03}Te_{1-2x}Se_xS_x$ (x = 0-0.10) samples decrease with increase in x content (Figure 2.3a). The room temperature κ_{tot} of pristine $Sn_{1.03}Te$ is to be ~ 8 W/mK which further decreases to 3.5 W/mK at 710 K. Typically, $Sn_{1.03}Te_{0.80}Se_{0.10}S_{0.10}$ sample exhibits κ_{tot} value of ~ 4 W/mK at 300 K and decreases to 1.5 W/mK at 707 K. Figure 2.4a represents the κ_{lat} for all the samples obtained by subtracting the electronic contribution from total thermal conductivity by using Wiedemann-Franz's law, $\kappa_{el} = L\sigma T$. Temperature-dependent Lorenz number, L for all the samples were obtained based on fitting the respective temperature-dependent Seebeck value.[5b] The electrical thermal conductivity for all the sample decreases compared to SnTe because of the decrease in electrical conductivity which is due to the decrease in carrier concentration (Figure 2.3d). Se and S substitution in SnTe reduces the κ_{lat} values enormously throughout the measured temperature range compared to that of controlled $Sn_{1.03}Te$ sample. Typically, $Sn_{1.03}Te_{0.85}Se_{0.075}S_{0.075}$ sample exhibit κ_{lat} value of 0.52 W/mK at room temperature which is significantly lower than other reported SnTe based sample (Figure 2.4)[17,18,21,25-29] and reaches the theoretical minimum limit of SnTe (κ_{min}~ 0.5 W/mK). The $Sn_{1.03}Te_{0.85}Se_{0.075}S_{0.075}$ samples possess extensive solid solutions and big micron size (~20 μm) SnS rich precipitates.

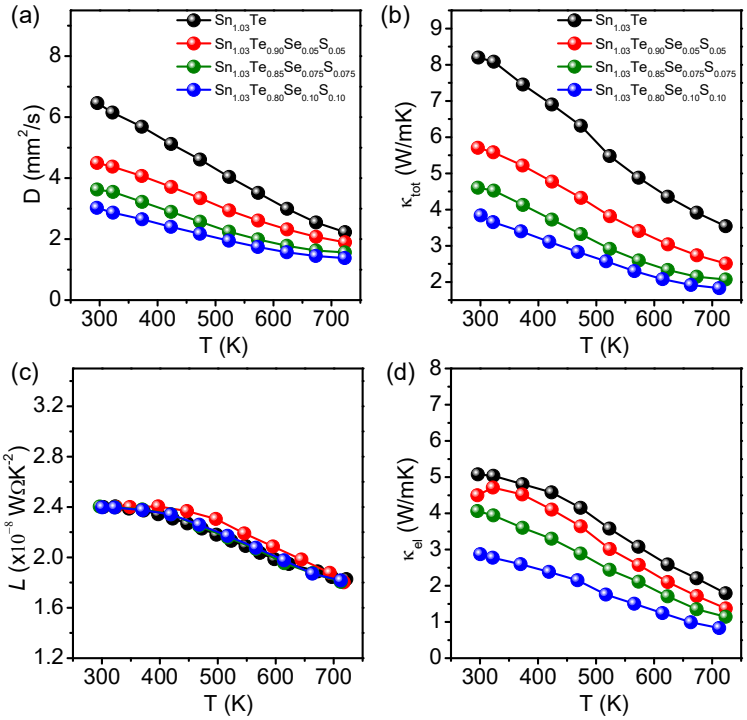

Figure 2.3 *Temperature variations of (a) diffusivity (D), (b) total thermal conductivity (κ_{tot}), (c) Lorenz number (L) and (d) electrical thermal conductivity (κ_{el}) of $Sn_{1.03}Te_{1-2x}Se_xS_x$ (x = 0–0.10) samples.*

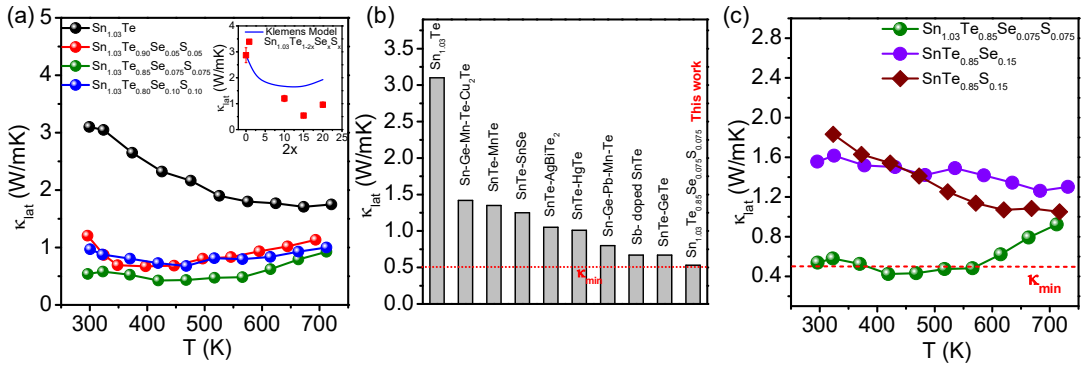

Figure 2.4 *(a) Temperature dependent lattice thermal conductivity (κ_{lat}) for $Sn_{1.03}Te_{1-2x}Se_xS_x$ (x = 0–0.10) samples. Inset of Figure 2.4a: Room-temperature lattice thermal conductivity as a function of total Se and S concentration, i.e. 2x in $Sn_{1.03}Te_{1-2x}Se_xS_x$. The solid blue line is a solid solution line predicted by the Klemens model. (b) The lattice thermal conductivity in this work in comparison with other previously reported SnTe-based samples.* [17,18,21,25-29] *(c) Comparison plot of κ_{lat} for $Sn_{1.03}Te_{0.85}Se_{0.075}S_{0.075}$, $Sn_{1.03}Te_{0.85}Se_{0.15}$ and $Sn_{1.03}Te_{0.85}S_{0.15}$ samples.*

We believe the big micron size precipitates do not affect much phonon scattering as the mean free path of heat-carrying phonons in SnTe lies in 2-20 nm range.[30]

To find microscopically the basic reason for ultralow thermal conductivity in $Sn_{1.03}Te_{0.85}Se_{0.075}S_{0.075}$ sample, we have calculated configurational entropy, vibrational entropy, and phonon dispersion *via* first-principles density functional perturbation theory (DFPT). For simplicity in the calculation, we have taken the $SnTe_{1-2x}Se_xS_x$ system instead of $Sn_{1.03}Te_{1-2x}Se_xS_x$ because excess Sn only controls the carrier concentration.

Configurational entropy increases when several initially separated systems of different atoms are mixed without chemical reaction. We consider pure elements have zero configurational entropy of mixing. Table 2.2 shows that the configurational entropy for pseudo-ternary system, $SnTe_{1-2x}Se_xS_x$ (2.8 J/K/mol) is significantly high compared to that of the pseudobinary phase, $SnTe_{1-2x}Se_x$ (0.55 J/K/mol) and $SnTe_{1-2x}S_x$ (0.95 J/K/mol). Thus, low κ_{lat} in the $Sn_{1.03}Te_{0.85}Se_{0.075}S_{0.075}$ sample can be attributed to entropically driven point defect scattering. It is worth noting that multi-component thermoelectric materials are capable of scattering phonons extensively because of highly tunable configurational entropy, resulting from complex crystal structure and bond inhomogeneity.[4,5]

Table 2.2: Change in vibrational entropy and configurational entropy at different concentrations of Se and S in SnTe.

Sample	% doped	Change in vibrational entropy (ΔS_{vibra})[4] (J/K/mol)	Change in configurational entropy(ΔS_{conf}) (J/K/mol)
Sn_8Te_8	0	0.0	0.0
Sn_8Te_7S	3.6	-58.24	0.96
$Sn_8Te_6S_2$	8	-114.45	1.54
Sn_8Te_7Se	8	-36.44	0.55
$Sn_8Te_6Se_2$	17.7	-38.18	2.55
Sn_8Te_6SeS	13.2 3.8(S) 9.4(Se)	-72.65	2.80

To confirm the effect of configurational entropy in the pseudo-ternary $Sn_{1.03}Te_{0.85}Se_{0.075}S_{0.075}$ system, we have prepared and measured the temperature-dependent κ_{lat} of controlled pseudo-binary $Sn_{1.03}Te_{0.85}Se_{0.15}$ and $Sn_{1.03}Te_{0.85}S_{0.15}$ samples (Figure 2.4c). $Sn_{1.03}Te_{0.85}Se_{0.075}S_{0.075}$ sample exhibits ultra-low κ_{lat}, especially from room temperature to 600 K compared to that of the pseudo-binary systems (Figure 2.4c). Thus, low κ_{lat} in the pseudo-ternary system can be attributed to the entropy-driven point defect phonon scattering due to enhanced mass fluctuation as several anions occupying the same position within the lattice. Similarly, configurational entropy plays an important role in decreasing the κ_{lat} in previously reported pseudo-ternary systems such as $(PbTe)_{1-2x}(PbSe)_x(PbS)_x$ and $(GeTe)_{1-2x}(GeSe)_x(GeS)_x$ [4,5], but none of those systems were able to reach their κ_{min} unlike the present case which hints about the presence of additional phonon scattering mechanisms operating in tandem with the point defect scattering to bring the κ_{lat} of SnTe down to its amorphous limit. The Klemens model was calculated to understand the effect of point defect scattering on lattice thermal conductivity of $Sn_{1.03}Te_{1-2x}Se_xS_x$ system (inset of figure 2.4a). However, experimental κ_{lat} for all the samples lies far below the theoretical line which further give an indication of additional mechanism which is complementary to the point defect phonon scattering.

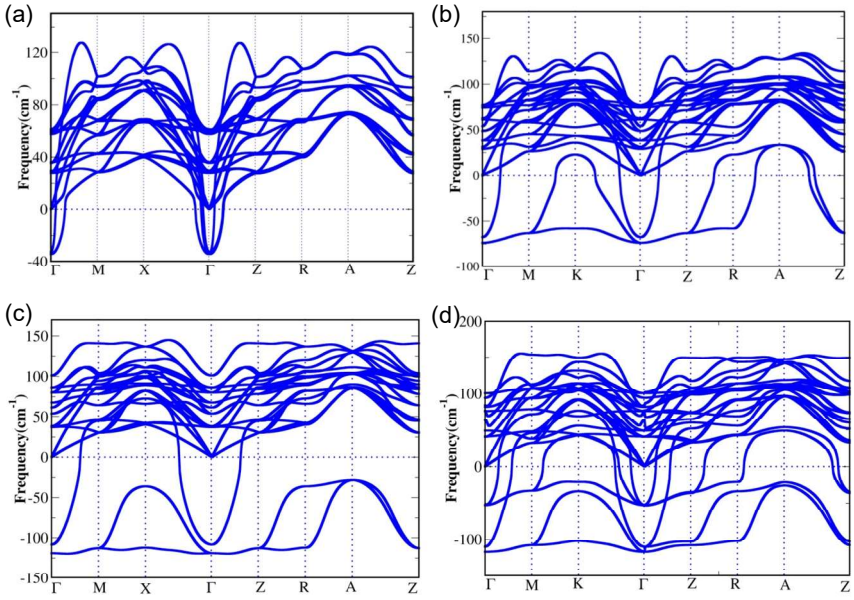

Figure 2.5 *Phonon dispersion of (a) Sn_8Te_8, (b) Sn_8Te_7Se, (c) Sn_8Te_7S and (d) Sn_8Te_6SeS as a function of q-points.*

We have also calculated vibrational entropy to check the phase stability at different concentration of S, Se and incorporating both S and Se in place of Te atom in SnTe crystal structure. The vibrational entropy decreases with the increasing concentration of S and Se in SnTe cubic crystal structure (Table 2.2). The rate of decrease is more for S atoms incorporation than that of the Se atoms in SnTe because of the ionic radius difference between Se and S atoms in the system. Since the atomic size of S is much lesser compared to the substituted Te atom, S atom vibrates more frequently as compared to the heavy element, hence vibrational contribution to entropy is very less. On the other hand, since the atomic size of Se atom is in between S and Te atoms, there is no significant change in vibrational entropy after Se substitution. Interestingly, in pseudo-ternary case, vibrational part of entropy decreases significantly because of the presence of S atom. Moreover, the decrease in vibrational entropy in the case of S substitution confirms that S is less soluble in the SnTe which was consistent with both PXRD and FESEM-BSE images (Figure 2.1a and Figure 2.2).

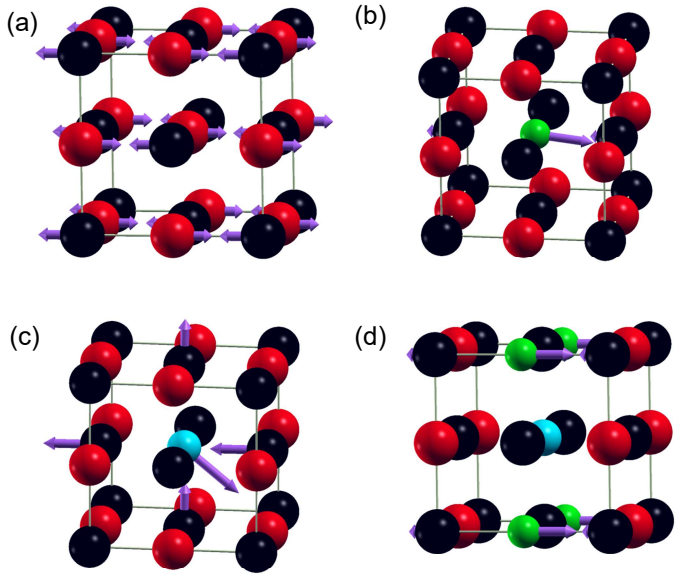

Figure 2.6 *Eigen vector of the imaginary phonon modes are shown for (a) SnTe, (b) SnTeSe, (c) SnTeS and (d) SnTeSeS (Sn, Black; Te, Red; Se, Cyan; S, Green). We have substituted Te with Se and S.*

To understand the origin of ultralow lattice thermal conductivity in $SnTe_{1-2x}Se_xS_x$ system, we further focused on various branches in the phonon dispersion curve of both SnTe and $SnTe_{1-2x}Se_xS_x$ (Figure 2.5). Phonon dispersion of pristine rocksalt SnTe exhibits imaginary modes (instability) with frequency of 36 cm^{-1} at Γ point, resulting from the rhombohedral distortion in the global cubic structure *via* Sn off-centering (Figure 2.5a).[31] Whereas, there is an appearance of flat bands in imaginary modes of frequency 117 cm^{-1} at Γ point (Figure 2.5d) for Sn_8Te_6SeS. The imaginary localized mode is originating from S atoms in Sn_8Te_6SeS which is visualized from the analysis of Eigen vectors (Figure 2.6). The other unstable localized flat mode of the frequency 53 cm^{-1} exhibits because of the Se in Sn_8Te_6SeS which is also confirmed from visualization of Eigen vector (Figure 2.6). The flat modes with imaginary frequency (117 cm^{-1}) are originated throughout the Brillouin zone along high symmetry path (Γ-M-K-Γ-Z-R). The high energy optical modes are also showing flat behavior. A significant band overlap between acoustics modes and low energy optical modes is obtained which scatters heat carrying acoustics phonons and reduces the lattice thermal conductivity in the $SnTe_{1-2x}Se_xS_x$ system. Six new imaginary phonon modes appear because of Se and S-substitution in SnTe. Interestingly, the bands which arose due to S substitution are flat throughout the irreducible Brillouin zone (BZ). The longitudinal acoustic phonon modes are more non-dispersive in Sn_8Te_6SeS than SnTe which also signifies that decreased phonon velocity. The reason for the band to be flat due to the off-centering of S atoms in Sn_8Te_6SeS lattice. In fact, S-atom makes weak metallic bonds with Sn. The phonon dispersion of Sn_8Te_6SeS is analogous to that of the $BaTiO_3$ where unstable localized mode originated due to off-centering of Ti atom along Ti-O-Ti chain.[32]

To confirm the off-center behavior of S atom in $SnTe_{1-2x}Se_xS_x$, we perform crystal orbital Hamiltonian population (COHP) analysis between the electronic states of S-3p and Se-4p with Sn-5s to indicate the bonding nature (Figure 2.7). COHP is defined as the DOS multiplied by the corresponding Hamiltonian matrix elements, and it indicates the strength and nature of bonding. The positive and negative values of COHP lead to bonding and anti-bonding interaction respectively. In Figure 2.7a, we have shown that there are strong interactions between the electronic states Sn 5s-S 3p and Sn 5s-Se 4p in the valence band near the Fermi level. The COHP analysis confirms the strong

interactions between Sn 5s and S 3p are bonding in nature with the S off-center configuration (Figure 2.7d) whereas anti-bonding nature appears when S is placed in its regular crystallographic site (Figure 2.7c).

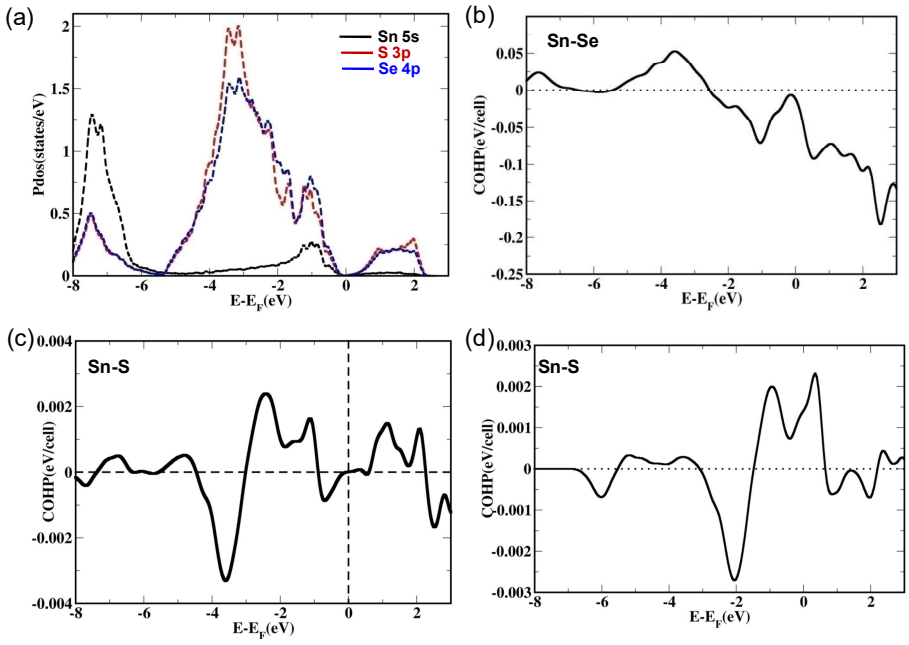

Figure 2.7 *(a) Electronic density of states of Sn 5s, S 3p and Se 3p where Fermi level is considered as a reference. Crystal orbital Hamiltonian analysis (COHP) of (a) Sn 5s - Se 4p orbitals, (b) Sn 5s – regular site S 3p orbitals and (c) Sn 5s and off-centered S 3p orbitals. The positive value of COHP leads to bonding interaction that stabilizes the structure. The negative value of COHP suggests to anti-bonding interaction that destabilizes the structure.*

On the other hand, the negative value of COHP indicates anti-bonding characteristics between the Sn 5s and Se 4p orbitals (Figure 2.7b). Interestingly, the strong anti-bonding interaction between Sn 5s and Se 4p orbitals are a larger negative value near the Fermi level compared to the COHP positive value of Sn 5s and S 3p orbitals. The positive value of COHP implies favorable bonding interactions of Sn 5s and S 3p in off-center configuration and stabilizes the system. We thus understand, there is a driving force on S atom to off-center towards the Sn which makes the bonds between them and stabilize the structure. Therefore, thermal energy could displace S atom from one potential well to others in a dynamic fashion which has a strong consequence in

phonon scattering. Similar behavior has been recently observed in PbSe-GeSe system where Ge off-center from its position to stabilize the structure and reduces thermal conductivity significantly.[33]

We calculated average phonon group velocity (ν_g) and Debye temperature (Θ_D) and showed that ν_g and Θ_D for $SnTe_{1-2x}Se_xS_x$ are lower than that of SnTe itself (Table 2.3). These lower values of the sound velocity can be attributed to the lower thermal conductivity of $SnTe_{1-2x}Se_xS_x$.

Table 2.3: Average phonon group velocity and Debye temperature for SnTe and $(SnTe)_{1-2x}(SnSe)_x(SnS)_x$.

Sample	Group velocity (ν_g, m/s)	Debye temperature (Θ_D, K)
SnTe	1470	220
SnTeSeS	1342	200

Large size mismatch between the constituent atoms (*i.e.,* size disorder) makes the system locally strained which is earlier observed in PbTe-PbS where S off-centering creates local dipole moment, resulting ferroelectric instability in the $PbTe_{1-x}S_x$ solid solution.[9] Similarly, large anion size mismatch is present in $SnTe_{1-2x}Se_xS_x$ system which gives rise to local distortion (thereby strain) in the global cubic crystal structure of SnTe. The effect of strain has been analyzed for both SnTe and SnTeSeS along with the phonon spectrum. The strain is calculated using formula $\frac{\partial\omega^2(\varepsilon)}{\partial\varepsilon}$, where, $\varepsilon = (a-a_0)/a_0$ (ω = frequency of unstable optical phonon modes; ε = applied strain in the system; a_0 = relaxed lattice parameter). The effect of strain on phonon has been examined using DFPT calculation at Γ point only (Figure 2.8). The higher slope in the plot of the square of the frequency of phonon modes as a function of strain in $SnTe_{1-2x}Se_xS_x$ (*i.e.* strain-phonon coupling) leads to higher anharmonicity, hence a high value of the Gruneisen parameter (γ) is expected to be observed as $\gamma \propto -(d\omega/dV)$. All the above-mentioned effects synergistically contribute to reduce the lattice thermal conductivity of $SnTe_{1-2x}Se_xS_x$ near to the κ_{min}.

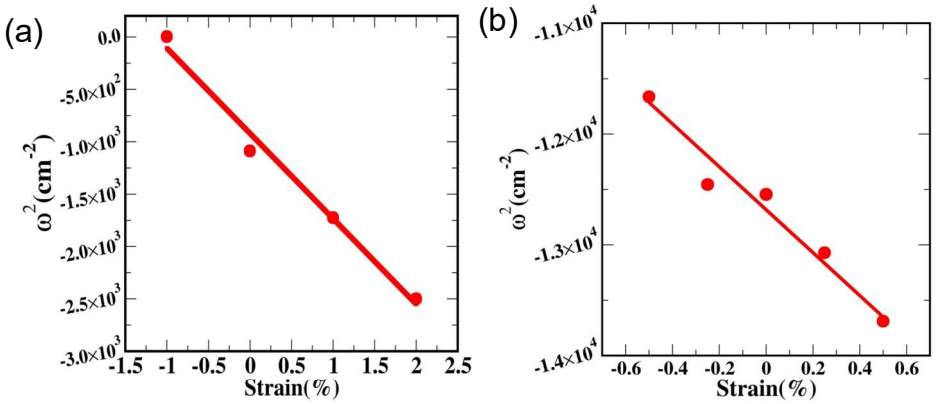

Figure 2.8 *Square of the frequency of phonon modes as a function of strain in all directions considering (a) a_0 = 6.41 Å for SnTe (b) a_0 = 6.21 Å for SnTeSeS. The slopes for SnTe and SnTeSeS are -812 and -1712 respectively. Slope signifies stain-phonon coupling.*

Although the theoretical calculation indicated towards bonding heterogeneity, with Sn-S having stronger bonding interaction as compared to Sn-Se or Sn-Te, a concomitant experimental proof was obtained using X-ray Pair Distribution Function (PDF) analysis (Figure 2.9-2.11). PDF being a total scattering technique provides a complete identity of the crystal structure, *i.e.*, both Brag reflection (long-range ordering) and diffuse scattering (short range ordering). Hence, it is very useful in correlating the structural aspects with the properties of the materials at a microscopic level. Full range X-ray PDF data of $Sn_{1.03}Te_{0.85}Se_{0.075}S_{0.075}$ at 300 K fits well with the rock salt cubic structure. Temperature-dependent PDF analysis indicates an increase in lattice parameter from 6.2846 Å at 300 K to 6.3137 Å at 500 K in $Sn_{1.03}Te_{0.85}Se_{0.075}S_{0.075}$ (Figure 2.9a). The thermal parameter for the cation and anions were also found to increase with increasing with temperature (Figure 2.9b). These observations are normal, as with the increase in the temperature, the lattice parameter increases due to thermal expansion, and also the thermal vibration of the atoms enhances (resulting in higher ADPs).

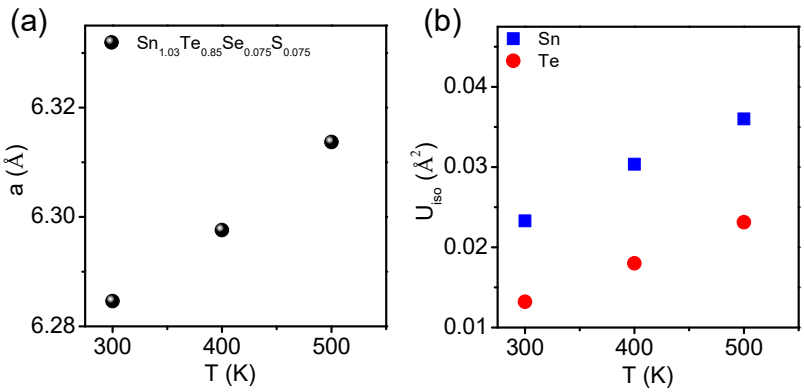

Figure 2.9 *Temperature dependence of (a) lattice parameter and (b) thermal ADPs of cation (Sn) and anion (Te) obtained from X-ray PDF of* $Sn_{1.03}Te_{0.85}Se_{0.075}S_{0.075}$ *sample.*

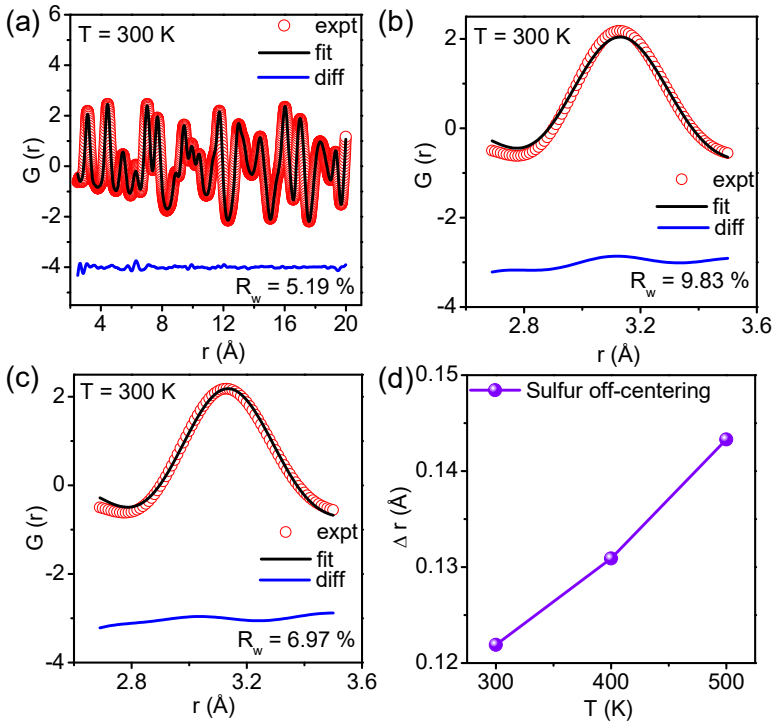

Figure 2.10 *(a) Global fit of X-ray PDF with cubic structure in* $Sn_{1.03}Te_{0.85}Se_{0.075}S_{0.075}$ *at 300 K. Fit of X-ray PDF for the nearest neighbor atomic correlation with the consideration of (b) cubic structure and (c) S off-centering along [111] direction at 300 K in* $Sn_{1.03}Te_{0.85}Se_{0.075}S_{0.075}$*. Although the global structure is well fitted with cubic phase, the local structure fits better with S off-centering along [111] direction. (d) Off-centering of S atoms in* $Sn_{1.03}Te_{0.85}Se_{0.075}S_{0.075}$ *due to local distortion as obtained from temperature dependent x-ray PDF analysis.*

To understand the chemical bonding of nearest atom-atom correlation in of $Sn_{1.03}Te_{0.85}Se_{0.075}S_{0.075}$, we have analyzed critically into the first peak in PDF (which gives information regarding the nearest atom-atom distances) (Figure 2.10b) and tried to rationalize the data using a distorted model, i.e., by off-centering the S anion (Figure 2.10c). We have observed that off-centering the S atom by 0.12 Å in [111] direction at 300 K properly describes the nearest neighbor correlation (R_w = 6.97 %, Figure 2.10c). Although the global structure of $Sn_{1.03}Te_{0.85}Se_{0.075}S_{0.075}$ fits well with cubic rock salt structure, the first PDF peak cannot well accounted by simple rock salt model (R_w = 9.83 %, Figure 2.10b).

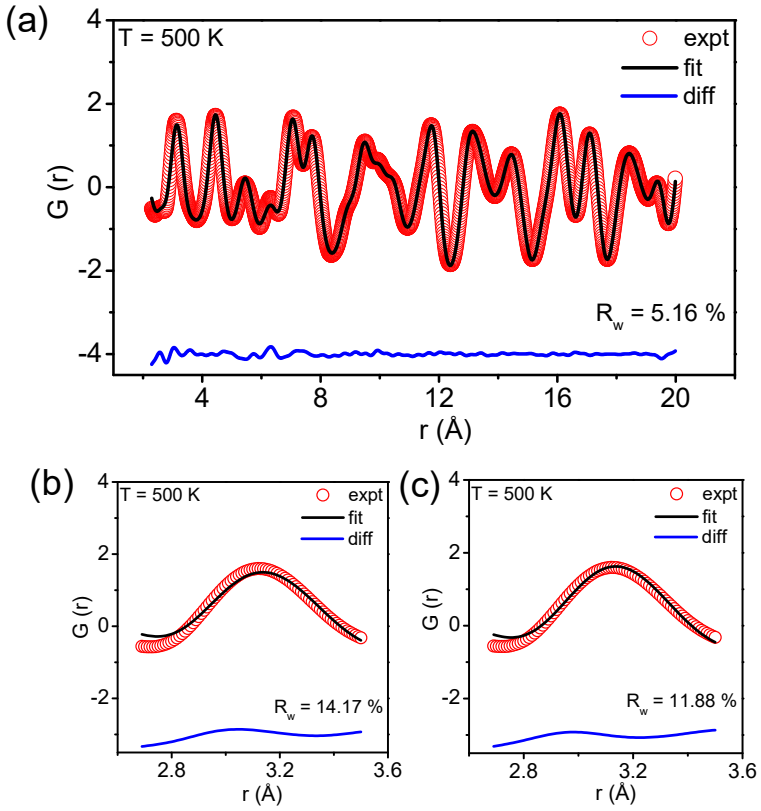

Figure 2.11 *(a) Global fit of X-ray PDF with cubic structure in $Sn_{1.03}Te_{0.85}Se_{0.075}S_{0.075}$ at 500 K. Fit of X-ray PDF for the nearest neighbor atomic correlation with the consideration of (b) cubic structure and (c) S off-centering along [111] direction at 500 K in $Sn_{1.03}Te_{0.85}Se_{0.075}S_{0.075}$. Although, the global structure is well fitted with cubic phase, the local structure fits better with S off-centering along [111] direction.*

The off-centering of S further increases to 0.14 Å at 500 K (Figure 2.10d and 2.11). The off-centering of S from its mean position suggest a bonding heterogeneity wherein a stronger bonding interaction between Sn-S acts as a catalyst for the S-off centering, which was predicted by DFT calculations. Similar local distortion results in the depletion of the thermal conductivity of few solids.[11, 33, 34] Thus, the local S off centering in global cubic $SnTe_{0.85}Se_{0.075}S_{0.075}$, is an important cause that inhibits the propagation of acoustic phonons and thereby decreasing the lattice thermal conductivity of the system.

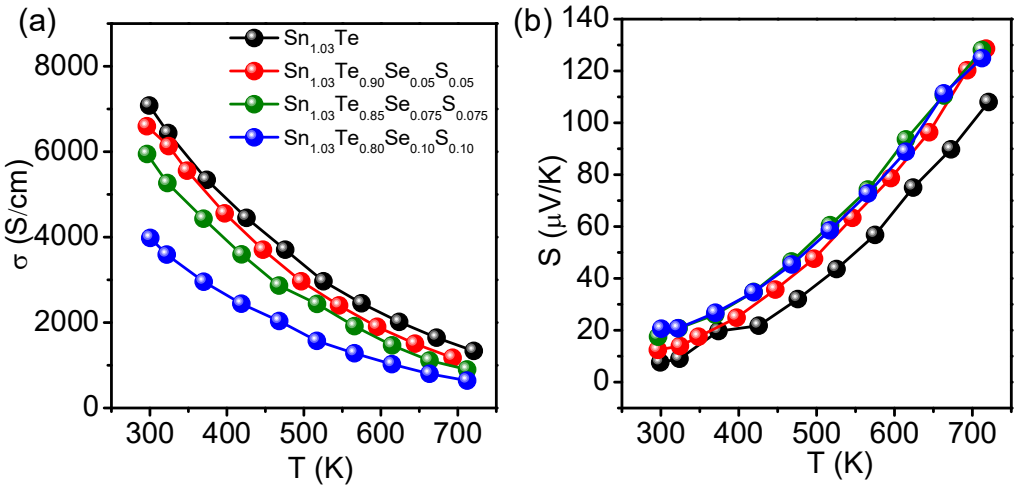

Figure 2.12 *Temperature dependent (a) electrical conductivity (σ), and (b) Seebeck coefficient (S) for* $Sn_{1.03}Te_{1-2x}Se_xS_x$ *(x = 0–0.10) samples.*

Figure 2.12 represent temperature dependent electronic transport properties of the $Sn_{1.03}Te_{1-2x}Se_xS_x$ (x = 0-0.10) samples. The electrical conductivity (σ) of all the samples exhibits the typical behavior of degenerate semiconductor. The electrical conductivity of SnTe decreases with the substitution of Se and S. Typically, the room temperature σ decreases from 7500 S/cm for $Sn_{1.03}Te$ to 4000 S/cm for $Sn_{1.03}Te_{0.80}Se_{0.10}S_{0.10}$ sample (Figure 2.12a). Whereas for all $Sn_{1.03}Te_{1-2x}Se_xS_x$ samples show slightly higher Seebeck coefficient compared to the pristine sample and remain unchanged with the increase in the Se and S content. Typically, the room temperature Seebeck value for all sample is ~20 μV/K which increases to ~130 μV/K at 707 K (Figure 2.12b). We have measured the carrier concentration (n = $1/eR_H$; where e and R_H are electronic charge and the Hall coefficient, respectively) for all the samples by Hall measurement by assuming a single parabolic model (Table 2.4). The Hall coefficient for all the samples shows positive

value, implying hole is the major carrier for all the system which is consistent with the temperature dependent Seebeck data. Room temperature electrical conductivity decreases with Se and S substitution because of the decreases in the *p*-type carrier concentration. Interestingly, the mobility for the $SnTe_{1-2x}Se_xS_x$ samples remain high and even higher compared to the other SnTe based samples with similar carrier concentration.[11]

Table 2.4: Electrical conductivity (σ), Seebeck coefficient (S), carrier concentration (p) and carrier mobility (μ) of $Sn_{1.03}Te_{1-2x}Se_xS_x$ (x = 0−0.10) samples at roomtemperature:

Sample	σ (S/cm)	S (μV/K)	p X 10^{19} (cm^{-3})	μ (cm^2/VS)
$Sn_{1.03}Te$	7078	7.6	10.8	409
$Sn_{1.03}Te_{0.90}Se_{0.05}S_{0.05}$	6595	12	4.36	944
$Sn_{1.03}Te_{0.85}Se_{0.075}S_{0.075}$	5943	17	4.17	889
$Sn_{1.03}Te_{0.80}Se_{0.10}S_{0.10}$	3981	20	3.43	724

Furthermore, it is not possible to reduce lattice thermal conductivity beyond the amorphous limit because the mean free path of the phonon is bounded by the inter-atomic distance. Thus, in the next step, we focused on the modification of the electronic structure of $Sn_{1.03}Te_{0.85}Se_{0.075}S_{0.075}$ sample to enhance the Seebeck coefficient. Ag and In co-doping improve the Seebeck coefficient of SnTe *via* the synergistic effect of resonance level formation (In doping) and valence band convergence (Ag doping).[35] Therefore, here, we choose Ag and In co-doping strategy to further improve the thermoelectric performance in $Sn_{1.03}Te_{0.85}Se_{0.075}S_{0.075}$ sample.

We have synthesized y mol% Ag and y mol% In co-doped $Sn_{1.03}Te_{0.85}Se_{0.075}S_{0.075}$ samples (y = 0 – 3 mol%) by vacuum sealed tube melting reaction followed by SPS and indexed the PXRD pattern with cubic SnTe (space group *Fm-3m*) (Figure 2.13a). Additional weak reflections could be indexed based on $SnSe_{1-x}S_x$ (space group *Pnma*) second phase.

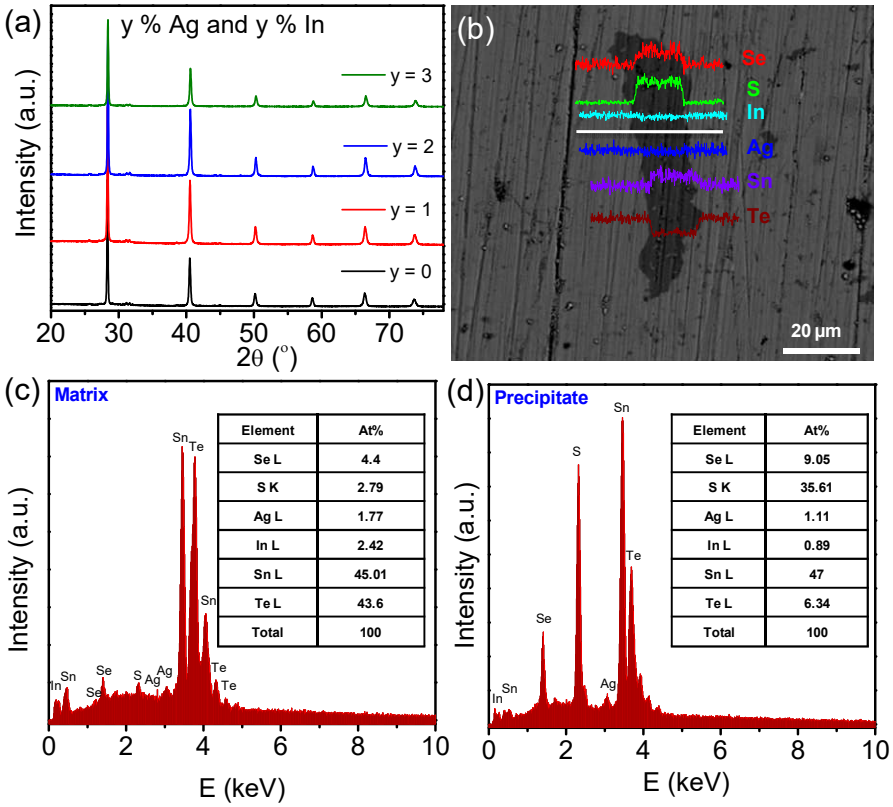

Figure 2.13 *(a) Powder X-ray diffraction pattern of* $Sn_{1.03}Te_{0.85}Se_{0.075}S_{0.075}$ *–y % Ag and y % In (y = 0 - 3), samples. (b) Backscattered FESEM image and EDS line scans along the precipitate of* $Sn_{1.03}Te_{0.85}Se_{0.075}S_{0.075}$*- 2% Ag and 2% In sample. EDS performed on both (c) matrix and (d) precipitate, respectively.*

We have performed BSE-FESEM and EDS to get better insight into the surface morphology and microstructure of $Sn_{1.03}Te_{0.85}Se_{0.075}S_{0.075}$ – 2% Ag and 2% In sample (Figure 2.13b-d). We have observed the presence of micrometer size (~20 μm) precipitate with dark contrast in the light contrast matrix (Figure 2.13b). EDS analysis reveals that matrix is $Sn_{1.03}Ag_yIn_yTe_{1-x}Se_x$ rich and precipitate is SnS rich (Figure 2.13c and d). Further, EDS line scanning on both matrix and precipitate verifies the presence of Ag and In in the $Sn_{1.03}Te_{1-x}Se_x$ matrix (Figure 2.13b) which have an important role in tailoring the electronic structure of $Sn_{1.03}Te_{0.85}Se_{0.075}S_{0.075}$ to optimize its thermoelectric performance.

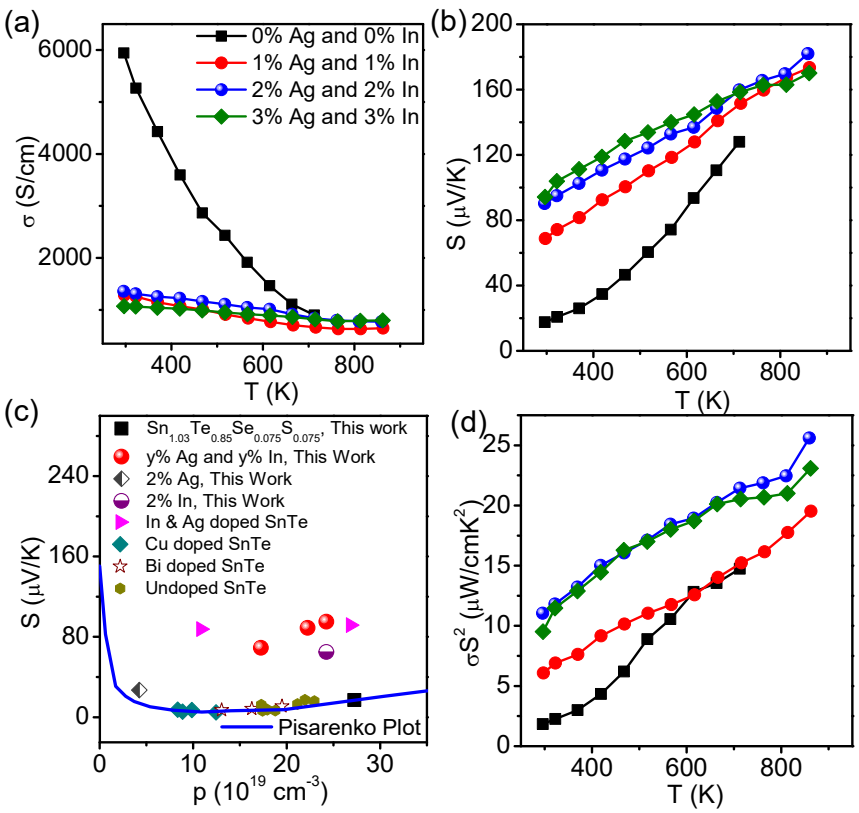

Figure 2.14 *Temperature dependent (a) electrical conductivity (σ) and (b) Seebeck coefficient (S) for $Sn_{1.03}Te_{0.85}Se_{0.075}S_{0.075}$ –y % Ag and y % In (y = 0 - 3) samples. (c) Room temperature Seebeck coefficient (S) vs. carrier concentration (p) plot of the present $Sn_{1.03}Te_{0.85}Se_{0.075}S_{0.075}$ and $Sn_{1.03}Te_{0.85}Se_{0.075}S_{0.075}$ - y % Ag and y % In samples. (d) Temperature dependent power factor (σS^2) for $Sn_{1.03}Te_{0.85}Se_{0.075}S_{0.075}$ –y % Ag and y % In (y = 0 - 3), samples.*

The electrical conductivities for $Sn_{1.03}Te_{0.85}Se_{0.075}S_{0.075}$ –y% Ag and y% In (y = 0 - 3) samples decrease with increasing temperature and also with the increasing amount of Ag and In over the entire measured temperature range (300 - 860 K) (Figure 2.14a). Substitution of Ag and In together decreases the electrical conductivity especially at room temperature because of the significant reduction in carrier mobility for all the samples due to resonant carrier scattering (Table 2.5). Typically, the room temperature σ decreases from 6000 S/cm (μ ~ 800 cm^2/Vs) for $Sn_{1.03}Te_{0.85}Se_{0.075}S_{0.075}$ to 1000 S/cm (μ ~ 135 cm^2/Vs) for $Sn_{1.03}Te_{0.85}Se_{0.075}S_{0.075}$ –3% Ag and 3 % In sample.

Table 2.5: Electrical conductivity (σ), Seebeck coefficient (S), carrier concentration (p) and carrier mobility (μ) of $Sn_{1.03}Te_{0.85}Se_{0.075}S_{0.075}$ – y% Ag and y % In (y = 1 - 3), $Sn_{1.03}Te_{0.85}Se_{0.075}S_{0.075}$ –2% Ag and $Sn_{1.03}Te_{0.85}Se_{0.075}S_{0.075}$ –2% In samples at room temperature:

Sample	σ (S/cm)	S (μV/K)	p X 10^{19} (cm^{-3})	μ (cm^2/VS)
$Sn_{1.03}Te_{0.85}Se_{0.075}S_{0.075}$ – 1 % Ag and 1% In	1283	69	20	40
$Sn_{1.03}Te_{0.85}Se_{0.075}S_{0.075}$ – 2 % Ag and 2% In	1356	90	25	33
$Sn_{1.03}Te_{0.85}Se_{0.075}S_{0.075}$ – 3% Ag and 3% In	1071	94	28	23
$Sn_{1.03}Te_{0.85}Se_{0.075}S_{0.075}$ – 2 % Ag	2723	27	7	242
$Sn_{1.03}Te_{0.85}Se_{0.075}S_{0.075}$ – 2 % In	793	65	27	18

Temperature-dependent Seebeck coefficients of the $Sn_{1.03}Te_{0.85}Se_{0.075}S_{0.075}$ –y% Ag and y% In (y = 0 - 3) samples are presented in Figure 2.14b. Positive Seebeck values indicate hole is the major carrier for all the samples which is consistent with positive Hall coefficient values. Seebeck coefficients for $Sn_{1.03}Te_{0.85}Se_{0.075}S_{0.075}$ –y% Ag and y% In (y = 0-3) samples are significantly higher over the entire temperature range compared to the controlled singly Ag and In-doped $Sn_{1.03}Te_{0.85}Se_{0.075}S_{0.075}$ sample (Figure 2.15). Typically, Seebeck value for $Sn_{1.03}Te_{0.85}Se_{0.075}S_{0.075}$ –2% Ag and 2% In sample is 90 μV/K at room temperature which further increases linearly to 180 μV/K at 856 K. This confirms the distinct and complementary role Ag and In on the thermoelectric properties of $Sn_{1.03}Te_{0.85}Se_{0.075}S_{0.075}$ which especially enhances the Seebeck coefficient throughout the measured temperature range.

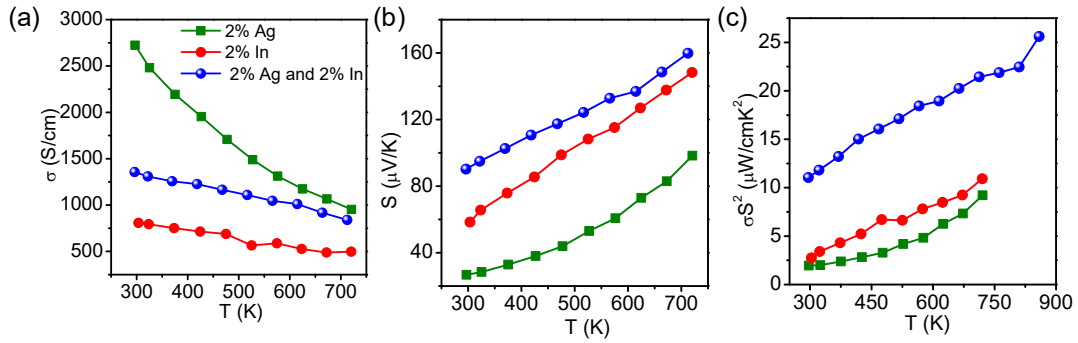

Figure 2.15 *Temperature dependent (a) electrical conductivity (σ), (b) Seebeck coefficient (S) and (c) power factor (σS²) for* $Sn_{1.03}Te_{0.85}Se_{0.075}S_{0.075}$ *–2% Ag and 2% In,* $Sn_{1.03}Te_{0.85}Se_{0.075}S_{0.075}$ *–2% Ag and* $Sn_{1.03}Te_{0.85}Se_{0.075}S_{0.075}$ *–2% In samples.*

We compared the room temperature Seebeck coefficient of $Sn_{1.03}Te_{0.85}Se_{0.075}S_{0.075}$ –y% Ag and y% In (y = 0 - 3) samples as a function of carrier concentration with the well-known Pisarenko line of SnTe to gain further insight into the origin of high Seebeck coefficient (Figure 2.14c). In doped sample exhibits higher Seebeck value compared to theoretical Pisarenko line due to the formation of resonance level near the valence band of $Sn_{1.03}Te_{0.85}Se_{0.075}S_{0.075}$ similar to previously reported In-doped SnTe.[35,36] Controlled Ag-doped $Sn_{1.03}Te_{0.85}Se_{0.075}S_{0.075}$ samples show slightly higher Seebeck value compared to Pisarenko line,which is attributed to the effective valence band convergence.[35-37] Interestingly, $Sn_{1.03}Te_{0.85}Se_{0.075}S_{0.075}$ –y% Ag and y% In co-doped samples exhibit much higher Seebeck coefficient than that of singly doped Ag and In samples which confirms that Ag and In synergistically enhance the Seebeck coefficient in $Sn_{1.03}Te_{0.85}Se_{0.075}S_{0.075}$ – y% Ag and y% In co-doped samples, where In act a resonant dopant and Ag increases the valence band convergence. The low carrier mobility for $Sn_{1.03}Te_{0.85}Se_{0.075}S_{0.075}$ –y% Ag and y% In co-doped samples can be attributed to the enhanced resonant carrier scattering and contribution of the heavy hole valence band.

The enhancement of the Seebeck coefficient can be understood by electronic structure calculations *via* DFT. We have considered √2 x √2 x 2 supercell in the simulation containing 32 atoms in the supercell. For this supercell, the light hole valence band maximum (VBM) and heavy hole valence band occur at the Γ point and Z+δ along the Z → R direction, respectively.

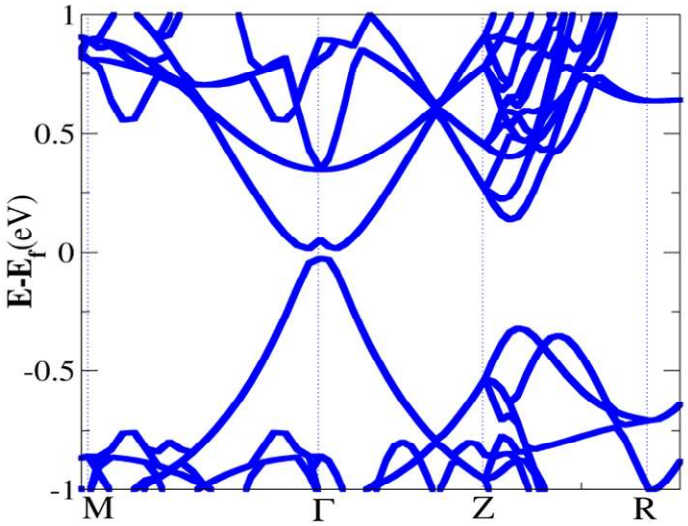

Figure 2.16 *Electronic structure of $Sn_{16}Te_{16}$ as a function of k-point in the supercell Brillouin zone. Fermi energy levels are set to zero and energy levels are shifted from Fermi level. The principal band gap appears at the Γ point and heavy hole valence band occurs at Z+δ along the Z ➞ R direction.*

Theoretically, the estimated band gap turns out to be 0.096 eV for SnTe after inclusion of spin-orbit coupling (Figure 2.16). DFT calculations have been further carried out to calculate electronic structures of $SnTe_{1-2x}Se_xS_x$, Ag-doped, In-doped, and Ag and In co-doped $SnTe_{1-2x}Se_xS_x$ systems (Figure 2.17a-d). Addition of Se and S further decreases the symmetry of the system and introduces new electronic levels near the Fermi energy which make the system metallic. We are unable to capture the small experimental band gap (~ 0.2 eV) in the electronic structure of $SnTe_{1-2x}Se_xS_x$ because of the typical underestimation of band gap by DFT calculation. For In-doped $SnTe_{1-2x}Se_xS_x$, a well-defined peak is observed in the valence band near the Fermi level, confirming the presence of a resonance state (Figure 2.17e). Interestingly, the energy separation between light and heavy hole valence band decreases from 0.35 eV for SnTe to 0.22 eV for $SnTe_{1-2x}Se_xS_x$, which further decreases to 0.19 eV Ag-doped $SnTe_{1-2x}Se_xS_x$, implying the effective valence band convergence after Ag substitution (Figure 2.17f). The energy separation between two valence band further decreases to ~0.10 eV for Ag and In co-doped sample which confirms the synergistic effect of Ag and In. Electronic structure of Ag and In co-doped $SnTe_{1-2x}Se_xS_x$ reveals the valence band convergence and resonance

state formation (Figure 2.17f). Thus, the synergistic effect of In and Ag co-doping in $(SnTe)_{1-2x}(SnSe)_x(SnS)_x$ is responsible for the observed notable augmentation in the Seebeck coefficient.

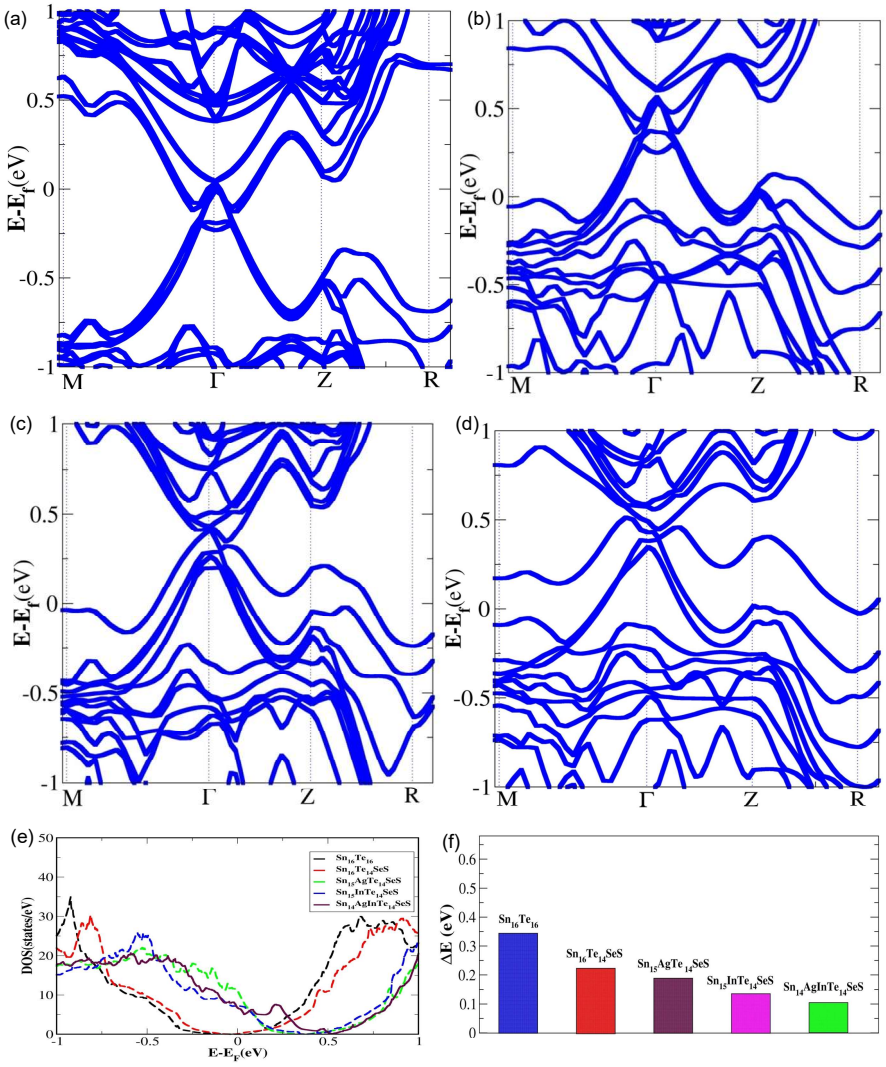

Figure 2.17 Electronic structure of (a) $Sn_{16}Te_{14}SeS$, (b) $Sn_{15}AgTe_{14}SeS$, (c) $Sn_{15}InTe_{14}SeS$ and (d) $Sn_{14}AgInTe_{14}SeS$ as a function of k-point in the supercell Brillouin zone. Fermi energy levels are set to zero and energy levels are shifted from Fermi level. The principal band gap appears at the Γ point and heavy hole valence band occurs at Z+δ along the Z ➞ R direction. (e) Density of states (DOS) and (f) the energy difference between light hole and heavy hole valence band maxima for pristine $Sn_{16}Te_{16}$, $Sn_{16}Te_{14}SeS$, $Sn_{15}AgTe_{14}SeS$, $Sn_{15}InTe_{14}SeS$ and $Sn_{14}AgInTe_{14}SeS$.

Figure 2.14d presents the temperature dependent power factor (σS^2) for $Sn_{1.03}Te_{0.85}Se_{0.075}S_{0.075}$ –y% Ag and y% In (y = 0 - 3) samples. In and Ag co-doped samples exhibit higher power factor compared to singly doped In and Ag over the entire temperature range because of optimum electrical conductivity and comparatively high Seebeck coefficient (Figure 2.15). This implies that In and Ag have a distinct but complementary role in enhancing the power factor of codoped samples. Typically, the room-temperature σS^2 value for $Sn_{1.03}Te_{0.85}Se_{0.075}S_{0.075}$ –2 % Ag and 2 % In sample is ~ 11 μW/cm·K^2 which further increases to ~27 μW/cm·K^2 at 856 K.

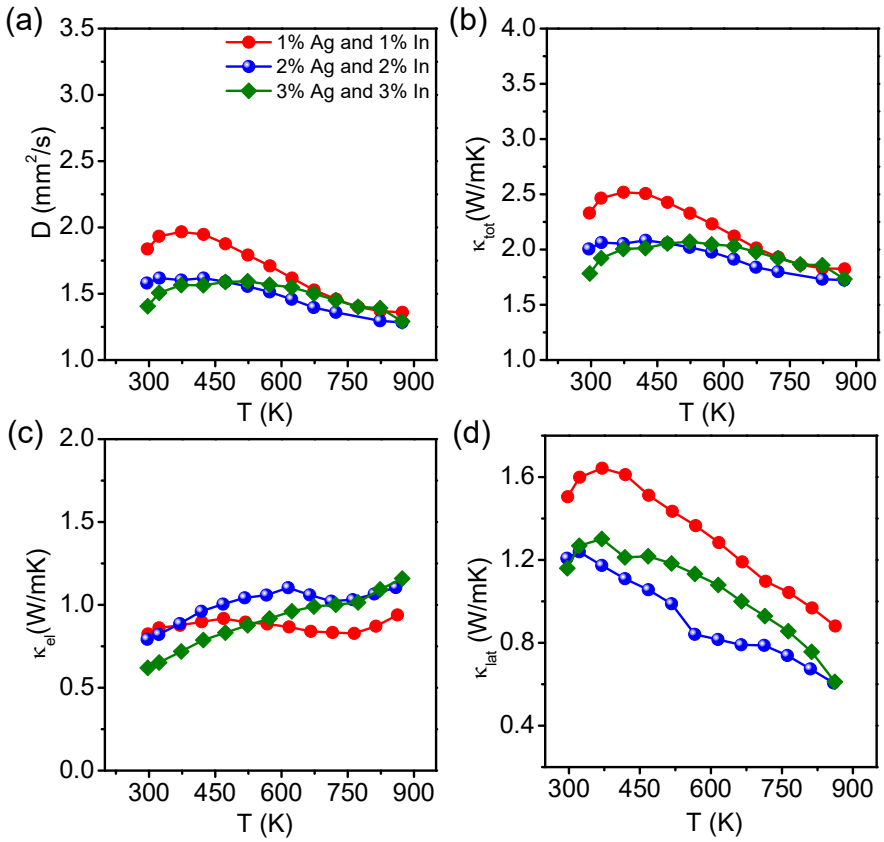

Figure 2.18 *Temperature variations of (a) diffusivity (D), (b) total thermal conductivity (κ_{tot}), (c) electrical thermal conductivity (κ_{el}) and (d) lattice thermal conductivity (κ_{lat}) of $Sn_{1.03}Te_{0.85}Se_{0.075}S_{0.075}$- y% Ag and y% In (y = 1 - 3) samples.*

.

Total thermal conductivity (Figure 2.18b) of $Sn_{1.03}Te_{0.85}Se_{0.075}S_{0.075}$ – y% Ag and y% In (y = 1 - 3) samples show a significant reduction with increasing In and Ag content, as the result of reduced electronic thermal conductivity, κ_{el} (Figure 2.18c). Typically, $Sn_{1.03}Te_{0.85}Se_{0.075}S_{0.075}$ –2 % Ag and 2% In sample exhibits κ_{tot} value of 2 W/mK at 300 K and decreases to 1.6 W/mK at 856 K. The κ_{lat} was estimated after subtraction of electronic contribution from total thermal conductivity. $Sn_{1.03}Te_{0.85}Se_{0.075}S_{0.075}$ – y% Ag and y% In (y = 1 - 3) sample exhibits κ_{lat} value of 1.2 W/mK at 300 K which decreases further to 0.6 W/mK at 856 K (Figure 2.18d). Mention must be made that κ_{lat} values for $Sn_{1.03}Te_{0.85}Se_{0.075}S_{0.075}$ –y% Ag and y% In (y = 1 - 3) samples do not follow any systematic trend with increasing the Ag and In content which is similar with previously reported Ag and In co-doped SnTe samples.[35]

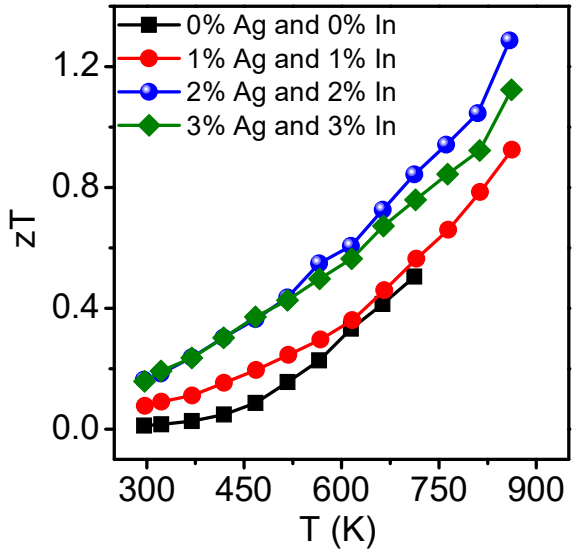

Figure 2.19 *Temperature dependent thermoelectric figure of merit (zT) for* $Sn_{1.03}Te_{0.85}Se_{0.075}S_{0.075}$*- y% Ag and y% In (y = 0 - 3) samples.*

The temperature dependent figure of merit, zT for $Sn_{1.03}Te_{0.85}Se_{0.075}S_{0.075}$ –y % Ag and y % In (y = 0 - 3) samples is presented in Figure 2.19. In and Ag co-doping synergistically enhances the zT significantly over the broad temperature range. $Sn_{1.03}Te_{0.85}Se_{0.075}S_{0.075}$ – 2 % Ag and 2% In sample exhibits the highest zT of ~ 1.3 at 854 K which is significantly higher than pristine SnTe and previously reported Ag and In co-doped SnTe sample (zT ~ 1 at 856 K).[35]

2.4 Conclusions

Although the scope of the investigations in $(SnTe)_{1-2x}(SnSe)_x(SnS)_x$ system is huge due to the possibility of vast compositional variation and complexity, here we have limited our investigation to study the thermoelectric properties of SnTe rich compositions with an equal fraction of SnSe and SnS. While with lower concentrations of SnSe and SnS, the system $(SnTe)_{1-2x}(SnSe)_x(SnS)_x$ (x = 0.05) represents solid solution, but with x>0.05 the system exhibits coexistence of solid solution and phase separation of $SnSe_{1-x}S_x$ rich precipitates (~20 μm) in $SnTe_{1-x}Se_x$ rich matrix. The solubility of SnSe is more in SnTe compared to that of SnS in SnTe due to large size mismatch of S and Te. The $(SnTe)_{1-2x}(SnSe)_x(SnS)_x$ system is significantly point defect rich due to high configurational entropy, which is confirmed by DFT calculation. Sulfur atoms locally off-center in global rock salt lattice of $(SnTe)_{1-2x}(SnSe)_x(SnS)_x$ due to strong covalent bonding between Sn-S, indicated by DFPT phonon calculation and synchrotron X-ray PDF analysis, resulted in local instability that induces coupling between optical and acoustic phonons. Synergistic effect of enhanced configurational entropy and S off-centering in pseudo-ternary system reduce the lattice thermal conductivity to its amorphous limit (κ_{min} ~ 0.5 W/mK). Further, Ag and In co-doping in $Sn_{1.03}Te_{0.85}Se_{0.075}S_{0.075}$ samples significantly enhance the Seebeck coefficient because of the synergistic effect resonance level formation and valence band convergence, respectively. As a result, the highest zT ~ 1.3 is achieved in $Sn_{1.03}Te_{0.85}Se_{0.075}S_{0.075}$ – 2 % Ag and 2% In sample at 854 K.

2.5 References

[1] B. Fultz, *Prog. Mater. Sci.* **2010**, *55*, 247.

[2] G. Tan, L. D. Zhao, M. G. Kanatzidis, *Chem. Rev.* **2016**, *116*, 12123.

[3] H. Wu, C. Chang, D. Feng, Y. Xiao, X. Zhang, Y. Pei, L. Zheng, D. Wu, S. Gong, Y. Chen, J. He, M. G. Kanatzidis, L.-D. Zhao, *Energy Environ. Sci*. **2015**, *8*, 3298.

[4] M. Samanta, K.Biswas, *J. Am. Chem. Soc.* **2017**, *139*, 9382.

[5] R. J. Korkosz, T. C. Chasapis, S. Lo, J. W. Doak, Y. J. Kim, C. Wu, E. Hatzikraniotis, T. P. Hogan, D. N. Seidman, C. Wolverton, V. P. Dravid, M. G. Kanatzidis, *J. Am. Chem. Soc.* **2014**, *136*, 3225.

[6] P. V. Vanitha, P. N. Santhosh, R. S. Singh, C. N. R. Rao, J. P. Attfield, *Phys. Rev. B* **1999**, *59*, 13539.

[7] A. K. Kundu, C.N.R. Rao, *Solid State Commun.* **2005**, *134*, 307.

[8] Z. Mao, D. N.Seidman, C. Wolverton, *APL Mater.* **2013**, *1*, 042103.

[9] J. W. Doak, C. Wolverton, V. Ozoliņs, *Phys. Rev. B* **2015**, *92*, 174306.

[10] A. Banik, B. Vishal, S. Perumal, R. Datta, K. Biswas, *Energy Environ. Sci*. **2016**, *9*, 2011.

[11] A Banik,. T. Ghosh, R. Arora, M. Dutta, J. Pandey, S. Acharya, A. Soni, U. V. Waghmare, K. Biswas, *Energy Environ. Sci.* **2019**, *12*, 589.

[12] A. P. Hammersley, S. O. Svensson, M. Hanfland, A. N. Fitch, D. Hausermann, *High Pressure Res.* **1996**, *14*, 235.

[13] X.Qiu, J. W Thompson,. S. J. L. Billinge, *J. Appl. Crystallogr.* **2004,** *37*, 678.

[14] C. L. Farrow, P. Juhas, J. W. Liu, D. Bryndin, E. S. Božin, J. Bloch, P. Th, S. J. L. Billinge, *J. Phys.: Condens. Matter.* **2007**, *19*, 335219.

[15] P. G. Klemens, *Phys. Rev.***1960**, *119*, 507.

[16] P. Giannozzi, S. Baroni, N. Bonini, M. Calandra, R. Car, C. Cavazzoni, D. Ceresoli, G. L. Chiarotti, M. Cococcioni, I. Dabo, A. L. Corso, S. de Gironkoli, S. Fabris, G. Fratesi, R. Gebauer, U. Gerstmann, C. Gougoussis, A. Kokalj, M. Lazzeri, L. Martin-Samos, N. Marzari, F. Mauri, R. Mazzarello, S. Paolini, A. Pasquarello, L. Paulatto, C. Sbraccia, S. Scandolo, G. Sclauzero, A. P. Seitsonen, A. Smogunov, P. Umari, R. M. Wentzcovitch, *J. Phys. Condens. Matter.* **2009**, *21*, 395502.

[17] A. Banik, S. Roychowdhury, K. Biswas, *Chem. Commun*. **2018**, *54*, 6573.

[18] A.Banik, K. Biswas, *J. Solid State Chem*. **2016**, *242*, 43.

[19] Z. Zhou, J. Yang, Q. Jiang, Y. Luo, D. Zhang, Y. Ren, X. He, J. Xin, *J. Mater. Chem. A* **2016**, *4*, 13171.

[20] G. Tan, L.-D. Zhao, F. Shi, J. W. Doak, S.-H. Lo, H. Sun, C. Wolverton, V. P. Dravid, C. Uher, M. G. Kanatzidis, *J. Am. Chem. Soc.* **2014**, *136*, 7006.

[21] A. Banik, K. Biswas. *J. Mater. Chem. A* **2014**, *2*, 9620.

[22] Q. Zhang, E. K. Chere, J. Sun, F. Cao, K. Dahal, S. Chen, G. Chen, Z. Ren, *Adv. Energy Mater***2015**, *5*, 1500360.

[23] Y.-M. Han, J. Zhao, M. Zhou, X.-X. Jiang, H.-Q. Leng, L.-F. Li, *J. Mater. Chem. A* **2015**, *3*, 4555.

[24] C. -C. Lin, R. Lydia, J. H. Yun, H. S. Lee, J. S. Rhyee, *Chem. Mater.* **2017**, *29*, 5344.

[25] G. J. Tan, F. Y. Shi, J. W. Doak, H. Sun, L. D. Zhao, P. L.Wang, C. Uher, C. Wolverton, V. P. Dravid, M. G. Kanatzidis, *Energy Environ. Sci*. **2015**, *8*, 267.

[26] H. Wu, C. Chang, D. Feng, Y. Xiao, X. Zhang, Y. Pei, L. Zheng, D. Wu, S. Gong, Y. Chen, J. He, M. G. Kanatzidis, L.-D. Zhao, *Energy Environ. Sci*. **2015**, *8*, 3298.

[27] L. Hu, Y. Zhang, H. Wu, J. Li, Y. Li, M. Mckenna, J. He, F. Liu, S. J. Pennycook, X. Zeng, *Adv. Energy Mater***2018**, *8*, 1802116.

[28] J. Tang, B. Gao, S. Lin, J. Li, Z. Chen, F. Xiong, W. Li, Y. Chen, Y. Pei, *Adv. Funct. Mater*. **2018**, *28*, 1803586.

[29] G. Tan, F. Shi, H. Sun, L.-D. Zhao, C. Uher, V. P. Dravid, M. G. Kanatzidis, *J. Mater. Chem. A* **2014**, *2*, 20849

[30] S. Lee, K. Esfarjani, T. Luo, J. Zhou, Z. Tian, G. Chen, *Nat. Commun.* **2014**, *5*, 3525.

[31] L. Aggarwal, A. Banik, S. Anand, U. V. Waghmare, K. Biswas, G. Sheet, *J. Materiomics* **2016**, *2*, 196.

[32] S. Baroni, S. de Gironcoli, A. Dal Corso, P. Giannozzi, *Rev. Mod. Phys.* **2001**, *73*, 515.

[33] Z.-Z. Luo, S. Hao, X. Zhang, X. Hua, S. Cai, G. Tan, T. P. Bailey, R. Ma, C. Uher, C. Wolverton, V. P. Dravid, Q. Yan, M. G. Kanatzidis, *Energy Environ. Sci.* **2018**, *11*, 3220.

[34] E. Rathore, R. Juneja, S. P. Culver, N. Minafra, A. K. Singh, W. G. Zeier, K. Biswas, *Chem. Mater.* **2019**, *31*, 2106.

[35] A. Banik, U. S. Shenoy, S. Saha, U. V. Waghmare, K. Biswas, *J. Am. Chem. Soc*. **2016**, *138*, 13068.

[36] Q. Zhang, B. Liao, Y. Lan, K. Lukas, W. Liu, K. Esfarjani, C. Opeil, D. Broido, G. Chen, Z. Ren, *Proc. Natl. Acad. Sci. U. S. A.* **2013**, *110*, 13261

[37] G. Tan, F. Shi, S. Hao, H. Chi, L.-D. Zhao, C. Uher, C. Wolverton, V. P. Dravid, M. G. Kanatzidis, *J. Am. Chem. Soc*. **2015**, *137*, 5100.

PART 5

Thermoelectric Properties of Silver Chalcogenides

Chapter 1

Soft Phonon Modes Leading to Ultralow Thermal Conductivity and High Thermoelectric Performance in AgCuTe

Chapter 1

Soft Phonon Modes Leading to Ultralow Thermal Conductivity and High Thermoelectric Performance in AgCuTe[†]

Summary

Crystalline solids exhibiting intrinsically low lattice thermal conductivity (κ_L) are crucial to realizing high-performance thermoelectric (TE) materials. In this chapter, we demonstrate an ultralow κ_L of 0.35 $Wm^{-1}K^{-1}$ in AgCuTe, which exhibits a remarkable TE figure-of-merit, zT of 1.6 at 670 K when alloyed with 10 mol% Se. First-principles DFT calculation reveals the presence of several soft phonon modes in its room-temperature hexagonal phase, which are also evident from low-temperature heat capacity measurement. These phonon modes, dominated by Ag vibrations, soften further with temperature giving a dynamic cation disorder and plausibly driving the superionic transition. Intrinsic factors such as hierarchical bond strengths, soft modes and optical-acoustic phonon coupling cause an ultralow κ_L in the room-temperature hexagonal phase, while the dynamic disorder of Ag/Cu cations leads to reduced phonon frequencies and mean free paths in the high-temperature rocksalt phase. Despite the significant cation disorder at elevated temperatures, the crystalline conduits to carrier-transport provided by the rigid anion sublattice render a high power factor.

[†]*Paper based on this study has been published in Angew. Chem. Int. Ed.* ***2018****, 57, 4043.*

1.1 Introduction

Thermoelectric (TE) materials, being functional in converting waste heat into electricity, are reckoned to play a significant role in the future energy management. Among the various successful approaches,[1] suppression of κ_L is imperative for efficient TE performance.[2-4] While the extrinsic routes to suppress the κ_L through all-scale hierarchical architectures or nanostructuring are effective in phonon-scattering,[2-4] an undesirable degradation of carrier transport is usually not entirely averted. Thus, solids with intrinsically low κ_L, are being capable of offering independent control over electrical properties.

Unconventional phonon-scattering processes have been unravelled to originate from intrinsic factors such as resonant bonding,[5] anharmonicity,[6] and crystallographic heterogeneity with coexisting rigid and fluctuating sublattices.[7] Notably, the site-disorder of cations compounded with lone-pair induced bond-anharmonicity leads to ultralow κ_L in the I-V-VI_2 compounds.[8,9] While the random rattling of guest atoms causes a low κ_L in caged compounds such as skutterudites[10] and clathrates,[11] anharmonic rattle-like coherent vibrations of cations engender an ultralow κ_L in $AgBi_3S_5$,[12] $CsAg_5Te_3$,[13] Cu_3SbSe_3[7] and Zintl tellurides such as $TlInTe_2$[14] and InTe.[15] Furthermore, in rocksalt $Cu_{2-\delta}X$ (X = Se/S)[16-18] and its derivatives such as AgCuX (X = Se, S),[19,20] the cations become superionic within rigid anionic framework above a transition temperature leading to intrinsically low κ_L, which resembles 'phonon-glass electron-crystal' (PGEC), as first envisaged by Slack,[21] are of considerable interest and are actively pursued in the thermoelectric research.

In this chapter, we demonstrate an ultralow κ_L of 0.35 $Wm^{-1}K^{-1}$ and a remarkable zT of 1.6 at 670 K in AgCuTe. AgCuTe is found to exhibit a hexagonal-to-rocksalt superionic transition in the 380 - 510 K range which has been investigated by temperature - dependent synchrotron X-ray diffraction and positron annihilation spectroscopy. Whereas the electrical properties considerably vary across the phase transition, κ_L remains extremely low (0.35 $Wm^{-1}K^{-1}$) throughout the temperature-range (300 - 723 K) studied. While the dynamic disorder of cation sublattice is responsible for an ultralow κ_L in the high-temperature rocksalt phase, the extremely low κ_L in the room-temperature hexagonal phase suggests the role of intrinsic factors such as structural complexity and weak

bonding characteristics of cations in suppressing its κ_L. DFT-based first-principles calculation reveals several soft vibrations of Ag in the hexagonal AgCuTe, which are also evident in its experimental heat capacity at low temperatures. These low-lying soft phonons scatter the heat-carrying acoustic phonon modes thereby suppressing the κ_L in AgCuTe. A strong phonon-strain coupling responsible for this is clearly revealed in our first-principles theoretical analysis of hexagonal AgCuTe. As a result of ultralow κ_L coupled with reasonably high power factors, high zT values of 1.4 and 1.6 are achieved respectively in the *p*-type AgCuTe and $AgCuTe_{0.90}Se_{0.10}$ at ~ 700 K.

1.2 Methods

1.2.1 Reagents

Silver (Ag, Aldrich 99.999%), copper (Cu, Alfa Aesar 99.9999%), selenium (Se, Alfa Aesar 99.9999%), and tellurium (Te, Alfa Aesar 99.999+ %) were used for synthesis without further purification.

1.2.2 Synthesis

Ingots (weighing a total of 10 g) of $AgCuTe_{1-x}Se_x$ (x = 0, 0.10 and 0.15) were synthesized by mixing stoichiometric ratios of elemental Ag, Cu, Te and Se in quartz ampoules. The ampoules were sealed under vacuum (10^{-5} Torr) and slowly heated to 723 K over 12 h, heated up to 1323 K in 5 h, annealed for 12 h and then slowly cooled down to room temperature in 20 h.

1.2.3 Powder X-ray diffraction

Powder X-ray diffraction patterns for finely ground samples were recorded at room-temperature using Cu K_α (λ = 1.5406 Å) radiation on a Bruker D8 diffractometer. Temperature-dependent synchrotron X-ray diffraction measurements (300 - 623 K) under N_2 flow were carried out with synchrotron X-ray beam of λ = 0.9016 Å, at BL-18B (Indian beam line), Photon Factory, KEK, Tsukuba, Japan. The energy of the beam was set by a Si (111) double crystal monochromator, which was cross-checked with Si (640b NIST) standard. All the measurements were carried out in Bragg–Brentano geometry with a divergence slit (300 μm), an anti-scattering slit (350 μm), and a receiving slit (300

μm). High-temperature measurements were carried out with Anton Paar DHS 1100 heating stage.

1.2.4 Differential scanning calorimetry

DSC data were measured by DSC Q2000 with a heating rate of 5 K/min between 320 K and 600 K in N_2 atmosphere.

1.2.5 Electrical transport

Electrical conductivity and Seebeck coefficients were measured simultaneously under He-atmosphere from room-temperature to 723 K using the commercial ULVAC-RIKO ZEM-3 instrument. Rectangular specimens cut and polished from ingots with typical dimensions of ca. 2×2×8 mm^3 were used for the measurements. The longer direction of the sample coincides with the ingot's growth direction. For determining the carrier concentrations, Hall measurements were carried out on the rectangular samples in four-contact geometry in a magnetic field of 0.57 T at room-temperature in custom-built equipment developed by Excel Instruments.

1.2.6 Thermal conductivity

Thermal diffusivity, D, was measured in the 300 − 723 K range by a laser flash diffusivity method in a commercial Netzsch LFA-457 instrument. Coins with 8 mm diameter and 2 mm thickness were used for the measurements. Heat capacity, C_p, in the 300 - 723 K range was indirectly derived using a standard sample (pyroceram) in LFA-457, which is in good agreement with the Dulong-Petit value. The total thermal conductivity, κ_{total}, was calculated using the formula $\kappa_{total} = D \times Cp \times \rho$, where ρ is the density of the sample (~ 97%).

1.2.7 Heat capacity experiment and fitting

Specific heat capacity at low temperatures (2 - 30 K) was measured using Physical Property Measurement System (PPMS).

1.2.8 Positron annihilation spectroscopy

Positron annihilation spectroscopy (PAS) is a powerful technique to study the point defects in solids and relies on the affinity of positrons to get trapped in the open volume

defects such as vacancies. Generally, the injected energetic positrons, after thermalization, annihilate with either low-momentum valence electrons or high-momentum core electrons in the specimen, thereby emitting two oppositely directed 511 keV gamma rays. The two primary PAS techniques to characterize vacancies in a given material are based on positron annihilation lifetime, and Doppler broadening of positron annihilated gamma radiation (DBPAR). Doppler broadening arises due to the momentum-distribution of electrons annihilating with thermalized positrons. The positron annihilation lifetimes have been measured with a fast-fast coincidence assembly with a time-resolution of 220 ps.[22] The positron lifetime spectrum (~ 5×10^6 coincidence counts) recorded at room-temperature has been analyzed by the computer programme PATFIT-88 with necessary source corrections to evaluate different positron lifetime states with their relative intensity.[23] The temperature-dependent measurement of Doppler broadening of positron annihilation radiation (DBPAR) has been carried out with a single high-purity Ge detector (*Efficiency:* 12 %; *Type*: PGC 1216 sp of DSG, Germany). The sample-source (~ 10 μCi ^{22}Na enclosed between ~ 1.5 μm thin nickel foils)-sample sandwich has been placed in a heating oven with a temperature accuracy of ± 2 ^{o}C. Complete details of the experimental setup are discussed elsewhere.[24] The DBPAR data have been analyzed by calculating the line-shape parameter (i.e., S-parameter), which is defined as the ratio of counts in the central area of the 511 keV photo peak (|511 keV - $E\gamma| \leq 0.85$ keV) to the total area of the photo peak (|511 keV - $E\gamma| \leq 4.25$ keV). The *S*-parameter represents the fraction of positrons annihilating with the low-momentum valence electrons with respect to the total number of positrons annihilated. When a positron is trapped in a vacant site, the wave function of positron is localized, and as a result, its annihilation with the deeply bound core electrons is less probable. The trapped positrons are, however, more probable to annihilation with the outer valence electrons.

1.2.9 Computational details

This part has been done in collaboration with Prof. Umesh V. Waghmare's group in JNCASR. First principles density functional theory (DFT) simulation package VASP 5.4.1 with projector-augmented (PAW) method and plane wave basis set are used in this study.[25] Perdew-Burke-Ernzerhof (PBE) exchange-correlation function with an energy cutoff of 500 eV is used.[26] To capture the onsite Columbic interaction we have used a

Hubbard U value of 5 eV for Ag and Cu atoms. The Brillouin zone integrations in hexagonal and rocksalt phases were sampled on 3 × 3 × 1 and 4 × 4 × 4 uniform meshes of points. We determined the vibrational frequencies of both the phases within a harmonic phonon approximation using second order force constants derived from DFT simulations.

1.3 Results & Discussion

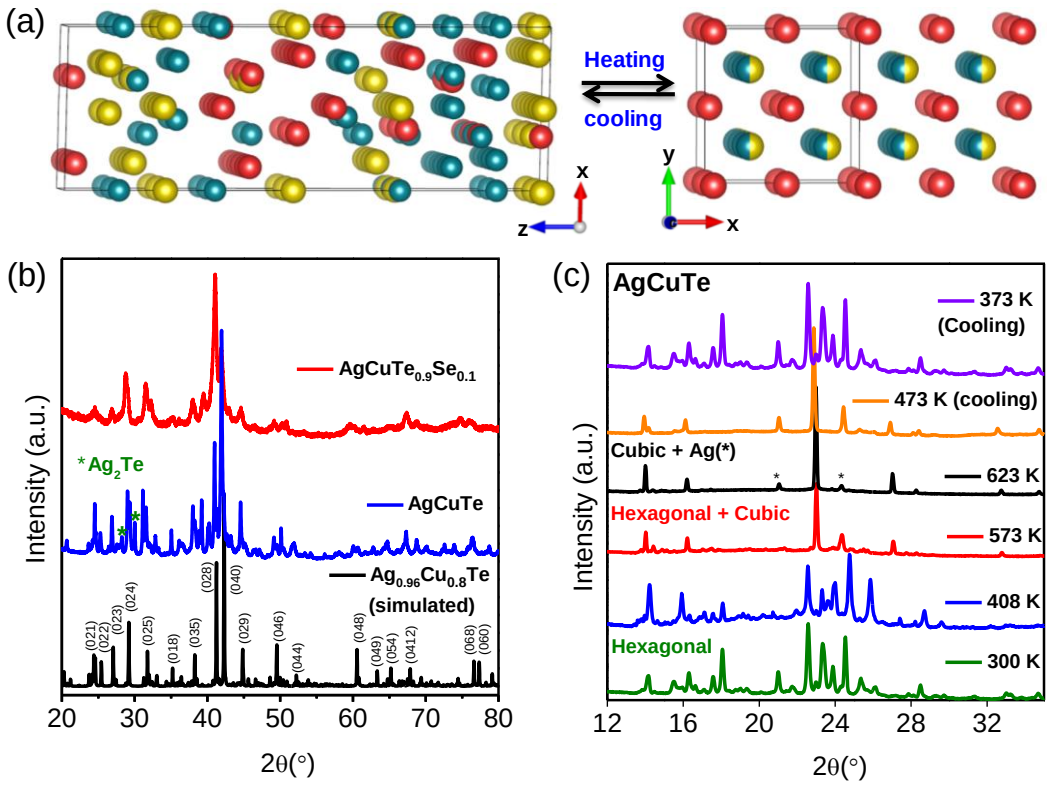

Figure 1.1 *(a) Structural transition in AgCuTe from the hexagonal phase at room-temperature (left) to rocksalt phase (right) at elevated temperatures. Yellow, blue and red atoms denote Ag, Cu and Te atoms, respectively. (b) PXRD patterns of AgCuTe and $AgCuTe_{0.90}Se_{0.10}$ recorded at room temperature using a laboratory source (Cu Kα; λ = 1.5406 Å) alongside the simulated pattern. (c) Temperature-dependent (300 – 623 K) synchrotron (λ = 0.9016 Å) PXRD patterns of AgCuTe measured during heating or cooling cycles.*

AgCuTe is a polymorphous semiconductor in the Ag_2Te - Cu_2Te pseudo-binary phase diagram.[27] At room temperature, AgCuTe crystallizes in a complex hexagonal structure (*P3m1*) (Figure 1.1a),[28] which undergoes a superionic phase transition (~ 460 K)

to a rocksalt phase (*Fm-3m*) in which the Ag and Cu are disordered around the face-centered cubic (fcc) sublattice of Te atoms (Figure Figure 1.1a).[29] Based on the Ag_2Te-Cu_2Te pseudo-binary phase diagram,[27] a stoichiometric AgCuTe is not stable at room-temperature, which always contains very small amounts of α-Ag_2Te (*P12$_1$/C1*) as a second phase, implying the matrix to be Ag-deficient (Figure 1.1b). The Ag deficiencies give rise to *p*-type conduction. The TE properties of AgCuTe can, therefore, be optimized by controlling the concentration of Ag vacancies, achieved here by alloying Se at the Te site. The relatively stronger Ag-Se/Cu-Se bonds compared to Ag-Te/Cu-Te bonds [30,31] effectively suppress the concentrations of cation vacancies in $AgCuTe_{1-x}Se_x$ samples and reduce the hole-concentrations (see below).

The laboratory powder X-ray diffraction (PXRD) patterns of $AgCuTe_{1-x}Se_x$ at 300 K could be indexed based on primarily hexagonal AgCuTe phase (Figure 1.1b), with weak diffraction peaks corresponding to the α-Ag_2Te phase (*P121/C1*). Upon heating, a superionic transition occurs in all the samples from hexagonal to rocksalt phase beyond 470 K, which is reversible and passes through a phase mixture as clearly seen from the temperature-dependent synchrotron PXRD ($\lambda = 0.9016$ Å) (Figure 1.1c). A high ionic conductivity of 0.8 Scm^{-1} was previously observed at 523 K in AgCuTe arising due to high cationic diffusivities of the order of 10^{-5} $cm^{-2}s^{-1}$, with about 60% of the total ionic diffusivity being due to the Ag cations.[32] Such high ionic conductivity of rocksalt AgCuTe resembles that found in molten salts (1 Scm^{-1})[16] and reflects a 'part-crystalline-part-glassy' state where the crystalline Te-sublattice coexists with a disordered superionic cation sublattice. Beyond 580 K, the hexagonal phase transforms completely into the superionic rocksalt phase. We also find that metallic Ag diffuses out of the material at high temperatures (which enhances the concentration of Ag vacancies), and redissolves into the matrix when cooled down to room-temperature (Figure 1.1c).

Interestingly, these peaks disappear upon incorporating 10 mol% Se in AgCuTe. Incorporation of Se suppresses the Ag vacancies and increases the solubility of α-Ag_2Te in the AgCuTe matrix, which was further verified by DSC experiment (Figure 1.2). Two endothermic peaks at 522 K and 412 K were observed for pristine AgCuTe which correspond to phase transition of AgCuTe from hexagonal to cubic and $\alpha - \beta$ structural transition of Ag_2Te, respectively. Endothermic peak at 412 K has almost disappeared for the $AgCuTe_{0.90}Se_{0.10}$ sample, which confirms the blocking of Ag_2Te formation on Se

doping in AgCuTe. Furthermore, upon Se-incorporation, the hexagonal to cubic phase transition temperature of AgCuTe decreases from 522 K to 466 K, which is consistent with the electrical transport measurement.

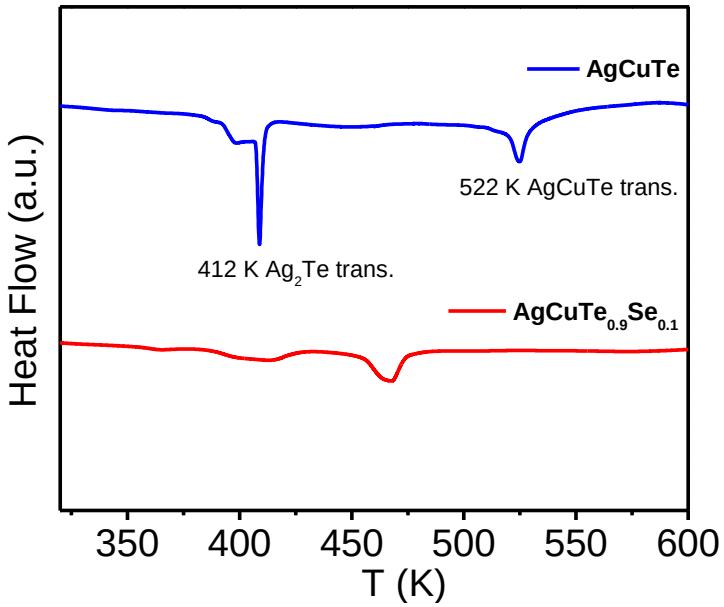

Figure 1.2 *DSC curves for $AgCuTe_{1-x}Se_x$ (x = 0 and 0.10) samples.*

Positron annihilation spectroscopy (PAS) is a powerful technique to study the vacancy in solids.[19,33] Deconvolution of the positron annihilation lifetime spectrum (Figure 1.3a) of AgCuTe recorded at room-temperature yields three lifetime components. The shortest lifetime component of 165 ± 4ps with 20 ± 1 % intensity is due to free annihilation of positrons whereas the longest lifetime component of 1227 ± 35 ps with 6 % intensity is related to the formation of positronium at the surface or the macroscopic voids inside the sample. The intermediate lifetime component of 304 ± 3ps with 74 ± 1 % intensity is ascribed to the trapping and subsequent annihilation of positrons in the open volume defects such as cation vacancies or their clusters.[19,33] The high intensity of the intermediate component indeed suggests a significant number of cation vacancies in our AgCuTe sample. The positron lifetime component in the 275 - 340 ps range has been ascribed to the Ag vacancies earlier in $AgBiSe_2$[33] and AgCuS[19]. Thus we conclude the lifetime component of 304 ± 3 ps in our AgCuTe sample to be primarily associated with

the Ag vacancies which comply with the presence of α-Ag_2Te phase in the room-temperature PXRD pattern (Figure 1.1b).

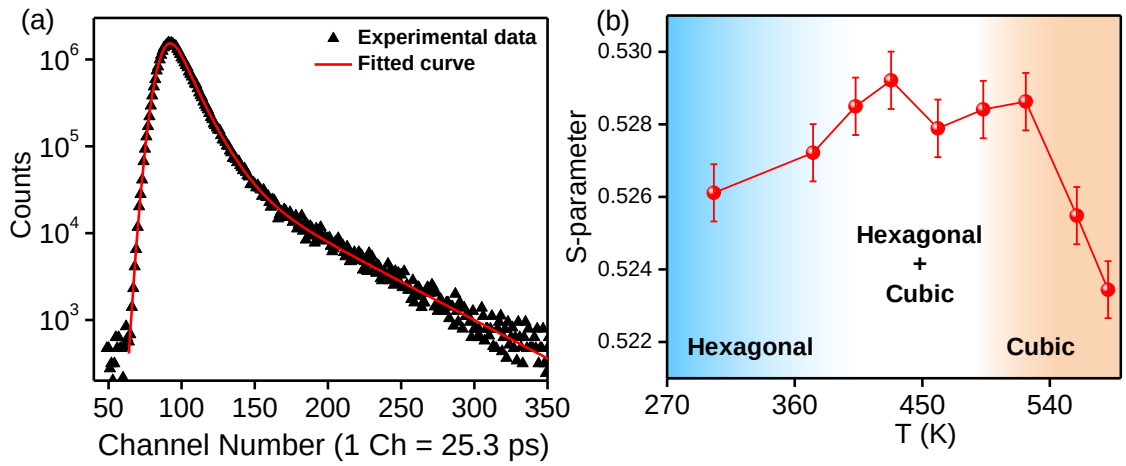

Figure 1.3 *(a) Positron annihilation lifetime spectrum for the AgCuTe sample at room temperature. Positron lifetime components were determined from the fitted curve shown as solid line. (b) Temperature-dependent Doppler broadening S-parameter of AgCuTe.*

To study the evolution of cation vacancies in AgCuTe as a function of temperature, we have obtained the Doppler-broadened spectrum (DBS) of annihilated gamma radiation. When a positron is trapped in a vacant site, the wave function of positron is localized, and as a result, its annihilation with the deeply bound core electrons is less probable. The trapped positrons are, however, more probable to annihilation with the outer valence electrons. The S - parameter (*i.e.*, the line-shape parameter of DBS), therefore, represents the contribution of valence electrons to the annihilation of positrons trapped in vacancies (see methods for the definition of S-parameter). Figure 1.3b shows the evolution of S-parameter for the AgCuTe sample as a function of temperature (300 - 580 K). The increase in S-parameter between 300 K and 524 K suggests an increase in number of Ag vacancies upon heating, consistent with the appearance of metallic Ag diffraction peaks in the PXRD patterns recorded at high temperatures (see figure 1.1c). Beyond 524 K, as the rocksalt phase is entirely formed, the S-parameter is found to fall rapidly. In the rocksalt phase where the vacancies act like 'hole' channels for superionic liquid-like conduction of cations, the effective access to the vacancies plausibly decreases for the positrons, and as a result, the S-parameter decreases. Thus, we have been able to

trace the evolution of cation vacancies and superionic phase transformation in AgCuTe using PAS as a function of temperature. The temperature-dependence of S-parameter indeed suggests the superionic transition in AgCuTe is essentially driven by the cation vacancies.

Electrical conductivity (σ) decreases with temperature for all the samples reflecting a degenerate semiconductor-like behaviour (Figure 1.4a). For AgCuTe, σ is 1055 S/cm near 300 K, which reaches to value of 148 S/cm at 710 K. σ decreases with Se-alloying in AgCuTe at 300 K, but remains slightly higher at high T (Figure 1.4a).

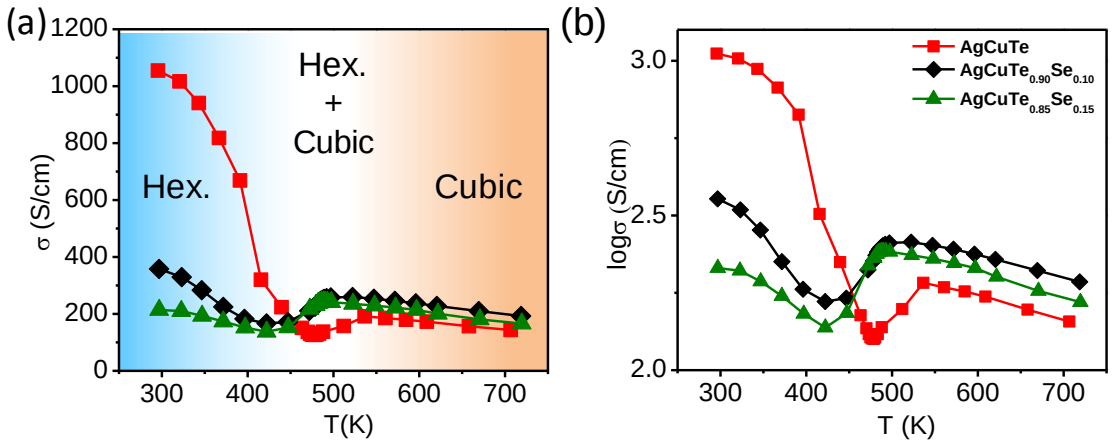

Figure 1.4 *(a) Temperature dependent electrical conductivity (σ) for the $AgCuTe_{1-x}Se_x$ (x= 0, 0.10, 0.15) samples. (b) Plot of logarithmic electrical conductivity (log σ) vs. temperature for the $AgCuTe_{1-x}Se_x$ (x = 0, 0.10, 0.15) samples.*

All the samples exhibit a broad minimum in the electrical conductivity during the phase transition, which shifts to lower temperatures with increasing Se-incorporation. A similar broad dip in the electrical conductivity is observed for the $Cu_{2-x}Se$ during its monoclinic-to-rocksalt superionic phase transition (350 - 410 K).[34] As the superionic phase transformation in AgCuTe proceeds through an inhomogeneous phase-mixture region, large spatial variations in the volume, density and crystal symmetry of both the phases can lead to an excess scattering of charge carriers during the phase transformation resulting in the observed minimum in the electrical conductivity.[17] The decreases in σ at 300 K is due to reduced hole-concentration, p_H which typically decreases from 9.74×10^{18} cm^{-3} for AgCuTe to 4.5×10^{18} cm^{-3} for $AgCuTe_{0.85}Se_{0.15}$ (Table 1.1).

Table 1.1: Carrier concentration (p_H) and carrier mobility (μ_H) of $AgCuTe_{1-x}Se_x$ (x= 0, 0.10, and 0.15) samples at room temperature.

Sample	Carrier Concentration (cm^{-3})	Mobility (cm^2/Vs)
AgCuTe	9.74 X 10^{18}	676
$AgCuTe_{0.90}Se_{0.10}$	6.24 X 10^{18}	361
$AgCuTe_{0.85}Se_{0.15}$	4.53 X 10^{18}	297

The high p_H in AgCuTe arises from the Ag vacancies in the system as also evident from the PAS. The relatively strong Ag-Se/Cu-Se bonds in $AgCuTe_{1-x}Se_x$ fix the Ag and Cu atoms in the crystal lattice and suppress the Ag/Cu vacancies resulting in a decreased hole-concentration in $AgCuTe_{1-x}Se_x$. A similar isovalent substitutional effect has been observed for the S-alloyed $Cu_{2-x}Se$ due to suppression of Cu vacancies.[31]

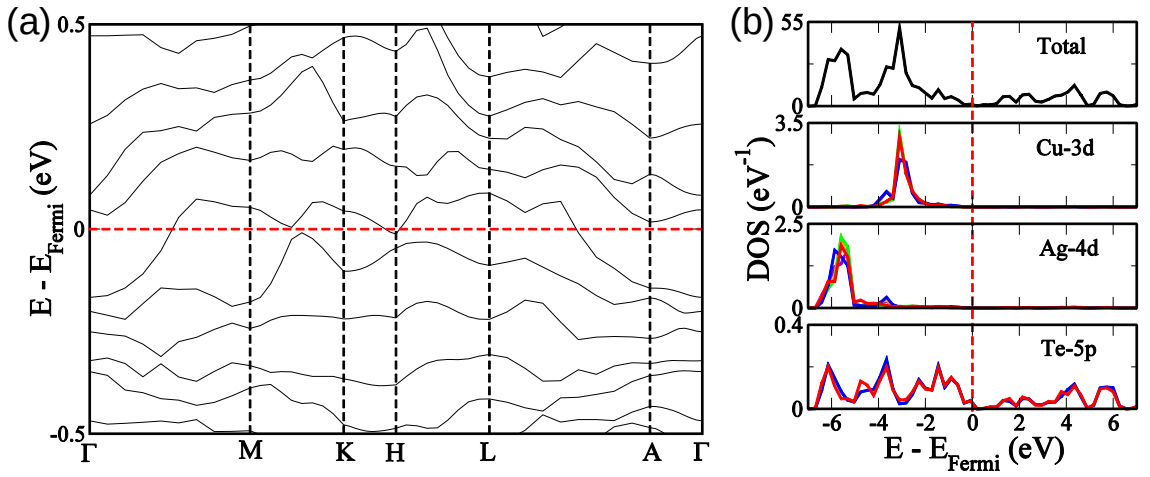

Figure 1.5 *(a) The electronic structure and (b) the electronic density of states (DOS) of hexagonal AgCuTe.*

Interestingly, the estimated room-temperature Hall mobility of the hexagonal AgCuTe phase is as large as 676 $cm^2V^{-1}s^{-1}$, which, however, decreases with Se-incorporation to 361 $cm^2V^{-1}s^{-1}$ in the $AgCuTe_{0.90}Se_{0.10}$ sample. Our first-principles calculations show that the electronic structure of hexagonal AgCuTe is semimetallic (Figure 1.5a), and hence the high carrier mobility observed at room-temperature, similar to the case of previously reported AgCuSe with a semimetallic electronic structure.[20] The

reduction in carrier mobility with Se-incorporation indicates an alloy scattering of charge carriers in the $AgCuTe_{1-x}Se_x$ (x = 0, 0.10, 0.15) samples. Furthermore, the projected electron density of states (DOS) (Figure 1.5b) reveals the valence band (VB) maximum in AgCuTe to have a dominant contribution from Te p-states with d-states of Ag and Cu located deeper in the VB, suggesting that the electrical transport is mainly governed by the anionic rigid Te-sublattice. The projected electronic density of states shows that both Cu-3d and Ag-4d bands are ~ 3eV and ~ 5eV below the Fermi level, respectively.

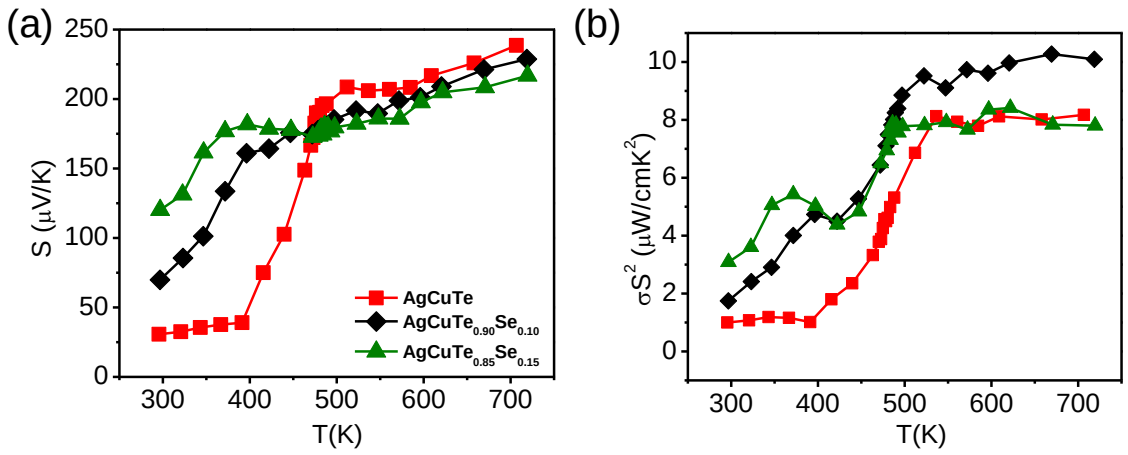

Figure 1.6 *Temperature dependent (a) Seebeck coefficient (S) and (b) power factor (σS^2) for the $AgCuTe_{1-x}Se_x$ (x= 0, 0.10, 0.15) samples.*

A positive sign of the Seebeck coefficient (*S*) throughout the temperature-range studied (Figure 1.6a) indicates a dominant conduction by holes in all the samples which is consistent with our Hall measurements. For the AgCuTe, *S* is 31 μV/K at 300 K in the hexagonal phase, which increases to 240 μV/K at 710 K in the rocksalt phase. A rapid rise in *S* between 400 K and 480 K is consistent with the rapid decrease in electrical conductivity (Figure 1.4b). $AgCuTe_{0.90}Se_{0.10}$ and $AgCuTe_{0.85}Se_{0.15}$ samples, on the other hand, exhibit higher *S* values of 70 μV/K and 120 μV/K, respectively at 300 K due to reduced hole-concentrations (Table 1.1), which increase to 228 μV/K and 216 μV/K, respectively at 710 K (Figure 1.6a). The power factors (σS^2) for the AgCuTe and $AgCuTe_{0.90}Se_{0.10}$ samples are 1 and 1.8 $\mu Wcm^{-1}K^{-2}$ respectively at 300 K, and increase to 8.2 and 10.3 $\mu Wcm^{-1}K^{-2}$, respectively at 710 K in the rocksalt phase (Figure 1.6b).

The hexagonal phase of AgCuTe shows a κ_{total} as low as 0.9 $Wm^{-1}K^{-1}$ at 300 K which further reduces to 0.4 $Wm^{-1}K^{-1}$ at 710 K in the rocksalt phase (Figure 1.7c). In the case of $AgCuTe_{0.90}Se_{0.10}$, κ_{total} remains extremely low (0.3 - 0.5 $Wm^{-1}K^{-1}$) throughout the range of temperature (300 - 723 K) investigated.

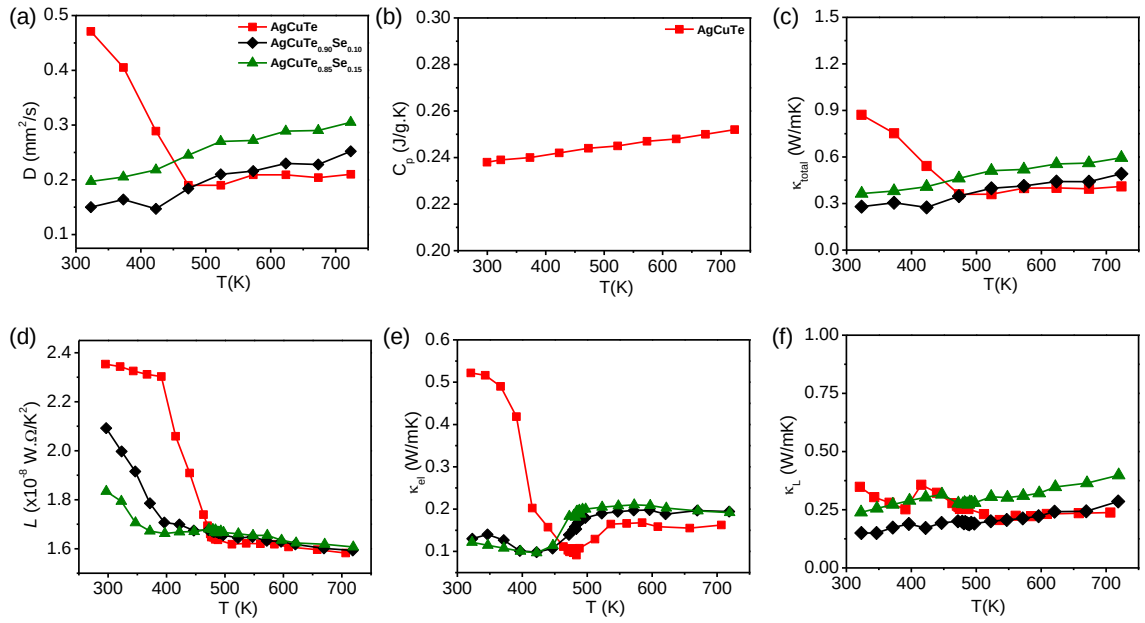

Figure 1.7 *Temperature dependent (a) diffusivity (D), (b) heat capacity (C_p), (c) total thermal conductivity (κ_{total}), (d)Lorenz number (L), (e) electrical thermal conductivity (κ_{el}) and (f) lattice thermal conductivity (κ_L) for the $AgCuTe_{1-x}Se_x$ (x= 0, 0.10, 0.15) samples. Heat capacity of AgCuTe is used for calculations of total thermal conductivity of other samples also.*

All the samples exhibit significantly low values of κ_L between 0.2 and 0.4 $Wm^{-1}K^{-1}$ (Figure 1.7f). These values are much lower compared with the binary tellurides such as Ag_2Te[35] and Cu_2Te[36] and many state-of-the-art TE materials. In crystalline solids, κ_L usually varies with temperature due to varying phonon mean free path. In AgCuTe, the κ_L is nearly independent of temperature in the 450 - 723 K range which is ascribed to the dynamic nature of Ag/Cu cations in the rock salt phase where the itinerant cations suppress the phonon mean free path close to a temperature-independent limit of the order of inter-atomic spacing. Despite the glass-like low κ_L, all the samples maintain relatively high electrical conductivity (Figure 1.4a) and carrier mobility (Table 1.1) typical of semiconductors due to crystalline conduits for charge carriers provided by the rigid anion sublattice, thus resembling a 'PGEC'.

Hexagonal AgCuTe exhibits extremely low κ_L near room-temperature although its cations are localized (*i.e.*, not superionic). To get further insight, we have measured the heat capacity of AgCuTe at low temperatures (2 - 30 K).

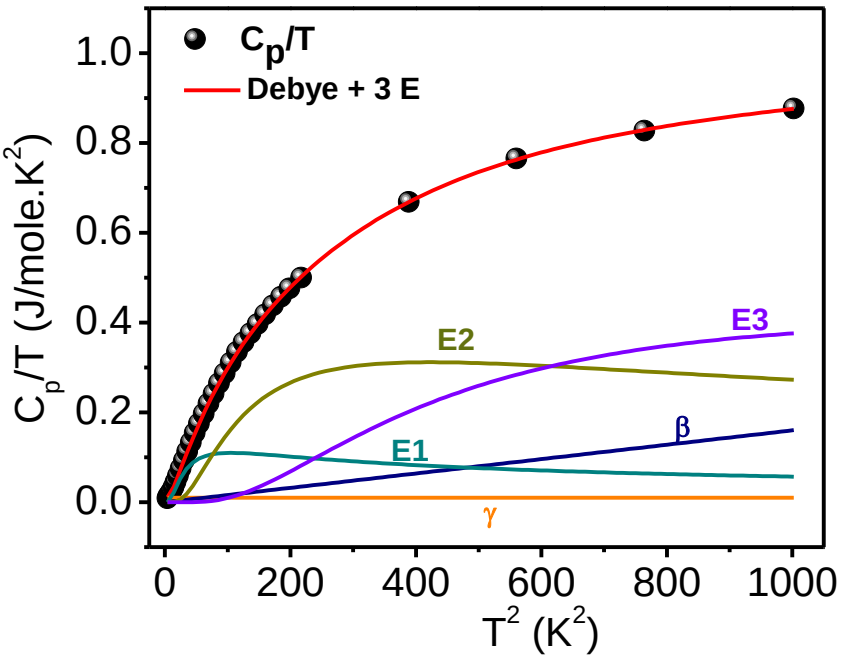

Figure 1.8 *C_p/T vs T^2 plot in 2 – 30 K range. The solid line is calculated using the combined Debye-Einstein model. The individual contributions from electronic (γ), Debye (β) and the three Einstein terms (E1, E2, E3) are also plotted.*

The plot of C_p/T *vs.* T^2 has been modelled using the combined Debye-Einstein model as (see figure 1.8):[14]

$$\frac{C_p}{T} = \gamma + \beta T^2 + \sum_n \left(A_n (\Theta_{E_n})^2 . \ (T^2)^{-3/2} . \ \frac{e^{\Theta_{E_n}/T}}{\left(e^{\Theta_{E_n}/T} - 1\right)^2} \right) \qquad (1.1)$$

In the above equation, γ corresponds to the electronic contribution and βT^2, to the Debye mode contribution where $\beta = C.(12\pi^4 N_A k_B/5).(\Theta_D)^{-3}$ with N_A, κ_B, θ_D being the Avogadro number, Boltzmann constant and Debye temperature, respectively. The Debye temperature (θ_D) for AgCuTe is estimated to be 179 K from the value of β. The parameter C is given as $C = 1 - \sum_n A_n/(3NR)$, where N is the number of atoms per formula unit and R, the gas constant. The third term corresponds to the contribution of Einstein modes where A_n is the pre-factor of the i^{th} mode. C_p of AgCuTe cannot be adequately modelled

with the Debye contribution alone. Three Einstein modes whose characteristic temperatures are estimated from the fits to be 26.52 K (θ_{E1} ~ 18.4 cm^{-1}), 52.98 K (θ_{E2} ~ 36.8 cm^{-1}) and 103.32 K (θ_{E3} ~ 71.8 cm^{-1}) (Table 1.2).

Table 1.2: Parameters obtained by fitting low-temperature heat capacity to the Debye–Einstein model.

Parameters	Debye-Einstein Model
γ /10 $^{-3}$ J mol $^{-1}$ K $^{-2}$	10.08
β /10^{-4} J mol $^{-1}$ K $^{-2}$	1.614
ΘE_1 (K)	26.52
ΘE_2 (K)	52.98
ΘE_3 (K)	103.32
Debye temperature, Θ_D (K)	179
R^2	0.99997

The Einstein modes represent quasi-localized optical phonon modes arising from the vibrations of weakly bound atoms. In AgCuTe, the Einstein modes arise from the low-frequency vibrations of Ag cations as indicated by our first-principles calculations below. These low-energy optical modes can effectively scatter the heat-carrying acoustic phonons thereby deteriorating the phonon transport of heat.

To get further insight into the observed low κ_L in the low-temperature AgCuTe phase, we have determined its electronic structure and dynamic structure based on first-principles density function theory, DFT. In calculation of the electronic structure of the room-temperature AgCuTe phase, a complex hexagonal structure (*P3m1*) reported by Avilov *et al.* (1976)[28] was used as a model. It has a complex hexagonal structure of AgCuTe phase with 73 atoms per unit cell and featuring an inhomogeneity in the chemical coordination and bonding of constituent atoms (Figure 1.1a). A wide range of bond distances between Ag/Cu and Te ions implies an inhomogeneous bonding strength among these ions (Table 1.3). Visualization of the calculated valence charge density indeed shows the inhomogeneity in bonding in the hexagonal phase with different

coordination environments around Ag/Cu/Te ions across the lattice (Figure 1.9). Such atomic scale heterogeneity in bonding is not conducive to efficient phonon transport.

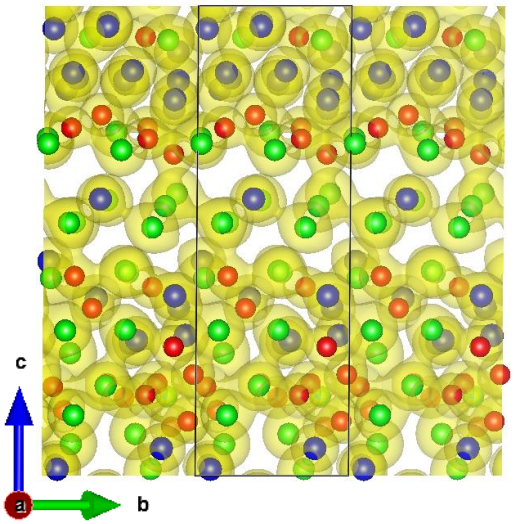

Figure 1.9 *The calculated valence charge density plot for the hexagonal AgCuTe phase with strong dexterity in chemical bonding. (Cu: red, Ag: blue and Te: green).*

Table 1.3: Bond distances between different Ag/Cu and Te ions in hexagonal AgCuTe structure.

Cu-Te bond	Bond length (Å)	Ag-Te bond	Bond length (Å)
Cu10-Te8	2.805	Ag9-Te10	2.648
Cu11-Te8	2.603	Ag8-Te9	2.647
Cu10-Te6	2.083	Ag6-Te9	2.712
Cu9-Te7	2.324	Ag5-Te7	2.594
Cu9-Te5	2.201	Ag1-Te1	2.509
Cu9-Te4	2.767	Ag2-Te2	2.387
Cu2-Te1	2.867	Ag3-Te4	2.352
Cu1-Te2	2.604		
Cu7-Te4	2.768		
Cu3-Te1	2.690		
Cu2-Te2	2.746		
Cu5-Te2	2.682		
Cu4-Te3	2.391		

The calculated phonon density of states (Ph-DOS) of the hexagonal phase reveals unusually many "soft' vibrational modes with frequencies lower than 50 cm^{-1} (Figure 1.10a).

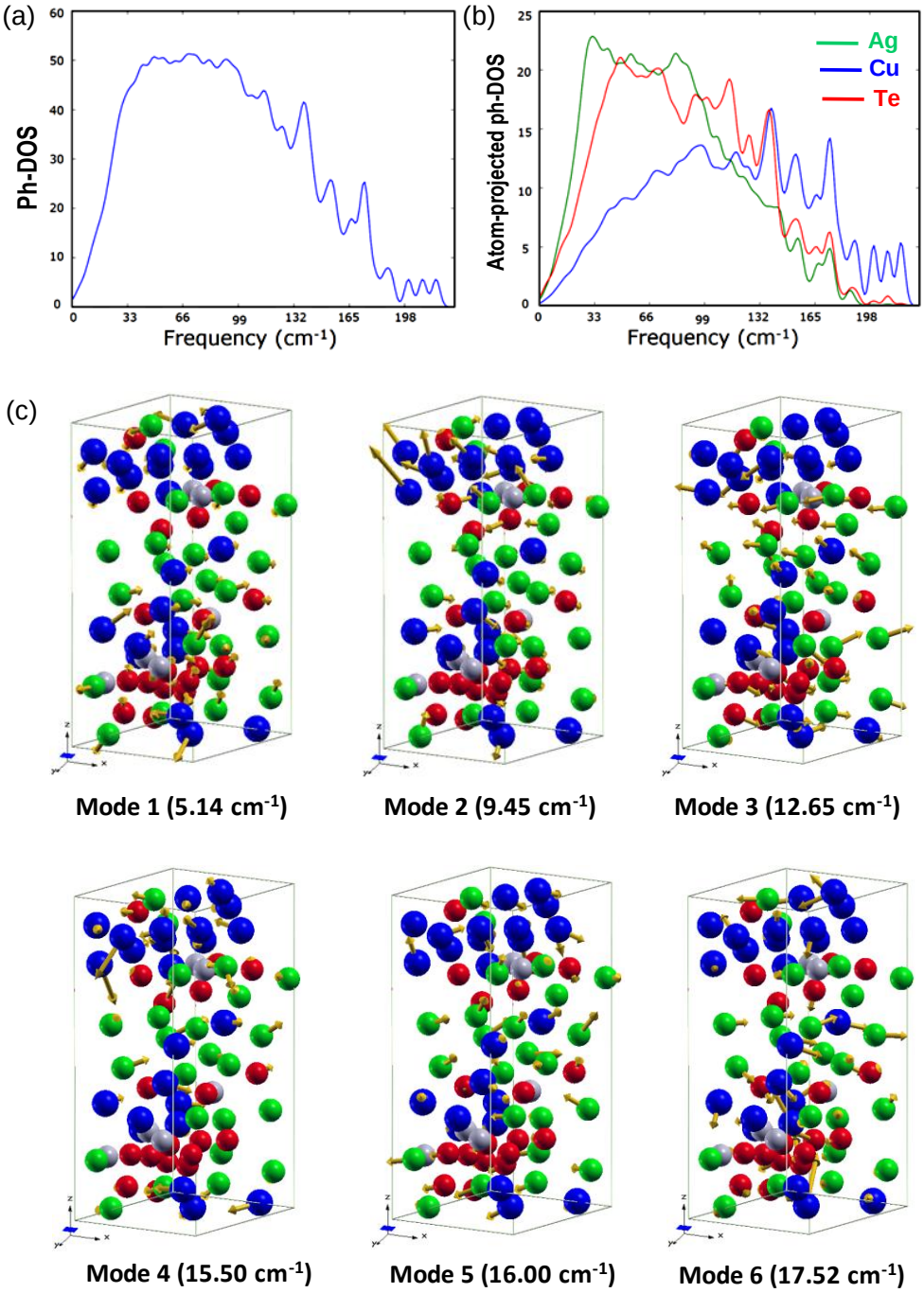

Figure 1.10 *(a) Zone centre phonon density of states, (b) atom projected phonon density of states and (c) visualization of soft vibration modes of hexagonal AgCuTe (Ag: blue, Cu: red, Te: green and Vacancy: light gray).*

These soft modes are optical phonons, which do not directly contribute to heat-transport. The atom-projected phonon DOS in Figure 1.10b shows dominant contributions from Ag and Te ionic displacements to modes in the low-frequency region. Visualization of the Eigen modes displacements of a few of the low-frequency modes at the Brillouin zone-centre reveals dominant vibrations of Ag followed by Te ions (Figure 1.10c). The amplitudes of vibration of Ag cations near the vacancies in the hexagonal structure are especially large (see Figure 1.10c). These low-lying optical phonon modes contribute to the experimental C_p at low-temperatures. In contrast, Cu atoms with higher coordination numbers contribute to phonon modes with higher frequency.

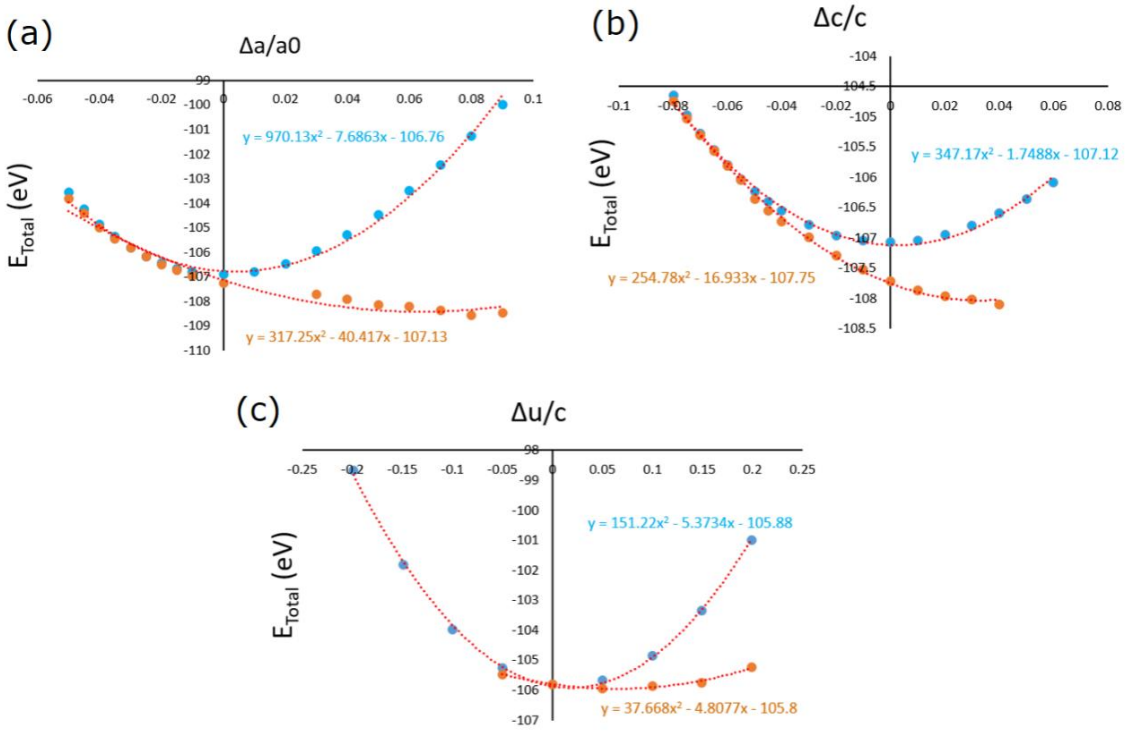

Figure 1.11 *Effect of longitudinal strain along (a) a-direction and (b) c-direction and of shear strain (c) on the energy of hexagonal AgCuTe. (Blue: unrelaxed structure, Orange: relaxed structure, Red: trend line)*

During thermal transport, heat energy carried by acoustic modes is dissipating in excitation of these optical modes. The cumulative effect can be seen through renormalization of sound velocity or elastic constants due to coupling of optical and acoustic phonons. The third order optical phonon-strain coupling is relevant to the

scattering of acoustic phonons by optic phonons. It reduces the elastic modulus effectively to

$$C_{relaxed} = C_{unrelaxed} - \sum_{\mu} \frac{L_{\mu}^2}{M_{\mu}\omega_{\mu}^2} \tag{1.2}$$

where, L_{μ} is the coupling of an optical phonon, μ with strain, ω_{μ} is its frequency and $M\mu$ its effective mass. $C_{unrelaxed}$ is the bare elastic modulus when positions of atoms in the unit cell are frozen during deformation, while $C_{relaxed}$ is a renormalized due to relaxation of atoms to minimize the energy.

For example, we examine two elastic moduli,

$$C_{Longitudinal} = \frac{1}{V}(\partial^2 E)/(\partial \varepsilon_h^2) \tag{1.3}$$

$$C_{Shear} = \frac{1}{4V}(\partial^2 E)/(\partial \varepsilon_s^2) \tag{1.4}$$

where, $\varepsilon_h = \partial a/a_0$ and $\varepsilon_s = \partial a_{\perp}/a_0$ where, a_0 is the lattice parameter and V is the volume of the unit cell. We find strong coupling of optical phonons with strain in the pseudo-hexagonal AgCuTe. We find a reduction in longitudinal elastic constant reduces by 67% (in *a*-direction), and 27% (in *c*-direction) and in the shear elastic modulus decreases by 76% (Figure 1.11). Thus, strong phonon-strain coupling of soft modes in the hexagonal AgCuTe phase is responsible for the extensive phonon scattering, and hence its ultralow κ_L ($\kappa_L = \frac{1}{3}C_v v^2 \tau \; and \; v \sim \sqrt{(C/\rho)}$ where v, τ, C and ρ denote sound velocity, relaxation time, elastic coefficient and density, respectively.

Visualization of the calculated charge density of the high-temperature rocksalt phase of AgCuTe (Figure 1.12a) reveals directional covalent bonds between Te and Ag/Cu cations. Its phonon dispersion exhibits modes with imaginary frequencies besides several soft phonon modes (Figure 1.12b). The electronic structure of rocksalt AgCuTe phase (Figure 1.12d) shows that the highest energy valence band and the lowest energy conduction band touch at the Γ-point.

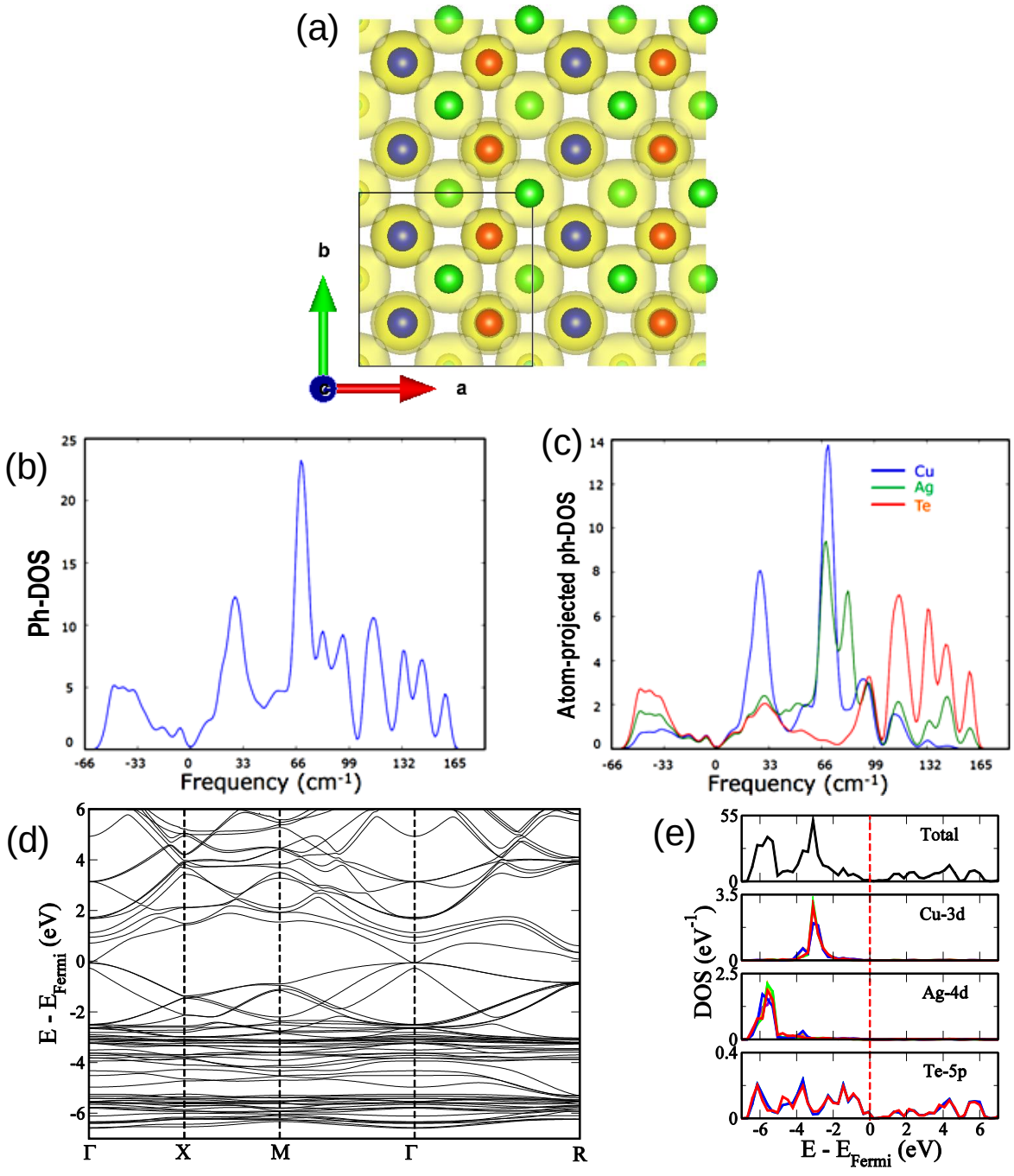

Figure 1.12 *(a) The calculated valence charge density plot for rocksalt AgCuTe phase. (Cu: red, Ag: blue and Te: green). (b) phonon density of states (Ph-DOS), (c) atom projected phonon DOS, (d) electronic band structure and (e) electronic DOS of rocksalt AgCuTe phase.*

From the electronic density of states (Figure 1.12e), it is clear that the states near Fermi level are located of Te-5p bands, while both Cu - 3d and Ag - 4d states are situated ~ 3 eV and ~ 5 eV below the Fermi level. Overlap of Cu - 3d and Ag - 4d states with Te-5p states in energy indicates hybridization and covalency of Cu - Te and Ag - Te bonds in both the phases of AgCuTe.

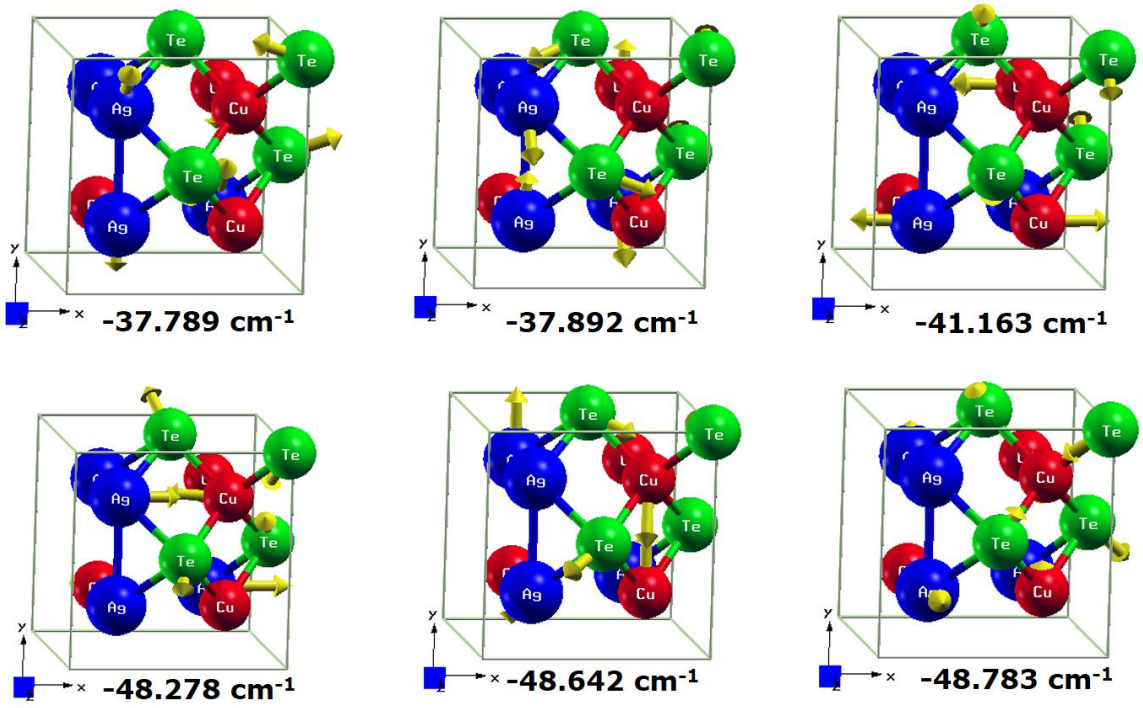

Figure 1.13 *Visualization of negative frequency modes of rocksalt AgCuTe (Cu: red, Ag: blue and Te: green).*

Visualization of these unstable modes (Figure 1.13) shows that they involve rotation of MTe_6 (M = Ag/Cu) octahedral with a primary contribution from Te ions. Phonon DOS (Figure 1.12c) of the rocksalt AgCuTe further shows that low energy modes are primarily constituted of Cu/Ag cationic vibrations.

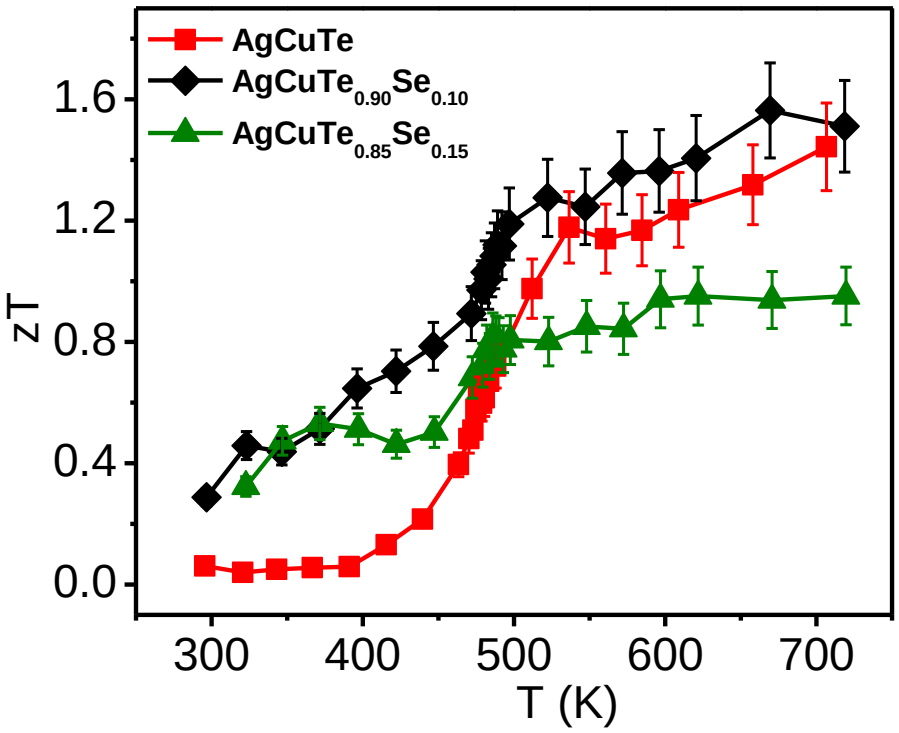

Figure 1.14 *Temperature dependent zT of $AgCuTe_{1-x}Se_x$ samples with 10% error bar.*

Pristine AgCuTe and $AgCuTe_{0.90}Se_{0.10}$ exhibits a high zT_{max} value of 1.45 and 1.6, respectively, at ~ 700 K (Figure 1.14) due to extremely low κ_L coupled with a reasonably high power factor.

1.4 Conclusions

In conclusion, AgCuTe exhibits an ultralow κ_L of 0.35 $Wm^{-1}K^{-1}$ and a high zT of 1.6 at 670 K. A superionic transition from the hexagonal to rocksalt phase of AgCuTe is evident from the temperature dependent XRD, Doppler broadening of PAS and TE properties. The intrinsic cation vacancies render AgCuTe a degenerate semiconductor with high hole-concentration. Alloying Te with Se is found to suppress the cation vacancies and enhance the power factor at elevated temperatures. Although its electrical properties vary significantly across the superionic transition, κ_L remains extremely low throughout the temperature range as a consequence of soft optical phonons and their strong coupling with strain/acoustic modes in the hexagonal phase and a dynamic disorder of cations in the rocksalt phase at elevated temperatures. A combination of low κ_L and reasonably high electrical conductivity and mobilities demonstrates 'PGEC-like' behaviour of AgCuTe.

1.5 References

[1] J. Sootsman, D. Y. Chung, M. G. Kanatzidis, *Angew. Chem. Int. Ed.* **2009**, *48*, 8616.

[2] K. Biswas, J. He, I. D. Blum, C.-I. Wu, T. P. Hogan, D. N. Seidman, V. P. Dravid, M. G. Kanatzidis, *Nature* **2012**, *489*, 414.

[3] B. Poudel, Q. Hao, Y. Ma, Y. Lan, A. Minnich, B. Yu, X. Yan, D. Wang, A. Muto, D. Vashaee, X. Chen, J. Liu, M. S. Dresselhaus, G. Chen, Z. Ren, *Science* **2008**, *320*, 634.

[4] G. Tang, W. Wei, J. Zhang, Y. Li, X. Wang, G. Xu, C. Chang, Z. Wang, Y. Du, L.-D. Zhao, *J. Am. Chem. Soc.* **2016**, *138*, 13647.

[5] S. Lee, K. Esfarjani, T. Luo, J. Zhou, Z. Tian, G. Chen, *Nat. Commun.* **2014**, *5*, 3525.

[6] L.-D. Zhao, S.-H. Lo, Y. Zhang, H. Sun, G. Tan, C. Uher, C. Wolverton, V. P. Dravid, M. G. Kanatzidis, *Nature* **2014**, *508*, 373.

[7] W. Qiu, L. Xi, P. Wei, X. Ke, J. Yang, W. Zhang, *Proc. Natl. Acad. Sci. U.S.A.* **2014**, *111*, 15031.

[8] S. N. Guin, A. Chatterjee, D. S. Negi, R. Datta, K. Biswas, *Energy Environ. Sci.* **2013**, *6*, 2603.

[9] M. D. Nielsen, V. Ozolins, J. P. Heremans, *Energy Environ. Sci.* **2013**, *6*, 570.

[10] X. Shi, J. Yang, J. R. Salvador, M. Chi, J. Y. Cho, H. Wang, S. Bai, J. Yang, W. Zhang, L. Chen, *J. Am. Chem. Soc.* **2011**, *133*, 7837.

[11] T. Takabatake, K. Suekuni, T. Nakayama, E. Kaneshita, *Rev. Mod. Phys.* **2014**, *86*, 669.

[12] G. Tan, S. Hao, J. Zhao, C. Wolverton, M. G. Kanatzidis, *J. Am. Chem. Soc.* **2017**, *139*, 6467.

[13] H. Lin, G. Tan, J.-N. Shen, S. Hao, L.-M. Wu, N. Calta, C. Malliakas, S. Wang, C. Uher, C. Wolverton, M. G. Kanatzidis, *Angew. Chem. Int. Ed.* **2016**, *55*, 11431.

[14] M. K. Jana, K. Pal, A. Warankar, P. Mandal, U. V. Waghmare, K. Biswas, *J. Am. Chem. Soc.* **2017**, *139*, 4350.

[15] M. K. Jana, K. Pal, U. V. Waghmare, K. Biswas, *Angew. Chem. Int. Ed.* **2016**, *55*, 7792.

[16] H. Liu, X. Shi, F. Xu, L. Zhang, W. Zhang, L. Chen, Q. Li, C. Uher, T. Day, G. J. Snyder, *Nat. Mater.* **2012**, *11*, 422.

[17] H. Liu, X. Yuan, P. Lu, X. Shi, F. Xu, Y. He, Y. Tang, S. Bai, W. Zhang, L. Chen, Y. Lin, L. Shi, H. Lin, X. Gao, X. Zhang, H. Chi, C. Uher, *Adv. Mater.* **2013**, *25*, 6607.

[18] A. A. Olvera, N. A. Moroz, P. Sahoo, P. Ren, T. P. Bailey, A. A. Page, C. Uher, P. F. P. Poudeu, *Energy Environ. Sci.* **2017**, *10*, 1668.

[19] S. N. Guin, J. Pan, A. Bhowmik, D. Sanyal, U. V. Waghmare, K. Biswas, *J. Am. Chem. Soc.* **2014**, *136*, 12712.

[20] S. Ishiwata, Y. Shiomi, J. S. Lee, M. S. Bahramy, T. Suzuki, M. Uchida, R. Arita, Y. Taguchi, Y. Tokura, *Nat. Mater.* **2013**, *12*, 512.
[21] G. A. Slack, *CRC Handbook of Thermoelectrics (ed. Rowe, D. M.)* **1995**, 407.
[22] A. Sarkar, C. Mahuya, S. K. Ray, D. Bhowmick, D. Sanyal, *J. Phys.: Condens. Matter.* **2011**, *23*, 155801.
[23] P. P. N. J. Kirkegaard, M. Eldrup, *Report of Riso National Lab (Riso-M-2740)* **1989**.
[24] H. S. D. Luitel, N. Gogurla, A. Sarkar, *J. Mat. Sci.* **2017**, *52*, 7615.
[25] G. Kresse, J. Furthmuller, *Phys. Rev. B* **1996**, *54*, 11169.
[26] J. P. Perdew, K. Burke, M. Ernzerhof, *Phys. Rev. Lett.* **1996**, *77*, 3865.
[27] A. S. M. Agaev M. I., and Zargarova M. I. , *Dokl. Akad. Nauk Az. SSR* **1971**, *27*, 15.
[28] A. S. B. Avilov, R.V.;Pinsker, T.G, *Sov. Phys., Crystallography* **1976**, *21*, 45.
[29] I. R. S. Nuriev, E.Yu.; Nabiev, R.N., *Izvestiya Akademii Nauk SSSR, Neorganicheskie Materialy* **1983**, *19*, 1074.
[30] B. Du, H. Li, J. Xu, X. Tang, C. Uher, *Chem. Mater.* **2010**, *22*, 5521.
[31] K. Zhao, A. B. Blichfeld, H. Chen, Q. Song, T. Zhang, C. Zhu, D. Ren, R. Hanus, P. Qiu, B. B. Iversen, F. Xu, G. J. Snyder, X. Shi, L. Chen, *Chem. Mater.* **2017**, *29*, 6367.
[32] J. B. Boyce, B. A. Huberman, *Phys. Rep.* **1979**, *51*, 189.
[33] C. Xiao, X. Qin, J. Zhang, R. An, J. Xu, K. Li, B. Cao, J. Yang, B. Ye, Y. Xie, *J. Am. Chem. Soc.* **2012**, *134*, 18460.
[34] K. Stephen Dongmin, A. D. Sergey, A. Umut, A. Maxim, S. Andrew, G. J. Snyder, *New J. Phys.* **2016**, *18*, 013024.
[35] J. Capps, F. Drymiotis, S. Lindsey, T. M. Tritt, *Phil. Mag. Lett.* **2010**, *90*, 677.
[36] Y. He, T. Zhang, X. Shi, S.-H. Wei, L. Chen, *NPG Asia Mater.* **2015**, *7*, e210.

Chapter 2

High Thermoelectric Figure of Merit and Enhanced Mechanical Stability of *p*-type $AgSb_{1-x}Zn_xTe_2$

Chapter 2

High Thermoelectric Figure of Merit and Enhanced Mechanical Stability of *p*-type $AgSb_{1-x}Zn_xTe_2$[†]

Summary

High performance thermoelectric materials are desirable in the lower-medium temperature range (450 - 650 K) for low grade waste heat recovery. In this chapter, we report a thermoelectric figure of merit (zT) of 1.9 at 585 K in p-type $AgSb_{1-x}Zn_xTe_2$, which is the highest value measured among the p-type materials in 450 - 650 K range. A high average thermoelectric figure of merit (zT_{avg}) of 1.3 is achieved in $AgSb_{0.96}Zn_{0.04}Te_2$. Moreover, $AgSb_{1-x}Zn_xTe_2$ sample exhibits hardness value of ~ 6.3 GPa (nano-indentation), which is significantly higher than that of the pristine $AgSbTe_2$. Substitution of Zn in $AgSbTe_2$ suppresses the formation of intrinsic Ag_2Te impurity phases, which indeed increases the thermal and mechanical stability. The lattice thermal conductivity for $AgSb_{1-x}Zn_xTe_2$ samples are reasonably reduced compared to the pristine $AgSbTe_2$ due to the significant solid solution point defect phonon scattering. Aliovalent Zn^{2+} doping in Sb^{3+} site in $AgSbTe_2$ increases the p-type carrier concentration, which boosts the electrical conductivity of $AgSb_{1-x}Zn_xTe_2$.

[†]*Paper based on this study has been published in ACS Energy Lett.* ***2017****, 2, 349.*

2.1 Introduction

$AgSbTe_2$ is considered as promising thermoelectric material for power generation application in the temperature range of 400 – 700 K due to its glass-like anomalously low thermal conductivity (0.6 - 0.7 $Wm^{-1}K^{-1}$).[1-5] At room temperature, $AgSbTe_2$ crystallizes in to disordered rock-salt structure (space group, *Fm-3m*) where Ag and Sb randomly occupy the cation site and Te occupies the anion site.[6] Previous studies indicate that strong anharmonicity in Sb-Te bonds is responsible for ultralow thermal conductivity, which is mainly caused due to the existence of stereochemically active $5s^2$ lone pair on Sb.[3] Moreover, narrow band gap semiconductor, $AgSbTe_2$, exhibits *p*-type conduction with high thermopower due to the presence of multiple flat valence band valleys.[7] Notably, alloys of $AgSbTe_2$ with PbTe rich $[(AgSbTe_2)_{1-x}(PbTe)_x$ (LAST)][8] and GeTe rich $[(AgSbTe_2)_{1-x}(GeTe)_x$ (TAGS)][9] phases are famous for their excellent thermoelectric performance.

Thermoelectric materials must be thermodynamically stable and mechanically robust for long-term applications. Despite of its high thermoelectric performances, thermodynamic stability of $AgSbTe_2$ still remains a challenging issue since its discovery.[10-11] Detailed studies on pseudo-binary Sb_2Te_3 - Ag_2Te and Sb_2Te_3 - Ag_2Te - Te phase diagrams confirm the non existence of thermodynamically stable compound with the exact stoichiometric composition of $AgSbTe_2$.[12-14] A stable cubic phase with a wide range of compositions ($Ag_{1-x}Sb_{1+x}Te_{2+x}$; x = 0.06 - 0.28) is the only ternary compound in the Sb_2Te_3 - Ag_2Te phase diagram. This nonstoichiometric $AgSbTe_2$ slowly decomposes into solid solution of Ag in Sb_2Te_3 and solid solution of Sb in β - Ag_2Te at 630 K.[12-15] Moreover, several groups have reported that presence of small amount of α - Ag_2Te as second phase in $AgSbTe_2$ at room temperature despite of their different synthesis procedures such as melting and slow cooling,[10,11] mechanical alloying[16] and zone melting,[17] which indicates that matrix is always Sb rich (Ag poor) in $AgSbTe_2$. Ag_2Te impurity may have negative impact on the thermoelectric properties of $AgSbTe_2$ because of its *n* - type conduction and structural phase transition at ~ 425 K.[13] Thus, blocking the formation of Ag_2Te impurity during synthesis of $AgSbTe_2$ is important for optimization of the thermoelectric and mechanical properties of $AgSbTe_2$. Another major drawback of $AgSbTe_2$ compound is its low electrical conductivity caused by the heavy hole carriers,

which is due to the effect of flat valence band maximum. Nevertheless, enhancement in the electrical conductivity has been achieved in Na doped non-stoichiometric $AgSbTe_2$, which exhibited a zT of 1.5 at 570 K.[5]

Cubic $AgSbSe_2$, an analogue of $AgSbTe_2$ is thermodynamically stable below its melting point and shows promising thermoelectric properties for practical application.[18-20] Recently, Du *et al.* have shown that partial substitution of Se in place of Te in $AgSbTe_2$ suppresses the formation of impurity phases such as Ag_2Te and $Ag_{0.35}Sb_{0.09}Te_{0.56}$.[13] A zT value of ~ 1.35 at 565 K is reported for the nominal composition of $AgSbTe_{1.98}Se_{0.02}$.[13] Recently, In doping in $AgSbTe_2$ resulted a zT of 1.35 at 650 K.[21] Moreover, Zn doping in $AgSbSe_2$ boosts the thermoelectric performance through synergistic effect of nanostructuring, carrier engineering and bond anharmonicity.[19] Motivated by the above fact, we have studied the effect of Zn doping (x= 0 - 6 mol%) on thermoelectric properties of $AgSbTe_2$.

In this chapter, we report a remarkably high thermoelectric figure of merit, *zT*, of 1.9 at 585 K in *p*-type $AgSb_{1-x}Zn_xTe_2$ (x = 0 - 0.06) ingots *via* simultaneous carrier engineering and reduction of lattice thermal conductivity. The *z*T of 1.9 at 585 K in $AgSb_{0.96}Zn_{0.04}Te_2$ is the highest *z*T value measured for *p*-type materials so far in the lower-medium temperature range (450 - 650 K). Importantly, $AgSb_{0.96}Zn_{0.04}Te_2$ possesses an average thermoelectric figure of merit, zT_{avg}, value of ~ 1.3 in the 300 - 600 K range, which is highest value so far measured for $AgSbTe_2$ based compounds. Since Zn^{2+} doping in place of Sb^{3+} in $AgSbTe_2$ acts as an acceptor, it increases *p*-type carrier concentration and thereby enhances the electrical conductivity. Increased *p*-type carriers in $AgSb_{1-x}Zn_xTe_2$ easily access the multiple flat valence band valleys in $AgSbTe_2$, which results in large Seebeck coefficient. In addition, reduction in lattice thermal conductivity has observed upon Zn doping in $AgSbTe_2$ due to phonon scattering due to solid solution point defects. Interestingly, substitution of Zn at Sb site in $AgSbTe_2$ suppresses the unavoidable formation of Ag_2Te, by increasing the solubility of Ag_2Te in $AgSbTe_2$, which indeed increases the thermal and mechanical stability of $AgSbTe_2$. The maximum hardness value of ~ 6.3 GPa was measured by nano-indentation method for $AgSb_{0.96}Zn_{0.04}Te_2$ sample, which is significantly higher than that of the pristine $AgSbTe_2$.

2.2 Methods

2.2.1 Reagents

Silver (Ag, Aldrich 99.999%), antimony (Sb, Alfa Aesar 99.9999%), zinc (Zn, Alfa Aesar 99.999%) and tellurium (Te, Alfa Aesar 99.999+ %) were used for synthesis without further purification.

2.2.2 Synthesis

High quality crystalline ingots (~ 6 g) of $AgSb_{1-x}Zn_xTe_2$ (x = 0, 0.02, 0.04 and 0.06) were synthesized by mixing appropriate ratios of high purity starting materials of Ag, Sb, Zn and Te in a quartz tube. The tubes were sealed under vacuum (10^{-5} Torr) and slowly heated to 673 K over 12 h, then heated up to 1123 K in 4 h, annealed for 10 h and then slowly cool down to room temperature over a period of 20 h.

2.2.3 Powder X-ray diffraction

Powder X-ray diffraction patterns for finely ground samples were recorded at room-temperature using Cu K_α (λ = 1.5406 Å) radiation on a Bruker D8 diffractometer.

2.2.4 Differential scanning calorimetry

DSC data were measured by DSC Q2000 with a heating rate of 5 K/min between 290 K and 660 K in N_2 atmosphere.

2.2.5 Field emission scanning electron microscopy

FESEM experiments were performed using NOVA NANO SEM 600 (FEI, Germany) operated at 15 KV.

2.2.6 Electrical transport

Electrical conductivity and Seebeck coefficients were measured simultaneously under He-atmosphere from room-temperature to 635 K using the commercial ULVAC-RIKO ZEM-3 instrument. Rectangular specimens cut and polished from ingots with typical dimensions of ca. 2×2×8 mm^3 were used for the measurements. The longer direction of the sample coincides with the ingot's growth direction.

2.2.7 Hall measurement

Carrier concentrations were determined using Hall coefficient measurements at room temperature with a PPMS system. Four-contact Hall-bar geometry was used for the measurement. At 300 K, we have estimated the carrier concentration, *n*, from the formula: $n = 1/eR_H$, where e is the electronic charge and R_H is Hall coefficient.

2.2.8 Thermal conductivity

Thermal diffusivity, D, was measured in the 300 − 650 K range by a laser flash diffusivity method in a commercial Netzsch LFA-457 instrument. Coins with 8 mm diameter and 2 mm thickness were used for the measurements. Heat capacity, C_p, in the 300 - 723 K range was indirectly derived using a standard sample (pyroceram) in LFA-457, which is in good agreement with the Dulong-Petit value. The total thermal conductivity, κ_{total}, was calculated using the formula $\kappa_{total} = D \times Cp \times \rho$, where ρ is the density of the sample (~ 97%).

2.2.9 Nanoindentation

The mechanical properties, reduced elastic modules and hardness of $AgSb_{1-x}Zn_xTe_2$ samples were measured by means of nanoindentation experiment using Hysitron TI 900 TriboIndenter. Nanoindentation was performed on the attached Berkocich three-sized pyramidal diamond tip. Before indentation, pellets of all the samples were polished with a diamond paste to obtain a mirror-like surface with a roughness of μm level. The constant load of ~ 5 mN was applied to the samples and the holding time was kept to be 10s during the indentation. The hardness (*H*) and reduced modulus (E_r) values were derived from the load (*P*) *vs*. displacement (*h*) curve of unloading region of applied load. In particular, hardness value was calculated from the equation, $H = P_{max}/A$, where P_{max} is maximum indentation load and *A* is projected area of hardness impression.

2.3 Results & Discussion

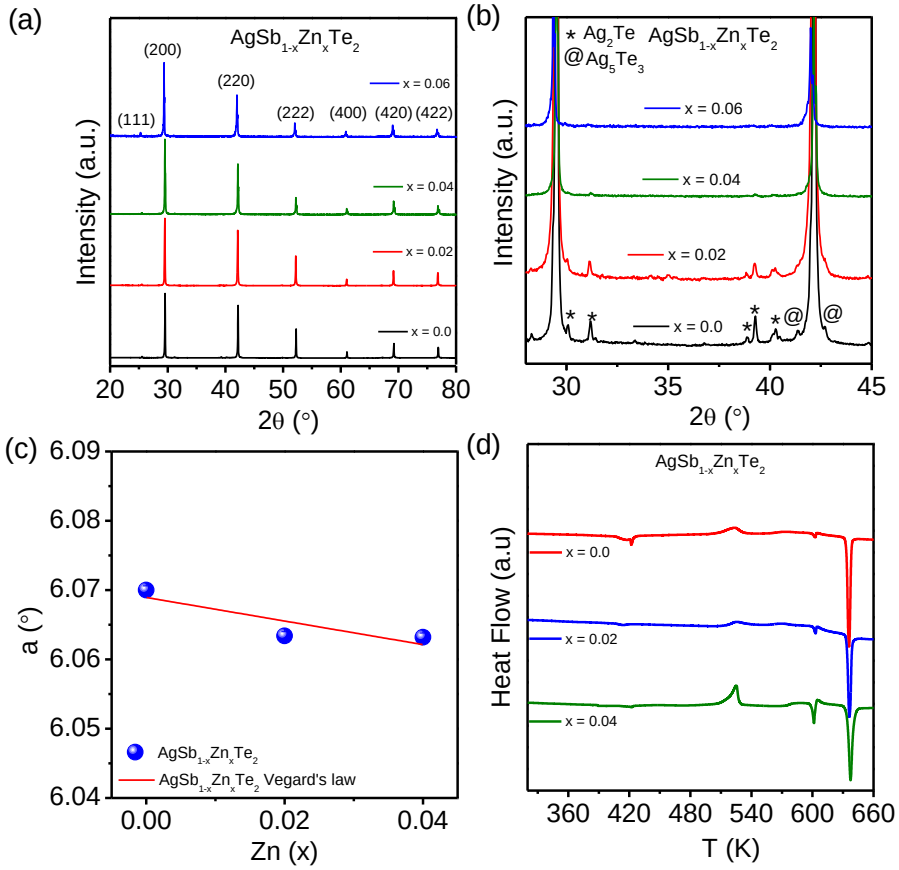

Figure 2.1 *(a) Powder X-ray diffraction pattern and (b) Zoomed version (2θ =28-45 ^{0}) of PXRD pattern of $AgSb_{1-x}Zn_xTe_2$ (x = 0.0, 0.02 0.04, 0.06) samples. (c) Variation of lattice parameter as a function of Zn (x) concentration in $AgSb_{1-x}Zn_xTe_2$ (x = 0 - 0.06) and (d) DSC curves for $AgSb_{1-x}Zn_xTe_2$ (x = 0.0, 0.02, 0.04) samples.*

Powder X-ray diffraction (PXRD) pattern of $AgSb_{1-x}Zn_xTe_2$ (x = 0, 0.02, 0.04, 0.06) samples could be indexed based on cubic $AgSbTe_2$ structure (space group, *Fm-3m*) (Figure 2.1a). Careful analysis of PXRD data for the compositions of x = 0 and x = 0.02 shows the weak diffraction peaks of Ag_2Te which is consistent with the previously reported literature (Figure 2.1b).[2,11,13] Interestingly, with the addition of Zn (x = 0 - 6 mol%) in $AgSbTe_2$, impurity peaks corresponding to Ag_2Te become weaker and finally disappear with higher concentration of Zn (Figure 2.1b). This suggests that substitution of Sb with Zn in $AgSbTe_2$ suppresses the formation of Ag_2Te phase. The lattice parameter of $AgSb_{1-x}Zn_xTe_2$ depends linearly on the concentration of Zn which is consistent with solid solution Vegard's law (Figure 2.1c).

The DSC curves for $AgSb_{1-x}Zn_xTe_2$ (x = 0, 0.02, 0.04) samples are presented in Figure 2.1d. A small endothermic peak observed around 425 K is associated with α - β structural transition of Ag_2Te for the pristine $AgSbTe_2$ and $AgSb_{0.98}Zn_{0.02}Te_2$. Transition due to Ag_2Te disappears completely for the composition of $x \geq 0.04$, which also confirms the blocking of Ag_2Te formation on Zn doping in $AgSbTe_2$. The exothermic peak around 510 K in DSC curve is responsible for the appearance of unstable phase Sb_7Te, which is earlier observed in Cu and Mn doped $AgSbTe_2$ sample.[22,23] Additionally, one endothermic peak around 602 K is observed for all the samples that correspond to the presence of Ag_5Te_3.[14] The DSC curves show the presence of the large endothermic peak at about 635 K which is corresponding to the decomposition of $AgSbTe_2$ into Ag_2Te and Sb_2Te_3.[14,15] This decomposition limits the thermoelectric studies of $AgSbTe_2$ in the 300 - 600 K range and here, we have focused our thermoelectric measurement in the same temperature range.

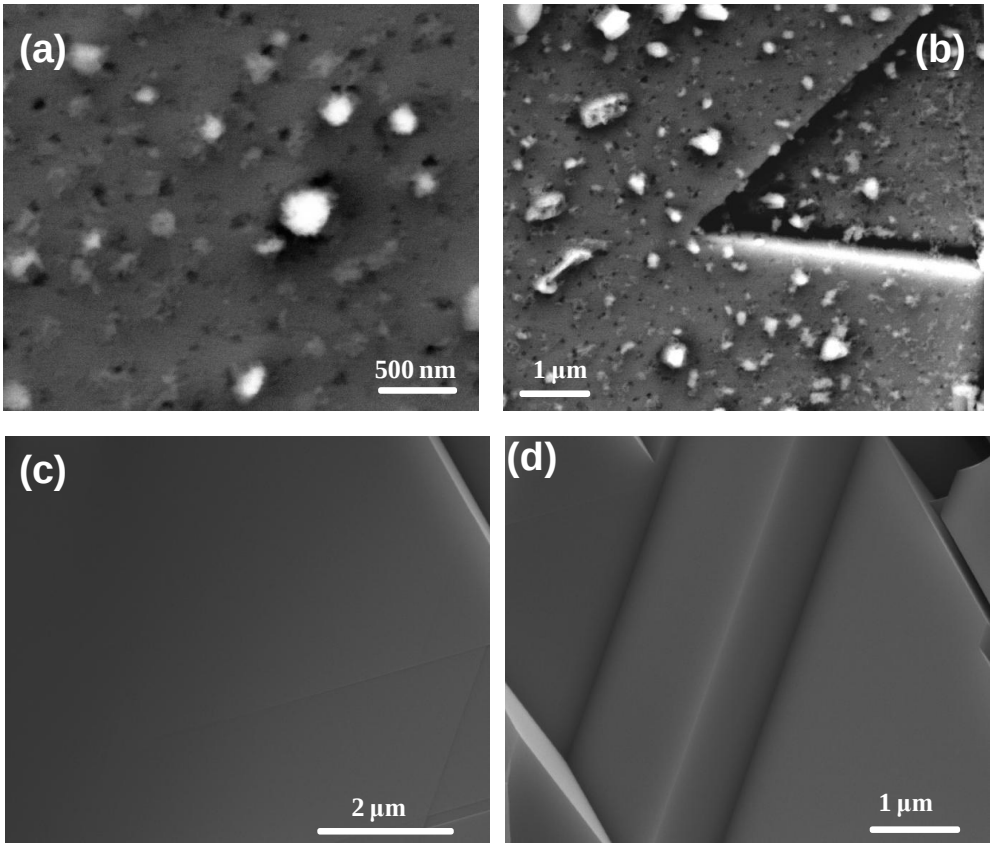

Figure 2.2 *Backscattered electron images taken during FESEM for (a - b) pristine $AgSbTe_2$ and (c - d) $AgSb_{0.96}Zb_{0.04}Te_2$ samples.*

To understand the surface morphology and microstructure compositions, back-scattered electron imaging (BSE) are performed during FESEM measurement. Figure 2.2 shows BSE - FESEM micrograph of $AgSbTe_2$ (a - b) and $AgSb_{0.96}Zn_{0.04}Te_2$ (c - d) samples. For pristine $AgSbTe_2$ sample, we have observed nano-precipitates with lighter contrast with respect to dark contrast $AgSbTe_2$ matrix. The light contrast nanoprecipitates observed in BSE-FESEM are α - Ag_2Te. Substitution of Zn in $AgSbTe_2$ suppresses the formation of Ag_2Te in matrix, thus we do not see any nanoprecipitates in $AgSb_{0.96}Zn_{0.04}Te_2$ (Figure 2.2c and d). We have prepared ingots by melt-cooling synthesis route. In the cooling process, Ag_2Te with higher melting point solidifies and slowly grows into microscale precipitates in $AgSbTe_2$ matrix, resulting inhomogeneous multiphase material. With addition of Zn, concentration of Ag_2Te decreases which is similar to Se doped $AgSbTe_2$ sample where, Se helps to reduce Ag_2Te phase.[13] Actually, Zn increases the solubility limit of Ag_2Te in $AgSbTe_2$ matrix because Ag_2Te form solid solution with ZnTe in lower concentration range. Similar behaviour is observed in GeTe, where 3 mol % Bi_2Te_3 increases the solubility limit of Pb in GeTe.[24]

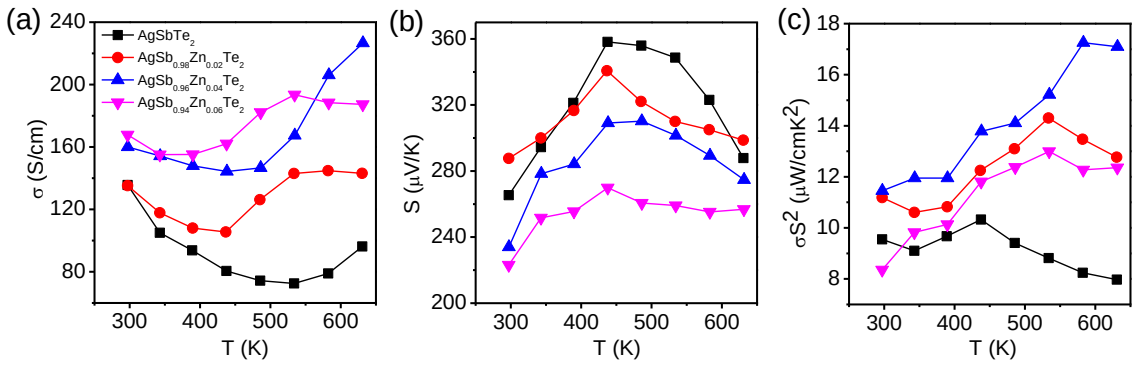

Figure 2.3 *Temperature dependent (a) electrical conductivity (σ), (b) Seebeck coefficient (S) and (c) power factor (σS^2) for $AgSb_{1-x}Zn_xTe_2$ (x = 0 - 0.06) samples.*

Figure 2.3a represents the temperature dependence of electrical conductivity (σ) for $AgSb_{1-x}Zn_xTe_2$ (x = 0 - 0.06) samples in the 300 – 635 K range. Aliovalent substitution of Zn^{2+} at Sb^{3+} site in $AgSbTe_2$ increases the σ from ~ 136 S/cm for pristine $AgSbTe_2$ to ~ 160 S/cm for $AgSb_{0.96}Zn_{0.04}Te_2$ at 300 K. With the increase in temperature, electrical conductivity of $AgSb_{1-x}Zn_xTe_2$ passes through minima, and then starts to increase at high temperature, which is due to onset of bipolar conduction in narrow band gap semiconductor. Typically, $AgSb_{0.96}Zn_{0.04}Te_2$ sample exhibits σ value of ~ 160 S/cm at

room temperature, which decreases to ~145 S/cm at 475 K and finally increases to ~ 227 S/cm at 632 K. With addition of Zn (4 - 6 mol%) in $AgSbTe_2$ the concentration of Ag_2Te decreases significantly, but small amount of Sb_7Te and Ag_5Te_3 phases still exist in $AgSbTe_2$ which can be shown from the DSC plot (Figure 2.1d) of $AgSb_{1-x}Zn_xTe_2$.

To understand the effect of Zn doping on electrical transport behaviour in $AgSbTe_2$ system, Hall measurement was carried out to estimate the carrier concentration (n) and carrier mobility (μ) of $AgSb_{1-x}Zn_xTe_2$ samples, which are summarized in Table 2.1. Doping of Zn in $AgSbTe_2$ increases the *p*-type carrier concentration from ~ 1.14 x 10^{19} cm^{-3} for pristine $AgSbTe_2$ to ~ 4.8 x 10^{19} cm^{-3} for $AgSb_{0.96}Zn_{0.04}Te_2$ sample. This indicates that Zn^{2+} dopes at Sb^{3+} sub-lattice and contributes one hole per doping in $AgSbTe_2$. Increase in *p*-type carrier concentration indeed increases the σ in $AgSb_{1-x}Zn_xTe_2$.

Table 2.1: Carrier concentration (n), carrier mobility (μ) and effective mass (m*) of $AgSb_{1-x}Zn_xTe_2$ (x = 0.0, 0.02, 0.04 and 0.06) samples at room temperature.

Sample	***n*** ***(cm^{-3})***	***μ*** ***($cm^2V^1S^{-1}$)***	***m****
$AgSbTe_2$	$1.14X10^{19}$	74	1.32 m_0
$AgSb_{0.98}Zn_{0.02}Te_2$	$2.7X10^{19}$	31	2.82 m_0
$AgSb_{0.96}Zn_{0.04}Te_2$	$4.8X10^{19}$	32.5	2.65 m_0
$AgSb_{0.94}Zn_{0.06}Te_2$	$5.14X10^{19}$	20.4	2.53 m_0

Temperature dependence of Seebeck coefficients (S) of $AgSb_{1-x}Zn_xTe_2$ samples are presented in Figure 2.3b. Positive Seebeck coefficient value indicates *p*-type conduction, which is consistent with the Hall coefficient data. Seebeck value for pristine $AgSbTe_2$ sample is ~ 264 μV/K at room temperature, which increases to ~ 360 μV/K at ~ 438 K. Large Seebeck value of $AgSbTe_2$ is attributed to the presence of flat and multi-valley valence band.[7] Typically, $AgSb_{0.96}Zn_{0.04}Te_2$ sample shows room temperature Seebeck value of ~ 235 μV/K and which increases to ~ 275 μV/K at 610 K. The high S value in $AgSbTe_2$ based compounds is owing to high density of state effective mass (m*). Calculated values of m* for $AgSbTe_2$ and $AgSb_{0.96}Zn_{0.04}Te_2$, samples are 1.32m_0, and 2.65 m_0, respectively (Table 2.1). Similar high m* values have also been observed in case of doped $AgSbSe_2$ and $AgSbTe_2$.[18, 25, 26] The increase in m* value with the increase in Zn

concentration in $AgSbTe_2$ is attributed to increase in *p*-type carriers, which easily accesses the multiple flat valence band valleys of $AgSbTe_2$. Notably, we have also observed that Zn doped samples exhibit relatively low hole mobility (μ) than that of pristine sample due to the presence of heavy holes (Table 2.1).

Figure 2.3c represents the temperature dependent power factors (σS^2) for $AgSb_{1-x}Zn_xTe_2$ samples. Typically, $AgSbTe_2$ exhibits the $S^2\sigma$ value of ~ 9.6 $\mu Wcm^{-1}K^{-2}$ at 300 K, which decreases to ~ 7.9 $\mu Wcm^{-1}K^{-2}$ at 610 K. However, $AgSb_{0.96}Zn_{0.04}Te_2$ sample exhibits the $S^2\sigma$ value of ~ 11.5 $\mu Wcm^{-1}K^{-2}$ at 300 K, which reaches to the maximum value of ~ 17.3 $\mu Wcm^{-1}K^{-2}$ at 585 K.

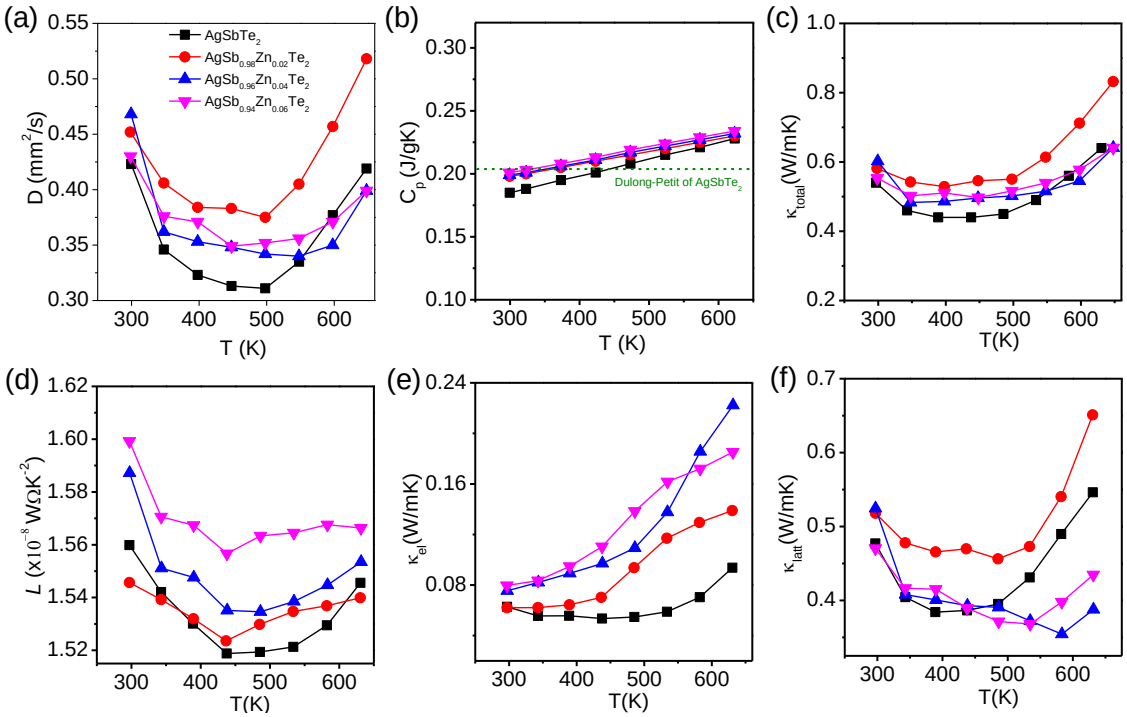

Figure 2.4 *Temperature dependent (a) diffusivity (D), (b) heat capacity (C_p), (c) total thermal conductivity (κ_{total}), (d) Lorenz number (L), (e) electrical thermal conductivity (κ_{el}) and (f) lattice thermal conductivity (κ_{latt}) for $AgSb_{1-x}Zn_xTe_2$ (x = 0-0.06) samples.*

Temperature dependent thermal conductivities of $AgSb_{1-x}Zn_xTe_2$ samples are illustrated in Figure 2.4. The total thermal conductivities, κ_{total} of all the samples were estimated by using the formula, $\kappa_{total} = DC_p\rho$, where, *D* is the thermal diffusivity (Figure 2.4a) and C_p is specific heat (Figure 2.4b) of the sample in the temperature range of 300 -

650 K. At 300 K, κ_{total} for all the samples ranges from 0.55 W/mK to 0.65 W/mK which is concurred with previous result (Figure 2.4c).[1, 2-5] However, with increasing temperature; we observe the enhanced contribution of bipolar thermal conductivity, which is typical of narrow band gap semiconductor. Previous theoretical electronic structure calculation indicates that $AgSbTe_2$ exhibits semi-metallic band structure where conduction band goes below the top of the valence band.[7] It is well-known that most DFT calculations tend to underestimate the band gaps of semiconductors and we cannot exclude the possibility that $AgSbTe_2$ is a semiconductor with a small band gap. Previous diffuse reflectance measurement in $AgSbTe_2$ provided an apparent band gap (0.35 eV), whereas electrical conductivity suggested a band gap of 0.1 eV.[7] These results clearly indicate that $AgSbTe_2$ is narrow band gap semiconductor. Substitution of small amount of Zn at the position of Sb in $AgSbTe_2$ does not change the narrow-band gap nature of $AgSbTe_2$ which can be seen from temperature dependent thermal conductivity which shows similar onset temperature for bipolar thermal conduction compared to pristine $AgSbTe_2$.

κ_{total} of $AgSb_{1-x}Zn_xTe_2$ is mainly governed by its lattice component, κ_{latt}, which corresponds to proliferation of phonons (Figure 2.4f). Temperature dependent κ_{latt} for $AgSb_{1-x}Zn_xTe_2$ samples were estimated by subtracting electronic thermal conductivity ($\kappa_{el} = L\sigma T$ (Figure 2.4e), where, L is Lorenz number which can be obtained based on the fitting of the respective Seebeck values that estimate the reduced chemical potential Figure 2.4d) from κ_{total}. Intrinsically low thermal conductivity of $AgSbTe_2$ arises due to presence of strong bond anharmonicity, resulting from the stereo chemically active $5s^2$ lone pair on Sb, which deforms lattice vibration significantly.[1] At 600 K, $AgSb_{0.96}Zn_{0.04}Te_2$ sample exhibits a κ_{latt} value of ~ 0.36 W/mK, which reaches close to the theoretical minimum limit of the thermal conductivity (~ 0.3 W/mK) in $AgSbTe_2$ calculated using the formula described by Cahill *et al.*[27] Reduction in the lattice thermal conductivity was ~ 26 % in $AgSb_{0.96}Zn_{0.04}Te_2$ when compared to the pristine $AgSbTe_2$. The reason for the decrease in κ_{latt} of $AgSb_{0.96}Zn_{0.04}Te_2$ compared to pristine $AgSbTe_2$ is due to scattering of heat carrying phonons via solid solution point defects.

We have estimated the dimensionless figure of merit (zT) for $AgSb_{1-x}Zn_xTe_2$ (x = 0, 0.02, 0.04, 0.06) samples by using measured value of σ, S and κ in 300 - 635 K temperature range (Figure 2.5a). Although, room temperature zT values of all the samples were comparable, the advantage of addition of Zn is clearly distinguishable at elevated

temperatures. We have obtained a maximum *z*T of ~ 1.9 at ~ 585 K for $AgSb_{0.96}Zn_{0.04}Te_2$, which is significantly higher compared to the pristine $AgSbTe_2$. The reproducibility of such high thermoelectric performance is confirmed by repeating the entire experiments for four times and Figure 2.5b presents the measured data taken from four different $AgSb_{0.96}Zn_{0.04}Te_2$ samples.

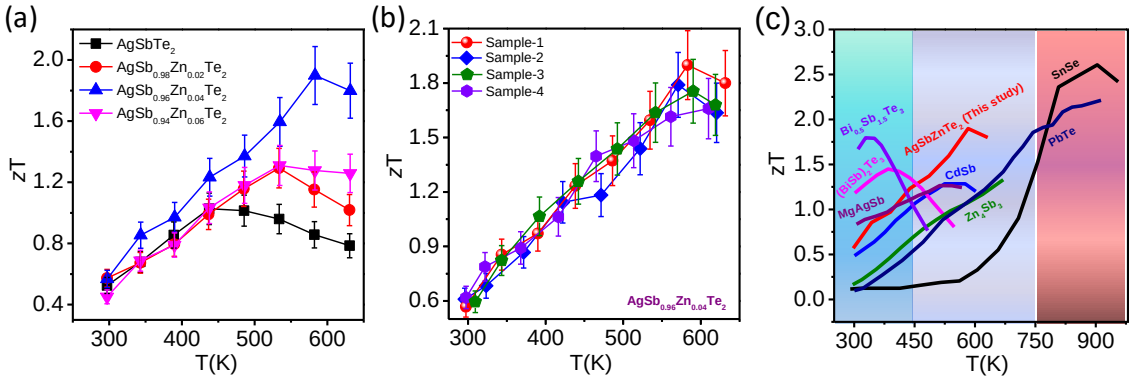

Figure 2.5 *(a) Temperature dependent thermoelectric figure of merit (zT) of* $AgSb_{1-x}Zn_xTe_2$ *(x = 0 - 0.06) samples. (b) Reproducibility of thermoelectric figure of merit (zT) for* $AgSb_{0.96}Zn_{0.04}Te_2$ *sample. For zT measurement, we consider 10 % error bar, which include error in electrical conductivity, Seebeck coefficient and thermal conductivity measurement. (c) the best zT obtained in this study compared with some of the state-of-the-art thermoelectric materials. p-type Zn doped* $AgSbTe_2$ *shows a highest zT in the lower-medium temperature range (450 to 650 K).*

p-type $Bi_{0.5}Sb_{1.5}Te_3$[28,29] based materials exhibit high performance in 300 - 400 K range, whereas *p* - type PbTe[30] and SnSe[31,32] based materials show high performance in 700 - 900 K range (Figure 2.5c). High performance *p*-type materials are desirable in the 450 - 650 K range for lower-medium temperature power generation application. *p*-type MgAgSb,[33] CdSb[34] and Zn_4Sb_3[35] based materials show promising performance in 450 - 650 K range (Figure 2.5a). *p*-type $AgSb_{0.96}Zn_{0.04}Te_2$ exhibits zT of 1.9 at 584 K, which is highest value obtained in the 450 - 650 K among the *p*-type materials. Average *z*T value (zT_{avg}) of $AgSb_{0.96}Zn_{0.04}Te_2$ is estimated to be ~ 1.3 by considering the cold and hot side temperatures of 300 and 600 K, respectively, which is in par with the high performance state of the art thermoelectric materials and other literature reported doped $AgSbTe_2$ samples (Figure 2.6).[30- 33, 36,37]

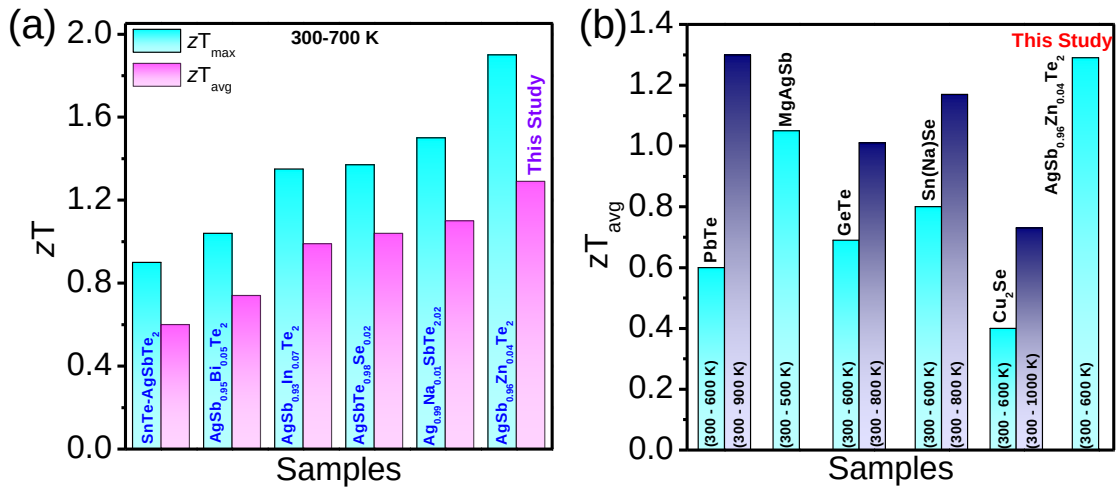

Figure 2.6 *(a) Comparison of zT_{max} and zT_{avg} (300 - 700 K) between $AgSb_{0.96}Zn_{0.04}Te_2$ samples in the present study and other reported $AgSbTe_2$ based materials.. (b) zT_{avg} values for several popular polycrystalline thermoelectric materials compared with the present $AgSb_{1-x}Zn_xTe_2$.*

In addition to high *z*T and high zT_{avg}, material should possess high mechanical stability for device applications. The mechanical properties, reduced elastic modules and hardness, of $AgSb_{1-x}Zn_xTe_2$ samples were measured by nano-indentation method (Table 2.2).

Table 2.2: Reduced elastic modules and hardness values of $AgSb_{1-x}Zn_xTe_2$ (x = 0.0, 0.04) samples.

Sample	Reduced elastic modules, E_r (GPa)	Hardness, H_v (GPa)
$AgSbTe_2$	57	2.54
$AgSb_{0.96}Zn_{0.04}Te_2$	72	6.30

Figure 2.7 shows the load (P) vs. displacement (h) curve of $AgSbTe_2$ and $AgSb_{0.96}Zn_{0.04}Te_2$ samples. Pristine $AgSbTe_2$ sample possesses the hardness value of ~ 2.54 GPa whereas $AgSb_{0.96}Zn_{0.04}Te_2$ sample shows the maximum hardness value of ~ 6.3 GPa. Substitution of Zn in $AgSbTe_2$ increases the hardness of the matrix significantly by increasing the rigidity of the material. Generally, hardness or strength of materials can be defined by dislocation motion in the lattice of matrix material.[38]

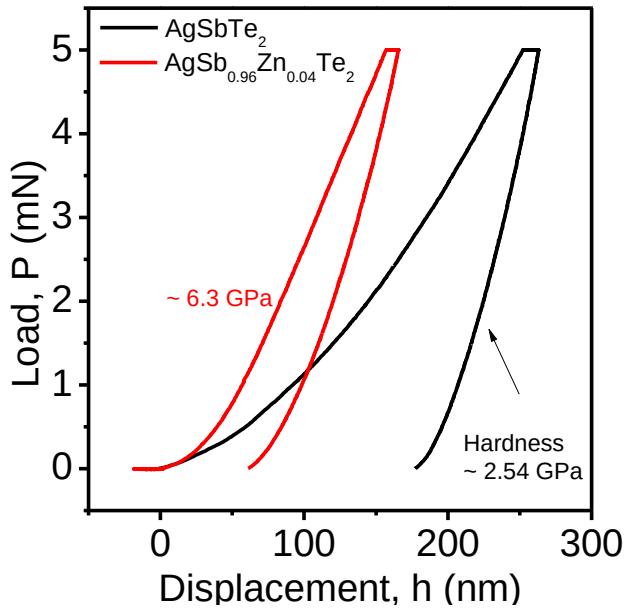

Figure 2.7 *The load (P) vs. displacement (h) curve and hardness value (GPa) of* $AgSb_{1-x}Zn_xTe_2$ *(x = 0.0, 0.04) samples measured by nanoindentation.*

Hardness can be effectively controlled by introducing solid solution, grain boundaries and second phase nanoprecipitates in the matrix, where solute atoms in solid solution, grain boundaries and small nanoprecipitates impede the motion of a dislocation, thereby increases the strength/ hardness of the material.[39] Since Zn doping increases the solubility of Ag_2Te in $AgSbTe_2$ matrix, we anticipate that the increased point defects due to solid solution impede the dislocation propagation, thereby enhances the hardness of the material. This result indicates that Zn doped $AgSbTe_2$ based materials have significantly high mechanical stability, which is useful during large scale device fabrication.

2.4 Conclusions

In conclusion, crystalline ingots of *p* - type $AgSb_{1-x}Zn_xTe_2$ exhibits a zT of 1.9 at 585 K, which is highest in the lower-medium temperature range (450 – 600 K). An average zT_{avg} value of 1.3 is obtained in the 300 - 600 K range for the $AgSb_{0.96}Zn_{0.04}Te_2$ sample, which is comparable to the best polycrystalline thermoelectric materials. Moreover, we have achieved a hardness value of ~ 6.3 GPa for high performance $AgSb_{0.96}Zn_{0.04}Te_2$ sample, which is significantly higher than that of the pristine $AgSbTe_2$. Zn doping in $AgSbTe_2$ suppresses the formation of Ag_2Te impurity phase, which indeed increases the thermal and mechanical stability. Zn^{2+} act as an acceptor dopant in $AgSbTe_2$, thereby enhances the electrical conductivity and power factor. Moreover, the lattice thermal conductivities for $AgSb_{1-x}Zn_xTe_2$ samples were reduced substantially due to the increased phonon scattering resulted from solid solution point defects.

2.5 References

[1] D. T. Morelli, V. Jovovic, J. P. Heremans, *Phys. Rev. Lett.* **2008**, *101*, 035901.

[2] J. Ma, O. Delaire, A. F. May, C. E. Carlton, M. A. McGuire, L. H. VanBebber, D. L. Abernathy, G. Ehlers, T. Hong, A. Huq, W. Tian, V. M. Keppens, Y. Shao-Horn, B. C. Sales, *Nat. Nanotech.* **2013**, *8*, 445.

[3] S. N. Zhang, T. J. Zhu, S. H. Yang, C. Yu, X. B. Zhao, *Acta Mater.* **2010**, *58*, 4160.

[4] M. D. Nielsen, V. Ozolins, J. -P. Heremans, *Energy Environ. Sci.* **2013**, *6*, 570.

[5] B. L. Du, H. Li, X. F. Tang, *J. Alloys Compd.* **2011**, *509*, 2039.

[6] R. W. Armstrong, J. W. Faust, W. A. Tiller, *J. Appl. Phys.* **1960**, *31*, 1954.

[7] K. Hoang, S. D. Mahanti, J. R. Salvador, M. G. Kanatzidis, *Phys. Rev. Lett.* **2007**, *99*, 156403.

[8] K. F. Hsu, S. Loo, F. Guo, W. Chen, J. S. Dyck, C. Uher, T. Hogan, E. K. Polychroniadis, M. G. Kanatzidis, *Science* **2004**, *303*, 818.

[9] Rosi, F. D.; Dismukes, J. P.; Hockings, E. F. *Electr. Eng.* **1960**, *79*, 450.

[10] Wojciechowski, K. T.; Schmidt, M. *Phys. Rev. B* **2009**, *79*, 184202.

[11] J. D. Sugar, D. L. Medlin, *J. Alloys Compd.* **2009**, *478*, 75.

[12] R. M. Ayralmarin, G. Brun, M. Maurin, J. C. Tedenac, *Eur. J. Solid State Inorg. Chem*. **1990**, *27*, 747.

[13] B. Du, H. Li, J. Xu, X. Tang, C. Uher, *Chem. Mater.* **2010**, *22*, 5521.

[14] P. M. Wyzga, K. T. Wojciechowski, *J. Elec. Mater.* **2015**, *45*, 1548.

[15] B. Du, Y. Yan, X. Tang, *J. Elec. Mater.* **2015**, *44*, 2118.

[16] H. Wang, J. Li., M. Zhou, T. Sui, *Appl. Phys. Lett.* **2008**, *93*, 202106.

[17] R. Wolfe, J. Wernick, S. Haszko, *J. Appl. Phys.***1960**, *31*, 1959.

[18] S. N. Guin, A. Chatterjee, Negi, D. S. Negi, R. Datta, K. Biswas, *Energy Environ. Sci.* **2013**, *6*, 2603.

[19] S. N. Guin, D. S. Negi, R. Datta, K. Biswas, *J. Mater. Chem. A* **2014**, *2*, 4324.

[20] S. N. Guin, K. Biswas, *J. Mater. Chem. C* **2015**, *3*, 10415.

[21] R. Mohanraman, R. Sankar, K. M. Boopathi, F.-C. Chou, C.-W. Chu, C.-H. Lee, Y.-Y. Chen, *J. Mater. Chem. A* **2014**, *2*, 2839.

[22] H. Zhang, J. Luo, H. T. Zhu, Q. L. Liu, J. K. Liang, G. H. Rao, *Acta Phys. Sin.* **2012**, *61*, 086101.

[23] Z. He, L. Jun, Z. Hang-Tian, L. Quan-Lin, L. Jing-Kui, L. Jing-Bo, L. Guang-Yao, *Chin. Phys. B* **2012**, *21*, 106101.

[24] D. Wu, L-D. Zhao, S. Hao, Q. Jiang, F. Zheng, J. W. Doak, H. Wu, H. Chi, Y. Gelbstein, C. Uher, C. Wolverton, M. G. Kanatzidis, J. He, *J. Am. Chem. Soc.* **2014**, *136*, 11412.

[25] V. Jovovic, J. P. Heremans, *Phys. Rev. B* **2008**, *77*, 245204

[26] K. Wojciechowski, J. Tobola, M. Schmidt, R. Zybaia, *J. Phys. Chem. Solids* **2008**, *69*, 2748.

[27] D. G. Cahill, S. K. R. O. Watson Pohl, *Phys. Rev. B* **1992**, *46*, 6131.
[28] S. Kim, K. H. Lee, H. A. Mun, H. S. Kim, S.W. Hwang, J. W. Roh, D. J. Yang, W. H. Shin, X. S. Li, Y. H. Lee, G. J. Snyder, S. W. Kim, *Science* **2015**, *348*, 109.
[29] B. Poudel, Q. Hao, Y. Ma, Y. Lan, A. Minnich, B. Yu, X. Yan, D. Wang, A. Muto, D. Vashaee, X. Chen, J. Liu, M. S. Dresselhaus, G. Chen, Z. Ren, *Science* **2008**, *320*, 634.
[30] K. Biswas, J. He, I. D. Blum, C. I. Wu, T. P. Hogan, D. N. Seidman, V. P. Dravid, M. G. Kanatzidis, *Nature* **2012**, *489*, 414.
[31] K. Peng, X. Lu, H. Zhan, S. Hui, X. Tang, G. Wang, J. Dai, C. Uher, G. Wang, X. Zhou, *Energy Environ. Sci.* **2016**, *9*, 454.
[32] L.-D. Zhao, S.-H. Lo, Y. Zhang, H. Sun, G. Tan, C. Uher, C. Wolverton,V. P. Dravid, M. G. Kanatzidis, *Nature* **2014**, *508*, 373.
[33] J. Shuai, H. S. Kim, Y. C. Lan, S. Chen, Y. Liu, H. Z. Zhao, J. H. Sui, Z. F. Ren, *Nano Energy*, **2015**, *11*, 640.
[34] S. Wang, J. Yang, L. Wu, P. Wei, J. Yang, W. Zhang, Y. Grin, *Chem. Mater.* **2015**, *27*, 1071.
[35] G. J. Snyder, M. Christensen, E. Nishibori, T. Caillat, B. B. Iversen, *Nat. Mater.* **2004**, *3*, 458.
[36] S. Perumal, S. Roychowdhury, D. S. Negi, R. Datta, K. Biswas, *Chem. Mater.* **2015**, *27*, 7171.
[37] H. Liu, X. Shi, F. Xu, L. Zhang, W. Zhang, L. Chen, Q. Li, C. Uher, T. Day, G. J. Snyder, *Nat. Mater.* **2012**, *11*, 422.
[38] K. Lu, L. Lu, S. Suresh, *Science* **2009**, *324*, 349.
[39] H. W. Zandbergen, S. J. Andersen, J. Jansen, *Science* **1997**, *277*, 1221.

Chapter 3

Ultrahigh Thermoelectric Figure of Merit, zT> 2.5 in Heavily Doped $AgSbTe_2$

Chapter 3

Ultrahigh Thermoelectric Figure of Merit, zT>2.5 in Heavily Doped $AgSbTe_2$[†]

Summary

The realization of high thermoelectric (TE) performance in the low- to mid-temperature range (300−650 K) is imperative for the waste heat recovery applications. Herein, we report the excellent thermoelectric performance of $AgSbTe_2$ over a wide temperature range (300-600 K). We observed a significant enhancement in the room temperature thermoelectric figure of merit (zT) from 0.6 to 1.6 at 300 Kin polycrystalline $AgSbTe_2$ upon M doping and obtained a maximum zT (zT_{max}) of 2.6 at ~ 573 K in polycrystalline $AgSb_{1-x}M_xTe_2$ Moreover, we obtained a highest device figure of merit (ZT_{dev}) of ~2 in polycrystalline $AgSb_{1-x}M_xTe_2$ which outperforms all other state-of-the-art p-type thermoelectric materials in the 300 – 600 K temperature regimes. The unprecedented thermoelectric performance is attributed to the ultralow thermal conductivity caused by enhanced phonon scattering due to the formation of spontaneous nanoscale superstructure domains with chemical ordering in the cationic sublattice and high-power factor stemming from high electrical conductivity augmented with high Seebeck coefficient resulting from valance band convergence. The obtained high zT in polycrystalline $AgSbTe_2$ materials over a wide temperature range also shows possibility of relieving the necessity of different materials for different temperature regimes with a single material starting from low- to mid-temperatures. This finding makes Pb- free polycrystalline $AgSbTe_2$ a promising candidate for thermoelectric applications in the room- and mid-temperature regimes.

[†]*Manuscript under preparation and submitted to the patent office*

3.1 Introduction

Thermoelectric materials with their ability to convert waste heat into electricity offer a promising solution to the increasing global energy demand. Over the years many materials such as PbTe with high zT have been discovered.[1,2] However, most of the high performance thermoelectric materials are based to toxic elements such as Pb.[1-3] The utmost challenge in the thermoelectric (TE) research is to develop environment-friendly high performance thermoelectric materials, particularly for applications in the low- to mid-temperature regime (300 – 600 K). Recently, a record high zT ~ 2.6 at 923 K has been realized in single crystal SnSe along b axis.[4] However, the difficulty to prepare materials in large scale in their single crystalline form often limit the practical applicability. High performance polycrystalline thermoelectric materials, on the other hand, with their relatively easy and quick synthesis process and scalability are more promising for practical applications. Moreover, high zT over a broad temperature range (ZT_{dev}) is the critical factor rather than zT_{max} as the heat to electrical energy conversion efficiency (η_{TE}) directly depends on ZT_{dev}:[1, 5]

$$\eta_{TE} = \left(\frac{T_h - T_c}{T_h}\right) \frac{\left(\sqrt{1 + (ZT)_{dev}} - 1\right)}{\left(\sqrt{1 + (ZT)_{dev}} + \frac{T_c}{T_h}\right)}$$

Where, T_h and T_c represent the hot and cold end temperature, respectively.

The efficiency of a thermoelectric material depends on the three interdependent parameters – electrical conductivity (σ), Seebeck coefficient (S), and total thermal conductivity (κ) via the following expression $zT = \sigma S^2 T/\kappa$.[1-5] Unfortunately, the strong interdependence among σ, S, and κ_{el} (κ_{el} electronic thermal conductivity) makes it challengingto realize high zT over a broad temperature range.[1,5] Several strategies, such as the enhancement of *S via* valance band convergence and introduction of resonant states near Fermi level[6-8] and/or reduction in κ by introducing point defect, nano-structuring and all-scale hierarchical architecturing[2,9-11] have been developed over the years to improve the thermoelectric performance. The recent advancements in thermoelectrics indicate that materials with intrinsically low thermal conductivity originating from intrinsic factors such as resonant bonding, anharmonic lattice vibration, large molecular weight and

complex crystal structure are the most promising candidate for the realization of high performance thermoelectrics.[12]

The intrinsically glass-like ultralow thermal conductivity (0.6 - 0.7 W/mK) of $AgSbTe_2$ makes it a promising candidate for thermoelectric applications in the mid-temperature range.[13,14] Theoretical studies indicate anharmonic effects in Sb-Te bonds due the presence of stereochemically active $5s^2$ lone pair on Sb might be the possible reason of ultralow thermal conducting behavior of this material[15-17]. Recent inelastic neutron scattering studies on the single crystalline samples, however, attributes the glass-like ultralow thermal conductivity to the phonon scattering from the spontaneously formed nanostructure with cationic ordering.[13] The experimental verification of cationic ordering in polycrystalline $AgSbTe_2$ specimens, however, is still elusive. Moreover, the thermodynamic stability of $AgSbTe_2$ is a long-term issue as it decomposes into binary compounds Ag_2Te and Sb_2Te_3 at a relatively low temperature, 630 K.[14] The formation of *n*-type Ag_2Te (space group *P121/C1*) impurity phase in the $AgSbTe_2$ matrix, which degrades the *p*-type thermoelectric performance of $AgSbTe_2$, is also a recurring challenge.

In this chapter, we demonstrate that M doping in polycrystalline $AgSbTe_2$ gradually dissolves the n-type Ag_2Te impurity phases with increasing M concentration and consequently, the hole concentration and electrical conductivity of the system increases. More importantly, we showed that increasing M doping in the system facilitates the cationic ordering and results in the formation of nanoscale superstructures. The spontaneous formation of these nanoscale superstructures increases phonon scattering and further suppresses the thermal conductivity. The room temperature lattice thermal conductivity decreases from 0.48 W/mK in pristine $AgSbTe_2$ to 0.19 W/mK in $AgSb_{1-x}M_xTe_2$. Consequently, room temperature zT ~0.6 of $AgSbTe_2$ increases to 1.6 in $AgSb_{1-x}M_xTe_2$. The highest obtained zT (zT_{max}) in $AgSb_{1-x}M_xTe_2$ is 2.6 at 573 K which outperforms state-of-the-art *p*-type polycrystalline material in the 300 - 600 K temperature range. Moreover,we obtained highest device ZT (ZT_{dev}) of ~ 2 in the 300-600 K temperature range due to high zT over a wide temperature range.

3.2 Methods

3.2.1 Reagents

Silver (Ag, Aldrich 99.999%), antimony (Sb, Alfa Aesar 99.9999%), M (M, Aldrich 99.5%) and tellurium (Te, Alfa Aesar 99.999+ %) were used for synthesis without further purification. We have submitted this work to the patent office. For this reason, we are not reavealing the details of the dopant (M) in this chapter. We hope examiners will understand the situation.

3.2.2 Synthesis

High quality polycrystalline ingots (~ 10 g) of $AgSb_{1-x}M_xTe_2$ ($x = 0$, x_1, x_2 and x_3; $x_1 > x_2 > x_3$) were synthesized by mixing appropriate ratios of high purity starting materials of Ag, Sb, M and Te in a quartz tube. The tubes were sealed under vacuum (10^{-5} Torr) and slowly heated to 673 K over 12 h, then heated up to 1123 K in 4 h, soaked for 10 h and then slowly cool down to room temperature over a period of 20 h.

3.2.3 Powder X-ray diffraction

Powder X-ray diffraction patterns for finely ground samples were recorded at room-temperature using Cu K_α ($\lambda = 1.5406$ Å) radiation on a Bruker D8 diffractometer.

3.2.4 Differential scanning calorimetry

DSC data were measured by TA instrument (DSC Q2000) with a heating rate of 5 K/min between 290 K and 660 K in N_2 atmosphere.

3.2.5 Electrical transport

Electrical conductivity and Seebeck coefficients were measured simultaneously under He-atmosphere from room-temperature to 623 K using the commercial ULVAC-RIKO ZEM-3 instrument. Rectangular specimens cut and polished from ingots with typical dimensions of ca. 2×2×8 mm^3 were used for the measurements. The longer direction of the sample coincides with the ingot's growth direction.

3.2.6 Hall measurement

Hall measurement of all the samples was carried out in a setup developed by Excel instrument where a variable magnetic field of 0-0.55 T and dc-current of 100 mA were used at room temperature.

3.2.7 Heat capacity measurement

Specific heat capacity at low temperatures (2-30 K) was measured using Physical Property Measurement System (PPMS).

3.2.8 Thermal conductivity

Thermal diffusivity, D, was measured in the 300 – 623 K range by a laser flash diffusivity method in a commercial Netzsch LFA-457 instrument. Coins with 8 mm diameter and 2 mm thickness were used for the measurements. Heat capacity, C_p, in the 300 - 623 K range was indirectly derived using a standard sample (pyroceram) in LFA-457, which is in good agreement with the Dulong-Petit value. The total thermal conductivity, κ_{total}, was calculated using the formula $\kappa_{total} = D \times C_p \times \rho$, where ρ is the density of the sample (~ 97%).

3.2.9 Computational details

This part has been done in collaboration with Prof. Umesh V. Waghmare's group in JNCASR. We use density functional theoretical (DFT) methods using QUANTUM ESPRESSO (QE) code[18] which takes into account only the valence electrons and replaces the potential of the ionic core with a smooth pseudopotential. We used Generalised Gradient Approximation (GGA)[19] to the exchange-correlation energy functional as parametrized by Perdew, Burke, and Ernzerhof (PBE)[20]. To describe the interactions between electrons and ions we use ultra-soft pseudopotentials for both $AgSbTe_2$ and M doped $AgSbTe_2$. $AgSbTe_2$ crystallizes in cubic structure belonging to *Fd-3m* space group. The primitive unit cell of $AgSbTe_2$ contains 16 atoms per unit cell and the conventional one contains 64 atoms per unit cell. Pristine and M substituted $AgSbTe_2$ were simulated using cubic conventional unit cell containing 64 atoms. The electronic wave function and the charge density expansion in terms of plane wave basis set were truncated with cut-off energies of 50 R_y and 400 R_y respectively. The Brillouin Zone (BZ) integrations were sampled on a 6X6X6 uniform mesh of k-points for both pristine and doped $AgSbTe_2$. The

discontinuity in occupation numbers of electronic states was smeared using Fermi-Dirac distribution functions with a broadening of $k_BT = 0.003\ R_y$. We determined the electronic structure and lattice dynamical properties of both the systems using structures obtained after full relaxation at the experimental lattice parameter[4]. Electronic spectrum was determined at Bloch vectors along high symmetry lines (Γ - X - M -Γ - R - X - M - R) in the Brillouin zone.

3.3 Results & Discussion

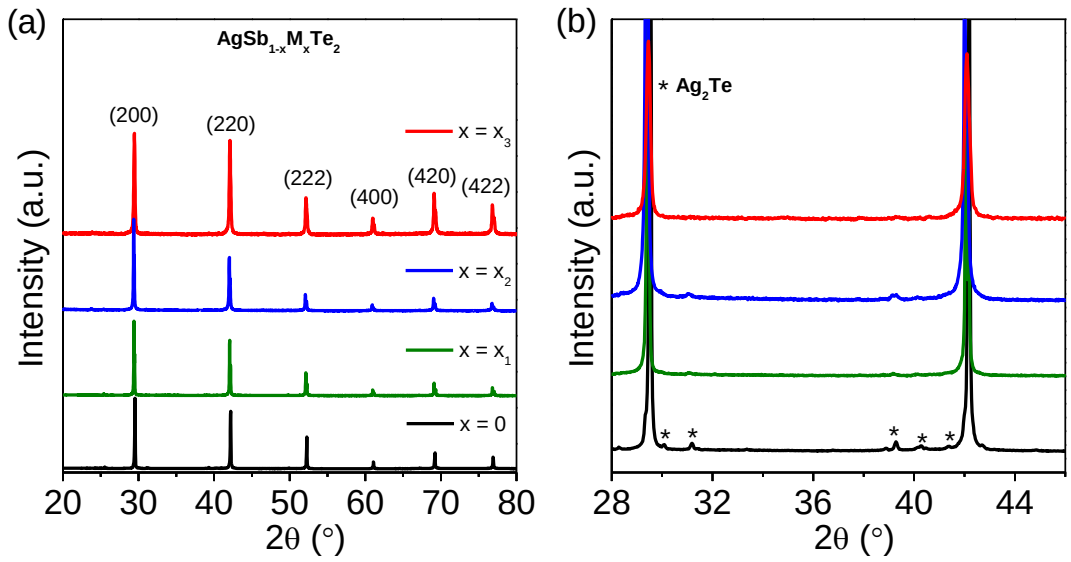

Figure 3.1 *(a) Powder X-ray diffraction pattern and (b) Zoomed version (2θ =28-45 ^{0}) of PXRD pattern of $AgSb_{1-x}M_xTe_2$ (x = 0, x_1, x_2, x_3) samples.*

Powder X-ray diffraction (PXRD) patterns (Figure 3.1a) of the as-synthesized polycrystalline $AgSb_{1-x}M_xTe_2$ samples could be indexed with cubic rocksalt type structure (space group, *Fm-3m*). We observed, similar to the previous reports, the presence of diffraction peaks corresponding to the Ag_2Te impurity phase in the pristine $AgSbTe_2$.[13,14] With increasing dopant concentration in the system, however, the impurity peaks gradually disappear confirming the positive role of dopant in blocking the Ag_2Te phase formation (Figure 3.1b). The suppression of the formation of Ag_2Te impurity phase is

further confirmed by DSC analysis (Figure 3.2). Endothermic peak at 425 K corresponding to the structural transition of α-Ag_2Te to β-Ag_2Te disappears completely for higher dopant concentration.

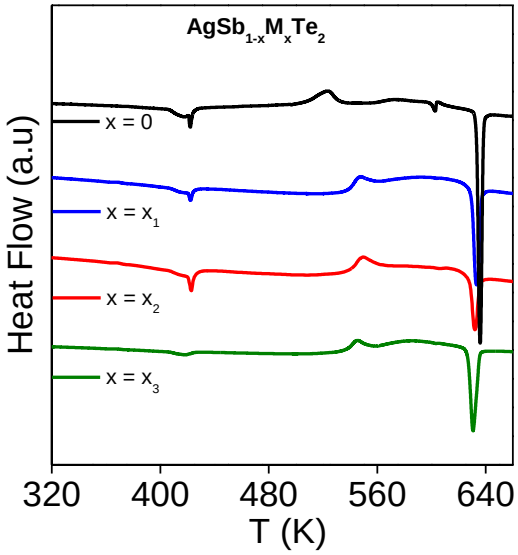

Figure 3.2 *DSC curves for $AgSb_{1-x}M_xTe_2$ (x = 0, x_1, x_2, x_3) samples.*

M substitution in $AgSbTe_2$ significantly enhances the thermoelectric figure of merit, zT, throughout the measured temperature range (300 - 600 K). At 300 K, zT increases from 0.6 for $AgSbTe_2$ to 1.6 at 300 K for doped $AgSbTe_2$ and further increases to 2.6 at 573 K (Figure 3.3a). The reproducibility of such high thermoelectric performance is confirmed by repeating the entire experiments for six times and Figure 3.3b presents the measured data taken from six different batches. Importantly, doped $AgSbTe_2$ outperforms all other state-of-the-art *p*-type (both polycrystalline and single crystalline) thermoelectric materials (Figure 3.3c). [2,4,9,21-27] The high zT throughout the measured temperature range (300 - 600 K) in doped $AgSbTe_2$ results in record high ZT_{dev} of ~ 2 (Figure 3.3d).[2,14,22,25-28] As a result of high zT over a wide temperature range, doped $AgSbTe_2$ exhibit a calculated efficiency of ~ 18.7% by considering hot and cold temperature 300 K and 600 K, respectively.

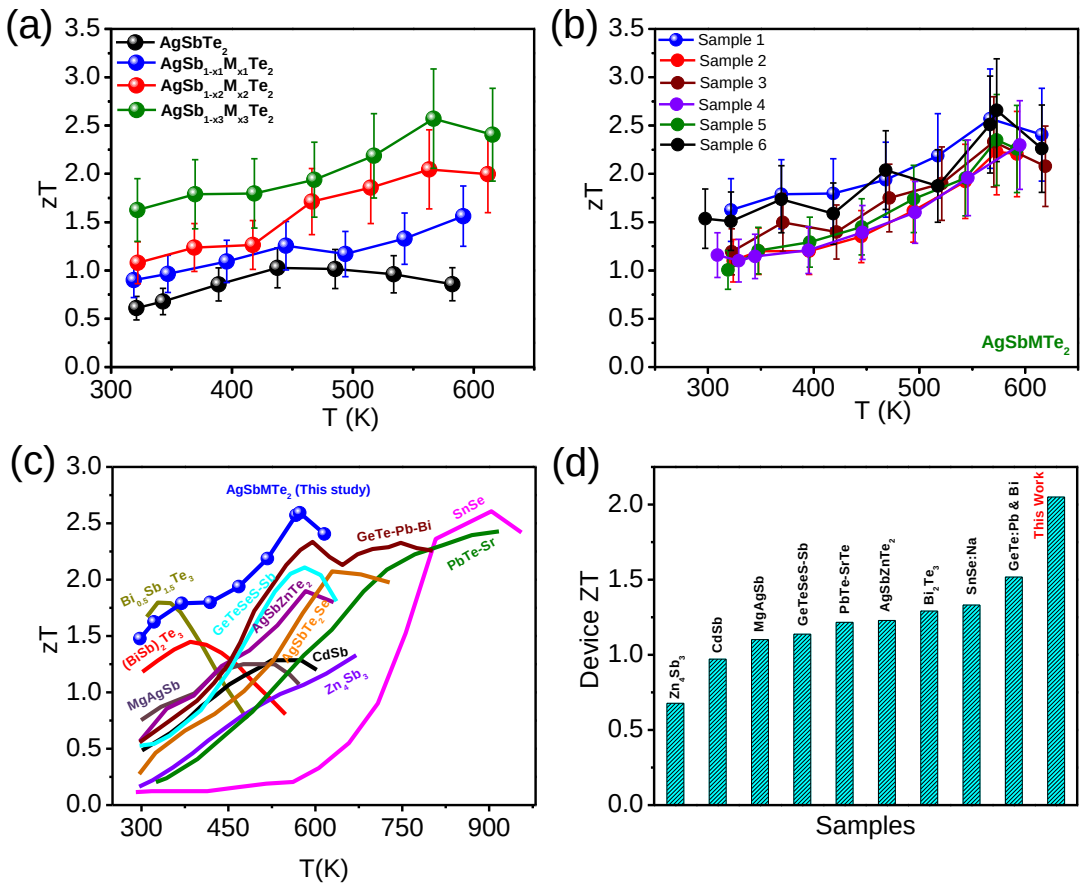

Figure 3.3 *(a) Temperature dependent thermoelectric figure of merit (zT) of* $AgSb_{1-x}M_xTe_2$ *(x = 0, x1, x2, x3) samples. (b) Reproducibility of thermoelectric figure of merit (zT) for* $AgSbMTe_2$ *sample. For zT measurement, we consider 20 % error bar, which include error in electrical conductivity, Seebeck coefficient and thermal conductivity measurement. (c) The best zT obtained in this study compared with some of the state-of-the-art thermoelectric materials. p-type doped* $AgSbTe_2$ *shows a highest zT in the lower-medium temperature range.*[2,4,9,21-27] *(d) Device ZT (*ZT_{dev}*) for several popular thermoelectric materials compared with the present* $AgSbMTe_2$ *sample.*[2,14,22,25-28]

We obtained record high thermoelectric performance in doped $AgSbTe_2$ sample, arising from advantageous effect of dopant on both electronic and phonon structure of $AgSbTe_2$. The temperature variation of electrical conductivity σ of polycrystalline $AgSb_{1-x}M_xTe_2$ is shown in Figure 3.4a. The aliovalent substitution in $AgSbTe_2$ increases the room temperature hole concentration in the system from 1.1 X 10^{19} cm^{-3} for pristine $AgSbTe_2$ to 5 X 10^{19} cm^{-3} for doped $AgSbTe_2$ (Table 3.1). Furthermore, the formation of *n*-type Ag_2Te impurity phase also decreases with increasing the dopant concentration. As

a result, the room temperature electrical conductivity σ increases from ~ 136 S/cm for pristine $AgSbTe_2$ to ~ 230 S/cm for doped $AgSbTe_2$.

Table 3.1: Carrier concentration (n), carrier mobility (μ) and effective mass (m*) of $AgSb_{1-x}M_xTe_2$ (x = 0, x_1, x_2 and x_3) samples at room temperature.

Sample	*n* (cm^{-3})	*μ* ($cm^2V^{-1}s^{-1}$)	*m**
$AgSbTe_2$	1.14 X 10^{19}	75	1.32 m_0
$AgSb_{1-x1}M_{x1}Te_2$	1.83 X 10^{19}	55	1.42 m_0
$AgSb_{1-x2}M_{x2}Te_2$	4.44 X 10^{19}	26	2.65 m_0
$AgSb_{1-x3}M_{x3}Te_2$	5.00 X 10^{19}	27	2.90 m_0

Temperature dependence of Seebeck coefficient (*S*) of $AgSb_{1-x}M_xTe_2$ samples are presented in Figure 3.4b. Positive Seebeck coefficient value indicates the *p*-type electronic conduction, which is also consistent with the Hall coefficient data. The Seebeck coefficient of pristine $AgSbTe_2$ is 264 μV/K at 300 K which further increases to 360 μV/K at 430 K. The origin of this large Seebeck coefficient in $AgSbTe_2$ is the presence of flat and multi-valley valence band near the Fermi level. The M doping gradually increases the hole concentration in the system and as a result, room temperature Seebeck coefficient decreases from 264 μV/K for pristine $AgSbTe_2$ to ~ 248 μV/K for doped $AgSbTe_2$.

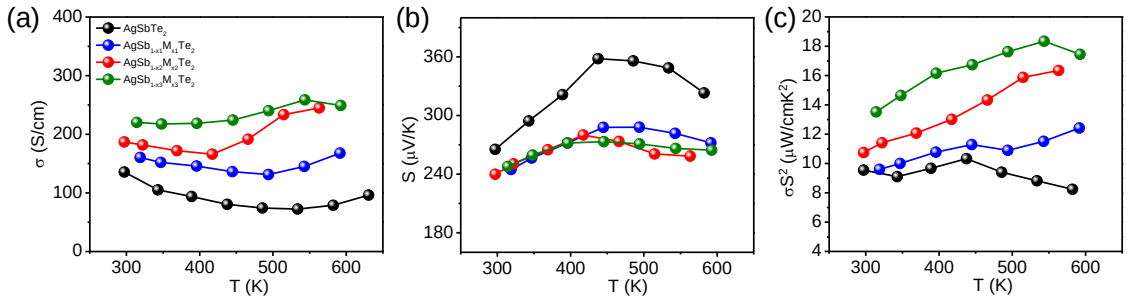

Figure 3.4 *Temperature dependent (a) electrical conductivity (σ), (b) Seebeck coefficient (S), and (c) power factor (σS^2) for $AgSb_{1-x}M_xTe_2$ (x = 0, x_1, x_2, x_3) samples.*

Although the hole carrier concentration increases with increasing dopant concentration, $AgSb_{1-x}M_xTe_2$ samples exhibit comparatively large Seebeck coefficient compared to other state of art materials which can be attributed to the high density of state effective mass of the doped samples (Table 3.1). The calculated values of m* for $AgSbTe_2$ and doped $AgSbTe_2$ samples are $1.32m_0$, and $2.90m_0$, respectively (Table 3.1). Typically, doped $AgSbTe_2$ sample shows Seebeck coefficient of ~ 248 μV/K at room temperature which increases to 267 μV/K at 592 K.The increase in m* value along with the increase in carrier concentration can be attributed to the increasing accessibility to the multiple flat valence band valleys of $AgSbTe_2$ with increasing the dopant concentration.

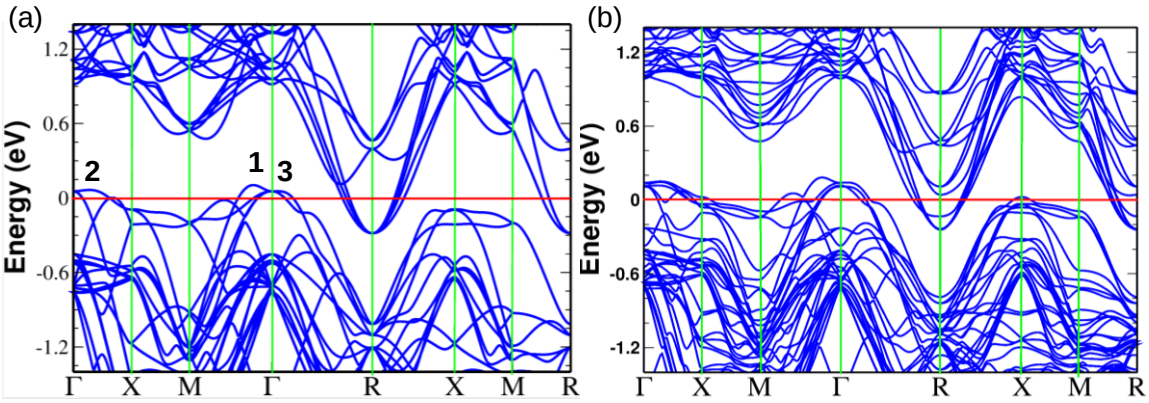

Figure 3.5 *Electronic structure of (a) $AgSbTe_2$ and (b) M doped $AgSbTe_2$.*

To obtain insight into the enhanced performance, we investigated the electronic structure of both $AgSbTe_2$ and M doped $AgSbTe_2$ *via* first principles density functional theory. Figure 3.5 represents the electronic structure of pristine $AgSbTe_2$ and reveals its semimetallic nature which is consistent with the previous reported band structure.[15-17,21] DFT confirms the presence of multi valence band near Fermi level for pristine $AgSbTe_2$ (Figure 3.5a). Primary valence band maximum locates in the M-Γ direction, labeled as VB_1 and other two valence band lie in Γ-X (VB_2) and Γ-R (VB_3) direction, respectively. The calculation shows very small energy gaps between the three valence bands (Table 3.2). Moreover, careful analysis reveals that top of the VB_1 is sharp with effective mass (m*) of 0.33 m_0 (m_0 is the mass of a free electron), while tops of both VB_2 and VB_3 are more flat with m* 2.91 m_0 and 3.22 m_0, respectively. Thus accessing the second and third valence will enhance the Seebeck coefficient instead of the increment in the carrier

concentration for M doped $AgSbTe_2$ samples. Interestingly, such small energy band gap between three valence bands is easily crossed by the Fermi level as the hole doping approaches (~4 to 5) $\times$ 10^{19} cm^{-3}. Whereas in case of PbTe and SnTe, the gap between two valence band is larger compared to the present case.[2,8] Mention must be made that electronic structure of $AgSbTe_2$ is much more complex compared to PbTe and SnTe which help to achieve high Seebeck coefficient in $AgSbTe_2$ compared to other rocksalt chalcogenides.[2,8] Pristine $AgSbTe_2$ is semimetallic with a pseudogap of -0.29 eV where as the gap increases to -0.24 eV and the energy gap between three valence bands also decreases for doped $AgSbTe_2$ sample, indicating the possibility of valence band convergence (Table 3.2). Such band convergence improves the Seebeck coefficient because of the contribution of three bands and asymmetric increase in the density of states near the Fermi energy. Similar electronic structure modifications have been observed in PbTe and SnTe samples.

Table 3.2: The energy separation between the three valence bands for $AgSbTe_2$ and M doped $AgSbTe_2$. M doping in $AgSbTe_2$ leads to valence band convergence.

UNDOPED $AgSbTe_2$ (meV)	**DOPED $AgSbTe_2$ (meV)**	**ΔE (meV)**
38	31	E_{v1}-E_{v2}
12.4	10.7	E_{v2}-E_{v3}
50	41	E_{v1}-E_{v3}

The high electrical conductivity and high Seebeck coefficient results in high power factor in the $AgSb_{1-x}M_xTe_2$ samples thorough out the measured temperature range (300 - 623 K) (Figure 3.4c). Power factor value of doped $AgSbTe_2$ sample (13.46 $\mu Wcm^{-1}K^{-2}$ at 312 K and 17.50 $\mu Wcm^{-1}K^{-2}$ at 594 K) is significantly high compared to that of pristine $AgSbTe_2$ (9.5 $\mu Wcm^{-1}K^{-2}$ at 300 K and 8.35 $\mu Wcm^{-1}K^{-2}$ at 582 K).

The temperature variation of total thermal conductivity, κ_{total}, of $AgSb_{1-x}M_xTe_2$ is shownin Figure 3.6b. The room temperature κ_{total} of pristine $AgSbTe_2$ is 0.6 W/mK and increases with temperature above 450 K because of the bipolar electrical conduction which is consistent with the electrical transport measurements. After doping, κ_{total} of

$AgSbTe_2$ further decreases. The room temperature κ_{total} of doped $AgSbTe_2$ sample is 0.25 W/mK and increases to 0.52 W/mK at 621 K. κ_{latt} also decreases with increasing the dopant concentration (Figure 3.6d). Doped $AgSbTe_2$ sample exhibits ultra-low κ_{latt} of ~ 0.19 W/mK at room temperature. Such low thermal conductivity value is close to the lattice thermal conductivity of single crystalline SnSe and lowers than other state-of-the-art chalcogenide-based materials.[1,4,5]

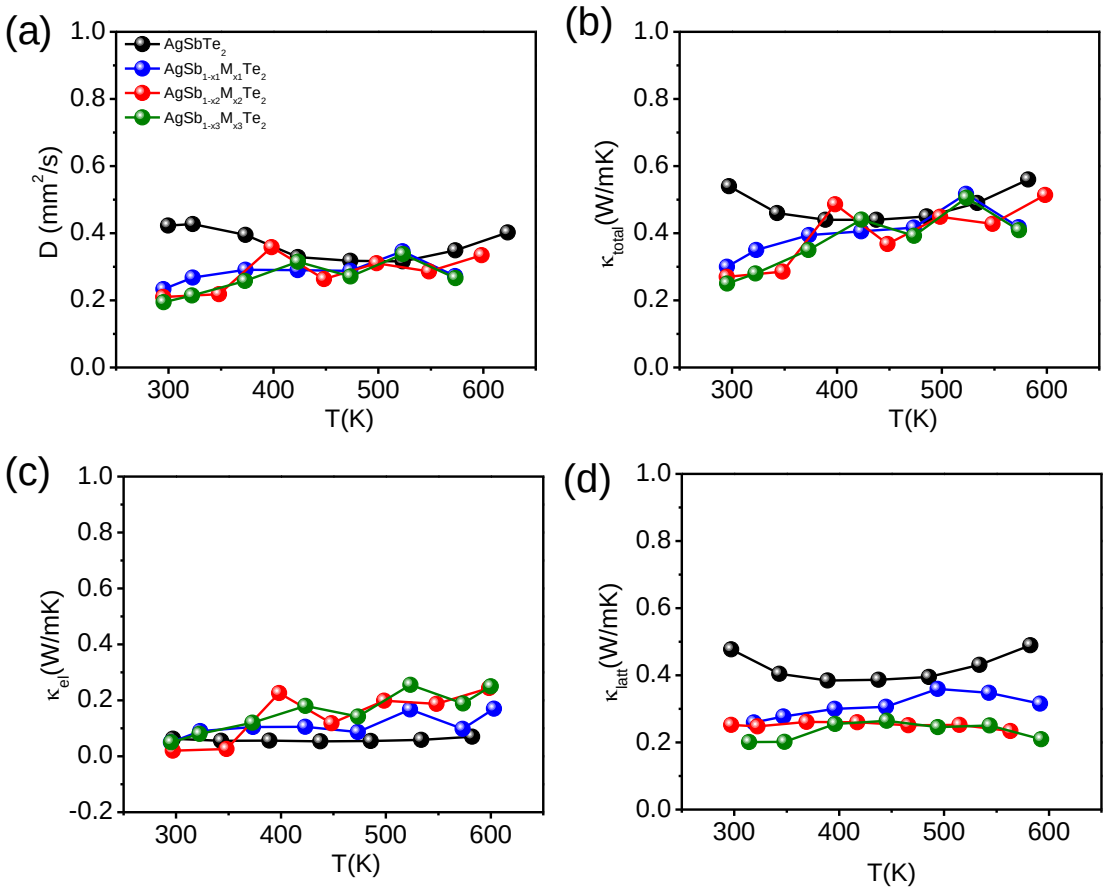

Figure 3.6 *Temperature dependent (a) diffusivity (D), (b) total thermal conductivity (κ_{total}), (c) electrical thermal conductivity (κ_{el}) and (d) lattice thermal conductivity (κ_{latt}) for $AgSb_{1-x}M_xTe_2$ (x = 0, x_1, x_2, x_3) samples.*

We have measured C_p (specific heat capacity) of doped $AgSbTe_2$ sample in the temperature range of 2 -30 K (Figure 3.7) to understand the origin of ultra-low κ_{lat} in polycrystalline doped $AgSbTe_2$ and fitted the experimental data by using Debye-Einstein model.[29]

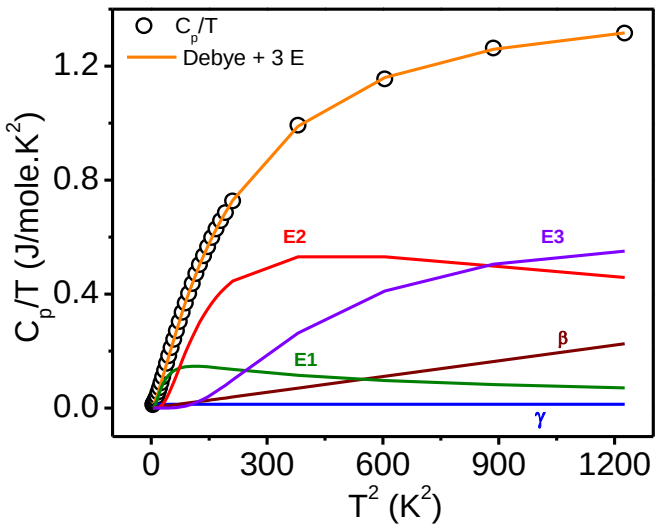

Figure 3.7 *C_p/T vs T^2 plot in 2 – 30 K range. The solid line is calculated using the combined Debye-Einstein model. The individual contributions from electronic (γ), Debye (β) and the three Einstein terms (E1, E2, E3) are also plotted.*

$$\frac{C_p}{T} = \gamma + \beta T^2 + \sum_n \left(A_n (\Theta_{E_n})^2 . \ (T^2)^{-3/2} \ . \ \frac{e^{\Theta_{E_n}/T}}{\left(e^{\Theta_{E_n}/T} - 1\right)^2} \right) \tag{3.1}$$

Where, γ and βT^2 represent electronic contribution and Debye mode contribution, respectively. β is given as $\beta = C\left(\frac{12\pi^4 N_A k_B}{5}\right).(\theta_D^{-3})$ (where, N_A, κ_B and θ_D are the Avogadro number, Boltzmann constant and Debye temperature, respectively). Here, C is presented as $C = 1 - \sum_n A_n/(3NR)$, where N and R are the number of atoms per formula unit and the gas constant, respectively. The last term in the above equation offers the contribution of Einstein modes and A_n is the pre-factor of the n^{th} mode. We find that the temperature variation of C_p in the low temperature regime cannot be adequately described only with Debye modes of acoustic phonons and requires at least three Einstein modes whose typical temperatures are obtained from the fits are 27 K (θ_{E1} ~ 18.8 cm^{-1}), 56 K (θ_{E2} ~ 38.9 cm^{-1}) and 105 K (θ_{E3} ~ 72.98 cm^{-1}) (Table 3.3). These low-frequency Einstein modes arise because of the soft vibrations of Ag and/or Sb cations in doped $AgSbTe_2$. These low-frequency optical phonons strongly couple with the heat-carrying acoustic phonons and suppress the lattice thermal conductivity of doped $AgSbTe_2$.

Table 3.3: Parameters obtained by fitting low-temperature heat capacity to the Debye–Einstein model.

Parameters	Debye-Einstein Model
γ /10 $^{-3}$ J mol $^{-1}$ K $^{-2}$	12.97
β /10^{-4} J mol $^{-1}$ K $^{-2}$	1.841
ΘE_1 (K)	27.76
ΘE_2 (K)	56.06
ΘE_3 (K)	105.71
Debye temperature, Θ_D (K)	160
R^2	0.99998

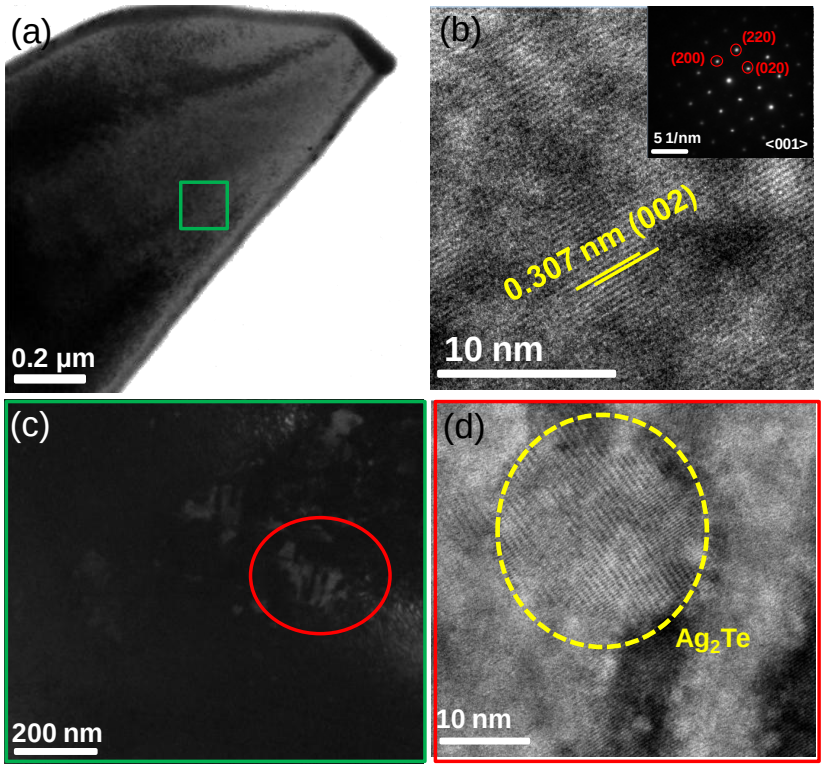

Figure 3.8 *(a) Low magnification TEM image of $AgSbTe_2$, (b) HRTEM of the highlighted area of (a). (c) Dark field image of the highlighted area in (a), showing the presence of Ag_2Te nanoprecipitates. (d) HRTEMof the highlighted area of (c), showing presence of small Ag_2Te precipitate with corresponding lattice spacing.*

Transmission electron microscopy (TEM) investigations of $AgSbTe_2$ and doped $AgSbTe_2$ samples were performed to further understand the microscopic origin and the

role of dopant in lowering the lattice thermal conductivity (Figure 3.8 and 3.9). High-resolution TEM (HRTEM) image shows the distance between two lattice fringes is 0.307 nm, corresponding to the (002) plane of cubic $AgSbTe_2$ (Figure 3.8b). Selected area electron diffraction (SAED) pattern confirms the single crystalline nature of the domains without the presence of any superstructure spots similar to the previous reports of polycrystalline $AgSbTe_2$ (inset of Figure 3.8b).[21] Dark-field TEM shows the presence of impurity phases in $AgSbTe_2$ matrix which was confirmed as α-Ag_2Te phase by HRTEM analysis. (Figure 3.8c and d) Interestingly, the SAED pattern of polycrystalline doped $AgSbTe_2$, however, shows superstructure spots (Figure 3.9 a and b). The presence of this superstructure spots confirms the cationic ordering in the nanoscale region. The presence of these nanoscale superstructures further increases the phonon scattering and reduces the lattice thermal conductivity in doped $AgSbTe_2$.

Figure 3.9a and b show the superlattice reflections of doped $AgSbTe_2$ sample which is present in the half way between all-even diffraction spots of the parent rocksalt structure along <001> direction. Different areas on the doped sample were analyzed and the electron diffraction patterns exhibited similar features. The superlattice reflections along the (001) zone axis corresponds to a cubic unit cell with lattice parameter of ~ 12.40 Å which implies doubling of the lattice parameter of pristine $AgSbTe_2$ (Figure 3.9c). HRTEM analysis further confirms the presence of few domains with spacing of 6.20 Å. Fast Fourier transformations (FFT) of these domains yield a doubling of cubic unit cell parameter of 12.40 Å (Figure 3.9c). Neighboring domains, however, show a spacing 3.1 Å which corresponds to the parent $AgSbTe_2$ structure.

The supercell originates from the breaking of symmetry from *Fm-3m* to *Pm-3m*. The number of crystallographic sites in the unit cell doubles when symmetry goes down to *Pm-3m* from *Fm-3m*. This is identical to ordered AF-I structure of $AgSbTe_2$ with alternating Ag-Te and Sb-Te crystallographic planes along to [100] direction. First principles calculations reveal that AF-I structure is energetically unfavorable compared to the competing AF-IIb structure, however, the energy penalty is relatively small (75 meV/formula unit). M doping facilitates the formation ofthe ordered AF-I structure due to the presence of strain in the $AgSbTe_2$ matrix system along <200> direction.

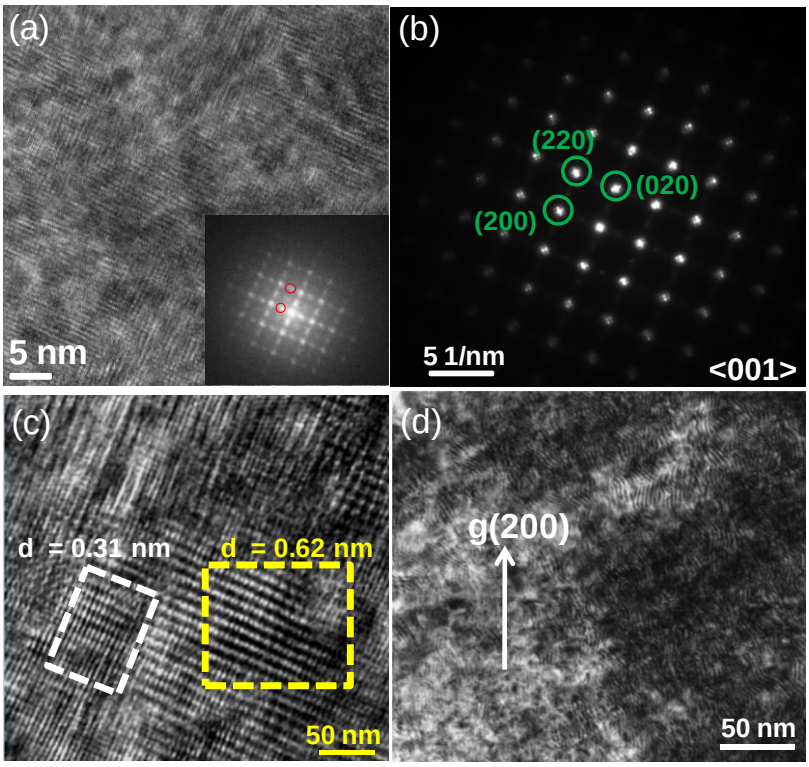

Figure 3.9 *(a) High-resolution TEM (HRTEM) image of doped $AgSbTe_2$ with fast Fourier transforms (FFT). Red circles indicate superstructure ordering spots at ½(h,k,l) with h,k,l even .(b) Electron diffraction pattern indexed to the cubic rocksalt parent structure with superstructure ordering spots. (c) HRTEM analysis confirms the presence of few domains with spacing of 0.62 nm. Fast Fourier transformations (FFT) of these domains yield a doubling of cubic unit cell parameter of 1.24 nm. Neighboring domains, however, show a spacing 0.31 nm which corresponds to the parent $AgSbTe_2$ structure (cell parameter 0.62 nm). (d) Two-beam (200) dark-field diffraction contrast showing oscillating strains.*

An oscillating contrast associated with the lattice strain is clearly evidentin Figure 3.9d, forming light and dark ripples with a period of 3.4 nm. This is consistent with chemical ordering of the cationic sublattice along (100) planes which reduces the symmetry from *Fm-3m* to *Pm-3m*. Moreover, The HRTEM image demonstrates a layering in the lattice, which is associated with the superlattice ordering similar tosingle crystalline $AgSbTe_2$ sample.[13] In $AgSbTe_2$, both Ag and Sb have octahedral coordination but the charge (Ag^+ and Sb^{3+}) and size (Ag^+ - 115 pm; Sb^{3+} - 76 pm) differences between them make their chemical ordering energetically unfavorable. Whereas, the charge and

size of M falls in between that of the Ag and Sb, lower the formation energy of the chemically ordered structure.

3.4 Conclusions

In summary, polycrystalline $AgSbTe_2$ samples demonstrate record high thermoelectric performance in the temperature range of 300-600 K. We observe a significant increase in room temperature zT from 0.6 for pristine $AgSbTe_2$ to 1.6 at 300 K for doped $AgSbTe_2$ and a maximum zT of 2.6 at 573 K in polycrystalline $AgSbTe_2$. High zT over a wide temperature range also resulted in a high ZT_{dev} of ~ 2 for the 300 - 600 K temperature regimes which is the highest value so far in thermoelectric materials. $AgSbTe_2$ outperforms all other state-of-the-art *p*-type polycrystalline and single crystalline thermoelectric materials in the temperature range of 300 - 600 K. This high thermoelectric performance originates from the doping as a result of increased electrical conductivity, the suppression of *n*-type Ag_2Te phase and decreased thermal conductivity due to the spontaneous formation of nanoscale superstructure with cationic ordering which causes enhance phonon scattering. The best thermoelectric material for room-temperature applications are Bi_2Te_3 based materials with zT of ~ 1.2 at 300 K whereas for mid-temperature applications, germanium chalcogenide and lead chalcogenide based materials are the best performer.[1,5,9,22] Interestingly, $AgSbTe_2$ samples cover both the region and shows possibility of relieving the necessity of different materials for different temperature regimes with a single material starting from room- to mid-temperature. This work promotes Pb-free polycrystalline $AgSbTe_2$ as a prime material for thermoelectric applications over a wide temperature range in the low- and mid-temperature regimes.

3.5 References

[1] J. Sootsman, D. Y. Chung, M. G. Kanatzidis, *Angew. Chem. Int. Ed.* **2009**, *48*, 8616.

[2] K. Biswas, J. He, I. D. Blum, C.-I. Wu, T. P. Hogan, D. N. Seidman, V. P. Dravid, M. G. Kanatzidis, *Nature* **2012**, *489*, 414.

[3] L. D. Zhao, V. P. Dravid, M. G. Kanatzidis, *Energy Environ. Sci.* **2014**, *7*, 251.

[4] L. -D. Zhao, S. -H. Lo, Y. Zhang, H. Sun, G. Tan, C. Uher, C. Wolverton, V. P. Dravid, M. G. Kanatzidis, Nature **2014**, *508*, 373.

[5] G. Tan, L. D. Zhao, M. G. Kanatzidis, *Chem. Rev.* **2016**, *116*, 12123.

[6] Y. Pei, X. Shi, A. LaLonde, H. Wang, L. Chen, G. J. Snyder, *Nature* **2011**, *473*, 66.

[7] J. P. Heremans, V. Jovovic, E. S.Toberer, A. Saramat, K. Kurosaki, A. Charoenphakdee, S. Yamanaka, G. J. Snyder, *Science* **2008**, *321*, 554.

[8] A. Banik, U. S. Shenoy, S. Saha, U. V. Waghmare, K. Biswas, *J. Am. Chem. Soc.* **2016**, *138*, 13068.

[9] B. Poudel, Q. Hao, Y. Ma, Y. Lan, A. Minnich, B. Yu, X. Yan, D. Wang, A. Muto, D. Vashaee, X. Chen, J. Liu, M. S. Dresselhaus, G. Chen, Z. Ren, *Science* **2008**, *320*, 634.

[10] L. D. Zhao, S. Hao, S. H. Lo, C. I. Wu, X. Zhou, Y. Lee, H. Li, K. Biswas, T. P. Hogan, C. Uher, C. Wolverton, V. P. Dravid, M. G. Kanatzidis, *J. Am. Chem. Soc*. **2013**, *135*, 7364.

[11] A. Banik, B. Vishal, S. Perumal, R. Datta, K. Biswas, *Energy Environ. Sci*. **2016**, *9*, 2011.

[12] M. K. Jana, K. Biswas, *ACS Energy Lett*. **2018**, *3*, 1315.

[13] J. Ma, O. Delaire, A. F. May, C. E. Carlton, M. A. McGuire, L. H. Van Bebber, D. L. Abernathy, G. Ehlers, T. Hong, A. Huq, et al. *Nat. Nanotech.* **2013**, *8*, 445.

[14] S. Roychowdhury, R.Panigrahi, S. Perumal, K. Biswas ACS Energy Lett. 2017, 2, 349.

[15] M. D. Nielsen, V. Ozolins, J. -P. Heremans, *Energy Environ. Sci. 2013*, *6*, 570.

[16] K. Hoang, S. D. Mahanti, J. R. Salvador, M. G. Kanatzidis, *Phys. Rev. Lett.* **2007**, *99*, 156403.

[17] D. T. Morelli, V. Jovovic, J. P. Heremans, *Phys. Rev. Lett.* **2008**, *101*, 035901.

[18] P. Giannozzi, S. Baroni, N. Bonini, M. Calandra, R. Car, C. Cavazzoni, D. Ceresoli, G. L. Chiarotti, M. Cococcioni, I. Dabo, A. L. Corso, S. de Gironkoli, S. Fabris, G. Fratesi, R. Gebauer, U. Gerstmann, C. Gougoussis, A. Kokalj, M. Lazzeri, L. Martin-Samos, N. Marzari, F. Mauri, R. Mazzarello, S. Paolini, A. Pasquarello, L. Paulatto, C. Sbraccia, S. Scandolo, G. Sclauzero, A. P. Seitsonen, A. Smogunov, P. Umari, R. M. Wentzcovitch, *J. Phys. Condens. Matter*. **2009**, *21*, 395502.

[19] X. Hua, X. Chen, W. A. Goddard III, *Phys. Rev. B* **1997**, *55*, 16103.

[20] P. Perdew, K. Burke, M. Ernzerhof, *Phys. Rev. Lett*. **1996**, *77*, 3865.
[21] M. Hong, Z. -G. Chen, L. Yang, Z. -M. Liao, Y. -C. Zou, Y. -H. Chen, S. Matsumura, J. Zou, *Adv. Energy Mater*. **2017**, *8*, 1702333.
[22] M. Samanta, K. Biswas, *J. Am. Chem. Soc*. **2017**, *139*, 9382.
[23] S. Kim, K. H. Lee, H. A. Mun, H. S. Kim, S. W. Hwang, J. W. Roh, D. J. Yang, W. H. Shin, X. S. Li, Y. H. Lee, *et al. Science* **2015**, *348*, 109.
[24] J. Shuai, H. S. Kim, Y. C. Lan, S. Chen, Y. Liu, H. Z. Zhao, J. H. Sui, Z. F. Ren, *Nano Energy* **2015**, *11*, 640.
[25] S. Wang, J. Yang, L. Wu, P. Wei, J. Yang, W. Zhang, Y. Grin, *Chem. Mater*. **2015**, *27*, 1071.
[26] G. J. Snyder, M. Christensen, E. Nishibori, T. Caillat, B. B. Iversen, *Nat. Mater*. **2004**, *3*, 458.
[27] J. Li, X. Zhang, Z. Chen, S. Lin, W. Li, J. Shen, IT Witting, A. Faghaninia, Y. Chen, A. Jain, L. Chen, G. J. Snyder, Y. Pei, *Joule* **2018**, *2*, 976.
[28] L.-D. Zhao, G. Tan, S. Hao, J. He, Y. Pei, H. Chi, H. Wang, S. Gong, H. Xu, V. P. Dravid, C. Uher,G. J. Snyder, C. Wolverton, M. G. Kanatzidis, *Science* **2016**, *351*, 141.
[29] M. K. Jana, K. Pal, A. Warankar, P. Mandal, U. V. Waghmare, K. Biswas, *J. Am. Chem. Soc.* **2017**, *139*, 4350.

List of Publications

- Included in thesis

1. **S. Roychowdhury,** M. Samanta, A. Banik, K. Biswas, "Thermoelectric energy conversion and topological materials based on heavy metal chalcogenides", *J. Solid State Chem.*, **2019**, *275*, 103. (Review article)
2. **S. Roychowdhury**, M. Dutta, K. Biswas, "Enhanced thermoelectric performance in topological crystalline insulator *n*-type $Pb_{0.60}Sn_{0.40}Te$ by simultaneous tuning of the band gap and chemical potential", *J. Mater. Chem. A*, **2018**, *6*, 24216.
3. **S. Roychowdhury**, T. Ghosh, R. Arora, U. V. Waghmare, K. Biswas, "Stabilizing n-type cubic GeSe by entropy driven alloying of $AgBiSe_2$: Ultralow thermal conductivity and promising thermoelectric performance", *Angew. Chem. Int. Ed.*, **2018**, *57*, 15167.
4. **S. Roychowdhury**, M. K. Jana, J. Pan, S. N. Guin, D. Sanyal, U. V. Waghmare, K. Biswas, "Soft phonon modes leading to ultralow thermal conductivity and high thermoelectric performance in AgCuTe", *Angew. Chem. Int. Ed.*, **2018**, *57*, 4043.
5. **S. Roychowdhury**, M. Samanta, S. Perumal, K. Biswas, "Germanium Chalcogenide Thermoelectrics: Electronic Structure Modulation and Low Lattice Thermal Conductivity", *Chem. Mater.*, **2018**, *30*, 5799. (Perspective article)
6. **S. Roychowdhury**, R. Panigrahi, S. Perumal, K. Biswas, "Ultrahigh Thermoelectric Figure of Merit and Enhanced Mechanical Stability of *p*-type $AgSb_{1-x}Zn_xTe_2$", *ACS Energy Lett.*, **2017**, *2*, 349.
7. **S. Roychowdhury**, U. S. Shenoy, U. V. Waghmare, K. Biswas, "An Enhanced Seebeck coefficient and high thermoelectric performance in *p*-type In and Mg co-doped $Sn_{1-x}Pb_xTe$ *via* co-adjuvant effect of resonance level and heavy hole valence band", *J. Mater. Chem. C*, **2017**, *5*, 5737.
8. **S. Roychowdhury**, U. S. Shenoy, U. V. Waghmare, K. Biswas, "Effect of potassium doping on electronic structure and thermoelectric properties of topological crystalline insulator", *Appl. Phys. Lett.*, **2016**, *108*, 193901.
9. **S. Roychowdhury**, S. Ghara, S. N. Guin, A. Sundaresan, K. Biswas, "Large linear magnetoresistance in topological crystalline insulator $Pb_{0.6}Sn_{0.4}Te$", *J. Solid State Chem.*, **2016**, *233*, 199.
10. S. Perumal,[#] **S. Roychowdhury**,[#] K. Biswas, "High performance thermoelectric materials and devices based on GeTe", *J. Mater. Chem. C*, **2016**, *4*, 7520. ([#] Equal authorship) (Review article)
11. S. Perumal,[#] **S. Roychowdhury**,[#] K. Biswas, "Reduction of thermal conductivity through nanostructuring enhances the thermoelectric figure of merit in $Ge_{1-x}Bi_xTe$", *Inorg. Chem. Front.*, **2016**, *3*, 125. ([#] Equal authorship)

12. **S. Roychowdhury**, U. S. Shenoy, U. V. Waghmare, K. Biswas, "Tailoring of electronic structure and thermoelectric properties of topological crystalline insulator by chemical doping", *Angew. Chem. Int. Ed.*, **2015**, *54*, 15241.
13. S. Perumal, **S. Roychowdhury**, D. S. Negi, R. Datta, K. Biswas, "High Thermoelectric Performance and Enhanced Mechanical Stability of *p*-type $Ge_{1-x}Sb_xTe$", *Chem. Mater.*, **2015**, *27*, 7171.

- Not included in thesis

14. **S. Roychowdhury**, K. Biswas, "Slight Symmetry Reduction in Thermoelectrics", *Chem*, **2018**, *4*, 939. (Preview)
15. A. Banik, **S. Roychowdhury**, K. Biswas, "The journey of tin chalcogenides towards high- performance thermoelectrics and topological materials", *Chem. Comm.*, **2018**, *54*, 6573. (Feature article)
16. M. Samanta, **S. Roychowdhury**, J. Ghatak, S. Perumal, K. Biswas, "Ultrahigh Average Thermoelectric Figure of Merit, Low Lattice Thermal Conductivity and Enhanced Microhardness in Nanostructured $(GeTe)_x(AgSbSe_2)_{100-x}$", *Chem. Eur. J.*, **2017**, *23*, 7438.
17. S. Das, L. Aggarwal, **S. Roychowdhury**, M. Aslam, S. Gayen, K. Biswas, G. Sheet, "Unexpected superconductivity at nanoscale junctions made on the topological crystalline insulator $Pb_{0.60}Sn_{0.40}Te$", *Appl. Phys. Lett*. **2016**, *13*, 132601.

Book Chapter

1. A. Dan, B. Basu, **S. Roychowdhury**, K. Biswas, B. Raj, "Nanotechnology and energy conversion: A solution using spectrally selective solar absorbers and thermoelectrics" in the book "Nanoscience and Nanotechnology: Advances and Developments in Nano-sized Materials", Ed. M. V. de Voorde, Walter de Gruyter GmbH & Co KG, **2018**.

BIOGRAPHY

Subhajit Roychowdhury received his B.Sc. (2012) degree from the University of Burdwan and M.Sc. (2014) degree in Chemistry from the Indian Institute of Technology (IIT), Kharagpur, West Bengal, India. He is currently pursuing his PhD under the supervision of Prof. Kanishka Biswas at the New Chemistry Unit, Jawaharlal Nehru Centre for Advanced Scientific Research (JNCASR), Bangalore, India. His research work focuses on topological materials and the thermoelectric properties of heavy metal chalcogenides. He is a recipient of the best-poster award at the "Annual In-House Symposium (2017), JNCASR, India" and "IUMRS-ICYRAM Singapore (2016), Bangalore, India". He is also a recipient of "Graduate student silver award", Materials Research Society (MRS), 2019. He has been selected for oral presentation in "2019 MRS Spring Meeting and Exhibits" Phoenix, Arizona, USA, April, 2019 and "Gordon Research Seminar", New London, USA, July, 2018.